Unleashing Reactivity by Silylation in Lewis Acid Organocatalysis

Inaugural-Dissertation

zur

Erlangung des Doktorgrades

der Mathematisch-Naturwissenschaftlichen Fakultät

der Universität zu Köln

vorgelegt von

Benjamin Mitschke

aus Jena

Köln 2024

Berichterstatter:	Prof. Dr. Dr. h.c. Dr. h.c. Benjamin List
	Prof. Dr. Hans-Günther Schmalz
	Prof. Dr. Shu Kobayashi
Tag der mündlichen Prüfung:	03.09.2024

Dedicated to the memory of my mother,
Margitta Mitschke.

Everybody wants to be a cat
It's cool to be a cat

– Thundercat

ACKNOWLEDGEMENTS

Ben, thank you for taking me in. Over the past five years, I have had the privilege of your unwavering trust in my abilities, not only to bring your ideas into the lab but also to stand on my own two feet. You have profoundly shaped how I think about chemical reactions and synthesis in general, and I consider this to be one of the most valuable lessons of my PhD.

Thank you, Prof. Dr. Hans-Günther Schmalz, for agreeing to review this thesis, and thank you, Prof. Dr. Mathias Wickleder and Dr. Monika Lindner, for serving on my thesis committee.

I am deeply grateful to the Chemical Industry Fund (VCI) for a Kekulé fellowship, which funded a large portion of my PhD studies, and the Studienstiftung des deutschen Volkes for supporting me throughout my undergraduate studies.

During my stay at the Max-Planck-Institut für Kohlenforschung, I had the pleasure of working with many talented scientists. Especially in my early years, I found myself in teams with experienced and highly capable Post-Docs; thank you, Dr. Chandra Kanta De, Dr. Sayantani Das, Dr. Carla Obradors, and Dr. Miles Aukland for giving me the opportunity to learn from you. I additionally would like to thank Lennart Brücher for his help with the Mukaiyama–Mannich reaction, and Kate Kryvous for a marvelous Master's thesis on nitroalkene activation. To everyone involved in numerous interactions and collaborations, it was a pleasure to share this experience with you, and I hope you had some fun, too.

Several special people have greatly influenced the last years on a personal level. Manuel, your impact on me is not only reflected in the thousands of catalysts screened in this thesis, but most importantly, in our countless discussions and shared moments. I am looking forward to exploring Zurich with you. Mathias, thanks for the companionship and insight. Many thanks to Bruni and Luc for being such fantastic humans and lab mates.

Vijay, I could not have asked for a better bench partner than you. A special thank you to Natascha Sadlowski for technical support in box 1, as well as to all the technicians of the List laboratory for their invaluable contributions. The same goes for the service departments of the institute, especially Dr. Markus Leutzsch for his extensive NMR contributions to this thesis.

Thank you to Lenni, Nils, Manuel, and Wencke for proofreading this thesis. Thank you, Alexandra Kaltsidis, for exceptional administrative support.

Lastly, none of this would have been possible without the support of my friends and family. Wencke, you have saved me more than once.

CONTENTS

ABSTRACT

This thesis explores advancements in the field of Lewis acid organocatalysis, more specifically silylium catalysis and silylium asymmetric counteranion-directed catalysis. Across three chapters, the effect of silylation and deprotosilylation on various chemical species is examined, resulting in the *unleashing* of their reactivity.

After an introduction of the conceptual framework (Chapter 1), Chapter 2 investigates the effect of silylation on nitronate anions, which led to the development of their catalytic asymmetric polarity inversion, culminating in an efficient and highly enantioselective catalytic synthesis of β-amino acids. The chapter also describes the spectroscopic characterization of the fundamental catalyst-substrate ion pair intermediate, critical for both reactivity and stereoselectivity, aided by density functional theory computations. Additionally, the direct deprotosilylation of nitroalkanes is described, serving as an inspiration for subsequent studies.

Chapter 3 deconvolutes the development of silyl ketene acetal catalysis through alkyl ester deprotosilylation. Despite their high nucleophilicity and central role in asymmetric catalysis, silyl ketene acetals have been challenging to synthesize. In the first part, the silicon-catalytic Mukaiyama–Mannich reaction of alkyl esters is described. After several unsuccessful asymmetric attempts of chiral ammonium-catalyzed and chiral silane-catalyzed variants of this transformation, mechanistic guidance facilitated the disovery of silylsulfonamides as versatile reagents for the catalytic stereoselective generation of silyl ketene acetals. This effort climaxed in the development of the silylium asymmetric counteranion-directed catalysis-enabled Mukaiyama–Mannich reaction of esters, with possible implications for the whole field of Mukaiyama reactivity.

Chapter 4 contains studies on silylium-catalyzed C-glysoylation reactions of arenes. It highlights the silylation of D-ribose as a pivotal step for both reactivity and stereoselectivity in a ring-opening addition of the nucleophile. Further efforts on the diastereoselective cyclization of the linear polyol products towards C-ribosides set the stage for the following total synthesis of GS-441524, the nucleoside core of the antiviral drug remdesivir, achieved in five steps from D-ribose.

KURZZUSAMMENFASSUNG

Diese Dissertation erforscht Fortschritte auf dem Gebiet der Lewis-Säure-Organokatalyse, insbesondere der Silylium-Katalyse und der asymmetrischen Silylium-Gegenanion-vermittelten Katalyse. Über drei Kapitel hinweg wird der Effekt der Silylierung und Deprotosilylierung auf verschiedene chemische Spezies untersucht, was letztlich zu einer *Entfesselung* ihrer Reaktivität führt.

Nach einer Einführung in den konzeptionellen Rahmen (Kapitel 1) untersucht Kapitel 2 die Wirkung der Silylierung auf Nitronat-Anionen, die zur Entwicklung ihrer katalytischen asymmetrischen Umpolung führte, gipfelnd in einer effizienten und hoch enantioselektiven katalytischen Synthese von β-Aminosäuren. Das Kapitel beschreibt auch die spektroskopische Charakterisierung des grundlegenden Katalysator-Substrat-Ionenpaar-Intermediats, das sowohl für Reaktivität als auch Stereoselektivität entscheidend ist, unterstützt durch Dichtefunktionaltheorie-Berechnungen. Zusätzlich wird die direkte Deprotosilylierung von Nitroalkanen beschrieben, die als Inspiration für nachfolgende Studien dient.

Kapitel 3 entwirrt die Entwicklung der Silylketenacetal-Katalyse durch Deprotosilylierung von Alkylestern. Trotz ihrer hohen Nukleophilie und zentralen Rolle in der asymmetrischen Katalyse war die Synthese von Silylketenacetalen bisher eine Herausforderung. Im ersten Teil wird die siliziumkatalytische Mukaiyama–Mannich-Reaktion von Alkylestern beschrieben. Nach mehreren erfolglosen asymmetrischen Versuchen mit chiralen Ammonium-katalysierten und chiralen Silan-katalysierten Varianten dieser Transformation wurden Silylsulfonamide als vielseitige Reagenzien für die katalytische stereoselektive Erzeugung von Silylketenacetalen entdeckt. Diese Bemühungen gipfelten in der Entwicklung der durch asymmetrische Silylium-Gegenanion-vermittelte Katalyse ermöglichten Mukaiyama–Mannich-Reaktion von Estern, mit potenziellen Implikationen für das gesamte Gebiet der Mukaiyama-Reaktivität.

Kapitel 4 enthält Studien zu Silylium-katalysierten *C*-Glykosylierungsreaktionen von Aromaten. Es hebt die Silylierung von D-Ribose als entscheidenden Schritt sowohl für die Reaktivität als auch für die Stereoselektivität bei einer ringöffnenden Addition des Nukleophils hervor. Weitere Bemühungen um die diastereoselektive Zyklisierung der linearen Polyolprodukte zu *C*-Ribosiden ebneten den Weg für die nachfolgende Totalsynthese von GS-441524, dem Nukleosidkern des antiviralen Medikaments Remdesivir, erreicht in fünf Schritten aus D-Ribose.

LIST OF ABBREVIATIONS

Ac	acyl
ACDC	asymmetric counteranion-directed catalysis
Alk	alkyl
Ar	aryl
aq.	aqueous
BALT	binaphthyl-allyl-tetrasulfone
BINOL	1,1'-bi-2-naphthol
Bn	benzyl
Boc	*tert*-butyloxycarbonyl
brsm	based on recovered starting material
Bu	butyl
BSA	*N*,*O*-bis(trimethylsilyl)acetamide
BSTFA	*N*,*O*-bis(trimethylsilyl)trifluoroacetamide
Bz	benzoyl
CPA	chiral phosphoric acid
Cy	cyclohexyl
DCE	1,2-dichloroethane
DCM	dichloromethane
DFT	density functional theory
DIBAL	diisobutylaluminium hydride
DMAP	4-dimethylaminopyridine
DMF	*N*,*N*-dimethylformamide
DMSO	dimethylsulfoxide
DSI	disulfonimide
d	doublet or day(s)
dr	diastereomeric ratio
ee	enantiomeric excess
er	enantiomeric ratio
equiv.	equivalents
ESI	electrospray ionization
EWG	electron-withdrawing group
GC	gas chromatography
h	hour(s)

HATU	hexafluorophosphate azabenzotriazole tetramethyl uronium
HMDS	hexamethyldisilazane
HOMO	highest occupied molecular orbital
HPLC	high performance liquid chromatography
i	*iso*
IDP	imidodiphosphate
iIDP	iminoimidodiphosphate
IDPi	imidodiphosphorimidate
JINGLE	1,1'-binaphthyl-2,2'-bis(sulfuryl)imides
LA	Lewis acid
LB	Lewis base
LDA	lithium diisopropylamide
LUMO	lowest unoccupied molecular orbital
m	multiplet
M	molar
[M]	metal with ligand field
Me	methyl
min	minute(s)
Ms	methylsulfonyl
MS	mass spectrometry or molecular sieves
NFSI	*N*-fluorobenzenesulfonimide
NHPI	*N*-hydroxyphthalimide
NMR	nuclear magnetic resonance (spectroscopy)
NOE	nuclear Overhauser effect
NTPA	*N*-triflyl phosphoramide
PADi	phosphoramidimidate
PES	potential energy surface
PG	protecting group
Ph	phenyl
Pr	propyl
p-TSA	4-toluenesulfonic acid
q	quartet
quant.	quantitative
r.t.	room temperature
sat.	saturated
t	*tert* or time
t	triplet

T	temperature
TBAF	tetra-*N*-butylammonium fluoride
TBS	*tert*-butyldimethylsilyl
TES	triethylsilyl
Tf	trifluoromethanesulfonyl (triflyl)
TFA	trifluoroacetic acid
THF	tetrahydrofuran
TIPS	triisopropylsilyl
TLC	thin-layer chromatography
TMS	trimethylsilyl
TPP	tetraphenylporphyrin
TRIP	3,3'-bis(2,4,6-triisopropylphenyl)-1,1'-binaphthyl-2,2'-diylhydrogenphosphate
TS	transition state
via	by way of

CHAPTER I

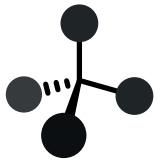

INTRODUCTION

Chemical synthesis is the science of the making and breaking of bonds. The key to any chemical synthesis is *selectivity*. Selectivity itself is a collective term and manifests itself as the preference of a chemical reaction for well-defined products over a seemingly infinite number of others. Specifically, chemists regularly observe selectivity in the form of *regioselectivity* (the preference for certain regions of a molecule), *chemoselectivity* (the preference for certain functional groups of a molecule), and *stereoselectivity* (the preference for certain diastereo- and enantiomers of a molecule), among others.

Because most chemical reactions tend to be non-selective, the need for selectivity stems from a desire to develop *ideal* syntheses. For reactions to be selective, guidance is required. This control can be introduced by a structural predisposition of the substrate or a reagent to undergo a particular transformation selectively—the well-known notions of substrate and reagent control—or by another concept: *catalysis*. This term was coined by Berzelius in 1836 in his work on *catalytic bodies*,[1] surrounded by an almost mystical aura:

> *"This power seems definitely to consist, in a faculty of bodies, by their simple presence, and without any chemical participation, to rouse up the play of certain affinities which at that temperature remained inactive [...]"*

In essence, this sentence still holds up after almost 200 years, because (1) the catalyst is another species of some kind (*"faculty of bodies"*), (2) the catalyst is not consumed during a chemical reaction (*"without any chemical participation"*)—although it readily engages with its substrates—, and (3) the catalyst enables reaction pathways that could hardly be achieved otherwise (*"rouse up the play of [...] affinities"*).

We now know that, in a simplified version, the rate of formation of a reaction product is determined by the energy required to reach the transition state—the unique point connecting both substrate and product on the multi-dimensional potential energy surface. Catalysts are able to lower the activation energy by offering alternative reaction pathways. This not only means that selectivity can be dialed into the reaction system or, in some cases, altered with

sub-stoichiometric, *catalytic* amounts of another substance; it is also a more efficient and thus economic approach to chemical synthesis. In this regard, models such as Trost's *atom economy* have been brought forward.[2]

Over the past 123 years, the Nobel Prize in chemistry has been awarded to research related to chemical catalysis 10 times. Sparked by the conceptualization of catalysis (Ostwald, 1909), the development of modern society would not have been possible without a catalytic ammonia synthesis (Haber, 1918), coal liquefaction (Bergius, 1931), or polymerization reactions (Ziegler and Natta, 1963). Advancements such as these have shaped the chemical industry; consequently, it is not surprising that an estimated 80–90 % of all modern chemical processes are catalyzed, contributing to approximately one-third of the global gross domestic product.[3]

Organic synthesis, which constitutes the greater part of anthropogenic synthesis, focuses mainly on the (de)construction of carbon–carbon, carbon–hydrogen, carbon–nitrogen, and carbon–oxygen bonds. Since organic synthesis revolves around the element carbon, its tetravalent nature leads to the emergence of a property associated with symmetry-breaking—*chirality*. Sodium ammonium tartrate crystals that appeared as mirror images of each other were separated and analyzed by Pasteur only 12 years after Berzelius' work on catalytic bodies.[4] This initially strange observation of *enantiomers* was conceptually solidifed by van't Hoff's[5] and Le Bel's[6] tetrahedral model for the carbon atom in 1874, and ultimately proven after the development of X-ray crystallography.

The existence of enantiomers leads to a special subclass of stereoselectivity; that is, *enantioselectivity*. As discussed above, all kinds of selectivities can be induced *via* the action of a well-defined catalyst. The studies by Knowles,[7] Noyori,[8] and Sharpless[9] led to the development of the field of *asymmetric catalysis*, which deals with the effective induction of enantioselectivity onto the substrates by the catalyst.

In the 1980s and 1990s, this field was dominated by approaches using transition metals and proteins as catalysts, and somewhat paralleled by chiral auxiliary-based methods. In the latter, enantiopure small organic molecules are covalently introduced into the substrate, allowing subsequent diastereoselectivity through substrate control. Associated with obvious disadvantages in terms of step[10] and atom economy, it was the work by List[11] and MacMillan[12] in the late 1990s that finally emancipated asymmetric synthesis from chiral auxiliaries. From that point on, small organic molecules not so different from the previously employed auxiliaries were used as *organocatalysts*, and a subsequent revolution in asymmetric catalysis was on the horizon (Nobel Prize in chemistry 2021).

Over the past 25 years, efforts in organocatalysis have culminated in the synthesis of chiral Brønsted superacids and their application within the concept of *asymmetric counteranion-directed catalysis*,[13] resorting to enantioinduction through ion-pairing interactions in the con-

text of Brønsted acid and Lewis acid organocatalysis. Lewis acid asymmetric counteranion-directed catalysis, along with Brønsted acid catalysis, is the conceptual foundation of this thesis and will be deconvoluted in the following sections.

1 Entering the Mukaiyama World

Over the past 50 years, the advancement of chemical synthesis has correlated strongly with the advancement of the aldol reaction.[14,15] Arguably, there is no other reaction that is so deeply intertwined with the dominion of asymmetric transition metal catalysis in the second half of the last century, the emergence of organocatalysis, and the most recent groundbreaking contributions to Lewis acid organocatalysis altogether.[16,17] The challenge and timeline of developing a catalytic asymmetric variant of this reaction will be discussed in the following part.

Aldol reactions based on magnesium and zinc enolates had already been published by House in 1973,[18] however, a specific variant of the aldol reaction based on enol silanes as preformed enol equivalents was developed by Mukaiyama in the same year (Scheme 1.1).[19]

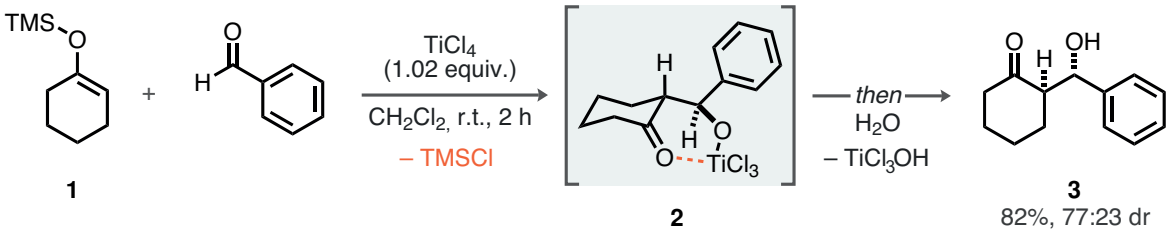

Scheme 1.1: The Mukaiyama aldol reaction.

Although enol silanes had been used as precursors to metal enolates by Stork in 1968[20] and Murai for α-haloalkylations and -sulfenylations,[21,22] this was the first report of a *direct* use as nucleophiles in highly useful aldol reactions. Cyclohexanone-derived enol silane **1** was reacted with benzaldehyde in the presence of stoichiometric amounts of $TiCl_4$, liberating TMSCl in the process and providing the aldol product **3** after aqueous workup. Retrospectively a seemingly intuitive step forward, this reaction offered a possible solution to the main problem of cross-aldol reactions at the time. Transformations of ketones as nucleophiles suffered from poor regioselectivities due to unselective enolate formation, and the preformed enol silane could be synthesized selectively under either kinetic or thermodynamic control.[23] It also allowed for the transformation of otherwise highly basic enolate equivalents such as silyl ketene acetals, formally corresponding to ester enolates that would limit the functional group tolerance of α-enolizable aldehyde acceptors.[24] Finally, many other famous organic reactions such as the Hosomi–Sakurai allylation[25] or Danishefsky's hetero-Diels–Alder reaction[26] were inspired by Mukaiyama's work.

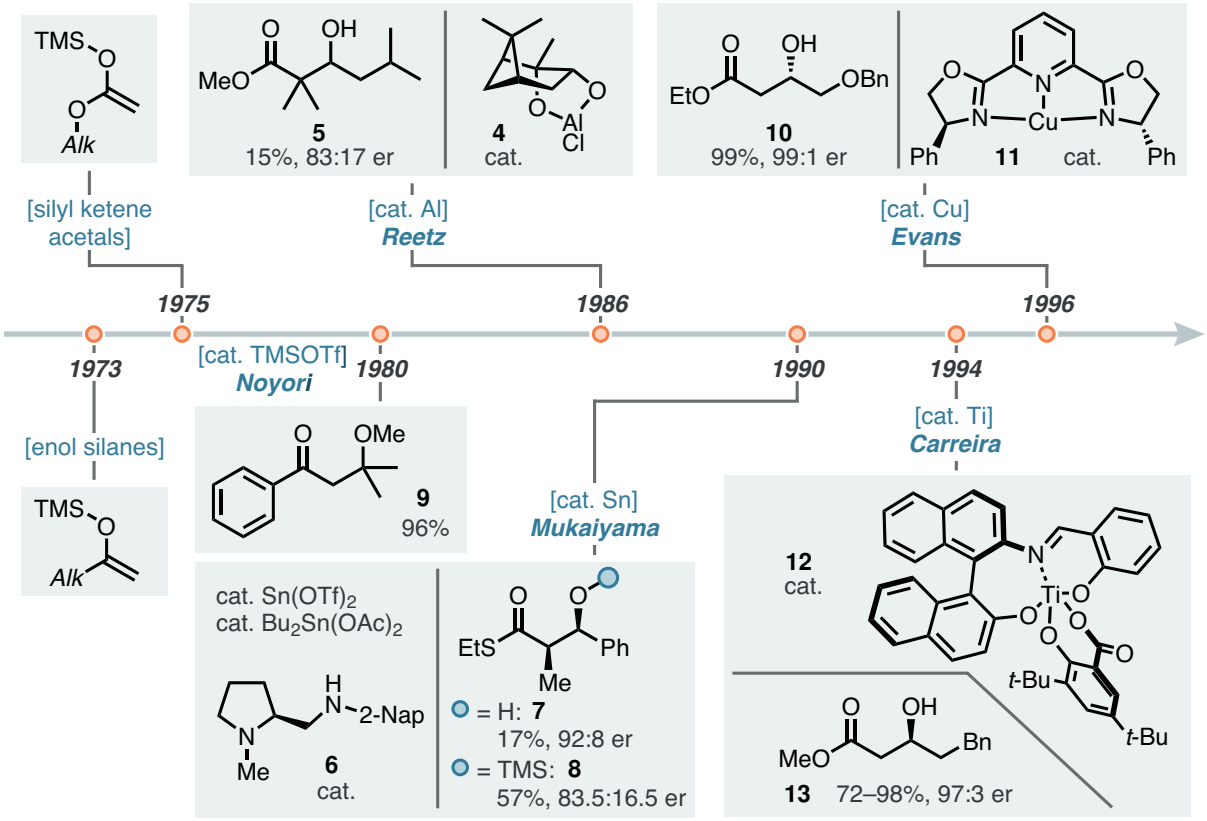

Scheme 1.2: Key milestones in the development of the Lewis acid-catalyzed Mukaiyama aldol reaction.

Considering the timeline of the development of the first asymmetric Mukaiyama aldol reactions (Scheme 1.2), it took another 13 years until Reetz presented a series of three different chiral enantiopure Lewis acid catalysts, with the (+)-pinene-derived aluminum chloride **4** providing the aldol **5** in 83:17 er.

Mukaiyama had moved on to tin(II)-mediated aldol reactions,[27–31] and found the addition of stoichiometric amounts of proline-derived chiral diamine **6** along with $Sn(OTf)_2$ and $Bu_2Sn(OAc)_2$ to provide **7** with excellent enantioselectivities of up to >99:1 er. Strikingly, when catalytic amounts of all three reagents were used, the TMS ether of the product **8** was isolated as the major product with a greatly reduced enantioselectivity of 83.5:16.5 er. The presence of the TMS ether product **8** established the mechanistic regime in which this reaction operated, and the lower enantioselectivity indicated non-asymmetric background reactivity (Scheme 1.3).[31]

In principle, the tin(II) complex **14** was a competent catalyst for this reaction, most likely providing enantiofacial selectivity through π-π stacking interactions as depicted in **15**. When stoichiometric amounts of tin were used in this reaction, the aldolate **16** provided the free alcohol **7** with high enantioselectivity after hydrolysis. However, one equivalent of TMSOTf was released for each nucleophilic addition. Considering the reduced amounts of tin in the

reaction mixture, the aldolate **16** had to undergo rather slow tin-silicon metathesis before the catalyst could re-enter the catalytic cycle. This emphasizes the importance of Noyori's findings. He discovered TMSOTf to be an effective catalyst for the Mukaiyama aldol reaction in 1980, after it had become commercially available in Japan in the late 1970s.[32] The accumulated TMSOTf could then coordinate to unreacted benzaldehyde through *silylium* activation to form the siloxocarbenium ion intermediate **17**, followed by nucleophilic attack by the silyl thioketene acetal. Ultimately, the low enantioselectivity of the product **8** was caused by silylium catalysis.

Consequently, asymmetric transition metal catalysis at the time, maybe even unknowingly so, faced a great challenge. Non-asymmetric *parasitic* catalysis due to the inevitable formation of TMSOTf or similarly activated species *in situ* has been the conceptual disadvantage for all metal-based Lewis acid-catalyzed approaches to the Mukaiyama aldol reaction, therefore requiring high catalyst loadings. The community quickly became aware of this problem by virtue of silyl crossover experiments,[33] and notable exceptions were still able to provide elegant solutions.[34,35]

In Mukaiyama's tin(II)-catalyzed variant, slow addition of the aldehyde over the course of the reaction allowed for the isolation of the TMS ether **8** in excellent yield and enantiomeric ratio of 95.5:4.5 er. The (acyloxy)borane fragment in Masamune's oxazaborolidene-catalyzed Mukaiyama aldol was also able to catalyze the silyl transfer step,[36] similar to Carreira's salicylate complex **12** in its catalytic variant (*"silyl shuttle"*, Scheme 1.2).[35] Evans demonstrated a fascinatingly active copper(II) pybox complex **11** in 1996 that provided the product **10** in >99:1 er, although control experiments confirmed active silicon scrambling.[37] It was thought

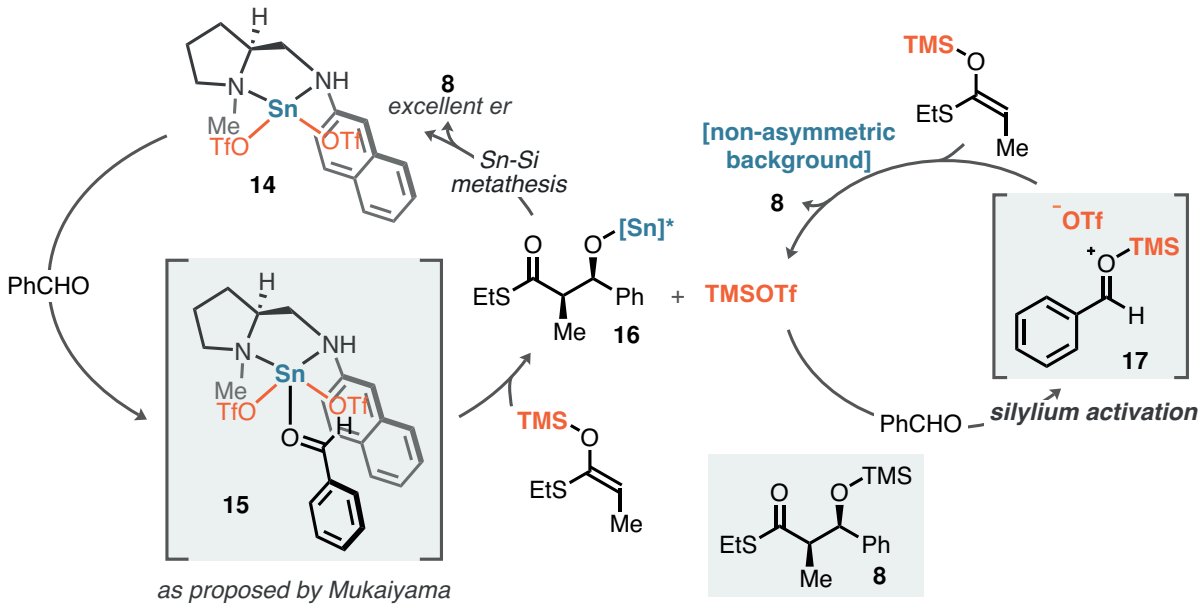

Scheme 1.3: The competition between asymmetric tin(II) and non-asymmetric TMSOTf catalysis.

that the activation of the α-benzoxyaldehyde by bidentate coordination within a Jahn–Teller-distorted square-pyramidal copper(II) Lewis acid was so strong that non-asymmetric background catalysis by R_3SiSbF_6 could not compete at -78 °C.

Besides Lewis acid catalysis, Denmark pioneered the development of chiral phosphoramide Lewis base catalysts.[34] This approach solved the problem of silyl transfer, however, fairly Lewis acidic trichlorosilyl groups were required to ensure efficient coordination of both aldehyde and Lewis base catalyst *via* putative *Si*-hexacoordinate closed transition states.[38]

Over the years, a number of different transformations based on enol silanes and silyl ketene acetals as nucleophiles have been developed, such as vinylogous aldol,[39] Mukaiyama–Michael,[40], or Mukaiyama–Mannich reactions.[41] Despite numerous efforts, however, asymmetric transition metal catalysis has not been able to provide a comprehensive general solution to this world of reactivity, which may be closely related to the observation of non-asymmetric background reactivity. An arguably more direct and elegant approach would be to use chiral versions of the triflate anion, and enantioinduction could occur in the highly activated siloxocarbenium ion pair **17**, converting the problem of into a solution for asymmetric catalysis without the need for a transition metal catalyst. Such a general process would offer a robust approach to the wide variety of organic transformations catalyzed by silylium Lewis acids in particular and Brønsted acids in general.[42]

2 Asymmetric Counteranion-Directed Catalysis

This section will highlight key steps in the development of chiral enantiopure and confined acids, which have been shown not only to be effective in inducing enantioselectivity through asymmetric counteranion-directed catalysis (ACDC), but also to exhibit effects such as shape- and size-selectivity normally observed in the fields of heterogeneous catalysis, supramolecular catalysis, and biocatalysis.[43,44] ACDC is a *general reactivity mode* to describe and rationalize enantioinduction in asymmetric catalysis.

> *For chemical reactions proceeding through an ACDC mechanism, enantioselectivity is induced by ion-pairing of a cationic intermediate with a chiral enantiopure anion, provided by the catalyst.*[13]

2.1 Ion Pairing in ACDC

The notion of *ion pairing* requires further discussion in this context. The term somewhat misleadingly implies that the Coulomb force is the sole source of attractive interactions; however, this is only true for idealized point charges in absolute vacuum. Whenever real systems

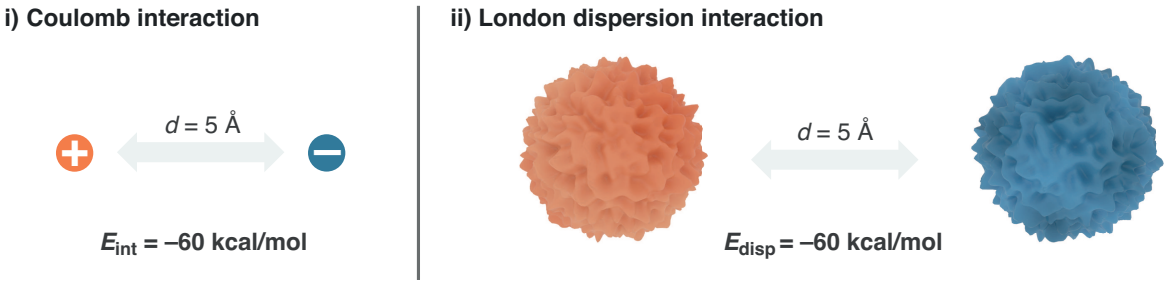

Fig. 1.1: Comparison of i) Coulomb interactions with ii) dispersion interactions. Both fragments in ii) are uncharged and consist of 100 organic atoms, giving 10 000 interacting atom pairs. Adapted from *The Chemical Bond*, p. 478.[45]

of small organic molecules of about 100–250 atoms are at play, a multitude of *additional*, otherwise classified weak, non-covalent interactions contribute to the overall attraction or repulsion by effects of scaling. First, directional electrostatic forces, which act on dipole-based increments of *polarization*—such as non-classical hydrogen and halogen bonds—can be present within the context of ion pairing. The strength of those interactions decreases with the polarization of the interacting partners until the complete absence of permanent polarization is reached and attraction is purely based on *polarizability* (π-π, London dispersion). Whereas organic chemists can often intuitively understand directional electrostatic interactions, the principles of non-covalent interactions and especially dispersion forces are harder to grasp. However, their importance cannot be overstated. In his chapter on *Dispersion Interaction and Chemical Bonding* in *The Chemical Bond*, Stefan Grimme has drawn an intriguing comparison (Fig. 1.1).[45] Two opposite point charges at a distance of 5 Å exhibit an interaction energy of $E_{\text{int}} \approx -60$ kcal/mol. A comparable interaction energy can be observed between two uncharged fragments of 100 light atoms (H, C, N, O) at the same distance. This effectively explains the attention in the field of chemical synthesis recently attracted by London dispersion and other non-covalent interactions—a progress that has also been facilitated by the advent of modern computational chemistry methods.[46]

Asymmetric catalysis as a field capitalizes on very small energy differences between diastereomeric transition states to favor one enantiomer of the product. To achieve an enantiomeric ratio (er) of 95:5 at room temperature an energy difference between the two competing ensembles of transition states of only 1.75 kcal/mol is required.[47,48] Consequently, this means that all of the discussed interactions within ion pairs can completely shift the selectivity landscape and should ideally be considered systemically.

2.2 Establishing the Concept

As discussed in Section 1, the development of ACDC has its roots in the field of asymmetric organocatalysis. Enantioinduction typically proceeded *via* covalent bond formation of

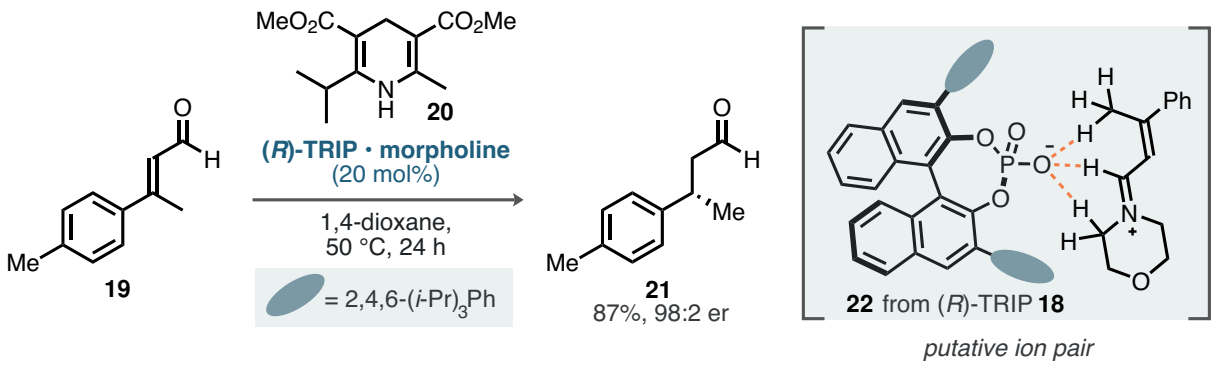

Scheme 1.4: List's introduction of ACDC by the transfer hydrogenation of enals.

aldehydes or ketones with chiral Lewis-basic catalysts (for example L-proline) followed by diastereoselective reaction of the enamine or iminium ion.[49]

Mayer and List established ACDC as a concept in 2006, by unorthodoxly transposing the chiral information from the iminium ion onto a chiral phosphate anion through ion pairing (see Section 2.1).[50] BINOL-based chiral phosphoric acids had been introduced two years earlier by Akiyama and Terada as Brønsted acid catalysts in Mannich reactions.[51,52] Importantly for this reaction, List's (*R*)-TRIP **18** was used, featuring highly congested 2,4,6-triisopropylphenyl-substituents in the 3,3'-positions of the BINOL backbone.[53,54] Using a range of aromatic α,β-unsaturated aldehydes, such as **19**, in combination with the sophisticated Hantzsch ester **20**, several derivatives of the phenylpropanal family such as **21** were synthesized with excellent yields and enantioselectivities. Mechanistically, the study demonstrated for the first time how enantioselectivity (*via* chiral phosphate) can be merged with reactivity of an achiral catalyst (*via* iminium ion formation from morpholine) through ion pairing, as illustrated with the putative ion pair **22**. Additionally, concurrent interactions, as discussed in Section 2.1, become evident: non-classical CH···O hydrogen bonds, originating from the highly polarized positions of the iminium, facilitate substrate recognition by the catalyst, along with probable dispersion interactions from the 2,4,6-triisopropylphenyl fragments. Those close contacts furthermore serve as a possible explanation for enantioconvergence when (*E*)/(*Z*)-mixtures of the substrate were employed, through deprotonative dienamine formation, as effectively demonstrated in the transfer hydrogenation of citral to give citronellal. Strikingly, superior enantioselectivities were achieved compared to the seminal works by List[55] and MacMillan[56] on iminium-catalyzed transfer hydrogenations.

The power of ACDC has also been recognized in the field transition metal-catalysis. In 2007, Toste and co-workers generated an Au^I/(*R*)-TRIP salt *in situ* for intramolecular hydroalkoxylation, hydrolactonization, and hydrosulfonamidation reactions of allenes.[57] Stereoselectivity is notoriously difficult to control with chiral ligands in Au^I catalysis due to the formation of linear bicoordinate gold species, thus displacing the chiral information from the

typical outer-sphere nucleophilic approach. Coulomb interactions, however, closely assembled the reactive gold species with the chiral anion, while presenting further possibilities of interactions with the substrate through hydrogen bonding. ACDC also found widespread applications in the context of supramolecular chemistry. In recent years, the work of Jacobsen in particular demonstrated that an achiral anion can be recognized by a chiral *anion binding* catalyst, resulting in a chiral supramolecular hydrogen-bonded complex that is then able to infer enantioinduction.[58–60]

Revisiting List's introduction of ACDC in 2006, it is essential to highlight the pioneering character of this work. This aspect is seen in the recognition of all the principles governing reactivity and selectivity within a novel concept at a time when the technology to effectively implement this concept was still developing. Naturally, ACDC is entangled with the field of Brønsted acid catalysis. This inherent connection was recognized early on, and in the years following the seminal work on transfer hydrogenation, development of increasingly stronger Brønsted acid catalysts followed.

2.3 From Brønsted Acid Catalysis to Silylium ACDC

Efforts to generalize the acidity scale beyond dilute aqueous solutions have culminated in the Hammett acidity function H_0 as a formal extension to the pH scale.[61] Hall and Conant investigated mixtures of sulfuric and acetic acid in the late 1920s and coined the term *superacid* as a consequence of the increased proton activity.[62] This has probably led to the most intuitive definition: an acid becomes a superacid when the acidity is higher than that of sulfuric acid.[63]

Groundbreaking work has been brought forward by Olah and co-workers, who thoroughly investigated chemical reactions in superacidic media.[68] Harsh reaction conditions, oftentimes employing $FSO_3H \cdot SbF_5$ (*"magic acid"*), enable reactions to proceed through dicationic mechanisms, or oligomerize methane by virtue of protonation to the carbonium ion CH_5^+ and subsequent dehydrogenation, just to name two examples.[69]

The axially chiral structural framework of BINOL and its binaphthyl derivatives has proven to be one of the most privileged in the entire field of asymmetric synthesis,[70] which is also deeply reflected in the structures of chiral Brønsted acids developed over the past years.[71] Those efforts are fueled by the vision to engage substrates with a decreased predisposition, i. e., their basicity. Consequently, this can be achieved by stronger acids, a progression in the field that is naturally represented by the pK_a values of the corresponding acids (in MeCN, Scheme 1.5). It is worth noting that, in a sense, the seminal work on proline-catalyzed aldol reactions also falls within the realm of Brønsted acid catalysis. Besides the enamine activation of the ketone reaction partner, the carboxylic acid fragment of

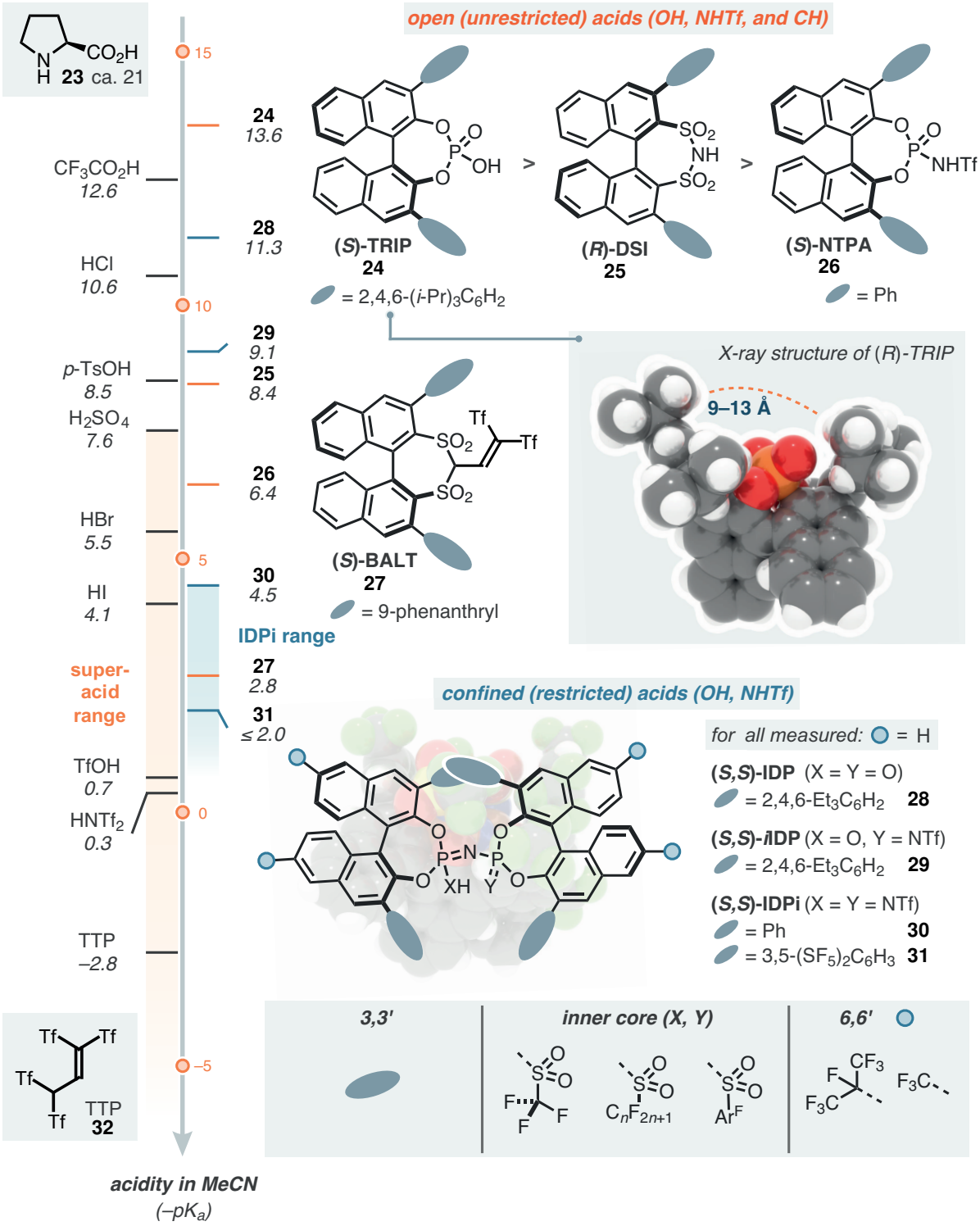

Scheme 1.5: Overview of a selection of chiral Brønsted acid organocatalysts including pK_a values in MeCN[16,64–66] as well as X-ray crystal structure of *(R)*-TRIP.[67]

proline has also been shown to be vital for reactivity and stereoselectivity, thus underlining the bifunctionality of this simple organocatalyst.[72,73] Typical pK_a values of carboxylic acids are in the range of 21–22.[64–66]

Chiral phosphoric acids are bifunctional in a similar sense; they are comprised of a Lewis basic (P=O) and Brønsted acidic site (P−OH). List's TRIP **24**, representing all chiral phosphoric acids, displays mild acidity (13.6) and has been demonstrated as a potent catalyst for the activation of imines.[53,54] The mild acidity of chiral phosphoric acids also allows compatibility with delicate keto–enol tautomerization equilibria; the regioselective functionalization of α-substituted cyclic ketones through thermodynamically controlled enol formation has been introduced *via* the concept of *enol catalysis* in contrast to traditional enamine-based methods.[74,75] In 2006, Yamamoto utilized the structure of chiral phosphoric acids as a template and introduced an acidifying structural modification that was proposed by Koppel, Yagupolskii and Taft ten years earlier: the replacement of an oxygen atom by an *N*-triflyl group.[76] Chiral *N*-triflyl phosphoramide **26** was found to be approximately 10,000,000 times more acidic than typical chiral phosphoric acids and expanded the electrophilic activation scope of Brønsted acid catalysis to ketones.[77]

Structurally more distinct motifs were presented by List and Ishihara in 2008, including BINSA (BINOL-disulfonic acids, not shown)[78–80] and by Berkessel in 2011, who established JINGLE (BINOL-bis(sulfuryl)imides, not shown).[81] However, especially noteworthy from this development phase is the DSI motif **25** ($pK_a = 8.4$), first synthesized by List and later by Giernoth in 2009.[82,83]

Fascinatingly, DSI catalysts were shown to effectively catalyze the asymmetric Mukaiyama aldol reaction of simple aldehydes, which puts this development in the direct context of the previous limitations in the field as discussed in Section 1 and opened up a novel avenue for asymmetric catalysis in the form of a distinct mechanistic regime: *silylium ACDC*. This approach catapulted organocatalysis into the realm of Lewis acid catalysis—a field that was completely dominated by (transition) metals and boron.

In Brønsted acid-catalyzed reactions, the chiral enantiopure catalyst **33** activates the substrate *via* protonation to form a most likely hydrogen-bonded, activated complex represented by **34** (Scheme 1.6). This protonation renders **34** susceptible to attack by an additional reagent or triggers an intramolecular reaction in proximity to the chiral anion. Ultimately, this leads to the formation of the product complex **35**, which then collapses to regenerate the Brønsted acid catalyst **33** and liberate the product. If a suitable silyl source is used in conjunction with a strong Brønsted acid, deprotosilylation of the catalyst generates a silylium Lewis acid *in situ*. The elementary steps involving substrate activation to form **37**, the stereoselective reaction to **38**, and subsequent product desilylation mirror those observed in Brønsted acid catalysis. Nonetheless, these mechanisms operate on distinct activation modes, potentially leading to differences in reactivity. First of all, silicon's high oxophilicity offers very specific activation modes that can be complementary to Brønsted acid-based approaches, especially considering traditional thermodynamic basicity arguments.[86] The ox-

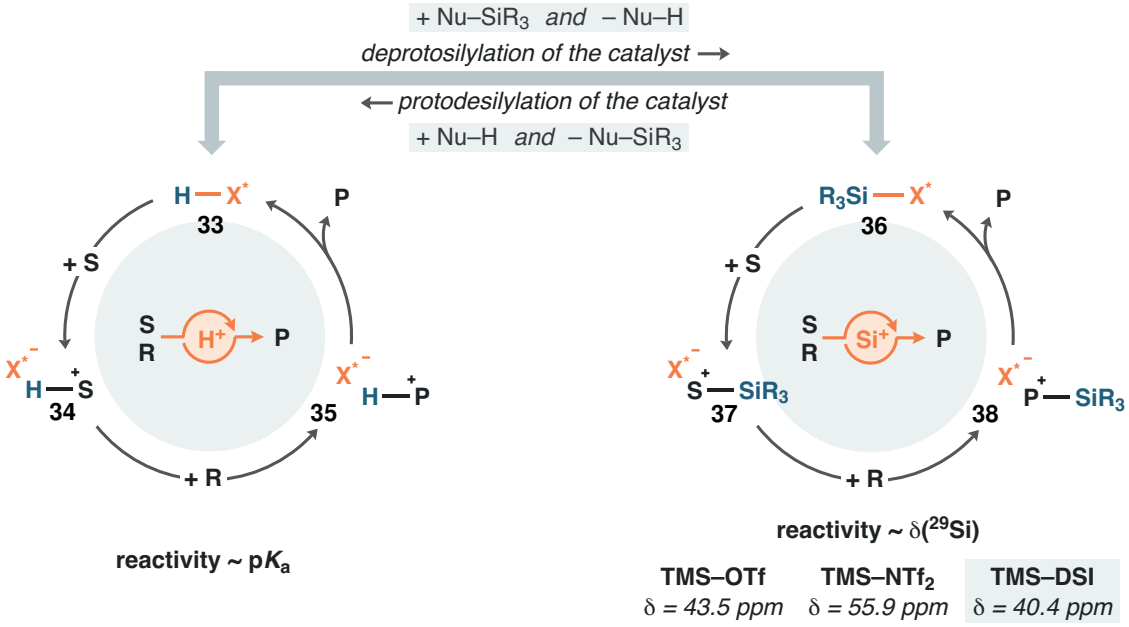

Scheme 1.6: Brønsted acid catalysis (left) vs. silylium ACDC (right). ^{29}Si NMR shifts from ref. [84, 85]; the chemical shift of the *O*-silyl isomer was chosen for the DSI.

ophilicity of silicon is also linked to another feature of silylium ACDC, which is self-drying. The activated silylium Lewis acid **36** readily deprotosilylates proton sources such as alcohols, amines, or water, eventually leading to complete silylation provided enough (sacrificial) silyl source Nu−SiR_3 is present in the system (Scheme 1.6 right).

Another highly important element is the nature of the silyl group. The substitution pattern at the central silicon atom of a R_3Si^+ group determines (1) the steric demands of the silylium ion and (2) the inherent Lewis acidity.[87] The structural nature of the silyl group is especially important in the context of asymmetric catalysis. Within ACDC, the chiral anion will be located in the vicinity of the activated species, and the steric demand of the silylium Lewis acid can potentially have a great influence on selectivity. Moreover, silyl groups have been found to be efficient dispersion energy donors by Schreiner.[88]

In terms of the determination of the silylium Lewis acidity, (2), a direct although almost completely computational measure is found in the fluoride ion affinity.[89] Additionally, the Gutmann–Beckett method is one of the most established estimates for Lewis acidity through the measurement of the change of the chemical shift of triethylphosphine oxide upon complexation, especially for nonstabilized trialkylsilyliums.[90–92] The arguably most intuitive correlation between reactivity and a measurable parameter that simultaneously includes the effect of the counteranion is found in the ^{29}Si NMR chemical shift of the activated silylium acid, as initially concluded by Mathieu and Ghosez.[84,93]

In List's chiral DSI-catalyzed Mukaiyama aldol reaction (Scheme 1.7), 2-naphthaldehyde **39** and the dimethyl silyl ketene acetal **40** reacted to provide TMS aldol product **41**. NMR

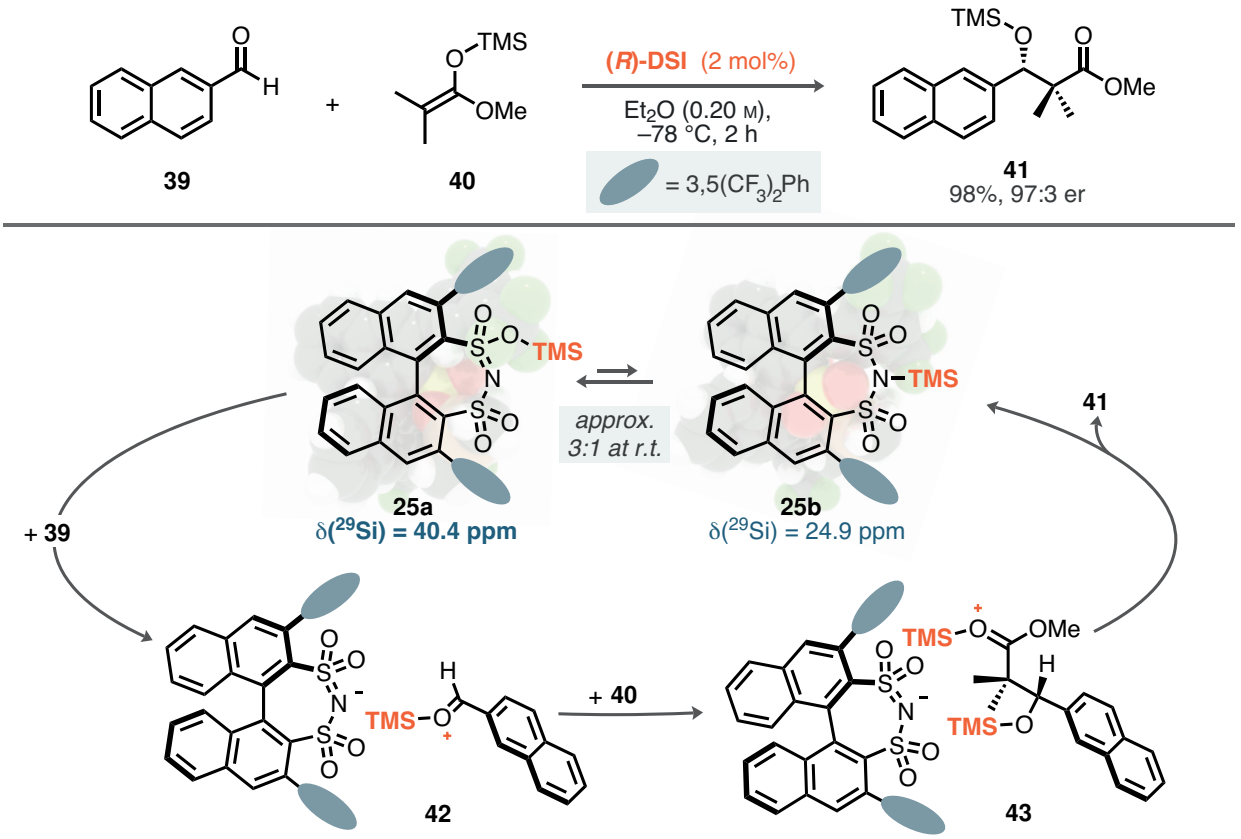

Scheme 1.7: The first application of chiral sulfonimides solved the main challenge of the Mukaiyama aldol reaction *via* silylium ACDC.

studies offered deep insights into the reaction mechanism. Rapid silylation of the disulfonimide **25** was observed upon the addition of **40**. The products of this reaction were characterized as the *O*- and *N*-silyl isomers **25a** and **25b**, respectively, which are connected by a dynamic equilibrium at room temperature in a 3:1 ratio in favor of **25a**.[85] Considering the ^{29}Si NMR shifts of both tautomers, the *O*-isomer displayed significant deshielding of the TMS group (*cf.* TMSOTf and $TMSNTf_2$, Scheme 1.6 right). This leads to the conclusion that **25a** is the stronger and thus more active catalytic silyl transfer agent. Consequently, activation of **39** furnished chiral siloxocarbenium ion **42**, closely resembling the one in the TMSOTf-catalyzed Mukaiyama aldol reaction (**17**, Scheme 1.3). The key difference is that subsequent nucleophilic attack by **40** occurs with high levels of enantioselectivity, due to the chiral, enantiopure disulfonimide anion. Silyl transfer within the product-DSI complex **43** onto the catalyst regenerates the active species equilibrium between **25a** and **25b**.

After the establishment of the proof-of-principle of silylium ACDC, the concept has found widespread applications in the community of chemical synthesis.[94] Several years later, List presented the even more acidic BALT catalysts in the Diels–Alder reaction of (fluoren-9-yl)methyl esters, which still remains as the single example of C–H acids in asymmetric

catalysis.[95] Exploring the limitations of these classes of open and unconfined catalysts quickly revealed that enantioselectivity could be induced effectively only for large substrates. For example, in the Mukaiyama aldol reaction shown in Scheme 1.7, aliphatic-like dihydrocinnamaldehyde reacted with a sterically less demanding α-unsubstituted silyl ketene acetal to provide the product with a lower yield of 59 % and 75:25 er. This was a symptom of a much deeper problem in asymmetric catalysis, with only two opposing solutions possible: (1) modifying the substrate, thus deviating from the initial system—a process that, at extreme levels, may be called *substrate engineering*, or (2) synthesizing different catalysts or novel catalyst motifs to address the *real* problem. Undoubtedly, the challenge to activate the smallest and most unbiased substrates has been the main driver for developing new catalyst frameworks in the past and was also a key element in the most recent breakthroughs in ACDC.[96–98]

The main problem of BINOL-based Brønsted acid catalysts was recognized and is clearly visible in the representative X-ray crystal structure of (*R*)-TRIP in Scheme 1.5. The 3,3'-substituents are key determinants of the shape of the chiral pocket, however, the distance between both 2,4,6-triisopropylphenyl groups is in the range of 9–13 Å, offering a plausible explanation for the observed high enantioinduction only for large substrates. A possible solution to decrease the size of the chiral pocket is found in supramolecular catalysis. Ishihara and co-workers demonstrated that the association of boron Lewis acids with chiral BINOL-based Lewis bases forms a well-defined chiral cavity, which is—depending on its size—able to completely alter the *endo*/*exo*-selectivity in Diels–Alder reactions of cyclopentadiene with α,β-unsaturated aldehydes.[99–101] This approach can be viewed as a direct conceptual offspring of Yamamoto's work on large aluminium Lewis acids in the 1980s, which demonstrated similar effects depending on the nature of the acid.[102–105]

Ishihara's method allowed for a high degree of tunability *via* combinatorial chemistry, however, the prerequisite of catalyst complex formation through Lewis pairing inherently limited the functional group compatibility. This concept of *confining* a catalyst's active site has been translated into small-molecule catalysis by Čorić and List in 2012, while retaining the highly important bifunctional nature of the chiral phosphoric acids.[106] The resulting imidodiphosphoric acid (IDP) **28** (see Scheme 1.5) displayed slightly increased acidity as compared to CPAs ($\mathrm{p}K_\mathrm{a} = 11.3$), which led to comparable reactivity. The X-ray crystal structure, as shown in Scheme 1.8, revealed the C_2-symmetrical combination of two BINOL subunits. Entry from the lower face into the active site was conformationally blocked by two of the four 3,3'substituents, and the *O,O-syn* conformation of the inner P=N−P core created a highly confined yet reasonably flexible pocket. It is plausible that an open conformer of **28** existed within the accessible conformational landscape, allowing substrate entry and stabilization through various non-covalent interactions. The consequences of this confined active site were demonstrated in the spiroacetalization reaction of dihydropyran **44**, producing

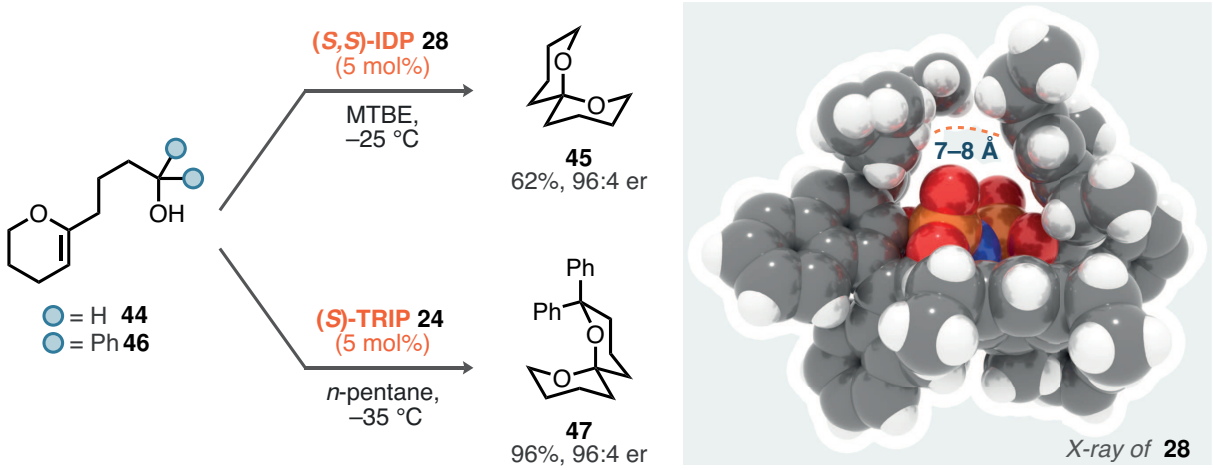

Scheme 1.8: Comparison of List's (top left) with Nagorny's (bottom left) spiroacetalization reaction and X-ray crystal structure of IDP **28** (right).

the insect pheromone olean (**45**) with good yield and excellent enantioselectivity (96:4 er). The fundamental advancement in achieving such drastic selectivity for this small, aliphatic substrate was especially highlighted in comparison to a complementary study using chiral phosphoric acids by Nagorny and co-workers.[107] The decoration of the substrate with two geminal phenyl fragments **46** was necessary to effectively induce enantioselectivity in **48** and kinetically favor the cyclization reaction *via* the Thorpe–Ingold effect.[108] This comparison emphasizes that confinement is crucial not only for stereoselectivity but also for preventing side reactions and potentially controlling chemo- as well as regioselectivity. The notion that an *"ideal confined catalyst shapes a reaction volume that is exclusively complementary to the transition state of the desired transformation by specifically limiting the degrees of freedom of the interacting reactants"*, is clearly evident in the catalyst motifs developed subsequently.[17]

Following the same =O/=NTf exchange logic that led to the development of *N*-triflyl phosphoramides **26** from chiral phosphoric acids, List was able to synthesize imino-imidodiphosphates (*i*IDP **29**, pK_a = 9.1) and imidodiphosphorimidates (IDPi **30** and **31**, pK_a = 4.5 and $\leq$ 2.0, respectively). In particular, the IDPi class of catalysts combines the aforementioned features of confinement with superacidity, positioning them at the tip of the spear of asymmetric catalysis as general anions for a wide variety of transformations.[16,17] The modularity of this catalyst framework (see Scheme 1.5 bottom), offers high potential for structural and electronic modifications, which is crucial for achieving finely tuned properties. Additionally, their acidity establishes them as highly active catalysts for silylium ACDC *via* protodesilylation of a silyl source (see Scheme 1.6).

Using acetaldehyde-derived TES enol silane **51** as nucleophilic reaction partner, IDPi **49** enabled the single aldolization to yield **52** as the sole reaction product with 95 % yield and 99:1 er (Scheme 1.9).[109] Comparable bistriflimide-catalyzed reactions developed by Ya-

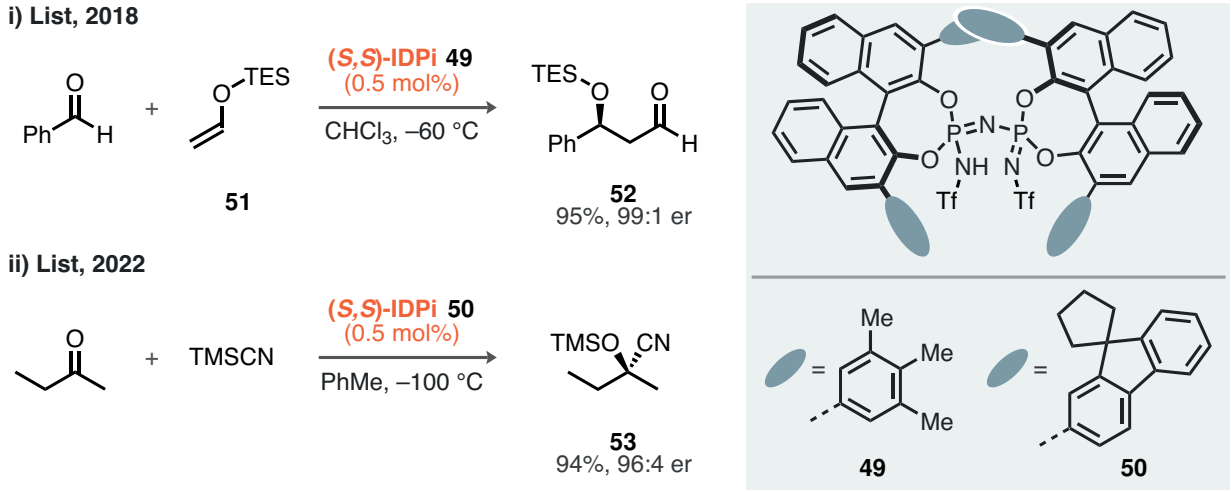

Scheme 1.9: Mukaiyama aldol reaction of acetaldehyde-enol silanes (top) and cyanosilylation of small ketones (bottom) developed by List.

mamoto and co-workers required extremely bulky silyl groups to prevent overreaction;[110] in this case, complete catalyst control excluded the reaction product from the catalytic cycle. Similarly, **50**-catalyzed cyanosilylation of 2-butanone with TMSCN provided TMS-cyanohydrin **53** with excellent yield and enantioselectivity of 96:4 er.

Enantiodifferentiation of this challenging substrate has been rationalized through in-depth density functional theory (DFT) calculations (Figure 1.2). The formation of an equilibrium between the silylated catalyst and HCN was observed by NMR spectroscopy, which supported the conclusion that HCN may form a hydrogen-bonded complex with the silylated IDPi. Prior to nucleophilic attack, isomerization of HCN to HNC and subsequent addition was found to be the lowest-energy pathway. Tight hydrogen-bonding facilitates an *inside attack* by the hydrogen isocyanide onto the siloxocarbenium ion, and the cation is stabilized through a network of non-covalent interactions, primarily involving the fluorenyl substituent of the BINOL backbone and the sulfonyl oxygen atoms of the catalyst's inner core.

These examples of silylium ACDC define the state-of-the-art not only in organocatalysis but also in chemical synthesis as a whole, surpassing the performance of both transition metal catalysis and biocatalysis with engineered enzymes. The advancements made by List and many others over the past 25 years have established organocatalysis as an active field of research, offering complementary activation modes and inspiring further developments.

All three following chapters of this thesis explore the realm of silylium catalysis. Chapter 2 introduces a novel electrophile in asymmetric catalysis, the bis(siloxy)iminium ion, and discusses efforts toward its synthesis *in situ*. These endeavors inspired the design of highly active deprotosilylating agents, silylsulfonamides, which are able to deprotonate alkyl esters; Chapter 3 details their development and application, the first catalytic and stereoselective synthesis of silyl ketene acetals, as well as their direct use in a silicon-catalyzed asymmetric

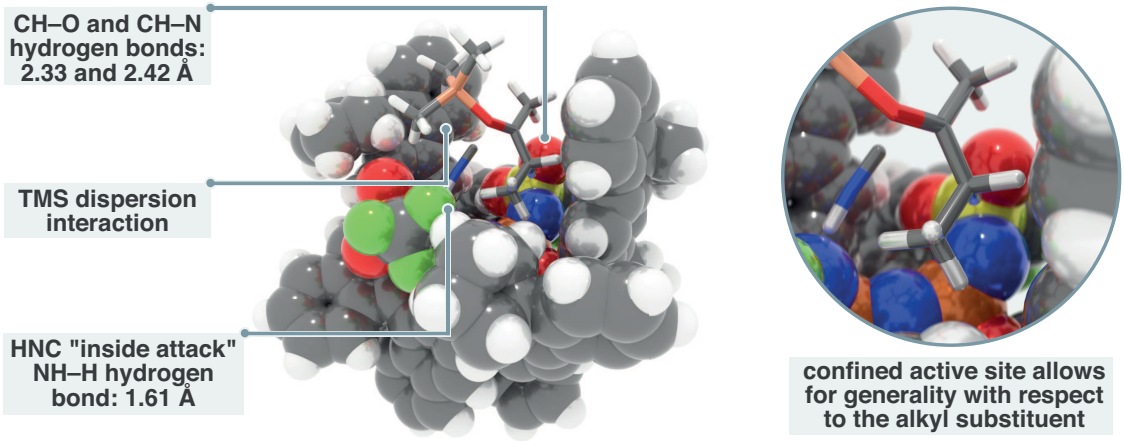

Fig. 1.2: Key interactions in the transition state leading to the major enantiomer of TMS-cyanohydrin **53** in List's cyanosilylation of ketones (B3LYP-D3/def2-TZVP//PBE-D3/def2-SVP).

Mukaiyama–Mannich reaction. The final chapter of this thesis, Chapter 4, steps back from asymmetric catalysis to explore studies towards the total synthesis of the nucleoside core GS-441524 of remdesivir *via* silylium catalysis.

CHAPTER II

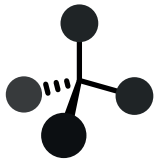

CATALYTIC ASYMMETRIC POLARITY INVERSION OF SILYL NITRONATES

1 Literature Background

The nitro group is one of the fundamental functional groups in chemical synthesis, and nitration chemistry is linked to the very origin of the modern chemical industry. Woulfe was probably the first to use nitric acid for electrophilic nitration in 1771, accidentally synthesizing picric acid from indigo.[111] He was followed by Mitscherlich,[112] Laurent[113], who was the first to distill naphthalene from coal tar, and Muspratt and Hoffmann, who systematically studied the nitration of benzene and toluene.[114] Nitrobenzene, which became known as *essence of mirbane* and a cheap alternative to almond oil, realized its full potential through the discovery of its reduction to aniline using sulfides by Zinin[115,116] and iron by Béchamp,[117] setting the stage for Perkin's first synthesis of mauveine in 1856.[118] These developments laid the foundation for the dye industry, which eventually evolved into the chemical industry as we know it today. Aniline remains the largest single product based on nitration, and only 4 % of its production is used for colorants.[119]

1.1 Transformations of Nitronate Anions: The Henry Reaction

The discovery of nitroalkanes likely dates back to Meyer's discovery of the nucleophilic substitution of alkyl halides with $AgNO_2$.[120] Some of the most powerful functionalizations of nitroalkanes, leveraging their α-acidity, are the Henry[121,122] and aza-Henry[123] reactions, which followed 21 years later. These transformations proceed through the initial deprotonation of nitroalkanes to form nucleophilic nitronate anions, which can react with aldehydes or imines to produce valuable β-amino alcohols and vicinal diamines following subsequent hydrogenation. The significant potential of catalytic asymmetric Henry reactions has been

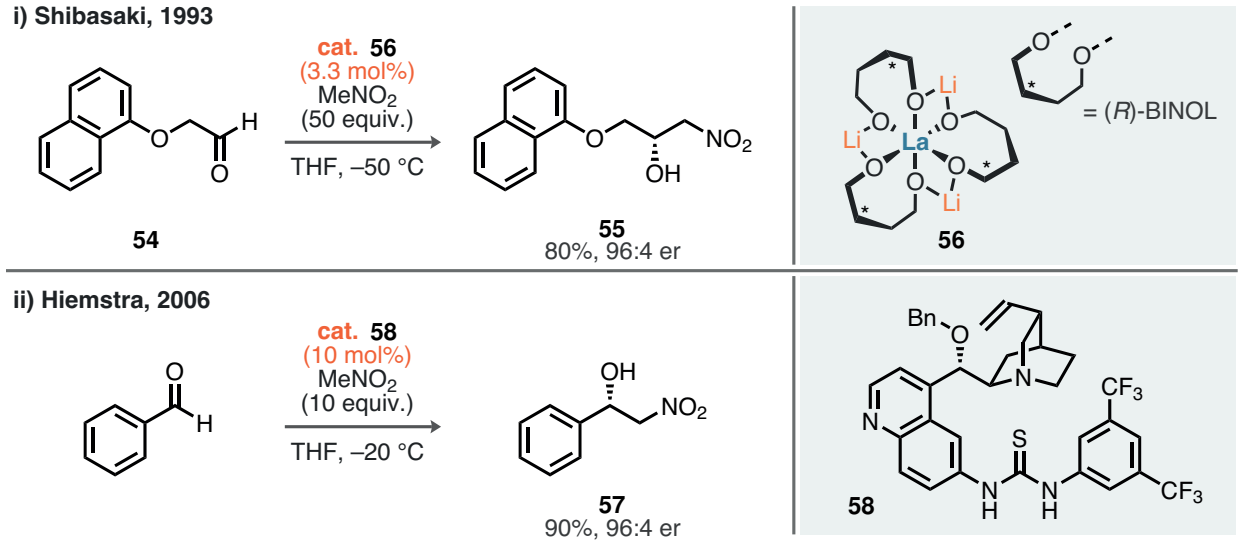

Scheme 2.1: First application of heterobimetallic alkoxide complexes by Shibasaki (i) and first highly enantioselective organocatalytic Henry reaction by Hiemstra (ii).

recognized due to the widespread occurrence of β-amino alcohol motifs in natural products. In the early 1990s, Shibasaki and co-workers developed basic rare earth/alkali metal alkoxide catalysts, with the Henry reaction being the first to showcase their potential (Scheme 2.1).[124,125] For example, the reaction of the aldehyde **54** with nitromethane, catalyzed by the La-Li-(*R*)-BINOL complex **56**, produced a β-nitro alcohol **55** with good yield and excellent enantioselectivity (96:4 er). This product could subsequently be transformed into the β-blocker propanolol through a one-pot hydrogenation/reductive amination sequence.[126,127] Inspired by the high basicity of Shibasaki's heterobimetallic catalyst, significant contributions emerged from his laboratory on the concept of *direct* α-functionalizations of sufficiently acidic pronucleophiles.[128] This topic will be explored further in Chapter 3.

Regarding organocatalytic methods, cinchona alkaloids were early recognized as efficient Brønsted base catalysts; however, they initially yielded only low enantioselectivities.[129] By integrating Schreiner's thiourea hydrogen bonding catalyst motif[130] into the structural framework of quinidine, Hiemstra accomplished the first highly enantioselective organocatalytic Henry reaction.[131] In this transformation, benzaldehyde was treated with nitromethane in the presence of 10 mol% of **58**, resulting in the product **57** with excellent enantioselectivity (96:4 er). The anion-binding capabilities of the thiourea combined with the basicity of quinidine likely played a crucial role in accelerating the enantioselective pathway of this transformation, profiting from several interactions.

Additionally, the high electron density of nitronate anions makes them excellent polarity-matched radical acceptors for electron-poor alkyl radicals. This characteristic was recently demonstrated by Hyster and co-workers in an ene-reductase-catalyzed cross-electrophile coupling between alkyl halides and nitroalkanes.[132]

1.2 The Discovery of Silyl Nitronates

In contrast to uncharged nitrones and nitrile oxides, which undergo rapid (3+2) cycloaddition reactions, direct cycloadditions of nitronate anions are typically not feasible. However, in 1974, Kashutina, Ioffe, and Tartakovskii demonstrated that nitroalkanes can undergo (3+2) cycloadditions with simple olefins when reacted with bis(trimethylsilyl)acetamide (BSA). This reaction generates a silyl nitronate *in situ*, a neutral form of the nitronate.[133] Subsequent studies on cycloadditions of silyl nitronates were conducted by Torssell,[134] while Seebach explored their application in classical nitronate anion chemistry. This involved anion-initiated Henry reactions[135–137] and the successive deprotonation of nitroalkanes.[138] Seebach and Dunitz were pioneers in conducting in-depth structural studies on silyl nitronates, as illustrated in Scheme 2.2 (right).[139] Although the use of silyl nitronates as nitronate anion precursors has proven highly valuable from the perspectives of functional group tolerance and catalysis—Maruoka developed an asymmetric phase transfer-catalyzed bifluoride-initiated variant of Seebach's reaction[140]—these studies did not explore the arguably most intriguing characteristic of silyl nitronates. This aspect links back to the discovery of the Nef reaction (Scheme 2.2 left); when attempting to hydrolyze the sodium nitronate **59** of nitroethane with diluted sulfuric acid, Nef did not detect any traces of nitroethane but instead found acetaldehyde and nitrous oxide.[141] The formation of a protonated nitronic acid species, such as **60**, most likely facilitated the nucleophilic attack by water, leading to an α-hydroxy nitroso acetal **61**, which immediately decomposed into formal hydrolysis products. These studies highlighted that after initial protonation, the tautomerization of the nitronic acid to the nitroalkane was sufficiently slow to allow for a second protonation event, adequately activating **60** for a subsequent nucleophilic attack *via* overall polarity inversion (*Umpolung*[142]) of the sodium nitronate **59**. In principle, this concept of electrophilic nitronate activation could be directly applied to silyl nitronates, particularly when considering the resonance structures **62a** and **62b**.

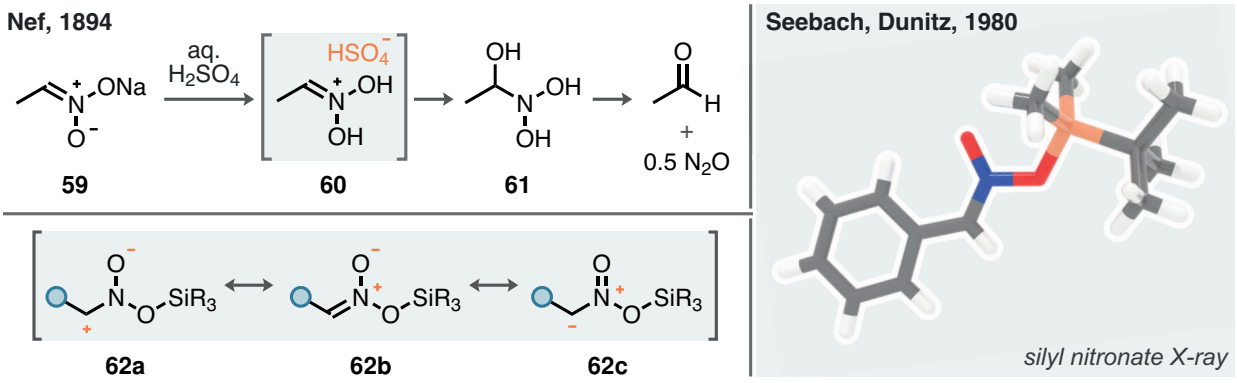

Scheme 2.2: The Nef reaction (top), Seebach's and Dunitz's X-ray crystal structure of a (nitromethyl)benzene-derived silyl nitronate (right), and resonance structure analysis (bottom).

1.3 Polarity Inversion of Alkyl and Silyl Nitronates

After Nef's foundational studies at the end of the 19th century, the polarity inversion chemistry of nitronates remained dormant for over 100 years. Advancements in the area of [4+2] cycloadditions between nitroalkanes and alkenes have facilitated access to cyclic alkyl nitronates,[143] and Ioffe showcased the addition of a wide array of silyl nucleophiles to alkyl nitronates (Scheme 2.3 top).[144] NMR studies on the association of alkyl nitronate **63** with TBSOTf indicated significant deshielding of the α-proton from 6.51 to 8.08 ppm, suggesting the formation of alkylsiloxyiminium ion **64**, similar to **60**. The addition of various nucleophiles, such as an acetophenone-derived enol silane, *N*-silyl enamine, and methallyl stannane, yielded nitroso acetals **65**–**67** in moderate to good yields. This methodology was

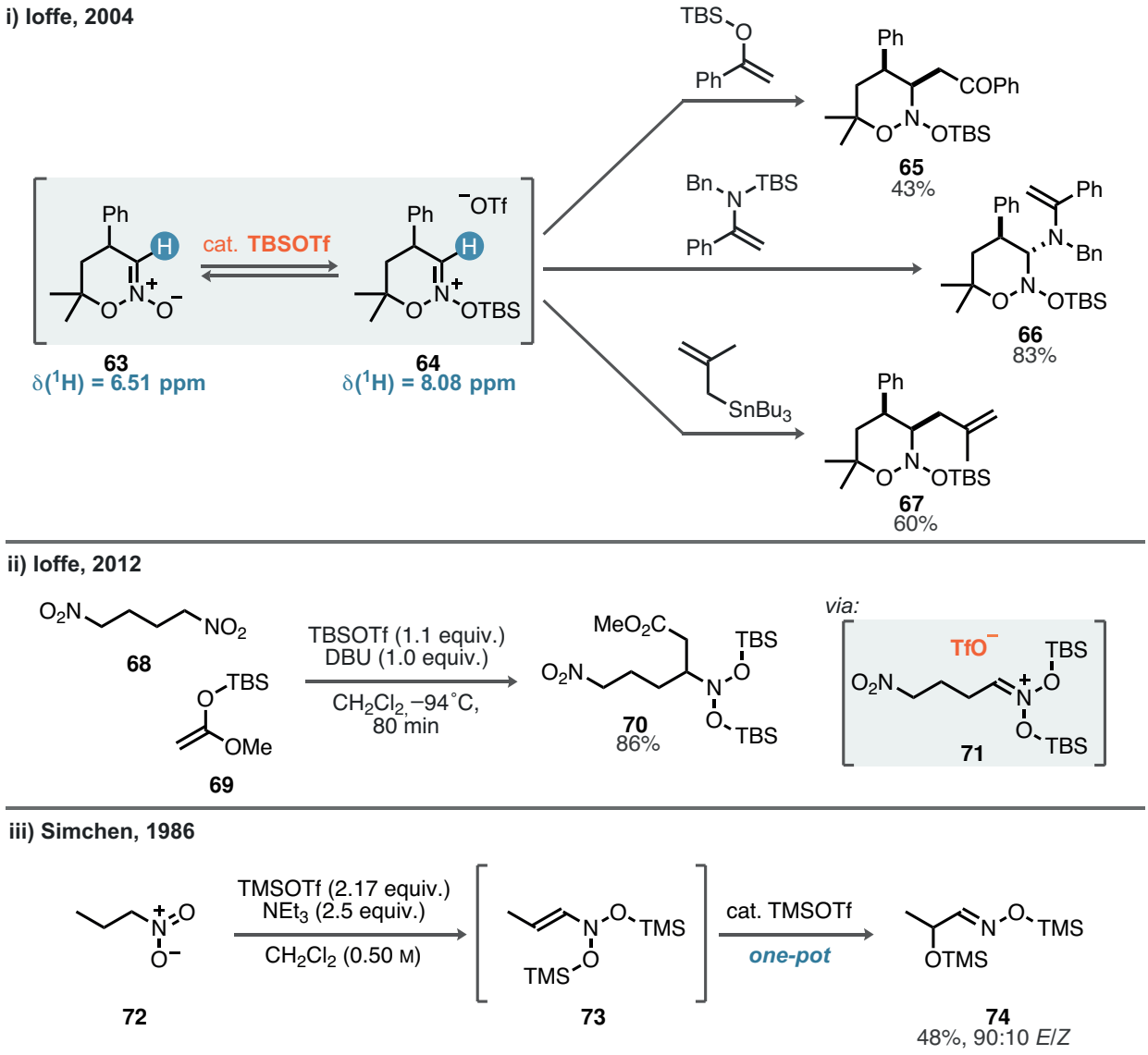

Scheme 2.3: Ioffe's alkyl nitronate (top) and acyclic one-pot silyl nitronate polarity inversion reactions (middle), as well as Simchen's successive silylation experiments (bottom).

later extended to include cyano- and aminosilylations of cyclic nitronates.[145–147] A collaborative kinetic study described by Mayr and Ioffe involved a series of reactions with a single silyl nitronate,[148] while the comprehensive scope of silyl nitronate polarity inversion was delineated by Ioffe in 2012 (Scheme 2.3 middle).[149] The reaction of 1,4-dinitrobutane **68** with silyl ketene acetal **69** and a slight excess of TBSOTf in the presence of DBU produced the silyl nitronate *in situ*. Subsequent activation by TBSOTf led to the formation of bis(siloxy)iminium ion **71**, which rapidly underwent nucleophilic addition by **69** to give **70** with 86 % yield.

The combination of large silyl electrophiles with bulky bases relates to the concept of Frustrated Lewis Pairs (FLPs), which consist of two highly Lewis-acidic and Lewis-basic components whose interaction is constrained by steric repulsion.[150,151] Although the modern approach to FLPs predominantly resides within inorganic chemistry and explores the activation of small molecules (such as H_2 or N_2), Simchen investigated the *in situ* silylation of nitroalkanes as early as the late 1980s using combinations of silyl triflates with NEt_3.[152,153] The *in situ* generated silyl nitronate was further silylated and deprotonated by the excess base present, forming bis(siloxy)enamine **73**. Simchen discovered that these compounds easily undergo Lewis acid-catalyzed heterolytic *N,O*-cleavage followed by oxa-Michael addition to the resulting silyl-nitrosylium ion. This process results in an overall β-polarity inversion of enamines, yielding α-siloxy oxime **74** in moderate yield. Isolation of bis(trimethylsiloxy)enamines, such as **73**, was straightforward, and larger silyl groups were found to favor the rearrangement.

Although the field of asymmetric catalysis acknowledged the utility of silyl nitronates in organic synthesis, their applications were primarily restricted to serving as precursors for nitronate anions, as demonstrated by Maruoka and Jørgensen,[140,154,155] or as radical acceptors, as shown by MacMillan.[156] However, the true potential of silyl nitronates lies in their ability to undergo activation by silylium Lewis acids, rendering them exceptionally potent electrophiles. This potential has been effectively demonstrated by Ioffe.[144–149] Given the confirmed intermediacy of bis(siloxy)iminium ions **71**, this challenge is particularly compelling in the context of silylium ACDC.

Our findings regarding the introduction of bis(siloxy)iminium ions into the field of silylium ACDC for the synthesis of aliphatic β^3-amino acids will be presented in Section 3 of this chapter.

2 Objectives

As discussed in the previous section, the strong activation of silyl nitronates to produce bis(siloxy)iminium ions stands in stark contrast to the lack of methods for their catalytic asymmetric functionalization with nucleophiles. Preliminary computational analysis of the molecular electrostatic potential (MEP) in the successive silylation series from a nitronate anion to a bis(siloxy)iminium further solidifies the polarity inversion of these species (Scheme 2.4). The consequences of silylium activation of a nitronate are also well reflected in the natural population analysis (NPA) charge[157] at the α-carbon atom. This analysis indicates *nucleophilicity* in nitronate **75** (-0.24), *ambiphilic* behavior in the silyl nitronate **76**, and *electrophilicity* in the bis(siloxy)iminium ion **77** (0.20).

The objective of this chapter is to introduce bis(siloxy)iminium ions such as **77** into the realm of silylium ACDC. Starting from silyl nitronate **78**, the reaction with a silyl nucleophile, such as an alkyl ester-derived silyl ketene acetal **79**, would activate **78** *in situ*, forming the chiral complex **80** through ion-pairing with the catalyst anion (Scheme 2.5). Given the extreme levels of reactivity and confinement achieved with the IDPi class of catalysts, these will be primarily investigated (see Section 2.3). Strong interactions with the catalyst anion, *via* a range of non-covalent interactions, would ideally grant highly enantioselective access to β-alkylcarboxy nitroso acetals **81**. Moreover, if substituted silyl ketene acetals **79** could be utilized, two stereocenters would be generated through the formation of a single strategic C$-$C σ-bond with potentially high diastereoselectivity under complete catalyst

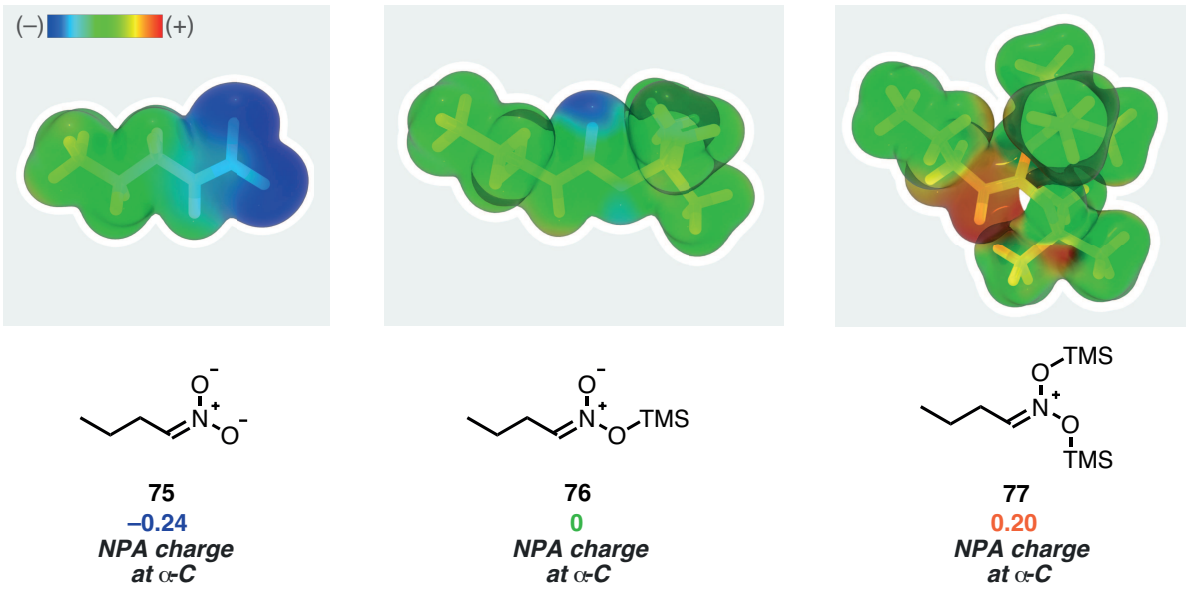

Scheme 2.4: Electron density surface (isovalue 0.007) colored by molecular electrostatic potential and natural population analysis of the successive silylation series from **75** to **77** (M06-2X/def2-QZVP//r2SCAN-3c).

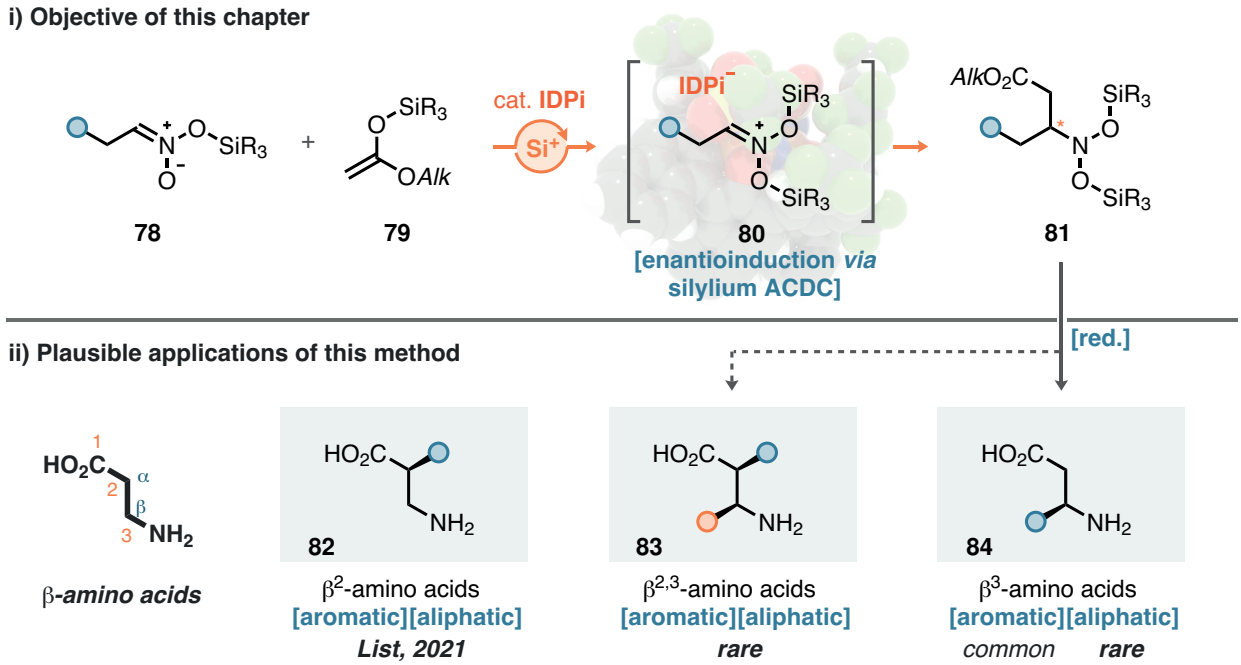

Scheme 2.5: Objective of this chapter (top) and plausible applications in the synthesis of β^3-amino acids (bottom).[160]

control. Considering the detailed NMR studies by Ioffe and Mayr,[148] who observed silyl transfer from TBSOTf to the nitronate, similar experiments could provide profound insight into the mechanism of ion pairing in silylium ACDC.

In addition to the fundamental potential of achieving the first catalytic asymmetric polarity inversion of silyl nitronates, the overall transformation mirrors the retrosynthetic disconnection of the Mannich reaction.[158,159] Nitroso acetals **81** would require only a simple reduction step to reach the amine oxidation state, positioning this proposed transformation in the highly sought-after context of β-amino acids.[161] The confined active site of the IDPi catalyst is ideally suited for the transformation of small aliphatic substrates, offering a complementary strategy to existing methods.[162,163]

Once a successful stereoselective method has been developed, a *direct* variant starting from nitroalkanes, instead of silyl nitronates, capitalizing on their sufficient α-acidity, will be explored.

3 Results and Discussion

The work described in Sections 3.1–3.3 was conducted in collaboration with Dr. Sayantani Das and Dr. Chandra Kanta De.

3.1 Establishing Reactivity, Challenging Selectivity

We commenced our initial investigations with the TBS-silyl nitronate **85**, selected for its stability,[164] in the reaction with silyl ketene acetal **69** to produce **86**, catalyzed by 2.5 mol%

Table 2.1: Initial catalyst screening of the reaction between **85** and **69**. Reactions performed on 0.025 mmol scale; conversion determined by ^{1}H NMR using Ph_3CH as an internal standard; [a] PhMe-d_8/*n*-pentane 1:1 *v*/*v*, −120 °C.

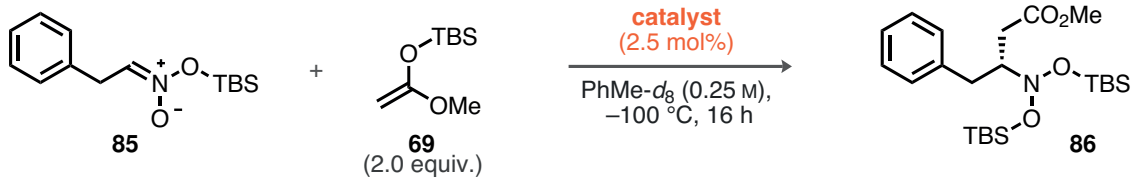

entry	catalyst	conversion	er **86**
1	**25**	traces	76:24
2	**30**	>95 %	27:73
3	**87**	>95 %	75:25
4	**88**	>95 %	62.5:37.5
5	**89**	>95 %	35:65
6	**90**	>95 %	92.5:7.5
7	**91**	>95 %	94:6
8[a]	**91**	22 %	96:4

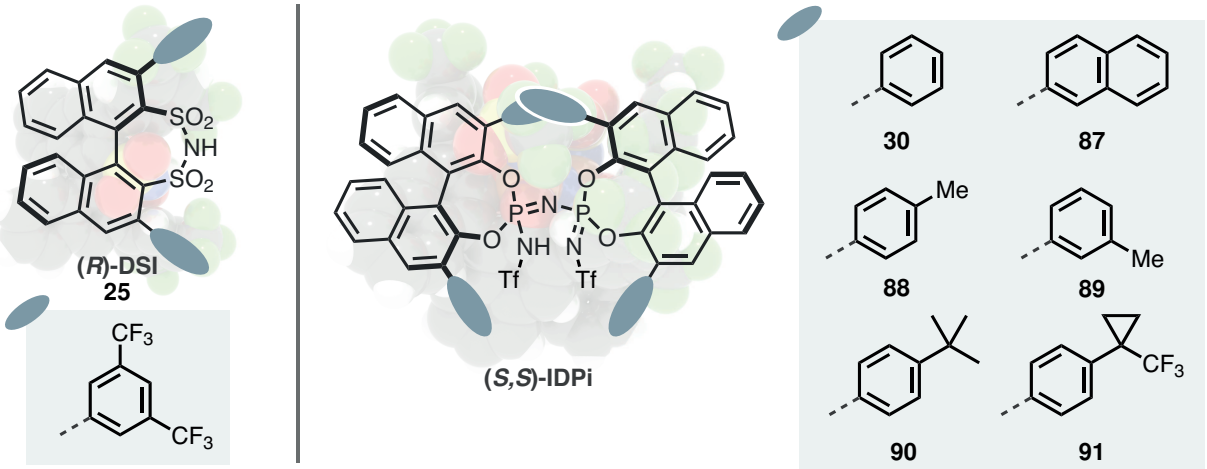

of DSI **25** or IDPi **30** at −100 °C (Table 2.1). The choice of solvent is crucial for asymmetric catalysis. Non-polar solvents that favor ion pairing are highly important; chlorinated solvents like $CHCl_3$ or CH_2Cl_2 were found to be detrimental for similar transformations by List,[165] making toluene a natural choice. DSI **25** ($pK_a = 8.4$) provided **86** in only trace amounts with moderate enantioselectivity (entry 1, 76:24 er). Switching to significantly more acidic IDPi catalysts led to a drastic increase in exclusive reactivity towards **86** in all cases (entries 2–7). It should be noted that, although only conversions of the starting material were determined, all reactions discussed proceeded selectively towards the product. Phenyl-substituted catalyst **30** ($pK_a = 4.5$) yielded the product with promising enantioselectivity (entry 2, 27:73 er), and an interesting change in selectivity for the preferred enantiomer was observed upon the introduction of a 2-naphthyl substituent in the 3,3'-positions (entry 3). This shift in selectivity was observed again by changing the position of the methyl group in the 3,3' substituent (entries 4 and 5). However, the 4-substituted phenyl fragments were identified as the best for this transformation; IDPi **91** with a particularly interesting trifluoromethyl cyclopropane-modified phenyl substituent in the 3,3'-positions was identified as the best catalyst, providing the product with very good enantioselectivity (94:6 er). Attempts to lower the reaction temperature further were limited due to the melting point of toluene (−95 °C); using a 1:1 (v/v) mixture of toluene-d_8 and n-pentane allowed the reaction to proceed slowly at −120 °C, resulting in the product with excellent selectivity (96:4 er).

Confronted with the challenge of exploring this reaction further by investigating several silyl nitronates besides **85**, we chose to elongate the alkyl chain between the nitronate and phenyl moieties and investigate silyl nitronate **92** (Table 2.2). In contrast to the high levels of enantioselectivity achieved with the initial substrate **85**, selectivity for product **93** was drastically reduced (entry 1, 73:27 er). Fluorenyl-substituted IDPi catalysts have been established as privileged motifs for a range of different transformations,[166,167] and drew our attention to this particular substrate. Systematic investigation of the effect of the inner core substituents demonstrated a stark preference for perfluoroalkyl cores (entries 2 and 3, IDPis **95** and **94d**), resulting in an optimal enantioselectivity of 98.5:1.5 er with triflyl core-IDPi **94** (entry 7).

Substrates **85** and **92** differ by the presence or absence of a methylene group; the requirement for two distinct catalyst frameworks to achieve high enantioselectivity is intriguing and may suggest very strong interactions between the plausible bis(siloxy)iminium ion and the catalyst anion. Although this difference is fundamentally interesting and indicative of a highly confined microenvironment, we aimed to expand the already high levels of selectivity achieved to a broad scope of nitroso acetals. For this reason, and in light of the success and efficiency of multi-substrate screening approaches in the past,[168,169] we decided to follow a substrate-pooling strategy.

Table 2.2: Initial screening for reactivity and enantioselectivity in the reaction between **92** and **69**. Reactions performed on 0.025 mmol scale; conversion determined by ^{1}H NMR using Ph_3CH as an internal standard.

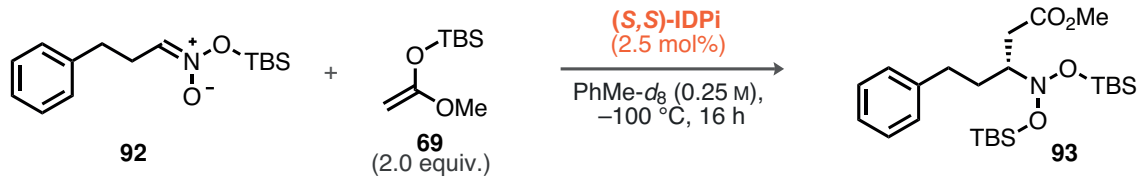

entry	catalyst	conversion	er **93**
1	**91**	>95 %	73:27
2	**94e**	>95 %	46.5:53.5
3	**94d**	>95 %	94.5:5.5
4	**94c**	>95 %	95.5:4.5
5	**94b**	>95 %	96:4
6	**94a**	>95 %	96:4
7	**94**	>95 %	98.5:1.5

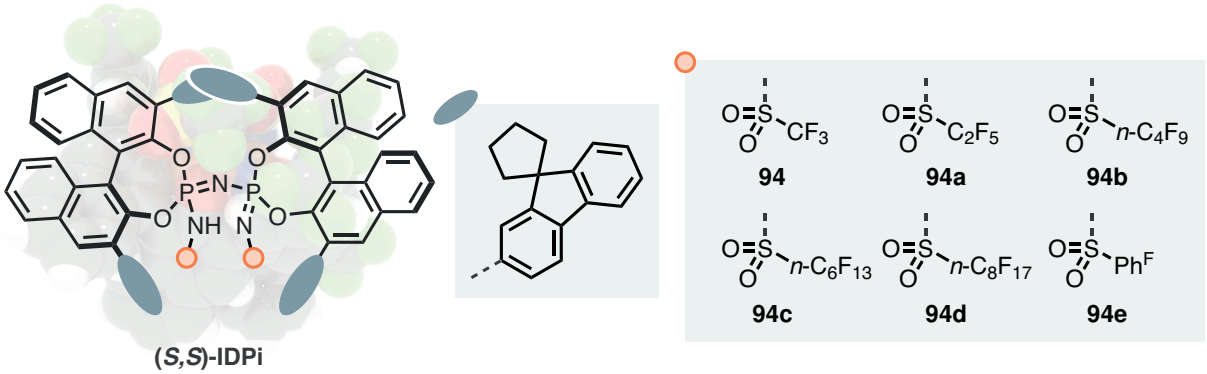

3.2 Multi-Substrate Screening: Accelerating Catalyst Discovery

We focused on the reactions of mixtures of four different silyl nitronates in the presence of an excess of silyl ketene acetal **69** and distinct IDPi catalysts, yielding a theoretical 24 enantiomeric ratios from just six reaction vessels. To represent structural features reflected in our preliminary screening efforts, we chose the model substrate (product **86**). Additionally, we elongated the alkyl chain between the silyl nitronate and the phenyl ring further (product **98**). We investigated the substitution at the phenyl ring of the model substrate (product **97**) and incorporated the effect of functional group tolerance using a heterocyclic substrate (product **96**).

Separation of the respective racemic mixtures is a key requisite for successful multi-substrate screening. Straightforward optimization using a reverse-phase HPLC approach

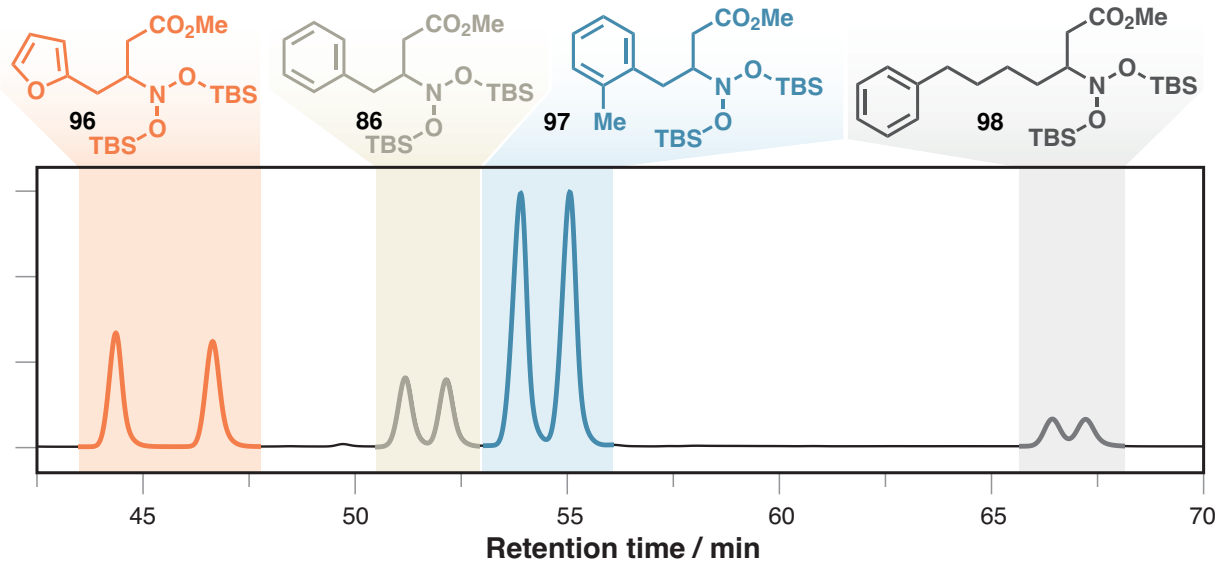

Scheme 2.6: Optimized RP-HPLC chromatogram of a mixture of the racemates chosen for the multi-substrate screening study (OJ-3R, 60:40 MeCN/H_2O, 1.0 mL/min).

provided complete baseline separation of all peaks (Scheme 2.6). To ensure full conversion of the silyl nitronates, we conducted the reactions at −100 °C for an extended period (20 vs. 16 h). If needed for improved enantioselectivity, reactivity would still be maintained even at −120 °C (Table 2.1, entries 7 and 8).

The silica-gel chromatographic properties of the nitroso acetal products were ideally suited for substrate-pooling: on NEt_3-deactivated silica gel TLC plates, all compounds investigated showed similar R_f values with 4 % MTBE in hexanes, allowing for the isolation of pure mixtures of the four products after simple preparative TLC. In principle, reverse-phase HPLC systems should also be able to tolerate the direct injection of crude reaction mixtures; however, this strategy was not pursued in the study described herein.

Scheme 2.7 shows the result of the multi-substrate screening. The color-coded product (see Scheme 2.6) is plotted against the respective IDPi catalyst (Scheme 2.7 top), with the height of the bar indicating the enantiomeric excess. For simplicity and to avoid switches in enantioselectivity, the absolute values of the enantiomeric excess are shown (for a full list of enantiomeric ratios, please see the Appendix, Table A.1). Several trends and differences become visible upon inspection of Scheme 2.7. The 2-furanyl nitroso acetal **96** exhibits inferior selectivity performance with the optimal IDPi catalyst **91** compared to the model substrate **86** (84.5:15.5 vs. 93:7 er). Additionally, the enantioselectivity with the spiro-fluorenyl IDPi **94**, which was identified by a traditional screening round for substrate **93**, was observed to be moderate (80:20 er), emphasizing the importance of this multi-substrate approach. Interestingly, a 3-biphenyl-substituted IDPi, which provided almost racemic product with a triflyl core (**99b**, 55.5:44.5 er), showed a strong preference for a perfluorophenylsulfonyl inner core

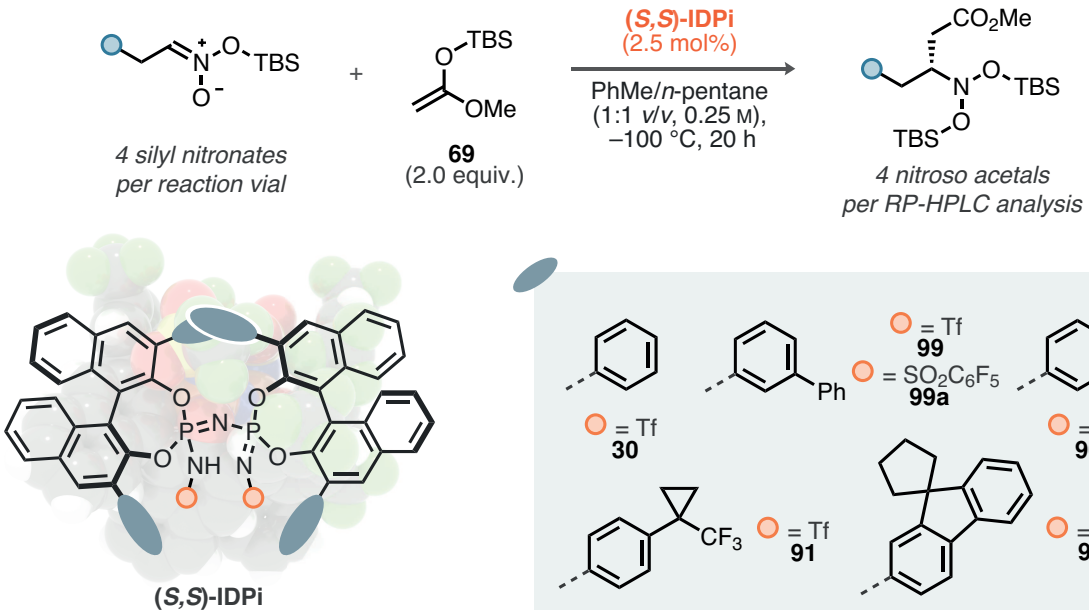

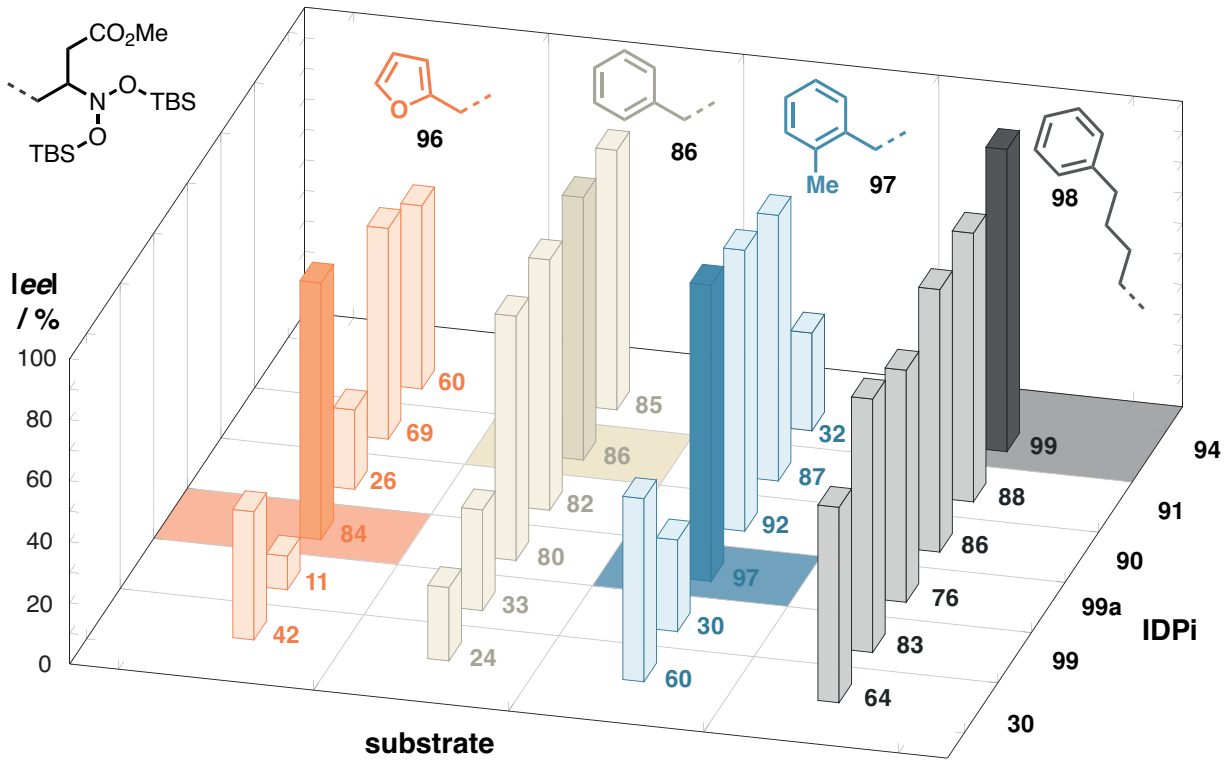

Scheme 2.7: Reaction conditions (top, total scale of 0.025 mmol) and results of the multi-substrate screening (bottom); full conversion was determined by ^{1}H NMR spectroscopy; HPLC conditions: OJ-3R, 60:40 MeCN/H_2O, 1.0 mL/min.

in **99a**, resulting in the best selectivity obtained (92:8er).

IDPi **99a** also demonstrated excellent performance for the 2-tolyl substrate **97** (98.5:1.5 er) compared to the trifluoromethyl-cyclopropane IDPi **91** (93.5:6.5 er). The comparison between the 4-(*tert*-butyl)phenyl **90** and 4-((trifluoromethyl)cyclopropyl)phenyl IDPi **91** is particularly intriguing; while **91** provided higher enantioselectivity for the model substrate **86** (Table 2.1, entries 6 and 7), the enantioselective conversion of the 2-tolyl silyl nitronate **97** appears to be preferred by IDPi **90** (96:4 vs. 93.5:6.5 er). Moreover, the preference of spiro-fluorenyl IDPi **94** for aliphatic-like substrates continued to improve, providing the nitroso acetal **98** with near-perfect enantioselectivity (99.5:0.5 er).

In summary, the optimization of enantioselectivity in this particular reaction efficiently demonstrated the limits of single-substrate optimization. When dealing with weak interactions, such as in asymmetric catalysis, seemingly small differences can tip the scale in either direction. This makes multi-substrate approaches an essential method for gaining a comprehensive understanding of the reactivity and selectivity landscape.[170]

3.3 Scope, Limitations, and Practicability

With our optimized IDPi catalysts **91**, **94**, and **99a** in hand, we set out to explore the scope and limitations of this method (Scheme 2.8).

Generally, all derivatives of the homobenzyl model substrate **86** required reaction times of 3 d at −120 °C and were obtained in excellent yields with very good to excellent enantioselectivities. The dichotomy of these substrates necessitating either IDPi **91** or **99a**—as indicated by the multi-substrate screening—persisted upon inspection of a larger portion of chemical space, with no clear trend visible. Taking all those results together, it seems reasonable to conclude that IDPi **99a** is a more general catalyst for this transformation. We also evaluated the reaction of two silyl nitronates with vinyl silyl ketene acetal **100** (E/Z=11:89) and were able to obtain the α,β-unsaturated methyl ester nitroso acetals **105** and **123** in very good yields and excellent enantioselectivities (99.5:0.5 and >99.5:0.5 er, respectively).

The most striking performance of spiro-fluorenyl IDPi **94** was revealed in the reactions of aliphatic and heteroatom-containing aliphatic substrates. In total, 17 distinct nitroso acetals could be synthesized using this single catalyst, all in excellent yields and enantioselectivities. Among those investigated, only *N*-indolyl product **109** required re-optimization of the catalyst (87:13 er with IDPi **94**), resulting in a *tert*-butyl-modified variant **122** of catalyst **94**. Overall, higher selectivities allowed for higher reaction temperatures and, consequently, shorter reaction times. Aliphatic nitriles (**110**, 95:5 er), ethers (**111** and **112**, 98:2 er and 97.5:2.5 er, respectively), esters (**113**, >99.5:0.5 er) and amides (**119**, 96:4 er), as well as halogens (**114** and **115**, both 97.5:2.5 er) were well tolerated under the reaction conditions.

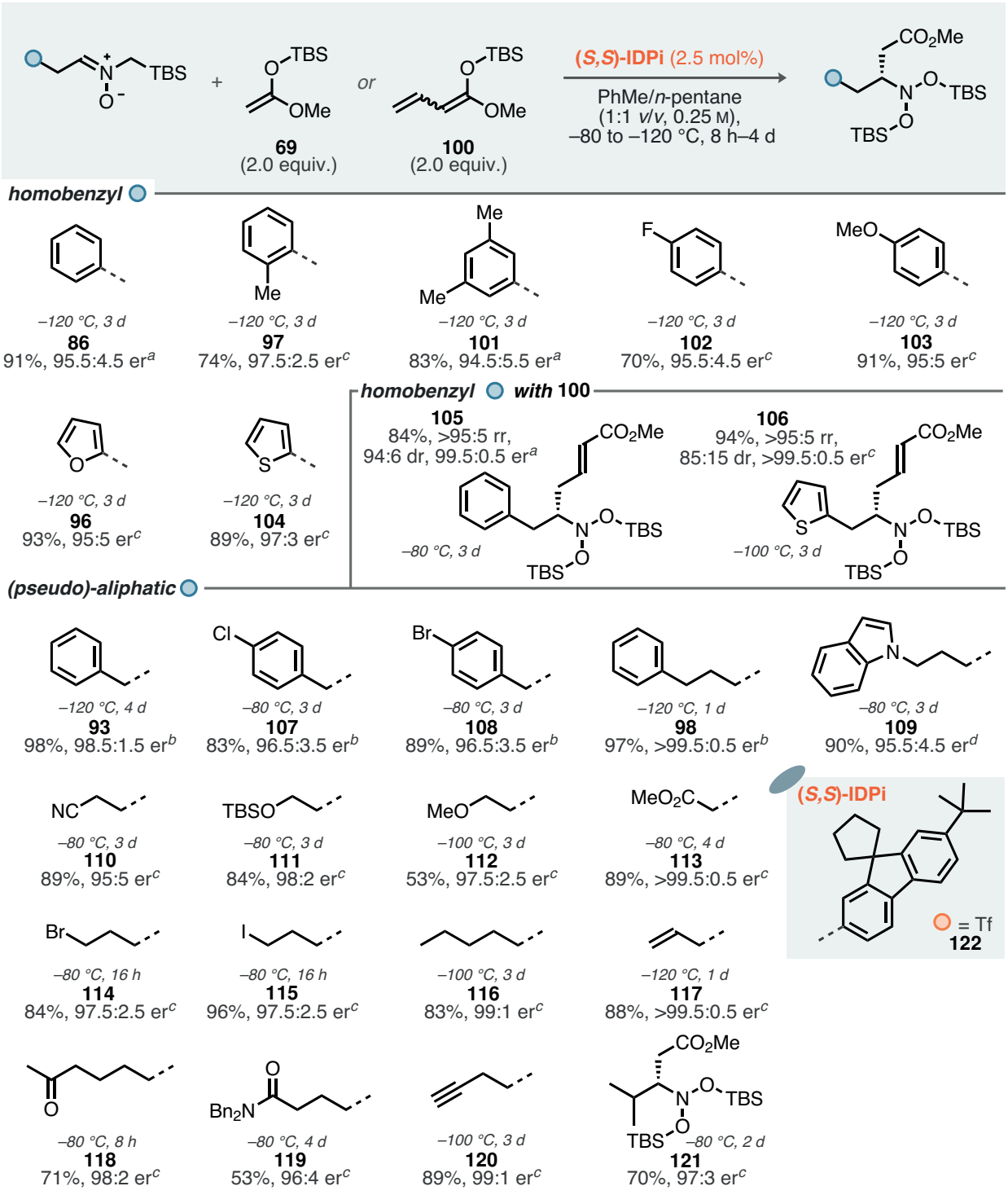

Scheme 2.8: Substrate scope of the IDPi-catalyzed nucleophilic addition of silyl ketene acetals **69** and **100** to silyl nitronates. Reactions performed on 0.1 mmol scale; isolated yields and enantiomeric ratios are reported; dr and rr were determined by ^{1}H NMR analysis of the crude mixtures; [a] with IDPi **91**; [b] with IDPi **94**; [c] with IDPi **99a**; [d] with IDPi **122**.

Strong chemoselectivity was observed in the selective formation of ketone-containing nitroso acetal **118**, showing no indication of the Mukaiyama aldol reaction in the crude reaction mixture. This result underscores the facile activation of silyl nitronates by silylium catalysis and opens up possible avenues toward the late-stage functionalization of complex molecules.

We furthermore investigated the reactions of methyl propionate-derived silyl ketene acetals **124a** and **124b** (Table 2.3).

Initial screening efforts on the optimized catalyst **91** for the addition of the unsubstituted silyl ketene acetal **69** to **85** revealed inferior levels of enantioselectivity (75:25 er), which shifted the focus to IDPis **99a** and **94**. The reactions of the (*E*)-enriched silyl ketene acetal **124a** were highly selective, with spiro-fluorenyl IDPi **94** providing both diastereoisomers with better enantioselectivity but lower diastereoselectivity compared to 3-biphenyl IDPi **99a** (entries 1 and 2).

Using identical reaction conditions for (*Z*)-enriched **124b**, a constrasting *diastereodivergence* was observed, with IDPi **99a** selectively providing **125a** (entry 3, >95:5 dr) and IDPi **94** the *anti*-diastereomer **125b** with lower levels of diastereoselection (entry 4, 29:71 dr). In addition to the high selectivity and diastereodivergence between both sets of reaction conditions, *enantiodivergence* for the *syn*-diastereomer with respect to the silyl ketene acetal was observed (see the major enantiomer of **125a** for entries 1–4). Conducting the reactions with **124b** at lower temperatures (−80 °C and −100 °C) further increased the diastereodivergence, resulting in a virtually complete selectivity for either diastereomer with excellent enantioselectivities (96:4 er for **125a** and >99.5:0.5 er for **125b**). The yields and selectivities were also consistent in the translation to the isolation-scale conditions (entries 7 and 8).

In principle, by just using two different IDPi catalysts and silyl ketene acetals, we were able to gain access to 3 out of the 4 possible stereoisomers of nitroso acetal **125**. In contrast to transformations of boron-enolates, which proceed *via* closed transition states, reactions of silyl ketene acetals typically operate through open transition states.[171]

This invites the possibility for modulation of the diastereoselectivity by the catalyst, and a pronounced effect of absolute catalyst control over this highly strategic C−C bond formation was observed here. Control experiments of monitoring the relative configuration of **124** in the presence of silylated IDPi catalysts **99a** and **94** by ^{1}H NMR excluded the possibility of isomerization prior to nucleophilic addition. The observed diastereodivergence is likely a consequence of the strong interactions between the bis(siloxy)iminium ion and the anion. Depending on the exact catalyst structure, the confined active site allows for only one of the two diastereomers to be formed. In case of IDPi **99a**, the selectivity may be governed by CH···π interactions, whereas the spiro-fluorenyl IDPi **94** may operate by virtue of dispersion interactions. However, the results also demonstrate that the structure of the silyl ketene acetal is somewhat recognized by the catalyst, and the exact origin of the change

Table 2.3: Optimization of the diastereoselective addition of **124a** and **124b** to **85**. Reactions conducted on 0.025 mmol scale; yields and diastereomeric ratios determined by ^{1}H NMR using mesitylene as an internal standard; [a] at −80 °C; [b] at −100 °C; [c] for 92 h, 0.10 mmol scale, isolated yield.

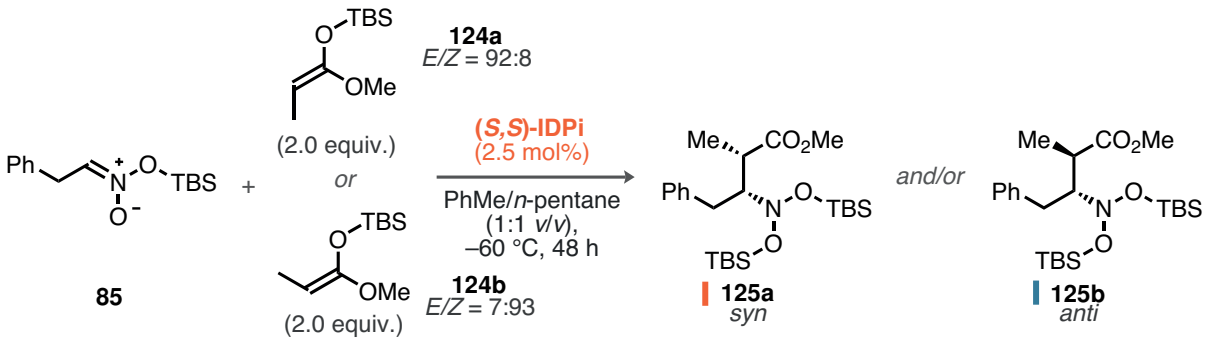

entry	cat.	**124**	yield	dr (*syn*:*anti*)	er (*syn*)	er (*anti*)
1	**99a**	**a**	15 %	>95:5	14:86	91:9
2	**94**	**a**	94 %	73:27	4:96	99:1
3	**99a**	**b**	79 %	>95:5	93.5:6.5	72:28
4	**94**	**b**	92 %	29:71	93:7	98.5:1.5
5[a]	**99a**	**b**	65 %	>95:5	96:4	79:21
6[b]	**94**	**b**	89 %	9:91	95:5	>99.5:0.5
7[a,c]	**99a**	**b**	60 %	>95:5	96:4	79.5:20.5
8[b,c]	**94**	**b**	87 %	10:90	95.5:4.5	>99.5:0.5

in enantioselectivity for **124a** as compared to **124b** remains unclear. One may conclude a stronger recognition of the (*E*)-silyl ketene acetal by the catalyst.

3.3.1 Limitations

The broad scope of nitroso acetals is contrasted by the inability of our method to convert the (nitromethyl)benzene-derived silyl nitronate selectively (Table 2.4). In general, the best catalyst motifs for the majority of the substrates, except for spiro-fluorenyl IDPi **94**, also performed best for **126** (catalysts **99**, **91**). Two reasons could be identified for the lower enantioselectivity in the formation of **127**. (1) Reactivity of the silyl nitronate **126** was comparably low, requiring higher reaction temperatures and reducing the applicability of perfluoroarylsulfonyl-core IDPis such as **99a** due to their assumed lower acidity. (2) The enantioselectivity was found to be less temperature-dependent. Comparing entries 5 and 6 in Table 2.4, the enantioselectivity increased from 73:27 er (at −40 °C) to 78:22 er (at

Table 2.4: Screening of the reactivity and enantioselectivity of silyl nitronate **126** with **69**. Reactions performed on 0.025 mmol scale; conversion determined by ^{1}H NMR using Ph_3CH as an internal standard.

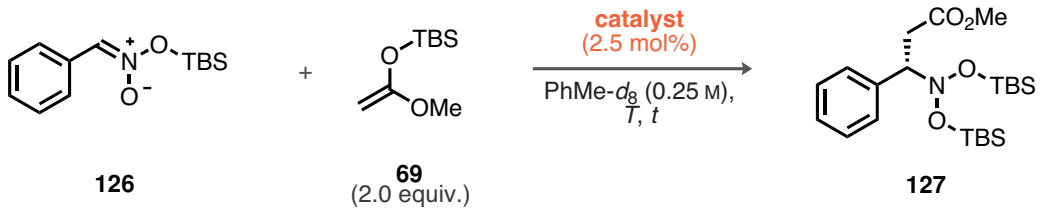

126 **69** (2.0 equiv.) **127**

entry	catalyst	T/°C	t/h	conversion	enantiomeric ratio
1	**30**	−40	18	>95 %	54:46
2	**99**	−40	18	93 %	75:25
3	**99**	−80	96	80 %	81.5:18.5
4	**99a**	−40	18	traces	84:16
5	**90**	−40	18	>95 %	73:27
6	**90**	−80	96	66 %	78:22
7	**91**	−100	18	traces	82.5:17.5
8	**87**	−40	18	>95 %	71:29
9	**94**	−40	18	73 %	56:44

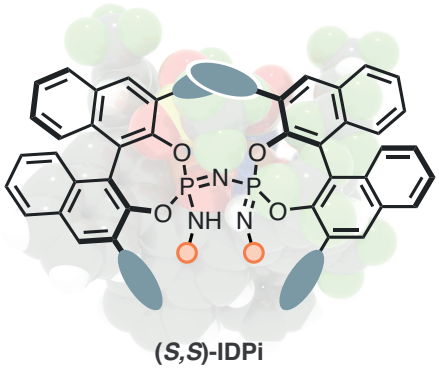

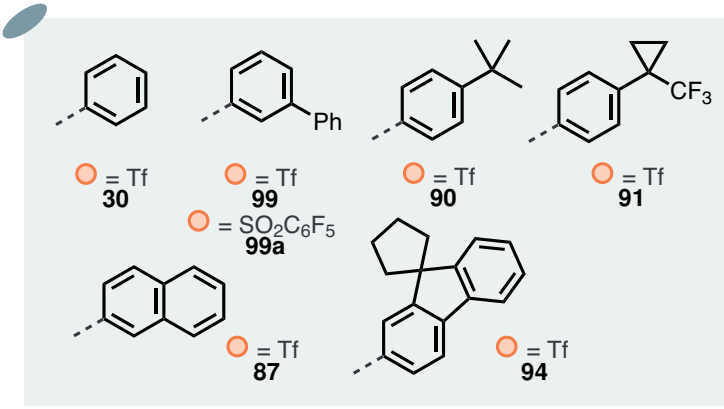

−80 °C) upon cooling of the reaction mixture by 40 K. The reaction of model substrate **86** at −45 °C proceeded with a comparable selectivity of 79:21 er; however, at −80 °C, the product was obtained with 91:9 er. Speculating with the implications of transition state theory, a lower temperature-dependence of the enantioselectivity manifests in a greater importance of the entropy of activation $\Delta\Delta S^{\ddagger}$. This lower temperature-dependence also means that there is a stronger dependence on the catalyst structure. Additional rounds of framework screening are very likely to provide a solution to this problem. Considering the vast majority of Mannich reactions of aromatic imines that have been developed,[162,172,173] further work

was discontinued. Aside from this particularly hard to optimize substrate in the reaction with silyl ketene acetal **69**, the reactions with allyl- and methallylsilanes instead of **69** were investigated with nitronates **85** and **128**. Using our optimal reaction conditions with IDPi **91** at −120 °C or 10 mol% of TBSOTf in toluene at −80 °C, no reaction was observed with either nitronate and TBS allyl- as well as methallylsilane. This is most likely a consequence of the low temperatures and the reduced nucleophilicity of allylsilanes as compared to silyl ketene acetals.[174] Higher temperatures generally led to decomposition of the silyl nitronate in our hands.

3.3.2 Practicability

Considering the breadth of aliphatic nitroso acetals accessible enantioselectively with IDPi catalyst **94**, we chose to focus on several reactions on a larger preparative scale in order to expand on the practicability of our method. Before engaging in these multi-gram syntheses, we were determined to re-optimize reaction parameters such as temperature, solvent, and concentration, to allow for the lowest possible catalyst loading. We chose to conduct these screening experiments on a 0.1 mmol scale to better simulate scale-up effects. The reaction toward aliphatic nitroso acetal **116** was selected due to the high levels of selectivity achieved in the substrate scope evaluation (Scheme 2.8) and the lack of asymmetric syntheses thereof.

IDPi catalysts have been shown to be catalytically active in the sub-ppm regime of loading,[165] and the impurity profile of the reagents is of critical importance. Especially amine residues in both the silyl ketene acetal **69** and silyl nitronate **129** can influence the catalyst by virtue of Brønsted or Lewis basicity.[175]

Silyl nitronate **129** was prepared from 1-nitrohexane using $TBSCl/NEt_3$ without any further purification other than inert filtration to remove $Et_3N \cdot HCl$ and drying under high-vacuum (>95 % pure by ^1H NMR). Fascinatingly, with a drastically reduced catalyst loading of 0.10 mol% (1000 ppm), the reaction proceeded smoothly at lower temperatures, providing the product **116** in excellent yields and enantioselectivities (Table 2.5, entries 1–5). Particularly impressive is the transformation at −15 °C, which proceeded to full conversion within just 1 h, resulting in 93 % yield and very high selectivity (96.5:3.5 er). Reducing the catalyst loading even further to 0.01 mol% (100 ppm) led to diminished reactivity (entries 6 and 7); however, increasing the concentration to 2.50 mol/L restored reactivity while compromising selectivity only minimally (entry 9).

For reasons of practicability, we selected the conditions shown in entry 4 for further consideration. Most important for this decision was the short reaction time, which enabled us to perform this reaction using a simple NaCl/ice bath (−20 °C) without any need for energy-, space- and time-intensive cryostats.

Table 2.5: Optimization of the reaction between hexyl silyl nitronate **129** and **69**. Reactions performed on 0.1 mmol scale; conversion determined by ^{1}H NMR using mesitylene as an internal standard. [a] with IDPi **94**; [b] with IDPi **99a**.

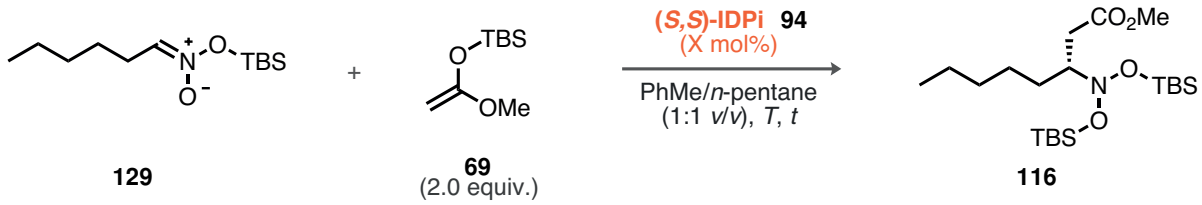

129 + **69** (2.0 equiv.) → **116**

entry	cat. loading	c/(mol/L)	T/°C	t/h	yield	enantiomeric ratio
1	0.10 mol%	0.25	−100 °C	16	26 %	99.5:0.5
2	0.10 mol%	0.25	−60 °C	16	quant.	98.5:1.5
3	0.10 mol%	0.25	−40 °C	16	quant.	98:2
4	0.10 mol%	0.25	−15 °C	1	93 %	96.5:3.5
5	0.10 mol%	0.25	0 °C	0.5	95 %	94.5:5.5
6	0.01 mol%	0.25	−40 °C	16	traces	97:3
7	0.01 mol%	0.25	−15 °C	16	30 %	95.5:4.5
8	0.01 mol%	1.00	−15 °C	16	87 %	95.5:4.5
9	0.01 mol%	2.50	−15 °C	16	quant.	95:5
10	0.01 mol%	5.00	−15 °C	16	quant.	94:6
11	0.01 mol%	10.00	−15 °C	16	quant.	93.5:6.5
12	0.01 mol%	neat	−15 °C	16	quant.	92.5:7.5

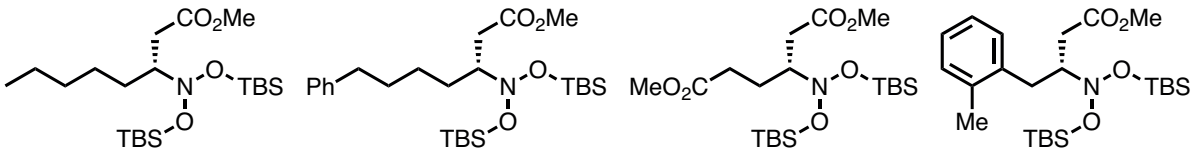

0.1 mol%, –20 °C, 1.5 h
116
99%, 96:4 er[a]
[15 mmol scale, 6.50 g]

0.1 mol%, –40 °C, 6 h
98
95%, 97.5:2.5 er[a]
[5 mmol scale, 2.30 g]

0.5 mol%, –40 °C, 15 h
113
93%, 97.5:2.5 er[a]
[5 mmol scale, 2.10 g]

0.5 mol%, –70 °C, 24 h
97
95%, 96.5:3.5 er[b]
[5 mmol scale, 2.20 g]

Accordingly, the reaction was performed at −20 °C for 1.5 h with 0.10 mol% (27.2 mg) IDPi **94** to provide the product with excellent enantioselectivity (96:4 er). In this particular case, the virtually pure nitroso acetal **116** was obtained after evaporation of the solvent mixture (toluene/*n*-pentane), methyl acetate, and excess silyl ketene acetal **69**, as judged by ^{1}H NMR spectroscopy. The catalytic amounts of IDPi **94** were carried on for further derivatizations (see section 3.4).

To further emphasize the practicability of this method, additional reactions toward nitroso

acetals **98**, **113**, and **97** were performed on a scale of 5.0 mmol. In summary, all three compounds were obtained in near-quantitative yields following simple flash chromatography, achieving excellent selectivities.

3.4 Nitroso Acetal Derivatizations – Hydrogenation

The hydrogenation of nitroso acetals traces back to Denmark's total syntheses of pyrrolizidine alkaloids *via* cascade [4+2]/(3+2) cycloadditions of nitroalkenes and alkyl nitronates,[176,177] where Raney nickel was identified as the most active mediator. Interestingly, a complete lack of reactivity was observed with standard catalysts such as Pd/C, Pearlman's $Pd(OH)_2$, or Adam's catalyst (PtO_2). These studies most likely served as an inspiration for Ioffe's hydrogenation of silyl nitroso acetals using Raney nickel.[149] TBS nitroso acetals required the addition of a fluoride source such as KF or KHF_2 to facilitate reduction, with deuterium incorporation at the stereocenter almost quantitatively conserved throughout the reaction.

Motivated by the promising literature precedents, we focused on the hydrogenation of nitroso acetal **86** using Raney nickel (Table 2.6). Because larger quantities of **86** needed to be synthesized for this optimization, we relied on the less selective but readily available IDPi catalyst **90** at higher temperatures over several iterations. Consequently, the enantiomeric ratio of the starting material **86** in Table 2.6 varies and is referenced by a blue-colored vertical line. This compromise proved inconsequential as we optimized for the *loss* of enantiomeric excess.

To our surprise, although the *N*-Boc-protected β-amino acid methyl ester readily formed, we observed a significant erosion of enantioselectivity under Ioffe's conditions using either KF or KHF_2 as a starting point (entries 1 and 2). We also investigated a possible pressure-dependence of this erosion but could not detect any effect (entries 3 and 4).

Substitution of the inorganic fluoride sources with the soluble silicate tetrabutylammonium difluorotriphenylsilicate (TBAT, entry 5) completely removed any stereoenrichment from **130**. Recognizing the potential influence of fluoride solubility, we chose to investigate the solvent for this transformation and observed only moderate conversion in *i*-PrOH but with improved change in *ee* of only −8 % (entries 6–8).

A reinvestigation of the hydrogenation catalyst to simple Pd on activated charcoal cleanly afforded the product without any loss in enantioselectivity (entry 9). These conditions also allowed us to decrease the hydrogen pressure to 1 bar using a straightforward balloon setup (entry 10) as well as the complete omission of the fluoride source with only a minor detrimental effect on the enantiomeric purity of **130** (entry 11). (*S*)-β-Homophenylalanine was purchased and subjected to Boc protection; this process enabled the determination of the absolute configuration of **130** and therefore **86** by comparison of the corresponding HPLC traces.

The absolute configuration of the remaining nitroso acetals was assigned by analogy.

In summary, the sensitivity of silyl nitroso acetals complicated the selective hydrogenation toward β-amino acids. In our hands, nitroso acetals readily eliminated the silanol to produce achiral *O*-silyl oximes under acidic conditions, however, we believe this mechanism was not primarily responsible for our observations. Considering the detrimental effect of a more soluble (thus more active) fluoride source (entry 5), it is plausible that immediate fluoride-induced desilylation of **86** produced highly basic nitroso acetal anions. Proton transfer to the protic solvent may have occurred, and highly basic species such as nitroso acetal, alkoxide, or fluoride anions could have racemized the stereocenter before hydrogenation could proceed. The contrast to Ioffe's findings might consequently be related to the activity of the Raney nickel. It has to be noted that, in our case, the Pd catalyst provided by Merck (product number 75990) was the most active of all Pd catalysts from the commercial vendors investigated.

Table 2.6: Optimization of the hydrogenation of nitroso acetal **86** with hydrogen, Boc_2O, fluoride sources, and various heterogeneous catalysts. Reactions performed on 0.025 mmol scale; conversion determined by ^{1}H NMR using mesitylene as an internal standard; blue line: starting material, orange circle: product.

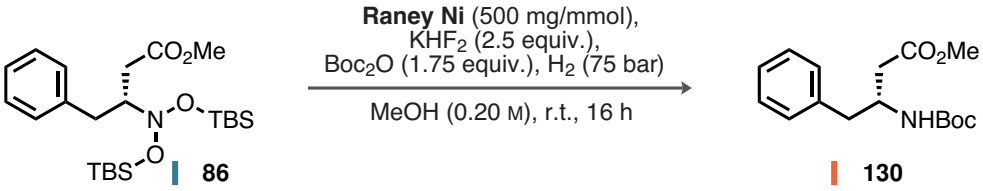

entry	deviation	conv.	er (**130**)		Δee
1	–	>95 %		86:14	–19 %
2	KF, 35 bar	>95 %		81:19	–29 %
3	125 bar	>95 %		70:30	–20 %
4	KF, 125 bar	>95 %		64:36	–32 %
5	TBAT	86 %		50:50	–60 %
6	*n*-heptane	–		–	–
7	EtOAc	–		–	–
8	*i*-PrOH	30 %		76:24	–8 %
9	Pd/C (20 mol%), 0.10 mol/L	>95 %		91.5:8.5	0 %
10	Pd/C (20 mol%), 1 bar, 0.10 mol/L	>95 %		91:9	–1 %
11	see entry 10, no KHF_2	>95 %		**90:10**	–3 %

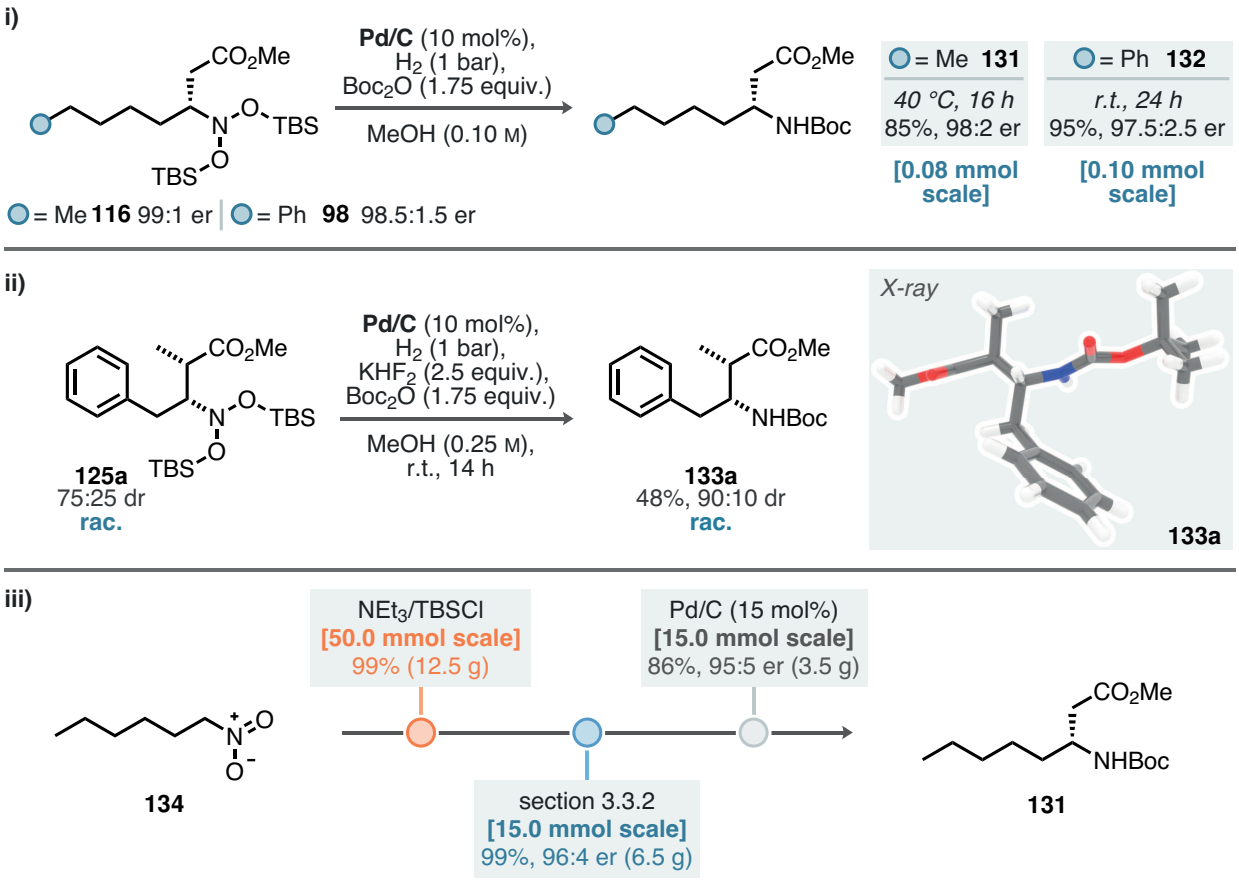

Scheme 2.9: Hydrogenative downstream modifications of enantioenriched nitroso acetals using the optimized hydrogenation conditions.

Scheme 2.9 illustrates our combined hydrogenation efforts using the optimized conditions. Aliphatic-chain nitroso acetals **116** and **98** were successfully reduced at either slightly elevated temperatures of 40 °C or room temperature within 1 d, and the *N*-Boc-protected β-amino acid methyl esters **131** and **132** were obtained in very good yields and enantioselectivities (Scheme 2.9 i, 98:2 er and 97.5:2.5 er).

Hydrogenation of a racemic mixture of the propionate-silyl ketene acetal addition product **125** required the presence of KHF_2 for sufficient reactivity. The diastereomers of the β-amino acid ester were partially separated by flash chromatography (48 %, 90:10 dr), and crystallization provided the pure *syn*-diastereomer, as verified by X-ray crystallography (Scheme 2.9 ii, right).

Having synthesized 6.50 g of hexyl nitroso acetal **116** (see Section 3.3.2), we were eager to investigate the feasibility of a large-scale hydrogenation (Scheme 2.9 iii). Accordingly, we were able to synthesize 3.53 g (95:5 er) of **131** after hydrogenation at 40 °C for 1 d. Overall, this three-step sequence from 1-nitrohexane **134** again emphasizes the practicability of our method for the synthesis of aliphatic β-amino acids.

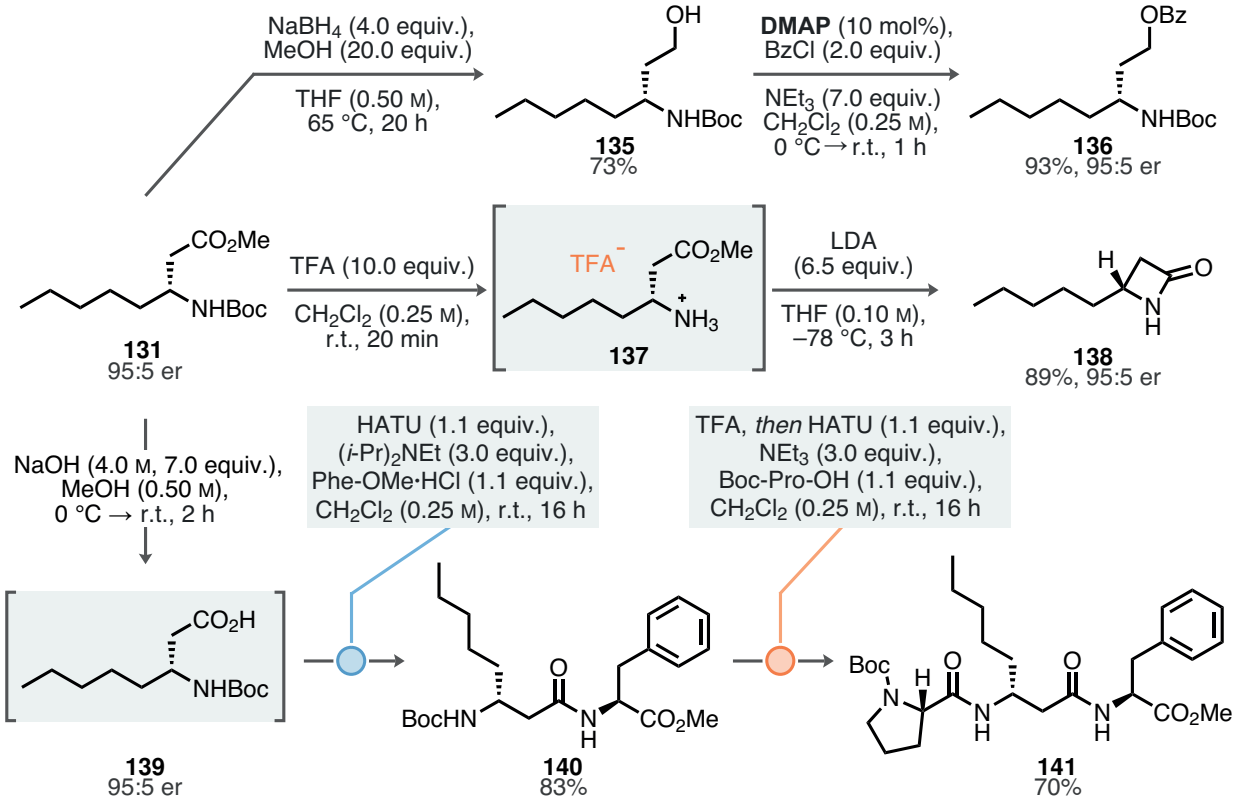

Scheme 2.10: Further modifications of *N*-Boc-β-amino acid methyl ester **131**.

The large amounts of **131** were subsequently applied in several illustrative downstream modifications (Scheme 2.10). Reduction of the ester fragment with $NaBH_4$ and MeOH provided γ-amino alcohol **135** in 73 % yield, the enantioconservation of which was determined *via* transformation to the benzoate **136** (93 %, 95:5 er). The Boc protecting group could be readily removed using standard conditions, and the trifluoroacetate ammonium salt **137** was further reacted with an excess of LDA at −78 °C to furnish aliphatic β-lactam **138** in excellent yield (89 %, 95:5 er).

Incorporation of β-amino acids into peptides and proteins can drastically alter their conformational and structural properties, as well as increase stability toward degradation by proteases.[161] Dipeptide **140** could be synthesized in a straightforward manner through hydrolysis of the ester to give **139** followed by HATU-mediated amide coupling with L-phenylalanine methyl ester hydrochloride. Finally, tripeptide **141** was synthesized following the same strategy with L-*N*-Boc-proline after Boc deprotection of **140**.

3.5 Mechanistic Studies

The work described in this section was conducted in collaboration with Dr. Chandra Kanta De, Dr. Ingolf Harden, and Dr. Giovanni Bistoni.

3.5.1 Ion Pair Characterization

The highly enantioselective and possibly diastereoselective addition of silyl ketene acetals to silyl nitronates raises intriguing questions about the mechanistic nuances of this transformation. We recognized that the key to answering some of these questions, not only in terms of selectivity but also reactivity, lies in an excact description of the ion pair. Considering the pioneering mechanistic studies laid out by Ioffe and Mayr,[148] we speculated that silyl transfer from the activated IDPi catalyst to the silyl nitronate might occur *spontaneously*, enabling us to observe and follow the formation of the ion pair spectroscopically by NMR.

Efforts to realize the spectroscopic observation and characterization of the ion pair involved choosing a suitable silyl source to ensure efficient deprotosilylation of the IDPi without nucleophilic addition to the bis(siloxy)iminium ion. Investigation of the limitations of this method (see Section 3.3.1) revealed a pronounced degree of orthogonality for allylsilanes, which is why we chose TBS methallylsilane as the activating agent. Further adjustment of the reaction conditions to facilitate NMR measurements was made with respect to the solvent. The viscosity of toluene increases drastically with lower temperatures, possibly creating detrimental concentration gradients able to compromise the integrity of the measurement. For this reason, we chose to monitor the silyl transfer in CD_2Cl_2 at −80 °C.

Scheme 2.11 i) shows the ^{31}P NMR spectrum of the protonated IDPi **91**, most likely broadened through inner core tautomerism. The average structure of the protonated IDPi catalyst, however, is C_2 symmetric, which results in the detection of a singlet. IDPi **91** was subsequently reacted with an excess of TBS methallylsilane **142** (10.0 equiv.) at room temperature, followed by another ^{31}P NMR measurement at −80 °C (Scheme 2.11 ii). Interestingly, four new doublets were observed as a result of deprotosilylation of **91** to furnish the silylated catalyst **143**. This symmetry-breaking event can be explained by selective silylation of the inner core sulfonyl oxygen atoms (C_1 symmetry), which creates an additional stereogenic center at sulfur. Accordingly, both (*S,S,R*)- and (*S,S,S*)-diastereomers appear in the NMR spectrum and are most likely connected *via* equilibrium, rendering the creation of a dynamic stereogenic center at sulfur inconsequential. Moreover, a singlet with comparably low intensity at −6.45 ppm can be observed in Scheme 2.11 ii), the identity of which remains unclear. It appears that this unknown species is linked to the silylation of **91**. Assuming C_2 symmetry, the formation of another ion pair by protonation of **142** (or silylation of isobutene) may seem plausible, forming a cationic species stabilized by the β-silicon effect.[178] *N*-silylation is an additional possibility.

Silylated IDPi **143** was used as a starting point for the investigation of the bis(siloxy)iminium ion pair. We reasoned that silyl transfer to silyl nitronate **85** would result in restoration of the C_2 symmetry in the IDPi anion; consequently, addition of 0.5 equiv. **85** led to the

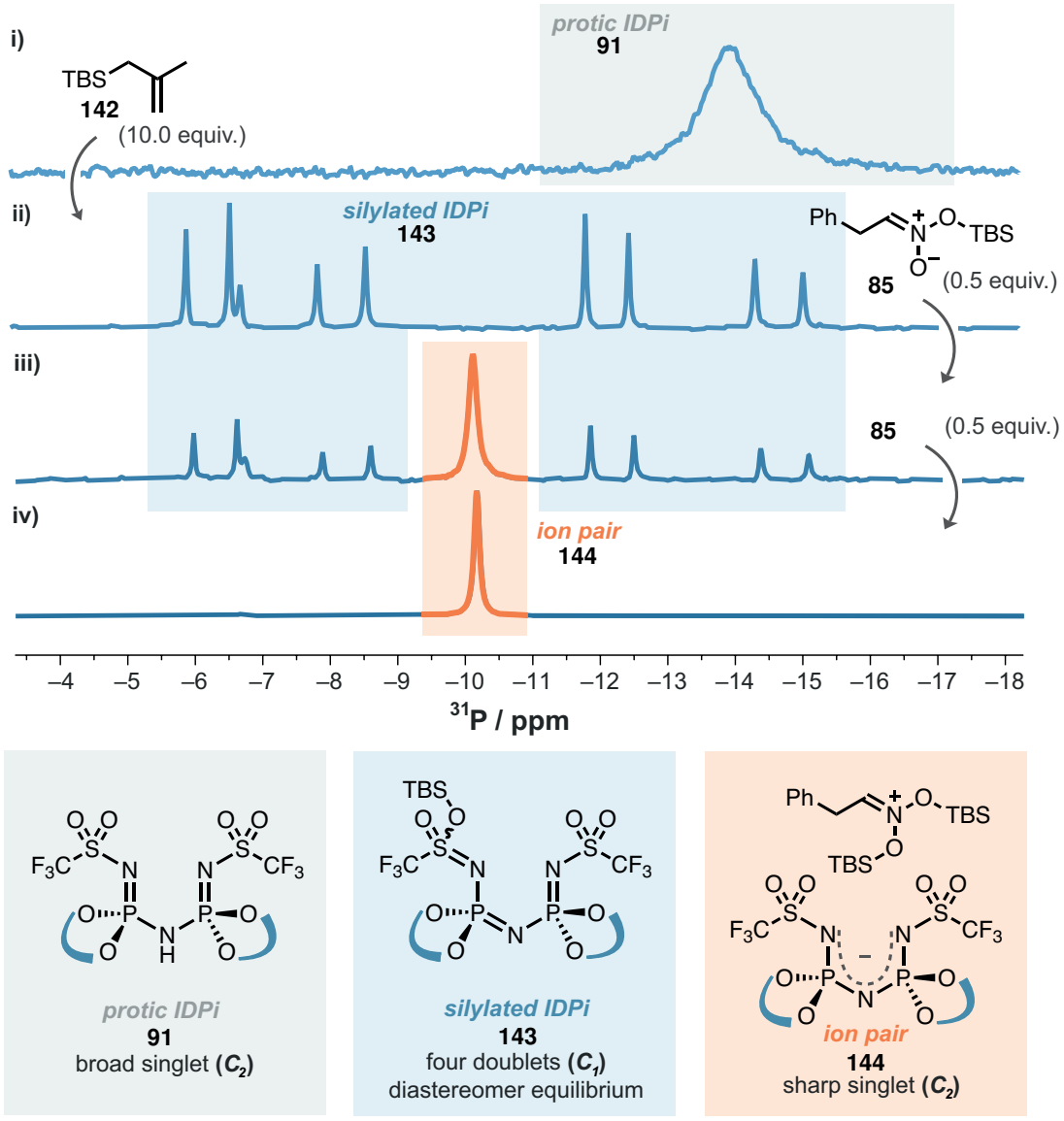

Scheme 2.11: ^{31}P NMR studies of the silylation of silyl nitronate **85** and observation of subsequent ion pairing; CD_2Cl_2, −80 °C.

appearance of a new singlet in the ^{31}P NMR spectrum at −10.12 ppm with a 1:1 ratio of this new singlet to **143** (Scheme 2.11 iii). Additional 0.5 equiv. **85** allowed us to exclusively observe the ion pair singlet (Scheme 2.11 iv), emphasizing the quantitative nature of this silyl transfer.

To further characterize the newly formed sharp singlet, we resorted to ^{1}H NMR analysis. Although this effort was highly complicated by the overlap with catalyst signals, we were able to fully characterize the formation of the bis(siloxy)iminium ion pair. ^{1}H,^{1}H-COSY analysis of the catalyst-dominated aromatic region in the ^{1}H NMR of the ion pair mixture from Scheme 2.11 iv) revealed a characteristic cross-peak from 7.63 ppm to 3.47 ppm. Following this indication of bis(siloxy)iminium formation according to **144**, we subjected the mixture

to a 1D-selective ROESY measurement (Figure 2.1 right) with excitation at 3.47 ppm. This experiment allowed us to deconvolute the signals from the overall mixture, clearly showing a strong deshielding of the bis(siloxy)iminium α-proton consistent with cationic activation through silylation (the same position resonates at 6.31 ppm in the isolated silyl nitronate **85**). Additionally, the diastereotopicity of the benzylic methylene group at 3.47 ppm is characteristic for inclusion of this achiral cation into the active site of the IDPi anion.

Although these effects evidently demonstrate the formation of the ion pair **143**, no further interactions between the two components could be observed by through-space NMR methods (ROESY or ^{1}H,^{19}F-HOESY). It must be noted that in similar cases, where ion-pairing occurs between ions of significantly distinct molar masses, the resulting different signal decay in the measurement may complicate the observation of specific interactions. Another possibility to investigate the degree of ion pairing could be the independent measurement of the diffusion constant D, the same order of which may indicate a correlation in movement.[179]

The confirmation of the bis(siloxy)iminium ion pair **144** formation inspired a structural investigation *in silico*. Several features are highlighted in Figure 2.2. Plausibly, substrate recognition may occur by virtue of a tight CH···O hydrogen bond (1.84 Å), with further attractive interactions originating from the (trifluoromethyl)cyclopropylphenyl fragment of the IDPi catalyst (CH$-\pi$ to the phenyl fragment of **85**, 3.00 Å). Two CH hydrogen bonds anchor one TBS group of the bis(siloxy)iminium to one of the sulfonyl groups of the catalyst's inner core. The 3,3'-substituents of the IDPi engage in non-covalent interactions with one of the TBS groups, which could involve a substantial electrostatic component and would further underline the importance of the tailored trifluoromethylcyclopropyl substituent required for

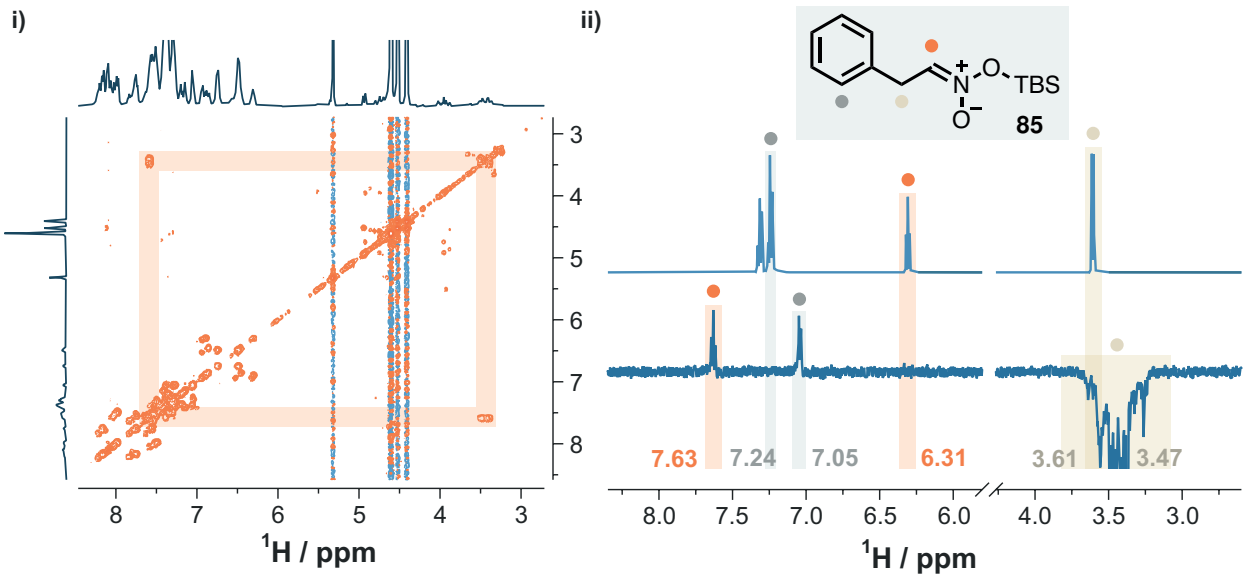

Fig. 2.1: ^{1}H,^{1}H-COSY NMR spectrum (left) as well as comparison of isolated **85** with the 1D-selective ROESY of the ion pair **144** (right, irradiation at 3.44 ppm).

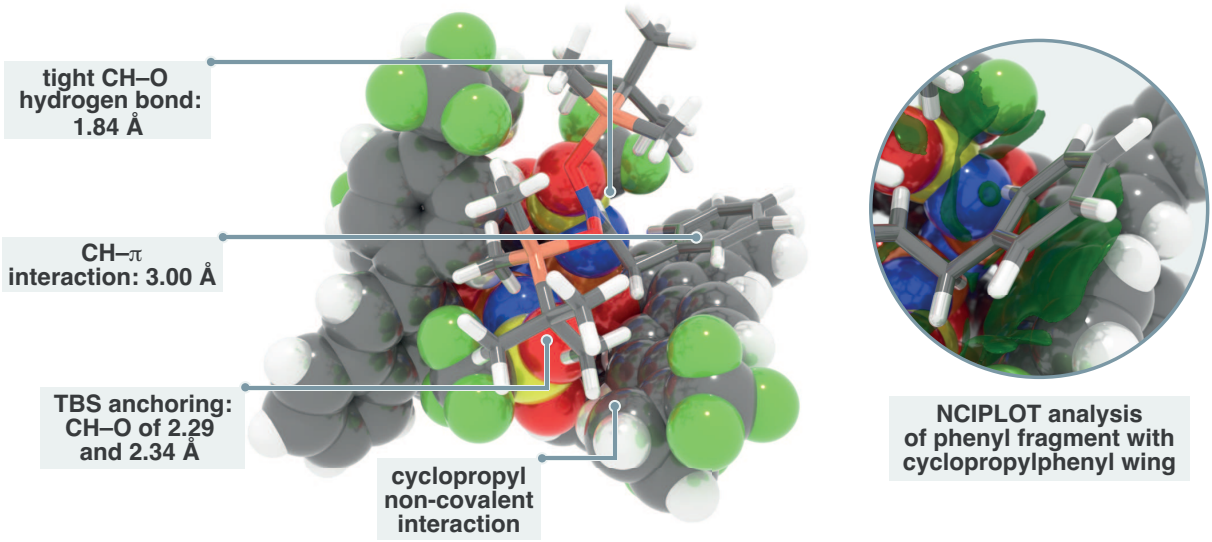

Fig. 2.2: DFT structure of ion pair **144** (PBE-D3/def2-SVP); NCIPLOT analysis: RDG isovalue of 0.35.

high enantioselectivities (see section 3.1). Altogether, the DFT structure demonstrates that the strong electrophilic activation of the silyl nitronate aligns with several stabilizing elements as well. For selective catalysis, both activation and stabilization relate to each other, which is in the spirit of *confinement*, as discussed in Chapter 1.

Based on the assumption that nucleophilic addition of the silyl ketene acetal **69** to the bis(siloxy)iminium ion is a highly exergonic process—which seems reasonable in light of the high energy-nature of both components—the Hammond postulate allows for speculation about the enantiodetermining transition states based on the structure of the ion pair. This leads to the conclusion that the C−H-π interaction of the aromatic tail, in combination with the tight CH−O hydrogen bond and the non-covalent interactions originating from the TBS groups of the bis(siloxy)iminium, might also be key attractive features in the respective transition states, governing the overall high levels of enantioselectivity achieved in this transformation. Attack of **69** to the exposed face of the cation in ion pair **144** matches with the absolute configuration of the obtained products.

3.5.2 Catalytic Cycle

The combined mechanistic experiments allowed us to distill our evidence into one proposed catalytic cycle of the nucleophilic addition of silyl ketene acetal to silyl nitronates, using the addition of **69** to **85** catalyzed by **91** as an example (Scheme 2.12). In the presence of silyl ketene acetal **69**, protic IDPi **91** undergoes fast deprotosilylation to furnish the silylated catalyst **143** (see Scheme 2.11). Silyl transfer to the silyl nitronate **85** produces the characterized ion pair **144**, susceptible to nucleophilic attack. Addition of silyl ketene acetal

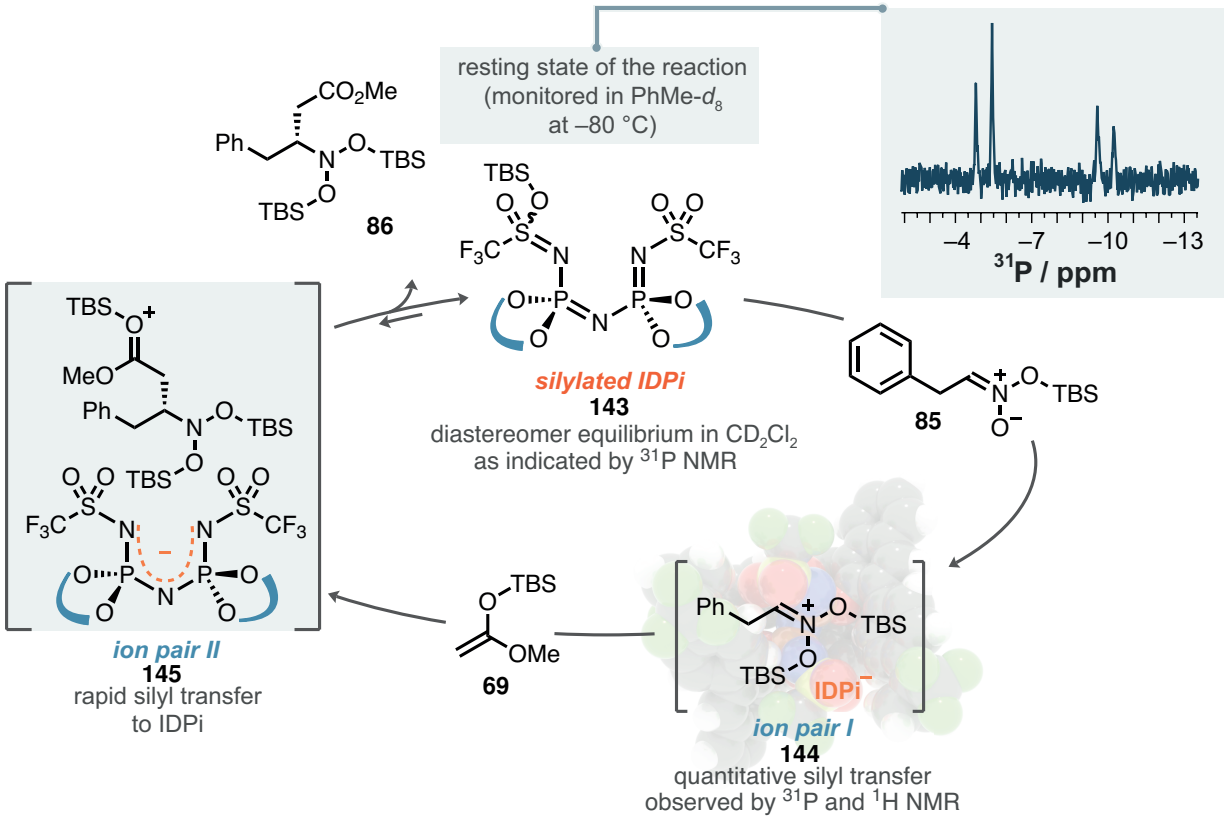

Scheme 2.12: Proposed catalytic cycle of the silyl ketene acetal addition to silyl nitronates.

69 provides another ion pair **145**, which can be expected to undergo fast silyl transfer of the TBS group to the anionic IDPi. We found the silylated IDPi **143** to be the resting state of the catalyst when we monitored the addition of **69** to 2-furanyl silyl nitronate leading to **96** in toluene-d_8 at −80 °C (this reaction did not proceed to full conversion and is therefore not shown here; raw data can be found in the Appendix, Table A.2). In light of this evidence, combined with the high levels of electrophilic activation in the bis(siloxy)iminium ion pair, it is plausible to assume that both nucleophilic addition and silyl transfer are kinetically fast steps. This kinetic behavior also explains the extreme levels of reactivity we were able to achieve with very low catalyst loadings, which would otherwise be complicated by elements such as product inhibition of the catalyst.

3.6 Development of a Direct Variant

The immense potential of the catalytic asymmetric polarity inversion of silyl nitronates is arguably limited by the sensitivity of the substrates. Although TBS silyl nitronates already represent one of the more stable available options,[164] they either have to be synthesized and used freshly or stored under a protective atmosphere of argon at −20 °C. For this reason, it is highly desirable to offer a possibility that starts one step earlier: at the nitroalkane.

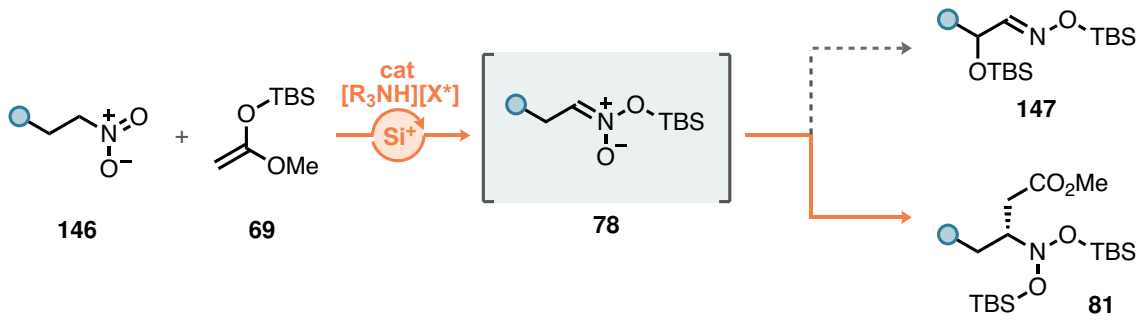

Scheme 2.13: Direct nitroalkane silylation approach discussed in this section.

This approach profits from Simchen's early contributions on the direct successive silylation of nitroalkanes (Scheme 2.3), who thoroughly investigated the cooperativity between amine bases and silylium Lewis acids. However, either Ioffe's or Simchen's reactions are incompatible with silylium ACDC since they required stoichiometric amounts of silyl triflate.

A hypothetical catalytic version would enable a highly step- and atom-economical approach to this transformation but is contrasted by the challenge of performing silylium ACDC in the presence of some of the strongest Lewis bases.[175] The necessity for additional bases most likely arises from the inherently low Lewis basicity of nitroalkanes and becomes particularly obvious in the comparison to ketones. Silyl transfer from allyl silanes to ketones occurs spontaneously without any base besides the IDPi anion or Tf_2N^- present,[180,181] because the lower α-acidity of ketones ($pK_a = 26.5$[182] in DMSO for acetone) is compensated by strong electrophilic silylium activation. Nitroalkanes on the other hand—nine orders of magnitude more acidic than ketones ($pK_a = 17.2$[182] in DMSO for $MeNO_2$)—do not readily undergo coordination to silylium Lewis acids, requiring Brønsted bases to initiate the reaction by deprotonation followed by nitronate silylation.

Given the high propensity of the IDPi class of catalysts to be activated by silyl ketene acetals, we reasoned that the acidity of an ammonium IDPi salt should still be sufficient for protodesilylation (Scheme 2.13). This would generate *catalytic* quantities of silylium IDPi and Brønsted base, which could then enable deprotosilylative transformations of nitroalkanes cooperatively. This overall process would correspond to a tautomerizing σ-bond metathesis between the nitroalkane **146** and commercially available silyl ketene acetal **69**, being a catalytic variant of Ioffe's first silyl nitronate synthesis with BSA at elevated temperatures. The overall driving force for this process would result from a higher stability of the silyl nitronate **78** compared to the silyl ketene acetal **69**.

3.6.1 Deprotosilylation of Ammonium IDPi Salts

Ammonium IDPi salt **91a** was readily accessible by simple protonation of NEt_3 followed by filtration (Scheme 2.14 i). Formation of the ion pair was corroborated by NMR analysis

(Scheme 2.14 ii). Similar to the bis(siloxy)iminium ion pair studies, a strong diastereotopic character can be noticed in the methylene groups of the triethylammonium fragment. Additionally, both methylene and methyl groups show NOE contacts to the aromatic region of the IDPi anion. These signals most likely originate from the ((trifluoromethyl)cyclopropyl)phenyl substituents, underlining the formation of a tight ion pair *via* significant stabilization of the ammonium ion.

Keen on studying the validity of our hypothesis, we synthesized several triethylammonium IDPi salts and tested their performance in the direct reaction of (2-nitroethyl)benzene **148** with **69** (Table 2.7). We could not observe any reactivity in toluene-d_8 (entries 1–3); however, generally good yields were observed in $CDCl_3$ (entries 4–8). Silyl ketene acetal addition product **86** was obtained as main product in most cases, accompanied by minor quantities of rearrangement product **149**. Aromatic-core IDPi salt **99c** demonstrated the highest selectivity of **86** over **149** but only at low levels of enantioselectivity (entry 8, 52.5:47.5 er). We believed that less polar solvents might favor ion-pairing, and higher levels of enantioselectivity could indeed be achieved in *n*-pentane (entries 9–13). This increase compromised reactivity significantly, although it was accompanied by complete selectivity for **86** (entry 11, 26 %, 62:38 er). This trend was amplified when the reaction was conducted in a mixture of toluene and *n*-pentane (entry 13, 69.5:30.5 er).

Although toluene has been shown to be superior in terms of selectivity, most likely because of favored ion-pairing, reactivity is also greatly influenced in this case because the initial step

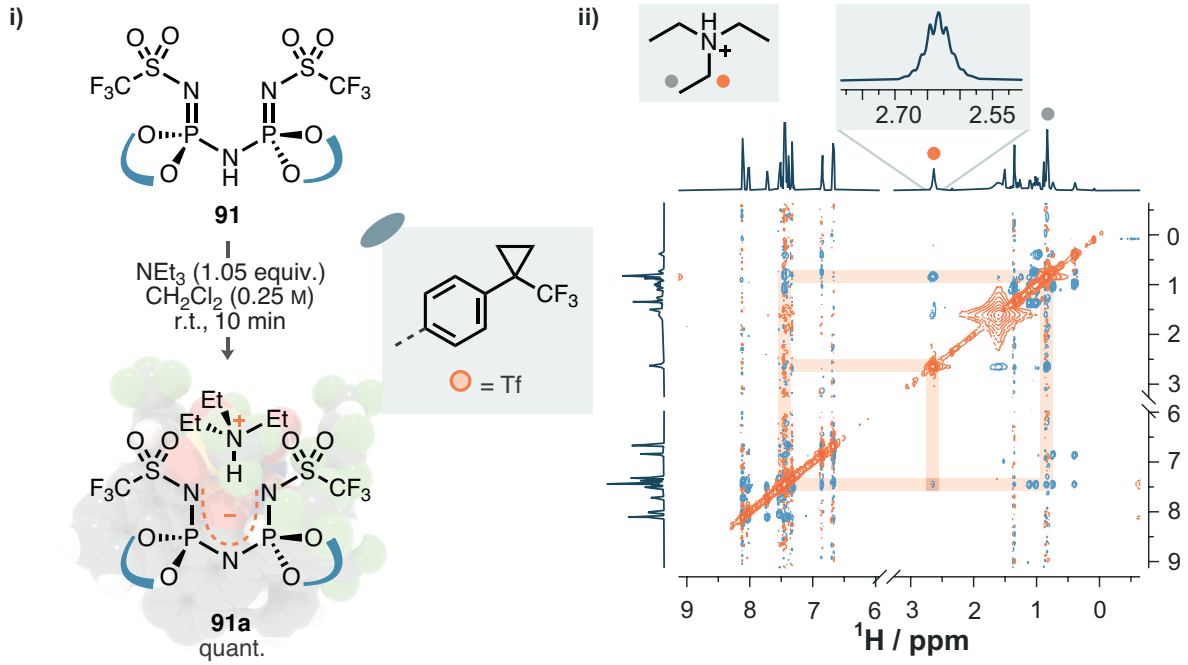

Scheme 2.14: i) Synthesis of triethylammonium IDPi salt **91a** as well as ii), ^{1}H,^{1}H-NOESY NMR spectrum with characteristic signals highlighted (CD_2Cl_2).

Table 2.7: Optimization of the reaction between nitroalkane **148** and **69** catalyzed by various triethylammonium IDPi salts. Reactions performed on 0.025 mmol scale; yield determined by ^{1}H NMR using mesitylene as an internal standard. [a] 1:1. The er of **149** was found to be 50:50 in all cases.

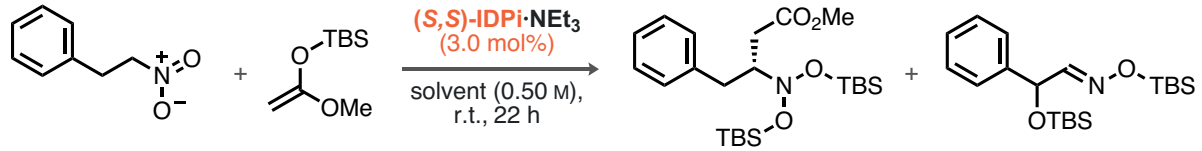

entry	solvent	IDPi	yield **86** and **149**		er **86**
1	PhMe-d_8	**94**	–	–	–
2	PhMe-d_8	**99**	–	–	–
3	PhMe-d_8	**99a**	–	–	–
4	$CDCl_3$	**91**	63 %, 12 %		60:40
5	$CDCl_3$	**150**	0 %, 15 %	–	–
6	$CDCl_3$	**94**	93 %, 8 %		52:48
7	$CDCl_3$	**99**	60 %, 7 %		52.5:47.5
8	$CDCl_3$	**99a**	98 %, 2 %		52.5:47.5
9	*n*-pentane	**91**	14 %, 6 %		55:45
10	*n*-pentane	**150**	–	–	–
11	*n*-pentane	**94**	26 %, 0 %		62:38
12	*n*-pentane	**99**	20 %, 0 %		51:49
13	*n*-pentane	**99a**	8 %, 4 %	–	n. d.
14	*n*-pentane/PhMe[a]	**94**	traces, 0 %		69.5:30.5

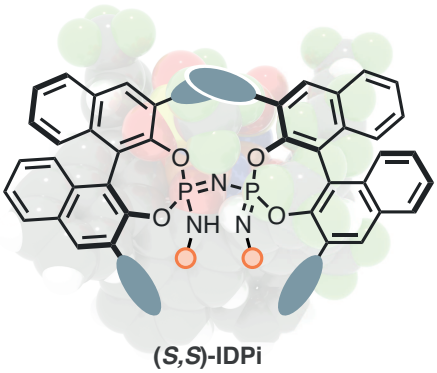

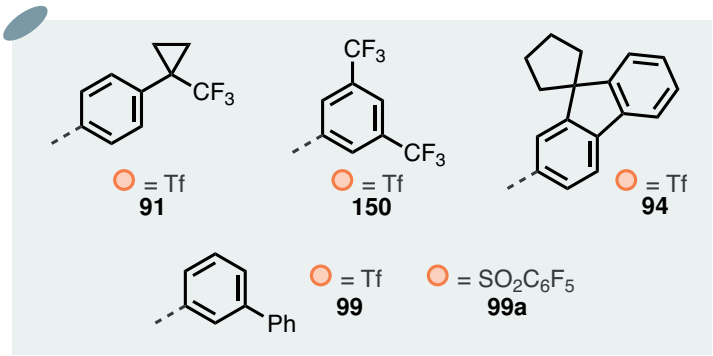

of this transformation involves the dissociation of an ammonium ion pair into a silylated IDPi and amine base. We recognized this inherent drawback of the design and attribute this kinetic challenge to the comparably high stability of the ammonium IDPi ion pair (see Scheme 2.14). For this reason, we investigated the effect of different ammonium cations with IDPi **94**, possibly favoring the extrusion of the ammonium ion from the active site. Conditions corresponding to entry 11 in Table 2.7 were used as a starting point. Tetramethylethylenediamine IDPi salt **94f** led to a slight increase in reactivity (entry 1, Table 2.8) with virtually no change in enantioselectivity (68:32 er). Interestingly, both Hünig's base and *N*-methylmorpholine (NMM) furnished no product at all (entries 2 and 3). Outstanding conversions were observed with bicyclic diamine 1,4-diazabicyclo[2.2.2]octane (DABCO) as well as quinuclidine, with the former providing mixtures of **86** and **149** in favor of the

Table 2.8: Influence of the trialkylammonium ion on the reactivity in the direct deprotosilylative reaction of **148**. Reactions performed on 0.025 mmol scale; yield determined by ^{1}H NMR using mesitylene as an internal standard. [a] 78 % conversion, remainder silyl nitronate **85**. [b] full conversion, remainder silyl nitronate **85**.

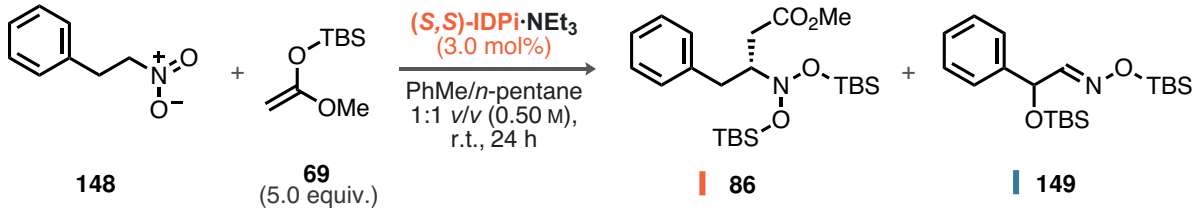

entry	catalyst	yield	er **86**
1	**94f**	14 %, 0 %	68:32
2	**94g**	0 %, 0 %	–
3	**94h**	0 %, 0 %	–
4	**94i**[a]	37 %, 5 %	70:30
5	**94j**[b]	0 %, 0 %	–

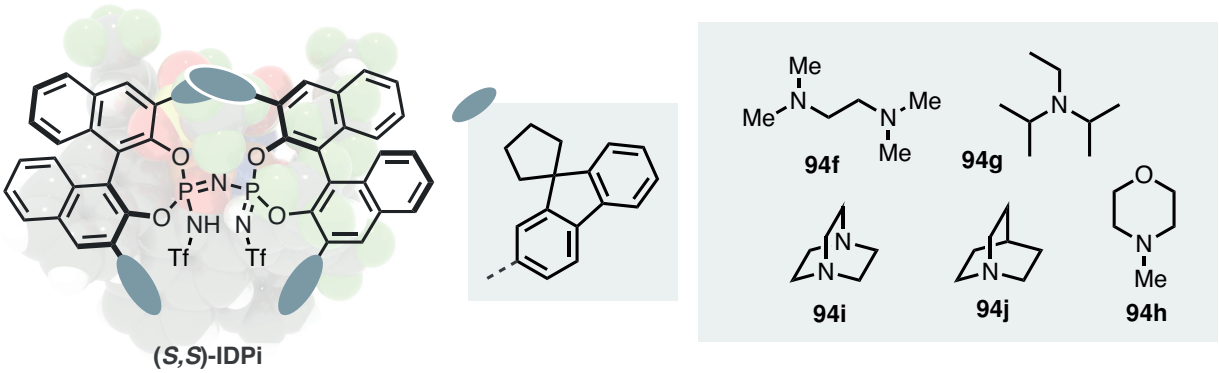

nucleophilic addition (37 %, 70:30 er) along with 36 % silyl nitronate **85**. Quinuclidine, on the other hand, showed no further activation of the silyl nitronate, and quantitatively stopped at the silyl nitronate (**85**) stage.

Several factors could contribute to these observations. The similarity of Hünig's base and NMM to NEt_3 might explain their similar behavior, and the slight difference to TMEDA could be a consequence of the additional free dimethylamino functionality that potentially protrudes from the active site of the IDPi. The strongest effect, however, was observed for bicyclic bases DABCO and quinuclidine.

The conformationally fixed sphere-like structure of the corresponding ammonium ions could potentially lower the attractive interactions to the anion, resulting in a kinetically favored activation. In addition to the structural features, the reactivity difference between DABCO and quinuclidine might involve a thermodynamic component. DABCO and NEt_3, both of which showed activation of the silyl nitronate, have similar pK_a values of the corresponding ammonium ions (8.93 and 9.00, respectively). The higher basicity of quinuclidine ($pK_a = 9.80$), on the other hand, explains the higher selectivity towards silyl nitronate formation.[182]

Using the higher reactivity and chemoselectivity of the DABCO IDPi salt in *n*-pentane/toluene 1:1 (*v*/*v*) as a screening platform, we were eager to improve the promising levels of enantioselectivity by fine-tuning of the fluorenyl substituent (Table 2.9).

Using several 7-substituted fluorenyl fragments with perfluorooctanesulfonyl core generally led to low reactivity combined with moderate improvements in enantioselectivity (entries 1–4). Investigation of the effect of perfluoroalkylsulfonyl core length was conducted for the 7-*tert*-butyl and 7-adamantyl fluorenes, with the perfluoroethanesulfonyl catalyst **122a** furnishing **86** in low yield and good enantioselectivity (entry 6, 84:16 er). The highest reactivity was observed for triflyl-core IDPi **122**, which allowed us to conduct the reaction at lower temperature for an elongated time (0 °C for 3.5 d), furnishing the product in 34 % and 87.5:12.5 er.

In summary, high reactivity in combination with high chemo- and enantioselectivities was not accomplished for the direct deprotosilylative transformation of nitroalkane **148**. Only low to moderate yields were achieved for a range of fluorenyl IDPi catalysts. As speculated earlier, this might be related to our design's inherent drawback of having to deconstruct a very stable ammonium IDPi ion pair. Optimization of the ammonium fragment did improve conversion; however, not to satisfactory levels of chemo- and enantioselectivity. Given the high selectivity for the silyl nitronate **85** achieved with a quinuclidinium IDPi salt (Table 2.8, entry 5), we chose to study an arguably more practicable and modular one-pot approach toward the realization of our goal.

Table 2.9: Influence of the fluorenyl substituent in the direct deprotosilylative reaction of **148**. Reactions performed on 0.025 mmol scale; yield determined by ^{1}H NMR using mesitylene as an internal standard. [a] 15 % yield silyl nitronate **85**; [b] at 0 °C for 3.5 d.

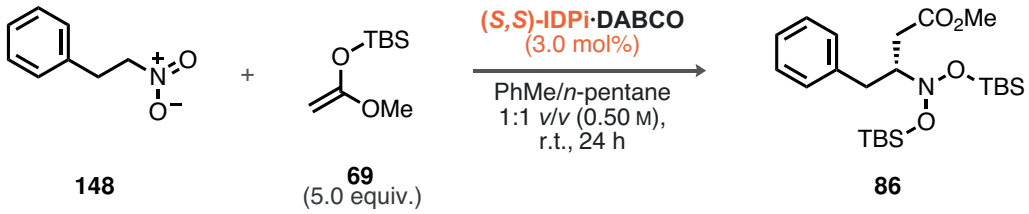

148 + **69** (5.0 equiv.) → **86**

entry	catalyst	yield	er **86**
0	**94**	37 %	70:30
1	**151a**	14 %	80.5:19.5
2	**122b**	14 %	86.5:13.5
3[a]	**152a**	0 %	–
4	**153a**	15 %	84:16
5	**153**	15 %	81:19
6	**122a**	15 %	84:16
7	**122**	31 %	82.5:17.5
8[b]	**122**	34 %	87.5:12.5

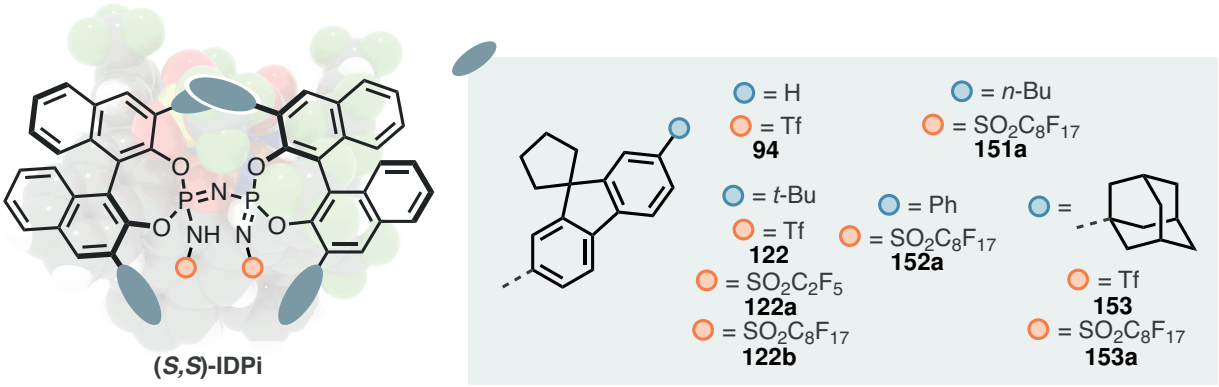

3.6.2 Achiral Quinuclidinium Organocatalysts

Instead of using an ammonium IDPi ion pair as starting point—exhibiting kinetically disfavored deionization *via* deprotosilylation—we chose to simplify the anion to triflate and trifluoroacetate. This approach would remove the kinetic imbalance and potentially increase reactivity. On the other hand, the main challenge is the selective formation of the silyl nitronate without any downstream Lewis-acidic activation to ensure high enantioselectivity

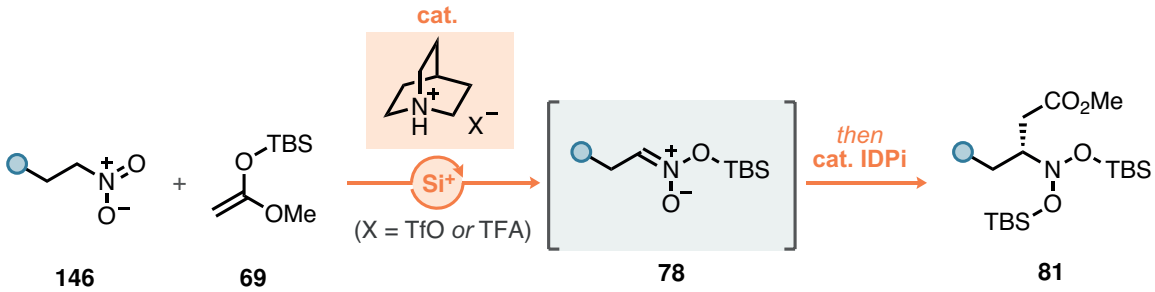

Scheme 2.15: Proposed one-pot approach, potentially overcoming previously encountered reactivity and selectivity limitations.

in the subsequent step. Enantioinduction might occur in an overall one-pot process by the addition of a suitable IDPi catalyst, provided the interference of the achiral anion used in the first step with the IDPi anion can be controlled (Scheme 2.15). Both salts, quinuclidinium triflate **154** and quinuclidinium trifluoroacetate **155**, were synthesized in quantitative yields through protonation by the corresponding acids in *n*-pentane followed by filtration. When these salts were subjected to an excess of silyl ketene acetal **69** in CD_2Cl_2 at room temperature, we observed immediate protodesilylation of **69** to form mixtures of free quinuclidine and TBS−X (X = OTf, TFA, Scheme 2.16 i). Analysis of the ^{29}Si NMR chemical shifts was in accordance with the expectation based on the pK_a values of the respective acids, with

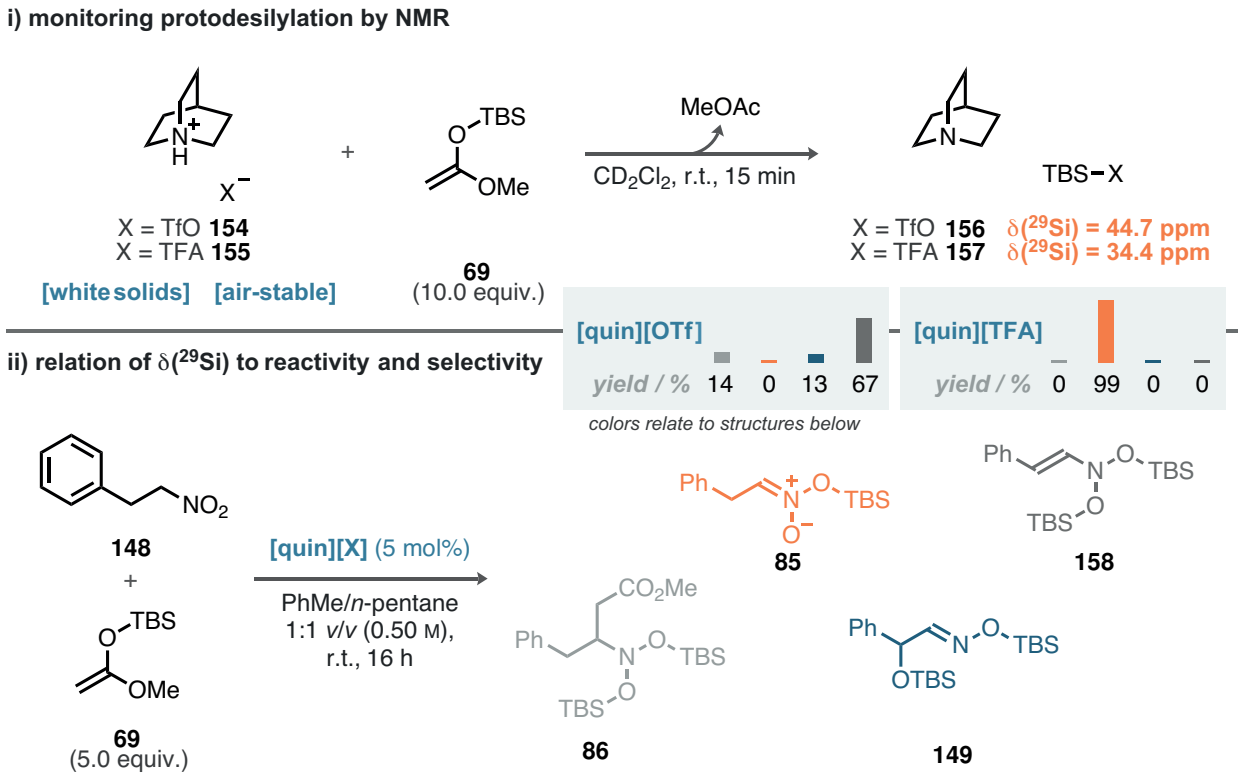

Scheme 2.16: i) Protodesilylation of quinuclidinium salts and ii) their difference in reactivity and selectivity in the catalysis of the reaction between **148** and **69**.

156 showing a comparable chemical shift to TBSOTf (43.3 ppm).[87] Employing 5 mol% of **154** and **155** as a catalytic platform for the investigation of the reaction between nitroalkane **148** and **69**, we observed a stark difference in their outcome (Scheme 2.17 ii).

Whereas quinuclidinium triflate provided a mixture of all four possible products, with bis(siloxy)enamine **158** being the main compound, quinuclidinium trifluoroacetate exhibited complete selectivity for the silyl nitronate **85**. As indicated by the stronger deshielding in the ^{29}Si NMR signal, the mixture of TBSOTf and quinuclidine demonstrated too strong Lewis-acidic potential, which eventually led to several successive silylation events.

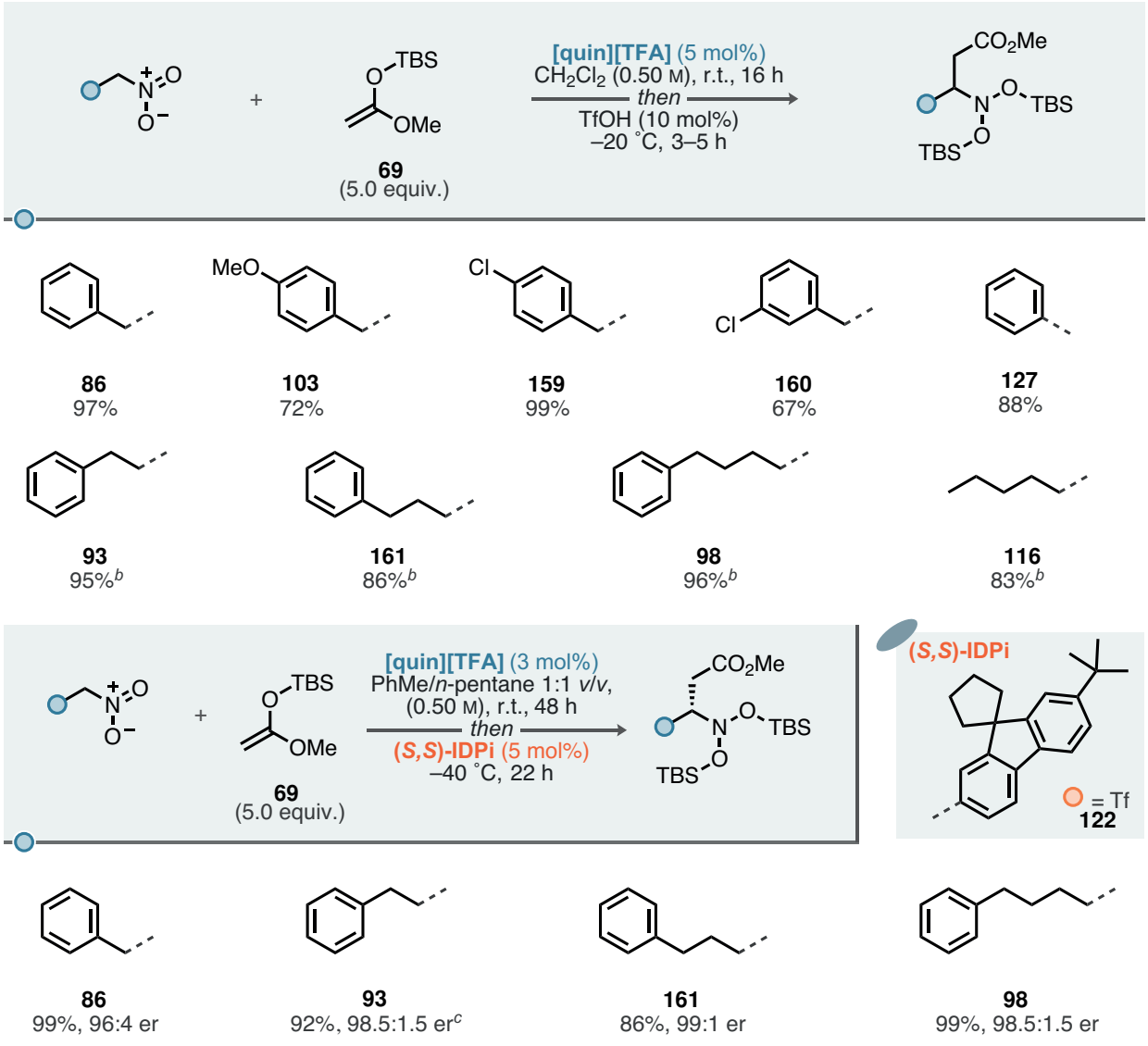

Scheme 2.17: Substrate scope of the direct deprotosilylative functionalization of nitroalkanes. Reactions with [quin][TFA] and TfOH on 0.50 mmol scale, isolated yields. Reactions with [quin][TFA] and *(S,S)*-IDPi on 0.025 mmol scale, yields determined by ^{1}H NMR using mesitylene as internal standard. [a] in toluene/*n*-pentane 1:1 *v*/*v*, no TfOH, NMR yield. [b] with 10 mol% [quin][TFA] and 15 mol% TfOH. [c] 0.10 mmol scale, isolated yield.

We used the mild silyl metathesis catalyst **155** as a starting point for the investigation of a one-pot catalytic silyl metathesis-nucleophilic addition sequence (Scheme 2.17). The second step of this sequence in the presence of quinuclidinium trifluoroacetate **155** was achieved when higher catalyst loadings of a stronger Brønsted acid than trifluoroacetic acid were added to the reaction mixture after full conversion to the silyl nitronate. This is most likely a consequence of quantitative salt formation of the stronger acid with quinuclidine.

In general, the highest reactivity in the silyl metathesis was achieved in CH_2Cl_2, and subsequent addition of 10 mol% TfOH after cooling to −20 °C selectively provided a range of nitroso acetals (Scheme 2.17, top). For (pseudo)aliphatic nitroalkanes, higher catalyst loadings of 10 mol% and 15 mol% of **155** and TfOH were necessary to achieve sufficient reactivity.

Intrigued by the clean reaction profiles achieved in the non-asymmetric variant, we were eager to investigate a possible catalytic asymmetric version of this direct transformation (Scheme 2.17, bottom). Informed by the results obtained for the nucleophilic addition to silyl nitronates, we performed these reactions in toluene/*n*-pentane for maximum enantioselectivities, slightly compromising the silyl metathesis reactivity. Employing 3 mol% **155** and 5 mol% of IDPi **122** with slightly prolonged reaction times, we were able to achieve excellent yields and enantioselectivities in the formation of nitroso acetals **86**, **93**, **161**, and **98**.

3.6.3 Proposed Catalytic Cycle

Based on the NMR-monitored salt activation experiments (Scheme 2.16), we propose the following catalytic cycle. Silyl ketene acetal **69** was found to readily activate **155** to form TBS−TFA, which is most likely in close contact with the Lewis-basic quinuclidine. Considering the mild Lewis acidity of TBS−TFA, this Lewis pair is probably not forming quantitatively, liberating enough free quinuclidine for the deprotonation of nitroalkane **146**. The

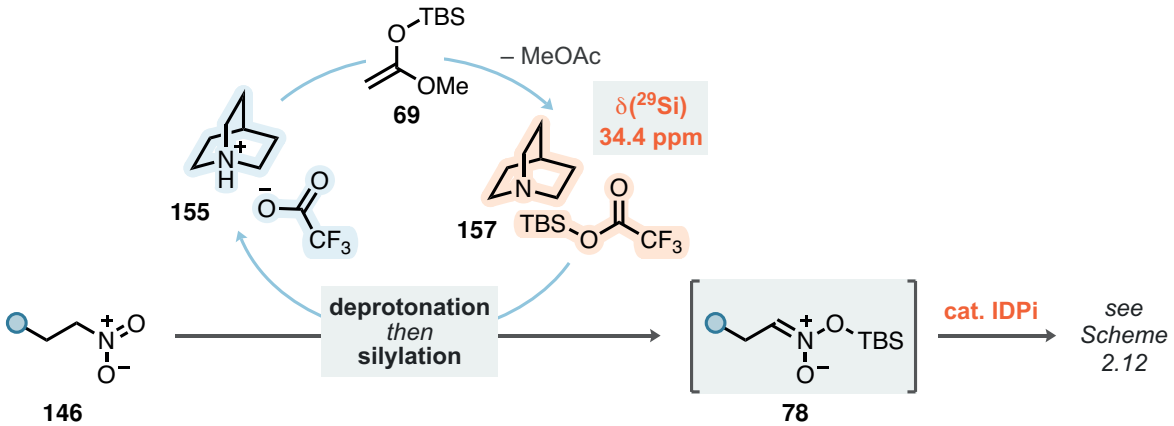

Scheme 2.18: Proposed catalytic cycle of the direct deprotosilylative activation of nitroalkanes by quinuclidinium organocatalysts.

divergent deprotosilylation of nitroalkanes and ketones has already been discussed in Section 3.6, and is again relevant in this context. Accordingly, the highly Lewis-basic quinuclidinium-nitronate anion complex resulting from nitroalkane deprotonation will then undergo fast silyl transfer from TBS−TFA, restoring the quinuclidinium trifluoroacetate **155** and liberating silyl nitronate **78** for further functionalizations (also see Scheme 2.12).

4 Summary and Outlook

The work discussed in this chapter encompasses the development of the first catalytic asymmetric addition of silyl ketene acetals to silyl nitronates *via* an overall polarity inversion process. Nitronate anions have been widely studied and were used as *nucleophiles* in asymmetric catalysis, whereas silyl nitronates mark their entry into the realm of *electrophilic activation*.

We recognized the high potential of silylium ACDC in the context of silyl nitronates and were able to rapidly identify multiple selective catalysts for their challenging transformation into chiral nitroso acetals. The process of catalyst identification was facilitated by a multi-substrate screening approach, after initial investigations revealed high levels of substrate-specificity in the enantioselectivity.

Ultimately, a set of four optimized IDPi catalysts enabled access to 27 distinct nitroso acetals with excellent yields and enantioselectivities. The most general catalyst out of the screened selection, decorated with a spiro-fluorenyl motif, was able to convert several aliphatic silyl nitronates to the corresponding nitroso acetals with excellent yields and enantioselectivities, which makes this catalytic asymmetric method especially appealing for the synthesis of aliphatic β^3-amino acids. To this end, we also optimized practical hydrogenation conditions to furnish *N*-Boc-protected β^3-amino acid methyl esters in a single step, as was effectively demonstrated in the gram-scale synthesis of *n*-hexyl acid **131**.

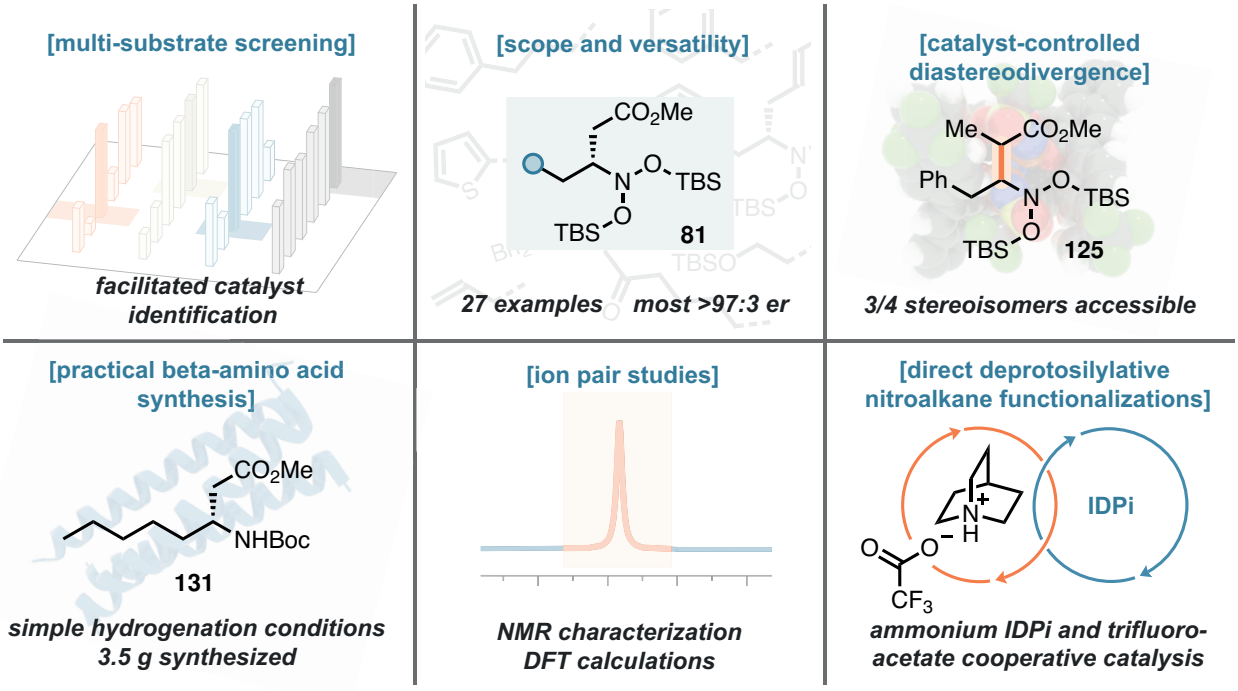

Scheme 2.19: Summary of the findings discussed in this chapter.

Several additional fundamental advances in asymmetric catalysis as a whole were brought forward along the path of discovery in this chapter. Using methyl propionate-derived silyl ketene acetals, in either (*E*)- or (*Z*)-enriched form, we could demonstrate a pronounced degree of catalyst control over the diastereo- and enantioselectivity in the formation of this strategic σ bond. This allowed us to synthesize three out of four possible stereoisomers of **125** by choice of IDPi catalyst and silyl ketene acetal.

We reasoned that such effects could only be achieved given strong ion-pairing interactions in the stereodetermining step and elucidated the formation of the ion pair by ^{1}H and ^{31}P NMR spectroscopy, in combination with in-depth DFT and NCIPLOT analyses. Those experimental studies revealed a facile silyl transfer to the silyl nitronate substrates, showing significant electrophilic activation *via* formation of bis(siloxy)iminium ions. In this context, we deconvoluted a range of non-covalent attractive interactions the catalyst anion offers to the activated substrate in order to accomodate this unleashed reactivity.

Lastly, we established the proof-of-concept of *direct* deprotosilylative transformations of nitroalkanes. Those investigations were fueled by the idea to use ammonium IDPi salts in order to perform cooperative Brønsted base-Lewis acid catalysis, resulting in an overall σ bond silyl metathesis to synthesize silyl nitronates *catalytically*. We recognized that the use of ammonium IDPi salts is limited by the high stability of the ammonium ion pairs, which resulted in the discovery of quinuclidinium trifluoroacetate as a mild silyl metathesis catalyst. This approach greatly profits from its practicability, with the commercially available silyl ketene acetal **69** fulfilling dual functions either as deprotosilylation reagent or nucleophile, depending on the reaction conditions. The stronger catalyst quinuclidinium triflate was shown to be less selective in the formation of the silyl nitronate but directly engaged in additional downstream modifications. Possible applications might be the optimization towards the clean formation of the α-siloxy oxime **149**, representing a possible catalytic entry into value-added products from early-stage nitroalkanes by virtue of redox transposition.

Although we demonstrated the validity of this concept, it is based on the inherent α-acidity of the nitroalkane substrates. A *truly catalytic* version of this transformation would be completely catalyst-dependent, able to functionalize all possible nitroalkanes without the

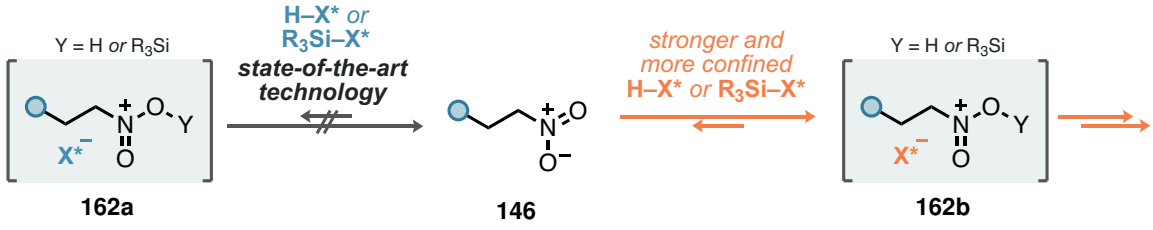

Scheme 2.20: Outlook: direct catalytic activation of nitroalkanes through protonation or silylation would remove the necessity for additional bases as well as overcome current limitations.

need for additional bases. Such a hypothetical transformation could be realized in the future through the development of even stronger and more confined Brønsted acids. Those systems would result in less coordinating anions for silylium ACDC or Brønsted acid catalysis, and might be able to activate nitroalkanes, which are known to belong to the least Lewis-basic substrates.[175] This fundamental breakthrough in acid catalysis could eventually overcome the limitations we encountered during our studies, such as the exclusive need for silyl ketene acetals as nucleophiles.

Lastly, the studies on nitroalkane deprotosilylation inspired efforts on the direct deprotosilylation of alkyl esters, which will be discussed in the following part, Chapter 3.

CHAPTER III

SILYL KETENE ACETAL CATALYSIS

1 Literature Background

1.1 The State-of-the-Art in Silylium ACDC

The development of silylium ACDC as a whole is deeply intertwined with the application of silyl ketene acetals (Scheme 3.1). As discussed in Chapter 1, Section 1, these nucleophiles

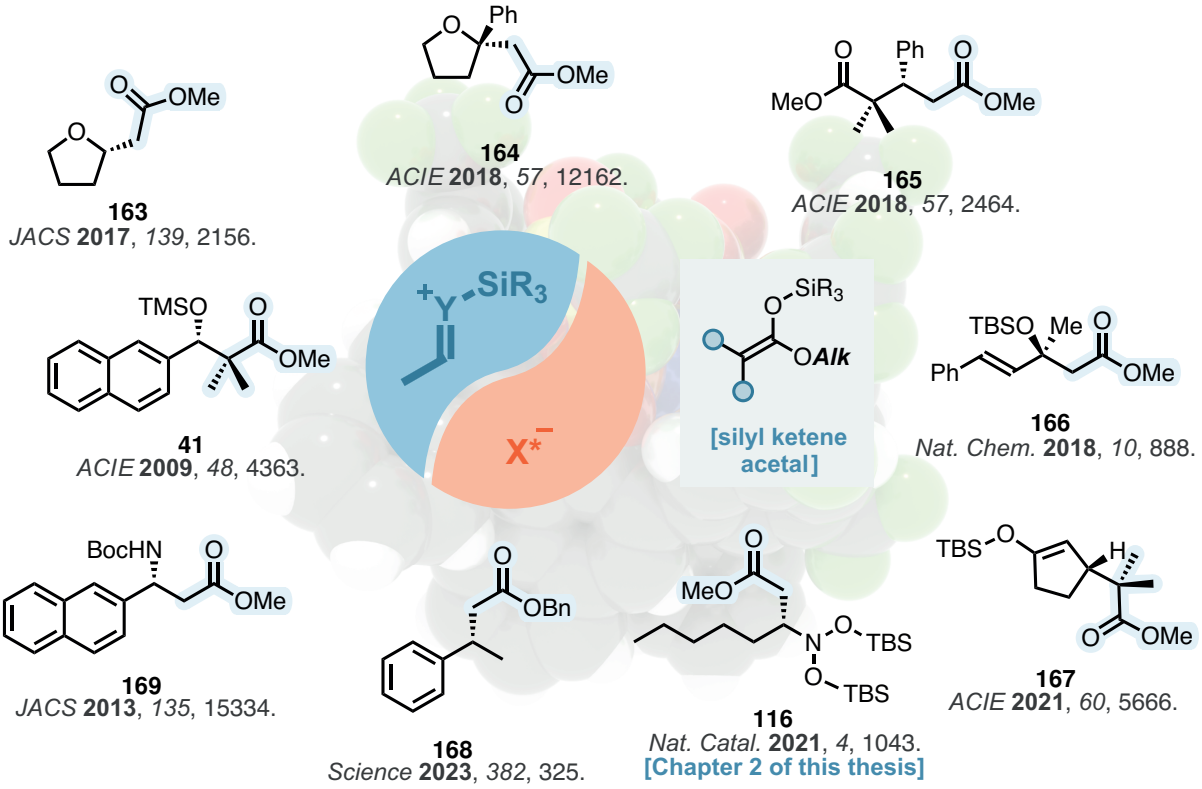

Scheme 3.1: Examples of silylium ACDC employing silyl ketene acetals as nucleophiles.[82,96,165,166,173,183–186]

hold a special place in chemical synthesis due to their compatibility with strong Brønsted and Lewis acids. In a sense, the fundamental interest in Mukaiyama-type transformations stems from the scarcity of methods for the catalytic asymmetric α-functionalization of carboxylic acid oxidation state equivalents. These transformations are highly desirable because esters, being early-stage industrial products, are directly accessible from crude olefins *via* carbonylation or hydroformylation.[187,188]

Traditionally, chiral auxiliaries have been and continue to be employed for similar problem sets, with the most recent advancements in catalysis distinguished by their complementarity and superiority to established protocols. Consequently, the List group has introduced additions to oxocarbenium ions,[183,184] benzylic cations,[96] α,β-unsaturated esters,[166] imines,[173] silyl nitronates (see Chapter 2),[186] enones,[185] ketones, and aldehydes.[82,165] Pioneering contributions to catalytic asymmetric functionalizations of silyl ketene acetals in the directly adjacent fields of Lewis base catalysis were made by Denmark,[171,189] while Jacobsen concentrated on supramolecular hydrogen-bonded complexes.[190–192] Chiral phosphoric acids are also known to catalyze vinylogous Mukaiyama–Mannich reactions.[193]

All of these developments—silylium ACDC, Lewis base catalysis, and anion-binding catalysis—share a common feature: silyl ketene acetals are employed as *stoichiometric* reagents.

1.2 Asymmetric Direct Functionalizations

The desire to enhance chemical synthesis generally aligns with the goal of breaking free from the constraints of stoichiometric reagents, and conceptual thoughts on its realization likely date back to the origins of organic synthesis itself. A recent emphasis on step-[10] and atom-economy[2] has been instrumental in intensifying these efforts. In this context, the term *direct functionalization* refers to the use of unfunctionalized starting materials—such as aldehydes, ketones, carboxylic acids, and esters—in an overall transformation that involves the generation of a nucleophilic species *in situ*.

As discussed in Section 1.1, Shibasaki's heterobimetallic complexes **56** are among the earliest developments within this conceptual framework, exhibiting high activity and selectivity in nitromethane-based Henry reactions (see Scheme 2.1).[124,126,127] Merely four years later, this concept was expanded to include *direct* aldol reactions of ketones.[194] However, for catalytic asymmetric transformations of ketones, enamine catalysis has arguably become the method of choice.[11,49]

Transposing these methods onto direct functionalizations of carboxylic acid derivatives, such as esters, amides, and nitriles, introduces a higher level of complexity due to the significantly lower α-acidity (acetone is 1000 times more acidic than *tert*-butyl acetate).[182]

Within the framework of asymmetric synthesis, the origins of such functionalizations can be traced back to the development of chiral auxiliaries and the aldol reaction. A significant amount of knowledge was gained from the corresponding transformations of ketones: Zimmerman and Traxler presented their insights into the nature of six-membered transition states in Ivanov and Reformatsky reactions in 1957,[195] and it was found that aldol reactions of metal enolates also proceed *via* these Zimmerman–Traxler transition states, evidenced by observed stereoconservation (*anti* from (*E*), *syn* from (*Z*)).[196,197] However, lower levels of diastereoselectivity were observed for smaller substituents on the metal enolates, presumably due to the comparatively large O–M (M = Li, ZnR, MgR, AlR_2) bond lengths, leading to loose transition states.[198,199] Mukaiyama introduced the formation of boron enolates (or vinyloxyboranes) by adding thioboronite $(n\text{-Bu})_2$BSPh to ketene and their application in aldol reactions as early as 1973.[200] These were later found to be *completely* diastereoconservative by Masamune and Evans, attributed to the formation of tight B–O bonds.[201,202] Their synthesis was notably straightforward using dialkylboron triflates and tertiary amines.[203]

Consequently, boron enolates became the method of choice, and two distinct approaches to asymmetric aldol reactions are highlighted herein, as depicted in Scheme 3.2. Chiral C_2-symmetric boranes were developed as transient auxiliaries for reactions with thioesters,

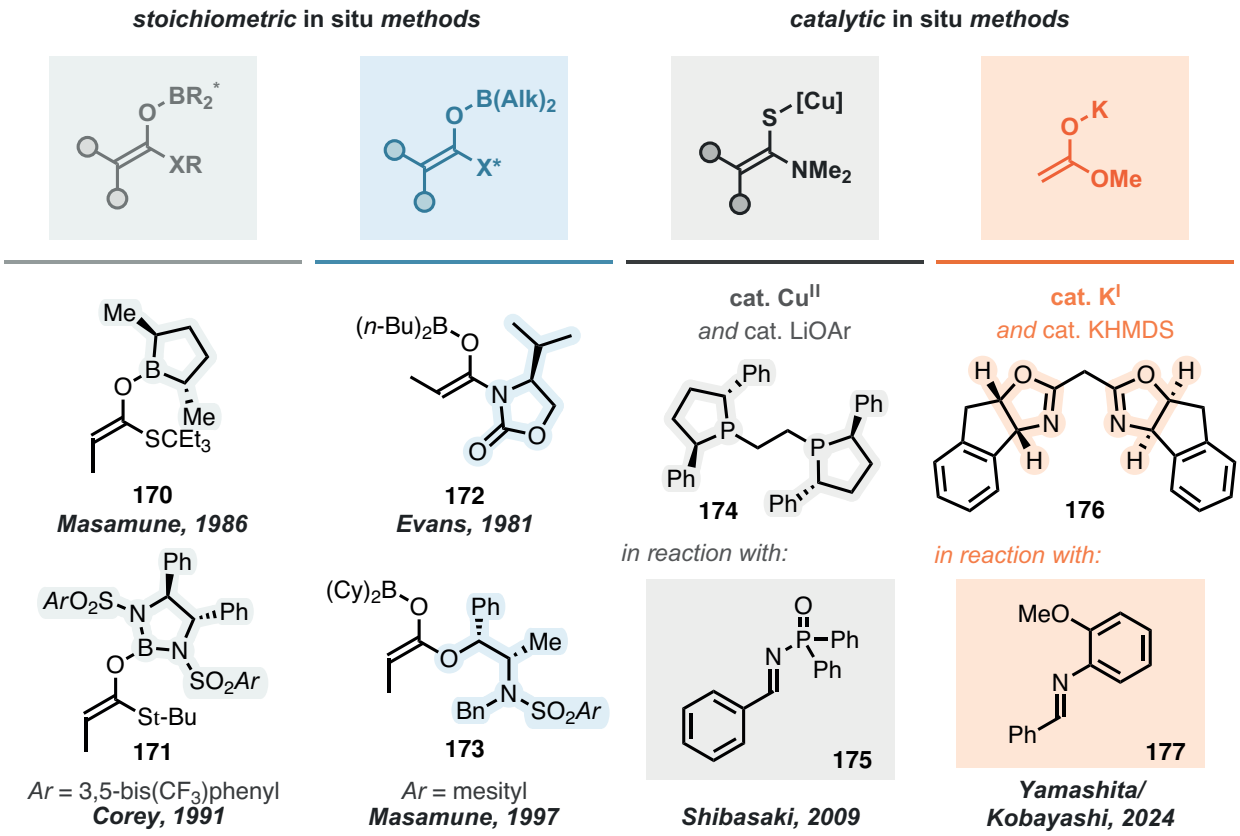

Scheme 3.2: Overview of methods for the asymmetric α-functionalization of carboxylic acid oxidation state equivalents.

and Masamune utilized **170** for *anti*-selective aldol reactions,[204] while Corey focused on diastereoselective synthesis of β-lactams using diazaborolidine **171**.[205] Evans' oxazolidinone auxiliary in reaction with (n-Bu)$_2$BOTf and triethylamine to yield **172** became renowned for *syn*-aldol reactions,[206,207] and complementarity was demonstrated in Masamune's *anti*-aldol reaction using the ephedrine-derived sulfonamide ester **173**.[208] The comparison of both auxiliaries **172** and **173** further underscores the critical role of the boron enolate double bond configuration for the diastereoselectivity in aldol reactions at that time.

The highest level of complexity is achieved in *catalytic* asymmetric direct transformations. Unlike the transient formation of boron enolates in auxiliary-mediated reactions, which occurs *via* stoichiometric amounts of boron triflate and tertiary amine, catalytic reactions introduce additional requirements for the catalyst. The entire transformation must operate based on the thermodynamic relationships between starting materials and products, necessitating sufficient activation and basicity for the generation of reactive species, while ensuring ample facial selectivity through kinetic preference for one of the diastereomeric transition states to achieve high enantioselectivity.

To this end, Shibasaki applied thioamides as highly Lewis-basic substrates, readily undergoing activation by a thiophilic copper(II) catalyst. Sub-stoichiometric amounts of lithium phenoxide efficiently deprotonated the thioamide (pK_a = 25.7 vs. 30.3 for t-BuOAc),[182] forming the copper enolate *in situ*, followed by an enantioselective Mannich reaction with Lewis-basic N-phosphinyl imine **175**.[209] A solitary example of a catalytic asymmetric direct reaction of alkyl esters was recently advanced by Yamashita and Kobayashi,[210] where strongly Brønsted-basic KHMDS in combination with a highly basic complex between potassium and a bis(oxazoline)ligand **176** successfully generated the methyl acetate-based potassium enolate. A subsequent Mannich reaction with sophisticated N-2-methoxyphenyl imines like **177** yielded high enantioselectivities up to 97.5:2.5 er. A key requisite of this transformation was the sufficient basicity of the potassium amide base formed immediately after nucleophilic attack to facilitate turnover. Direct activations of carboxylic acids with catalytic amounts of borane and superstoichiometric amounts of DBU are also known.[211,212]

1.3 Silyl Ketene Acetals

1.3.1 The Ireland–Claisen Rearrangement

The deprotonation of simple esters using lithium amide bases was pioneered by Rathke in 1971,[213] and just one year later, Ireland introduced the Claisen rearrangement of allyl ester enolates.[214] Lithium enolates of allyl propionates underwent rapid rearrangement, whereas predominantly side reactions were observed with allyl acetates. Consequently, silylation with TMSCl to form silyl ketene acetals facilitated a selective rearrangement at higher tempera-

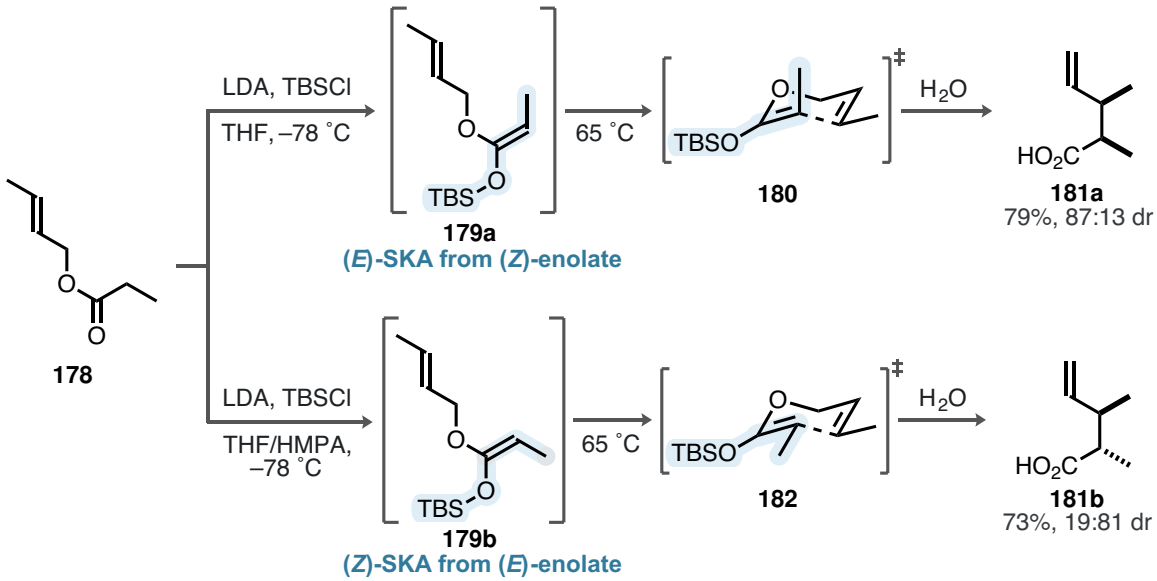

Scheme 3.3: Ireland's diastereodivergent silyl ketene acetal synthesis, as elucidated by analysis of the relative stereochemistry of the carboxylic acids **181a** and **181b**.

tures. These reactions are now recognized as Ireland–Claisen rearrangements, although the silyl ketene acetal variant has found broader application (Scheme 3.3).

The rearrangement products were initially obtained as a diastereomeric mixture of *syn*- and *anti*-products, which were not elaborated upon in the initial publication. Systematic investigations of the stereochemistry-defining factors were conducted in 1975 and 1976, respectively.[215,216] The six-membered chair-like nature of these pericyclic transition states had already been demonstrated,[217] which, combined with a stereodefined starting material, enabled the unambiguous assignment of the configuration of the double bond in the silyl ketene acetal based on the relative configuration of the rearrangement products (Scheme 3.3).

Accordingly, the subjection of (*E*)-crotyl propionate to straightforward deprotonation/silylation conditions using LDA and TBSCl at −78 °C yielded the *syn*-carboxylic acid **181a** (87:13 dr) after hydrolysis. Based on the analysis of the transition state **180**, Ireland concluded the reasonably selective formation of the (*E*)-silyl ketene acetal **179a**. Most importantly, synthesizing the silyl ketene acetal in a mixture of THF and highly Lewis-basic HMPA resulted in the inverted outcome, with *anti*-carboxylic acid **181b** from (*Z*)-silyl ketene acetal **179b** being the major diastereomer (81:19 dr).

What later became popularized as the *Ireland model* can be qualitatively understood *via* analysis of the deprotonation transition states (Scheme 3.4). Sterically demanding LDA was found to have a significant influence, and the tight transition state **183** in the absence of any Lewis-basic additives could be assumed to minimize potential 1,3-diaxial interactions of the ester α-substituent with one of the isopropyl groups.

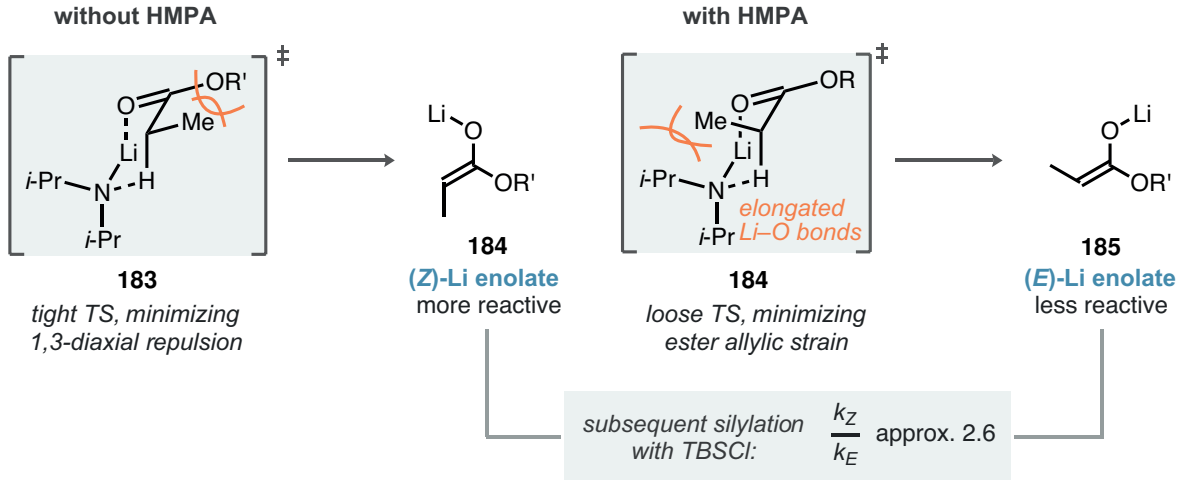

Scheme 3.4: The Ireland model, allowing for qualitative rationalization of the enolate structure as well as kinetic resolution of the respective enolates in a subsequent silylation with TBSCl.

Conversely, HMPA was expected to promote looser transition states through coordination to the lithium cations in the reaction mixture, thus shifting the focus of repulsive interactions onto the ester's allylic strain (see transition state **185**). Ireland later elucidated a *kinetic resolution* mechanism, providing deeper insight into the factors determining stereoselectivity in silyl ketene acetals.

It should be noted that silylation of an (*E*)-lithium enolate leads to a (*Z*)-silyl ketene acetal and vice versa—a result of the change in priorities of lithium versus silicon.

When a 30:70 (*E*)/(*Z*) mixture of lithium enolates in a 15 % solution of DMPU in THF was trapped with a sub-stoichiometric amount of TBSCl, a 14:86 mixture of (*Z*)/(*E*)-silyl ketene acetals was obtained, resulting in a 2.6 times higher reactivity of the (*Z*)-enolate.[218] Isomerization of the (*Z*)- to the (*E*)-enolate was excluded by control experiments, contrasting with the facile isomerization of ketone enolates *via* aldol/retro-aldol reaction[219] and likely related to a kinetically unfavored Claisen condensation pathway.

The differing reactivity of ester enolates adds complexity to the already step- and reagent-intensive synthesis of silyl ketene acetals. Ireland's diastereodivergent synthesis effectively established them as potent intermediates in chemical synthesis, also highlighting their *kinetic* properties. In the 1980s, Simchen further explored the synthesis of various silylated species—including silyl ketene acetals—using trialkylsilyl triflates and tertiary amines, thereby gaining significant insights into their *thermodynamic* properties, which will be discussed subsequently.

1.3.2 Soft Deprotosilylation Approaches

Simchen has presented a range of studies on the soft deprotosilylation of highly activated systems, such as esters bearing α-electron-withdrawing groups and highly Lewis-basic amides.[220–222] These efforts were further complemented by a systematic investigation of alkyl

esters (Scheme 3.5).[223]

He recognized the thermodynamic competition between silyl ketene acetals **187a** and α-silyl esters **188** as well as their substituent dependence, as depicted in Scheme 3.5 i. For alkyl esters with comparably small silyl groups (TMS), the thermodynamic minimum was found to be the α-silyl ester **189**, showing no sign of silyl ketene acetal formation. Conversely, esters with sterically large or electron-withdrawing substituents, such as ethyl phenylacetate, selectively furnished the (*Z*)-silyl ketene acetal **192a**. This evidence was further corroborated by the selective synthesis of α-trimethylsilyl ethyl phenylacetate **191** and its subjection to catalytic amounts of TMSOTf, demonstrating complete isomerization towards **192a**.

Regarding the dependence on the silyl group, soft deprotosilylation reactions were conducted with various trialkylsilyl triflates (Scheme 3.5 ii). Generally high reactivity was observed in the conversion of ethyl valerate **193**, yielding a 23:77 mixture of silyl ketene acetal and α-TMS ester after just 3 hour at room temperature. Larger silyl groups led to increased proportions of the silyl ketene acetal, and an interesting time-dependence was noted with TBSOTf. Initially, a mixture consisting of 87 % silyl ketene acetal and 13 % α-TBS ethyl valerate was obtained after 1 hour (full conversion). Prolonging the reaction time to 15 hour resulted in a mixture of 98 % (*Z*)-TBS silyl ketene acetal along with 2 % of the (*E*)-isomer.

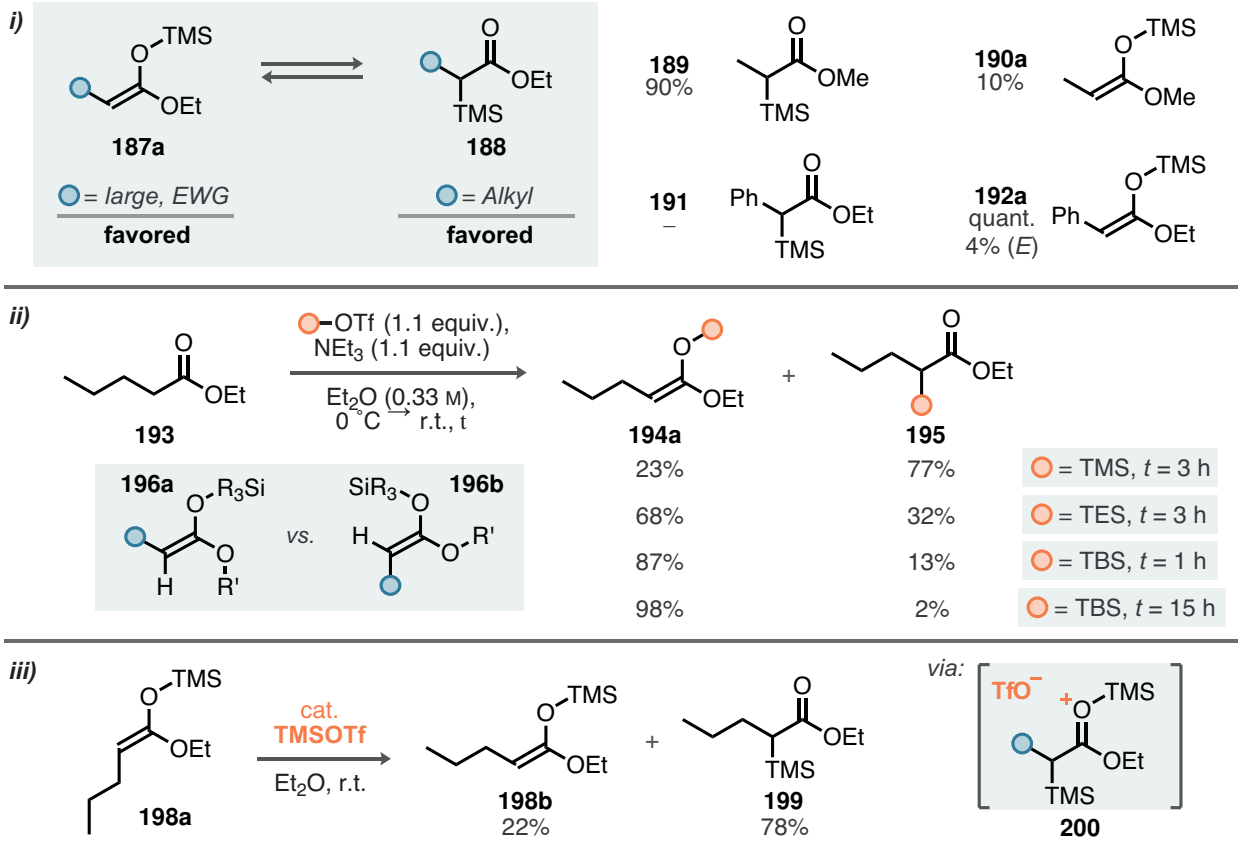

Scheme 3.5: Synthesis and isomerization studies of silyl ketene acetals of alkyl esters by Simchen.

Several key learnings can be extracted from these seminal studies: 1) Larger silyl groups favor the formation of the silyl ketene acetal over the α-silyl ester. 2) All isomers appear to be connected *via* silylium-catalyzed equilibration, leading to the thermodynamically most stable isomer after sufficient reaction time. The thermodynamic preference for the (*Z*)- over the (*E*)-silyl ketene acetal was further established by selective isomerization of (*E*)-**198a** to the equilibrium mixture of **194a** and **199** (*cf.* first entry in Scheme 3.5 ii), supported by similar studies by Wilcox.[224] Simchen proposed that this isomerization proceeds through a successive carbosilylation ion pair like **200**, facilitating access to either α-silyl or silyl ketene acetal isomers. It is likely that the higher stability of the (*Z*)-silyl ketene acetal originates from a series of allylic strain arguments, deriving from a preferable arrangement of substituents in **196a** over **196b**, even though the alkyl residue resides in a slightly unfavorable *s-cis* arrangement.

1.3.3 Silyl Ketene *N,O*-Acetal Intermediates in Catalysis

A notable study describing the catalytic and direct α-functionalization of tertiary amides to produce silyl ketene *N,O*-acetals was published by Kobayashi in 2011.[225] The reaction of *N,N*-dimethylacetamide with *N*-tosyl benzaldimine **201** was facilitated by 2 mol% of TIPSOTf and triethylamine, yielding the β-sulfonamido amide **203** in quantitative yield. Tertiary amides have also been a focus of Simchen's studies on activated systems in 1987,[220] which included descriptions of the spontaneous formation of *O*-silyl imidate salts such as **204**. The highly substituted nitrogen atom allows for rotation out of the plane, resulting in minimized overlap between the p-orbital and the π^* orbital of the carbonyl functionality. This *stereoelectronic bias* enables tertiary amides, such as **202**, to benefit from their high levels of Lewis basicity, yet also increases α-acidity in the ion pair **204** by minimizing allylic strain.

Nonetheless, Kobayashi's tertiary amide Mannich reaction has been instrumental in establishing the viability of the concept. It is plausible to assume that an active equilibrium between **204** and a silyl ketene *N,O*-acetal is established in the presence of triethylamine, with small amounts of the ketene acetal being continuously removed *via* nucleophilic addition.

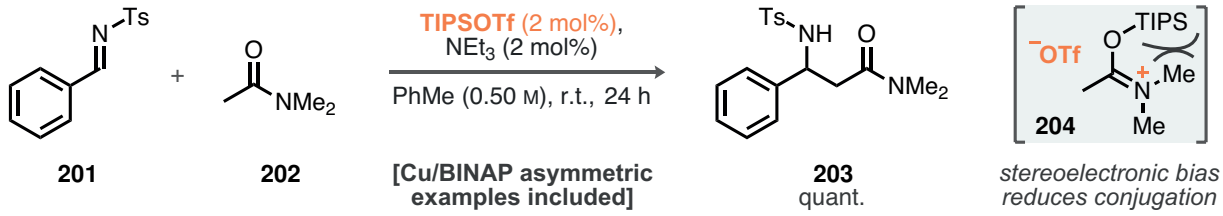

Scheme 3.6: Kobayashi's Mannich reaction of *N*-tosyl imines with stereoelectronically biased tertiary amides.

Turnover of silicon must occur through silyl transfer from an immediately formed silylated product, although either the intermediacy of silyl ketene acetals nor this mechanism were not further discussed by the authors.

2 Objectives

As effectively demonstrated in the previous sections, catalytic asymmetric and *direct* functionalizations offer advantages in terms of step and atom economy; however, they also present a wide array of thermodynamic and kinetic challenges, most of which must be addressed by the catalyst. This is particularly evident in the field of asymmetric organocatalysis, which struggles to provide a *general* solution for the activation of alkyl esters, frequently necessitating prefunctionalized starting materials.

We propose a *catalytic stereoselective* synthesis of silyl ketene *O,O*-acetals from simple alkyl esters, followed by their subsequent asymmetric functionalization *via* silylium ACDC, which could potentially overcome these existing challenges (Scheme 3.7). Literature precedent has demonstrated the viability of soft deprotosilylation methods for their synthesis (section 1.3.2), while the turnover of silicon has been established in Kobayashi's TIPSOTf-catalyzed Mannich reaction of *N*-sulfonyl imines (Section 1.3.3).

The overall goal shall be achieved through the development of an unprecedented direct silicon-catalyzed Mukaiyama–Mannich reaction of alkyl esters, predicated on the hypothesis that strong silylium activation of the ester substrates followed by subsequent deprotonation will generate silyl ketene acetals as *catalytically generated* intermediates.

If successful, this conceptual framework for conducting Mukaiyama-type reactions of simple esters catalytically, intertwined with a deep mechanistic understanding of the critical determinants, will pave the way for its ultimate realization—the integration with silylium ACDC. Considering the substantial number of catalytic asymmetric reactions in silylium

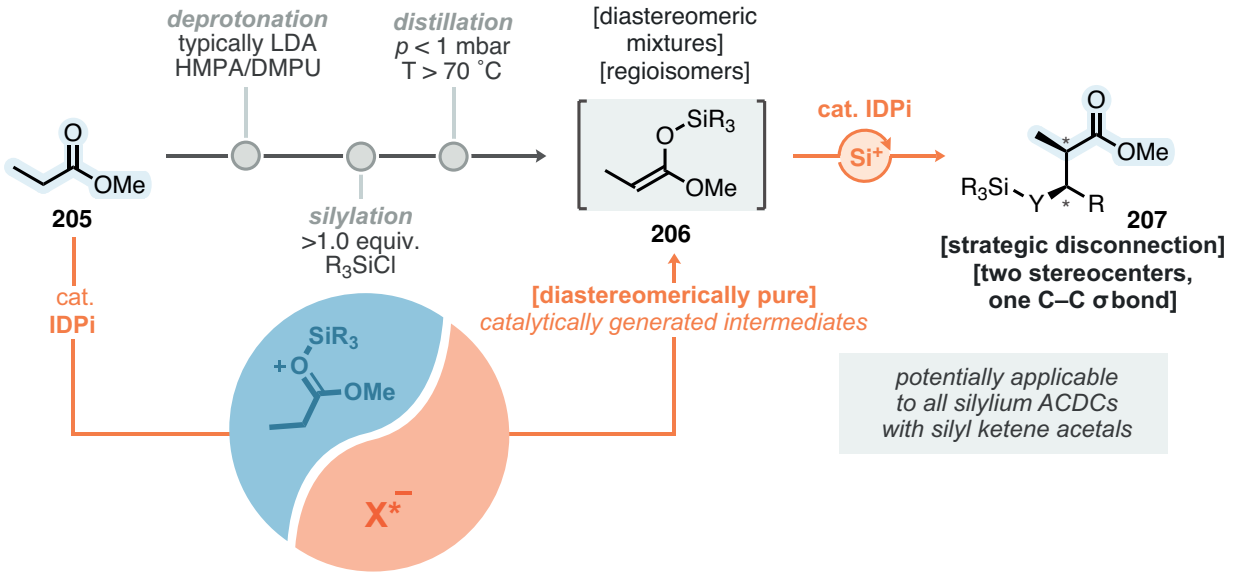

Scheme 3.7: Objective of this chapter: synthesis of silyl ketene acetals *via* silylium catalysis *in situ*, potentially resulting in catalytic asymmetric functionalizations catalytic in silicon.

ACDC primarily catalyzed by the IDPi class of catalysts (Scheme 3.1), these developments could significantly impact the field, making them potentially accessible from abundant alkyl esters rather than the laboriously synthesized and purified silyl ketene acetals.

A suitable highly confined and chiral enantiopure anion would therefore serve dual purposes: aiding in the silylium-catalyzed generation of catalytic amounts of silyl ketene acetal and inferring enantioinduction in a subsequent step with a specific electrophile. Not only would this enable the first silicon-catalyzed asymmetric Mukaiyama–Mannich reaction of alkyl esters, but it would also open up avenues toward *direct* functionalizations such as Mukaiyama–Michael and aldol reactions, as well as Ireland–Claisen rearrangements, and many more.

3 Results and Discussion

3.1 Computational Deprotosilylation Thermochemistry

Seeking to generate silyl ketene acetals as catalytically generated intermediates, we explored the thermodynamic landscape of carbonyl deprotosilylation reactions. Given that the conversion of ketones to enol silanes by reaction with allylsilanes is a well-established catalytic method using $HNTf_2$ and NEt_3[181] and in silylium ACDC,[180] we chose the reaction between acetone and allyltriisopropylsilane as a basis for computational comparison.

Isodesmic reactions are a specific type of *isogyric* reactions. Generally, isogyric reactions encompass all chemical reactions that maintain the same number of electron pairs in starting materials and products.[226] A subset of these, isodesmic reactions, are characterized by the *"retention of the number of bonds of a given formal type, albeit with a change in their relation to one another."*[227,228] These reactions have historical roots in a period when accurate thermochemical calculations were challenging due to the unavailability of vibrational frequencies, yet they often showed reasonable alignment with experimental data using what are now considered basic computational methods. Despite advancements in computational chemistry, the utility of isodesmic reactions has persisted in chemical synthesis due to their ability to provide rapid access to reliable thermochemical data and their error-cancelling nature.

Inspecting the transformations depicted in Scheme 3.8 separately, both the starting materials and products consist of 2 π and 17 σ bonds. Specifically, this reaction involves the transposition of one C−O π bond to a C−C π bond, as well as one C−Si σ bond to an O−Si σ bond, establishing an isogyric relation. In contrast, a reaction between two enol silane

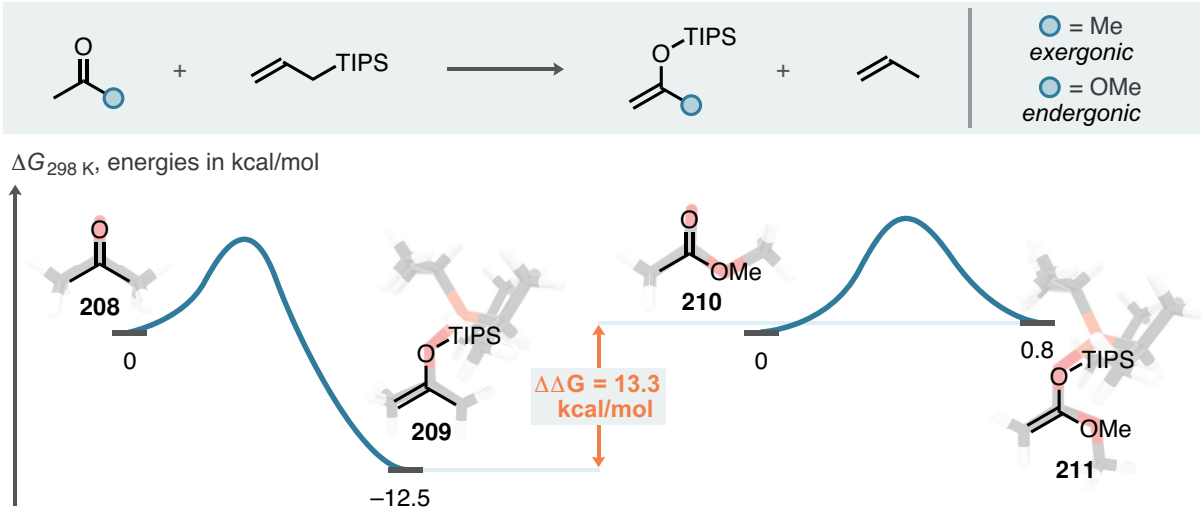

Scheme 3.8: Computational investigation of the deprotosilylation thermochemistry of acetone **208** and methyl acetate **210**; Gibbs free enthalpies (298 K) obtained at the DLPNO-CCSD(T)/cc-pVQZ//r2SCAN-3c level of theory.

equivalents would qualify as isodesmic.

Thermochemical data at 298 K for this comparison between acetone **208** and methyl acetate **210** was acquired using the r2SCAN-3c functional, followed by the computation of electronic energies at the DLPNO-CCSD(T)/cc-pVQZ level of theory. In alignment with experimentally feasible catalytic deprotosilylation of ketones, we calculated a Gibbs free energy of −12.5 kcal/mol for the deprotosilylation of acetone. Conversely, the challenge of rendering the same reaction with methyl acetate **210** became evident upon calculating an overall endergonic reaction pathway (0.8 kcal/mol). This results in an overall difference of $\Delta\Delta G = 13.3$ kcal/mol, primarily attributed to the higher stability of methyl acetate due to ester resonance.

For these reasons, it can be anticipated that direct deprotonation of silylium-activated alkyl esters by a weakly coordinating (and weakly basic) anion is an unfeasible pathway, necessitating the presence of additional basic species. Furthermore, the flat thermodynamic landscape suggests that highly reversible generation *in situ* might be operative, requiring the immediate subsequent removal of the silyl ketene acetal from the hypothetical equilibrium.

3.2 Development of a Silicon-Catalyzed Mukaiyama–Mannich Reaction of Alkyl Esters

3.2.1 Investigation of the Silylium Activation of Alkyl Esters

Given the inherently low acidity of alkyl esters and the thermodynamic endergonicity discussed in Section 3.1, we sought to investigate potential side reactions *via* NMR spectroscopy. These efforts were driven by the propensity of alkyl esters to undergo dealkylation rather than deprotonation under harsh conditions, as exemplified by the classical Krapcho reaction[229] with alkali metal (pseudo)halides at high temperatures, or the Jung–Olah–Voronkov reaction with highly Lewis-acidic TMSI.[230–232]

Consequently, we subjected 1.0 equiv. of $HNTf_2$ to rapid silylation conditions with an excess of TIPS 2-(methylallyl)silane (10.0 equiv.) in toluene-d_8 at room temperature (Fig. 3.1). This allowed us to observe immediate protodesilylation of the allylsilane, liberating isobutene and furnishing the strong Lewis acid $TIPSNTf_2$, as confirmed by ^{19}F and ^{29}Si NMR. The effect of subsequent methyl propionate addition (30.0 equiv.) as a model substrate was monitored using ^{1}H and ^{19}F NMR spectroscopy; the results are depicted in Fig. 3.1.

Upon addition of the ester, rapid decay of the signals corresponding to **214** was observed, while a new singlet at −73.9 ppm became visible in the ^{19}F NMR. This new species was identified as *N*-methyl bistriflimide **218a**, resulting from the collapse of the ion pair **220** to form **218a** and the silyl ester **219**. The overall concentration profile furthermore aligned well with first-order kinetics, as illustrated by the plotted curves in Fig. 3.1. It is likely

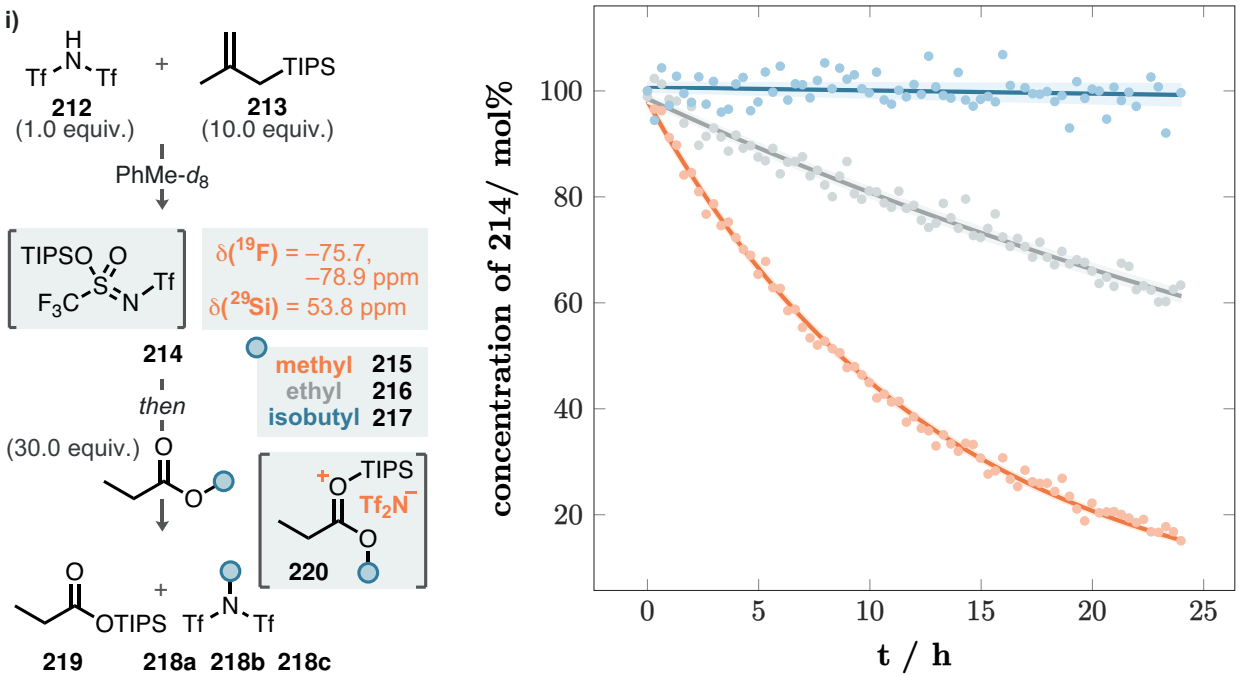

Fig. 3.1: Kinetic profile of the $TIPSNTf_2$ (**214**) alkylation by the three alkyl esters **215**–**217**; data points extracted from the relative integration of the ^1H (with **215**) or ^{19}F NMR (with **216** and **217**) signals corresponding to **214** and **218**. The plotted functions assuming first order-kinetics have been added for clarity; orange: reaction with **215**, gray: reaction with **216**; blue: reaction with **217**.

that the ion pair **220** forms readily and that charge-neutralizing alkylation of the anion is the rate-limiting step, although no further experiments were conducted to corroborate this hypothesis.

Overall, near-quantitative methylation of **214** occurred at room temperature, underscoring the extreme levels of activation that simple alkyl esters undergo in complexes such as **220**. Moreover, the unavailability of a deprotonation regime by the catalyst anion was verified experimentally, contrasting with the facile deprotosilylation of ketones.

Recognizing that this side reactivity offers potential pathways for catalyst deactivation *via* alkylation, we were intrigued by the possibility of investigating the effect of the alkyl group. For this reason, we chose to examine ethyl propionate **216** and isobutyl propionate **217**. As expected from the higher substitution, **216** reacted significantly slower towards *N*-ethyl bistriflimide **218b** compared to the methyl ester, yet still produced more than 30 % of **218b** after 24 hour at room temperature. The trend continued with isobutyl propionate, which showed no significant alkylation of $TIPSNTf_2$ **214** at room temperature.

Having realized the implications of alkyl ester silylium activation with the highly acidic and non-confined Lewis acid $TIPSNTf_2$, we considered the corresponding methylation using confined IDPi catalysts. To investigate these effects, we reacted IDPi **30** under identical reaction conditions as previously discussed at room temperature and 80 °C, analyzing aliquots

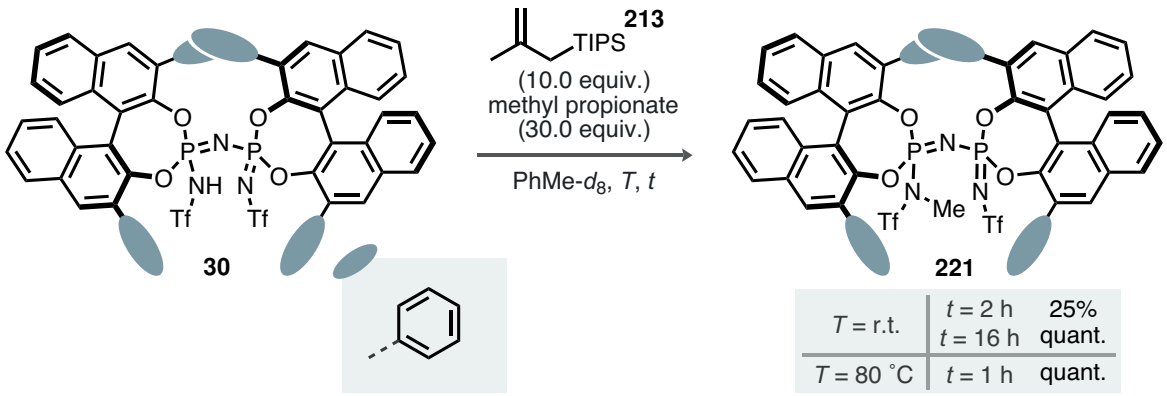

Scheme 3.9: *N*-methylation of IDPi **30** towards **221** by silylium-catalyzed reaction with methyl propionate **215**.

of the reactions by ^{31}P NMR spectroscopy (Scheme 3.9). Similar to the deprotosilylation studies discussed in Chapter 2, Section 3.5.1, we observed the formation of a desymmetrized species, displaying distinct doublets for each phosphorus atom. This species was formed at room temperature after 16 hour as the sole reaction product, and was formed quantitatively after just 1 hour at 80 °C.

Isolation and purification *via* silica gel chromatography ultimately led to the identification of the methylated IDPi **221**, demonstrating site-selective reactivity at one of the outer nitrogen atoms. This observation likely results from the enhanced accessibility of these nitrogen atoms, precluding any methylating reactivity at the central nitrogen atom.

Notably, the first-generation synthesis of IDPi **30** *via* the Staudinger reaction involved demethylation with 15.0 equiv. of TBAI at elevated temperatures as the final step.[233] This possibly renders a silylium-catalyzed methylation under our conditions irreversible, and therefore must be carefully considered in subsequent optimization efforts.

3.2.2 Initial Findings: TIPSOTf-Catalyzed Reactions

We initiated our efforts by investigating the reaction between *N*-tosyl benzaldimine **201** and methyl acetate **210** or methyl propionate **215** in the presence of 20 mol% TIPSOTf and NEt_3, following a protocol similar to that used by Kobayashi (Table 3.1).[225]

The reaction of methyl acetate in CH_2Cl_2 yielded 10 % of the desired Mannich product **222** after 16 h at room temperature. Since substituted silyl ketene acetals are more stable than their acetate-derived counterparts,[223] we speculated about a stronger driving force using methyl propionate. Accordingly, we observed increased reactivity towards **223** under otherwise identical conditions (entry 2, 39 %) with low diastereoselectivity (55:45 dr). Despite the low yield, this result demonstrated catalytic turnover of silicon in reactions of alkyl esters for the first time. An adjustment of the ester concentration further increased the yield to 73 % with unchanged diastereoselectivity (entry 3, 56:44 dr). The relative configuration was

Table 3.1: Screening of the reaction between imine **201** and methyl acetate **210** or methyl propionate **215** catalyzed by TIPSOTf and NEt_3. Reactions performed on 0.10 mmol scale; yields determined by ^1H NMR using mesitylene as an internal standard.

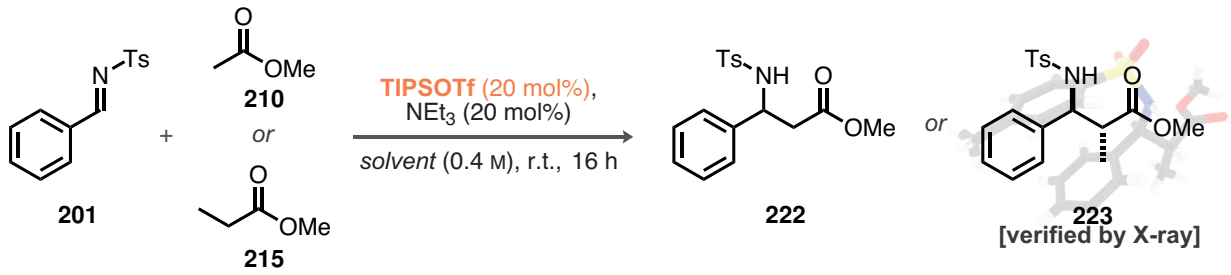

entry	ester (equiv.)	solvent	yield **222** or **223**	dr **223**
1	**210** (1.1)	CH_2Cl_2	10 %	–
2	**215** (1.1)	CH_2Cl_2	39 %	55:45
3	**215** (3.0)	CH_2Cl_2	73 %	56:44
4	**215** (3.0)	$CHCl_3$	41 %	51:49
5	**215** (3.0)	DCE	74 %	54:46
6	**215** (3.0)	PhMe	–	–
7	**215** (3.0)	PhCl	16 %	37:63
8	**215** (3.0)	THF	9 %	43:57

determined by separating both diastereoisomers, followed by crystallization, and subsequent X-ray crystal structure analysis of the *anti*-diastereomer.

Investigation of the effect of the solvent (entries 4–8) revealed a strong preference for chlorinated aliphatic solvents, showing a complete lack of reactivity in toluene (entry 6), which slightly recovered upon switching to chlorobenzene (entry 7). Intriguingly, chlorobenzene also led to a change in diastereoselectivity, favoring the *syn*-*N*-sulfonyl β-amino acid ester.

No conversion of the starting materials was observed when lower amounts of TIPSOTf and NEt_3 were used. Additionally, only traces of TIPSOTf methylation were detected by ^{19}F NMR analysis of the crude reaction mixtures, likely due to the overall reduced Lewis acidity in the presence of NEt_3.

Although these results effectively demonstrate the active regime of silicon catalysis, moderate reactivity was largely confined to chlorinated solvents. Given the importance of achieving maximum enantioselectivity for future applications of silylium ACDC, and considering that toluene has been identified as one of the best solvents in similar contexts,[173] which provided no conversion under these conditions, we opted to substitute TIPSOTf with the stronger Lewis acid $TIPSNTf_2$.[84]

3.2.3 $TIPSNTf_2$-Catalyzed Reactions

The most straightforward way to utilize $TIPSNTf_2$ is to generate it *in situ* by reacting with an allylsilane. To this end, and to avoid possible side reactivity from Hosomi–Sakurai-type allylation of the imine, we chose to presilylate 20 mol% of $HNTf_2$ with 1.0 equiv. allyltriisopropylsilane, rather than using the more nucleophilic methallylsilane **213** (Table 3.2).[174,234]

Generally, higher reactivity was observed with the stronger Lewis acid $TIPSNTf_2$, yielding improved results in CH_2Cl_2 (entry 1, 96 %) as well as diastereoselectivity (83:17 dr). Most notably, however, was the observed conversion towards **223** in toluene (entry 2), as well as the first instance of reactivity with catalyst loadings of less than 20 mol% (entry 3).

Motivated by this significant increase in reactivity, we hypothesized about the nature of the $TIPSNTf_2/NEt_3$ mixture. Assuming that triethylamine-mediated deprotonation of an ion pair like **220** (see Section 3.2.1) generates catalytic amounts of the silyl ketene acetal,

Table 3.2: Screening of the reaction between imine **201** and methyl propionate **215** catalyzed by $TIPSNTf_2$ and NEt_3. Reactions performed on 0.10 mmol scale with 3.0 equiv. **215**; yields determined by ^1H NMR using mesitylene as an internal standard; [a] at 0 °C; [b] at −25 °C; [c] at −50 °C.

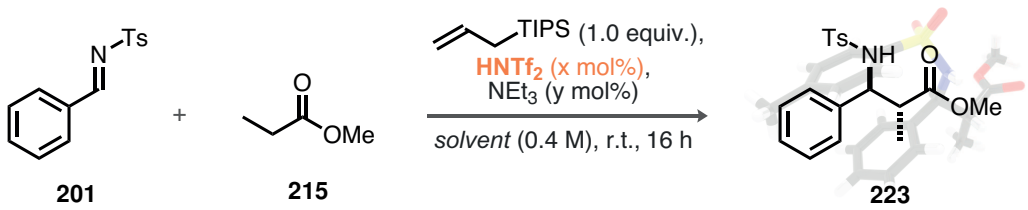

201 + **215** → **223**

entry	x	y	solvent	yield **223**	dr
1	20.0	20.0	CH_2Cl_2	96 %	83:17
2	20.0	20.0	PhMe	54 %	70:30
3	10.0	10.0	PhMe	11 %	71:29
4	25.0	20.0	PhMe	quant.	70:30
5	20.0	15.0	PhMe	quant.	81:29
6	15.0	10.0	PhMe	quant.	83:17
7	10.0	5.0	PhMe	quant.	86:14
8	5.0	2.5	PhMe	–	–
9[a]	15.0	10.0	PhMe	quant.	87:13
10[b]	15.0	10.0	PhMe	quant.	90:10
11[c]	15.0	10.0	PhMe	40 %	92:8

the formation of triethylammonium bistriflimide salt $[NEt_3H][NTf_2]$ would result. Although this species is still moderately acidic (see Section 3.6.2), its catalytic performance pales in comparison to the highly Lewis-acidic $TIPSNTf_2$. To ensure the constant presence of a "catalytic excess" of silylium Lewis acid in the system, we chose to reduce the amount of NEt_3 relative to $TIPSNTf_2$ (entries 4–11).

In our first experiment, employing 25 mol% $TIPSNTf_2$ and 20 mol% NEt_3, we observed quantitative formation of **223** with unchanged diastereoselectivity (entry 4, 70:30 dr). Subsequent reduction of the absolute amount of catalyst while retaining the difference of 5 mol% between $TIPSNTf_2$ and NEt_3 provided full conversion towards **223** up until a combination of 10 mol% $TIPSNTf_2$ with 5 mol% NEt_3 (entry 7). This trend was additionally accompanied by a gradual increase in diastereoselectivity (up to 86:14 dr).

Reaching a reactivity limit using the conditions shown in entry 7 at lower temperatures, we explored the effect of lower temperatures on the outcome of the reaction using a 15/10 mixture (entries 9–11). Consequently, silicon catalysis was active even at low temperatures of −50 °C, furnishing **223** in a reduced yield of 40 % with a diastereoselectivity of 92:8 dr.

3.2.4 Effect of the Silyl Group

Intrigued by the optimized reaction conditions, we investigated the effect of the silyl group by using 25 mol% of various allyltrialkylsilanes for deprotosilylation of $HNTf_2$ with imines **201** and **224** (Table 3.3).

For the reactions involving the *N*-tosyl imine **201** (entries 1–4), we observed no reactivity with allyltrimethylsilane and allyltriethylsilane as catalysts. Interestingly, reactivity was partially retained for the corresponding TBS allyl silane (47 %, 79:21 dr), while our standard conditions using allyltriisopropylsilane provided the product **225** in quantitative yield (86:14 dr).

In the reactions involving *N*-mesyl imine **224**, allyltriethylsilane (entry 6) exhibited no reactivity, while the corresponding TMS and TBS variants furnished the product in low yields (33 % and 27 %, entries 1 and 3). Based on the approximate range of these yields being close to the absolute amount of allylsilane added, it seems plausible to conclude an incompetent turnover of silicon. However, the lack of reactivity for the smaller allylsilanes with the *N*-tosyl imine suggests a significant divergence between **201** and **224**, emphasizing the importance of the larger TIPS group for effective silicon catalysis.

3.2.5 Exploration of the Scope

Having gained vital insights into the silicon-catalyzed activation of alkyl esters, we extended our investigation to include a variety of alkyl esters reacted with imines. This investigation

Table 3.3: Screening of the effect of the silyl group on the reaction between imine **201** or **224** and isobutyl propionate **217**. Reactions performed on 0.10 mmol scale with 3.0 equiv. **217**; yields determined by ^{1}H NMR using mesitylene as an internal standard.

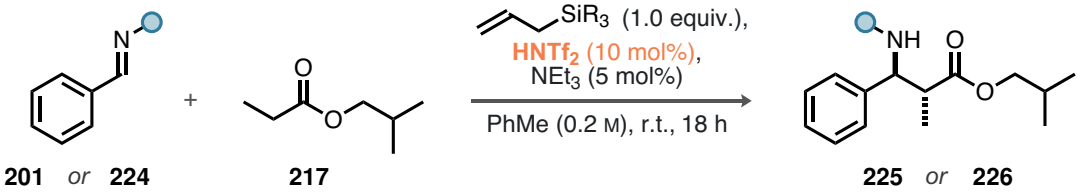

201 *or* **224** **217** **225** *or* **226**

entry	SiR_3		yield **225** or **226**	dr
1	TMS	Ts	–	–
2	TES	Ts	–	–
3	TBS	Ts	47 %	79:21
4	TIPS	Ts	quant.	86:14
5	TMS	Ms	33 %	86:14
6	TES	Ms	–	–
7	TBS	Ms	27 %	88:12
8	TIPS	Ms	quant.	88:12

is ongoing, and a selection of the already obtained examples is presented in Scheme 3.10.

All reactions were conducted using only 25 mol% of allyltriisopropylsilane, reinforcing the silicon-catalyzed nature of the process. Generally, the high yields and diastereoselectivities previously discussed in Section 3.2.3 were maintained upon expansion to include more diverse substrates. Specifically, conversions of not only methyl but also ethyl, isobutyl, and phenyl propionate were well tolerated, yielding the respective *N*-sulfonyl *β*-amino acid esters **227**, **225**, and **228**. Notably, the phenyl propionate-based product **228** exhibited visible precipitation from the apolar reaction medium, facilitating purification through simple filtration and washing with *n*-pentane. The corresponding C–C bond-forming reaction likely exhibited slightly lower diastereoselectivity, and the observed amplification could have been influenced by precipitation, especially considering the slightly reduced yield of 68 %.

Distinct sulfonyl functionalities beyond the tosyl group also facilitated rapid product formation, allowing access to mesyl-based *β*-amino esters **229**, **230**, and **226** in high yields and with good diastereoselectivities. The conversion of an *N*-ethanesulfonyl imine was also well tolerated.

The 4-methylphenyl-substituted product **231** marked our first entry into the reactions of substituted aromatic imines, providing promising data (86 %, 87:13 dr). A preliminary investigation into esters bearing longer alkyl chains was conducted for the reaction with

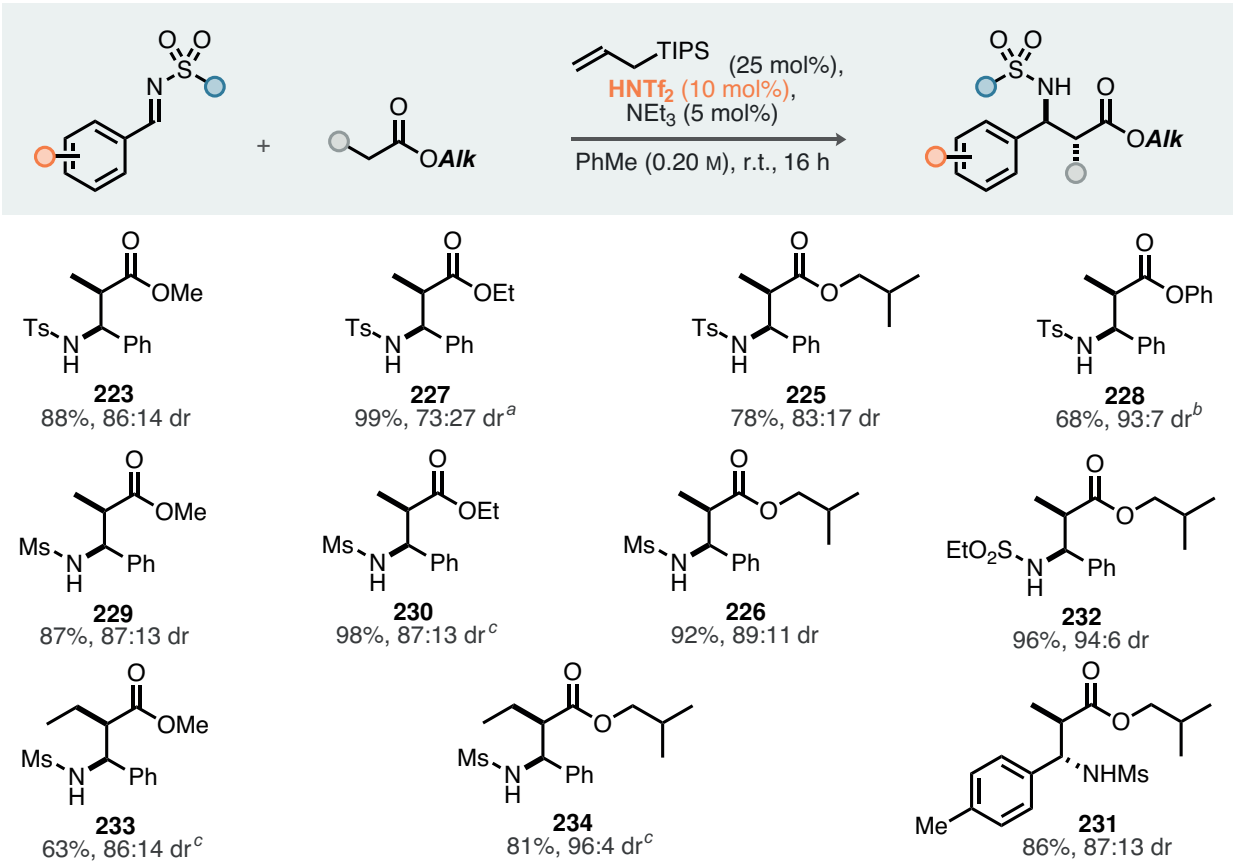

Scheme 3.10: Scope of the silicon-catalyzed reaction between selected aromatic imines and alkyl esters; reaction conducted on 0.40 mmol scale; isolated yields; diastereoselectivity determined by ^{1}H NMR analysis of the crude reaction mixtures; [a] on 0.05 mmol scale, NMR yield; [b] purified by filtration; [c] performed by Lennart Brücher.

methyl and isobutyl butyrate. Consistent with our previous results, these products were readily formed, underscoring the robustness of the catalytic system across a range of substrate complexities.

3.2.6 Proposed Reaction Pathway

Based on the results gained from our optimization and scope efforts, we propose the following reaction pathway (Scheme 3.11). Considering the entire reaction system, the alkyl ester is the most Lewis-basic component.[175] Following this assumption, coordination of $TIPSNTf_2$ would lead to the formation of a siloxocarboxonium bistriflimide ion pair such as **235**. Unlike the similar ion pair **220**, discussed in Section 3.2.1, the catalytic amounts of NEt_3 now make the deprotonation thermodynamically accessible, yielding (*Z*)-silyl ketene acetal **236a** *in situ* with the liberation of $[Et_3NH][NTf_2]$.

The formation of **236a** was additionally verified through stoichiometric experiments, inspired by the pioneering studies of Simchen. Reacting methyl propionate **215** with TIPSOTf

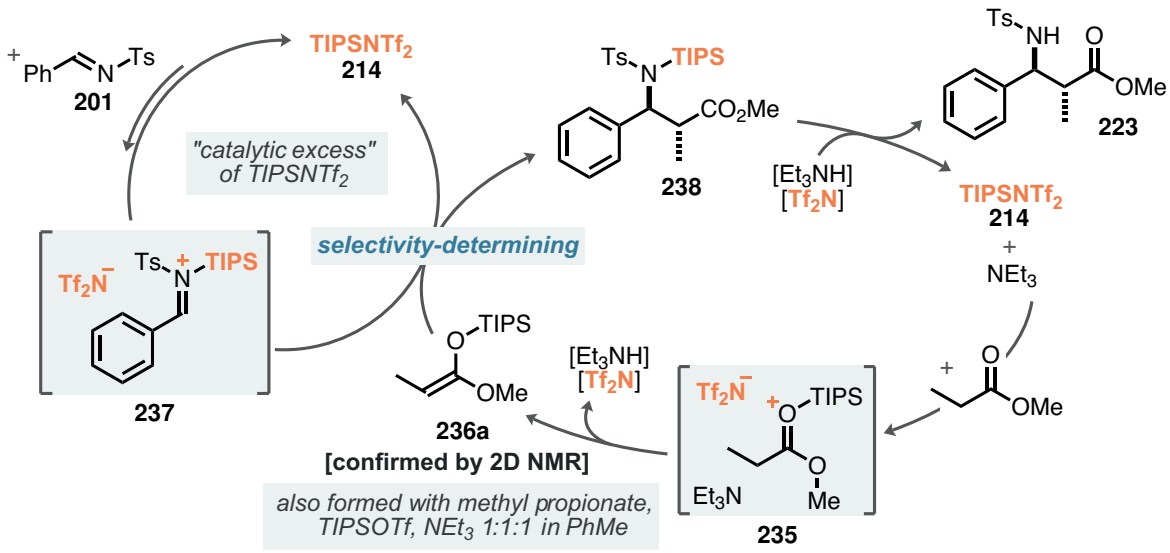

Scheme 3.11: Proposed reaction pathway of the silicon-catalyzed Mukaiyama–Mannich reaction between *N*-sulfonyl imine **201** and methyl propionate **215**, catalyzed by $TIPSNTf_2$ **214** and NEt_3.

and NEt_3 (1:1:1 ratio) in toluene-d_8 at room temperature for 16 h in an NMR tube resulted in 27 % clean conversion towards **236a**. The relative configuration of the silyl ketene acetal was not verified by NOESY experiments and was assigned based on literature precedent.[223,224]

The facile formation of **236a** is followed by a nucleophilic attack on the TIPS-activated imine **201**. Given the generally low Lewis basicity of *N*-sulfonyl imines,[175] an activated complex such as **237** likely forms only in minor quantities. We postulate that the ensuing activation compensates for this, with **236a** rapidly adding to yield the *N*-silyl-*N*-sulfonyl Mannich product **238**. This step likely determines diastereoselectivity, producing the *anti*-product through significant contributions of steric repulsion by the large TIPS group.

Additionally, while the relative configuration of the imine in **237** was not determined, based on the size of the substituents, we propose the depicted (*Z*)-configuration. Turnover of the two catalytic species is eventually established *via* proton-silicon metathesis between **238** and $[Et_3NH][NTf_2]$ to yield the sulfonamide product **223** through an overall silicon catalysis mechanism.

It is noteworthy that the "catalytic excess" of $TIPSNTf_2$ led to an acceleration of product formation, and that moderate to excellent yields were already achieved in toluene and CH_2Cl_2, respectively, even with equimolar amounts of $TIPSNTf_2$ and NEt_3. Considering these results, we hypothesize that in those reactions (Sections 3.2.2 and 3.2.3), no silylium activation of the imine occurs. Consequently, the mild Brønsted acid $[Et_3NH][NTf_2]$ acts as the active catalyst, promoting product formation through hydrogen bonding activation of **201**.

Reflecting on the outcomes of the silyl group screening (Section 3.2.4), it appears that smaller silyl groups do not facilitate silicon-hydrogen exchange between the silylated Mannich product **238** and $[Et_3NH][NTf_2]$. The accumulated ammonium salt would then engage in

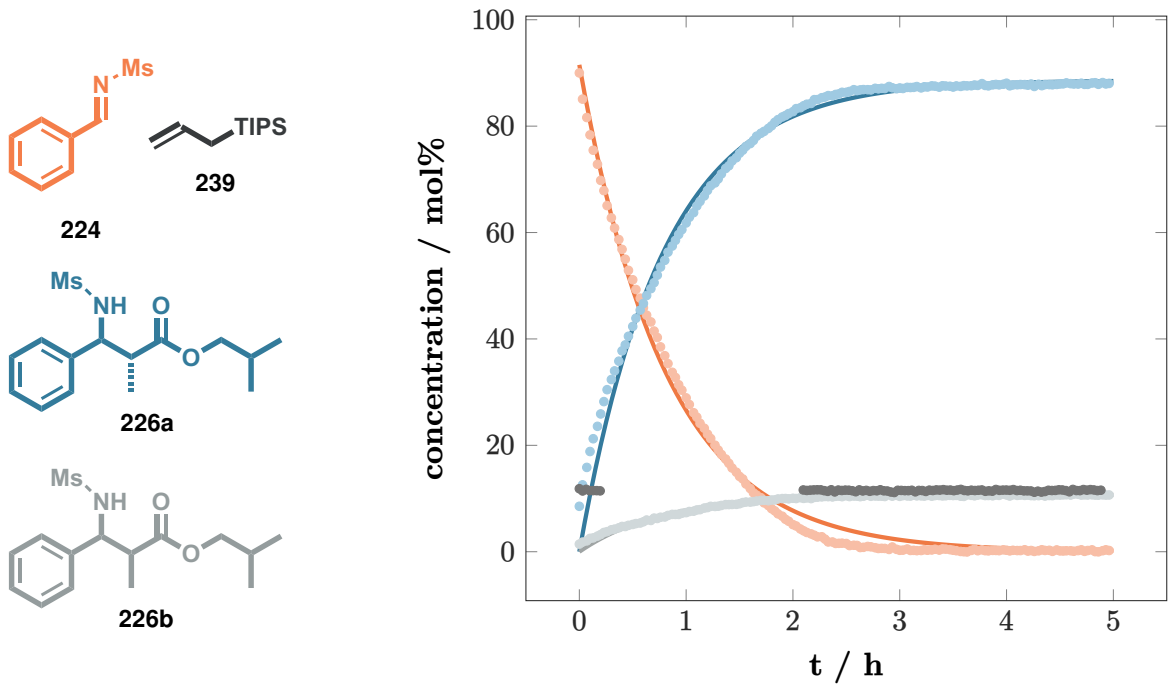

Fig. 3.2: Kinetic profile of the reaction between *N*-mesyl imine **224** and isobutyl propionate **217** as monitored by ^{1}H NMR; the reaction was conducted with 25 mol% allyltriisopropylsilane, 10 mol% $HNTf_2$, 5 mol% NEt_3 and 3.0 equiv. ester in toluene-d_8.

sluggish protodesilylation of the allylsilane until its complete consumption. This suggests a significant degree of frustration in **238**, which might be key to enabling overall turnover in the silicon catalysis.

We additionally monitored the reaction between *N*-mesyl imine **224** and isobutyl propionate **217** with 25 mol% allyltriisopropylsilane, 10 mol% $HNTf_2$, and 5 mol% NEt_3, by ^{1}H NMR spectroscopy (Fig. 3.2). High levels of reactivity were observed in this experiment, achieving full conversion towards both diastereomers of **226** after less than 3 h at room temperature. Several interesting features can be recognized in the kinetic profile.

The concentration of allyltriisopropylsilane **239** remained constant at approximately 12 % throughout the reaction, indicating no further deprotosilylation after initial activation of $HNTf_2$. Notably, the signal of **239** used for integration showed significant overlap with the NH proton of the *syn*-diastereomer **226b** from 20 minute to 2 hour, and therefore the concentration was not plotted for this time interval. This observation supports our proposed reaction pathway in Scheme 3.11, which is based on closed cycles of $TIPSNTf_2$ and $[Et_3NH][NTf_2]$ without the regeneration of $HNTf_2$. Interestingly, no traces of any silylated forms of the product **226** were detected, indicating rapid silicon-hydrogen exchange.

Moreover, exponential fits of the concentration profiles based on first-order kinetics were added in Fig. 3.2. As clearly visible from the profile of imine **224**, the experimental data does not qualitatively align with the kinetic model. For moderate conversions (50–70 %), the

reaction was slower, whereas for higher conversions (>80 %) it was faster than expected by a first-order dependence. This behavior could suggest a stronger influence of a pseudo-zero-order pathway, possibly explained mechanistically *via* a rate-limiting generation of the silyl ketene acetal **236a** followed by a kinetically fast nucleophilic addition to yield the *N*-silylated product **240**, which was not observed spectroscopically.

3.3 Possibilities for Asymmetric Organocatalysis

Mechanistic and kinetic studies have emphasized the instrumental roles of a catalytic Brønsted-basic species for the *in situ* generation of silyl ketene acetals, along with a TIPS silylium Lewis acid for catalytic turnover in silicon. Speculating about the possibilities to introduce chirality into either catalytic species, without further complicating the system, we propose three distinct approaches (Scheme 3.12). For the reactions involving equimolar amounts of $TIPSNTf_2$ and NEt_3, we considered the implications of the resulting triethylammonium bistriflimide salt for mild Brønsted acid catalysis in the activation of the imine. If a chiral tertiary amine base were used instead of NEt_3, asymmetric induction might occur in a complex similar to **241**.

Additionally, the overall silicon-catalyzed nature of this transformation potentially enables enantioinduction *via* a suitably designed chiral silane. The intriguing implications of this approach not only lie in the formation of a chiral complex with the imine **242**, but also in the *in situ* generation of a chiral enantiopure silyl ketene acetal. Historically, such silyl ketene acetals have primarily been used as stoichiometric chiral auxiliaries.[235,236]

Lastly, silylium ACDC offers the possibility of enantioinduction through ion-pairing to a chiral enantiopure counteranion. The development of highly acidic Brønsted superacid organocatalysts in recent years would allow for the substitution of $HNTf_2$ with an IDPi catalyst. However, our previous experience with direct nitroalkane silylation reactions (Chapter 2, Section 3.6) has demonstrated the high stability of ammonium IDPi salts, thus preclud-

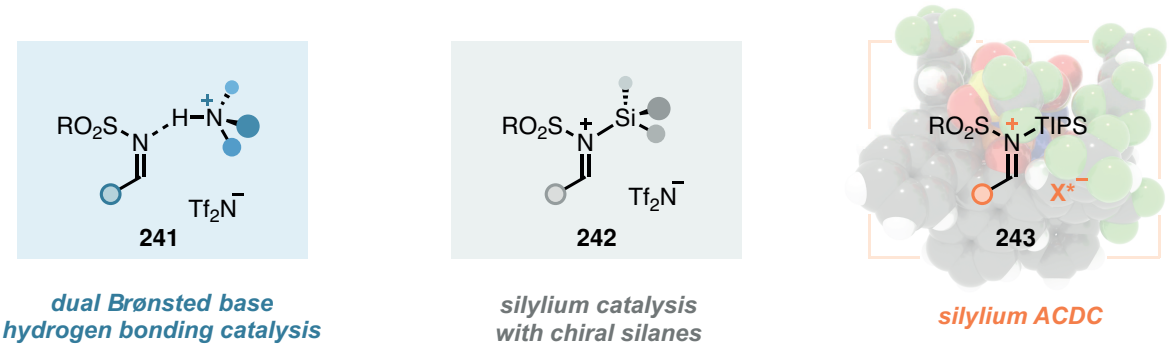

Scheme 3.12: Potential asymmetric silicon-catalyzed Mukaiyama–Mannich reactions based on three distinct approaches.

ing any promising compatibility with tertiary amines in this context. For this reason, we recognize that the potential success of a silylium ACDC approach lies in the development of silylium-compatible Brønsted-basic species that avoid transient salt formation.

The following sections will briefly discuss the first two concepts of chiral amine and chiral silane catalysis, and finally deconvolute our significant efforts towards the realization of an asymmetric silicon-catalyzed Mukaiyama–Mannich reaction *via* silylium ACDC.

3.4 Chiral Tertiary Amine-Catalyzed Mukaiyama–Mannich Reactions

Asymmetric quinine- or quinidine-catalyzed Strecker reactions[237] and ketene hydroalkoxylations[238] are among the first organocatalytic reactions known in the field. To investigate the influence of chiral tertiary amines on the silicon-catalyzed Mukaiyama–Mannich reaction from a proof-of-concept perspective, we utilized quinine as the catalyst framework. Although silylation of sterically demanding hydroxy functions, such as the encumbered secondary alcohol in quinine, with large silyl groups can be expected to be comparably slow, we opted to use the methylated catalyst **244** to avoid potential neutralization of the silylium Lewis acid.

Based on our mechanistic insights, we postulated a minimal influence of silylium catalysis in the nucleophilic addition of the silyl ketene acetal for stoichiometrically equal amounts of $TIPSNTf_2$ and tertiary amine. Thus, we employed conditions shown in Table 3.2 (entries 1 and 2) for our investigation, substituting NEt_3 with *O*-methylquinine **244** (Scheme 3.13).

Both reactions, either in CH_2Cl_2 or toluene, yielded the product in comparable yields and diastereoselectivity as the corresponding NEt_3-catalyzed variants. However, no measurable enantioselectivity was observed in CH_2Cl_2, while the reaction in toluene provided **223** with low enantioselectivity (53:47 er).

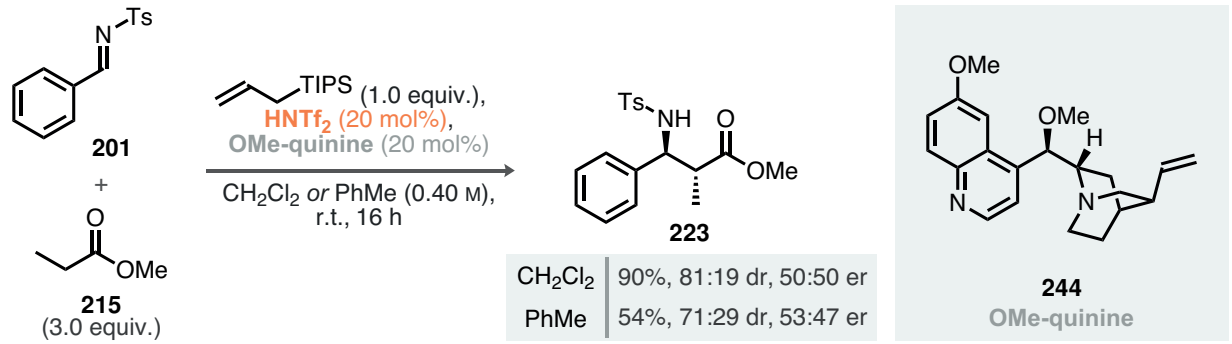

Scheme 3.13: Silicon-catalyzed Mukaiyama–Mannich reactions in the presence of chiral tertiary amine **244**; reactions on 0.10 mmol scale; yields and diastereoselectivities measured by ^{1}H NMR analysis of the crude reaction mixtures with mesitylene as internal standard; absolute configuration of **223** not determined.

The *O*-alkylation of cinchona alkaloids is a standard procedure for catalyst design in phase-transfer catalysis[239] and, for instance, is also the linkage point of Sharpless' dihydroxylation ligands.[240] Nonetheless, considering the absence of significant interactions originating from **244** except for π-π interactions of the quinoline fragment, we hypothesize that overly flexible transition states may have led to the observed low enantioselectivity. This might be overcome by systematically designing interaction donors, such as large electron-rich aryl groups on the secondary alcohol. Polar interactions to the comparably electron-poor quinoline would consequently lead to a more rigid catalyst structure, potentially enhancing enantioselectivity.

Additionally, although these results suggest some contribution of the chiral ammonium ion to the enantiodetermining step, more in-depth mechanistic studies under these exact conditions would be required. Given the high catalyst loadings (20 mol% each) needed for sufficient reactivity, further work was discontinued.

3.5 Chiral Silicon-Catalyzed Mukaiyama–Mannich Reactions

3.5.1 Overview of Existing Chiral Silane Catalysts

The majority of chiral silane catalysts have been developed for asymmetric Diels–Alder reactions over the past 26 years.[241–249] Despite the niche appeal due to a lack of generality and practicality in broader applications, these catalysts have made significant contributions to chemical catalysis.

The origins of chiral silane catalysts trace back to Noyori's first synthesis of an axially chiral binaphthyl-based dimethylsilane in 1982,[250] which was later evolved into the acetonitrilium ion **245** by Jørgensen and Helmchen in 1998.[241] Initially proposed to be a pure silylium ion with a persistent charge at silicon, its more likely coordination to the solvent was later clarified by Olah.[251] Recently, Hatanaka developed the corresponding bistriflimide silylium Lewis acid based on Jørgensen's and Helmchen's initial structure, achieving excellent

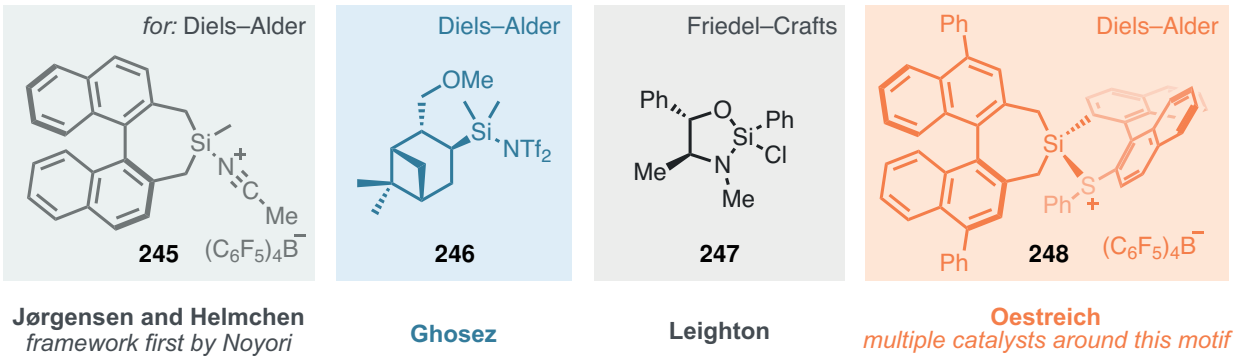

Scheme 3.14: Short overview of chiral silicon catalysts developed.

enantioselectivities in Diels–Alder reactions of α,β-unsaturated N-acyl oxazolidinones.[242]

Ghosez introduced the myrtenal-based silane **246** also for Diels–Alder reactions, achieving only moderate enantioselectivities. Interestingly, the primary methoxy group was found to be instrumental for enantioinduction.[243]

Leighton's development of strained chlorosilanes like **247**, where an electron-poor silicon atom is embedded within a *cis*-substituted five-membered cycle, has induced significant strain, favoring the formation of putative pentacoordination at silicon. This approach has proved successful for Friedel–Crafts reactions of hydrazones[252] and Diels–Alder reactions.[244]

The most recent advancements were introduced by Oestreich, who proposed increasing Lewis acidity through a constant cationic heteroatom-stabilized charge at silicon, akin to the acetonitrilium ion **245**. A series of catalysts based on this motif have been developed, demonstrating high potential as asymmetric catalysts for Diels–Alder reactions of chalcones.[245–249] Notably, **248** features phenyl-substitution at the binaphthyl backbone in the 4,4'-positions, diverging from the traditional 3,3'-positions.

3.5.2 Toward Chiral Trialkylsilane Catalysts

In our quest to synthesize a novel catalyst motif that potentially accommodates the several distinct requirements for the silicon-catalyzed Mukaiyama–Mannich reaction, we pursued a hybrid approach. For most BINOL-based catalysts, especially in organocatalysis, the 3,3'-positions have proven to be the most effective handles to modulate enantioinduction.[51,52]

Structures similar to **245** and **248** are particularly intriguing due to the positioning of the silicon atom within the C_2 axis of the structure, rendering this an overall chirotopic non-stereogenic center. This configuration suggests a higher potential for generality in these catalysts compared to **246** or **247**, for example.

Consequently, we chose to synthesize silicon catalysts similar to the original structure **245** synthesized by Jørgensen and Helmchen, incorporating substituents at the 3,3'-positions, using a phenyl group as a model. To establish a basis for comparison and reactivity optimization, we additionally synthesized the unsubstituted variant.

Our synthesis commenced with the triflation of readily available (S)-BINOLs **249** and **250** under standard conditions, providing **251** and **252** in quantitative yields following simple aqueous workup. Subsequent installation of the methyl groups proceeded *via* Kumada coupling with MeMgBr to yield **253** and **254** in 68 % and 84 % yield, respectively. Silepine **255** has been synthesized in the literature either through direct metalation of the parent binaphthyl compound[253] or tin-lithium exchange of the corresponding stannepine.[254] Since the tin route requires chlorination, Grignard formation, and addition of Me_2SnCl_2, we opted for the direct metalation approach.

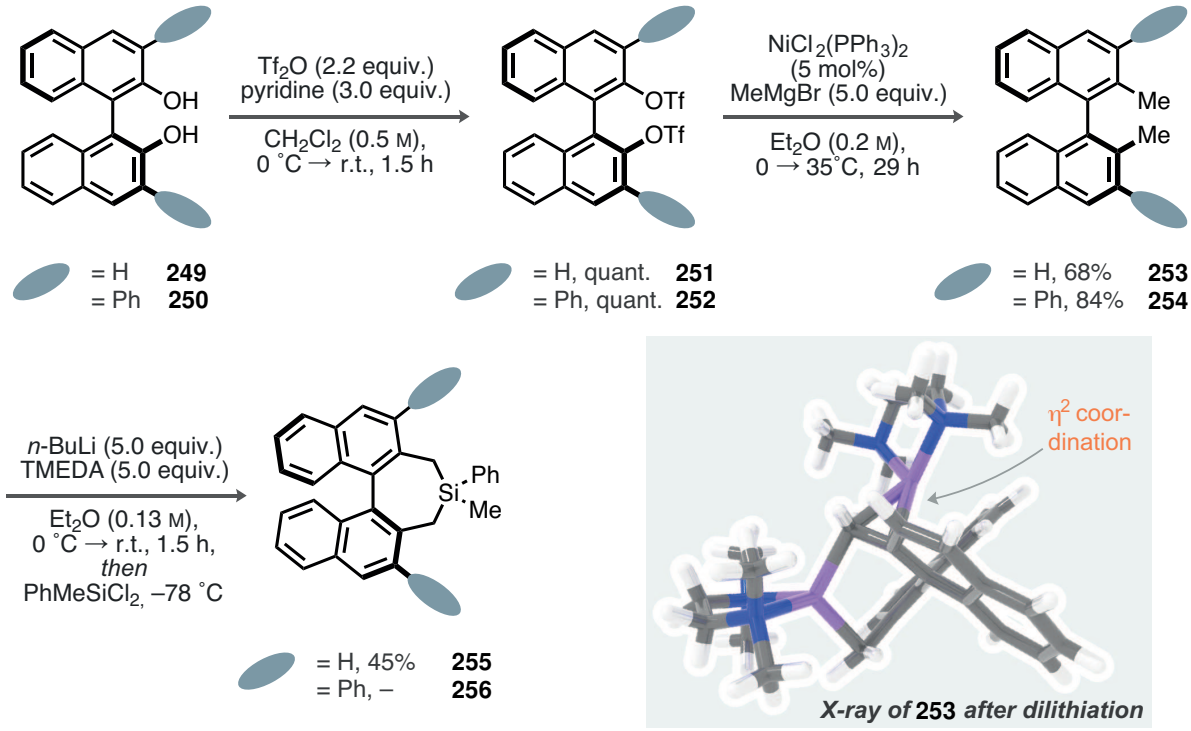

Scheme 3.15: Exploration route towards silepines **255** and **256** from (*S*)-BINOLs **249** and **250** (blue: nitrogen, purple: lithium).

After concentrating an *n*-BuLi solution in hexanes under vacuum, addition of a solution of 3,3'-unsubstituted (*S*)-binaphthyl **253** in THF and finally TMEDA, an immediate color change to dark red was observed, with the formation of a red precipitate after 1.5 h. This observation aligns with the literature, where synthesis of intensely colored organolithiums followed by recrystallization has, in some cases, been found to enhance the subsequent silylation step (see Scheme 3.15, bottom right, for an X-ray crystal structure of the dilithium salt of **253**).[253] We then added $PhMeSiCl_2$ (3.0 equiv.) to the crude reaction mixture after cooling to −78 °C, observing complete discoloration after 7 h. Ultimately, silepine **255** was obtained in 45 % yield.

Encouraged by this initial success, we proceeded to investigate the dilithiation-silylation sequence for the 3,3'-substituted binaphthyl **254**. However, attempts to obtain the desired silepine **256** were unsuccessful, with unspecific decomposition observed during lithiation and the appearance of the same intense red color. This result persisted even with extended lithiation periods of 16 h and 69 h at room temperature.

Several factors could explain these unsuccessful attempts. Firstly, etheral solvents tend to decompose in the presence of strong organolithium bases *via* formation of more stable lithium alkoxides.[255] This decomposition is also influenced by the aggregation state of the organolithium species, offering a possible explanation for the divergence between **253** and **254**.[256]

Additionally, the photolysis of organolithium compounds is a well-studied phenomenon, known to proceed through single electron-transfer processes.[257] The high degree of coloration of the putative lithium salts suggests significant susceptibility to visible light irradiation. The X-ray crystal structure, as reported in the literature,[253] of the 3,3'-unsubstituted dilithium salt (Scheme 3.15) already demonstrates a contribution of the aromatic binaphthyl backbone by means of η^2-coordination to the lithium atom—an interaction that could potentially influence the stability of the corresponding 3,3'-substituted binaphthyl species.

3.5.3 Toward Chiral Alkylaryloxysilane Catalysts

The time- and step-intensive synthesis of silepine **255**, along with the unsuccessful attempts to access **256**, prompted a reconsideration of a potentially more direct route to chiral and active silicon catalysts. Given that motifs similar to **255** are typically synthesized from (*S*)-BINOL and its derivatives through multiple steps, we hypothesized that direct silylation of the OH functionalities with a suitable (allyl)(alkyl)$SiCl_2$ species would furnish aryloxysilanes. These aryloxysilanes could then generate the active Lewis acid *in situ* through reaction with $HNTf_2$.

To assess the feasibility of this approach, we first chose to conduct model studies using achiral aryloxysilicon species (Scheme 3.16). Allyl(dimethyl)phenoxysilane **257** was synthesized *via* a straightforward substitution reaction between phenol and allyl(dimethyl)chlorosilane, achieving 98 % yield. Subjecting a solution of **257** in toluene-d_8 (0.20 M) to 10 mol%

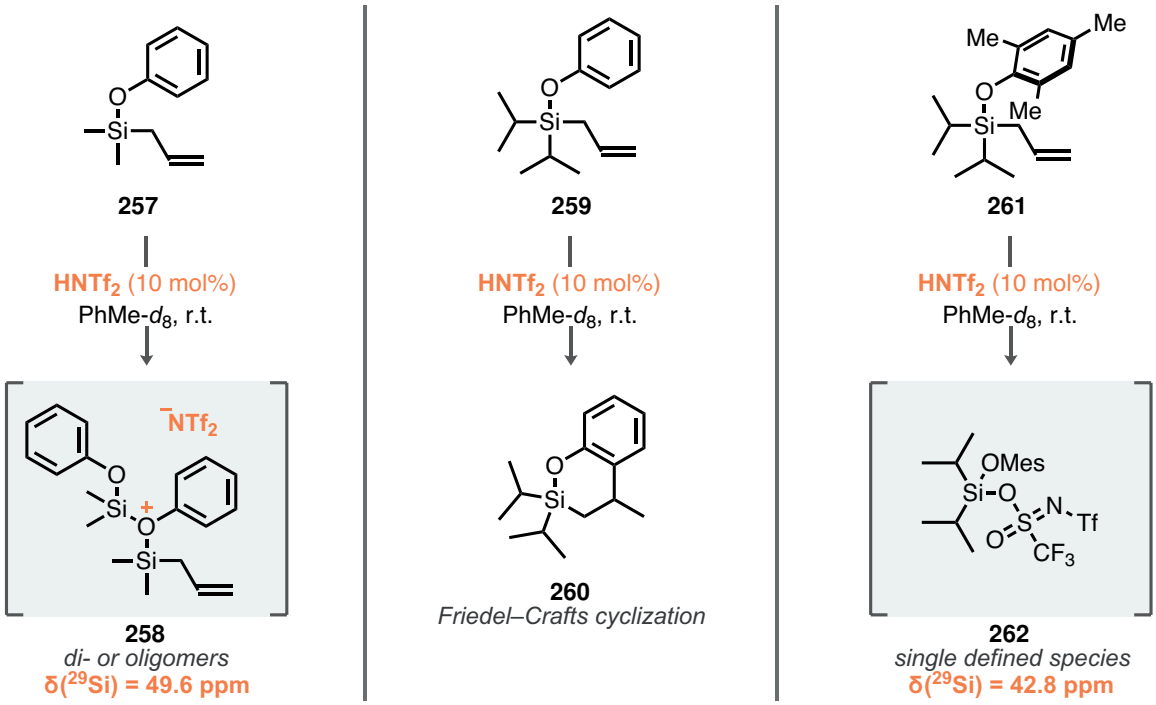

Scheme 3.16: Investigation of the newly synthesized aryloxysilanes **257**, **259**, and **261**.

$HNTf_2$ indicated the formation of an active silylium-like Lewis acid, as evidenced by ^{29}Si NMR (δ = 49.6 ppm). However, ^{19}F NMR analysis revealed very broad signals ranging from −76.0 to −79.0 ppm. Based on this evidence, we conclude that **257** most likely di- or oligomerized upon activation, as indicated by structure **258**.

Using the conditions described in Table 3.2, entry 7, with 50 mol% of **257**, no conversion of the starting material was observed. This observation aligns with the propensity of **257** to oligomerize, likely due to the small size of the methyl groups, which is similar to the reduced or absent reactivity observed with allyltrimethylsilane (Table 3.3).

To increase the size of the alkyl portion of the allylsilane, we synthesized the corresponding diisopropyl variant **259**. Allyl(diisopropyl)chlorosilane was synthesized from chlorodiisopropylsilane *via* substitution with allylmagnesium bromide, followed by copper-mediated oxidative chlorination, yielding 49 % over two steps. The final substitution reaction with phenol cleanly provided **259**, although in a significantly reduced yield of 19 %.

Subjecting **259** to the same reaction conditions as **257** resulted in complete consumption of the allylsilane, as observed in the first ^{1}H NMR measurement (after 10 min). Given the addition of only 10 mol% of $HNTf_2$, we were intrigued by this *catalytic* reactivity. Analysis of the selectively formed single species led to the structural assignment of the siloxacycle **260**. In retrospect, this reactivity is not surprising; the phenoxy substituent renders the overall aromatic fragment electron-rich, significantly activating the 2-position. Combined with the Thorpe–Ingold effect,[108] resulting from the geminal isopropyl groups, a highly favored Friedel–Crafts cyclization to form the six-membered silacycle **260** was observed.

Incorporating the key learnings from the reactions of **257** and **259**, we designed allylsilane **261** to overcome the previously encountered problems: 1) Installation of the sterically demanding isopropyl groups was found necessary for reactivity (as demonstrated by the catalytic incompetence of **257**), and 2) blocking the 2-position within the arene portion should preclude any Friedel–Crafts side-reactivity.

We were pleased to find that allyl(diisopropyl)mesityloxysilane **261**, synthesized in 84 % yield from mesitol and allyl(diisopropyl)chlorosilane, selectively converged to a single species upon reaction with 10 mol% of $HNTf_2$. The ^{19}F NMR displayed two sharp singlets at −75.3 and −78.4 ppm, indicating *O*-silylation of the bistriflimide anion. Furthermore, the ^{29}Si NMR chemical shift indicated significant Lewis-acidic character (δ = 42.8 ppm), similar to the trialkylsilylium-based counterparts (*cf.* TBSOTf: δ = 43.3 ppm).[87]

Using the optimized conditions (see Scheme 3.10) but with 50 mol% of **261** for the silicon-catalyzed Mukaiyama–Mannich reaction provided the product **225** in 29 % yield (81:19 dr). Although this result does not sufficiently demonstrate the silicon-catalytic nature of the reaction for this new system, we nevertheless proceeded to synthesize chiral BINOL-based variants of **261**.

To maintain the structural feature of mono-linkage to an aryloxy functionality, we chose to block one hydroxy group of BINOL *via* monotriflation and Kumada coupling, attaching the allyl(diisopropyl)chlorosilane to the remaining OH group. This overall synthetic endeavor was realized through a combination of well-established and straightforward steps, with a complete overview provided in Chapter 5. Overall, 3-substituted **266** as well as 3,3'-substituted **267** and **268** were synthesized from their corresponding BINOLs over 7 and 5 steps, respectively (Table 3.4, bottom).

Using the identical reaction conditions from the model studies, which yielded 29 % in the reaction between *N*-tosyl imine and isobutyl propionate **217**, we investigated the performance of the newly synthesized catalysts (Table 3.4, top).

In general, only low yields were observed in the reactions with imine **201** (entries 1, 2, and 4), irrespective of the silane used. The product **225** was obtained with moderate diastereoselectivities, and the enantioselectivity reached up to 45:55 er for the *syn*-diastereomer of **225** (entry 2). Higher reactivity was observed in the conversion of *N*-mesyl imine **224**, although

Table 3.4: Investigation of the catalytic performance of the BINOL-based allyl(diisopropyl)aryloxysilanes. Reactions performed on 0.10 mmol scale; yield determined by ^{1}H NMR using mesitylene as an internal standard; absolute configuration of **225** and **226** not determined.

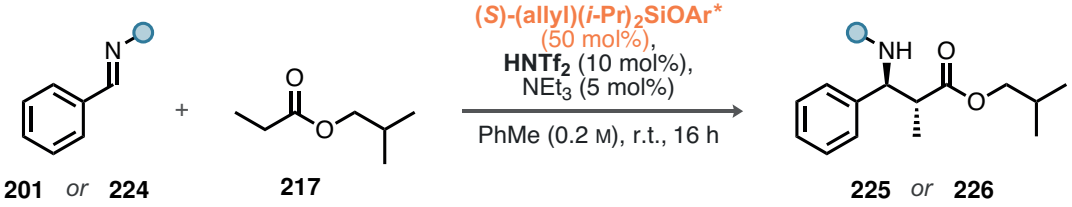

entry	cat.	○	yield	dr	er, major (*anti*)	er, minor (*syn*)
1	**266**	Ts	26 %	75:25	46:54	– –
2	**267**	Ts	20 %	72:28	48.5:51.5	45:55
3	**267**	Ms	80 %	76:24	48:52	50:50
4	**268**	Ts	44 %	76:24	52:48	46.5:53.5

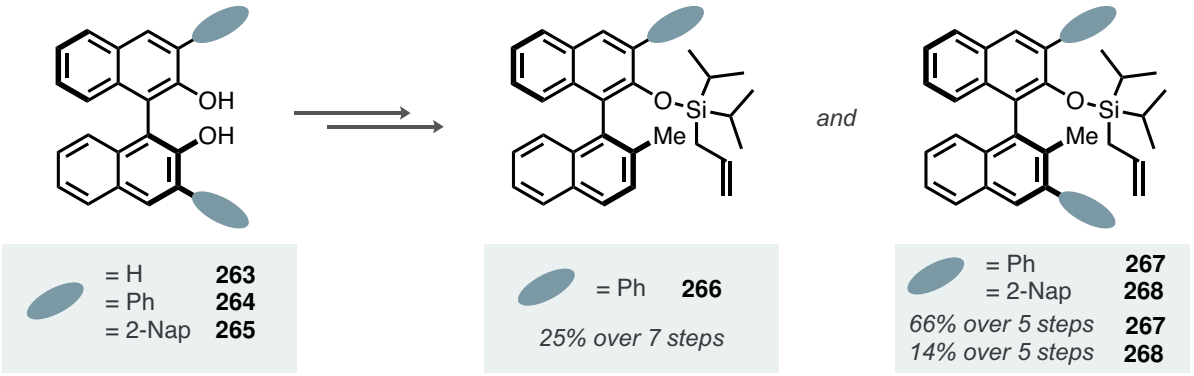

no significant enantioinduction was measured (entry 3).

Similar to the influence of chiral tertiary amines (Section 3.4), the levels of enantioselectivity obtained were generally low. One possible reason could be the inherent drawback of requiring NEt_3, which could potentially coordinate to all Lewis-acidic species in the mixture, thus influencing the outcome of the reactions. The possibility of combining the chiral tertiary amine approach with a chiral silane exists but was not further considered.

Another problem could arise from the freely rotatable lower binaphthyl fragment of **266**, **267**, and **268**. The attachment of the allyldiisopropyl fragment completely removed the conformational locking effect observed in chiral phosphoric acid-like systems. This not only put the newly developed system far from the initially discussed chirotopic non-stereogenic strategy but also introduced significant flexibility in the catalyst. While some degree of flexibility can be beneficial to allow for generality, similar to the plasticity of an enzyme, most highly successful asymmetric catalyst motifs share a certain rigidity in their structure.

Recognizing the limited conclusions that can be drawn from such an investigation, we optimized the three-dimensional structure of the silyl ketene acetal generated through ester activation by catalyst **267** at the r2SCAN-3c level of theory, without conducting a systematic conformational search (Fig. 3.3).

Considering these arguments qualitatively, several points can be addressed. The putative chiral enantiopure silyl ketene acetal is positioned significantly far from the chiral backbone due to the O−Si−O linker. A possible consequence is that, despite being attached to a large chiral backbone, the nucleophilic addition to the imine occurs through an outer-sphere mechanism, thereby minimizing the influence of the binaphthyl group. Furthermore, the

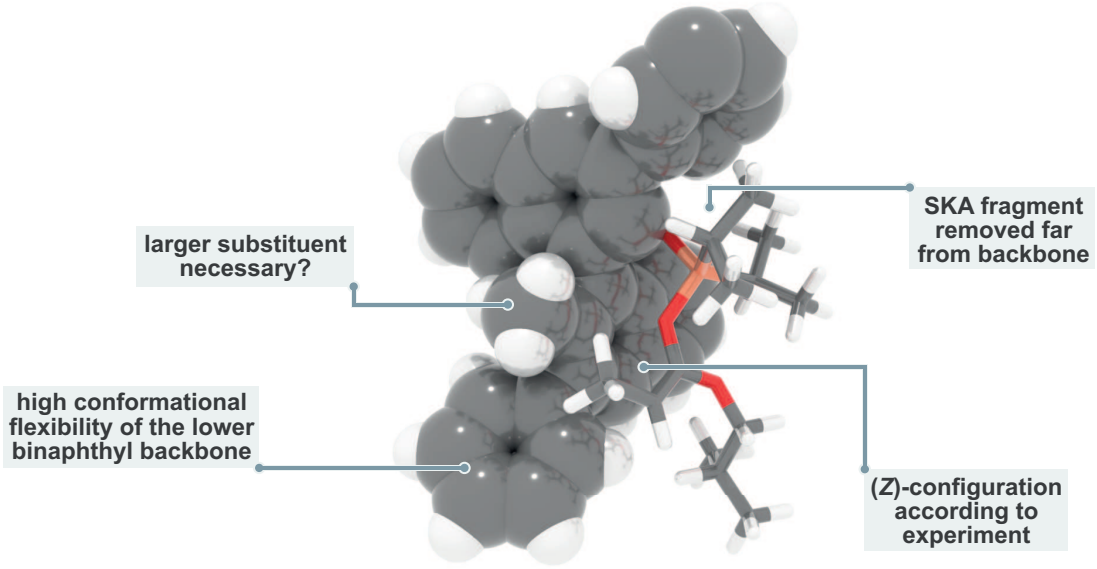

Fig. 3.3: Structure of the silyl ketene acetal generated from deprotosilylation of isobutyl propionate **217** with the active catalyst resulting from **267** (r2SCAN-3c; red: oxygen, salmon: silicon).

angle between the two naphthyl moieties appears almost orthogonal, a result of minimized steric repulsion. As discussed earlier, this increases the conformational flexibility of the system, leading to nonspecific diastereotopic transition states. The methyl group of the southern fragment is located directly next to the nucleophilic carbon atom of the silyl ketene acetal; this position could be of significant importance and may be optimized in future generations of catalysts.

For simplicity, the synergy between the formation of a chiral silyl ketene acetal *and* the addition to an iminium ion, activated by coordination to a chiral silylium Lewis acid, has not been discussed here. However, these factors would be crucial for future considerations, potentially leading to the development of dimeric catalysts.

It is noteworthy that the application of alkoxysilylium Lewis acids has rarely been described in the literature.[258] Along the path of synthesis, we encountered significant limitations in synthesizing 3,3'-substituted binaphthyl-based silanes, making the described alkoxysilanes an attractive alternative. Model studies demonstrated comparable acidity to traditional trialkylsilylium Lewis acids, suggesting potential applications as chiral Lewis acids not only for silicon-catalyzed Mukaiyama–Mannich reactions but also for Diels–Alder reactions and other transformations.

3.6 The Discovery of Silylsulfonamides

Considering the minor influence of chiral enantiopure tertiary amines and alkoxysilanes on the enantioselectivity of the silicon-catalyzed Mukaiyama–Mannich reaction, we were determined to develop a successful silylium ACDC-enabled approach. Although combinations of the very strong Lewis acid TIPSNTf$_2$ with NEt$_3$ retained high reactivity, we observed comparably low or even a lack of reactivity when substituting HNTf$_2$ with an IDPi at high catalyst loadings (see Appendix, Scheme A.1).

This is not only a consequence of the slightly lower Lewis acidity of the silylated IDPi—especially in the presence of NEt$_3$—but is also related to our postulated intermediacy of ammonium salts (Scheme 3.11). Section 3.6.1 discussed in detail the high stability of the corresponding trialkylammonium IDPi, a result of strong interactions within the confined cavity of the IDPi anion.

Therefore, we conclude that, in order to realize high reactivity for all deprotosilylative reactions *via* silylium ACDC, the formation of ammonium salt intermediates *must be avoided at all costs.*

This notion of charge-neutral isogyric silicon-hydrogen exchange is already present in the mildly basic reagents BSA[259] and bis(trimethylsilyl)trifluoroacetamide (BSTFA),[260] which were developed for deprotosilylations of amino acids and peptides. Having identified the

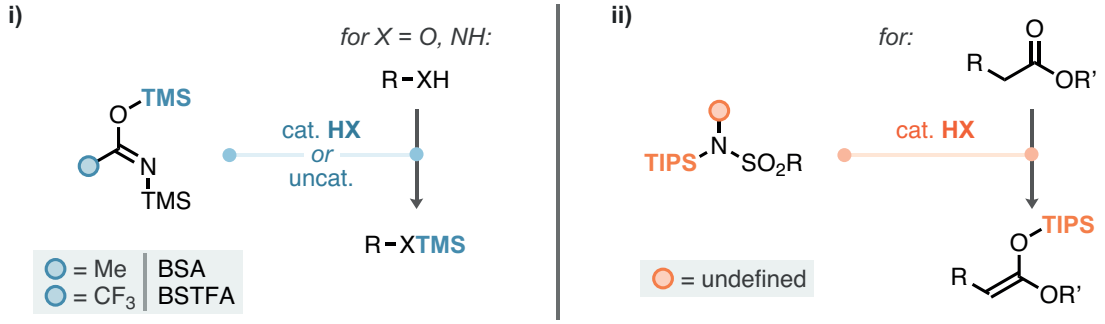

Scheme 3.17: Deprotosilylating agents. i) BSA and BSTFA, initially developed for deprotosilylations of amino acids and peptides, and ii) potential of *N*-silylsulfonamides for deprotosilylations of alkyl esters.

requirement for the large TIPS group to observe turnover in silicon, the potential of the silylsulfonamide intermediate **238** (Scheme 3.11) for the corresponding deprotosilylation of silylium-activated esters drew our attention (Scheme 3.17).

We hypothesized that the thermodynamic driving force would be comparable to amide-based silylating agents due to their similar pK_a values of approximately 17 in DMSO.[261,262] Moreover, sulfonamides are well-known for their propensity to form strong hydrogen-bonded networks, which could provide additional driving force, particularly in the non-polar solvents typically used in silylium ACDC.[263] The TIPS group could introduce additional steric repulsion, potentially adding to the driving force for deprotosilylation.

3.6.1 Novel Deprotosilylating Agents

Since the application of silylsulfonamides as silylating agents is unprecedented in the literature, we set out to examine the validity of this concept by synthesizing a series of three different reagents. The structural features of these reagents were chosen to systematically incorporate elements found in the *N*-silylated Mannich product **238**.

Accordingly, we synthesized *N*-tosyl-*N*-TIPS-methylamine **269**, *N*-tosyl-*N*-TIPS-β-alanine **270**, and the corresponding α-gem-dimethyl variant **271** (Scheme 3.18). Silylsulfonamide **269** was directly accessible from the commercially available sulfonamide through deprotosilylation with TIPSOTf/NEt_3. Interestingly, it demonstrated high stability towards moisture, facilitating purification *via* standard column chromatography, yielding the compound as a white crystalline solid (see Scheme 3.18 right for an X-ray crystal structure). Compound **270** was synthesized from β-alanine hydrochloride in two steps and was isolated as an air- and water-stable, colorless oil in 78 % yield over two steps. Access to **271** was obtained from ethyl cyanoacetate, producing the highly moisture-sensitive *N*-silylsulfonamide **271** in 15 % yield after five steps.

Investigating the deprotosilylation of 10 mol% $HNTf_2$ with all three reagents indicated

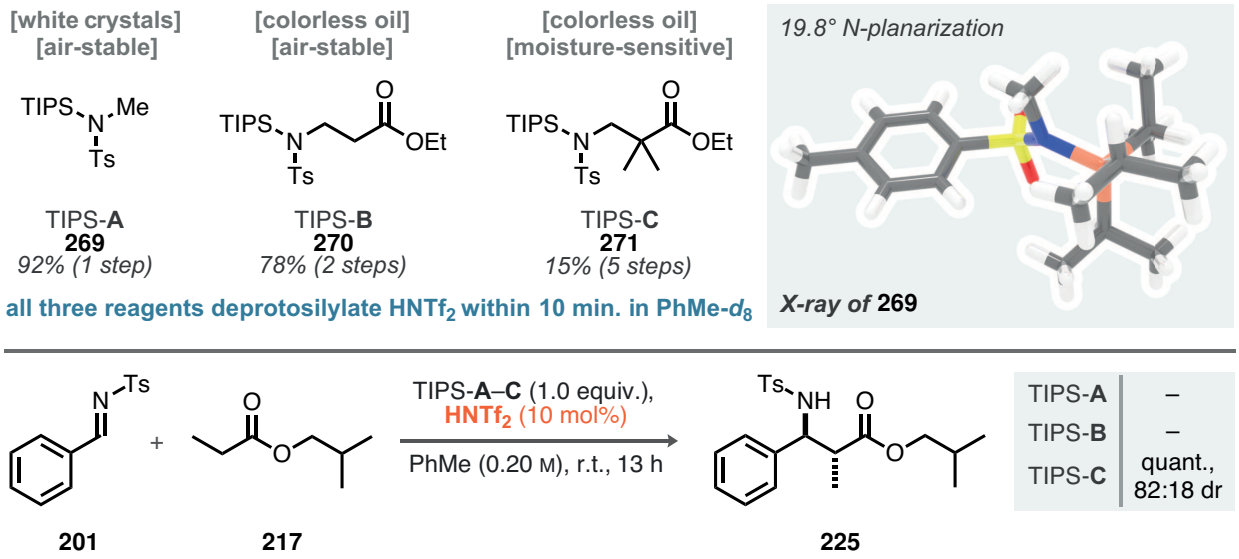

Scheme 3.18: Overview of newly synthesized deprotosilylating agents, based on inspiration drawn from **238** as well as investigation of their influence on the reaction between *N*-tosyl imine **201** and isobutyl propionate **217**.

rapid formation of $TIPSNTf_2$, showing quantitative conversion within 10 min at room temperature in toluene-d_8. Eager to test the silylsulfonamides in the silicon-catalyzed Mukaiyama–Mannich reaction, we used 1.0 equiv. of TIPS-**A**, -**B**, and -**C** under otherwise identical reaction conditions without NEt_3. While TIPS-**A** (**269**) and TIPS-**B** (**270**) did not yield any conversion of the starting materials, TIPS-**C** (**271**) furnished **225** in quantitative yield after just 13 h (82:18 dr). This high level of reactivity was conserved even at a low $HNTf_2$ loading of 2.0 mol% under otherwise identical reaction conditions (Table 3.5, entry 3). Further reduction of the $HNTf_2$ amount along with 25 mol% TIPS-**C** provided incomplete conversion of the *N*-tosyl imine **201**, while identical reaction conditions for the *N*-mesyl imine **224** furnished the product **226** quantitatively (86:14 dr).

Altogether, these initial results effectively demonstrate that silylsulfonamides combine

Table 3.5: Investigation of the $HNTf_2$ loading in the reactions mediated by TIPS-**C** (Scheme 3.18). Reactions performed on 0.10 mmol scale; yield and diastereoselectivity determined by ^1H NMR of the crude reaction mixtures using mesitylene as an internal standard; [a] conversion of the imine.

entry	imine	mol% $HNTf_2$	mol% TIPS-**C**	yield	dr
1	**201**	10.0	100	quant.	82:18
2	**201**	5.0	100	quant.	82:18
3	**201**	2.0	100	quant.	82:18
4[a]	**201**	1.0	25	52 %	85:15
5[a]	**224**	1.0	25	quant.	86:14

dual functions within a single structure: 1) They serve as silicon precatalysts, rapidly activating $HNTf_2$ to generate $TIPSNTf_2$, and 2) they are sufficiently basic to deprotosilylate the ester, presumably aided by silylium activation.

3.6.2 Silylsulfonamides of the First Generation

Having identified silylsulfonamides as key intermediates in the silicon-catalyzed Mukaiyama–Mannich reaction, we continued with a systematic investigation of their properties. These studies were driven by the apparent potential of the silylated sulfonamide to initiate the reaction by generating catalytic quantities of the silyl ketene acetal *in situ*, without the need for additional tertiary amine bases.

To this end, we designed a modular synthetic route towards derivatives of TIPS-**C** (Scheme 3.19). We chose to use isobutyl esters for all reagents to avoid the potential of catalyst alkylation (Section 3.2.1). The key disconnection was identified as a quaternary center-forging Mukaiyama–Mannich reaction of readily available and comparably stable tetrasubstituted TMS silyl ketene acetals **272**. This reaction proceeded to full conversion within a matter of minutes, which was clearly visible by the complete consumption of the insoluble amidosulfone **273**.[173]

Direct deprotonation/silylation using $TIPSOTf/R_3N$ of sulfonamide **274** to provide the silylsulfonamides appeared as an attractive solution; however, traces of the tertiary amine

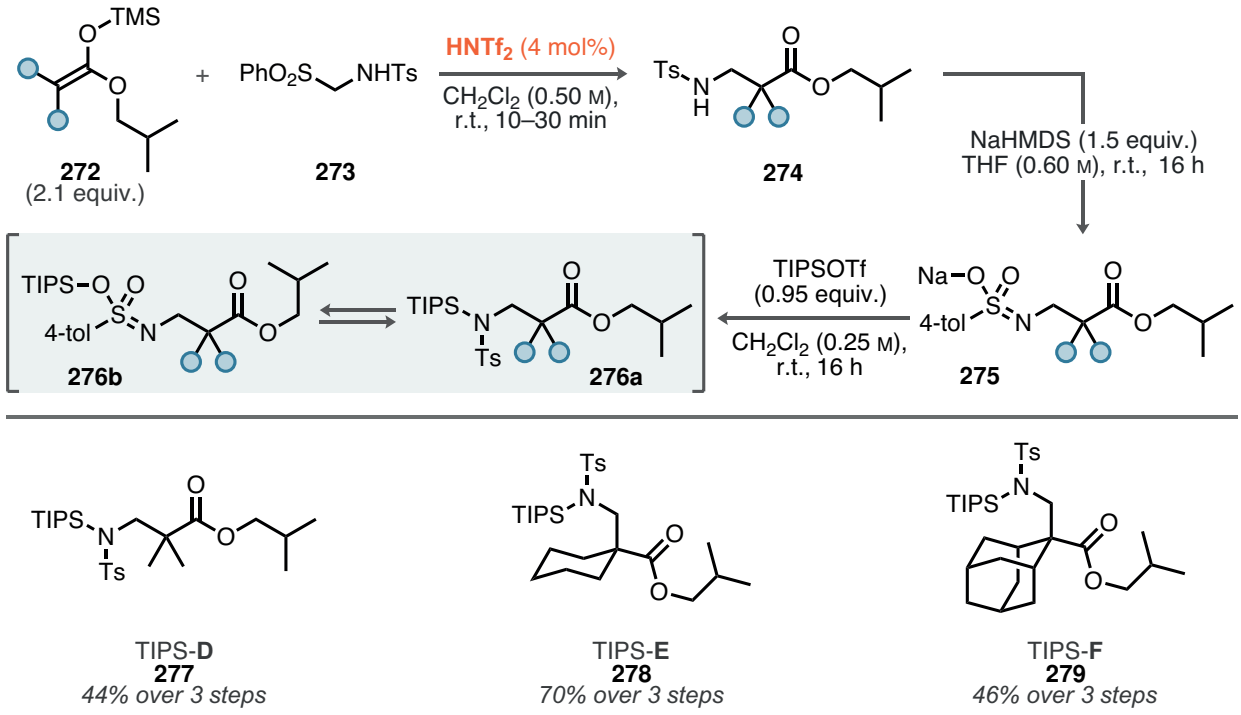

Scheme 3.19: Modular synthesis of first-generation *N*-silylsulfonamides based on a $HNTf_2$-catalyzed *N*-tosyl formaldimine Mukaiyama–Mannich reaction to form the quaternary center.

would be hard to remove from the highly sensitive compounds, rendering this approach less desirable. Interestingly, when **274** was subjected to a slight excess of NaHMDS in THF, visible precipitation was observed. Straightforward filtration revealed that the solids were the corresponding sodium sulfonimidates **275**, which were surprisingly stable even after storage under air for several weeks. Sodium-silicon metathesis with TIPSOTf, driven by the precipitation of NaOTf from the reaction mixture, cleanly provided the amine-free silylsulfonamides **276** as colorless oils after filtration under Ar. Rigorous exclusion of moisture provided analytically pure samples; however, up to 5 % of the NH sulfonamide **274** could be detected. Since **274** would be the product of the deprotosilylation, this minor impurity was tolerated if present.

Following this synthetic scheme, we successfully synthesized the isobutyl variant of TIPS-**C**, **277** (TIPS-**D**), as well as derivatives with increased steric demand of the α-gem-dialkyl substituents, **278** and **279** (TIPS-**E** and TIPS-**F**).

Careful NMR spectroscopic analysis of **277**–**279** indicated a varying degree of silatropism, shuffling between the *N*-silylsulfonamide **276a** and the *O*-silylsulfonimidate **276b**. Notably, silylation at one of the sulfonyl oxygens creates a configurationally stable stereogenic center at sulfur, which facilitated NMR assignment through the appearance of diastereotopicity, along with distinct ^{29}Si NMR shifts of both isomers. We further investigated the silatropism by examining the ratio between the two isomers using ^{29}Si and ^{1}H NMR measurements over a temperature range from −40 to 60 °C. Accordingly, we observed a reversible temperature-dependence in the distribution between *N*-TIPS **276a** and *O*-TIPS **276b**, indicating a dynamic equilibrium between the two isomers.

The temperature-dependence of the distributions allowed us to determine the thermodynamic parameters for the isomerization, resulting in a comprehensive description of the silatropism through the experimental determination of Gibbs free energy values. A summary

Table 3.6: Relative distribution of *N*-silylsulfonamide and *O*-silylsulfonimidate silatropisomers **276a** and **276b** for the series of TIPS-**D**–**F** in toluene-d_8, as determined by ^{29}Si and ^{1}H NMR over a temperature range of 100 K.

entry	reagent	*N*-TIPS / %	*O*-TIPS / %	$\Delta G_{N\rightarrow O}$(298 K) / (kcal/mol)
1	TIPS-**D** (Me_2)	94.3	5.7	1.63 ± 0.26
2	TIPS-**E** (Cy)	71.3	28.7	0.41 ± 0.19
3	TIPS-**F** (Ad)	6.0	94.0	-1.68 ± 0.42

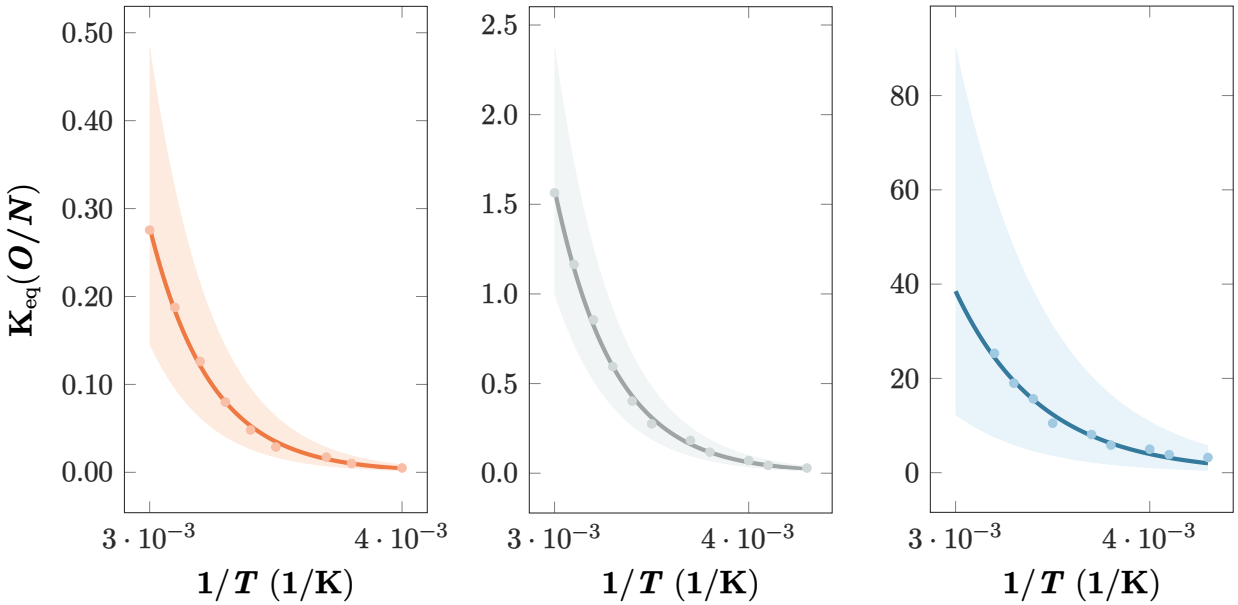

Fig. 3.4: Extracted equilibrium constants K_{eq} of the *O*- and *N*-silatropisomers versus the inverse temperature; orange: TIPS-**D** (**277**), gray: TIPS-**E** (**278**), blue: TIPS-**F** (**279**); the error of the exponential fit is indicated by a lighter shade of the respective color.

of the data is provided in Table 3.6, and the NMR distributions are displayed in Fig. 3.4.

The gem-dimethyl reagent TIPS-**D** favored the *N*-silylsulfonamide isomer (Table 3.6, entry 1), resulting in an overall endergonic isomerization to the *O*-silylsulfonimidate. This endergonicity was reduced in the transition to the cyclohexyl-based reagent TIPS-**E**, which exhibited a smaller energy difference between the isomers of (0.41 ± 0.19) kcal/mol. This could be attributed to the larger steric demand of the cyclohexyl fragment, weakening the stability of the *N*-silatropisomer through repulsive interactions. We observed a continuation of this trend upon the introduction of an even larger adamantyl substituent (TIPS-**F**, entry 3), displaying significantly exergonic isomerization towards the *O*-TIPS isomer.

Upon identifying their vital influence on the Mukaiyama–Mannich reaction and characterizing the silatropism, we were intrigued by the possibility of achieving high reactivity in a silylium ACDC-enabled silicon-catalyzed Mukaiyama–Mannich reaction by using these reagents as *initiators*. Therefore, we chose the reaction of *N*-mesyl imine **224**, due to its higher reactivity (Table 3.5), in conjunction with isobutyl propionate **217**, 75 mol% TIPS-**D**–**F**, and 4.0 mol% of highly acidic (*S,S*)-IDPi **150** at −20 °C for 21 h.

Notably, dimethyl and cyclohexyl *N*-silylsulfonamides TIPS-**D** and TIPS-**E** provided the product **226** in quantitative yield with excellent diastereoselectivity (>95:5 dr) and promising enantioselectivity of 28.5:71.5 er. This contrasted with the complete lack of reactivity observed for the adamantyl-based reagent TIPS-**F**. As both TIPS-**D** and -**E** exhibit endergonic *N*-to-*O* isomerization of the TIPS group, we speculated that this might relate to the higher stability of the *O* isomer for TIPS-**F**. Additionally, the confined active site of the IDPi

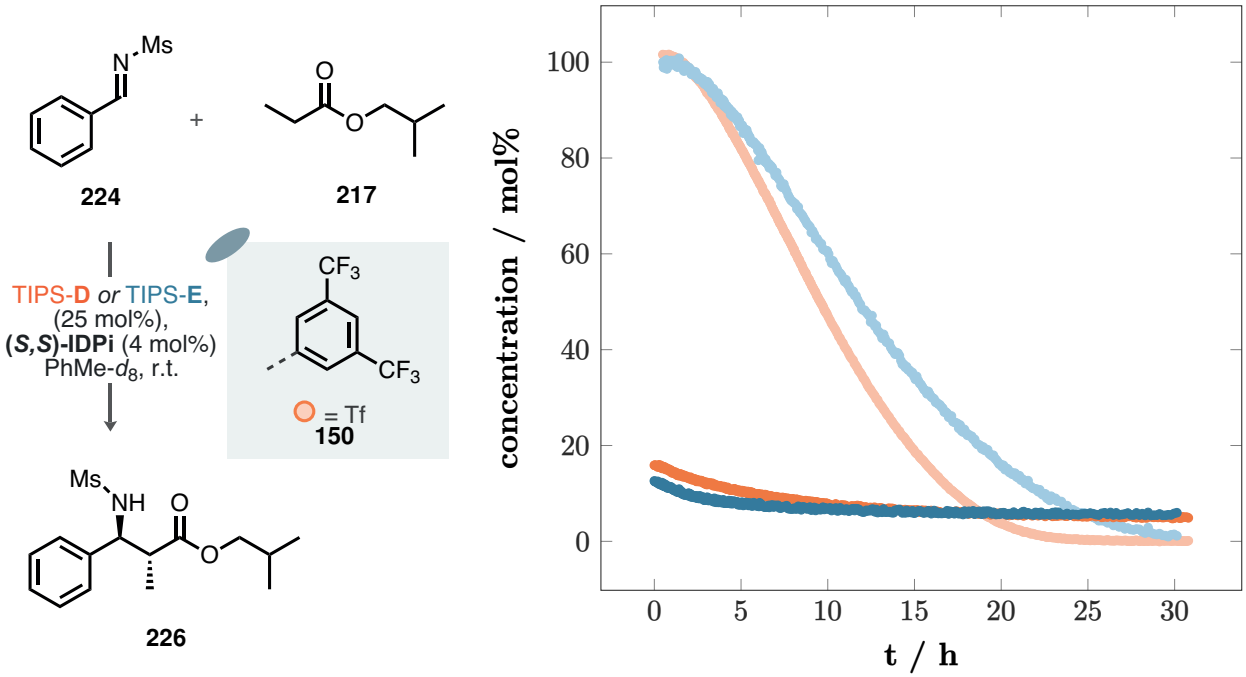

Fig. 3.5: Kinetic profile of the reaction between *N*-mesyl imine **224**, isobutyl propionate **217**, and TIPS-**D** and -**E**, catalyzed by IDPi **150**, as monitored by ^{1}H NMR; *N*-silylsulfonamides are indicated with bright orange and blue, and the concentration profile of the imine **224** in a lighter shade of the same color.

is highly substrate-specific. Considering the sterically demanding adamantyl substituent in TIPS-**F**, combined with our postulated *catalyzed* silyl ketene acetal formation, the observed lack of reactivity might also be related to the structural features of TIPS-**F**.

We chose next to verify the active regime of silicon catalysis for the IDPi-catalyzed reactions using ^{1}H NMR spectroscopy. Following this investigation, we aimed to explore the differences between the two reactive reagents TIPS-**D** and **E** (Fig. 3.5).

Both reactions proceeded to full conversion after 30 h, and their concentration profiles exhibited slight variations. Both TIPS-**D** and **E** reactions shared an initiation period, with an observable increase in rate after 2–3 h. Subsequent to this initiation period, both profiles displayed a constant rate over most of the reaction course, indicating a pseudo-zero order relationship with **224**. This observation aligns with a rate-determining generation of the silyl ketene acetal, followed by a kinetically rapid nucleophilic addition.

However, they differed in the slope of the presumably pseudo-zero order curve of **224**. This observation could be related to the fact that the concentrations of TIPS-**D** and **E** reached a plateau after approximately 10 h. Assuming that, after the initial reagent-based silyl ketene acetal generation and nucleophilic addition, the silylated product of the Mukaiyama–Mannich addition becomes the silyl-transfer reagent, it is plausible to conclude the presence of an active equilibrium between the silylated product and the protosulfonamides of TIPS-**D**

and **E**.

For this reason, both reagents lead to different concentration profiles, because the overall dynamic connection between all silylated and protonated sulfonamide species suggests a propensity of the confined IDPi catalyst to react with either of those. The high degree of structural dependence was already indicated by the lack of reactivity observed for the adamantyl reagent TIPS-**F**. It may be that the cyclohexyl-based variant reacts slower than the gem-dimethyl-*N*-silylsulfonamide TIPS-**D**.

3.6.3 A Catalytic Stereoselective Synthesis of Silyl Ketene Acetals

Motivated by our kinetic studies, we set out to observe the formation of the silyl ketene acetal spectroscopically. We hypothesized that, in the absence of a suitable electrophile and with higher concentrations of the silylsulfonamide **276**, enrichment of the nucleophile should occur. If successful, this experiment would provide proof not only for the intermediacy of silyl ketene acetals but also for the high degree of thermodynamic driving force associated with the desilylation of silylsulfonamides.

To facilitate the identification of newly formed species *via* coupling in the ^{1}H or directly in the ^{13}C NMR, we chose to use an excess of ^{13}C-labeled isobutyl propionate in the reaction with 1.0 equiv. TIPS-**E** catalyzed by $HNTf_2$ (Fig. 3.6). Based on the presumably shape-selective effects observed in Fig. 3.5, we used $HNTf_2$ as a small and achiral model catalyst to map out the thermodynamic landscape.

Immediately upon addition of the ester **217** to the mixture of **278** and $HNTf_2$ in toluene-d_8, we observed the consumption of the silylsulfonamide (Fig. 3.6). This observation was accompanied by the emergence of a new peak in the ^{13}C NMR spectrum at 156.5 ppm, which is consistent with literature-known values for silyl ketene acetals.[171] Enabled by the $^{3}J_{CH}$ coupling of the isobutyl methylene protons to the ^{13}C carbonyl carbon of 1.4 Hz, we were additionally able to unambiguously identify **280a** in the ^{1}H NMR spectrum. The complete (*Z*)-diastereoselectivity was further corroborated by measurement of 1D-selective NOESY experiments, and the key observed interactions are depicted in Fig. 3.6. This aligns well with Simchen's stoichiometric experiments[223] using combinations of trialkylsilyltriflates and tertiary amines, and demonstrates the first *catalytic* and completely stereoselective generation of silyl ketene acetals.

Based on the exact amounts of ester used, we were able to observe 13.9 % (with 4.0 equiv.) or 19.2 % (with 10.0 equiv.) silyl ketene acetal in less than 1 h. Consequently, the protodesilylation of TIPS-**E** introduces enough driving force into the system to render the overall generation of **280a** thermodynamically feasible. Regarding the comparatively small concentrations of silyl ketene acetal, it is reasonable to assume a highly reversible generation *in*

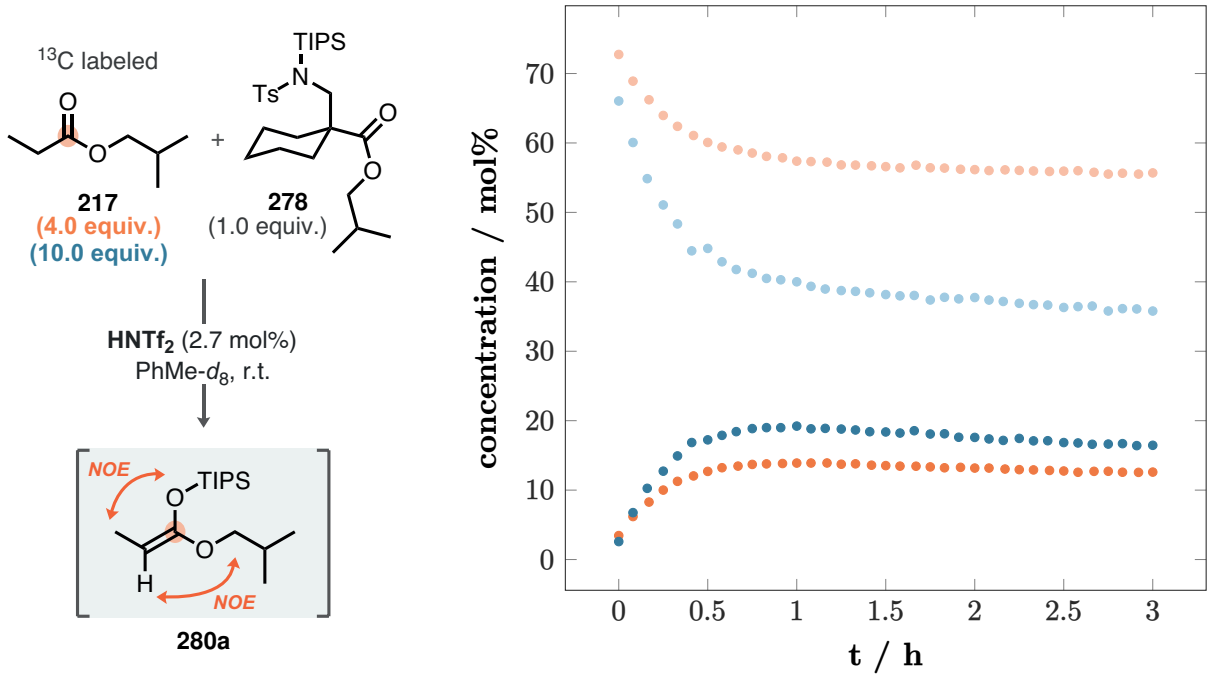

Fig. 3.6: Concentration profile of the reaction between ^{13}C labeled isobutyl propionate **217** and TIPS **E**, catalyzed by $HNTf_2$, as monitored by ^{1}H NMR; key NOE interactions are highlighted in **280a**; concentrations of **280a** are indicated with bright orange and blue, and the concentration profile of the silylsulfonamide in a lighter shade of the same color.

situ, which is consistent with the measured NMR data. Continuing efforts aim to influence this thermodynamic relationship to generate higher concentrations of nucleophile, which can be achieved by structural modification of the silylsulfonamide (Section 3.6.5).

Altogether, this reversible generation of the silyl ketene acetal is key to subsequent irreversible and potentially catalytic asymmetric functionalization, resulting in *direct* reactions of alkyl esters.

3.6.4 Key Findings of the First Generation

Thus far, we have successfully established the design of using silylsulfonamides as silicon precatalysts for the Mukaiyama–Mannich reaction (Scheme 3.20). NMR analysis has enabled the thermodynamic characterization of the silatropism in **276**, highlighting their potential as silyl transfer agents. Based on kinetic experiments, we have experimentally verified the generation of the silyl ketene acetal **280a** through a *catalytic* synthesis. In the context of the Mukaiyama–Mannich reaction, this *in situ* generation manifested as a comparably slow initial rate in the concentration profiles depicted in Fig. 3.5.

The freshly generated nucleophile **280a** then likely rapidly adds to the imine **224** to furnish the *N*-TIPS product **240**, which we propose to be the key intermediate for a second cycle of catalytic silyl ketene acetal generation. The presence of a constant concentration

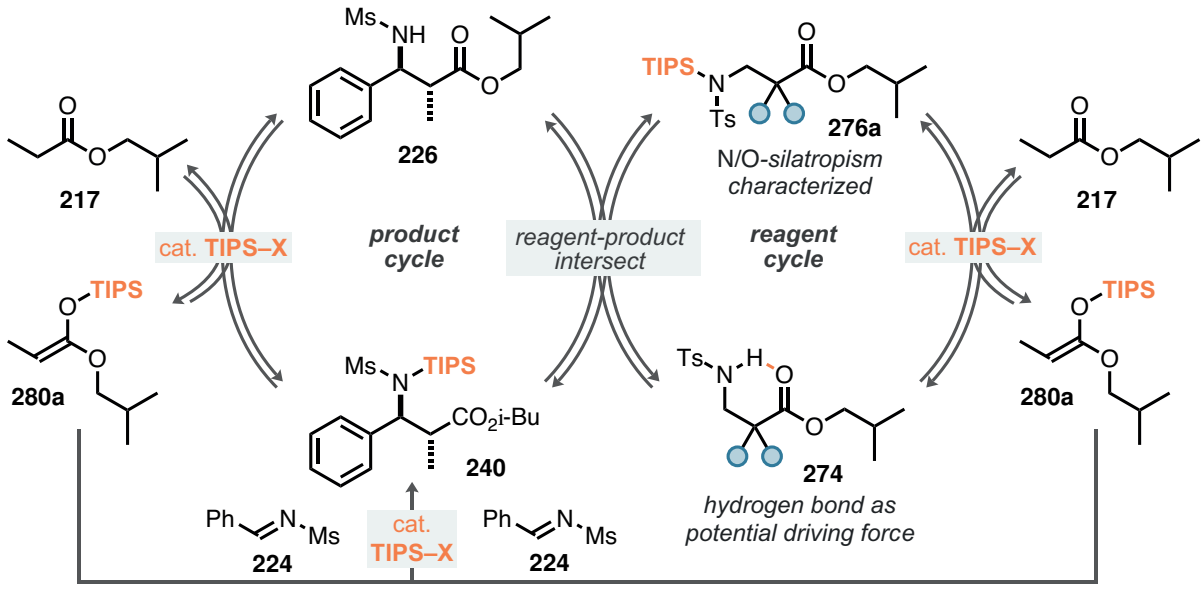

Scheme 3.20: Proposed intertwined mechanistic scenario of thermodynamically controlled silyl ketene acetal generation, followed by its kinetically controlled reaction with **224**, based on key findings of the development of the first-generation *N*-silylsulfonamides.

of **276** implies that silyl transfer might also occur between **240** and **274**, resulting in the observed differences in reactivity with confined IDPi catalysts based on the structural demand of **274**.

Overall, two important notions can be identified in Scheme 3.20. 1) All depicted catalytic cycles conserve the TIPS group, emphasizing its true catalytic nature for this particular transformation. 2) Each step involving a catalytic silylium Lewis acid proceeds *via* retention of silicon at the anion. This results in the overall high reactivity achieved, also for the first time with IDPi catalysts, completely removing the requirement for tertiary amine bases and avoiding potentially sluggish catalyst deprotosilylation steps.

On the other hand, we have not been able to fully understand the molecular features associated with the driving force of silylsulfonamide protodesilylation. Since all of them resemble β-amino acids, which are Mannich products, there is a significant implication of an intramolecular hydrogen bond between the sulfonamide N–H and the basic ester fragment.

3.6.5 Silylsulfonamides of the Second Generation

The work described in this section was conducted in collaboration with Lennart Brücher.

Efforts to gain a deeper understanding of the silylsulfonamide protodesilylation inspired the design of novel reagent structures. With regard to the intramolecular NH hydrogen bond (highlighted in structure **274** in Scheme 3.20), which warrants speculation about its influence on the overall driving force, we completely substituted the ester fragment with a methyl group

(TIPS-**G**). We believed that following this approach, the influence on the steric properties of the reagent would be minimized, while allowing for critical insight into the specific hydrogen-bonding interaction.

The corresponding neopentylamine-based silylsulfonamide TIPS-**G** (**281**) was obtained in 71 % yield after three straightforward steps, using our developed sodium sulfonimidate route (Scheme 3.19, 76.3:23.7 N/O-TIPS at 298 K). Seeking to obtain a single parameter that allows for the direct comparison of reagents, we hypothesized that measuring the equilibrium with the ester to form the silyl ketene acetal would provide access to the corresponding equilibrium constants K_{eq}, and therefore result in the determination of the Gibbs free energy.

Based on the successful reaction setup and characterization of **280a**, we used the initial gem-dimethyl reagent TIPS-**D**, its cyclohexyl variant TIPS-**E**, as well as the neopentylsilylsulfonamide TIPS-**G** (**281**) in combination with 10.0 equiv. of isobutyl propionate **217** (Scheme 3.21). The results corresponding to the reaction displayed in Scheme 3.21 are plotted in Fig. 3.7. The concentration profiles of the silylsulfonamides and the concentration of the silyl ketene acetal **280a** are displayed over time, with colors indicating the reagent used in each respective reaction.

Interestingly, we observed an improved performance of TIPS-**E** over TIPS-**D**, which contrasts with the reaction profiles measured for the reaction catalyzed by IDPi **150** (Fig. 3.6). Whereas TIPS-**D** reached equilibrium concentrations of 10.0 % after 1.2 h at room temperature, the direct comparison with TIPS-**E** revealed an almost twofold higher concentration of **280a** after 1 h. As discussed earlier, the kinetic preference for a faster Mukaiyama–Mannich reaction mediated by TIPS-**D** might result from fewer repulsive interactions with the confined IDPi catalyst, despite its thermodynamically inferior performance.

Most notably, however, was the performance of the neopentyl reagent **281**. Equilibrium concentrations of **280a** exceeded those of the other two reagents by more than 50 %, reaching 28.8 % in less than 30 min. It appears that the removal of the ester fragment not only improved the thermodynamic performance but also introduced a kinetic preference for

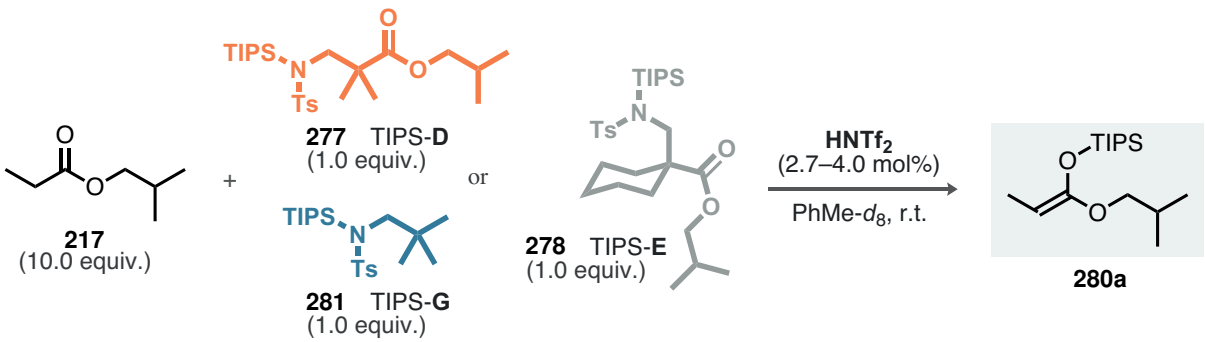

Scheme 3.21: Selection of N-silylsulfonamides chosen for the determination of the equilibrium concentrations in the reaction with **217** to form **280a** *via* ^{1}H NMR spectroscopy.

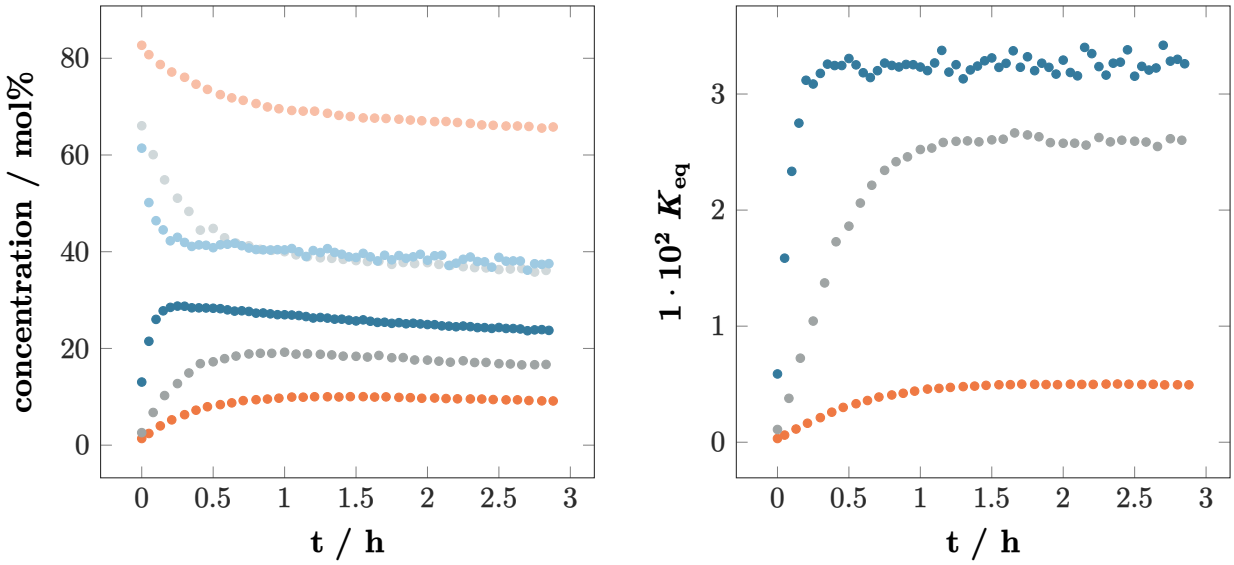

Fig. 3.7: Concentration profiles of **280a** corresponding to the reaction shown in Scheme 3.21 (left) and time-dependence of the equilibrium constant, assuming a 1:1 reaction; orange: with TIPS-**D**, gray: with TIPS-**E**, blue: with TIPS-**G**; the corresponding *N*-silylsulfonamides are indicated with a lighter shade of the same color.

protodesilylation, achieving equilibrium conditions in a significantly shorter time.

This is also effectively represented in the plot of the equilibrium constant K_{eq} over time, indicating both the verification of equilibrium conditions *via* reaching a plateau over time, as well as the superior performance of **281**.

Another interesting feature is the potentially divergent reactivity of both silatropisomers of the reagents. Since the aromatic protons of the tosyl fragment for TIPS-**D** and TIPS-**E** do not overlap in the NMR spectra, we were able to track the concentrations of both isomers over time. After calculating the ratio between the *N*- and *O*-TIPS isomers, we observed this ratio to remain constant over the course of the whole reaction (13.88 ± 0.19 for TIPS-**D** and 2.06 ± 0.02 for TIPS-**E**). Although this result does not provide information about the preferential reaction of one isomer over the other, it demonstrates that the *N*-to-*O* isomerization is fast compared to the deprotosilylation of isobutyl propionate **217**.

Ultimately, by using the mean concentrations after equilibrium was reached in each case, we were able to extract the Gibbs free energy for the deprotosilylation of isobutyl propionate

Table 3.7: Gibbs free energies of the deprotosilylation of isobutyl propionate **217** with TIPS-**D**, -**E** and -**G** at 298 K, calculated based on the mean equilibrium constants $\bar{K}_{eq}$.

entry	reagent	c_{max}(**280a**) / mol%	$\bar{c}$(**280a**) / mol%	ΔG(298 K) / (kcal/mol)
1	TIPS-**D**	10.0	9.2 ± 0.6	3.15 ± 0.10
2	TIPS-**E**	19.2	17.4 ± 1.0	2.16 ± 0.06
3	TIPS-**G**	28.8	25.9 ± 1.5	2.03 ± 0.05

217 with the three reagents at 298 K (Table 3.7). Analysis of these values indicates the importance of harnessing even the smallest thermodynamic contributions, as evidenced by the seemingly small difference in Gibbs free energy between TIPS-**E** and -**G** (entries 2 and 3) leading to a concentration difference in **280a** of approximately 50 %.

3.6.6 *N*-Silylation-Induced Conformational Interactions

Intrigued by the reactivity difference between the ester reagents TIPS-**D** and TIPS-**E** compared to the second-generation neopentyl reagent TIPS-**G**, we conducted a detailed analysis of the ^{1}H,^{1}H-NOESY NMR spectra of the ester-based reagents, aiming to identify key conformational interactions.

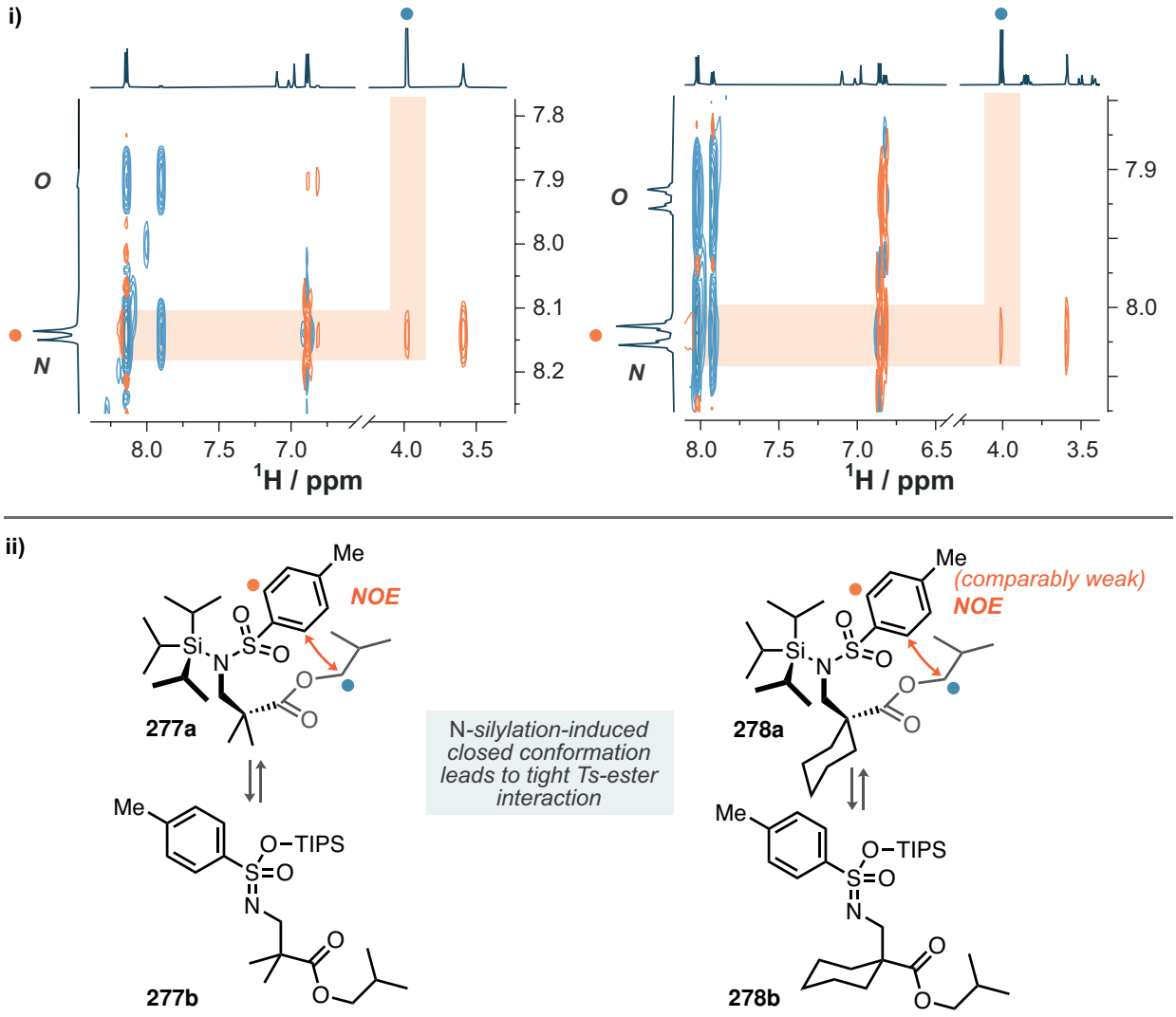

Scheme 3.22: i) ^{1}H,^{1}H-NOESY NMR spectra of *N*-silylsulfonamides TIPS-**D** (**277**) and -**E** (**278**) and ii) proposed *N*-silylation-induced closed conformation, explaining the observed NOE interactions.

Interestingly, we observed close interactions between the protons in the 2-position of the tosyl fragment and the methylene group of the isobutyl moiety (Scheme 3.22). This interaction was considerably more intense for the gem-dimethyl reagent TIPS-**D** compared to TIPS-**E**. In both cases, the tosyl protons are directly flanked by the signals of the corresponding *O*-silatropisomer, highlighting a total lack of this specific interaction for the *O*-isomer. This observation prompted a structural investigation of both silatropisomers, which is reflected in those depicted in Scheme 3.22, bottom.

Due to the sterically demanding nature of the large TIPS group, we propose that the non-TIPS residue of the reagents is forced into a closed conformation, orienting the tosyl fragment directly above the isobutyl ester. This effect is likely further amplified by the geminal-dialkyl substitution.

Using this experimental verification as a starting point, we conducted a systematic conformational analysis employing Grimme's CREST algorithm. All 234 (TIPS-**D**) and 444 conformers (TIPS-**E**) were subjected to further analysis of their respective Gibbs free energies (methyl esters were used for simplicity). This computational protocol successfully reproduced the experimentally deduced conformations, as displayed in the structures of the lowest-energy conformers (Fig. 3.8). Inspection of the 3D structures clearly indicates the location of the sulfonyl group in close proximity to the ester fragment, leading to calculated distances of 2.69 Å (TIPS-**D**) and 2.71 Å (TIPS-**E**).

Such a tight interaction suggests potential interactions between the two fragments, which was further elucidated for TIPS-**D** using second-order perturbation theory analysis as implemented in the Natural Bond Orbital (NBO) code. We found that both lone pairs of the closer sulfonyl oxygen donate into the π^* orbital of the ester *via* $n_O \rightarrow \pi^*(C{=}O)$ interaction. This interaction energy contributes to the stabilization of the *N*-silatropisomer by a total of 3.9 kcal/mol (2.5 kcal/mol and 1.4 kcal/mol), as depicted for one of the lone pairs in the middle structure of Fig. 3.8.

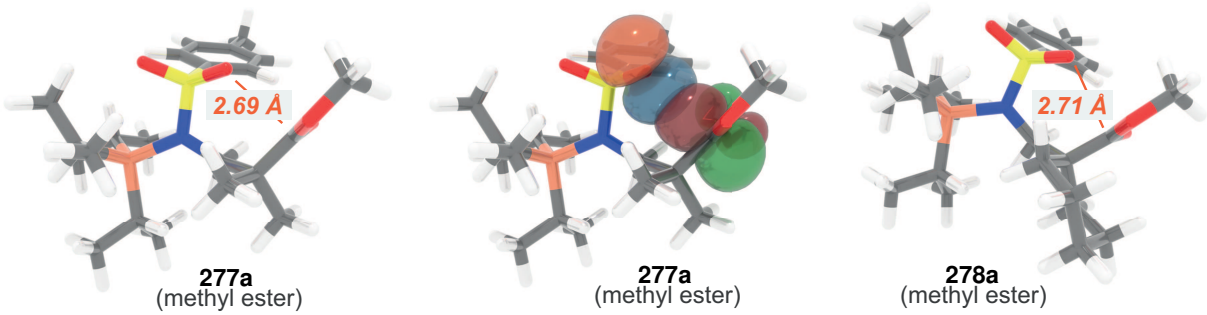

Fig. 3.8: Lowest-energy conformers of TIPS-**D** (**277a**) and -**E** (**278a**) calculated at the M06-2X/def2-QZVP//r2SCAN-3c level of theory as well as visualization of the sulfonyl oxygen lone pair and ester C=O π^* molecular orbitals (isovalue 0.05).

Caution is advised when comparing these computationally obtained values with the experimentally determined Gibbs free energies of the isobutyl propionate deprotosilylation. Although experimentally proven NOE contacts locate the tosyl fragment in the vicinity of the ester portion, significant conformational flexibility remains within the *N*-silylation-induced framework.

Nonetheless, this computational analysis provides a possible explanation for the reduced reactivity of the ester-based reagents through stabilization of the *N*-isomer. This interaction appears to be conserved in the cyclohexyl variant TIPS-**E** as well. However, the increased steric demand in the ester's α-position likely contributes to greater deprotosilylating activity due to intramolecular steric repulsion to the TIPS group.

Ultimately, through a combination of experimental and computational analyses, we attribute the main driving force for the protodesilylation of the newly developed silylsulfonamide reagents to intramolecular steric repulsion with the TIPS group. This effect is particularly evident in the highest catalytic potential observed with the neopentyl reagent, which lacks any strong interaction donors or acceptors in the sulfonamide backbone.

3.7 Silylium ACDC-Enabled Silicon-Catalyzed Mukaiyama–Mannich Reactions

The following work has been conducted in parallel with the investigation of the properties of silylsulfonamides, as discussed in Section 3.6. For all reactions, either TIPS-**D**, TIPS-**E**, or TIPS-**G** were used, with specific notation for each optimization step.

Unless specifically required, the enantioselectivity of the minor *syn*-diastereomer (if observed) will not be further discussed.

The high thermodynamic driving force of silylsulfonamide protodesilylation has made the *in situ* generation of silyl ketene acetals accessible *catalytically*. Motivated by the implications of this concept, combined with the promising diastereo- and enantioselectivities discussed in Section 3.6.2, we set out to develop a silylium ACDC-enabled silicon-catalyzed Mukaiyama–Mannich reaction through the optimization of all key reaction parameters.

3.7.1 Initial Catalyst Screening

During our initial catalyst screening, we noted reduced reactivity in IDPi-catalyzed Mukaiyama–Mannich reactions when using *N*-tosyl imine **201**, consistent with the observations recorded in Table 3.5. Additionally, enantioselectivity was generally low across all cases examined. Detailed screening data are available in the Appendix (Table A.3).

Given these results, we selected *N*-mesyl imine **224** as the model substrate for a comprehensive screening of IDPi catalysts. This screening was conducted in the reaction with

Table 3.8: Initial overview screening of the reaction between **224** and **217**. Reactions performed on 0.025 mmol scale; yields and diastereoselectivities determined by ^{1}H NMR using mesitylene as an internal standard; absolute configuration not determined; [a] 5 mol% used.

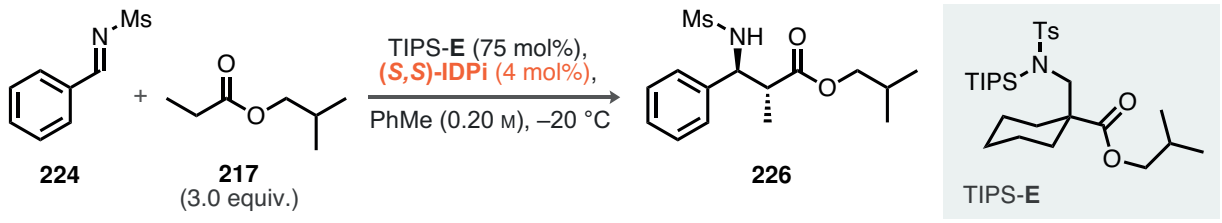

entry	catalyst	time	yield **226**	dr	er (*anti*)
1[a]	**30**	17 h	–	–	–
2[a]	**99b**	17 h	–	–	–
3[a]	**87**	17 h	–	–	–
4[a]	**87a**	17 h	–	–	–
5	**150**	60 h	quant.	95:5	25.5:74.5
6	**150a**	68 h	15 %	93:7	27:73
7	**150b**	68 h	13 %	95:5	27:73
8	**282**	62 h	quant.	>95:5	23:77
9	**282a**	50 h	95 %	>95:5	20:80
10	**282b**	62 h	quant.	95:5	29:71

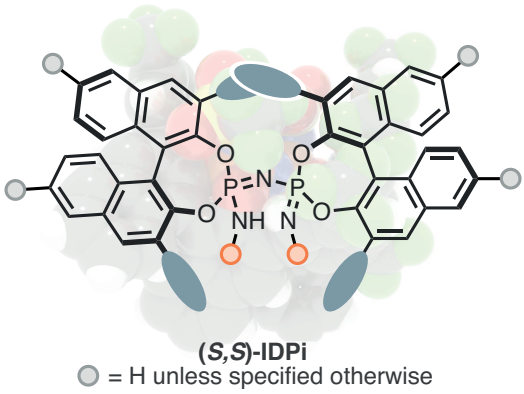

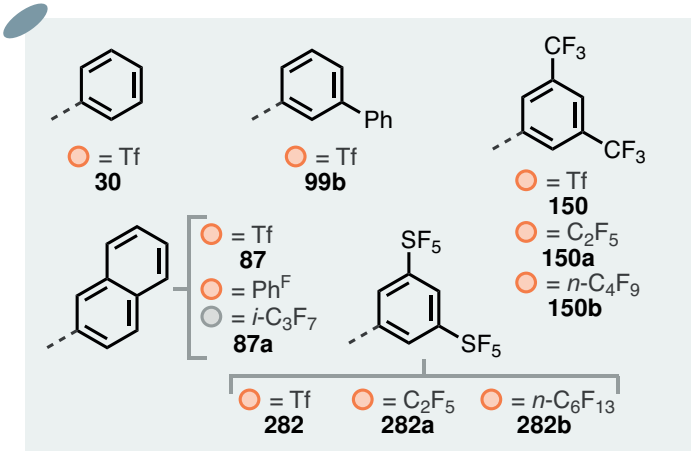

isobutyl propionate **217** (3.0 equiv.) in toluene at −20 °C, and the outcomes are documented in Table 3.8. The catalytic assessments of IDPi catalysts **30**, **99b**, and **87** showed no conversion under the experimental conditions. This lack of activity extended even to a derivative of IDPi with acidifying 6,6'-substituents, **87a**, which also failed to convert the starting materials (entries 1–4 in Table 3.8).

Expanding the scope to include IDPi structures with more acidic characteristics led to

a notable increase in reactivity, generally yielding **226** with excellent yields and diastereoselectivity, and moderate enantioselectivity (entries 5–10). The diminished reactivity observed in entries 6 and 7 could be attributed to insufficient acidification of the catalysts, as their structural resemblance to **283** suggests they should exhibit similar catalytic activity.

The most effective catalyst identified was **282a**, a 3,5-bis(pentafluorosulfanyl)phenyl-substituted IDPi, which produced **226** with outstanding diastereoselectivity (>95:5 dr) and promising enantioselectivity (20:80 er, entry 9). Interestingly, neither reducing the inner core length (IDPi **282**) nor extending it (IDPi **282b**) resulted in improved performance.

3.7.2 Benzofuranyl IDPi Screening

The work described in this and the following sections was conducted in collaboration with Lennart Brücher.

Given the moderate enantioselectivities observed with previous catalysts, we explored an alternative approach by incorporating 2-benzofuranyl residues into IDPi catalyst structures. These residues are known to be as acidifying as perfluoroalkyl-containing arene substituents in IDPi catalysts, offering a novel structural dimension while maintaining necessary catalytic reactivity.[264]

Employing the same reaction conditions that were successful in previous screenings (Table 3.8), we conducted an evaluation of a series of benzofuranyl-substituted IDPi catalysts with perfluoroalkyl inner cores. The results of this screening are detailed in Table 3.9.

Performing the reaction at −20 °C, which previously yielded **226** quantitatively with IDPi **150** (Table 3.8, entry 5), we observed notably different results with the 2-benzofuranyl-substituted IDPi **284**. This catalyst furnished the product at a low yield (15 %, entry 1) but exhibited promising enantioselectivity (80.5:19.5 er). Interestingly, all benzofuranyl-IDPi catalysts favored the opposite enantiomer of **226** compared to those detailed in Table 3.8.

To further explore the influence of the perfluoroalkyl core, these catalysts were also tested at room temperature (Table 3.9). Perfluoroethyl- and *n*-perfluorobutylsulfonyl cores provided **226** with similar selectivities, showing a slight preference for the longer *n*-C_4F_9 core (entries 2 and 3). The remarkable performance of the 5-(trifluoromethyl)-2-benzofuranyl IDPi **285**, even at −20 °C, which furnished the product quantitatively with moderate enantioselectivity (74.5:25.5 er, entry 4), led to further systematic investigations into the substituent effects on the benzofuran backbone. Analysis revealed a strong preference for the 6-methyl variant **287**, which achieved a good enantioselectivity of 79.5:20.5 er at room temperature (entry 6). Further exploration using naphtho[2,1-*b*]- and naphtho[1,2-*b*]furanyl-IDPi catalysts **290** and **291** showed both to lead to full conversion, providing the product quantitatively and with

Table 3.9: Screening of the reaction between **224** and **217** with benzofuranyl-substituted IDPis. Reactions performed on 0.025 mmol scale; yields and diastereoselectivities determined by ^{1}H NMR using mesitylene as an internal standard; absolute configuration not determined; [a] at −20 °C.

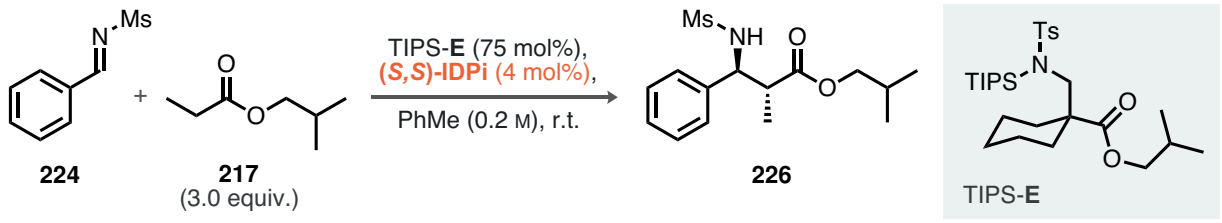

entry	catalyst	time	yield **226**	dr	er (*anti*)
1[a]	**284**	41 h	15 %	>95:5	80.5:19.5
2	**284a**	24 h	quant.	90:10	70.5:29.5
3	**284b**	24 h	quant.	90:10	73.5:26.5
4[a]	**285**	22 h	quant.	>95:5	74.5:25.5
5	**286**	24 h	66 %	91:9	75.5:24.5
6	**287**	24 h	53 %	94:6	79.5:20.5
7	**288**	24 h	55 %	91:9	69.5:30.5
8	**289**	24 h	quant.	94:6	79:21
9	**290**	24 h	quant.	93:7	82:18
10	**291**	24 h	quant.	95:5	81.5:18.5

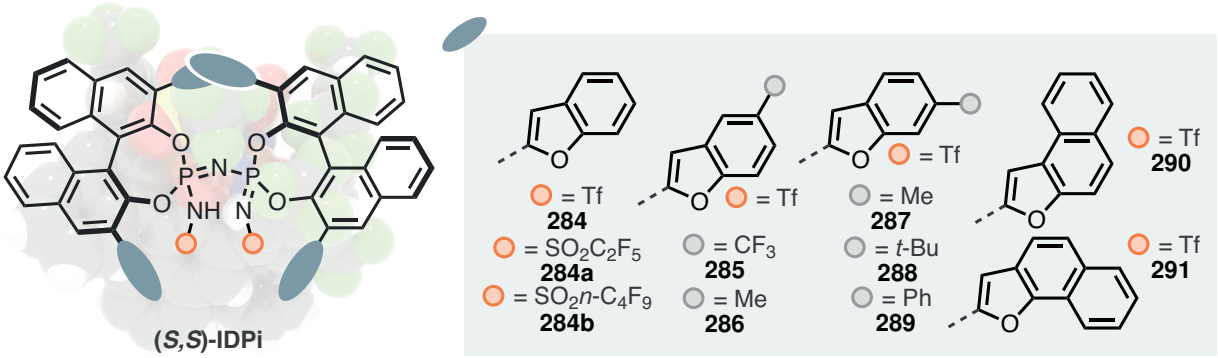

excellent diastereoselectivity. Notably, **290** displayed a slightly higher enantioselectivity of 82:18 er (entry 9).

Previous successes with benzofuranyl-substituted IDPi catalysts have been achieved by substitution of the perfluoroalkylsulfonyl cores with perfluoroarylsulfonyl derivatives.[264] Building on this, we embarked on an investigation of the impact of this substitution on the most promising catalysts detailed in Table 3.9, focusing particularly on the naphthofuran

Table 3.10: Screening of the reaction between **224** and **217** with benzofuranyl-substituted IDPis bearing a perfluorophenylsulfonyl inner core. Reactions performed on 0.025 mmol scale; yields and diastereoselectivities determined by ^{1}H NMR using mesitylene as an internal standard; absolute configuration not determined; [a] at 20 °C with TIPS-**D**; [b] in *m*-xylene.

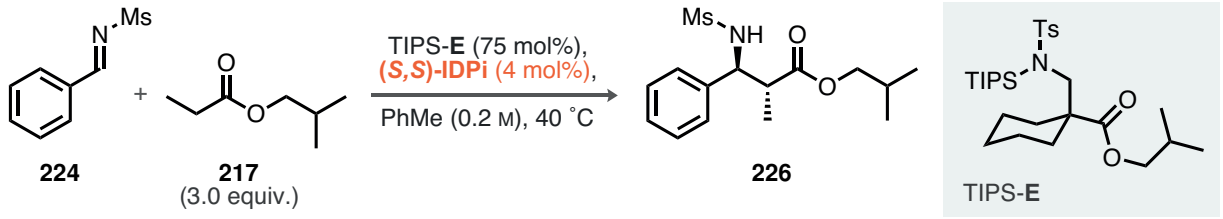

224 **217** (3.0 equiv.) **226**

entry	catalyst	time	yield **226**	dr	er (*anti*)
1[a]	**290a**	48 h	54 %	>95:5	90:10
2	**290a**	48 h	84 %	95:5	89.5:10.5
3	**284c**	48 h	18 %	89:11	84.5:15.5
4[b]	**285a**	4.5 d	71 %	90:10	89:11
5	**289a**	24 h	12 %	92:8	86:14
6	**292a**	24 h	25 %	92:8	91:9

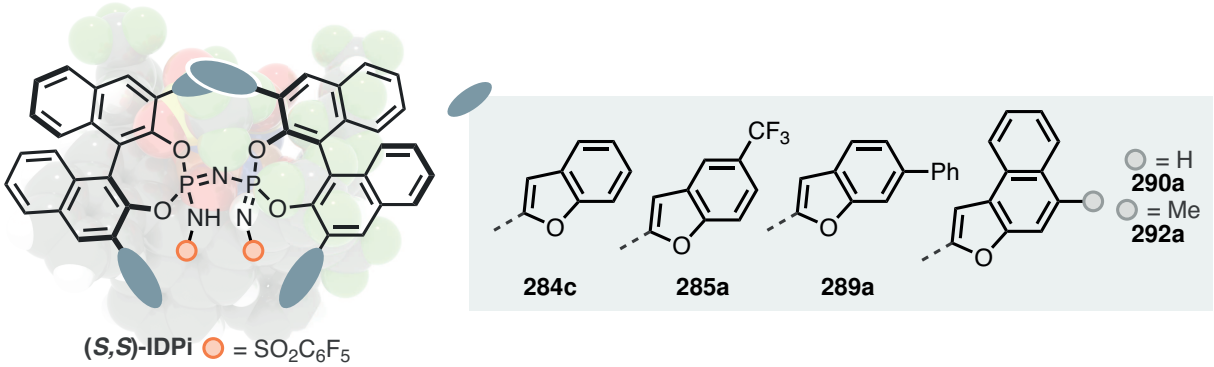

motifs and the beneficial effect of 6-substituents on the benzofuran fragment.

Due to observed reduced reactivity with certain variants, these reactions were conducted at an elevated temperature of 40 °C to ensure comparability (Table 3.10, *cf.* entries 1 and 2). Overall, enhanced diastereo- and enantioselectivities were observed for all perfluorophenylsulfonyl-core catalysts. Several interesting observations emerge from Table 3.10: firstly, the effect of temperature on the enantioselectivity of the reaction catalyzed by IDPi **290a** was minimal (90:10 er vs. 89.5:10.5 er). Moreover, a direct comparison between the catalyst **290a** and its counterpart featuring an unsubstituted benzofuran **284c** underscores the significant influence of the additional phenyl ring (entries 2 and 3, 89.5:10.5 er vs. 84.5:15.5 er).

The IDPi with a phenyl substituent in the 6-position of the benzofuran group **289a** did not exhibit as pronounced an improvement in enantioselectivity upon core substitution as

other catalysts; however, substitution at this position remains crucial, as evidenced by the high enantioselectivity achieved with IDPi **292a** (entry 6, 91:9 er), albeit at a reduced yield of **226**. Representing the best compromise between high reactivity and selectivity, naphtho[2,1-*b*]furan-substituted IDPi **290a** was chosen for further optimization of reaction conditions, including temperature, equivalents of ester, concentration, and solvent.

3.7.3 Effect of the Temperature

The influence of temperature on the reaction was preliminarily suggested by results shown in Table 3.10 (entries 1 and 2), prompting a detailed investigation into its systematic effects. For this purpose, our optimized IDPi **290a** was employed in the reaction between **224** and isobutyl propionate **217** (3.0 equiv.) across a range of temperatures (Table 3.11).

This investigation confirmed the previously noted minimal influence of temperature on enantioselectivity. At 40 °C, an enantiomeric ratio of 88:12 er was observed, with only an 8 % variation in enantiomeric excess observed down to −30 °C. To enhance our understanding of the reaction dynamics, we chose conditions from entry 6 at −10 °C to explore the impact of the solvent on yield and selectivity (Table 3.12).

Table 3.11: Effect of temperature on the reaction between **224** and **217** catalyzed by IDPi **290a**. Reactions performed on 0.025 mmol scale; yields and diastereoselectivities determined by ^{1}H NMR using mesitylene as an internal standard; absolute configuration not determined.

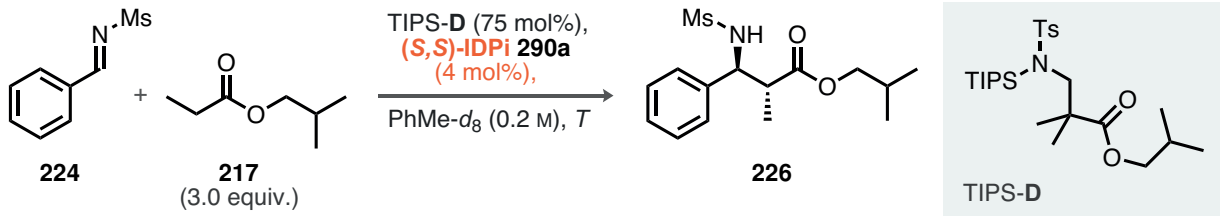

entry	T / °C	time	yield **226**	dr	er (*anti*)
1	40	48 h	93 %	>95:5	88:12
2	30	48 h	86 %	>95:5	89:11
3	20	48 h	54 %	>95:5	90:10
4	10	48 h	41 %	>95:5	90.5:9.5
5	0	96 h	93 %	>95:5	90:10
6	−10	96 h	37 %	>95:5	91:9
7	−20	96 h	23 %	>95:5	91:9
8	−30	96 h	8 %	>95:5	92:8

3.7.4 Effect of the Solvent

We chose a range of etheral, chlorinated, aliphatic, and aromatic solvents for the investigation of our model reaction (Table 3.12).

Despite the notable insolubility of the imine in MTBE and THF, MTBE still managed to provide **226** at a low yield but with good enantioselectivity (entry 1, 86:14 er), whereas THF resulted in no conversion. Similarly, *n*-hexane showed no reactivity, presumably due to solubility issues (entry 5).

Chlorinated solvents, particularly CH_2Cl_2, demonstrated better reactivity, achieving 43 % yield, yet neither CH_2Cl_2 nor $CHCl_3$ influenced the enantioselectivity (entries 3 and 4) at all.

The preference of this reaction both in terms of reactivity and selectivity for aromatic solvents was further emphasized in the examination of benzene, *m*-xylene, and mesitylene (entries 6–8). Compared to the previous conditions in toluene, furnishing the product with 91:9 er, we saw a further increase in enantioselectivity upon conducting the reaction in *m*-xylene (94:6 er, entry 7). Most notably, when using mesitylene, a solvent with an additional methyl group, the enantioselectivity peaked at an impressive 95.5:4.5 er, though the yield remained moderate at 30 %.

Table 3.12: Effect of various solvents on the reaction between **224** and **217** catalyzed by IDPi **290a**. Reactions performed on 0.025 mmol scale; yields and diastereoselectivities determined by ^{1}H NMR using mesitylene as an internal standard; absolute configuration not determined; [a] at 10 °C.

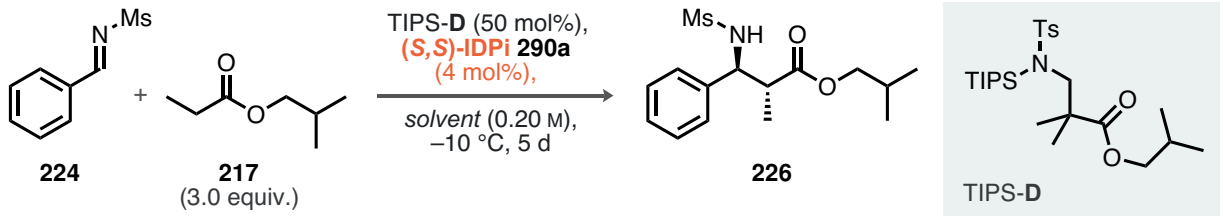

entry	solvent	yield **226**	dr	er (*anti*)
1	MTBE	23 %	>95:5	86:14
2	THF	–	–	–
3	CH_2Cl_2	43 %	>95:5	50:50
4	$CHCl_3$	11 %	>95:5	53:47
5	*n*-hexane	–	–	–
6[a]	benzene	28 %	>95:5	88:12
7	*m*-xylene	10 %	>95:5	94:6
8	mesitylene	30 %	>95:5	95.5:4.5

3.7.5 Effect of the Concentration

Addressing the potential to enhance the yield of **226**, our exploration into the equilibrium dynamics between the ester and silylsulfonamides indicated a substantial influence of ester concentration on the formation of silyl ketene acetal *in situ* (Fig. 3.6).

However, our hypothesis that merely increasing the ester concentration might adversely affect the polarity of the reaction mixture, potentially undermining the ion-pairing interactions critical for enantioinduction, was confirmed: Under standard conditions using 3.0 equiv. **217**, the product was formed in 8 % yield with 92:8 er. Yet, when 50.0 equiv. of the ester was used, although the yield increased to 69 %, the enantioselectivity decreased to 85.5:14.5 er.

To mitigate this reduction in enantioselectivity while enhancing the ester's absolute amount, we opted to maintain the ester concentration in mesitylene (Table 3.13).

Overall findings indicated that these factors had a minimal impact on reactivity, with a gradual decline in yield observed from 27 % at 0.20 mol/L to 6 % at 0.04 mol/L. Upon closer inspection of this trend, we observed a significant drop in yield when reducing the concentration below 0.05 mol/L, resulting in a total decrease of only 6 % (entries 1 and 4), while the enantioselectivity slightly increased to 96:4 er.

In summary, this investigation successfully mitigated the impact of using a higher amount of ester by adjusting the absolute dilution, albeit at the cost of reduced reactivity due to this concentration-dependence.

Table 3.13: Effect of the concentration, while maintaining the effective concentration of ester, on the reaction between **224** and **217** catalyzed by IDPi **290a**. Reactions performed on 0.025 mmol scale; yields and diastereoselectivities determined by ^{1}H NMR using mesitylene as an internal standard; absolute configuration not determined.

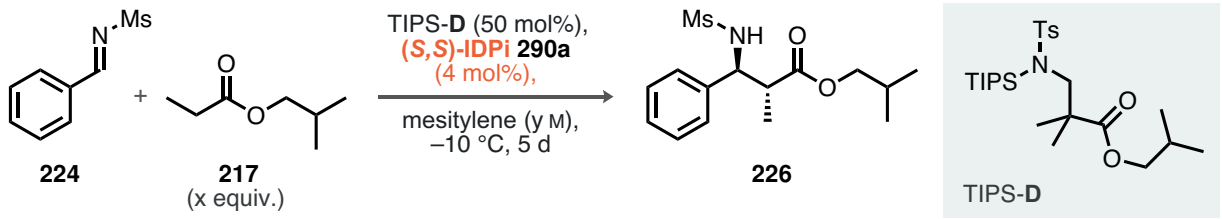

entry	x	y	yield **226**	dr	er (*anti*)
1	3.0	0.20	27 %	>95:5	95.5:4.5
2	6.0	0.10	23 %	>95:5	95.5:4.5
3	9.0	0.07	21 %	>95:5	96:4
4	12.0	0.05	27 %	>95:5	96:4
5	15.0	0.04	6 %	>95:5	96:4

3.7.6 Final Fine-Tuning of the Reaction Conditions

At this stage in the optimization of enantioselectivity, we introduced the second-generation silylsulfonamides. Our mechanistic studies revealed a stronger thermodynamic driving force for protodesilylation using the neopentyl reagent TIPS-**G** (**281**) in reaction with isobutyl propionate **217**. Eager to leverage this finding to enhance reactivity, we applied the conditions from Table 3.13, entry 4, for a final series of adjustments in temperature and solvent (Table 3.14). To our delight, an increase of over 100 % in yield was observed, producing **226** in 47 % yield with virtually unchanged enantioselectivity (95.5:4.5 er, entry 1). When the reaction was conducted at a slightly elevated temperature of 30 °C, the selectivity decreased, while we observed a significantly enhanced yield (entry 2). This was counteracted by modifying the solvent; using 1,3-diethylbenzene (entries 3–5) demonstrated superior reactivity compared to mesitylene, facilitating nearly quantitative formation of the Mannich product **224** in 93 % yield and excellent enantioselectivity (95:5 er).

In summary, these screening efforts identified the optimal reaction conditions for the first asymmetric silicon-catalyzed Mukaiyama–Mannich reaction of simple alkyl esters *via* silylium ACDC. This achievement was realized through a combination of mechanistic insights and continuous screening, highlighting the importance of both approaches.

Several mechanistic nuances, particularly those influencing key enantioselectivity-determining factors, will be further discussed in Section 3.7.8.

Table 3.14: Final optimization parameters of the reaction between **224** and **217** catalyzed by IDPi **290a**. Reactions performed on 0.025 mmol scale; yields and diastereoselectivities determined by ^{1}H NMR using mesitylene as an internal standard; absolute configuration not determined; [a] 3 d reaction time.

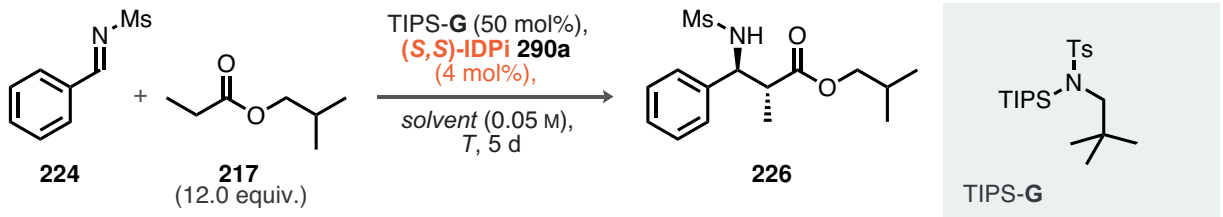

entry	solvent	T / °C	yield **226**	dr	er (*anti*)
1	mesitylene	−10	47 %	>95:5	95.5:4.5
2	mesitylene	30	91 %	>95:5	94:6
3	1,3-diethylbenzene	−10	67 %	>95:5	95:5
4	1,3-diethylbenzene	0	75 %	>95:5	95:5
5	1,3-diethylbenzene	10	93 %	>95:5	95:5

3.7.7 Preliminary Exploration of the Scope and Limitations

With our optimized conditions in place, employing naphthofuranyl IDPi **290a** and silylsulfonamide TIPS-**G**, we were keen to explore the scope and limitations of our reaction (Scheme 3.23).

This exploration was supported by the prior synthesis of several racemic compounds using our newly developed $HNTf_2$-catalyzed reaction (Scheme 3.10). Generally, the products were obtained as single diastereomers. In addition to the model substrate, which was obtained in 93 % yield and 95:5 er, we investigated the performance with different ester substituents.

Interestingly, both ethyl and methyl propionate furnished **230** and **229** in good to excellent yields, albeit with slightly reduced enantioselectivities of 91:9 er and 91.5:8.5 er, respectively. Methyl substitution at the 4-position of the imine's phenyl ring was well tolerated, yielding 90 % with an enantioselectivity of 93.5:6.5 er.

Current limitations appear related to the *N*-sulfonyl substituent and the alkyl chain length of the ester. Using an *N*-ethanesulfonyl imine, we observed a significant decrease in both yield and enantioselectivity (72:28 er). A similar but more pronounced trend was

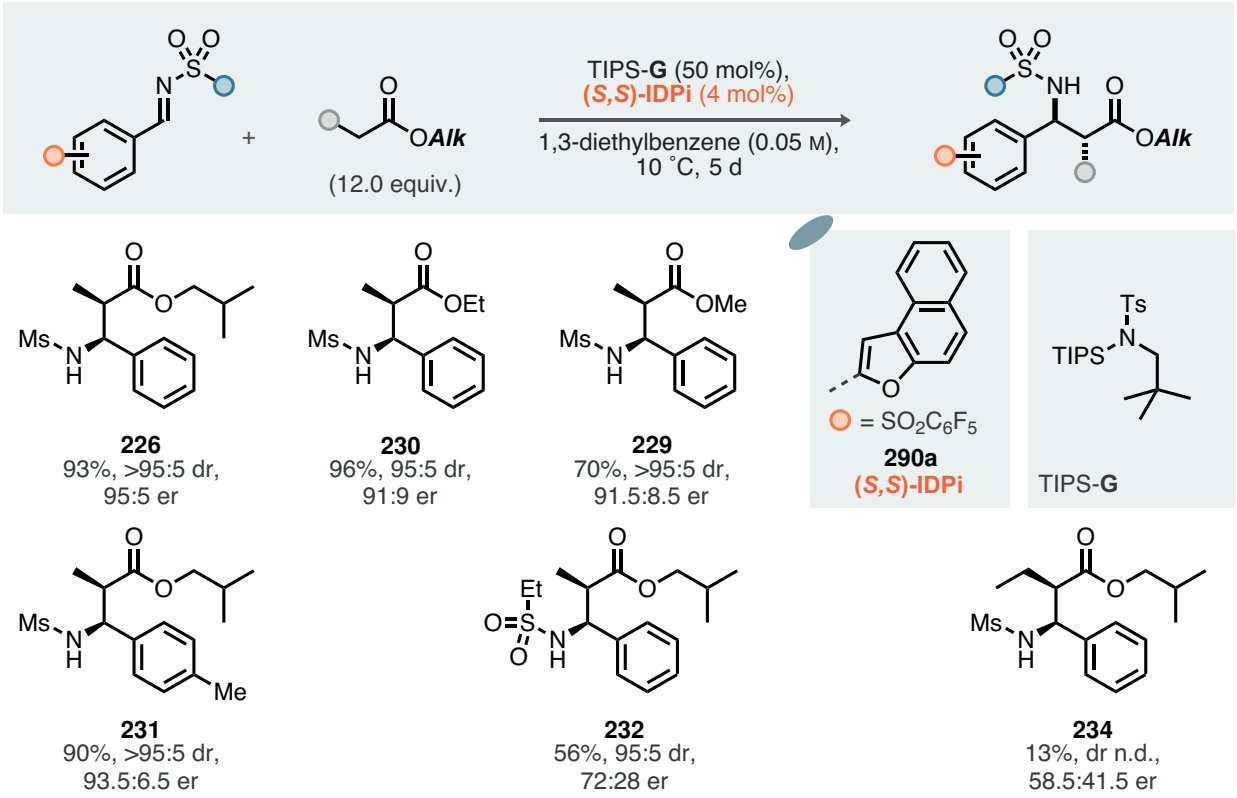

Scheme 3.23: Preliminary investigation of the scope and limitations of the silylium ACDC-enabled silicon-catalyzed Mukaiyama–Mannich reaction; reactions conducted on 0.025 mmol scale; yields and diastereoselectivities determined by ^{1}H NMR using mesitylene as an internal standard; absolute configuration not determined.

observed with isobutyl butyrate; the corresponding product **234** displayed only very low levels of enantioselectivity.

These limitations suggest strong interactions of these positions with the catalyst backbone, clearly indicating that a more systematic investigation is necessary and is currently underway.

3.7.8 Proposed Reaction Pathway

Condensing our mechanistic insights with the observed reactivity and selectivity, we propose the following all-silylium-catalyzed, silicon-catalytic reaction pathway (Scheme 3.24).

The overall reaction is initiated by the deprotosilylation of the IDPi catalyst **290a** upon its reaction with the neopentyl silylsulfonamide TIPS-**G** (**281**), which was observed to be a rapid initiation process for all silylsulfonamides. The combination of the high acidity of **290a** and the strong driving force for protodesilylation in **281** renders this activation reaction irreversible. Moreover, monitoring of the reaction progress by ^{31}P NMR clearly indicates that the *O*-silylated IDPi catalyst is the resting state. This observation validates our initial hypothesis to avoid any intermediate salt-forming processes, which is likely crucial for achieving the high reactivity observed in this reaction.

Following IDPi silylation, we hypothesize that an equilibrium between the reagent TIPS-**G** and the alkyl ester **293** is established. We characterized this equilibrium using isobutyl propionate **217**, which demonstrated a flat thermodynamic landscape. The Gibbs free energy of this reaction was determined to be $\Delta G = (2.03 \pm 0.05)$ kcal/mol at 298 K, yielding low but significant quantities of the (*Z*)-configured silyl ketene acetal **294a** *in situ*. The relative configuration of the double bond was unambiguously determined to be (*Z*) by 1D-selective NOESY experiments performed on the silyl ketene acetal generated from isobutyl propionate **217** under the specific reaction conditions devoid of imine **224**. Thus far, the inherent stereoselectivity of the deprotonation step has not been elucidated. Simchen's studies[223] have described the (*E*)-to-(*Z*)-isomerization of TBS silyl ketene acetals, yet no information was provided on the sterically more demanding TIPS variants. Given the increased steric demand, it is conceivable that isomerization becomes less relevant, and that the deprotonation step itself is highly stereoselective. Investigating this phenomenon will involve using preformed (*E*)-silyl ketene acetal and subjecting it to our reaction conditions. Additionally, we have yet to gather information about the kinetic properties of the ester deprotosilylation step. We attribute the higher performance of TIPS-**G** compared to first-generation reagents to the absence of a Lewis-basic ester fragment, thereby reducing competition for the Lewis-acidic TIPS–IDPi.

Overall, the demonstration of *thermodynamic control*, which the IDPi catalyst imposes on the reaction system, is complemented by the need for *kinetic control* during the stereoselective

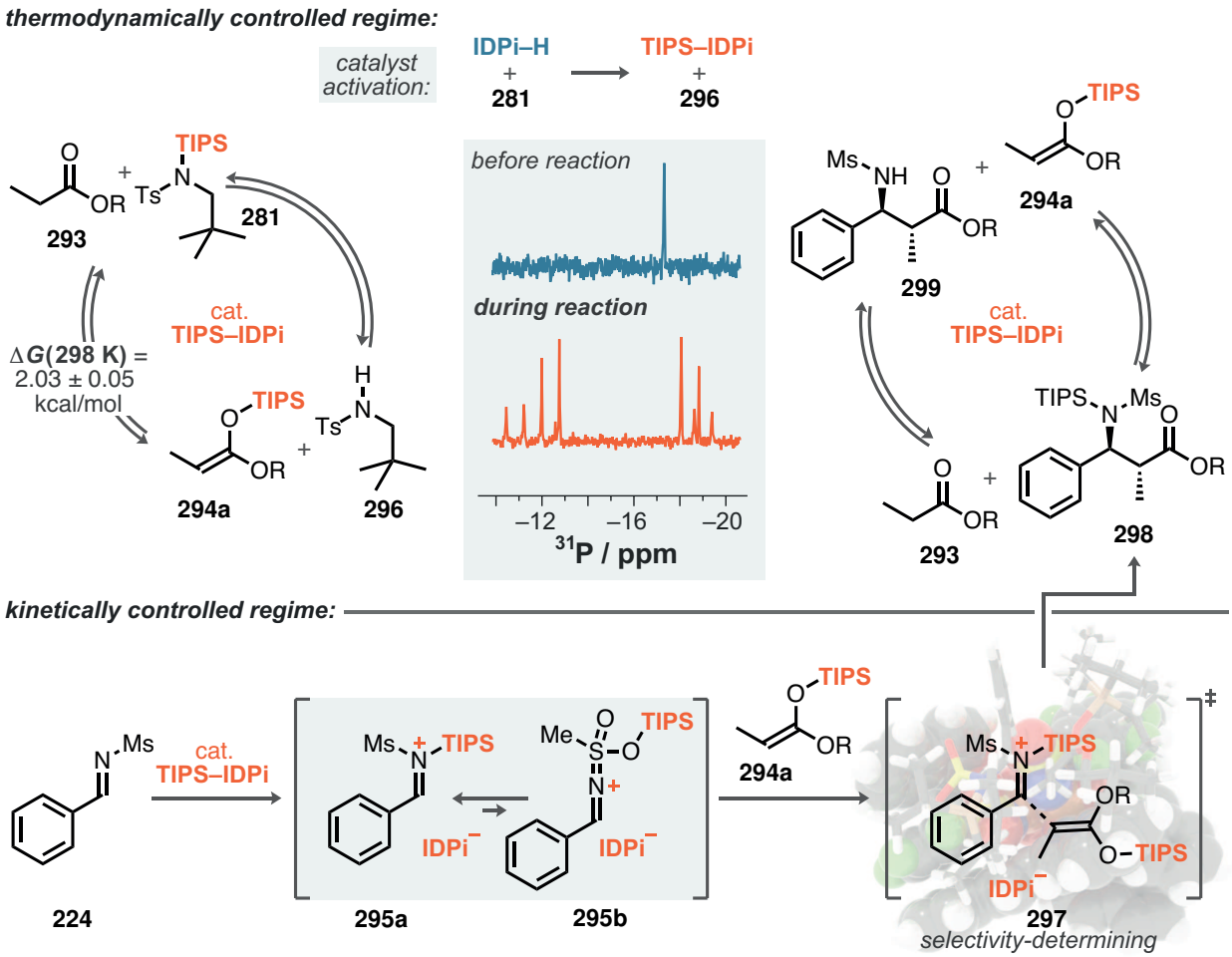

Scheme 3.24: Proposed reaction pathway of the silylium ACDC-enabled, silicon-catalyzed Mukaiyama–Mannich reaction.

addition of the freshly generated silyl ketene acetal **294a**. The activation of the imine is likely facilitated through silylation, forming the ion pair **295**.

Similarly to the silatropism observed with the silylsulfonamides, this imine may also undergo a dynamic equilibration process. For the *N*-silylated variant, we propose the indicated (*Z*)-configuration **295a** due to the sterically demanding TIPS group. Additional stereochemical complexity is introduced during isomerization to the corresponding *O*-isomer. The iminium ion is hypothesized to form a sulfoxazacumulene-like structure **295b**, which possesses not only a stereogenic center at sulfur but also axial chirality. Such a species would likely exhibit strong match-mismatch interactions with the chiral, enantiopure counteranion, potentially rendering its formation stereoselective. In this context, there is a possibility for stereoinduction at the ion pair stage, and the selectivity of the subsequent nucleophilic addition of **294a** may primarily result from the stereodifferentiation induced in **295b**.

However, the contribution of the nitrogen lone pair from the imine **224** to the sulfur atom is considerably low. This is attributed not only to the significant size difference between

nitrogen and sulfur, potentially leading to inefficient orbital overlap, but also to the sp^3 configuration of the sulfur atom, which precludes any substantial π-donation necessary for the formation of **295b**. Therefore, we believe that the *N*-TIPS-activated imine **295a** is the predominant species, rendering the stereochemical arguments discussed for **295b** likely inconsequential.

Consequently, the addition of the silyl ketene acetal **294a** *via* a potential transition state, as depicted in structure **297**, would result in the formation of the *N*-silylated product **298** in the selectivity-determining step. Preliminary investigations into the scope of the reaction revealed a strong preference for *N*-mesyl substitution in the imine, as well as higher selectivities for propionate esters, suggesting that these features act as recognition elements for the chiral enantiopure counteranion. The silylium activation of the imine in **295** might acidify the sulfonyl methyl group, leading to the likely formation of non-classical CH···O hydrogen bonds with the core fragments of the IDPi catalyst. A similar interaction may be expected for the α-methyl group of the propionate-derived silyl ketene acetal in reactions with highly activated substrates. Significant dispersion interactions can furthermore be expected as a consequence of the large TIPS groups. A comprehensive transition state analysis and further scope exploration are currently underway.

The silylated product **298** generated in this manner is expected to establish an equilibrium with the excess ester **293** present in the reaction mixture, similar to that observed with TIPS-**G** (**281**). It is plausible to assume a different thermodynamic profile for this equilibrium, as these reactions have been found to be highly substituent-dependent (Section 3.6).

Since **298** itself contains two stereocenters (three, if considering the *O*-silylated variant), different interaction energies of these stereoisomers with the chiral enantiopure counteranion could lead to kinetic resolution during the protodesilylation. An extreme scenario would involve reversible C−C bond formation between silyl ketene acetal **294a** and the imine **224**, with irreversible protodesilylation of **298** to form **299**, making this final step stereodetermining. Control experiments with independently synthesized, racemic silylated product **298**, subjected to catalytic amounts of IDPi **290a** in the presence of an ester, and the measurement of the enantiomeric ratio of **299** over time could provide insight into this hypothesis. However, no dependence of the enantioselectivity on the conversion of the reaction has been observed in all cases studied so far, which we attribute to the less likely nature of this mechanistic scenario. Another possibility is that the reaction of the *N*-TIPS product **298** with an excess of a different silyl ketene acetal in the presence of IDPi **290a** might show evidence of scrambling in the final product, if the C−C bond-forming step were reversible, since low amounts of imine **224** would be regenerated over the course of this reaction. This control experiment might be realized by using an isotope-labeled silyl ketene acetal, or a nucleophile with a different alcohol portion of the ester fragment.

Nonetheless, the fundamentally silicon-catalyzed nature of this process is underscored by the equilibrium involving the product **299**, which is eventually liberated due to the deprotosilylating nature of its silylated variant **298**. The relatively small quantities of silyl ketene acetal generated through this mechanism are sufficient for quantitative reaction, as they combine with a subsequent irreversible, kinetically controlled nucleophilic addition step, leading to the constant regeneration of **294a**. We interpret this behavior as a pseudo-zero order behavior in the concentration of the imine over time; however, more in-depth kinetic studies are required to quantitatively describe this phenomenon.

Lastly, we hypothesize that both variants of silylsulfonamides, TIPS-**G** (**281**) and **298**, are linked through an additional equilibrium, which is not depicted in Scheme 3.24 for reasons of clarity. We believe that this potential connection is governed by the stronger protodesilylating agent, but also likely proves inconsequential due to the catalytic competence of both species in the generation of the silyl ketene acetal.

4 Summary and Outlook

This chapter has demonstrated the development of the concept of *silyl ketene acetal catalysis*. Analogous to enamine catalysis, which is based on the reversible generation of an α-nucleophilic species from ketones and aldehydes *in situ*, we have successfully generated and fully characterized highly reactive silyl ketene acetals as catalytic intermediates.

This overall process was facilitated by the development of a silicon-catalytic Mukaiyama–Mannich reaction of alkyl esters. Literature precedent had already established that Mannich reactions of *N*-sulfonyl imines with tertiary amides can be catalytic in silicon. This mechanistic peculiarity inspired our efforts not only to fully understand the key determining factors but also to expand the methodology to include unbiased substrates. This effort culminated in a set of reaction conditions capable of efficiently converting a range of abundant alkyl esters into their corresponding *N*-sulfonyl β-amino esters.

However, in our attempts to develop a complementary catalytic *asymmetric* variant, we encountered several challenges. Using highly acidic and confined IDPi catalysts along with tertiary amines resulted in low yields and selectivities, consistent with observations made in Chapter 2. Substitution of NEt_3 with a chiral tertiary amine derived from quinine also yielded only modest levels of enantioinduction. Similarly, newly developed and synthesized chiral BINOL-based allyl(diisopropyl)aryloxysilanes provided low enantioselectivities as well. Although these catalyst motifs have not yet succeeded in our desired transformation, their straightforward synthesis and high potential for modularity may still open avenues for other

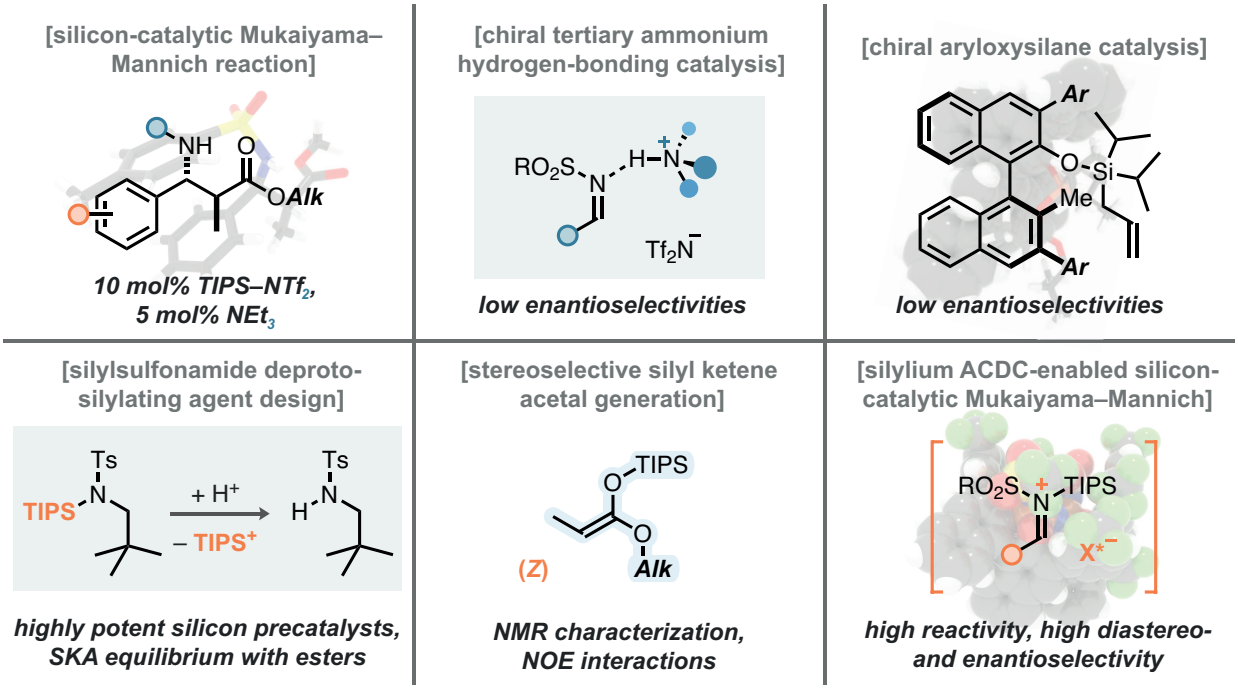

Scheme 3.25: Summary of the findings discussed in this chapter.

catalytic asymmetric transformations.

Ultimately, these highly challenging attempts inspired a deeper mechanistic and kinetic investigation, which led us to elucidate the key connection between the alkyl ester and silyl ketene acetal. Silylsulfonamides, structurally related to the silylated Mannich products generated during our reactions, have been found to be highly potent deprotosilylating reagents. Throughout this investigation, we synthesized a small library of new reagents and investigated their reactivity-determining features. These reagents are capable of completely (*Z*)-stereoselectively deprotosilylating alkyl esters *via* an overall catalytic reaction, with the latest-generation neopentylamine-based silylsulfonamide generating up to 29 mol% of silyl ketene acetal through the establishment of a fast equilibrium.

Having identified and widened this catalytic window to silyl ketene acetals, we successfully developed the silylium ACDC-enabled silicon-catalytic Mukaiyama–Mannich reaction of alkyl esters. Our optimization efforts revealed the high importance of a naphthofuran-decorated IDPi catalyst, which imparts complete diastereo- and excellent enantioselectivities in the transformation of several *N*-sulfonyl imines with a range of alkyl esters.

4.1 Outlook on the Mukaiyama–Mannich Reaction

With our newly developed reagents and the established set of reaction conditions for the catalytic asymmetric Mukaiyama–Mannich reaction in hand, we will next expand our investigation of the substrate scope. These crucial details will continue to inform our mechanistic understanding and will be complemented by in-depth DFT calculations conducted in parallel. Section 3.7.8 has already discussed and proposed several key experiments to gain deeper insight into this transformation.

Preliminary investigations of the substrate scope revealed a pronounced substrate-specificity for the *N*-mesyl substituent as well as for propionate esters over isobutyl butyrate. We believe that to address these challenges, a broader approach to catalyst screening will be the most effective strategy moving forward. This endeavor may also involve a multi-substrate screening approach, similar to that described in Chapter 2.

4.2 Outlook on the Development of Silylsulfonamides

Continuing efforts to increase reactivity align with our desire to further steepen the thermodynamic landscape of ester deprotosilylation. For this reason, we have embarked on a preliminary computational exploration of new deprotosilylating agents.

Our initial computational studies (Scheme 3.26) have nearly quantitatively reproduced the experimentally determined Gibbs free energy for the reaction of TIPS-**G** with isobutyl propionate, showing a difference of only 1.9 kcal/mol. While further refinement is still re-

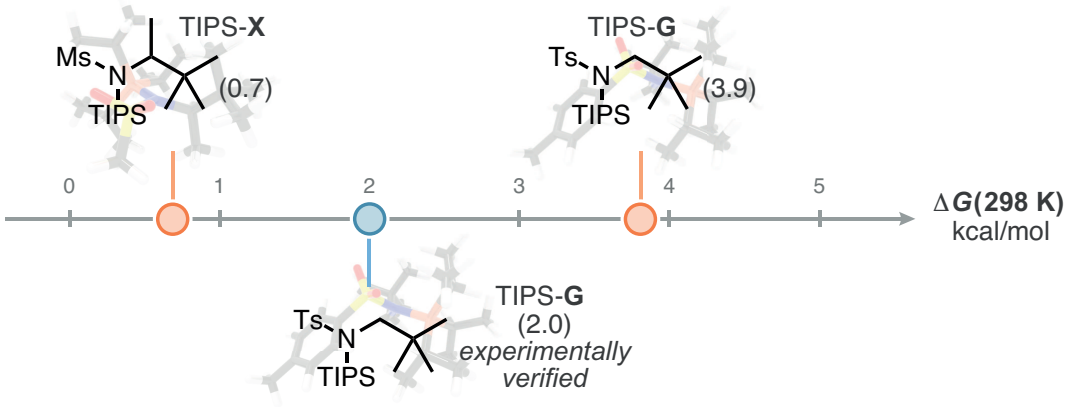

Scheme 3.26: Computational deprotosilylation thermochemistry of the lowest-Gibbs free energy conformers of TIPS-**G** and TIPS-**X** with methyl propionate (M06-2X/def2-QZVP//r2SCAN-3c).

quired and ongoing, we observed a significant increase in the driving force for ester deprotosilylation upon installation of an α-methyl group *in silico* (TIPS-**X**, 0.7 kcal/mol). Eventually, we believe that the design of novel reagents like TIPS-**X** will not only enhance our understanding of this reactivity but also enable a completely catalytic stereoselective *synthesis* of silyl ketene acetals.

In the context of silylium ACDC, whose compatibility we have demonstrated in the development of the catalytic asymmetric Mukaiyama–Mannich reaction, more active reagents will lead to milder reaction conditions and facilitate the overall process of generalizing enantioinduction.

4.3 Beyond the Mukaiyama–Mannich Reaction

In parallel to our computational design of more active reagents, we have conducted initial investigations of other Mukaiyama-type transformations from alkyl esters using our first-generation reagents.

By employing methyl cinnamate instead of the *N*-mesyl imine in a mixture of toluene and isobutyl propionate (1:1 *v*/*v*, 0.10 mol/L), we observed quantitative formation of the Mukaiyama–Michael addition product **300** at −20 °C. This reaction achieved promising diastereoselectivity (76:24 dr) and enantioselectivity (81.5:18.5 er) using a naphthofuran-substituted IDPi catalyst **290**. Similarly, we identified 72 % yield of the Mukaiyama aldol product in the reaction with benzaldehyde, exhibiting a low degree of stereoinduction (67:33 dr, 52:48 er) when conducted at room temperature.

Altogether, these results showcase both the high reactivity and compatibility of our silylsulfonamide deprotosilylating reagents within the context of silylium ACDC. These transformations serve as exemplary cases for virtually all conceivable silylium-catalyzed transfor-

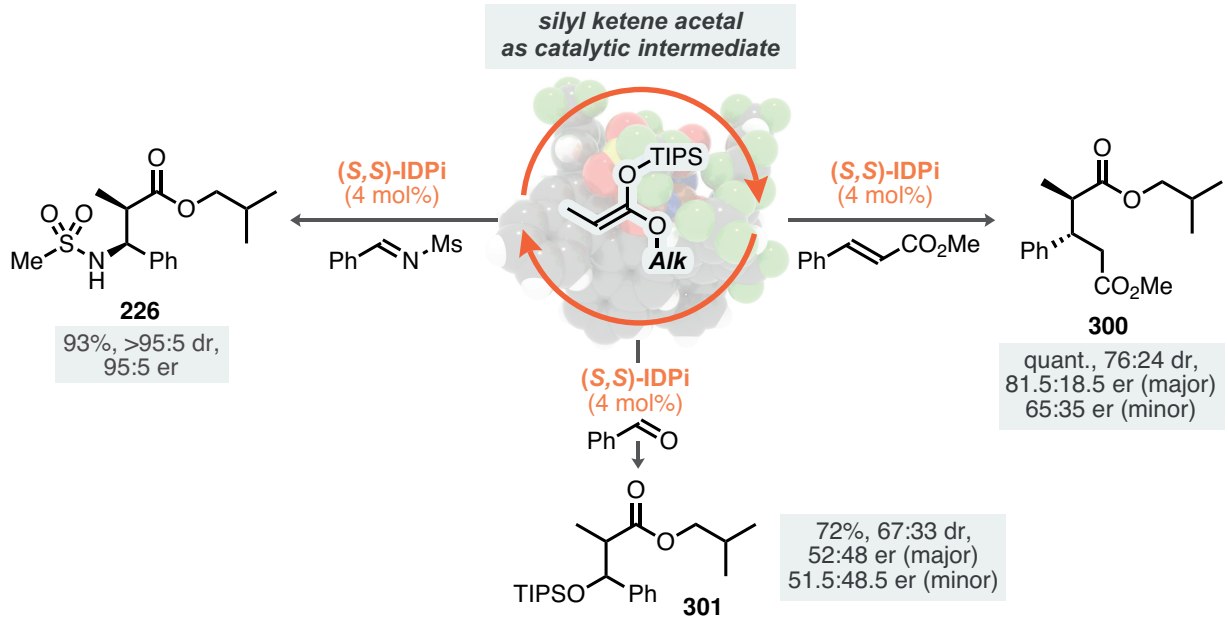

Scheme 3.27: Preliminary exploration of different Mukaiyama reactions from alkyl esters; reactions conducted on 0.025 mmol scale; aldol: IDPi **150**, 2.0 equiv. silylsulfonamide; Michael: IDPi **290**, 2.0 equiv. silylsulfonamide; yields and diastereoselectivities determined by crude ^{1}H NMR analysis; absolute configurations not determined; relative configuration of **300** assigned by analogy.[166]

mations that involve silyl ketene acetals, making their direct application from simple alkyl esters highly attractive. The optimization of these preliminary stereoselectivities is ongoing.

Besides Mukaiyama–Michael and aldol reactions, we plan to investigate Mukaiyama–Mannich reactions of *N*-carbamoyl imines, which are highly attractive due to their practicality, as well as direct Ireland–Claisen rearrangements. Given the implications outlined in Chapter 4, we will also initiate studies on the direct stereoselective *C*-glycosylation of alkyl esters.

Lastly, the Mukaiyama–Mannich reaction has cemented the overall concept of silicon catalysis within asymmetric Lewis acid organocatalysis. Although the silylsulfonamide reagents facilitate Mukaiyama–type reactions directly from alkyl esters, these transformations still require the addition of stoichiometric amounts of silicon. We hope that this work will inspire the development of more silicon-catalytic asymmetric reactions in the future, potentially extending to the aforementioned Mukaiyama–Michael or aldol reactions, and many more.

CHAPTER IV

SILYLIUM-CATALYZED *C*-GLYCOSYLATION: TOTAL SYNTHESIS OF GS-441524

1 Literature Background

The evolution of life is directly related to the evolution of disease. Human infections, typically spread through person-to-person or animal-to-person contact, are increasingly transmitted due to growing population densities. This intimate connection likely exists as long as we do and has had widespread societal and cultural manifestations (see Munch's *Self Portrait with the Spanish Flu*, Fig. 4.1).

Fig. 4.1: *Self Portrait with the Spanish Flu*, Edvard Munch, 1919

Bacterial infections, such as the bubonic plague, or *Black Death*, annihilated approximately 50 % of Europe's population within just six years during the 14th century.[265] Although such infections have been largely controlled with the development of antibiotics, the rise of multiresistent pathogens—mainly caused by antimicrobial misuse—poses a significant threat.[266] Viral infections, on the other hand, are notoriously difficult to control and have been the origin of several pandemics, such as the Russian flu (1889–1895, 1 million deaths), the Spanish flu (1918–1919, 50–100 million deaths), HIV/AIDS (since 1981, 40 million deaths), and—most recently—COVID-19 (since 2020). The novel virus SARS-CoV-2, the origin of the coronavirus disease 2019, has reportdely led to 7 million casualties, although estimates based on excess mortality are significantly higher.[267]

The last pandemic saw significant mitigation efforts through the rapid development of mRNA technology.[268] This approach is expected to expand into multiple future applications. However, small-molecule antivirals continue to serve as a primary defense against viruses. The COVID-19 crisis demonstrated that the development of such drugs could proceed at a similarly rapid pace—Pfizer's Paxlovid (nirmatrelvir/ritonavir) progressed from design to clinical studies within just 12 months.[269]

1.1 Small-Molecule Antivirals

The use of small molecules as antiviral agents began with iododeoxyuridine (iodoxuridine) for treating herpes simplex in 1963. Since then, 90 distinct antivirals have been developed up to 2016.[270] These agents are classified based on their mechanism of action into several categories: among others are entry inhibitors, as well as protease, integrase, and neuraminidase inhibitors. Antivirals that target viral replication mechanisms include reverse transcriptase and polymerase inhibitors, which are dominated by nucleoside analogues. Additionally, non-nucleoside reverse transcriptase inhibitors (NNRTIs) and non-nucleoside inhibitors of RNA (for RNA viruses) and DNA (for DNA viruses) polymerases are also employed. Providing a full overview of small-molecule antivirals is beyond the scope of this thesis; therefore, a

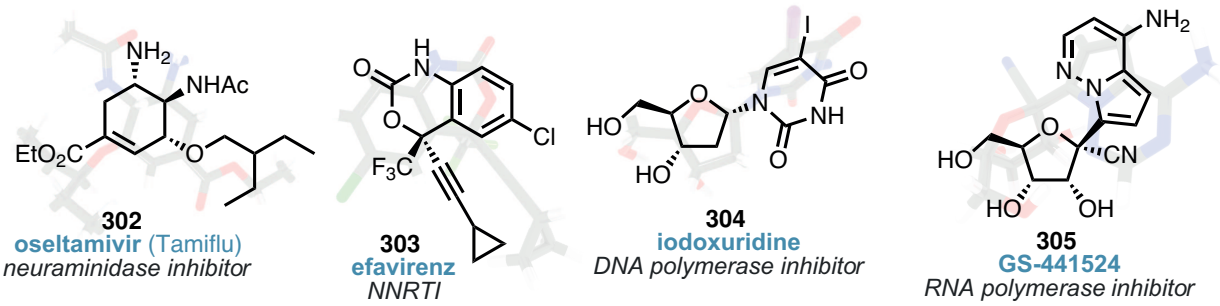

Scheme 4.1: Selected examples of small-molecule antivirals; 3D structures are based on X-ray data.[271–274]

selection is presented in Scheme 4.1.

Oseltamivir (Tamiflu), an orally administered drug, is used in high-risk patients to prevent severe flu progression. It acts by inhibiting neuraminidase, a glycoprotein on the viral surface crucial for releasing the virus from infected host cells.[275] Due to a significant political interest in the early 2000s, oseltamivir has also sparked notable synthetic research efforts in several prominent laboratories, including those led by Shibasaki,[276] Trost,[277] and Corey.[278]

Efavirenz is an NNRTI used for the treatment of HIV and, like all NNRTIs, selectively binds to a hydrophobic pocket of the HIV reverse transcriptase,[279] implying significant enzyme tolerance for various ligands. The conformational plasticity of this pocket has been extensively investigated.[280]

Iodoxuridine, approved in 1963, was the first small-molecule antiviral and is used to treat herpes simplex. It is a deprotoiodinated version of deoxyuridine and acts as a DNA polymerase inhibitor by mimicking deoxythymidine.[281] Similarly, due to structural resemblances with adenosine, GS-441524 (**305**) effectively inhibits RNA polymerase.[282] The active form of all nucleoside analogues is the triphosphate, which consequently requires phosphorylation of these drugs *in vivo*. Remdesivir (Veklury, **306**), which incorporates GS-441524 **305** as its nucleoside core, has received considerable attention during the onset of the SARS-CoV-2 pandemic. Further details will be discussed below.

1.2 GS-441524 and Remdesivir

Remdesivir (**306**), originally developed by Gilead Sciences for treating Ebola and Marburg viruses (Scheme 4.2 i),[282,283] was rapidly repurposed at the beginning of the COVID-19 crisis. Significant efforts were devoted to examine existing (antiviral) drugs, leading to the realization of the SOLIDARITY trial, led by the World Health Organization (WHO). This global initiative analyzed the mortality of hospitalized patients treated with several drugs, including remdesivir, lopinavir, hydroxychloroquine, and interferon β-1a, from March 2020 until January 2021.

In May 2022, the final results of the SOLIDARITY trial were presented; further investigation was discontinued for three out of the four drugs studies, leaving only remdesivir to continue in randomized studies. It was found to have no effect on patients already on ventilators, and only minor effects on the progression to death or the need for ventilation.[284] Despite these findings, remdesivir remained a recommended treatment for high-risk COVID-19 patients, especially at the early stages of the pandemic, able to prevent severe progressions.[285] Additionally, although it has never officially been approved for this use, the nucleoside GS-441524 is used to treat feline infectious peritonitis (FIP)—a deadly disease in FCoV-infected cats, illustrating its broader therapeutic potential.[286,287]

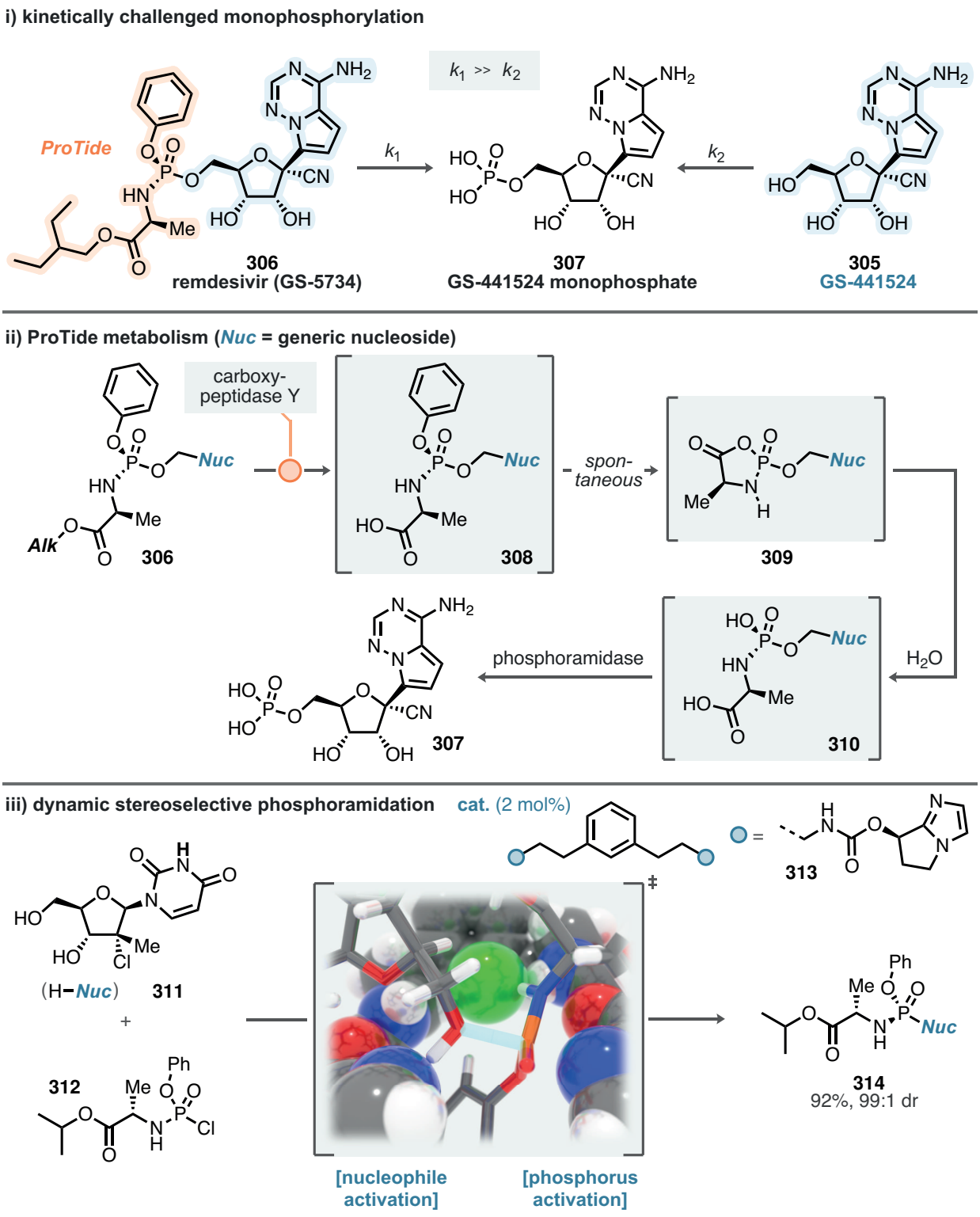

Scheme 4.2: i) ProTide technology to overcome kinetically disfavored nucleoside monophosphorylation; ii) postulated mechanism of ProTide hydrolysis; iii) catalytic dynamic stereoselective phosphoramidate synthesis. All compounds have been drawn in their neutral form, acknowledging that (partial) deprotonation might occur under physiological conditions; blue: nitrogen, red: oxygen, orange: phosphorus, green: chloride.

Structurally, the compound features a *C*-nucleoside core attached to an aryloxy phosphoramidate ester side chain at the 5-position. Remdesivir itself is a prodrug; its design utilizes the *ProTide* technology, developed by McGuigan and colleagues, which is known for its rapid hydrolysis kinetics of the phosphoramidate group.[288,289] This approach aligns with the phosphonate side-chain concept introduced by De Clercq and Holý in their development of acyclic nucleoside monophosphonates (ANPs).[290–292] The active pharmaceutical ingredient of nucleoside analogues is the corresponding triphosphate; however, for GS-441524, the monophosphorylation process is the limiting factor for bioavailability. The postulated enzymatic initiation of ProTide hydrolysis effectively addresses this challenge, enhancing drug delivery and efficacy (Scheme 4.2 ii).[282]

An abundant carboxypeptidase is postulated to initiate the hydrolytic sequence by forming the carboxylic acid **308**, which then undergoes spontaneous cyclization to form oxazaphospholidinone **309**. Subsequent ring opening by water ultimately furnishes **307**. This compound is then able to undergo downstream phosphorylations to provide the pharmaceutically active agent.

Although the ProTide technology offers an elegant solution to the bioavailability issue, it comes with several drawbacks. From a pharmacological perspective, the metabolical sensitivity of the side chain necessitates that remdesivir be administered *via* intravenous injection. Furthermore, it introduces stereochemical complexity, which can have dramatic effects in biological systems.

To address this synthetic challenge, researchers at Merck have developed a catalytic dynamic kinetic resolution of chlorophosphoramidate **312** (Scheme 4.2 iii). The reaction exhibited a second-order dependence on the catalyst. Inspired by the development of dimeric catalysts by Denmark[293] and Jacobsen[294], the synthesis of a novel phenyl-bridged imidazole dimer **313** ultimately led to the completely stereoselective formation of ProTide nucleoside **314**.[295]

DFT transition state analysis revealed that the stereoselectivity is governed by a chloride-templated framework, with the dimeric nature of **313** enabling bifunctional activation of the nucleophile and electrophile. Rapid epimerization of the stereocenter at phosphorus in **312** allowed for an overall dynamic process. Zhang and co-workers presented a variant of this chemistry tailored for the phosphoramidation of GS-441524.[296]

1.2.1 Reported Syntheses of Remdesivir

Three generations of remdesivir syntheses have been described in patents by Gilead Sciences,[297–299] however, yields for the third generation are not reported.[300] Consequently, this section will focus on the second generation synthesis (Scheme 4.3).

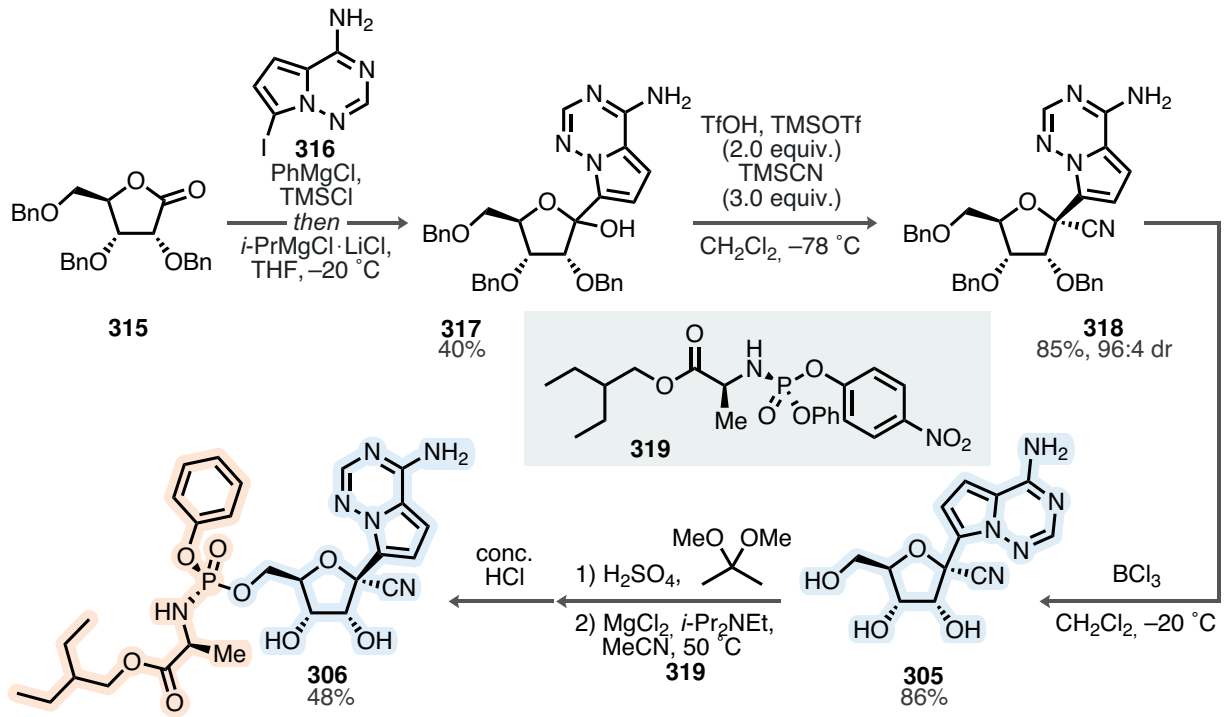

Scheme 4.3: Second-generation synthesis of GS-441524 and remdesivir.

The main challenge was achieving the stereoselective formation of the highly substituted stereocenter at the 2-position. This was complicated by the *C*-nucleosidic linkage to the aminopyrrolotriazine nucleobase. To address this, perbenzylated ribonolactone **315** was selected as the starting material, establishing the correct oxidation state needed for subsequent cyanation.[301]

This choice, however, resulted in a compromise regarding step economy, necessitating a multi-step synthesis from D-ribose, yielding **315** in either 61 % over three steps[302] or 43 % over four steps.[303] The synthesis of 2-iodoaminopyrrolotriazine **316** had already been well-established *via* regioselective iodination of aminopyrrolotriazine with NIS.

The unsubstituted nucleobase has been synthesized starting from either pyrrole[304] or 2,5-dimethoxytetrahydrofuran[305], with yields of 28 % over three steps and 27 % over four steps, respectively. In September 2020, Garg and colleagues presented an alternative synthesis for the nucleobase.[306]

Concerning the connection of both fragments **315** and **316**, deprotonation of the amino functionality in **316** with PhMgCl was followed by silylation with TMSCl. This step then set the stage for a transmetalation using Knochel's Turbo Grignard conditions.[307] The addition to **315** yielded lactol **317** in 40 % yield, with inconsequential diastereoselectivity at the anomeric center. The development of the subsequent cyanation step has received considerable attention; factors such as temperature and the nature of the employed Brønsted acid were found to be crucial for achieving high yields and stereoselectivity in the reaction.[308]

Under optimized conditions—employing superstoichiometric amounts of TfOH, TMSOTf and TMSCN at −78 °C—perbenzylated cyanoriboside **318** was obtained in 85 % yield with excellent diastereoselectivity (96:4 dr). Subsequent BCl_3-mediated debenzylation followed by acetonide formation on GS-441524 **305** and stereoretentive phosphoramidation with enantiopure **319** ultimately led to the synthesis of remdesivir **306** in 48 % yield (14 % from **315** over 6 steps, 9 % from D-ribose over 9 steps).

1.3 An Overview of Methods for *C*-Glycosylation

C-glycosides, such as GS-441524 and remdesivir, are structural frameworks of great importance in drug development.[309] Their significance stems from the replacement of the heteroatomic glycosidic bonds—typically involving oxygen and nitrogen—with carbon. This modification leads to increased metabolic stability and potentially enhanced specificity for their target enzymes or receptors.

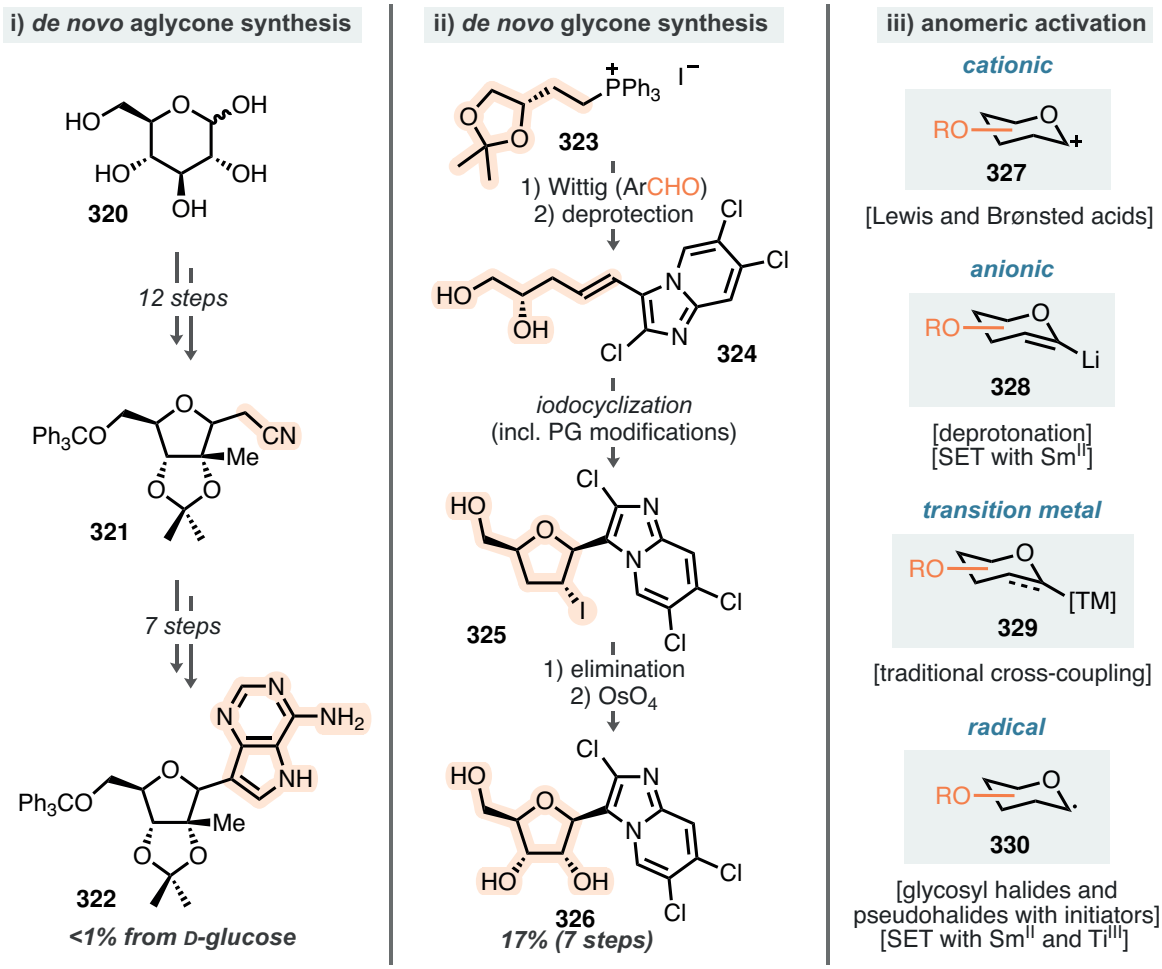

Scheme 4.4: Common approaches toward *C*-glycosides *via* i) synthesis of the aglycone, ii) synthesis of the glycone, and iii), anomeric activation.

They have found widespread applications not only as antivirals but also as anthropogenic drugs, and they are common motifs in a variety of natural products.[310] The overall strategies for synthesizing *C*-glycosides can be classified into three distinct regimes: i) *de novo* synthesis of the arene (aglycone) fragment, ii) *de novo* synthesis of the carbohydrate (glycone) fragment, and iii) anomeric activation of the carbohydrate (Scheme 4.4). Approaches i) and ii) for synthesizing *C*-glycosides are highly substrate-specific and often involve multi-step syntheses. For instance, the methylenecyanoglycoside **321** was synthesized from D-glucose **320** in 12 steps, requiring an additional 7 steps to produce the final *C*-adenosine derivative **322**.[311,312] Parallel to this, the synthesis of the glycone fragment is illustrated by the creation of the chloroimidazopyridine riboside **326**. Starting from readily available phosphonium salt **323**, the arene fragment was introduced *via* a straightforward Wittig reaction. The styrenyl moiety in **324** allowed for iodocyclization subsequent to acetonide deprotection, yielding the iodoglycoside **325**. Elimination and a well-established diastereoselective *syn*-dihydroxylation finally provided the riboside **326** in 17 % yield over 7 steps.[313]

The arguably most powerful and versatile approach for *C*-glycosylation, known as *anomeric activation*, encompasses a range of techniques (Scheme 4.4 iii).[310] These methods can be broadly categorized into cationic and anionic activation, as well as radical- and transition metal-based reactions. Cationic activation involves the departure of a leaving group at the anomeric position, complemented by anionic activation which proceeds either through deprotonation using strong bases like *t*-BuLi or by successive single electron transfer with Sm^{II} reagents. Traditional cross-coupling reactions typically utilize transition metal catalysis. Radical reactions are particularly notable for their funtional group tolerance, often allowing the hydroxy functionalities to remain unprotected, due to their orthogonality to RO−H bonds. Specific structural requirements of the *C*-glycoside structure dictate the exact synthetic strategy; the installation of electron-rich arenes typically proceeds through cationic activation, while electron-poor arenes may be functionalized through nucleophilic aromatic substitution reactions.

A notable example of cationic anomeric activation, which is of particular importance to this thesis and to silylium catalysis in general, is the Vorbrüggen method (Scheme 4.5). This approach has its conceptual roots in traditional *O*- and *N*-glycosylation reactions, more specifically, the Hilbert–Johnson reaction, which first described the addition of *O*-alkyl imidates to sugars.[314] This concept was later expanded to include *O*-silyl derivatives.[315] Vorbrüggen pioneered the use of metal-based Lewis acids[316] and subsequently TMSOTf and $TMSClO_4$[317] as catalysts for these transformations. Notably, the introduction of the Vorbrüggen method predates Noyori's TMSOTf-catalyzed Mukaiyama aldol reactions[32] by five years (see Chapter 1, Scheme 1.2), establishing it as one of the founding figures of silylium catalysis.

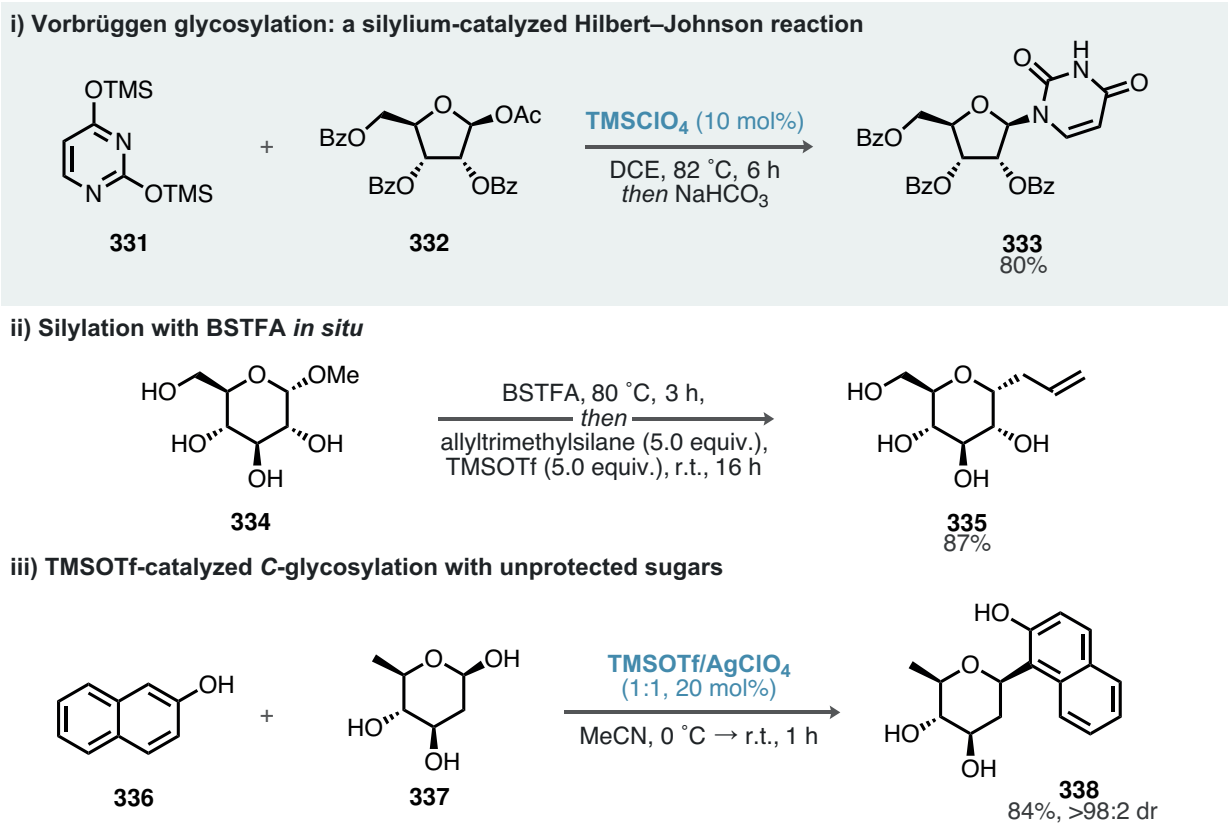

Scheme 4.5: i) Vorbrüggen's modification of the silyl Hilbert–Johnson reaction, ii), Gray's BSTFA-mediated *in situ* silylation, and iii), TMSOTf-catalyzed *C*-glycosylation with unprotected deoxyglucose **337**.

In a practical application of this method, persilylated uracil **331**, which was readily prepared *via* exhaustive silylation of uracil with TMSCl/HMDS, was found to readily react with perbenzoylated ribosyl acetate **332** under the influence of 10 mol% of $TMSClO_4$. This reaction produced benzoylated uridine **333** in 80 % yield and with excellent diastereoselectivity (Scheme 4.5 i). Besides achieving high selectivities, the Vorbrüggen method also addressed challenges such as the solubility of the nucleobase or carbohydrates through persilylation. This process has been further improved by the development of trimethylsilylating agents like BSA[259] and BSTFA.[260] Vorbrüggen's modification has been extensively applied in the synthesis of *N*-glycosides,[318] yet there has been a notable lack of its application in silylium-catalyzed *C*-glycosylation reactions.[319] Gray reported the silylation of carbohydrates with BSTFA *in situ* followed by deoxygenation with Et_3SiH in 1987, which also included a single example of allyl-glycosylation and subsequent desilylation (Scheme 4.5 ii).[320] The *C*-glycoside **335** was synthesized from 1-*O*-methyl-D-glucose **334** under harsh conditions, requiring 5.0 equiv. of TMSOTf and allyltrimethylsilane each. Additionally, pioneering studies by Toshima in 1992 introduced a TMSOTf/$AgClO_4$ mixture as an efficient catalyst for the reaction between 2-naphthol **336** and bis-deoxy-D-glucose **337** (Scheme 4.5 iii).[321] This

methodology was later expanded to include *C*-glycosylations with allyl silanes,[322] and found several applications in total synthesis.[323,324] Although these latter examples raise questions about whether the active catalyst is likely *in situ*-generated triflic acid instead of TMSOTf, they powerfully underscore the potential of this activation mode in transforming unprotected substrates.

2 Objectives

Section 1 has illustrated the importance of antivirals, with a particular focus on remdesivir (**306**) and its nucleoside core, GS-441524 (**305**). Considering the existing synthesis routes toward remdesivir, we recognized the elegant organocatalytic dynamic stereoselective phosphoramidation (Scheme 4.2 iii) and focused our attention on the nucleoside core GS-441524. This was furthermore supported by the recent availability of clinical data showing the potential of the direct oral administration of **305** instead of the prodrug remdesivir.[325,326] The primary *C*-glycosylation reaction currently requires extensive prefunctionalization of both ribonolactone and iodoaminopyrrolotriazine, despite the inherent polarity match present in the *unfunctionalized* starting materials (Scheme 4.6).

To address this, we propose a complementary approach starting directly from aminopyrrolotriazine **341** and D-ribose (**342**) to synthesize **340**. Drawing from Vorbrüggen's contributions to the Hilbert–Johnson reaction, we aim to utilize silylium catalysis to potentially activate **342**. This method would not only simplify the synthesis by reducing the need for prefunctionalization but also eliminates the requirement for cryogenic conditions. Challenges related to solubility and selectivity may be addressed by employing *in situ* traceless silylation using trimethylsilylating agents such as BSA or BSTFA.

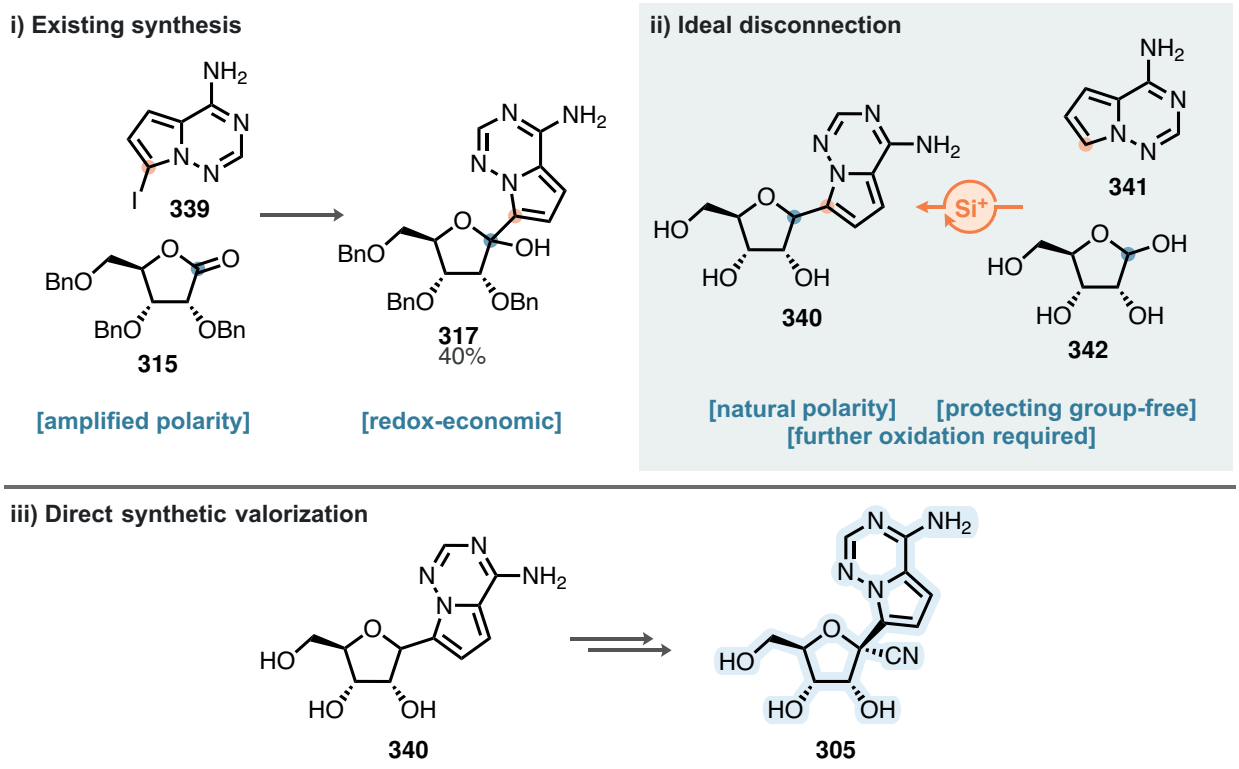

Scheme 4.6: Silylium catalysis-enabled direct *C*-glycosylation with unprotected starting materials and subsequent downstream modifications towards GS-441524 (**305**).

The generality of this method and its potential application will be a significant focus. However, the primary challenge lies in adjusting the oxidation state of the anomeric carbon (Scheme 4.6 iii, *cf.* C2 in **340** and **305**). Possible solutions could include transition metal-catalyzed C−H oxidations and direct oxidative cyanations.

3 Results and Discussion

The work described in this section was conducted in collaboration with Dr. Carla Obradors, Dr. Miles Aukland, and Dr. Markus Leutzsch.

3.1 Development of a Direct Catalytic *C*-Glycosylation

3.1.1 Initial Findings

We began our synthetic studies by reacting aminopyrrolotriazine **341** with D-ribose (**342**), using an excess of BSTFA (10.0 equiv.) at elevated temperatures, in line with the persilylation conditions previously described by Gray (see Scheme 4.5). To make the glycosylation reaction more efficient and less dependent on large quantities of TMSOTf, we opted for a loading of 25 mol%, aiming to maintain catalytic activity while minimizing the chemical excess typically required.

After stirring a mixture of D-ribose and **341** with TMSOTf in BSTFA at room temperature for 15 min, we observed that the initially heterogeneous mixture dissolved, likely due to the silylation of **342** and **341**. After continuing the reaction for 16 h at 50 °C, we achieved full conversion to a single product: the ring-opened polyol silyl ether **343** in 99 % yield as a single diastereomer (Scheme 4.7). The formation of **343** was unexpected when compared to typical outcomes of TMSOTf- and other Lewis acid-catalyzed glycosylation reactions (see Scheme 4.5). Desilylation with TBAF yielded the free polyol **344**. Given the potential ambiguity in determining the relative configuration of acyclic systems due to their conformational

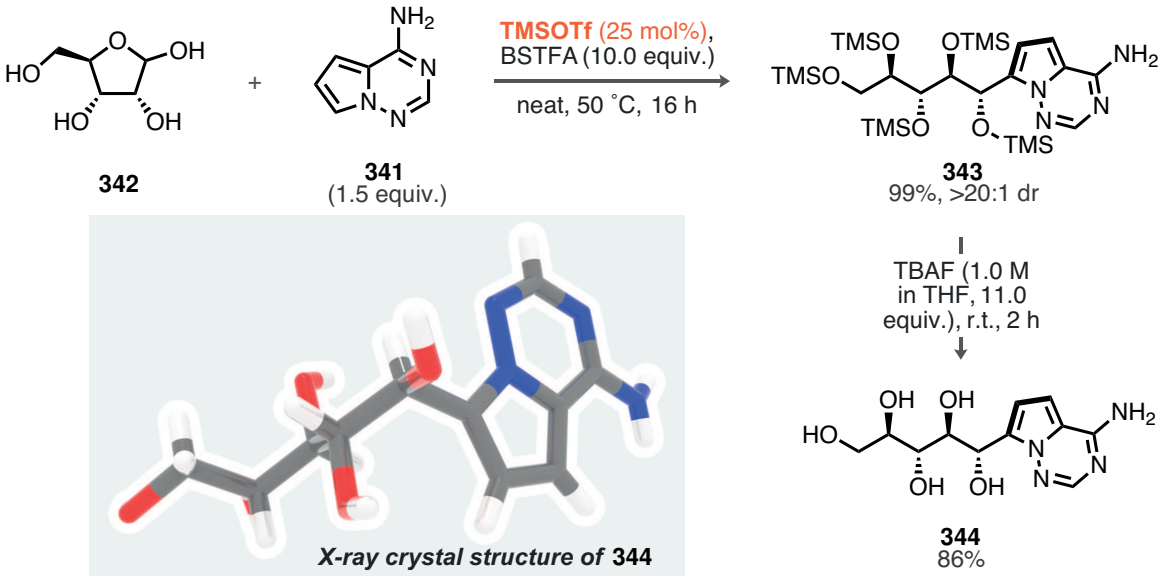

Scheme 4.7: Initial studies revealed high reactivity and diastereoselectivity towards ring-openend product **343**.

flexibility, the linear structure and the relative configuration of the post-anomeric benzylic center were ultimately confirmed through X-ray single crystal structure analysis of **344**.

3.1.2 Diastereoconvergent Ribose Persilylation

Intrigued by the high levels of diastereoselectivity observed in the formation of the ring-opened products **343**, we aimed to explore how exhaustive silylation affects the anomeric configuration of D-ribose **342**. Therefore, the standard reaction mixture without aminopyrrolotriazine **341** was stirred at room temperature until complete dissolution was observed after 15 min. Subsequently, the mixture was transferred to an NMR tube equipped with a coaxial insert filled with DMSO-d_6.

Carbohydrates, including D-ribose, are known for their complex stereochemical behavior, constantly equilibrating between α- and β-pyranose (**342b**) and -furanose (**342a**) forms, as well as the open aldehyde: it was not until 2010 that the X-ray crystal structure of D-ribose was resolved.[327] In our spectroscopic experiments, we observed a significant diastereoconvergence primarily towards the β-persilylribofuranose **345a** (21 %) and -pyranose **345b** (77 %), with only a minor presence of approximately 2 % of the α-persilylribofuranose.

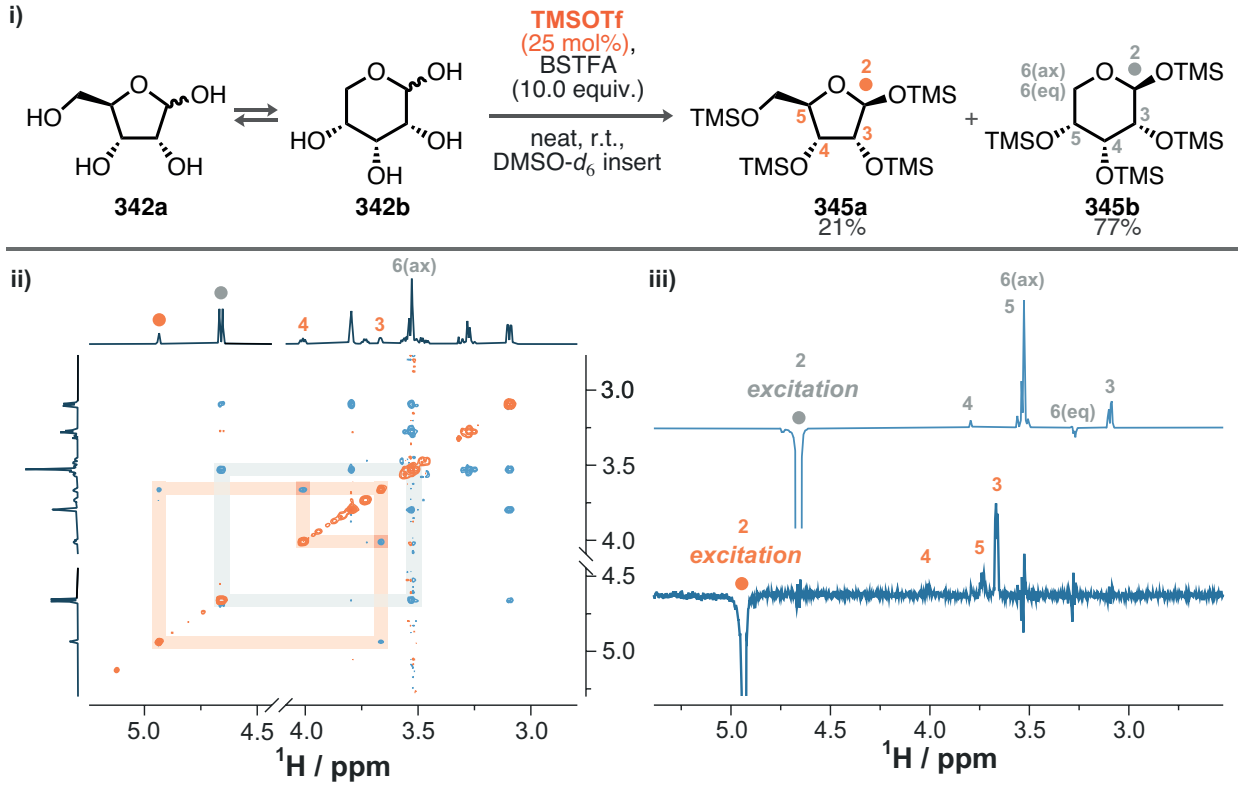

Scheme 4.8: i) Diastereoconvergent persilylation of D-ribose, ii), ^{1}H,^{1}H-NOESY of the reaction mixture, and iii) selective 1D-gradient NOESY with excitation at 4.66 ppm (top) and 4.94 ppm (bottom), respectively.

The detailed anomeric configuration of these isomers was elucidated using ^{1}H,^{1}H-NOESY as well as selective 1D-gradient NOESY techniques (Scheme 4.8 ii and iii). These experiments revealed strong NOE interactions between the proton in the 2-position and the axial proton in the 6-position of the pyranose isomer **345b**. The relative configuration of the furanose **345a** proved more challenging to assign due to the flexibility of the five-membered ring. However, observable NOE contacts between the protons in the 2- and 5-positions, as well as the comparably weak interaction between the 2- and 3-positions, allowed us to confidently assign the β-configuration for **345a**.

Luo and colleagues also investigated similar persilylation conditions for carbohydrates, including D-ribose.[328] They obtained a 50:50 diastereomeric mixture of persilylribofuranose **345a** (α/β) under basic conditions using TMSOAc/NEt_3, and a slight increase in β-selectivity (25:75 α/β) under moderately acidic conditions (*p*-TSA/HMDS).

In our experiments, we hypothesize that the observed diastereodivergence upon silylation primarily results from the equilibrated repulsion; the introduction of sterically demanding TMS groups tends to disfavor the *cis*-configuration of the anomeric center relative to the neighboring 3-position. Given the more acidic conditions of our TMSOTf/BSTFA system compared to Luo's studies, which likely renders the connection between all stereoisomers dynamic, we observed equilibration to the thermodynamically more stable anomer. Notably, these steric effects appear to dominate over the α-selectivity typically observed due to the anomeric effect, where the non-bonding electron pair of the oxygen n(O) donates into the antibonding orbital of the C−O bond σ^*(C−O). This suggests that the steric hindrance induced by silylation can override the electronic preferences typically governing the formation of glycosidic bonds.

Ultimately, the origin of the regioisomeric mixture—comprising 21 % ribofuranose **345a** and 77 % ribopyranose **345b**—in our experiment remains unclear. Notably, the distribution between pyranose and furanose isomers of D-ribose has been reported as 71:29 upon melting at approximately 90 °C.[327] This information suggests that the solid-state distribution of these forms might be directly persilylated under our reaction conditions. We hypothesize that subsequent equilibration likely occurs at the stereochemical level without significant regiochemical changes.

3.1.3 Kinetic Profile of the *C*-Glycosylation Reaction

After identifying the β-configured ribopyranose and -furanose isomers and determining their respective concentrations following persilylation, immediate questions arose about the subsequent steps in the nucleophilic addition reaction. Notably, the nature of the isolated products, **343** and **344**, implied that the addition of **341** might involve ring-opening. However, the

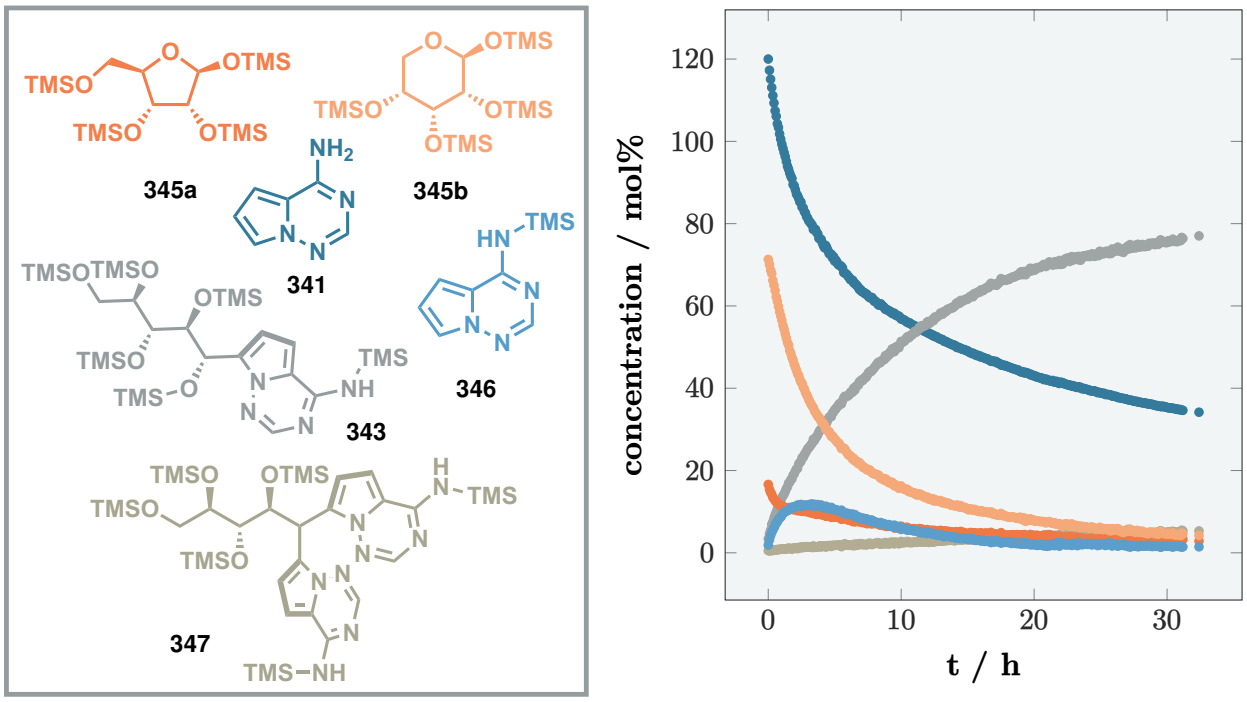

Fig. 4.2: Kinetic profile of the reaction between D-ribose **342** and **341** (1.20 equiv.) in 10.0 equiv. BSTFA at 50 °C as monitored by ^{1}H NMR spectroscopy; the concentrations of all species in the mixture were referenced to **341**.

origin of the observed high diastereoselectivity in this reaction remained elusive. Considering the electron-rich nature of aminopyrrolotriazine **341**, a possibly unselective ring-opening addition might be followed by a completely diastereoselective epimerization of the benzylic stereocenter. On the other hand, the selectivity might be fully controlled by kinetics, providing the single diastereomers based on substrate control.

In order to gain deeper insight, we once again turned to NMR spectroscopy to monitor the *C*-glycosylation reaction dynamics between D-ribose **342** and the aminopyrrolotriazine **341** over time. Building on the methodology employed in our D-ribose persilylation studies, we began by reacting **342** with 25 mol% TMSOTf at room temperature. After stirring the mixture for 15 min, we added **341**. To facilitate the glycosylation reaction, the mixture was stirred for 10 min at room temperature and subsequently heated to 50 °C.

This experimental setup provided information about the reaction mechanism (Fig. 4.2). Notably, we observed the formation of the *N*-silylated aminopyrrolotriazine **346**. At high concentrations of the parent arene **341**, silylation initially led to an enrichment of **346**, which subsequently decreased due to the nucleophilic addition of both species.

As previously noted in the D-ribose persilylation experiments (see Section 3.1.2), a similar mixture of β-ribofuranose **345a** and -ribopyranose **345b** was obtained, with a distribution of 19 % **345a** and 81 % **345b**. Both **345a** and **345b** were involved in the formation of the product **343**, showing a slight kinetic preference for the reaction involving the pyranose isomer

345b. After 5 h, the concentration of **345b** decreased by 64 %, whereas β-furanose **345a** reacted by 47 %. Intriguingly, we also detected the product **347** resulting from the silylium activation of compound **343**, which was formed in quantities of up to 5 % after 32 h. Crucially, no other *C*-glycosylation products or stereoisomers besides **343** were observed, leading to the conclusion that the high diastereoselectivity is established primarily in the C–C bond-forming step, thereby precluding any downstream epimerization. The slow emergence of the successive activation product **347** supports this hypothesis, indicating a comparably slow activation of **343** under the Lewis-acidic conditions.

3.1.4 Proposed Reaction Pathway

Condensing out experimental findings into a single reaction pathway, we propose a diastereoconvergent funneling mechanism, as depicted in Scheme 4.9. We have efficiently ruled out the possibility of background Brønsted acid catalysis influencing our results. This conclusion is supported by the presence of a large excess of BSTFA, which immediately silylates any traces of TfOH that might form due to moisture intrusion. Consequently, kinetic silylation of the initial 71:29 mixture of pyranose **342b** and furanose **342a** yields a similar distribution of regioisomers **345b** and **345a** at approximately 77:21, with an additional 2 % of α-persilylribofuranose.

The β-configuration of the anomeric center in both **345b** and **345a** was confirmed through

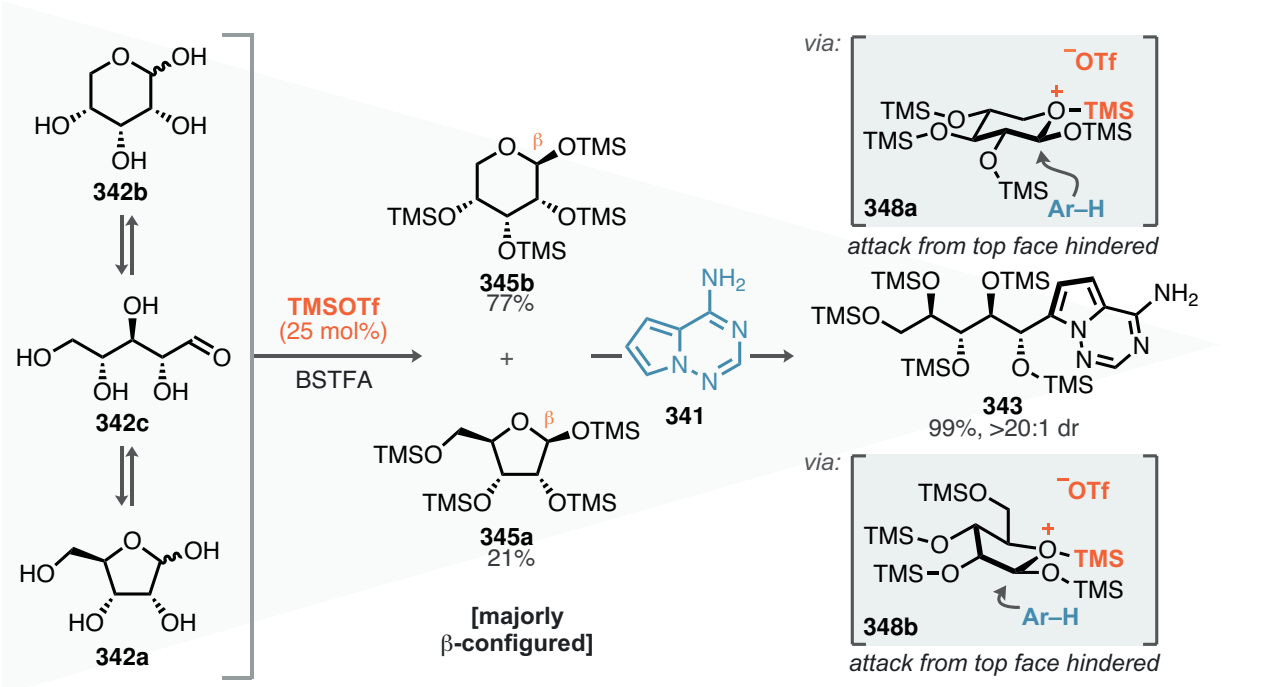

Scheme 4.9: Dynamic kinetic diastereoconvergent mechanism enabled by silylium-catalyzed persilylation and endocyclic oxygen activation.

NOESY experiments. This configuration is most likely influenced by the large steric demands of the TMS groups under the strongly Lewis-acidic conditions that favor equilibration.

We propose that the nucleophilic addition of the aminopyrrolotriazine **341** proceeds *via* a diastereoselective ring-opening mechanism, primarily driven by the activation of the endocyclic oxygen atom. This hypothesis is supported by a control experiment with 2-methylpentanal as a substrate under identical conditions, which resulted in no conversion, thus excluding the possibility of a direct addition of the arene to the aldehyde. This type of ring-opening reactivity aligns with observations made by Zhang, Park, and Chang in their borane-catalyzed ionic reduction of carbohydrates.[329]

Further, the subsequent silylation of a TMS silyl ether by another TMS group is likely kinetically unfavorable due to repulsive steric interactions, making the endocyclic oxygen atom a more likely candidate for reaction. The specific conformation at this position may also facilitate coordination to the Lewis acid due to stereoelectronic effects, ideally orienting the lone pair on the oxygen for this interaction. Additionally, the methylene group adjacent to the activated oxygen atom in **348a** may contribute to the slightly higher reactivity observed in the conversion of β-persilylribopyranose **345b** due to steric effects around this site.

Ultimately, this second level of diastereodivergence—characterized by the stereoselective formation of β-isomers in the silylation—enables the selective formation of polyol **344** in quantitative yield and as a single diastereoisomer.

We recognize, however, that our proposed mechanism is specifically based on the persilylation and kinetic experiments conducted with the combination of D-ribose and aminopyrrolotriazine **341**. Considering the diversity of carbohydrates and their differing chemical behaviors, it is important to acknowledge that crucial findings might vary depending on the specifics of each system.

3.2 Scope and Limitations

Continuing upon the optimal conditions established for the formation of the polyol **344**, we aimed to explore the generality of our synthetic method across different carbohydrate and arene substrates (Scheme 4.10). To mitigate the formation of successive activation products similar to **347** (see Fig. 4.2), we adjusted the molar ratios of arene to carbohydrate for all examples, except for those involving **344**. Specifically, we used a ratio of 1.0 equiv. arene to 1.5 equiv. carbohydrate. Applying this modified protocol, we synthesized the xylose-based polyol **349**, which was isolated in a moderate yield of 53 % as a single diastereoisomer following its reaction with aminopyrrolotriazine **341**.

The high diastereoselectivity was consistently maintained when different arenes were added to D-ribose. This versatility is demonstrated by the selective formation of the *N*-

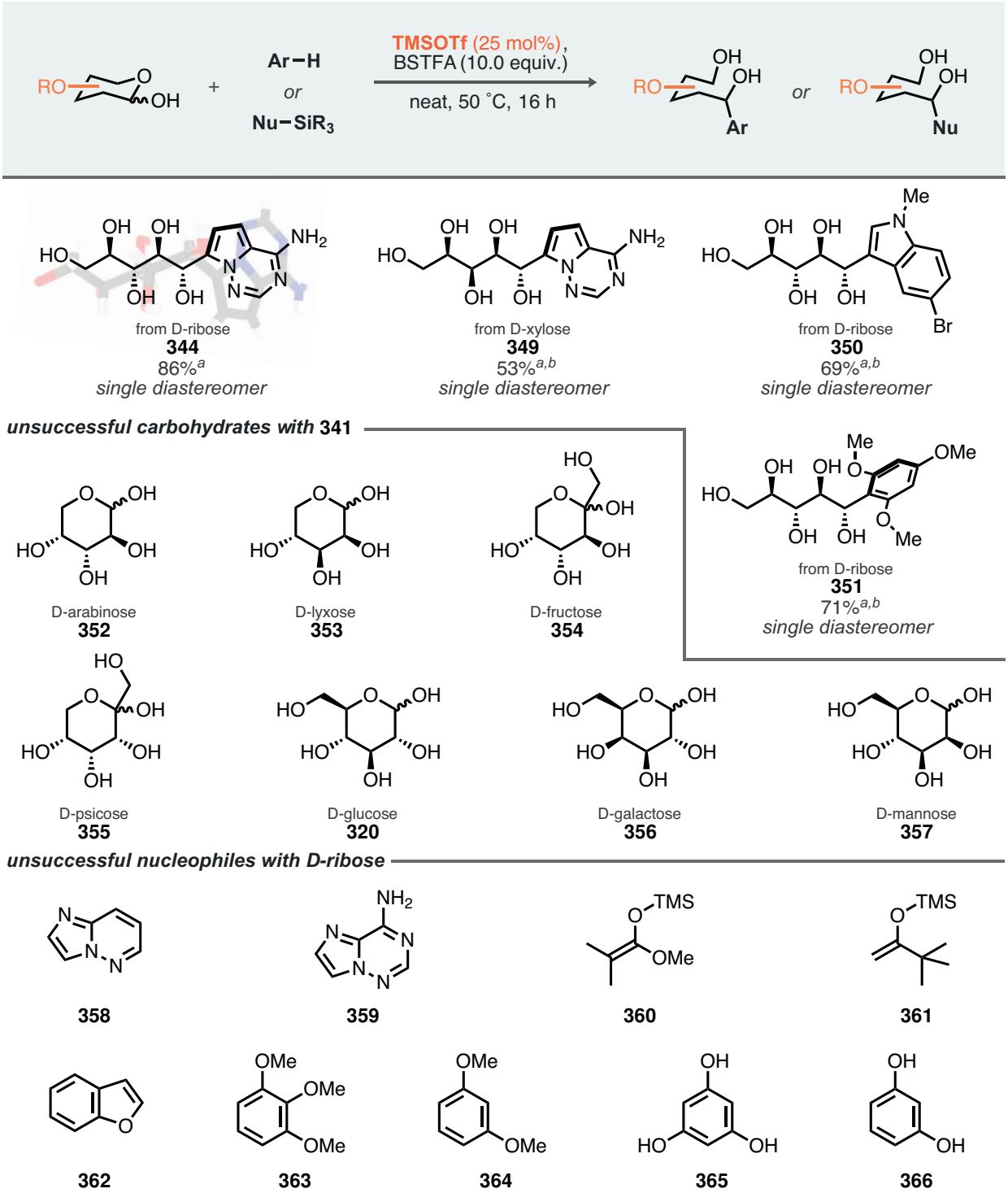

Scheme 4.10: Scope and limitations of the silylium-catalyzed *C*-glycosylation reaction; [a] isolated yield after desilylation with TBAF in THF, 0.20 mmol scale. [b] reaction with 1.0 equiv. arene and 1.5 equiv. carbohydrate.

methyl-5-bromoindole addition product **350**, which was isolated in 69 % yield. Similiarly, the 1,3,5-trimethoxybenzene-based product **351** was obtained in 71 % yield.

In order to expand the scope of transformable arene acceptors, we investigated a range of widely available carbohydrates. Among all of those shown in Scheme 4.10, none reacted towards the desired product, resulting in rather low generality. A plausible hypothesis, informed by our previous mechanistic studies, involves the sterically demanding nature of the hexoses such as D-glucose **320**, D-galactose **356**, and D-mannose **357**, which lack the vicinal methylene functionality found in ribopyranose **345b**. This difference could drastically influence either the activation of the endocyclic oxygen atom or hinder the trajectory of an incoming arene nucleophile. Contrary to this hypothesis, however, is the lack of reactivity observed for the pentoses D-arabinose **352** and D-lyxose **353**. To gain a fundamental understanding of the limiting factors in these reactions, persilylation studies similar to those discussed in Section 3.1.2 would be required.

The low generality observed in the activation of different glycosyl donors was further confirmed through the investigation of several nucleophiles. Less nucleophilic but structurally similar heterocycles **358** and **359** showed no conversion, as did a range of highly nucleophilic oxygen-containing aromatic rings (**362**–**366**). Reactions conducted with silyl ketene acetal **360** and enol silane **361** aligned with the previously discussed results.

In general, we observed low generality in our silylium-catalyzed *C*-glycosylation reaction. Several factors likely contribute to this limitation in reactivity, with the primary reason being the high steric demand of the persilylated carbohydrate fragments. Since the development of this transformation was inspired by the connection between D-ribose **342** and aminopyrrolotriazine **341**, we focused on the total synthesis of GS-441524 **305**.

3.3 Polyol Cyclization Toward *C*-Furanosides

3.3.1 Polyol Cyclization as an Entry to GS-441524

Expanding on the high reactivity and selectivity observed in the ring-opening silylium-catalyzed *C*-glycosylation reaction, which yielded polyol **344**, we explored various synthetic routes towards GS-441524. The initial key challenge identified was achieving selective cyclization to form furanoside **340**, followed by the adjustment of the oxidation state through catalytic C−H oxidation chemistry (Scheme 4.11). This approach aligns our synthetic efforts with previous developments by Gilead,[297–299] allowing us to benefit from existing literature on deoxycyanation reactions. These transformations would complete our proposed synthesis of GS-441524 and the formal total synthesis of remdesivir.

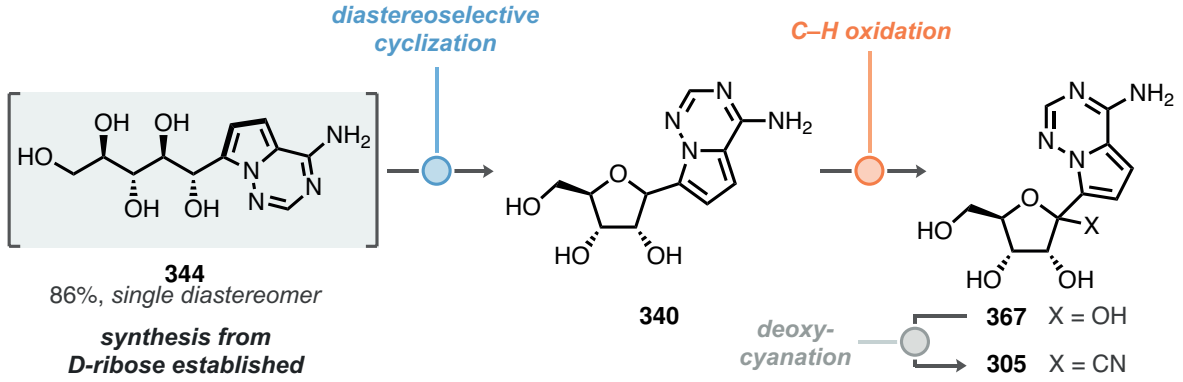

Scheme 4.11: Proposed downstream modifications of polyol **343** toward the total synthesis of GS-441524.

3.3.2 Acid-Mediated Diastereodivergent Cyclization

We identified the need for the polyol **344** to cyclize diastereoselectively into the α- **340a** and β-riboside **340b** isomers, which are essential for successful downstream modifications. Ideally, the polyol would cyclize immediately after the nucleophilic addition of the arene under acidic conditions. The acidic environment serves two primary roles: 1) it facilitates the desilylation of the persilylated polyol **343** and any excess BSTFA, and 2) it promotes mild and regioselective furanoside formation.

Accordingly, when we added a solution of HCl in 1,4-dioxane to the crude mixture containing polyol TMS ether **343** at 0 °C, and subsequently increased the temperature to room temperature, we were pleased to observe selective formation of the α-furanoside **340a** (Scheme 4.12) in good yield (71 %) and with high diastereoselectivity (90:10 dr). The formation of the corresponding pyranose was not observed. The selective formation of **340a** raised questions

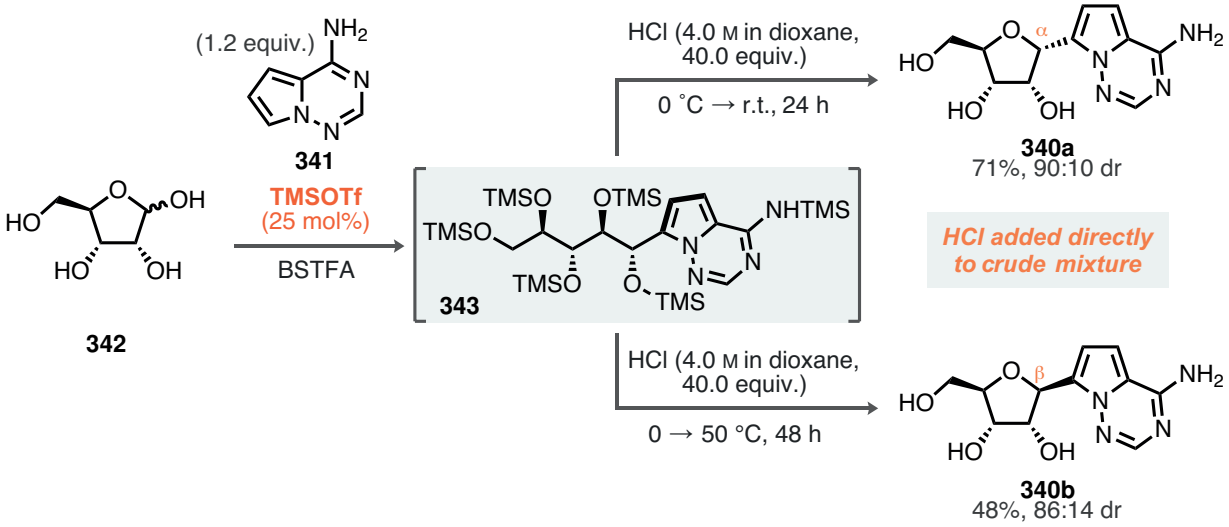

Scheme 4.12: Diastereodivergent either kinetically or thermodynamically controlled cyclization of polyol **343** to α- **340a** or β-furanoside **340b**.

about the potential for diastereodivergence starting from **343**. We speculated that desilylation occurs prior to cyclization, with the hydroxy groups in the 3- or 6-positions of the polyol chain potentially favoring the α-selective transition state kinetically *via* hydrogen bonding to the relatively basic DMAP-like nitrogen atom of the heterocycle. This interaction becomes evident upon structural inspection of **340a**. Similar to the D-ribose persilylation studies (Section 3.1.2), the β-furanoside may be the thermodynamically more stable isomer, likely avoiding strain associated with the *cis,cis*-configuration. This hypothesis also aligns with previous studies on the selective acid-mediated epimerization of *C*-glycosides by Kool.[330]

To investigate this hypothesis, we subjected isolated **340a** to the conditions with HCl, normally used for the cyclization, and observed selective epimerization toward **340b** (86:14 dr) after 18 h at 50 °C, as monitored by crude ^{1}H NMR of reaction mixture aliquots. Continuing the reaction for 10 h at room temperature, after cooling down, still revealed the same diastereomeric ratio, which excluded the possibility of an active equilbrium between **340a** and **340b**. Translating these results to the direct desilylation-cyclization conditions shown in Scheme 4.12, we were able to invert the diastereoselectivity, achieving selective formation of **340b** in moderate yield (48 %) with good diastereoselectivity (86:14 dr). Additionally, the NMR epimerization experiments indicated a decline of the purity profile with prolonged reaction time at 50 °C, which may explain the lower yield observed in the formation of the β-furanoside.

Overall, the temperature-dependence of the diastereoselectivity suggests that the cyclization of crude **343** is diastereodivergent. However, this characteristic more results from a subsequent epimerization rather than being an intrinsic property of the cyclization process itself.

3.4 Development of a Selective C−H Oxidation

We initiated our studies on the selective C−H oxidation of the benzylic position by examining several transition metal-based approaches. Entry into this avenue was driven by the assump-

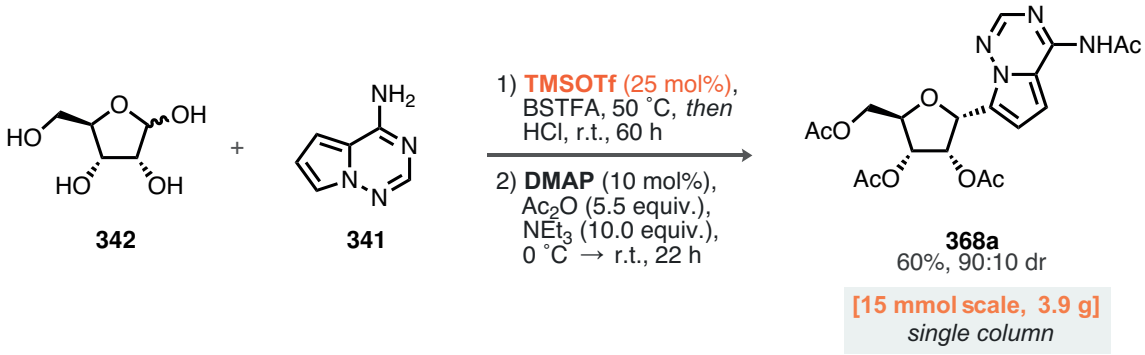

Scheme 4.13: Telescoped synthesis of acetylated furanoside **368a**.

tion that the benzylic C−H bond in **340** has the lowest bond dissociation energy (BDE). This characteristic potentially allows for the *selective* abstraction of a hydrogen atom (in radical-based reactions) or a hydride (in closed-shell oxocarbenium reactions). Simultaneously, we recognized the high functional group density in the furanoside **340**, which could potentially interfere with a metal catalyst or its ligand.

To establish a reliable platform for this investigation, we selected the acetyl-protected α-furanoside **368a**, the synthesis of which was conducted on a larger scale of 15.0 mmol, providing 3.91 g of the product after a single flash column chromatography (Scheme 4.13).

3.4.1 Initial Experiments

Regarding the first oxidation experiments with **368a**, we employed Stahl's Cu^{I}/NFSI radical-relay system to generate NSI radicals *in situ*.[331] Stahl also described the use of a Co^{II}/NHPI combination under aerobic conditions for efficient hydrogen atom abstraction.[332] Unfortunately, these approaches were unsuccessful: the Cu^{I}/NFSI lacked complete reactivity, while the Co^{II}/NHPI system caused decomposition of the furanoside **340**.

Metalloporphyrins play a central role in biological systems, particularly for oxidative transformations.[333,334] Their potential for organic synthesis was recognized by Groves in 1979, who disclosed Fe(TPP)Cl-catalyzed epoxidations and C−H oxidations using iodosylbenzene (PhIO) as the oxidant.[335] Similarly, Hirobe developed ruthenium porphyrin-catalyzed transfer oxygenations between alkenes and pyridine-*N*-oxides for selective epoxidation reactions,[336] which were further advanced by Nagano to include C−H oxidations of alkanes.[337]

However, as with the copper- and cobalt-based reactions, these attempts were unsuccessful in our hands; the Ru(TPP)CO/pryidine-*N*-oxide method yielded only starting materials, and the Fe(TPP)Cl/PhIO resulted in complete decomposition of **340**.

Similarly, manganese-catalyzed reactions have been developed and are known to proceed *via* metal-oxo species, comparable to Fe(TPP)Cl-mediated transformations.[338] We started with a modified manganese porphyrin bearing perfluorinated phenyl substituents **369** and systematically investigated the influence of the catalyst structure (Table 4.1, entry 1).[339] Although only traces of conversion were observed in this experiment, high-resolution mass spectrometry (HRMS) analysis of the crude reaction mixture indicated the presence of a compound with the target mass. Expanding the conditions to include a range of different Mn porphyrins significantly increased reactivity, resulting in 38 % conversion with good selectivity towards the desired product **370** (entry 2, Mn(TPP)Cl). Additionally, we identified a side product, ribonolactone **371**, which likely formed from the fragmentation of lactol **370**.

Further modification of the porphyrin with electron-rich (entry 3) or sterically demanding substituents (entry 4) did not improve the reaction profile. Additionally, the manganese-salen

Table 4.1: Optimization of the Mn-catalyzed C–H oxidation of α-furanoside **368a**; PhIO added in six portions over the course of 5 h; reactions conducted on 125 µmol scale; conversion determined by crude ^{1}H NMR with integration relative to unreacted **368a**; ^{b} 10 h reaction time.

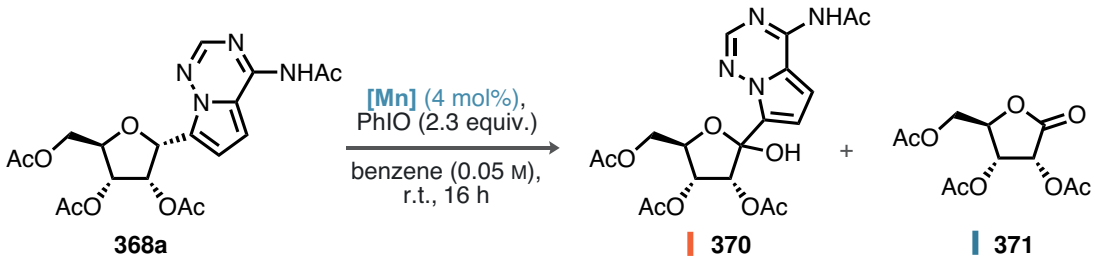

entry	[Mn]	conversion	toward **370** and **371**	
1	**369**	traces	–	–
2^b	**372**	38 %	27 %, 11 %	
3	**373**	51 %	17 %, 34 %	
4	**374**	5 %	5 %, 1 %	
5	**375**	24 %	12 %, 12 %	

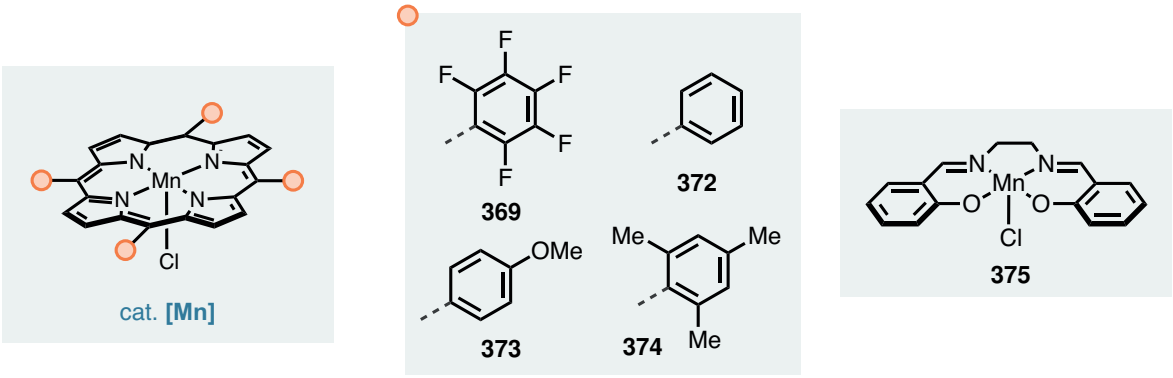

complex **375** was found to be reactive but unselective (entry 5).

Intrigued by the moderately selective formation of **370**, we aimed to enhance the feasibility of this transformation. Using the conditions shown in entry 2 on a larger reaction scale of 0.55 mmol provided 27 % of **370**, with re-isolation of the starting material **368** resulting in an overall yield of 58 %, based on recovered starting material.

We performed preliminary control experiments to investigate the potential for catalyst inhibition by the highly basic DMAP-like nitrogen atom in the pyrrolotriazine portion in **368**. To this end, we synthesized the *para*-toluenesulfonate salt of **368** and subjected it to the reaction conditions outlined in Table 4.1. The conversion was reduced to 20 %, and 2 % of the ribonolactone **371** was formed.

We also considered the possibility of removing the oxidation product **370** from the reaction mixture. Given that lactol **370** is more polar than the starting material **368**, we

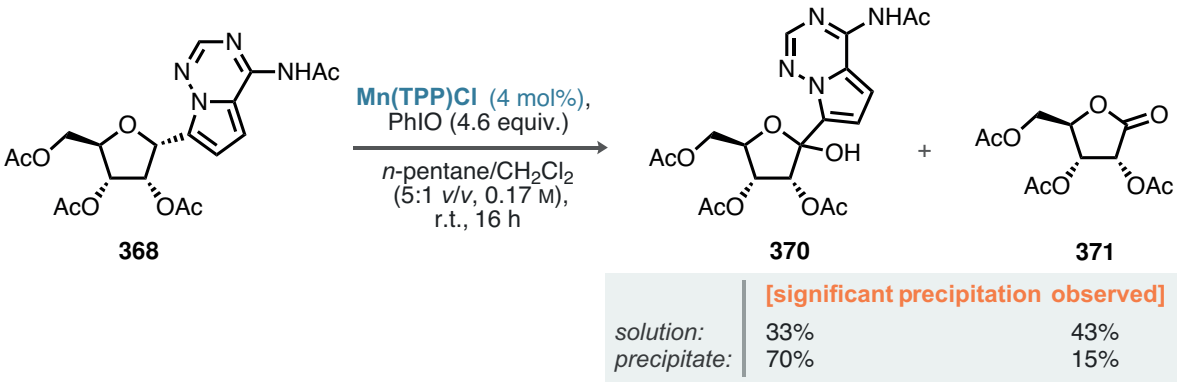

Scheme 4.14: Decreasing the polarity of the reaction medium led to preferred precipitation of the polar lactol **370**; ratios determined by relative integration of **368**, **370**, and **371** in the crude ^{1}H NMR.

speculated that using a less polar reaction medium might facilitate the precipitation of a product-enriched mixture. This could prevent further oxidative cleavage leading to **371**.

Using slightly modified conditions, we observed significant precipitation when conducting the C−H oxidation reaction in a mixture of *n*-pentane/CH_2Cl_2 (5:1 *v*/*v*, Scheme 4.14). Although the relative distribution was determined in the absence of an internal standard, a qualitative trend was still observable. Analysis of the homogeneous solution showed an enrichment of ribonolactone **371** (43 %), along with unreacted starting material and lactol **370** (33 %), whereas the solid mainly consisted of the desired product **370** (70 %).

We subsequently performed this reaction twice on a slightly increased scale (1.25 and 0.50 mmol) to provide sufficient material for subsequent steps. We were able to obtain lactol **370** with increased and, most importantly, synthetically useful yield of 45 % and 37 %, respectively.

3.4.2 Stereodynamic Lactol-Ketone Equilibrium

Upon identifying and isolating reasonable quantities of lactol **370**, we observed that it exists in both diastereomeric forms, **370a** and **370b**, as well as the ketone isomer **376**. We were able to fully characterize all isomers and verify their dynamic connection through a lactol-ketone equilibrium (Scheme 4.15). Analysis in CD_2Cl_2 revealed an isomer distribution with a ratio of 46:34:20 **376**:**370a**:**370b**. The major acyclic ketone species **376** exhibited an exchange signal to the α-diastereoisomer of the lactol **370a** in the ^{1}H,^{1}H-NOESY (Scheme 4.15 bottom left).

Mild acids are known to catalyze acetalization equilibria, which is consistent with our observations. Upon adding 6.0 equiv. of AcOH to the NMR tube followed by the same measurement, we observed a significantly enhanced exhange signal of **376** with both **370a** and **370b**. This overall dynamic equilibration likely renders the low diastereoselectivity inconse-

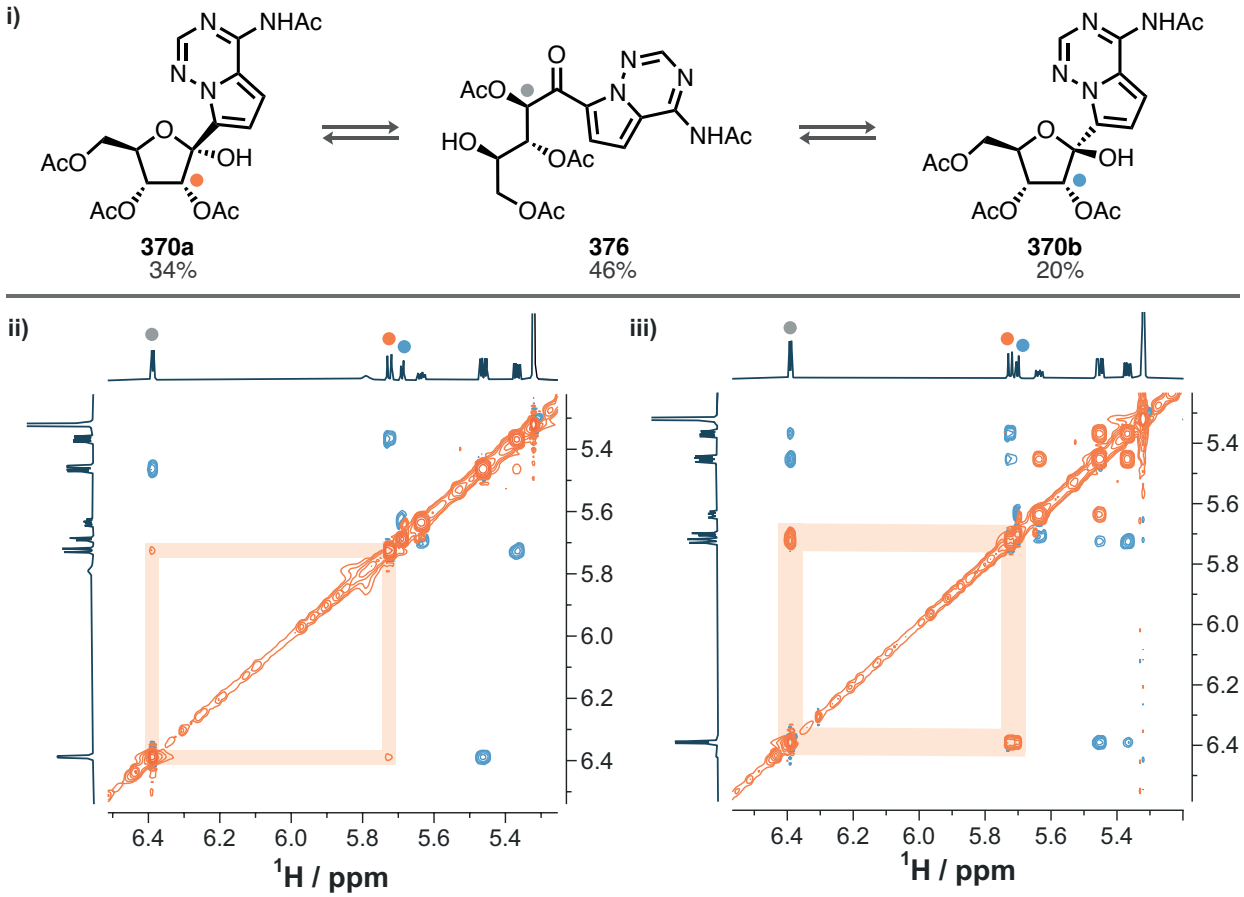

Scheme 4.15: i) Equilibrium between both lactol diastereomers **370a**, **370b**, and ketone **376**; ii) ^{1}H,^{1}H-NOESY of the pure isolated compound in CD_2Cl_2; iii) ^{1}H,^{1}H-NOESY of the pure isolated compound in CD_2Cl_2 with 6.0 equiv. AcOH.

quential for the subsequent deoxycyanation step, provided it is conducted under sufficiently acidic conditions to facilitate dynamic exchange.

3.4.3 Diastereoselectivity of the C−H Oxidation

With the diastereodivergent cyclization conditions providing facile access to both α- and β-furanosides, we investigated the potential diastereoselectivity in the Mn-catalyzed C−H oxidation. Using reaction conditions in benzene with either **368a** (90:10 dr) or **368b** (86:14 dr), we observed exclusive reactivity of the α-diastereomer. This resulted in 18 % conversion toward **370**, along with 6 % **371** (Scheme 4.16 i).

This divergent reactivity is intriguing and could be rationalized by structural analysis of computationally generated structures of **368a** and **368b** (Scheme 4.16 ii). Overlaying all conformers generated at the GFN2-xTB level of theory, within an energy window of 1.0 kcal/mol with respect to the lowest conformer, which is inside the thermal energy window of approximately 0.6 kcal/mol, revealed a striking difference between the two diastereoisomers.

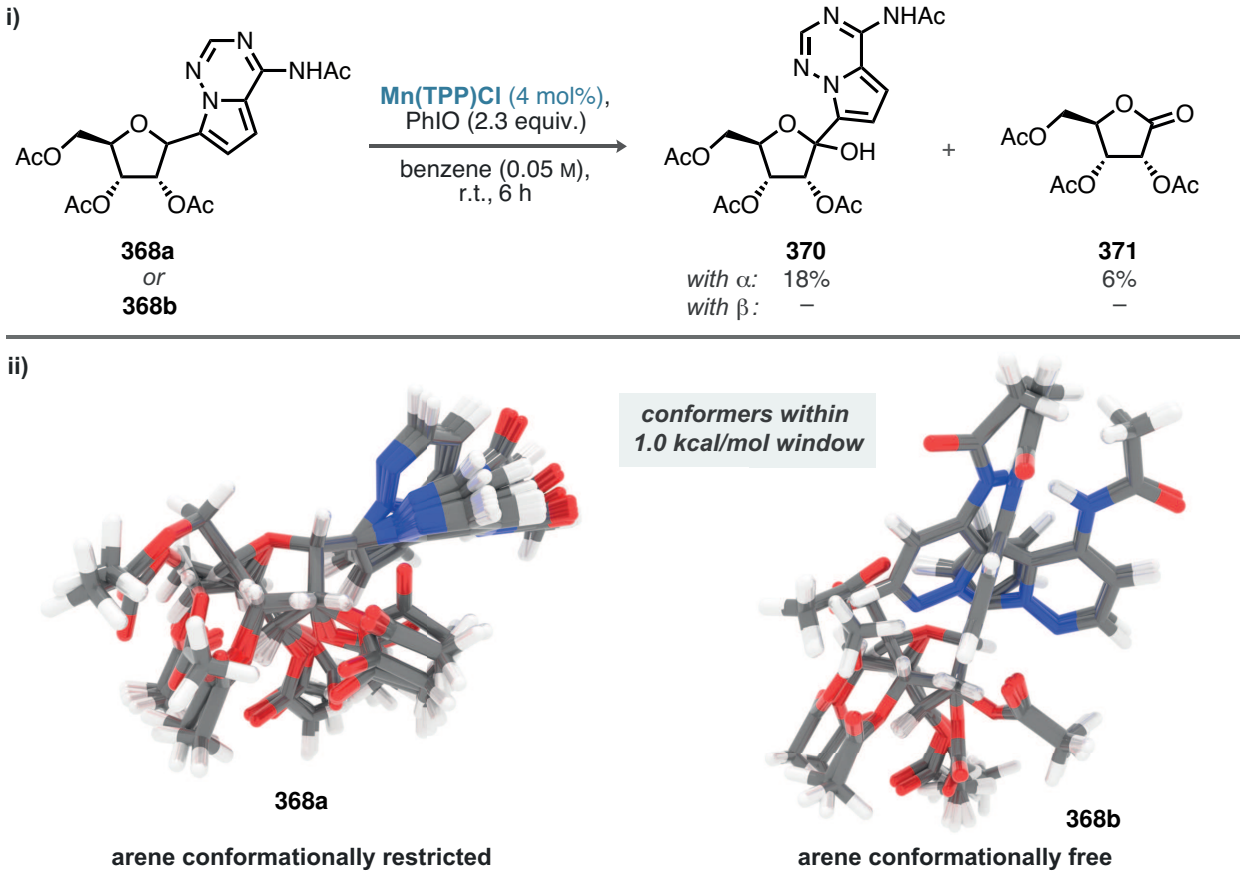

Scheme 4.16: i) Diastereoselectivity in the C–H oxidation of **368a** or **368b**, conversion determined by integration relative to unreacted **368** in the crude ^{1}H NMR; ii) Overlay of the GFN2-xTB conformers within an energy window of 1.0 kcal/mol (13 for **368a**, 8 for **368b**).

In **368a**, the arene fragment is conformationally restricted due the vicinal *cis*-acetyloxy group. Conversely, in the β-furanoside **368b**, the arene has access to a broader conformational space. We believe that this steric and conformational effect is the main determinant of the observed reactivity. The more exposed benzylic hydrogen atom in **368a**, due to the *cis,cis*-configuration of the neighboring acetyloxy functionalities, also likely contributes to the enhanced reactivity.

3.5 Development of a Selective Deoxycyanation

3.5.1 Initial Experiments

The deoxycyanation method has been established for Gilead's tribenzylated lactone in the synthesis of GS-441524 and remdesivir. This allowed us to use these conditions as a starting point for our experiments (see Scheme 4.3).[308] Adjusting the amount of TMSCN to account for potential hydrolysis in these small-scale reactions at cryogenic temperatures, we achieved full conversion of **370** in all cases (Table 4.2). Analysis of the reaction profile revealed a

Table 4.2: Optimization of the deoxycyanation of **370**; reactions conducted on 0.025 mmol scale; conversion determined by crude ^{1}H NMR with integration relative to **377**.

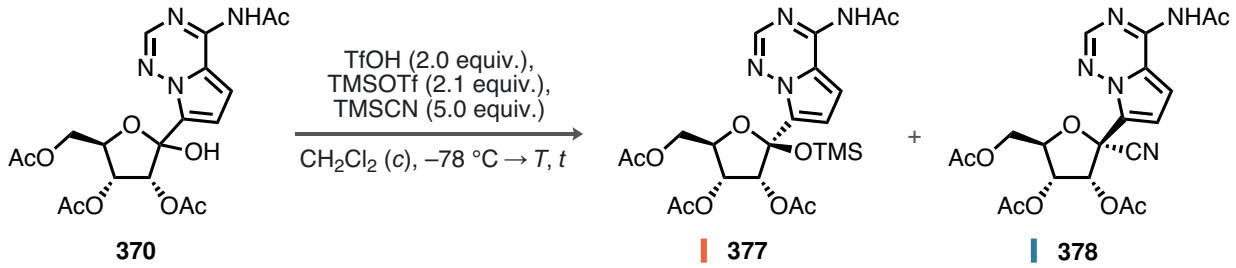

entry	T	t	c	conversion	toward **377** and **378**	dr of **378**
1	r.t.	24 h	0.50 mol/L	>95 %	45 %, 55 %	62:38
2	r.t.	24 h	1.00 mol/L	>95 %	10 %, 90 %	75:25
3	0 °C	48 h	1.00 mol/L	>95 %	50 %, 50 %	81:19

mixture of three species: silylated β-configured lactol **377** and both diastereomers of the deoxycyanated product **378** (62:38 dr, entry 1). Increasing the concentration of the reaction improved the conversion to **378** with moderate diastereoselectivity (90 %, 75:25 dr, entry 2). We hypothesized that lower temperatures over prolonged periods could further enhance diastereoselectivity. Consequently, after 48 h at 0 °C upon warm-up from −78 °C, the cyanated product was formed with improved diastereoselectivity (81:19 dr), albeit in lower yield (50 %, entry 3).

While these experiments demonstrate that strongly acidic conditions successfully convert the isomeric mixture of lactol **370** (see Section 3.4.2) to a cyclic isomer **379**, the conversion to and diastereomeric ratio of **378** were insufficient for further consideration. This difference compared to Gilead's conditions, which provide the cyanated product in near-quantitative yield and excellent diastereoselectivity (96:4 dr), is likely due to the choice of protecting group. The more Lewis-basic acetyl functionalities may reduce the overall acidity of the system through coordination of the silylium Lewis acid.

3.5.2 Substitution with a Stronger Acid

We substituted TfOH with the more acidic $HNTf_2$ (Scheme 1.5) to overcome the inherent limitations, aiming for higher conversions of **377** and selectivities in forming the desired product **378** (Table 4.3). Using a higher stoichiometric amount of $HNTf_2$ successfully realized this endeavor. However, this increase in reactivity led to a decrease in selectivity; the major product formed was the bicyclic gem-dicyanodihydro-1,3-oxazine **380** (entry 1, 58 %). The formation of **380** was likely triggered by the subsequent activation of the desired cyanation product **378** by catalytic amounts of $TMSNTf_2$ or TMSOTf (Scheme 4.17).

Table 4.3: Optimization of the deoxycyanation of **370** with $HNTf_2$; reactions conducted on 0.025 mmol scale; conversion determined by crude ^1H NMR with integration relative to **377**; [a] remaining amount was **377**.

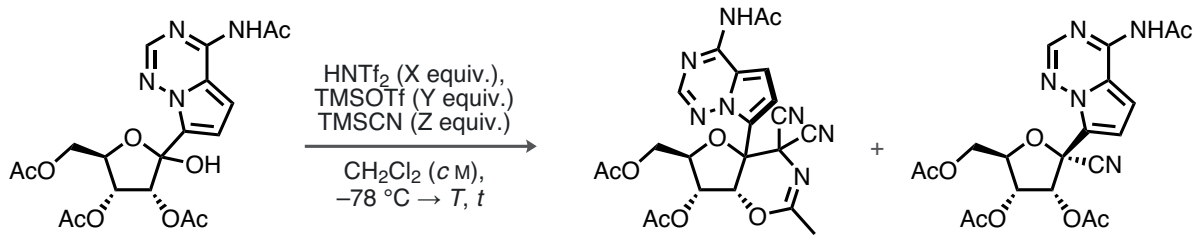

370 **380** **378**

entry	T	t	c	X	Y	Z	conv.	**380**	**378**	dr of **378**
1	0 °C	20 h	1.00	3.5	2.1	5.0	>95 %	58 %	42 %	87:13
2	0 °C	18 h	0.25	3.5	2.1	3.0	>95 %	–	>95 %	82:18
3	0 °C	18 h	0.25	3.5	–	3.0	>95 %	–	>95 %	75:25
4	−20 °C	28 h	0.25	3.5	–	3.0	>95 %	–	>95 %	82:18
5	−40 °C	20 h	0.25	3.5	–	3.0	>95 %	–	>95 %	87:13
6	−60 °C	20 h	0.25	3.5	–	3.0	60 %[a]	–	60 %	88:12
7	−40 °C	20 h	0.25	2.0	–	3.0	>95 %	–	>95 %	80:20

The proposed mechanism involves the consecutive addition of TMSCN to form α-gem-dicyano bis(trimethylsilyl)amine **381**, which then condenses with the neighboring acetyl group to form the bicyclic compound **380**, liberating TMS_2O. The relative stereochemistry of **380** could not be determined using NMR spectroscopy. However, the slightly higher diastereoselectivity of **378** suggests the preferential conversion of the minor diastereomer.

Realizing that reducing the amount of TMSCN in the reaction mixture could prevent overreaction of the desired product, we continued our experiments with 3.0 equiv. of TMSCN. Combined with an adjustment with respect to the concentration enabled a clean conversion to **378** with good diastereoselectivity (entry 2, 82:18 dr).

To simplify the reaction, we questioned the necessity of TMSOTf. Given that super-stoichiometric amounts of $HNTf_2$ were present, immediate protodesilylation of the reasonably basic TMSCN would generate the active Lewis acid $TMSNTf_2$ *in situ*. Consequently, performing the reaction without TMSOTf selectively yielded **378** with slightly reduced diastereoselectivity (entry 3, 75:25 dr). This implied an influence of TMSOTf on the overall diastereoselectivity; prioritizing a more practical reaction setup over this minor difference in selectivity, we proceeded to investigate the effect of temperature (entries 4–6).

Ultimately, we were able to obtain **378** cleanly with over 95 % conversion and good diastereoselectivity (87:13 dr) at −40 °C. However, reducing the amount of $HNTf_2$ at the same temperature decreased diastereoselectivity (entry 7, 80:20 dr).

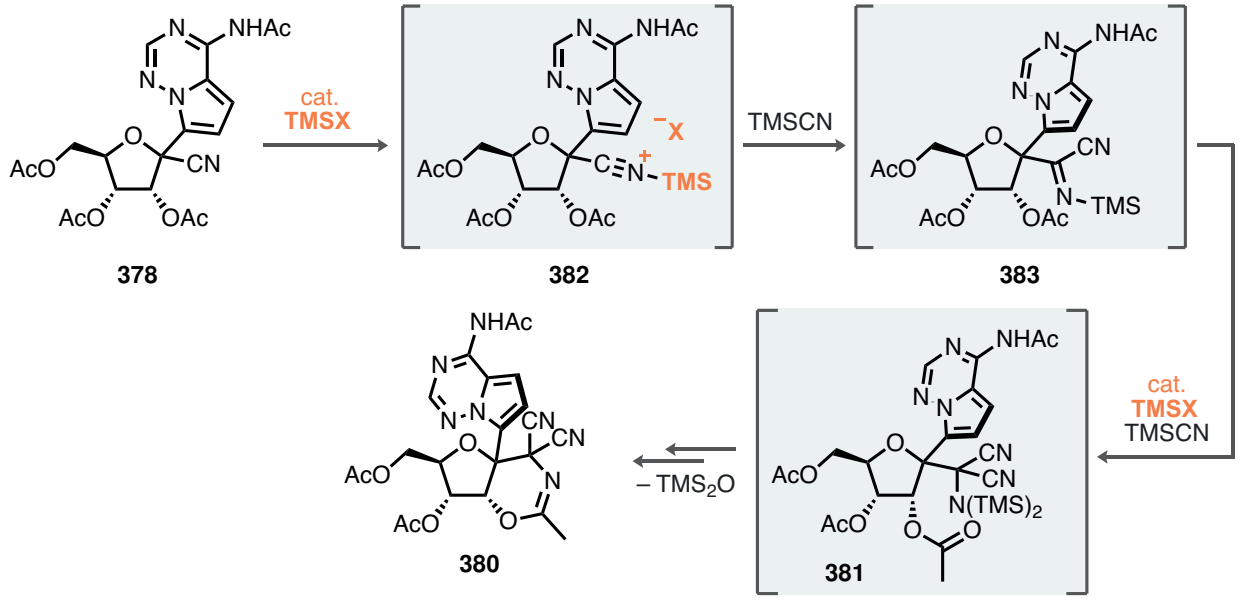

Scheme 4.17: Proposed mechanism of formation of gem-dicyanodihydro-1,3-oxazine **380**.

The conditions in entry 5 were eventually applied on a 0.10 mmol scale (45.0 mg of **370**), yielding **378** in 84 % with very good diastereoselectivity (89:11 dr) after purification by column chromatography.

3.6 Deacetylation of the Cyanated Furanoside

With a sufficient quantity of **378** in hand, we proceeded with the final deprotection to obtain GS-441524 (**305**). Using straightforward deacetylation conditions with catalytic amounts of NaOMe in MeOH, we achieved full conversion after just 1 h at room temperature (Scheme 4.18). Notably, we observed the precipitation of a white amorphous solid during the reaction. After simple filtration, washing with hexanes, and drying, we isolated **305** as a single diastereomer in 81 % yield. The higher concentration of the major diastereomer likely favors diastereoselective aggregation and precipitation, leaving the undesired diastereomer of **305** in solution. With respect to the major diastereomer of **378**, the yield of **305** was 91 %.

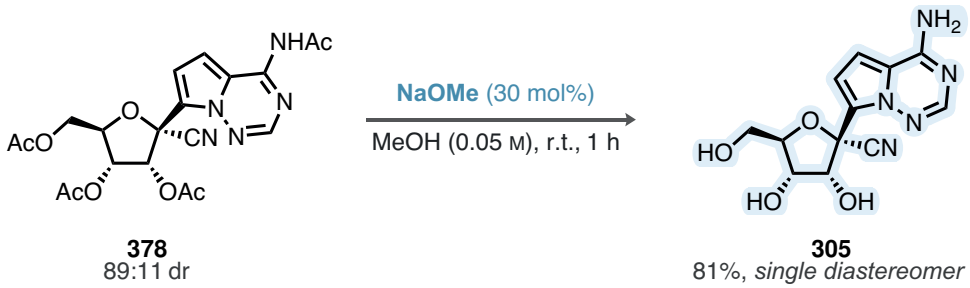

Scheme 4.18: Deacetylation of **378** as the last step in the total synthesis of GS-441524 **305**.

4 Summary and Outlook

This chapter describes the shortest total synthesis of the nucleoside drug GS-441524 to date. The advancements toward this goal were driven by the discovery of a silylium-catalyzed ring-opening *C*-glycosylation reaction between unprotected D-ribose **342** and aminopyrrolotriazine **341**.

Detailed NMR spectroscopic studies highlighted the critical role of persilylation in determining the anomeric configuration of the carbohydrate, leading to *complete diastereoconvergence* toward a single polyol product, **344**, *via* a proposed dynamic kinetic transformation (Scheme 4.19 i). As a proof-of-concept, this method has also been extended to distinct electron-rich arenes as nucleophiles. Further elaboration of **344** enabled us to explore *diastereodivergent* cyclization conditions, resulting in the formation of α-**340a** and β-enriched *C*-riboside **340b**, including straightforward peracetylation, which set the stage for the subsequent total synthesis (Scheme 4.19 ii).

We then realized a manganese-catalyzed C–H oxidation of α-**368a** to produce lactol **370**, with the stereoinconsequential lactol-ketone equilibrium fully characterized by NMR spectroscopy. Subsequent optimization of the deoxycyanation overcame existing reactivity limitations, converging all isomers into a single cyclic furanoside hemiacetal, which selectively

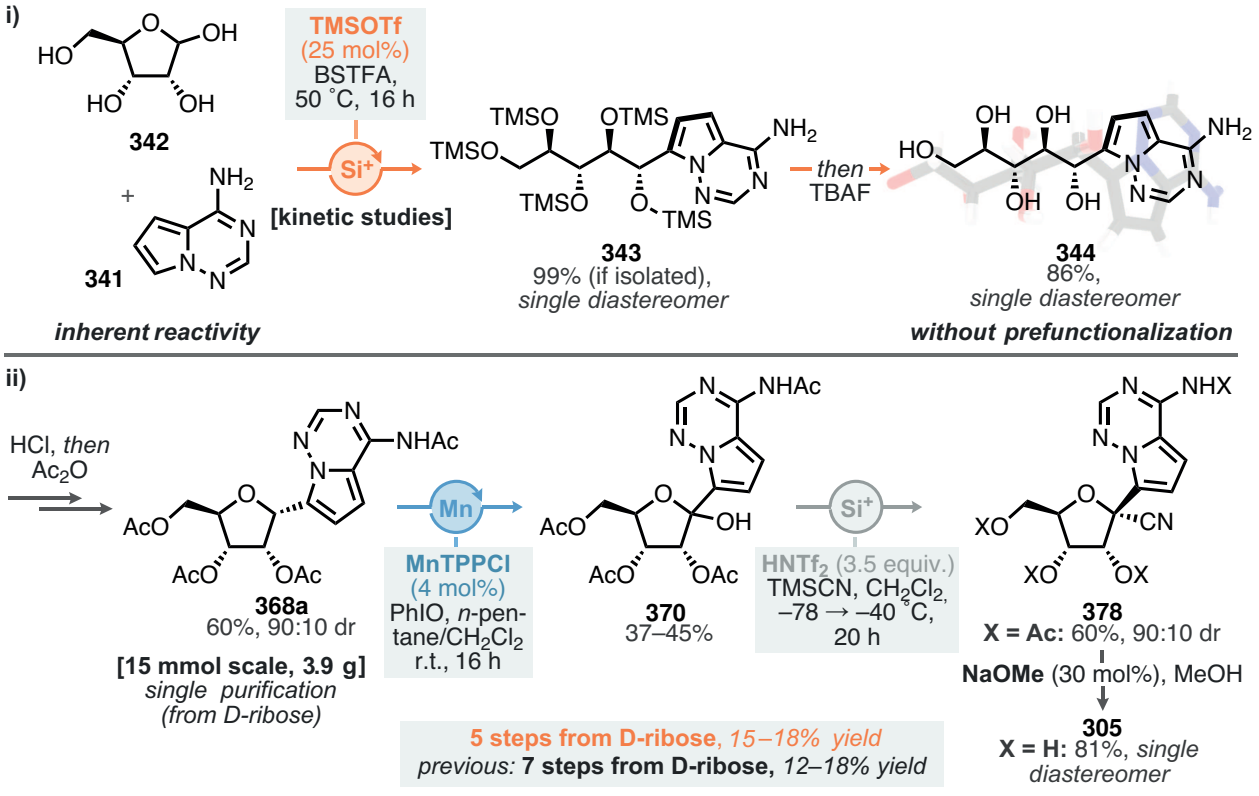

Scheme 4.19: Summary of the findings discussed in this chapter.

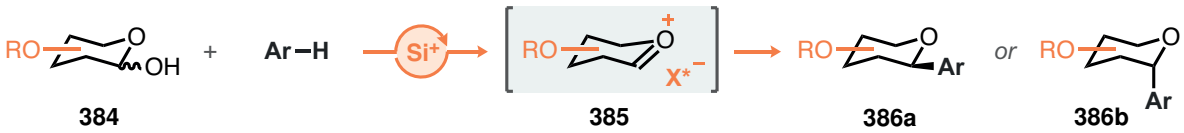

Scheme 4.20: Outlook: general catalytic diastereoselective *C*-glycosylation of carbohydrates with arenes, enabled by silylium ACDC.

reacted to form **378**. Established deprotection conditions directly furnished GS-441524 **305** as a single diastereomer following simple filtration.

In summary, our synthetic approach provided **305** in just five steps, with an overall yield of 15–18 %. Gilead's published second generation synthesis achieves a comparable yield of 12–18 %, but requires extensive prefunctionalization of both starting materials.

Although cost efficiency and process economy are crucial factors in deciding on a synthetic route, the need for prefunctionalization led us to develop a silylium-catalyzed *C*-glycosylation using *unfunctionalized* starting materials on a laboratory scale.

Our synthetic efforts also highlight the remaining limitations in the synthesis of *C*-glycosides, which can serve as a foundation for future developments. Silylium ACDC provides an ideal platform to achieve the goal of a diastereoselective (and potentially catalyst-controlled diastereodivergent) *C*-glycosylation reaction for a wide variety of arenes (Scheme 4.20) with **384**.

Selectivity toward an oxocarbenium-based mechanism, in contrast to our observations, could be achieved by carefully designing a catalyst with a confined active site, capable of facilitating multiple stabilizing interactions within ion pair **385**. This ion pair would also strongly activate the carbohydrate donor, allowing for a broader range of transformable arenes.

Since all naturally occurring carbohydrates are chiral and enantiopure, a significant challenge would be managing the matched and mismatched interactions related to the absolute configuration of the catalyst anion. However, this challenge also presents an opportunity to fine-tune these interactions, enabling diastereodivergence based solely on the structure of the catalyst. This could result in an overall α- or β-selective *C*-glycosylation reaction, producing **386a** and **386b**, respectively.

CHAPTER V

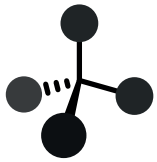

EXPERIMENTAL PART

1 General Experimental Information

Unless stated otherwise, all reagents were purchased from commercial suppliers and used without further purification. All solvents used in the reactions were distilled from appropriate drying agents prior to use.

Reactions were monitored by thin layer chromatography (TLC) on silica gel pre-coated glass (0.2 mm, Macherey-Nagel). Visualization was accomplished by irradiation with UV light at 254 nm, or appropriate stain solutions, such as ceric ammonium molybdate (CAM) oder $KMnO_4$.

Column chromatography was carried out using Merck (60 Å, 230–400 mesh, particle size 40–63 μm) or VWR (40–63 μm) silica gel, using technical-grade solvents.

All reported yields refer to chromatographically and spectroscopically pure compounds, unless stated ohterwise.

^{1}H, ^{13}C, ^{19}F, ^{29}Si, and ^{31}P NMR spectra were recorded on a Bruker AV-600, AV-500, or AV-300 spectrometer in deuterated solvents. ^{1}H chemical shifts (δ) are reported in ppm relative to residual protonated solvent resonance employed as the internal standard ($CDCl_3$ $\delta = 7.26$, C_6D_6 $\delta = 7.16$, CD_2Cl_2 $\delta = 5.32$, DMSO $\delta = 2.50$, CD_3OD $\delta = 3.31$, PhMe $\delta = 2.09$, CD_3CN $\delta = 1.94$).[340] Data are reported as follows: chemical shift, multiplicity (s = singlet, d = doublet, t = triplet, q = quartet, p = pentet, s = sextet, hept = heptet, m = multiplet), coupling constants (Hz), and integration. ^{13}C chemical shifts are reported in ppm with the solvent resonance as the internal standard ($CDCl_3$ $\delta = 77.16$, C_6D_6 $\delta = 128.06$, CD_2Cl_2 $\delta = 54.00$, DMSO $\delta = 39.52$, CD_3OD $\delta = 49.00$, PhMe $\delta = 20.40$, CD_3CN $\delta = 1.32$).[340] ^{19}F, ^{29}Si, and ^{31}P values were used as obtained by the spectrometer and are reported relative to common references.[341]

High resolution mass spectra were determined on a Bruker APEX III FTMS (7 T magnet).

Optical rotations were determined with an Autopol IV polarimeter (Rudolph Research Analytical) at 589 nm at 25 °C. Data are reported as follows: α_λ, concentration c (g/100 mL),

and solvent. Enantiomeric ratios were determined by HPLC analysis employing chiral stationary phase columns specified in the individual experiment, by comparing the samples with the corresponding racemic mixtures.

Dry argon was purchased from Air Liquide with >99.5 % purity.

Nomenclature follows the suggestions proposed by ChemDraw Professional, version 23.1.1. Stereochemical configuration is graphically depicted in the structural formulas throughout this thesis following the IUPAC recommendations.

Language corrections have been conducted using the ChatGPT language model, versions 4 and 4o. Suggested corrections have been reviewed carefully and were integrated if required for enhanced clarity and readability.

2 General Computational Information

Preliminary structures were generated at the GFN2-xTB level[342] using the xtb program version 6.6.0, followed by exploration of the conformational landscape at the same level of theory using Grimme's Conformer–Rotamer Ensemble Sampling Tool (CREST), version 2.12.[343] All resulting conformers were subsequently subjected to density functional theory (DFT) geometry optimizations.

DFT calculations were conducted using ORCA version 5.0.3.[344] For geometry optimizations, the r2SCAN-3c composite density functional electronic-structure method along with the def2-mTZVPP basis set was used (`verytightscf`).[345–347] The Resolution of Identity approximation in the Split-RI-J variant using a corresponding auxiliary basis set was used.[348–350] True ground-state structures were verified by subsequent vibrational frequency calculation at the same level of theory *via* absence of imaginary frequencies.

Refined electronic energies were either obtained using the M06-2X exchange-correlation functional[351] in conjunction with the def2-QZVP[345] basis set or using *ab initio* methods at the DLPNO-CCSD(T)[352–358]/cc-pVQZ[359] level of theory. Gibbs free energies were obtained by combining the thermochemical corrections from the vibrational frequency calculations, acquired by using Duarte's `otherm.py` in a 1 mol/L solution standard state at 298 K.[360]

Second order peturbation analysis was conducted for *N*-silylsulfonamide **277a** as implemented in the NBO 7.0 code, interfaced with ORCA.[361]

NCIPLOT analysis was conducted using promolecular densities as established in the NCIPLOT program, version 4.2.[362,363]

Structures and cube files were visualized using ChimeraX (version 1.7.1)[364] and Blender (version 4.1).

3 Synthetic Procedures for Chapter 2

3.1 Synthesis of Nitroalkanes

All nitroalkanes that were used for the synthesis of silyl nitronates or direct deprotosilylative functionalizations have been synthesized using literature-known procedures or were acquired from commercial vendors.[365–373]

(2-Nitroethyl)benzene (**148**):

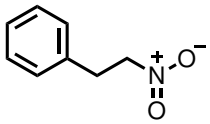

^{1}H NMR (500 MHz, $CDCl_3$): δ 7.36–7.31 (m, 2H), 7.30–7.25 (m, 1H), 7.24–7.18 (m, 2H), 4.62 (t, $J = 7.4$ Hz, 2H), 3.33 (t, $J = 7.4$ Hz, 2H).
^{13}C NMR (126 MHz, CD_2Cl_2): δ 135.8, 129.1, 128.7, 127.6, 76.4, 33.6.

(2-Nitropropyl)benzene (**387**):

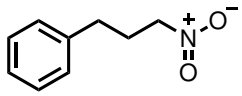

^{1}H NMR (500 MHz, $CDCl_3$): δ 7.38–7.28 (m, 2H), 7.26–7.21 (m, 1H), 7.21–7.16 (m, 2H), 4.37 (t, $J = 6.9$ Hz, 2H), 2.73 (t, $J = 7.5$ Hz, 2H), 2.42–2.23 (m, 2H).
^{13}C NMR (126 MHz, CD_2Cl_2): δ 139.6, 128.9, 128.6, 126.8, 74.8, 32.4, 29.0.

(2-Nitrobutyl)benzene (**388**):

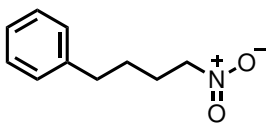

^{1}H NMR (500 MHz, $CDCl_3$): δ 7.34–7.27 (m, 2H), 7.24–7.19 (m, 1H), 7.19–7.15 (m, 2H), 4.39 (t, $J = 7.0$ Hz, 2H), 2.68 (t, $J = 7.6$ Hz, 2H), 2.04 (dt, $J = 15.5$, 7.0 Hz, 2H), 1.81–1.64 (m, 2H).
^{13}C NMR (126 MHz, CD_2Cl_2): δ 141.1, 128.6, 128.5, 126.3, 75.6, 35.1, 28.0, 26.9.

(2-Nitropentyl)benzene (**389**):

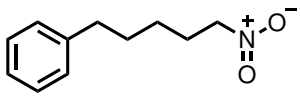

^{1}H NMR (500 MHz, $CDCl_3$): δ 7.32–7.27 (m, 2H), 7.23–7.14 (m, 3H), 4.37 (t, $J = 7.0$ Hz, 2H), 2.63 (t, $J = 7.7$ Hz, 2H), 2.14–1.96 (m, 2H), 1.68 (p, $J = 7.7$ Hz, 2H), 1.48–1.38 (m, 2H).
^{13}C NMR (126 MHz, CD_2Cl_2): δ 142.0, 128.5, 128.5, 126.1, 75.7, 35.7, 30.8, 27.4, 26.0.

1-Methoxy-4-(2-nitroethyl)benzene (**390**):

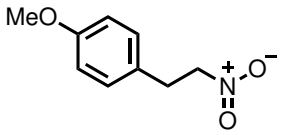

^{1}H NMR (500 MHz, $CDCl_3$): δ 7.16–7.09 (m, 2H), 6.90–6.83 (m, 2H), 4.57 (t, $J = 7.4$ Hz, 2H), 3.79 (s, 3H), 3.26 (t, $J = 7.4$ Hz, 2H).
^{13}C NMR (126 MHz, CD_2Cl_2): δ 159.1, 129.8, 127.7, 114.5, 76.7, 55.4, 32.9.

1-Chloro-4-(2-nitroethyl)benzene (**391**):

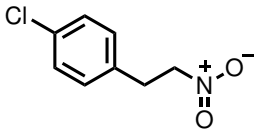

^{1}H NMR (500 MHz, $CDCl_3$): δ 7.34–7.28 (m, 2H), 7.18–7.10 (m, 2H), 4.59 (t, $J = 7.2$ Hz, 2H), 3.29 (t, $J = 7.2$ Hz, 2H).
^{13}C NMR (126 MHz, CD_2Cl_2): δ 134.2, 133.6, 130.1, 129.3, 76.1, 32.9.

1-Chloro-3-(2-nitroethyl)benzene (**392**):

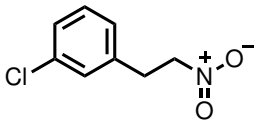

^{1}H NMR (500 MHz, $CDCl_3$): δ 7.32–7.24 (m, 2H), 7.22–7.20 (m, 1H), 7.13–7.01 (m, 1H), 4.61 (t, $J = 7.3$ Hz, 2H), 3.30 (t, $J = 7.3$ Hz, 2H).
^{13}C NMR (126 MHz, CD_2Cl_2): δ 137.7, 134.9, 130.4, 128.9, 127.9, 126.9, 75.9, 33.1.

3.2 Synthesis of Silyl Nitronates (GP1)

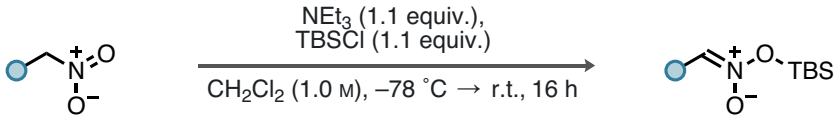

To a solution of the respective nitroalkanes (1.0 equiv.) and TBSCl (1.1 equiv.) in CH_2Cl_2 (1.0 mol/L) in a Schlenk flask under an atmosphere of Ar, NEt_3 (1.1 equiv.) was added dropwise at −78 °C. The reaction was stirred for 10 min at −78 °C, then allowed to warm to room temperature, followed by stirring for additional 16 h. Upon full conversion (as monitored by crude ^{1}H NMR), the solvent was removed under high vacuum, using an additional liquid nitrogen cooling trap. *n*-Pentane was added to the crude reaction mixture, and the liquid phase was purified through syringe filtration under Ar into another flame-dried Schlenk flask. This process was repeated three times, and the solution of the respective silyl nitronate in *n*-pentane was subsequently concentrated under reduced pressure.

All silyl nitronates were used directly and without further purification, unless stated otherwise. Due to their high sensitivity towards light, moisture, and oxygen, complete characterization was omitted, and only ^{1}H and ^{13}C NMR spectra are listed in the following.

***tert*-Butyldimethylsilyl (*E*)-(2-phenylethylidene)azinate (85):**

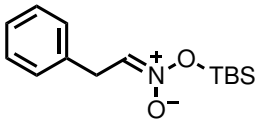

Obtained following GP1 as a yellow-brownish oil.

^{1}H NMR (500 MHz, CD_2Cl_2): δ 7.34–7.29 (m, 2H), 7.25 (td, J = 6.7, 1.7 Hz, 3H), 6.31 (t, J = 6.4 Hz, 1H), 3.61 (d, J = 6.4 Hz, 2H), 0.94 (s, 9H), 0.31 (s, 6H).
^{13}C NMR (126 MHz, CD_2Cl_2): δ 137.2, 129.2, 129.1, 127.4, 116.1, 33.4, 26.1, 18.2, −4.1.

***tert*-Butyldimethylsilyl (*E*)-(3-phenylpropylidene)azinate (92):**

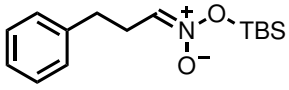

Obtained following GP1 as a clear oil.

^{1}H NMR (500 MHz, CD_2Cl_2): δ 7.30 (ddd, J = 7.5, 6.1, 2.1 Hz, 2H), 7.23–7.18 (m, 3H), 6.09 (t, J = 6.3 Hz, 1H), 2.81 (t, J = 7.6 Hz, 2H), 2.58 (q, J = 7.6, 6.3 Hz, 2H), 0.92 (s,

9H), 0.27 (s, 6H).

^{13}C NMR (126 MHz, CD_2Cl_2): δ 141.2, 129.0, 128.8, 126.8, 116.4, 32.1, 28.7, 26.2, 18.2, −4.1.

***tert*-Butyldimethylsilyl (*E*)-(2-(furan-2-yl)ethylidene)azinate** (**393**):

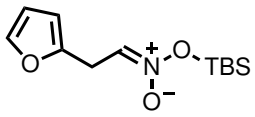

Obtained following GP1 as a clear oil.

^{1}H NMR (500 MHz, CD_2Cl_2): δ 7.35 (dd, J = 2.0, 0.8 Hz, 1H), 6.33 (t, J = 3.2, 2.0 Hz, 1H), 6.30 (t, J = 6.1 Hz, 1H), 6.16–6.13 (m, 1H), 3.64 (dd, J = 6.1, 0.9 Hz, 2H), 0.94 (s, 9H), 0.31 (s, 6H).

^{13}C NMR (126 MHz, CD_2Cl_2): δ 150.3, 142.4, 113.3, 111.0, 107.2, 26.5, 26.1, 18.2, −4.1.

***tert*-Butyldimethylsilyl (*E*)-(2-tolyl)ethylidene)azinate** (**394**):

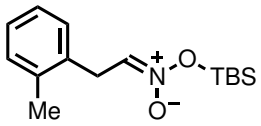

Obtained following GP1 as a bright yellow oil.

^{1}H NMR (500 MHz, CD_2Cl_2): δ 7.20–7.12 (m, 4H), 6.22 (t, J = 6.3 Hz, 1H), 3.60 (d, J = 6.3 Hz, 2H), 2.31 (s, 3H), 0.94 (s, 9H), 0.32 (s, 6H).

^{13}C NMR (126 MHz, CD_2Cl_2): δ 137.2, 135.4, 130.9, 129.8, 127.6, 126.7, 115.9, 31.4, 26.1, 19.8, 18.2, −4.1.

***tert*-Butyldimethylsilyl (*E*)-(5-phenylpentylidene)azinate** (**128**):

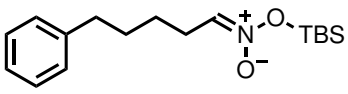

Obtained following GP1 as a clear oil.

^{1}H NMR (500 MHz, CD_2Cl_2): δ 7.28 (td, J = 7.3, 1.5 Hz, 2H), 7.21–7.15 (m, 3H), 6.09 (t, J = 6.3 Hz, 1H), 2.64 (t, J = 7.7 Hz, 2H), 2.30 (q, J = 7.6, 6.3 Hz, 2H), 1.71–1.63 (m, 2H), 1.58–1.49 (m, 2H), 0.95 (s, 9H), 0.30 (s, 6H).

^{13}C NMR (126 MHz, CD_2Cl_2): δ 142.9, 128.9, 128.8, 126.3, 117.3, 36.1, 31.7, 27.0, 26.2, 26.1, 18.2, −4.1.

***tert*-Butyldimethylsilyl (*E*)-hexylideneazinate (129)**:

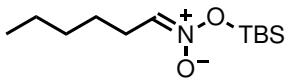

Obtained following GP1 as a clear oil.

^{1}H NMR (500 MHz, CD_2Cl_2): δ 6.08 (t, J = 6.3 Hz, 1H), 2.25 (q, J = 7.7, 6.3 Hz, 2H), 1.48 (dq, J = 11.8, 7.3 Hz, 2H), 1.37–1.26 (m, 4H), 0.94 (s, 9H), 0.92–0.87 (m, 3H), 0.28 (s, 6H).

^{13}C NMR (126 MHz, CD_2Cl_2): δ 117.6, 32.1, 27.1, 26.2, 26.1, 22.9, 18.2, 14.3, −4.1.

***tert*-Butyldimethylsilyl (*E*)-(2-(4-fluorophenyl)ethylidene)azinate (395)**:

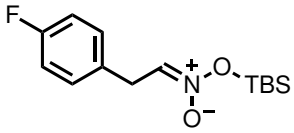

Obtained following GP1 as a yellowish oil.

^{1}H NMR (500 MHz, CD_2Cl_2): δ 7.24–7.20 (m, 2H), 7.04–6.98 (m, 2H), 6.29 (t, J = 6.4 Hz, 1H), 3.58 (d, J = 6.4 Hz, 2H), 0.93 (s, 9H), 0.30 (s, 6H).

^{13}C NMR (126 MHz, CD_2Cl_2): δ 162.4 (d, J = 244.1 Hz), 133.0 (d, J = 3.2 Hz), 130.7 (d, J = 8.0 Hz), 115.9 (d, J = 21.6 Hz), 32.5, 26.1, 18.2, −4.1.

^{19}F NMR (471 MHz, CD_2Cl_2): δ −116.9.

***tert*-Butyldimethylsilyl (*E*)-(2-(4-methoxyphenyl)ethylidene)azinate (396)**:

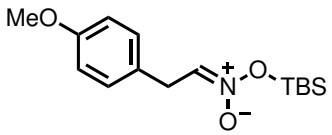

Obtained following GP1 as a yellow oil.

^{1}H NMR (500 MHz, CD_2Cl_2): δ 7.17–7.13 (m, 2H), 6.86–6.81 (m, 2H), 6.27 (t, J = 6.4 Hz, 1H), 3.77 (s, 3H), 3.54 (d, J = 6.4 Hz, 2H), 0.93 (s, 9H), 0.30 (s, 6H). 13.

^{13}C NMR (126 MHz, CD_2Cl_2): δ 159.2, 130.1, 129.1, 116.5, 114.6, 55.8, 32.5, 26.1, 18.2, −4.1.

***tert*-Butyldimethylsilyl (*E*)-(2-(3,5-dimethylphenyl)ethylidene)azinate (397):**

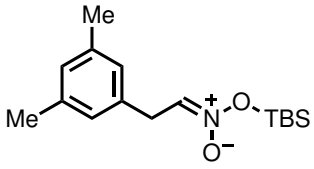

Obtained following GP1 as a bright yellow oil.

^{1}H NMR (500 MHz, CD_2Cl_2): δ 6.89 (s, 1H), 6.84 (s, 2H), 6.27 (t, J = 6.4 Hz, 1H), 3.52 (d, J = 6.4 Hz, 2H), 2.28 (s, 6H), 0.94 (s, 9H), 0.31 (s, 5H).
^{13}C NMR (126 MHz, CD_2Cl_2): δ 138.9, 136.9, 128.9, 126.9, 116.4, 33.2, 26.1, 21.5, 18.2, −4.1.

***tert*-Butyldimethylsilyl (*E*)-(3-(4-chlorophenyl)propylidene)azinate (398):**

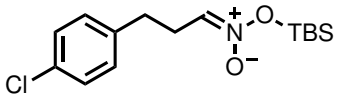

Obtained following GP1 as a clear oil. Due to rapid decomposition at room teperature, only a ^{1}H NMR spectrum is listed.

^{1}H NMR (500 MHz, CD_2Cl_2): δ 7.31–7.22 (m, 2H), 7.21–7.10 (m, 2H), 6.07 (t, J = 6.3 Hz, 1H), 2.79 (t, J = 7.6 Hz, 2H), 2.56 (td, J = 7.6, 6.2 Hz, 2H), 0.92 (s, 9H), 0.27 (s, 6H).

***tert*-Butyldimethylsilyl (*E*)-(3-(4-bromophenyl)propylidene)azinate (399):**

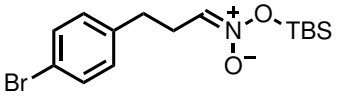

Obtained following GP1 as a clear oil.

^{1}H NMR (500 MHz, CD_2Cl_2): δ 7.42 (d, J = 8.4 Hz, 1H), 7.10 (d, J = 8.4 Hz Hz, 2H), 6.07 (s, 1H), 2.78 (t, J = 7.6 Hz, 3H), 2.56 (td, J = 7.5, 6.2 Hz, 3H), 0.92 (s, 13H), 0.26 (s, 8H).
^{13}C NMR (126 MHz, CD_2Cl_2): δ 140.4, 132.1, 130.7, 120.5, 116.0, 31.5, 28.4, 26.2, 18.2, −4.2.

***tert*-Butyldimethylsilyl (*E*)-(2-(thiophen-2-yl)ethylidene)azinate (400):**

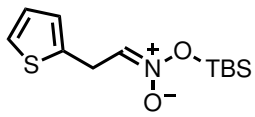

Obtained following GP1 as a dark brown oil.

^{1}H NMR (500 MHz, CD_2Cl_2): δ 7.19 (dd, J = 5.1, 1.2 Hz, 1H), 6.95 (dd, J = 5.1, 3.4 Hz, 1H), 6.91 (dq, J = 3.4, 1.2 Hz, 1H), 6.32 (t, J = 6.3 Hz, 1H), 3.80 (dd, J = 6.3, 1.0 Hz, 2H), 0.94 (s, 9H), 0.31 (s, 6H).
^{13}C NMR (126 MHz, CD_2Cl_2): δ 138.8, 127.5, 126.4, 125.0, 115.3, 27.7, 26.1, 18.2, −4.1.

***tert*-Butyldimethylsilyl (*E*)-(5-(1*H*-indol-1-yl)pentylidene)azinate (401):**

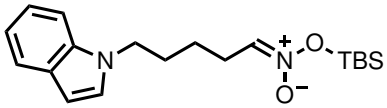

Obtained following GP1 as a clear oil.

^{1}H NMR (500 MHz, CD_2Cl_2): δ 7.59 (dt, J = 7.9, 1.0 Hz, 1H), 7.35 (dd, J = 8.2, 1.0 Hz, 1H), 7.18 (ddd, J = 8.3, 7.0, 1.2 Hz, 1H), 7.12 (d, J = 3.1 Hz, 1H), 7.06 (ddd, J = 8.0, 7.0, 1.0 Hz, 1H), 6.47 (dd, J = 3.1, 0.9 Hz, 1H), 6.06 (t, J = 6.4 Hz, 1H), 4.15 (t, J = 7.0 Hz, 2H), 2.28 (td, J = 7.6, 6.4 Hz, 2H), 1.95–1.82 (m, 2H), 1.50 (tdd, J = 10.2, 8.2, 4.5 Hz, 2H), 0.93 (s, 9H), 0.28 (s, 6H).
^{13}C NMR (126 MHz, CD_2Cl_2): δ 136.6, 129.2, 128.4, 121.9, 121.3, 119.7, 116.8, 109.9, 101.4, 46.5, 30.5, 26.6, 26.2, 23.9, 18.2, −4.1.

***tert*-Butyldimethylsilyl (*E*)-(4-cyanobutylidene)azinate (402):**

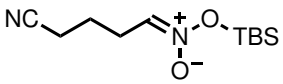

Obtained following GP1 as a clear oil. Due to rapid decomposition at room teperature, only a ^{1}H NMR spectrum is listed.

^{1}H NMR (500 MHz, CD_2Cl_2): δ 6.15 (t, J = 6.4 Hz, 1H), 2.45–2.33 (m, 4H), 1.87 (p, J = 7.2 Hz, 2H), 0.94 (s, 9H), 0.29 (s, 6H).

***tert*-Butyldimethylsilyl (*E*)-(4-((*tert*-butyldimethylsilyl)oxy)butylidene)azinate (403)**:

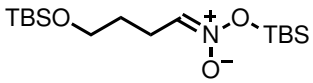

Obtained following GP1 as a clear oil.

^{1}H NMR (500 MHz, CD_2Cl_2): δ 6.14 (t, J = 6.3 Hz, 1H), 3.64 (t, J = 6.1 Hz, 2H), 2.32 (td, J = 7.4, 6.3 Hz, 2H), 1.69 (tt, J = 7.4, 6.1 Hz, 2H), 0.93 (s, 9H), 0.89 (s, 9H), 0.29 (s, 6H), 0.05 (s, 6H).
^{13}C NMR (126 MHz, CD_2Cl_2): δ 117.3, 63.1, 29.4, 26.3, 26.2, 24.2, 18.7, 18.2, −4.1, −5.1.

Methyl (*E*)-4-(((*tert*-butyldimethylsilyl)oxy)oxidoazaneylidene)butanoate (404):

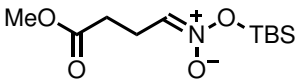

Obtained following GP1 as a clear oil.

^{1}H NMR (500 MHz, CD_2Cl_2): δ 3.66 (s, 3H), 2.58–2.47 (m, 4H), 0.93 (s, 9H), 0.28 (s, 6H).
^{13}C NMR (126 MHz, CD_2Cl_2): δ 173.0, 115.6, 52.0, 30.0, 26.0, 22.4, 18.0, −4.4.

***tert*-butyldimethylsilyl (*E*)-(6-(dibenzylamino)-6-oxohexylidene)azinate (405)**:

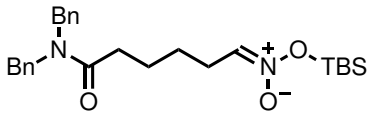

Obtained following GP1 as a clear oil. Due to rapid decomposition at room teperature, only a ^{1}H NMR spectrum is listed.

^{1}H NMR (500 MHz, CD_2Cl_2): δ 7.33–7.16 (m, 6H), 7.16–7.01 (m, 4H), 6.02 (t, J = 6.3 Hz, 1H), 4.50 (s, 2H), 4.39 (s, 2H), 2.39–2.32 (m, 2H), 2.19 (td, J = 7.5, 6.3 Hz, 2H), 1.69–1.60 (m, 2H), 1.47–1.40 (m, 2H), 0.86 (s, 9H), 0.20 (s, 6H).

***tert*-Butyldimethylsilyl (*E*)-(5-bromopentylidene)azinate (406)**:

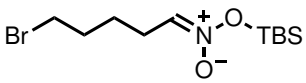

Obtained following GP1 as a clear oil. Due to rapid decomposition at room teperature, only

a ^{1}H NMR spectrum is listed.

^{1}H NMR (500 MHz, CD_2Cl_2): δ 6.10 (t, J = 6.4 Hz, 1H), 3.44 (t, J = 6.7 Hz, 2H), 2.29 (td, J = 7.6, 6.4 Hz, 2H), 2.00–1.82 (m, 2H), 1.69–1.59 (m, 2H), 0.94 (s, 9H), 0.29 (s, 6H).

***tert*-Butyldimethylsilyl (*E*)-(5-iodopentylidene)azinate** (**407**):

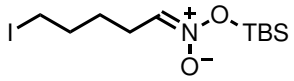

Obtained following GP1 as a clear oil.

^{1}H NMR (500 MHz, CD_2Cl_2): δ 6.10 (t, J = 6.4 Hz, 1H), 3.22 (t, J = 6.9 Hz, 2H), 2.37–2.22 (m, 2H), 1.91–1.81 (m, 2H), 1.68–1.57 (m, 2H), 0.94 (s, 9H), 0.29 (s, 6H).
^{13}C NMR (126 MHz, CD_2Cl_2): δ 116.7, 33.6, 27.3, 26.2, 26.0, 18.2, 6.8, −4.1.

***tert*-Butyldimethylsilyl (*E*)-(2-methylpropylidene)azinate** (**408**):

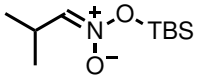

Obtained following GP1 as a clear oil.

^{1}H NMR (500 MHz, CD_2Cl_2): δ 5.95 (d, J = 7.3 Hz, 1H), 2.80–2.66 (m, J = 7.0 Hz, 1H), 1.08 (s, 3H), 1.07 (s, 3H), 0.93 (s, 9H), 0.28 (s, 6H).
^{13}C NMR (126 MHz, CD_2Cl_2): δ 122.8, 27.2, 26.2, 19.5, 18.2, −4.2.

***tert*-Butyldimethylsilyl (*E*)-(4-methoxybutylidene)azinat** (**409**):

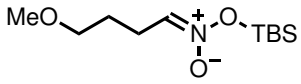

Obtained following GP1 as a clear oil. Due to rapid decomposition at room teperature, only a ^{1}H NMR spectrum is listed.

^{1}H NMR (500 MHz, CD_2Cl_2): δ 6.13 (t, J = 6.4 Hz, 1H), 3.37 (t, J = 6.3 Hz, 2H), 3.30 (s, 3H), 2.31 (td, J = 7.5, 6.4 Hz, 2H), 1.73 (tt, J = 7.5, 6.3 Hz, 2H), 0.94 (s, 9H), 0.28 (s, 6H).

***tert*-Butyldimethylsilyl (*E*)-pent-4-en-1-ylideneazinate** (**410**):

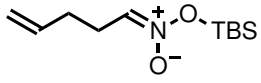

Obtained following GP1 as a clear oil.

^{1}H NMR (500 MHz, CD_2Cl_2): δ 6.09 (t, J = 6.2 Hz, 1H), 5.82 (ddt, J = 17.1, 10.2, 6.5 Hz, 1H), 5.07 (dq, J = 17.1, 1.6 Hz, 1H), 5.02 (dq, J = 10.2, 1.5 Hz, 1H), 2.41–2.33 (m, 2H), 2.25 (tdd, J = 8.3, 6.5, 1.2 Hz, 2H), 0.93 (s, 9H), 0.28 (s, 6H).
^{13}C NMR (126 MHz, CD_2Cl_2): δ 137.4, 116.6, 115.8, 30.2, 26.2, 26.0, 18.1, −4.3.

***tert*-Butyldimethylsilyl (*E*)-hex-5-yn-1-ylideneazinate (411)**:

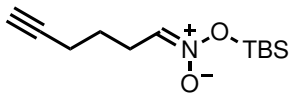

Obtained following GP1 as a clear oil.

^{1}H NMR (500 MHz, CD_2Cl_2): δ 6.12 (t, J = 6.4 Hz, 1H), 2.36 (m, 2H), 2.24 (td, J = 7.1, 2.7 Hz, 2H), 2.02 (t, J = 2.7 Hz, 1H), 1.71 (p, J = 7.3 Hz, 2H), 0.94 (s, 9H), 0.29 (s, 6H).
^{13}C NMR (126 MHz, CD_2Cl_2): δ 116.3, 84.0, 69.4, 26.2, 26.2, 25.3, 18.7, 18.2, −4.1.

***tert*-Butyldimethylsilyl (*E*)-(7-oxooctylidene)azinate (412)**:

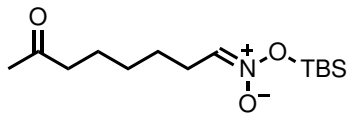

Obtained following GP1 as a clear oil.

^{1}H NMR (500 MHz, CD_2Cl_2): δ 6.08 (t, J = 6.4 Hz, 1H), 2.41 (t, J = 6.4 Hz, 2H), 2.25 (td, J = 7.6, 6.4 Hz, 2H), 2.09 (s, 3H), 1.61–1.41 (m, 4H), 1.37–1.28 (m, 2H), 0.93 (s, 9H), 0.28 (s, 6H).
^{13}C NMR (126 MHz, CD_2Cl_2): δ 209.0, 117.3, 43.9, 30.2, 29.4, 26.9, 26.2, 26.2, 24.0, 18.2, −4.1.

3.3 Synthesis of Silyl Ketene Acetals

(*E*)-*tert*-Butyl((1-methoxyprop-1-en-1-yl)oxy)dimethylsilane (124a):

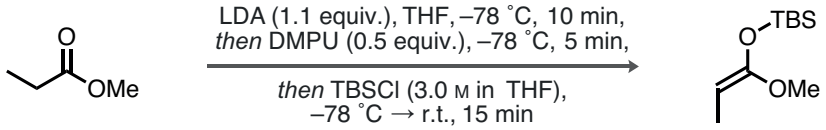

215

124a
E/*Z* = 92:8

Following a literature procedure by Denmark,[171,374] *n*-BuLi (2.5 mol/L in hexanes, 1.1 equiv., 55.0 mmol, 22.0 mL) was added dropwise to a solution of diisopropylamine (1.1 equiv., 55.0 mmol, 7.7 mL) in THF (55 mL) at 0 °C. Upon complete addition, the reaction was stirred for 15 min at 0 °C. Subsequently, methyl propionate **215** (1.0 equiv., 50.0 mmol, 4.8 mL) was added dropwise at −78 °C (acetone/dry ice bath), and the reaction was stirred for 10 min at −78 °C upon complete addition. DMPU (0.5 equiv., 25.0 mmol, 3.0 mL) was added at 78 °C, followed by TBSCl after 5 min (3.0 mol/L in THF, 1.1 equiv., 18.3 mL). The reaction was allowed to warm to room temperature, stirred for 15 min, and terminated by the careful addition of cold water. The reaction was diluted with *n*-pentane, the phases were separated, and the organic layer was washed with water (2x) and a sat. aq. $CuSO_4$ solution (3x). The organic layer was dried over Na_2SO_4, concentrated under reduced pressure, and directly purified *via* distillation using a Vigreux column (bp = 65 °C at 15 mbar). The title compound **124a** was obtained as a clear oil in 53 % yield (5.38 g, 26.6 mmol) as a mixture of diastereomers (E/Z = 92:8).

^{1}H NMR (500 MHz, CD_2Cl_2): δ 3.65 (q, J = 6.6 Hz, 1H), 3.52 (s, 3H), 1.47 (d, J = 6.6 Hz, 3H), 0.94 (s, 9H), 0.18 (s, 6H).
^{13}C NMR (126 MHz, CD_2Cl_2): δ 154.6, 78.7, 55.1, 25.8, 18.4, 9.6, −4.9

(*Z*)-*tert*-Butyl((1-methoxyprop-1-en-1-yl)oxy)dimethylsilane (124b):

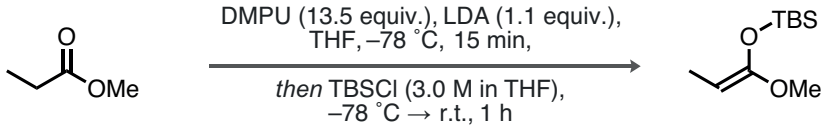

215 **124b** *E*/*Z* = 7:93

Following a literature procedure by Ireland,[214,216] *n*-BuLi (2.5 mol/L in hexanes, 1.1 equiv., 22.0 mmol, 8.8 mL) was added dropwise to a solution of diisopropylamine (1.1 equiv., 22.0 mmol, 3.1 mL) in THF (10 mL) at 0 °C. DMPU (13.5 equiv., 270.6 mmol, 32.7 mL) was added at −78 °C (acetone/dry ice bath), the reaction was stirred for 10 min at −78 °C, and a solution of methyl propionate **215** (1.0 mol/L in THF, 1.0 equiv., 20.0 mmol, 20.0 mL) was added dropwise, followed by stirring for additional 15 min. A solution of TBSCl (3.0 mol/L in THF, 1.1 equiv., 22.0 mmol, 7.3 mL) was added and the reaction was stirred for 15 min at −78 °C, after it was allowed to warm to room temperature, followed by stirring for 1 h. The reaction was terminated by the careful addition of cold water, diluted with *n*-pentane, and the phases were separated. The organic layer was washed with water (2x) and a sat. aq. $CuSO_4$ solution (2x). The organic layer was dried over Na_2SO_4, concentrated under reduced pressure, and directly purified *via* distillation (3x) using a Vigreux column (bp = 58 °C at 12 mbar). The title compound **124b** was obtained as a clear oil in 14 % yield (583 mg,

2.9 mmol) as a mixture of diastereomers (E/Z = 7:93).

^{1}H NMR (500 MHz, CD_2Cl_2): δ 3.47 (q, J = 6.4 Hz, 1H), 3.46 (s, 3H), 1.50 (d, J = 6.4 Hz, 3H), 0.94 (s, 9H), 0.14 (s, 6H).

^{13}C NMR (126 MHz, CD_2Cl_2): δ 157.4, 69.8, 54.8, 25.9, 18.3, 9.8, −4.2.

(*E*)-*tert*-Butyl((1-methoxyprop-1-en-1-yl)oxy)dimethylsilane (100):

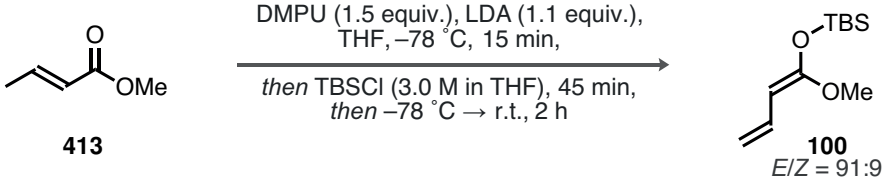

Following a slightly modified literature procedure by Ireland,[216] *n*-BuLi (2.5 mol/L in hexanes, 1.2 equiv., 36.0 mmol, 14.4 mL) was added dropwise to a solution of diisopropylamine (1.25 equiv., 28.0 mmol, 5.3 mL) in THF (45 mL) at 0 °C. DMPU (1.5 equiv., 37.5 mmol, 5.4 mL) was added at −78 °C (acetone/dry ice bath), stirred for 10 min, followed by the dropwise addition of methyl crotonate **413** (1.0 equiv., 30.0 mmol, 3.2 mL) and stirred for 15 min. A solution of TBSCl (3.0 mol/L in THF, 1.25 equiv., 37.5 mmol, 12.5 mL) was added dropwise and the reaction was stirred for 45 min at −78 °C, until it was allowed to warm to room temperature. The reaction was terminated after 1 h by careful addition of cold water, diluted with *n*-pentane, and the phases were separated. The organic layer was washed with water (2x) and a sat. aq. $CuSO_4$ solution (2x). The organic layer was dried over Na_2SO_4, concentrated under reduced pressure, and directly purified *via* distillation using a Vigreux column (bp = 31 °C at 0.023 mbar). The title compound **100** was obtained as a clear oil in 81 % yield (6.94 g, 32.4 mmol) as a mixture of diastereomers (E/Z = 91:9).

^{1}H NMR (500 MHz, CD_2Cl_2): δ 6.50 (dt, J = 17.2, 10.4 Hz, 1H), 4.81 (ddd, J = 17.2, 2.2, 0.6 Hz, 1H), 4.56 (ddd, J = 10.4, 2.2, 0.6 Hz, 1H), 4.48 (d, J = 10.4 Hz, 1H), 3.56 (s, 3H), 0.95 (s, 8H), 0.18 (s, 5H).

^{13}C NMR (126 MHz, CD_2Cl_2): δ 159.2, 132.9, 106.7, 80.7, 55.2, 25.8, 18.4, −4.2.

3.4 Catalytic Asymmetric Polarity Inversion of Silyl Nitronates (GP2)

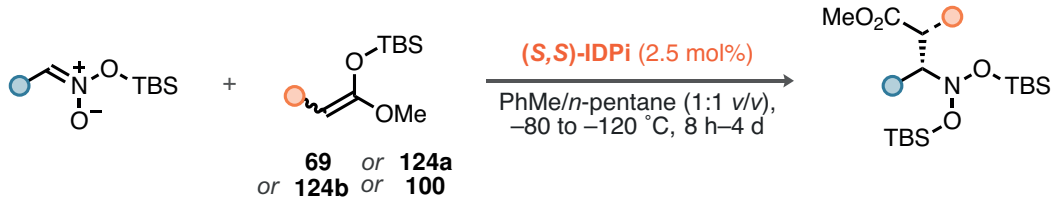

69 *or* **124a** *or* **124b** *or* **100**

In an oven-dried GC vial with septum, the respective catalyst (**91**, **94**, **99a**, or **414**, 4.0–4.5 mg, 2.5 mol%) was dissolved in toluene (200 µL, 0.50 mol/L with respect to the nitronate) and reacted with the silyl ketene acetal (**69**, **124a**, **124b**, or **100**, 2.0 equiv., 0.20 mmol) for 10 min at room temperature. After transfer to a cryostat maintaining the indicated temperature and stirring for additional 10 min, a solution of the silyl nitronate (0.50 mol/L in *n*-pentane, 1.0 equiv., 200 µL) was added dropwise to the reaction mixture. The reaction was stirred for the indicated time at the indicated temperature. Subsequently, the reaction was terminated by addition of NEt_3 and MeOH (1:1 *v*/*v*, 200 µL/mmol of silyl nitronate), stirred for 10 min at the indicated temperature and then allowed to warm to room temperature. The crude mixture was directly purified *via* flash column chromatography on silica gel (24:1 hexanes/MTBE, silica gel flushed with hexanes/EtOAc/NEt_3 18:1:1 prior to application of the crude mixture) to give the desired nitroso acetal.

Methyl (*R*)-3-(bis((*tert*-butyldimethylsilyl)oxy)amino)-4-phenylbutanoate (86):

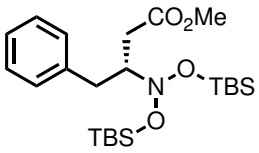

Obtained following GP2 using catalyst **91** and silyl ketene acetal **69** at −120 °C for 3 d. The title compound was isolated in 91 % yield (41.0 mg) after flash column chromatography.

^{1}H NMR (500 MHz, CD_2Cl_2): δ 7.32–7.24 (m, 2H), 7.23–7.14 (m, 3H), 3.64 (dddd, J = 9.2, 7.3, 5.6, 4.5 Hz, 1H), 3.50 (s, 3H), 3.33 (dd, J = 13.7, 4.5 Hz, 1H), 2.84 (dd, J = 16.1, 7.3 Hz, 1H), 2.62 (dd, J = 13.7, 9.2 Hz, 1H), 2.32 (dd, J = 16.0, 5.6 Hz, 1H), 0.97 (s, 9H), 0.92 (s, 9H), 0.22 (s, 3H), 0.21 (s, 3H), 0.18 (s, 3H), 0.10 (s, 3H).
^{13}C NMR (126 MHz, CD_2Cl_2): δ 173.0, 140.0, 130.0, 128.9, 126.6, 72.8, 51.7, 35.5, 34.3, 30.7, 30.3, 26.4, 26.3, 18.4, 18.4, −3.3, −3.5, −4.1, −4.5.
ESI-HRMS: calculated for $C_{23}H_{43}NO_4Si_2Na$ $[M+Na]^+$: 476.262 285, found: 476.262 210.
HPLC (OJ-3R, MeCN/H_2O = 55:45, 1.0 mL/min, λ = 215 nm, 298 K): t_r(minor) =

23.5 min, t_r(major) = 24.9 min, 95.5:4.5 er.
$[\alpha]_{\mathbf{D}}^{\mathbf{25}}$ = −4.3 (c = 0.51, n-heptane).

Methyl (*R*)-3-(bis((*tert*-butyldimethylsilyl)oxy)amino)-5-phenylpentanoate (93):

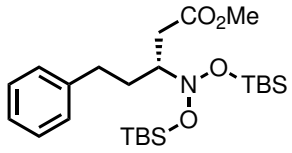

Obtained following GP2 using catalyst **94** and silyl ketene acetal **69** at −120 °C for 4 d. The title compound was isolated in 98 % yield (45.7 mg) after flash column chromatography.

^{1}H NMR (500 MHz, CD_2Cl_2): δ 7.31–7.23 (m, 2H), 7.23–7.13 (m, 3H), 3.64 (s, 3H), 3.39 (tdd, J = 7.4, 5.8, 4.9 Hz, 1H), 3.14 (dd, J = 16.0, 4.9 Hz, 1H), 2.78 (ddd, J = 13.9, 10.4, 6.1 Hz, 1H), 2.67 (ddd, J = 13.9, 10.3, 5.7 Hz, 1H), 2.37 (dd, J = 16.0, 7.3 Hz, 1H), 2.03 (dddd, J = 13.8, 10.3, 7.6, 6.1 Hz, 1H), 1.73 (ddt, J = 13.8, 10.3, 5.8 Hz, 1H), 0.90 (s, 9H), 0.89 (s, 9H), 0.21 (s, 3H), 0.18 (s, 3H), 0.18 (s, 3H), 0.09 (s, 3H).
^{13}C NMR (126 MHz, CD_2Cl_2): δ 173.8, 142.7, 128.9, 126.3, 70.6, 51.9, 33.4, 33.4, 33.1, 30.3, 26.3, 18.4, 18.2, −3.3, −3.4, −4.1, −4.3.
ESI-HRMS: calculated for $C_{24}H_{45}NO_4Si_2Na$ $[M + Na]^+$: 490.277 935, found: 490.278 200.
HPLC (OJ-3R, MeCN/H_2O = 60:40, 1.0 mL/min, λ = 215 nm, 298 K): t_r(minor) = 15.9 min, t_r(major) = 17.4 min, 98.5:1.5 er.
$[\alpha]_{\mathbf{D}}^{\mathbf{25}}$ = 19.0 (c = 0.51, n-heptane).

Methyl (*R*)-3-(bis((*tert*-butyldimethylsilyl)oxy)amino)-4-(furan-2-yl)butanoate (96):

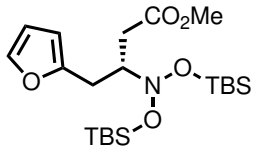

Obtained following GP2 using catalyst **99a** and silyl ketene acetal **69** at −120 °C for 3 d. The title compound was isolated in 93 % yield (41.4 mg) after flash column chromatography.

^{1}H NMR (500 MHz, CD_2Cl_2): δ 7.32 (dd, J = 2.0, 0.8 Hz, 1H), 6.28 (dd, J = 3.2, 1.9 Hz, 1H), 6.05 (dd, J = 3.2, 0.9 Hz, 1H), 3.73 (dddd, J = 9.0, 7.2, 5.8, 4.8 Hz, 1H), 3.58 (s, 3H), 3.28 (dd, J = 15.1, 4.7 Hz, 1H), 2.86 (dd, J = 16.1, 7.2 Hz, 1H), 2.73 (dd, J = 15.1, 9.0 Hz, 1H), 2.38 (dd, J = 16.1, 5.8 Hz, 1H), 0.93 (s, 9H), 0.91 (s, 9H), 0.19 (s, 3H), 0.19 (s, 3H), 0.17 (s, 3H), 0.12 (s, 3H).

^{13}C NMR (126 MHz, CD_2Cl_2): δ 172.8, 154.0, 141.8, 110.7, 107.1, 70.0, 51.8, 34.6, 30.3, 27.8, 26.3, 26.3, 18.4, 18.3, −3.4, −3.5, −4.3, −4.6.

ESI-HRMS: calculated for $C_{21}H_{41}NO_5Si_2Na$ $[M+Na]^+$: 466.241 550, found: 466.240 990.

HPLC (OJ-3R, MeCN/H_2O = 55:45, 1.0 mL/min, λ = 220 nm, 298 K): t_r(minor) = 17.2 min, t_r(major) = 19.4 min, 95:5 er.

$[\alpha]_D^{25}$ = −7.4 (c = 0.41, n-heptane).

Methyl (*R*)-3-(bis((*tert*-butyldimethylsilyl)oxy)amino)-4-(2-tolyl)butanoate (97):

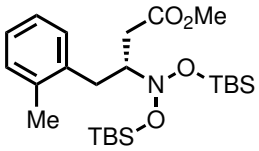

Obtained following GP2 using catalyst **99a** and silyl ketene acetal **69** at −120 °C for 3 d. The title compound was isolated in 74 % yield (34.9 mg) after flash column chromatography.

^{1}H NMR (500 MHz, CD_2Cl_2): δ 7.16–7.04 (m, 4H), 3.68 (dddd, J = 10.1, 7.2, 5.7, 4.4 Hz, 1H), 3.44 (s, 3H), 3.27 (dd, J = 13.8, 4.4 Hz, 1H), 2.87 (dd, J = 16.0, 7.1 Hz, 1H), 2.73 (dd, J = 13.8, 10.0 Hz, 1H), 2.33 (s, 3H), 2.28 (dd, J = 16.0, 5.6 Hz, 1H), 0.96 (s, 9H), 0.92 (s, 9H), 0.22 (s, 3H), 0.22 (s, 3H), 0.20 (s, 3H), 0.12 (s, 3H).

^{13}C NMR (126 MHz, CD_2Cl_2): δ 173.0, 137.6, 137.3, 130.9, 130.8, 126.9, 126.2, 71.1, 51.6, 34.0, 32.8, 30.3, 26.4, 26.3, 19.9, 18.4, 18.4, −3.3, −3.4, −4.1, −4.5.

ESI-HRMS: calculated for $C_{24}H_{45}NO_4Si_2Na$ $[M+Na]^+$: 490.277 935, found: 490.277 390.

HPLC (OZ-3R, MeCN/H_2O = 70:30, 1.0 mL/min, λ = 215 nm, 298 K): t_r(minor) = 7.9 min, t_r(major) = 8.7 min, 97.5:2.5 er.

$[\alpha]_D^{25}$ = −3.8 (c = 0.26, n-heptane).

Methyl (*R*)-3-(bis((*tert*-butyldimethylsilyl)oxy)amino)-7-phenylheptanoate (98):

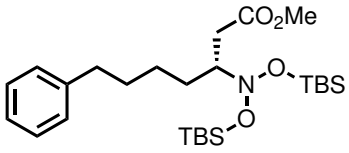

Obtained following GP2 using catalyst **94** and silyl ketene acetal **69** at −120 °C for 1 d. The title compound was isolated in 97 % yield (48.3 mg) after flash column chromatography.

^{1}H NMR (500 MHz, CD_2Cl_2): δ 7.30–7.21 (m, 2H), 7.20–7.11 (m, 3H), 3.63 (s, 3H), 3.32 (tdd, J = 7.7, 5.4, 4.5 Hz, 1H), 3.13 (dd, J = 15.9, 4.5 Hz, 1H), 2.60 (t, J = 7.7 Hz, 2H),

2.29 (dd, J = 16.0, 7.7 Hz, 1H), 1.74–1.54 (m, 3H), 1.54–1.44 (m, 1H), 1.44–1.32 (m, 2H), 0.89 (s, 9H), 0.89 (s, 9H), 0.20 (s, 3H), 0.15 (s, 3H), 0.13 (s, 3H), 0.13 (s, 3H).

^{13}C NMR (126 MHz, CD_2Cl_2): δ 174.0, 143.3, 129.0, 128.8, 126.1, 71.1, 51.8, 36.4, 33.2, 32.3, 31.7, 30.3, 26.9, 26.3, 18.4, 18.2, 3.3, −3.4, −4.0, −4.4.

ESI-HRMS: calculated for $C_{26}H_{49}NO_4Si_2Na$ $[M + Na]^+$: 518.309 235, found: 518.308 390.

HPLC (OZ-3R, MeCN/H_2O = 65:35, 1.0 mL/min, λ = 215 nm, 298 K): t_r(minor) = 17.3 min, t_r(major) = 19.0 min, >99.5:0.5 er.

$[\alpha]_D^{25}$ = 18.3 (c = 0.72, n-heptane).

Methyl (*R*)-3-(bis((*tert*-butyldimethylsilyl)oxy)amino)-4-(3,5-dimethylphenyl)butanoate (101):

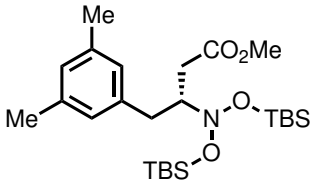

Obtained following GP2 using catalyst **91** and silyl ketene acetal **69** at −120 °C for 3 d. The title compound was isolated in 83 % yield (40.0 mg) after flash column chromatography.

^{1}H NMR (500 MHz, CD_2Cl_2): δ 6.83 (s, 1H), 6.79 (s, 2H), 3.60 (dddd, J = 9.1, 7.6, 6.5, 3.7 Hz, 1H), 3.52 (s, 3H), 3.25 (dd, J = 13.6, 4.6 Hz, 1H), 2.81 (dd, J = 16.0, 7.6 Hz, 1H), 2.53 (dd, J = 13.6, 9.2 Hz, 1H), 2.32 (dd, J = 16.1, 5.4 Hz, 1H), 2.27 (s, 6H), 0.97 (s, 9H), 0.92 (s, 9H), 0.21 (s, 3H), 0.21 (s, 3H), 0.18 (s, 3H), 0.11 (s, 3H).

^{13}C NMR (126 MHz, CD_2Cl_2): δ 173.1, 139.8, 138.3, 128.1, 127.8, 72.9, 51.7, 35.1, 34.3, 26.4, 26.3, 21.5, 18.4, 18.4, −3.3, −3.4, −4.1, −4.6.

ESI-HRMS: calculated for $C_{25}H_{47}NO_4Si_2Na$ $[M + Na]^+$: 504.293 585, found: 504.293 540.

HPLC (OD-3, n-heptane, 1.0 mL/min, λ = 220 nm, 298 K): t_r(minor) = 5.1 min, t_r(major) = 5.7 min, 94.5:5.5 er.

$[\alpha]_D^{25}$ = −1.7 (c = 0.47, n-heptane).

Methyl (*R*)-3-(bis((*tert*-butyldimethylsilyl)oxy)amino)-4-(4-fluorophenyl)butanoate (102):

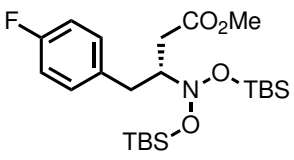

Obtained following GP2 using catalyst **99a** and silyl ketene acetal **69** at −120 °C for 3 d. The title compound was isolated in 70 % yield (32.2 mg) after flash column chromatography.

^{1}H NMR (500 MHz, CD_2Cl_2): δ 7.20–7.12 (m, 2H), 7.01–6.93 (m, 2H), 3.65–3.55 (m, 1H), 3.52 (s, 3H), 3.27 (dd, J = 13.8, 4.9 Hz, 1H), 2.87 (dd, J = 16.1, 6.9 Hz, 1H), 2.62 (dd, J = 13.9, 8.8 Hz, 1H), 2.31 (dd, J = 16.1, 6.0 Hz, 1H), 0.95 (s, 9H), 0.91 (s, 9H), 0.20 (s, 6H), 0.17 (s, 3H), 0.08 (s, 3H).
^{13}C NMR (126 MHz, CD_2Cl_2): δ 173.0, 162.0 (d, J = 243.2 Hz), 135.8 (d, J = 2.6 Hz), 131.4 (d, J = 7.7 Hz), 115.5 (d, J = 21.2 Hz), 72.8, 51.7, 34.9, 34.1, 26.4, 26.3, 18.4, 18.3, −3.4, −3.4, −4.1, −4.5.
^{19}F NMR (471 MHz, CD_2Cl_2): δ −118.10.
ESI-HRMS: calculated for $C_{23}H_{42}FNO_4Si_2Na$ $[M+Na]^+$: 494.252 863, found: 494.253 110.
HPLC (OD-3, *n*-heptane, 1.0 mL/min, λ = 220 nm, 298 K): t_r(minor) = 3.4 min, t_r(major) = 3.6 min, 95.5:4.5 er.
$[\alpha]_D^{25}$ = 1.1 (c = 0.18, *n*-heptane).

Methyl (*R*)-3-(bis((*tert*-butyldimethylsilyl)oxy)amino)-4-(4-methoxyphenyl)butanoate (103):

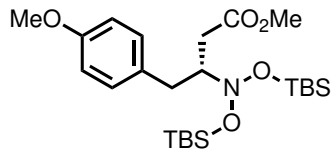

Obtained following GP2 using catalyst **99a** and silyl ketene acetal **69** at −120 °C for 3 d. The title compound was isolated in 91 % yield (44.4 mg) after flash column chromatography.

^{1}H NMR (500 MHz, CD_2Cl_2): δ 7.15–7.05 (m, 2H), 6.87–6.74 (m, 2H), 3.76 (s, 3H), 3.59 (dddd, J = 9.3, 7.2, 5.6, 4.5 Hz, 1H), 3.51 (s, 3H), 3.25 (dd, J = 13.8, 4.5 Hz, 1H), 2.83 (dd, J = 16.1, 7.2 Hz, 1H), 2.55 (dd, J = 13.9, 9.3 Hz, 1H), 2.30 (dd, J = 16.0, 5.6 Hz, 1H), 0.96 (s, 9H), 0.91 (s, 9H), 0.21 (s, 3H), 0.20 (s, 3H), 0.18 (s, 3H), 0.10 (s, 3H).
^{13}C NMR (126 MHz, CD_2Cl_2): δ 173.1, 158.7, 131.8, 130.8, 114.3, 73.0, 55.7, 51.7, 34.6, 34.1, 26.4, 26.3, 18.4, 18.4, −3.3, −3.4, −4.1, −4.5.
ESI-HRMS: calculated for $C_{24}H_{45}NO_5Si_2Na$ $[M+Na]^+$: 506.272 850, found: 506.272 860.
HPLC (OJ-3R, MeCN/H_2O = 55:45, 0.8 mL/min, λ = 215 nm, 298 K): t_r(minor) = 28.7 min, t_r(major) = 29.9 min, 95:5 er.
$[\alpha]_D^{25}$ = 1.1 (c = 0.38, *n*-heptane).

Methyl (*S*)-3-(bis((*tert*-butyldimethylsilyl)oxy)amino)-4-(thiophen-2-yl)butanoate (104):

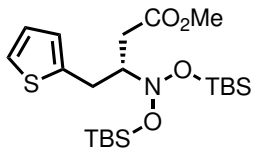

Obtained following GP2 using catalyst **99a** and silyl ketene acetal **69** at −120 °C for 3 d. The title compound was isolated in 89 % yield (41.0 mg) after flash column chromatography.

^{1}H NMR (500 MHz, CD_2Cl_2): δ 7.15 (dd, J = 5.1, 1.2 Hz, 1H), 6.92 (dd, J = 5.2, 3.4 Hz, 1H), 6.84–6.80 (m, 1H), 3.70–3.61 (m, 1H), 3.57 (s, 3H), 3.50 (ddd, J = 14.9, 4.6, 1.1 Hz, 1H), 2.90 (dd, J = 14.9, 8.9 Hz, 1H), 2.83 (dd, J = 16.1, 7.7 Hz, 1H), 2.40 (dd, J = 16.1, 5.3 Hz, 1H), 0.95 (s, 9H), 0.91 (s, 9H), 0.21 (s, 3H), 0.21 (s, 3H), 0.19 (s, 3H), 0.11 (s, 3H).
^{13}C NMR (126 MHz, CD_2Cl_2): δ 172.9, 142.6, 127.3, 126.3, 124.3, 72.9, 51.8, 34.5, 30.3, 29.3, 26.4, 26.3, 18.4, −3.4, −3.5, −4.1, −4.6.
ESI-HRMS: calculated for $C_{21}H_{41}NO_4SSi_2Na$ $[M + Na]^+$: 482.218 050, found: 482.218 708.
HPLC (OJ-3R, MeCN/H_2O = 55:45, 0.8 mL/min, λ = 230 nm, 298 K): t_r(minor) = 22.8 min, t_r(major) = 24.5 min, 97:3 er.
$[\alpha]_D^{25}$ = −13.7 (c = 0.47, n-heptane).

Methyl (*R*)-3-(bis((*tert*-butyldimethylsilyl)oxy)amino)-5-(4-chlorophenyl)butanoate (107):

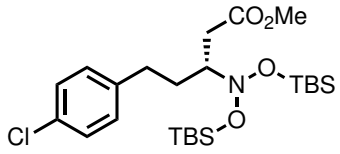

Obtained following GP2 using catalyst **94** and silyl ketene acetal **69** at −80 °C for 3 d. The title compound was isolated in 83 % yield (42.0 mg) after flash column chromatography.

^{1}H NMR (500 MHz, CD_2Cl_2): δ 7.29–7.21 (m, 2H), 7.18–7.10 (m, 2H), 3.64 (s, 3H), 3.36 (tdd, J = 7.5, 5.8, 4.9 Hz, 1H), 3.13 (dd, J = 16.1, 4.8 Hz, 1H), 2.76 (ddd, J = 14.1, 10.2, 6.1 Hz, 1H), 2.65 (ddd, J = 14.1, 10.1, 5.9 Hz, 1H), 2.36 (dd, J = 16.1, 7.3 Hz, 1H), 1.99 (dddd, J = 13.8, 10.2, 7.5, 6.1 Hz, 1H), 1.71 (ddt, J = 13.9, 10.2, 5.9 Hz, 1H), 0.89 (s, 9H), 0.88 (s, 9H), 0.20 (s, 3H), 0.18 (s, 3H), 0.16 (s, 3H), 0.08 (s, 3H).
^{13}C NMR (126 MHz, CD_2Cl_2): δ 173.8, 141., 131.9, 130.3, 128.9, 70.5, 51.9, 33.4, 32.9, 32.7, 26.3, 18.4, 18.2, −3.3, −3.4, −4.1, −4.3.

ESI-HRMS: calculated for $C_{24}H_{44}ClNO_4Si_2Na$ $[M+Na]^+$: 524.238 963, found: 524.238 810.
HPLC (OD-3, *n*-heptane, 0.7 mL/min, $\lambda = 220$ nm, 298 K): t_r(major) = 7.4 min, t_r(minor) = 8.0 min, 96.5:3.5 er.
$[\alpha]_D^{25} = 21.2$ ($c = 0.42$, *n*-heptane).

Methyl (*R*)-3-(bis((*tert*-butyldimethylsilyl)oxy)amino)-5-(4-bromophenyl)butanoate (108):

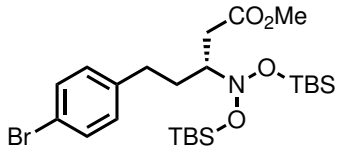

Obtained following GP2 using catalyst **94** and silyl ketene acetal **69** at −80 °C for 3 d. The title compound was isolated in 89 % yield (49.0 mg) after flash column chromatography.

^{1}H NMR (500 MHz, CD_2Cl_2): δ 7.44–7.35 (m, 2H), 7.13–7.05 (m, 2H), 3.64 (s, 3H), 3.36 (tdd, J = 7.5, 5.8, 4.9 Hz, 1H), 3.13 (dd, J = 16.1, 4.8 Hz, 1H), 2.74 (ddd, J = 14.0, 10.2, 6.1 Hz, 1H), 2.63 (ddd, J = 14.0, 10.1, 5.9 Hz, 1H), 2.36 (dd, J = 16.1, 7.4 Hz, 1H), 1.99 (dddd, J = 13.8, 10.1, 7.6, 6.1 Hz, 1H), 1.71 (ddt, J = 13.9, 10.2, 5.8 Hz, 1H), 0.88 (s, 9H), 0.88 (s, 9H), 0.20 (s, 3H), 0.18 (s, 3H), 0.16 (s, 3H), 0.08 (s, 3H).
^{13}C NMR (126 MHz, CD_2Cl_2): δ 173.8, 141.8, 131.9, 130.8, 119.9, 70.5, 51.9, 33.4, 32.81, 32.78, 26.3, 18.4, 18.2, −3.3, −3.4, −4.1, −4.3.
ESI-HRMS: calculated for $C_{24}H_{44}BrNO_4Si_2Na$ $[M+Na]^+$: 568.188 461, found: 568.188 430.
HPLC (OD-3, *n*-heptane, 1.0 mL/min, $\lambda = 230$ nm, 298 K): t_r(major) = 5.6 min, t_r(minor) = 6.5 min, 96.5:3.5 er.
$[\alpha]_D^{25} = 22.1$ ($c = 0.43$, *n*-heptane).

Methyl (*R*)-3-(bis((*tert*-butyldimethylsilyl)oxy)amino)-7-(1*H*-indol-1-yl)heptanoate (109):

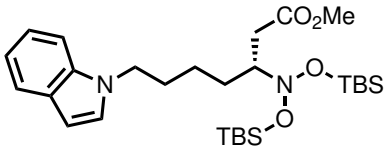

Obtained following GP2 using catalyst **414** and silyl ketene acetal **69** at −80 °C for 3 d. The title compound was isolated in 90 % yield (48.0 mg) after flash column chromatography.

^{1}H NMR (500 MHz, CD_2Cl_2): δ 7.58 (dt, J = 8.0, 1.0 Hz, 1H), 7.34 (dd, J = 8.3, 1.0 Hz, 1H), 7.16 (ddd, J = 8.2, 7.0, 1.2 Hz, 1H), 7.11 (d, J = 3.1 Hz, 1H), 7.05 (ddd, J = 7.9, 7.0,

1.0 Hz, 1H), 6.45 (dd, J = 3.2, 0.8 Hz, 1H), 4.12 (t, J = 7.1 Hz, 2H), 3.61 (s, 3H), 3.29 (qd, J = 7.9, 4.9 Hz, 1H), 3.12 (dd, J = 16.0, 4.3 Hz, 1H), 2.27 (dd, J = 16.1, 7.8 Hz, 1H), 1.82 (dq, J = 9.2, 7.3 Hz, 2H), 1.72–1.58 (m, 1H), 1.51–1.28 (m, 3H), 0.88 (s, 9H), 0.87 (s, 9H), 0.17 (s, 3H), 0.13 (s, 3H), 0.09 (s, 3H), 0.07 (s, 3H).

^{13}C NMR (126 MHz, CD_2Cl_2): δ 174.0, 136.6, 129.2, 128.3, 121.8, 121.3, 119.6, 109.9, 101.3, 70.9, 5.9, 46.8, 33.1, 31.4, 31.0, 26.3, 26.3, 24.7, 18.4, 18.2, −3.3, −3.5, −4.0, −4.5.

ESI-HRMS: calculated for $C_{28}H_{50}N_2O_4Si_2Na$ $[M+Na]^+$: 557.320 134, found: 557.320 500.

HPLC (IB-3, *n*-heptane/MTBE 95:5, 1.0 mL/min, λ = 210 nm, 298 K): t_r(minor) = 14.6 min, t_r(major) = 15.4 min, 95.5:4.5 er.

$[\alpha]_D^{25}$ = 17.1 (c = 0.37, *n*-heptane).

Methyl (*R*)-3-(bis((*tert*-butyldimethylsilyl)oxy)amino)-6-cyanohexanoate (110):

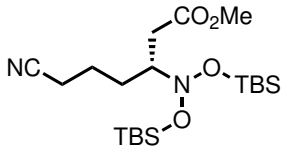

Obtained following GP2 using catalyst **94** and silyl ketene acetal **69** at −80 °C for 3 d. The title compound was isolated in 89 % yield (38.6 mg) after flash column chromatography.

^{1}H NMR (500 MHz, CD_2Cl_2): δ 3.65 (s, 3H), 3.34 (tt, J = 7.8, 4.9 Hz, 1H), 3.14 (dd, J = 16.3, 4.5 Hz, 1H), 2.43–2.26 (m, 3H), 1.94–1.77 (m, 2H), 1.76–1.63 (m, 1H), 1.58–1.45 (m, 1H), 0.90 (s, 9H), 0.89 (s, 9H), 0.21 (s, 3H), 0.18 (s, 3H), 0.18 (s, 3H), 0.14 (s, 3H).

^{13}C NMR (126 MHz, CD_2Cl_2): δ 173.6, 120.0, 70.4, 52.0, 33.3, 30.8, 26.3, 23.6, 18.4, 18.2, 17.8, −3.4, −3.4, −4.0, −4.4.

ESI-HRMS: calculated for $C_{20}H_{42}N_2O_4Si_2Na$ $[M+Na]^+$: 453.257 534, found: 453.257 750.

2D-HPLC (Zorbax RX-SIL, *n*-heptane/*i*−PrOH 99.5:0.5, 1.0 mL/min, λ = 210 nm, 298 K): t_r = 4.0 min, then (IB-3, *n*-heptane/MTBE 80:20, 1.0 mL/min, λ = 210 nm, 298 K): t_r(minor) = 3.7 min, t_r(major) = 3.9 min, 95:5 er.

$[\alpha]_D^{25}$ = 25.8 (c = 0.33, *n*-heptane).

Methyl (*R*)-3-(bis((*tert*-butyldimethylsilyl)oxy)amino)-6-((*tert*-butyldimethylsilyl)oxy)hexanoate (111):

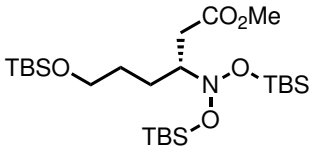

Obtained following GP2 using catalyst **94** and silyl ketene acetal **69** at −80 °C for 3 d. The title compound was isolated in 84 % yield (45.3 mg) after flash column chromatography.

^{1}H NMR (500 MHz, CD_2Cl_2): δ 3.63 (s, 3H), 3.60 (td, J = 6.3, 3.7 Hz, 2H), 3.33 (tdd, J = 7.4, 5.9, 4.6 Hz, 1H), 3.13 (dd, J = 15.9, 4.6 Hz, 1H), 2.31 (dd, J = 15.9, 7.4 Hz, 1H), 1.80–1.60 (m, 2H), 1.59–1.47 (m, 1H), 1.47–1.35 (m, 1H), 0.89 (s, 18H), 0.88 (s, 9H), 0.20 (s, 3H), 0.17 (s, 3H), 0.16 (s, 3H), 0.14 (s, 3H).
^{13}C NMR (126 MHz, CD_2Cl_2): δ 174.0, 71.2, 63.7, 51.8, 33.4, 30.7, 28.2, 26.32, 26.30, 18.8, 18.4, 18.2, −3.3, −3.5, −4.0, −4.3, −5.0.
ESI-HRMS: calculated for $C_{25}H_{57}NO_5Si_3Na$ $[M + Na]^+$: 558.343 679, found: 558.344 290.
2D-HPLC (Zorbax RX-SIL, *n*-heptane/*i*-PrOH 99.8:0.2, 1.0 mL/min, λ = 210 nm, 298 K): t_r = 1.6 min, then (OD-3, *n*-heptane, 1.0 mL/min, λ = 210 nm, 298 K): t_r(minor) = 2.5 min, t_r(major) = 3.8 min, 98:2 er.
$[\alpha]_D^{25}$ = 16.7 (c = 0.43, *n*-heptane).

Methyl (*R*)-3-(bis((*tert*-butyldimethylsilyl)oxy)amino)-6-methoxyhexanoate (112):

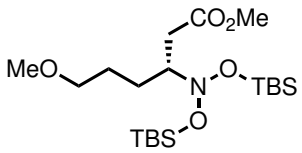

Obtained following GP2 using catalyst **94** and silyl ketene acetal **69** at −100 °C for 3 d. The title compound was isolated in 53 % yield (23.0 mg) after flash column chromatography.

^{1}H NMR (500 MHz, CD_2Cl_2): δ 3.64 (s, 3H), 3.38–3.30 (m, 3H), 3.28 (s, 3H), 3.13 (dd, J = 15.9, 4.6 Hz, 1H), 2.31 (dd, J = 16.0, 7.6 Hz, 1H), 1.77–1.63 (m, 2H), 1.63–1.54 (m, 1H), 1.42 (tdd, J = 10.2, 8.0, 5.5 Hz, 1H), 0.89 (s, 18H), 0.20 (s, 3H), 0.17 (s, 3H), 0.17 (s, 3H), 0.14 (s, 3H).
^{13}C NMR (126 MHz, CD_2Cl_2): δ 173.9, 73.2, 71.0, 58.8, 51.8, 33.3, 28.3, 27.4, 26.3, 18.4, 18.2, −3.3, −3.4, −4.0, −4.4.
ESI-HRMS: calculated for $C_{20}H_{45}NO_5Si_2Na$ $[M + Na]^+$: 458.272 850, found: 458.272 430.
HPLC (OZ-3R, MeCN/H_2O 55:45, 1.0 mL/min, λ = 205 nm, 298 K): t_r(minor) = 23.8 min, t_r(major) = 24.5 min, 97.5:2.5 er.
$[\alpha]_D^{25}$ = 17.7 (c = 0.35, *n*-heptane).

Dimethyl (*R*)-3-(bis((*tert*-butyldimethylsilyl)oxy)amino)hexanedioate (113):

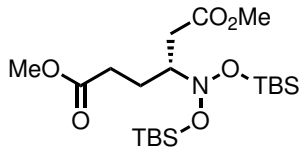

Obtained following GP2 using catalyst **94** and silyl ketene acetal **69** at −80 °C for 4 d. The title compound was isolated in 89 % yield (40.0 mg) after flash column chromatography.

^{1}H NMR (500 MHz, CD_2Cl_2): δ 3.64 (s, 3H), 3.64 (s, 3H), 3.43–3.27 (m, 1H), 3.15 (dd, J = 16.0, 4.4 Hz, 1H), 2.49 (ddd, J = 15.3, 9.3, 5.8 Hz, 1H), 2.41 (ddd, J = 16.1, 9.0, 6.8 Hz, 1H), 2.32 (dd, J = 16.0, 7.9 Hz, 1H), 1.92 (dtd, J = 14.7, 8.9, 5.8 Hz, 1H), 1.74 (dddd, J = 14.3, 9.3, 6.9, 5.0 Hz, 1H), 0.89 (s, 9H), 0.89 (s, 9H), 0.21 (s, 3H), 0.17 (s, 6H), 0.12 (s, 3H).
^{13}C NMR (126 MHz, CD_2Cl_2): δ 174.0, 173.6, 70.1, 51.9, 33.1, 31.7, 30.3, 27.1, 26.3, 18.4, 18.2, −3.3, −3.5, −4.1, −4.4.
ESI-HRMS: calculated for $C_{20}H_{43}NO_6Si_2Na$ $[M + Na]^+$: 472.252 115, found: 472.252 080.
2D-HPLC (Eclipse Plus C8, MeCN/H_2O 70:30, 1.0 mL/min, λ = 210 nm, 308 K): t_r = 11.7 min, then (OZ-3R, MeCN/H_2O 55:45, 1.0 mL/min, λ = 210 nm, 298 K): t_r(minor) = 18.2 min, t_r(major) = 19.1 min, >99.5:0.5 er.
$[\alpha]_D^{25}$ = 18.7 (c = 0.58, n-heptane).

Methyl (*R*)-3-(bis((*tert*-butyldimethylsilyl)oxy)amino)-7-bromoheptanoate (114):

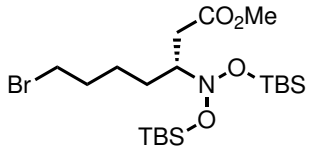

Obtained following GP2 using catalyst **94** and silyl ketene acetal **69** at −80 °C for 16 h. The title compound was isolated in 84 % yield (41.8 mg) after flash column chromatography.

^{1}H NMR (500 MHz, CD_2Cl_2): δ 3.64 (s, 3H), 3.42 (t, J = 6.8 Hz, 2H), 3.32 (tdd, J = 7.6, 5.6, 4.6 Hz, 1H), 3.13 (dd, J = 16.0, 4.6 Hz, 1H), 2.31 (dd, J = 16.0, 7.6 Hz, 1H), 1.90–1.81 (m, 2H), 1.73–1.55 (m, 2H), 1.51–1.36 (m, 2H), 0.89 (s, 18H), 0.21 (s, 3H), 0.18 (s, 3H), 0.17 (s, 3H), 0.15 (s, 3H).
^{13}C NMR (126 MHz, CD_2Cl_2): δ 173.9, 70.9, 51.9, 34.4, 33.5, 33.3, 30.8, 26.3, 25.9, 18.4, 18.2, −3.3, −3.4, −4.0, −4.4.
ESI-HRMS: calculated for $C_{20}H_{44}BrNO_4Si_2$ $[M + Na]^+$: 520.188 400, found: 520.188 460.

2D-HPLC (Zorbax RX-SIL, *n*-heptane/*i*-PrOH 99.9:0.1, 1.0 mL/min, $\lambda = 220$ nm, 308 K): $t_r = 2.8$ min, then (OD-3, *n*-heptane, 1.0 mL/min, $\lambda = 220$ nm, 298 K): t_r(minor) = 4.2 min, t_r(major) = 5.4 min, 97.5:2.5 er.
$[\alpha]_{\mathbf{D}}^{\mathbf{25}} = 17.4$ ($c = 0.27$, *n*-heptane).

Methyl (*R*)-3-(bis((*tert*-butyldimethylsilyl)oxy)amino)-7-iodoheptanoate (115):

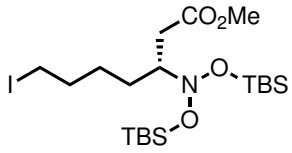

Obtained following GP2 using catalyst **94** and silyl ketene acetal **69** at −80 °C for 16 h. The title compound was isolated in 96 % yield (52.6 mg) after flash column chromatography.

^{1}H NMR (500 MHz, CD_2Cl_2): δ 3.64 (s, 3H), 3.35–3.29 (m, 1H), 3.21 (t, $J = 7.0$ Hz, 2H), 3.12 (dd, $J = 16.0$, 4.6 Hz, 1H), 2.31 (dd, $J = 16.0$, 7.6 Hz, 1H), 1.88–1.75 (m, 2H), 1.73–1.64 (m, 1H), 1.61–1.51 (m, 1H), 1.50–1.35 (m, 2H), 0.89 (s, 18H), 0.21 (s, 3H), 0.18 (s, 3H), 0.17 (s, 3H), 0.15 (s, 3H).
^{13}C NMR (126 MHz, CD_2Cl_2): δ 173.9, 70.9, 51.9, 34.2, 33.3, 30.5, 28.2, 26.3, 18.4, 18.2, 7.4, −3.3, −3.4, −4.0, −4.3.
ESI-HRMS: calculated for $C_{20}H_{44}INO_4Si_2$ $[M + Na]^+$: 568.175 380, found: 568.174 583.
2D-HPLC (Zorbax RX-SIL, *n*-heptane/*i*-PrOH 99.9:0.1, 1.0 mL/min, $\lambda = 220$ nm, 308 K): $t_r = 2.5$ min, then (OD-3, *n*-heptane, 1.0 mL/min, $\lambda = 220$ nm, 298 K): t_r(minor) = 4.1 min, t_r(major) = 5.7 min, 97.5:2.5 er.
$[\alpha]_{\mathbf{D}}^{\mathbf{25}} = -42.2$ ($c = 0.27$, *n*-heptane).

Methyl (*R*)-3-(bis((*tert*-butyldimethylsilyl)oxy)amino)octanoate (116):

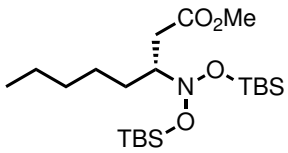

Obtained following GP2 using catalyst **94** and silyl ketene acetal **69** at −100 °C for 3 d. The title compound was isolated in 83 % yield (36.0 mg) after flash column chromatography.

^{1}H NMR (500 MHz, CD_2Cl_2): δ 3.63 (s, 1H), 3.39–3.25 (m, 1H), 3.12 (dd, $J = 15.9$, 4.6 Hz, 1H), 2.29 (dd, $J = 15.9$, 7.6 Hz, 1H), 1.64 (dq, $J = 12.2$, 7.8, 7.3 Hz, 1H), 1.50–1.40 (m, 1H), 1.39–1.21 (m, 7H), 0.91–0.86 (m, 11H), 0.20 (s, 3H), 0.17 (s, 3H), 0.16 (s, 3H), 0.14 (s, 3H).

^{13}C NMR (126 MHz, CD_2Cl_2): δ 174.0, 71.2, 51.8, 33.2, 32.5, 31.7, 30.3, 26.8, 26.3, 23.1, 18.4, 18.2, 14.4, −3.3, −3.5, −4.1, −4.4.
ESI-HRMS: calculated for $C_{21}H_{47}NO_4Si_2Na$ $[M+Na]^+$: 456.293 585, found: 456.293 390.
2D-HPLC (Multohigh U Si, *n*-heptane/*i*-PrOH 99.9:0.1, 1.0 mL/min, $\lambda = 210$ nm, 298 K): $t_r = 1.5$ min, then (OD-3, *n*-heptane, 1.0 mL/min, $\lambda = 210$ nm, 298 K): t_r(minor) = 4.0 min, t_r(major) = 4.2 min, 99:1 er.
$[\alpha]_D^{25} = 18.9$ ($c = 0.50$, *n*-heptane).

Methyl (*R*)-3-(bis((*tert*-butyldimethylsilyl)oxy)amino)hept-6-enoate (117):

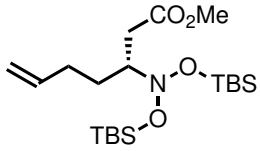

Obtained following GP2 using catalyst **94** and silyl ketene acetal **69** at −120 °C for 1 d. The title compound was isolated in 88 % yield (36.8 mg) after flash column chromatography.

^{1}H NMR (500 MHz, CD_2Cl_2): δ 5.82 (ddt, $J = 16.9$, 10.2, 6.5 Hz, 1H), 5.09–4.88 (m, 2H), 3.64 (s, 3H), 3.35 (tdd, $J = 7.8$, 5.5, 4.5 Hz, 1H), 3.15 (dd, $J = 15.9$, 4.5 Hz, 1H), 2.32 (dd, $J = 16.0$, 7.7 Hz, 1H), 2.26–2.16 (m, 1H), 2.16–2.06 (m, 1H), 1.76 (dddd, $J = 13.8$, 9.5, 7.9, 5.8 Hz, 1H), 1.47 (ddt, $J = 14.2$, 9.6, 5.9 Hz, 1H), 0.89 (s, 18H), 0.21 (s, 3H), 0.17 (s, 3H), 0.17 (s, 3H), 0.14 (s, 3H).
^{13}C NMR (126 MHz, CD_2Cl_2): δ 173.9, 139.0, 115.0, 70.5, 51.8, 33.1, 31.3, 31.0, 30.3, 26.3, 18.4, 18.2, −3.3, −3.5, −4.0, −4.4.
ESI-HRMS: calculated for $C_{20}H_{43}NO_4Si_2$ $[M+Na]^+$: 418.280 341, found: 418.280 080.
HPLC (IB-N3, *n*-heptane, 1.0 mL/min, $\lambda = 279$ nm, 268 K): t_r(minor) = 3.8 min, t_r(major) = 4.1 min, >99.5:0.5 er.
$[\alpha]_D^{25} = 25.5$ ($c = 0.38$, *n*-heptane).

Methyl (*R*)-3-(bis((*tert*-butyldimethylsilyl)oxy)amino)-9-oxodecanoate (118):

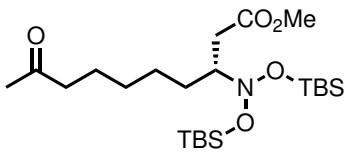

Obtained following GP2 using catalyst **94** and silyl ketene acetal **69** at −80 °C for 8 h. The title compound was isolated in 71 % yield (33.8 mg) after flash column chromatography.

^{1}H NMR (500 MHz, CD_2Cl_2): δ 3.62 (s, 3H), 3.34–3.24 (m, 1H), 3.11 (dd, $J = 16.0$, 4.6 Hz,

1H), 2.39 (t, J = 7.5 Hz, 2H), 2.28 (dd, J = 16.0, 7.6 Hz, 1H), 2.08 (s, 3H), 1.67–1.56 (m, 1H), 1.52 (p, J = 7.6 Hz, 2H), 1.48–1.40 (m, 1H), 1.38–1.20 (m, 4H), 0.88 (s, 18H), 0.19 (s, 3H), 0.15 (s, 3H), 0.15 (s, 3H), 0.12 (s, 3H).
^{13}C NMR (126 MHz, CD_2Cl_2): δ 209.2, 174.0, 70.9, 51.8, 44.0, 33.0, 31.5, 30.1, 29.7, 26.9, 26.2, 24.2, 18.3, 18.1, −3.4, −3.5, −4.1, −4.5.
ESI-HRMS: calculated for $C_{23}H_{49}NO_5Si_2$ $[M + Na]^+$: 498.304 010, found: 498.304 150.
2D-HPLC (VDSpher PUR 100 SIL, *n*-heptane/*i*-PrOH 99:1, 1.0 mL/min, λ = 210 nm, 298 K): t_r = 2.9 min, then (OD-3, *n*-heptane/MTBE 97:3, 1.0 mL/min, λ = 210 nm, 298 K): t_r(minor) = 10.7 min, t_r(major) = 12.6 min, 98:2 er.
$[\alpha]_D^{25}$ = 12.2 (c = 0.39, *n*-heptane).

Methyl (*R*)-3-(bis((*tert*-butyldimethylsilyl)oxy)amino)-8-(dibenzylamino)-8-oxo-octanoate (119):

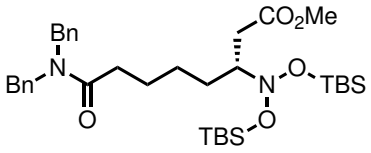

Obtained following GP2 using catalyst **94** and silyl ketene acetal **69** at −80 °C for 4 d. The title compound was isolated in 53 % yield (34.0 mg) after flash column chromatography.

^{1}H NMR (500 MHz, CD_2Cl_2): δ 7.40–7.34 (m, 2H), 7.33–7.23 (m, 4H), 7.22–7.18 (m, 2H), 7.18–7.12 (m, 2H), 4.56 (s, 2H), 4.46 (s, 2H), 3.62 (s, 3H), 3.31 (ddt, J = 10.6, 7.6, 4.9 Hz, 1H), 3.12 (dd, J = 16.0, 4.6 Hz, 1H), 2.40 (td, J = 7.4, 3.0 Hz, 2H), 2.28 (dd, J = 16.0, 7.5 Hz, 1H), 1.76–1.59 (m, 3H), 1.55–1.43 (m, 1H), 1.42–1.30 (m, 2H), 0.88 (s, 9H), 0.87 (s, 9H), 0.19 (s, 3H), 0.15 (s, 3H), 0.14 (s, 3H), 0.13 (s, 3H).
^{13}C NMR (126 MHz, CD_2Cl_2): δ 174.0, 173.7, 138.5, 137.6, 129.4, 129.1, 128.6, 128.0, 127.7, 127.0, 71.1, 51.8, 50.6, 48.7, 33.7, 33.2, 31.7, 27.1, 26.3, 26.1, 18.4, 18.2, −3.3, −3.4, −4.0, −4.4.
ESI-HRMS: calculated for $C_{35}H_{58}N_2O_5Si_2Na$ $[M + Na]^+$: 665.377 649, found: 665.377 750.
HPLC (OD-3, *n*-heptane/*i*-PrOH 97:3, 1.0 mL/min, λ = 220 nm, 298 K): t_r(minor) = 4.7 min, t_r(major) = 5.6 min, 96:4 er.
$[\alpha]_D^{25}$ = 14.1 (c = 0.34, *n*-heptane).

Methyl (*R*)-3-(bis((*tert*-butyldimethylsilyl)oxy)amino)oct-7-ynoate (120):

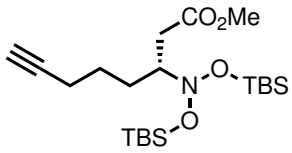

Obtained following GP2 using catalyst **94** and silyl ketene acetal **69** at −100 °C for 3 d. The title compound was isolated in 89 % yield (38.3 mg) after flash column chromatography.

^{1}H NMR (500 MHz, CD_2Cl_2): δ 3.64 (s, 3H), 3.33 (tdd, J = 7.7, 5.5, 4.4 Hz, 1H), 3.14 (dd, J = 16.0, 4.5 Hz, 1H), 2.31 (dd, J = 16.0, 7.7 Hz, 1H), 2.19 (td, J = 7.0, 2.7 Hz, 2H), 1.96 (t, J = 2.7 Hz, 1H), 1.84–1.62 (m, 2H), 1.60–1.41 (m, 2H), 0.89 (s, 18H), 0.21 (s, 3H), 0.18 (s, 3H), 0.17 (s, 3H), 0.14 (s, 3H).
^{13}C NMR (126 MHz, CD_2Cl_2): δ 173.9, 84.7, 70.8, 68.8, 51.9, 33.2, 30.9, 30.3, 26.3, 26.3, 19.0, 18.4, 18.2, −3.3, −3.4, −4.0, −4.4.
ESI-HRMS: calculated for $C_{21}H_{43}NO_4Si_2Na$ $[M + Na]^+$: 452.262 285, found: 452.261 900.
2D-HPLC (Multichrome 3-Si, *n*-heptane/*i*-PrOH 99.5:0.5, 1.0 mL/min, λ = 210 nm, 298 K): t_r = 3.7 min, then (OD-3, *n*-heptane, 1.0 mL/min, λ = 210 nm, 298 K): t_r(minor) = 7.6 min, t_r(major) = 8.0 min, 99:1 er.
$[\alpha]_D^{25}$ = 21.3 (c = 0.49, *n*-heptane).

Methyl (*R*)-3-(bis((*tert*-butyldimethylsilyl)oxy)amino)-4-methylpentanoate (121):

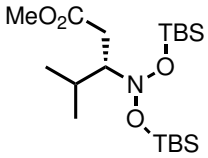

Obtained following GP2 using catalyst **94** and silyl ketene acetal **69** at −80 °C for 2 d. The title compound was isolated in 70 % yield (28.5 mg) after flash column chromatography.

^{1}H NMR (500 MHz, CD_2Cl_2): δ 3.64 (dd, J = 16.9, 3.1 Hz, 1H), 3.40 (ddd, J = 9.9, 7.2, 3.1 Hz, 1H), 3.36 (s, 3H), 3.27 (q, J = 7.0 Hz, 1H), 2.43 (dd, J = 16.9, 7.1 Hz, 1H), 1.86 (dp, J = 9.5, 6.7 Hz, 1H), 1.10 (d, J = 6.6 Hz, 3H), 0.99 (s, 9H), 0.92 (s, 9H), 0.91 (d, J = 6.6 Hz, 3H), 0.29 (s, 3H), 0.27 (s, 3H), 0.25 (s, 3H), 0.22 (s, 3H).
^{13}C NMR (126 MHz, CD_2Cl_2): δ 173.83, 76.88, 51.02, 31.39, 31.17, 26.20, 26.05, 21.05, 19.65, 18.16, 17.85, −3.3, −3.6, −3.7, −4.5.
ESI-HRMS: calculated for $C_{19}H_{43}NO_4Si_2Na$ $[M + Na]^+$: 428.262 285, found: 428.262 190.
2D-HPLC (Zorbax RX-SIL, *n*-heptane/*i*-PrOH 99.9:0.1, 1.0 mL/min, λ = 210 nm, 298 K):

$t_r = 1.9$ min, then (IA-3, *n*-heptane, 1.0 mL/min, $\lambda = 210$ nm, 298 K): t_r(minor) = 3.0 min, t_r(major) = 3.4 min, 97:3 er.
$[\alpha]_D^{25} = 6.2$ ($c = 0.26$, *n*-heptane).

Methyl (*S,E*)-5-(bis((*tert*-butyldimethylsilyl)oxy)amino)-6-phenylhex-2-enoate (105):

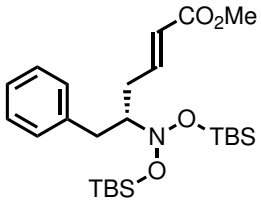

Obtained following GP2 using catalyst **99a** and silyl ketene acetal **100** at −80 °C for 3 d. The title compound was isolated as a mixture of diastereomers (E/Z = 94:6) in 84 % yield (40.3 mg) after flash column chromatography. The following NMR data are given for the (*E*)-diastereomer.

^{1}H NMR (500 MHz, CD_2Cl_2): δ 7.27 (dd, J = 8.6, 6.7 Hz, 2H), 7.18 (dd, J = 8.1, 6.4 Hz, 3H), 6.92 (dt, J = 15.2, 7.4 Hz, 1H), 5.71 (dt, J = 15.2, 1.5 Hz, 1H), 3.65 (s, 3H), 3.29 (dd, J = 13.7, 4.9 Hz, 1H), 3.20 (tt, J = 7.7, 5.1 Hz, 1H), 2.74–2.58 (m, 2H), 2.35 (dddd, J = 14.8, 7.4, 5.5, 1.5 Hz, 1H), 0.96 (s, 9H), 0.92 (s, 9H), 0.22 (s, 3H), 0.19 (s, 3H), 0.16 (s, 3H), 0.09 (s, 3H).
^{13}C NMR (126 MHz, CD_2Cl_2): δ 167.1, 148.4, 140.4, 129.9, 128.9, 126.6, 122.4, 75.8, 51.7, 35.8, 32.3, 26.5, 26.4, 26.3, 26.2, 18.4, 18.4, −3.2, −3.3, −3.9, −4.1.
ESI-HRMS: calculated for $C_{25}H_{45}NO_4Si_2Na$ $[M + Na]^+$: 502.277 935, found: 502.278 350.
HPLC (OJ-3R, MeCN/H_2O 55:45, 1.0 mL/min, $\lambda = 220$ nm, 298 K): t_r(minor) = 27.5 min, t_r(major) = 29.9 min, 99.5:0.5 er.
$[\alpha]_D^{25} = 11.4$ ($c = 0.48$, *n*-heptane).

Methyl (*S,E*)-5-(bis((*tert*-butyldimethylsilyl)oxy)amino)-6-(thiophen-2-yl)hex-2-enoate (105):

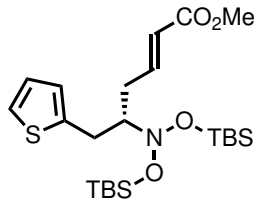

Obtained following GP2 using catalyst **99a** and silyl ketene acetal **100** at −100 °C for 3 d. The title compound was isolated as a mixture of diastereomers (E/Z = 85:15) in 94 % yield

(43.4 mg) after flash column chromatography. The following NMR data are given for the (*E*)-diastereomer.

^{1}H NMR (500 MHz, CD_2Cl_2): δ 7.14 (dd, J = 5.2, 1.2 Hz, 1H), 7.00–6.90 (m, 2H), 6.81 (dd, J = 3.4, 1.0 Hz, 1H), 5.76 (dt, J = 15.6, 1.5 Hz, 1H), 3.67 (s, 3H), 3.45 (ddd, J = 15.0, 5.0, 1.1 Hz, 1H), 3.22 (tt, J = 7.7, 5.2 Hz, 1H), 2.89 (dd, J = 15.0, 8.2 Hz, 1H), 2.70 (dtd, J = 14.7, 7.2, 1.6 Hz, 1H), 2.42 (dddd, J = 14.9, 7.5, 5.5, 1.5 Hz, 1H), 0.94 (s, 9H), 0.91 (s, 9H), 0.22 (s, 3H), 0.21 (s, 3H), 0.17 (s, 3H), 0.11 (s, 3H).
^{13}C NMR (126 MHz, CD_2Cl_2): δ 166.9, 147.8, 142.8, 127.1, 126.0, 124.0, 122.4, 75.7, 51.5, 32.3, 29.6, 26.2, 26.1, 18.2, −3.5, −3.5, −4.1, −4.2.
ESI-HRMS: calculated for $C_{23}H_{43}NO_4SSi_2Na$ $[M+Na]^+$: 508.234 358, found: 508.234 880.
HPLC (IB-N3, MeCN/H_2O 75:25, 1.0 mL/min, λ = 220 nm, 298 K): t_r(major) = 6.5 min, t_r(minor) = 6.9 min, >99.5:0.5 er.
$[\alpha]_D^{25}$ = −61.6 (c = 0.19, *n*-heptane).

Methyl (methyl (2*S*,3*R*)-3-(bis((*tert*-butyldimethylsilyl)oxy)amino)-2-methyl-4-phenylbutanoate (125a):

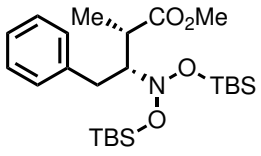

Obtained following GP2 using catalyst **99** and silyl ketene acetal **124b** at −80 °C for 4 d. The title compound was isolated in 60 % yield (28.0 mg) after flash column chromatography.

^{1}H NMR (500 MHz, CD_2Cl_2): δ 7.29–7.23 (m, 1H), 7.22–7.17 (m, 2H), 7.16–7.11 (m, 1H), 3.51 (dd, J = 14.7, 4.6 Hz, 1H), 3.33 (m, 4H), 2.80 (q, J = 7.0 Hz, 1H), 2.74 (dd, J = 14.7, 7.1 Hz, 1H), 1.26 (d, J = 7.0 Hz, 3H), 0.92 (s, 9H), 0.92 (s, 9H), 0.25 (s, 3H), 0.20 (s, 3H), 0.16 (s, 3H), 0.08 (s, 3H).
^{13}C NMR (126 MHz, CD_2Cl_2): δ 175.5, 141.3, 129.9, 128.5, 126.2, 77.8, 51.6, 42.0, 33.2, 26.4, 26.3, 18.4, 18.2, 16.3, −3.0, −3.4, −3.4, −4.3.
ESI-HRMS: calculated for $C_{24}H_{45}NO_4Si_2Na$ $[M+Na]^+$: 490.277 940, found: 490.277 935.
2D-HPLC (YMC-Pack PVA-SIL-NP, *n*-heptane/*i*-PrOH 99.9:0.1, 1.0 mL/min, λ = 210 nm, 298 K): t_r(minor) = 4.2 min, t_r(major) = 4.5 min, then (OD-3, *n*-heptane, 1.0 mL/min, λ = 210 nm, 298 K): t_r(minor) = 9.5 min, t_r(major) = 15.3 min, 96:4 er.
$[\alpha]_D^{25}$ = −3.3 (c = 0.30, *n*-heptane).

Methyl (methyl (2*R*,3*R*)-3-(bis((*tert*-butyldimethylsilyl)oxy)amino)-2-methyl-4-phenylbutanoate (125b):

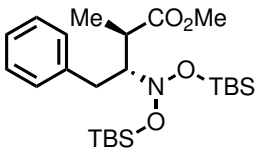

Obtained following GP2 using catalyst **94** and silyl ketene acetal **124a** at −100 °C for 4 d. The title compound was isolated as a mixture of diastereomers (*anti*/*syn* = 90:10) in 87 % yield (40.1 mg) after flash column chromatography.

^{1}H NMR (500 MHz, CD_2Cl_2): δ 7.25 (d, J = 4.4 Hz, 4H), 7.17–7.12 (m, 1H), 3.63 (td, J = 7.1, 4.8 Hz, 1H), 3.57 (s, 3H), 3.48 (dd, J = 15.2, 4.8 Hz, 1H), 3.08 (p, J = 7.2 Hz, 1H), 2.63 (dd, J = 14.9, 7.1 Hz, 1H), 1.11 (d, J = 7.2 Hz, 3H), 0.92 (s, 9H), 0.91 (s, 9H), 0.21 (s, 3H), 0.20 (s, 3H), 0.15 (s, 3H), 0.08 (s, 3H).

^{13}C NMR (126 MHz, CD_2Cl_2): δ 176.5, 141.7, 129.7, 128.6, 126.2, 76.8, 51.7, 41.6, 26.4, 26.3, 18.4, 18.3, 15.3, −3.1, −3.5, −3.9, −4.6.

ESI-HRMS: calculated for $C_{24}H_{45}NO_4Si_2Na$ $[M + Na]^+$: 490.277 940, found: 490.277 935.

2D-HPLC (YMC-Pack PVA-SIL-NP, *n*-heptane/*i*-PrOH 99.9:0.1, 1.0 mL/min, λ = 210 nm, 298 K): t_r(major) = 4.2 min, t_r(minor) = 4.5 min, then (OD-3, *n*-heptane, 1.0 mL/min, λ = 210 nm, 298 K): t_r(minor) = 8.1 min, t_r(major) = 8.4 min, >99.5:0.5 er.

$[\alpha]_D^{25}$ = 10.3 (c = 0.39, *n*-heptane).

3.5 Hydrogenation of Nitroso Acetals (GP3)

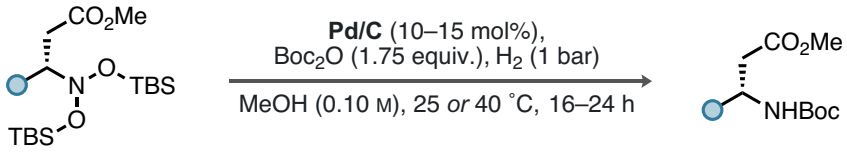

In a round-bottom flask, Pd (10 % on activated charcoal, Merck, product number 75990, batch number BCCD3509) was carefully suspended in methanol (0.10 mol/L) under an atmosphere of Ar. After the nitroso acetal (1.0 equiv.) and di-*tert*-butyldicarbonate (1.75 equiv.) were added, the flask was closed with a septum, purged with hydrogen gas for 1 min, and, after attachment of two hydrogen-filled balloons (double-layered), stirred at room temperature or 40 °C for the indicated time. Upon full conversion, the reaction atmosphere was purged with Ar, the crude mixture filtered over a pad of Celite, and washed with copious amounts

of methanol. After the solvent was removed under reduced pressure, the crude product was directly purified by flash column chromatography on silica gel (hexanes/EtOAc = 4:1).

Methyl (*R*)-3-((*tert*-butoxycarbonyl)amino)octanoate (131):

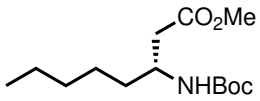

Obtained following GP3 using 10 mol% of catalyst at 40 °C for 16 h. The title compound was isolated as a colorless oil in 85 % yield (18.4 mg).

^{1}H NMR (500 MHz, CD_2Cl_2): δ 4.81 (d, J = 7.5 Hz, 1H), 3.85 (q, J = 7.5 Hz, 1H), 3.64 (s, 3H), 2.63–2.43 (m, 2H), 1.57–1.38 (m, 1H), 1.41 (s, 9H), 1.37–1.26 (m, 7H), 0.92–0.85 (m, 3H).
^{13}C NMR (126 MHz, CD_2Cl_2): δ 172.6, 155.7, 79.4, 52.0, 48.3, 39.9, 35.2, 32.1, 28.7, 26.3, 23.1, 14.3.
ESI-HRMS: calculated for $C_{14}H_{27}NO_4$ $[M+H]^+$: 274.201 284, found: 274.201 300.
HPLC (IC-3, MeCN/H_2O 50:50 → 20:80 after 10 min, 1.0 mL/min, λ = 220 nm, 298 K): t_r(major) = 4.9 min, t_r(minor) = 5.3 min, 98:2 er.

Methyl (*R*)-3-((*tert*-butoxycarbonyl)amino)-7-phenylheptanoate (132):

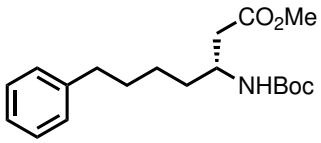

Obtained following GP3 using 10 mol% of catalyst at room temperature for 24 h. The title compound was isolated as a colorless oil in 95 % yield (31.7 mg).

^{1}H NMR (500 MHz, CD_2Cl_2): δ 7.39–7.32 (m, 2H), 7.30–7.23 (m, 3H), 4.99 (d, J = 9.3 Hz, 1H), 4.00 (q, J = 7.2 Hz, 1H), 3.76 (s, 3H), 2.69 (t, J = 7.7 Hz, 2H), 2.59 (dt, J = 15.3, 7.6 Hz, 2H), 1.63–1.44 (m, 16H).
^{13}C NMR (126 MHz, CD_2Cl_2): δ 172.3, 155.5, 142.5, 128.5, 128.4, 125.8, 79.3, 51.7, 47.7, 39.3, 35.9, 34.6, 31.2, 28.5, 25.9.
ESI-HRMS: calculated for $C_{19}H_{29}NO_4Na$ $[M+Na]^+$: 358.198 878, found: 358.198 820.
HPLC (AD-3, *n*-heptane/*i*-PrOH 98:2, 1.0 mL/min, λ = 210 nm, 298 K): t_r(minor) = 14.7 min, t_r(major) = 17.2 min, 97.5:2.5 er.

***syn*-Methyl-3-((*tert*-butoxycarbonyl)amino)-2-methyl-4-phenylbutanoate (133a):**

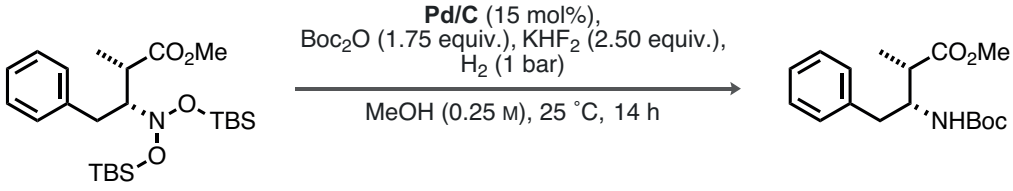

In a round-bottom flask, Pd (10 % on activated charcoal, Merck, product number 75990, batch number BCCD3509) was carefully suspended in methanol (1.0 mL, 0.25 mol/L) under an atmosphere of Ar. After the nitroso acetal (1.0 equiv., 0.25 mmol, 118.0 mg) and di-*tert*-butyldicarbonate (1.75 equiv., 0.44 mmol, 95.9 mg, 101 µL) were added, the flask was closed with a septum, purged with hydrogen gas for 1 min, and, after attachment of two hydrogen-filled balloons (double-layered), stirred at room temperature for 14 h. Upon full conversion, the reaction atmosphere was purged with Ar, the crude mixture filtered over a pad of Celite, and washed with copious amounts of methanol. After the solvent was removed under reduced pressure, the crude product was directly purified by flash column chromatography on silica gel (hexanes/EtOAc = 4:1) to provide two fractions (F1: 10.0 mg, *anti*/*syn* = 76:24, F2: 29.0 mg, *anti*/*syn* = 10:90) of the product (65 % combined yield, 48 % F2). The title compound was obtained as a pure diastereomer (*anti*/*syn* <1:20) after crystallization of F2 from hexanes/MTBE at room temperature. The relative configuration was determined by X-ray single crystal structure analysis.

^{1}H NMR (500 MHz, CD_2Cl_2): δ 7.29 (t, J = 7.5 Hz, 2H), 7.24–7.17 (m, 3H), 4.65 (d, J = 9.0 Hz, 1H), 4.13–4.03 (m, 1H), 3.67 (s, 3H), 2.81 (dd, J = 14.0, 5.3 Hz, 1H), 2.73–2.55 (m, 2H), 1.33 (s, 9H), 1.18 (d, J = 7.2 Hz, 3H).
^{13}C NMR (126 MHz, CD_2Cl_2): δ 175.3, 155.5, 138.6, 129.7, 128.7, 126.8, 79.3, 52.0, 43.6, 38.8, 28.4, 13.1.
ESI-HRMS: calculated for $C_{17}H_{25}NO_4Na$ $[M + Na]^+$: 330.167 578, found: 330.167 140.

Absolute Configuration

The absolute configuration was determined to be (*R*) by comparison of the HPLC trace of **130** with commercially purchased *N*-Boc-(*S*)-β-homophenylalanine and subsequent derivatization to the methyl ester. All other products were assigned by analogy.

3.6 Downstream Modifications

***tert*-butyl (*R*)-(1-hydroxyoctan-3-yl)carbamate (135):**

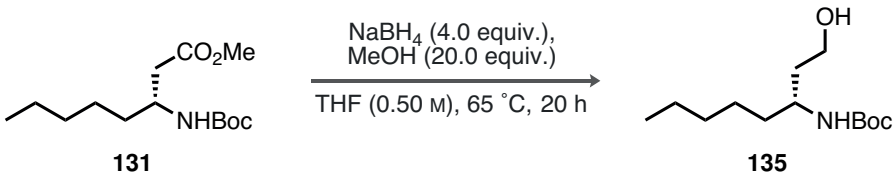

Following a literature procedure,[375] methanol (20.0 equiv., 20.0 mmol, 0.8 mL) was added dropwise over a period of 20 min to a solution of the *N*-Boc-protected β-amino acid methyl ester **131** (1.0 equiv., 1.0 mmol, 273.2 mg) and $NaBH_4$ (4.0 equiv., 4.0 mmol, 151.0 mg) in THF (2.0 mL, 0.50 mol/L) at 65 °C and the resulting mixture was stirred for 20 h. Upon full conversion, the reaction was allowed to cool to room temperature and terminated by the careful addition of water. The phases were separated and the aqueous phase was extracted with EtOAc (3 x 10 mL). The combined organic extracts were washed with brine, dried over Na_2SO_4, concentrated under reduced pressure, and directly purified by flash column chromatography on silica gel (hexanes/EtOAc = 3:1). The title compound was obtained as a colorless oil in 73 % yield (180.0 mg).

^{1}H NMR (500 MHz, CD_2Cl_2): δ 4.41 (d, J = 8.6 Hz, 1H), 3.70 (d, J = 12.3 Hz, 1H), 3.60–3.52 (m, 2H), 3.18 (t, J = 7.0 Hz, 1H), 1.78 (dddd, J = 13.5, 9.6, 6.5, 3.3 Hz, 1H), 1.52–1.20 (m, 18H), 0.89 (t, J = 6.9 Hz, 3H).

^{13}C NMR (126 MHz, CD_2Cl_2): δ 157.7, 79.9, 59.2, 47.8, 39.8, 36.2, 32.2, 28.6, 26.4, 23.1, 14.4.

ESI-HRMS: calculated for $C_{13}H_{27}NO_3Na$ $[M + Na]^+$: 268.188 313, found: 268.188 190.

(*R*)-3-((*tert*-butoxycarbonyl)amino)octyl benzoate (136):

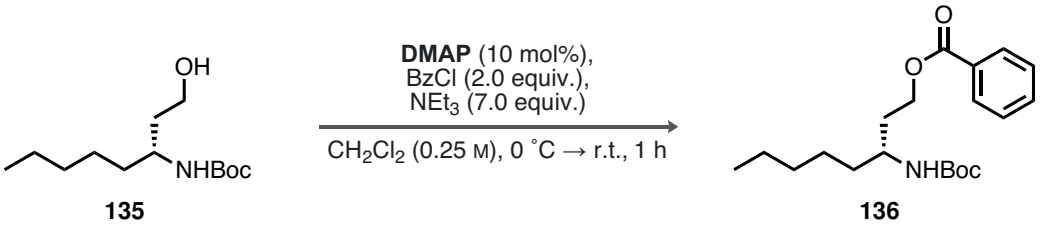

Following a literature procedure,[376] DMAP (10 mol%, 20.0 µmol, 2.44 mg) and benzoyl chloride (2.0 equiv., 0.4 mmol, 46 µL) were added to a solution of NEt_3 (7.0 equiv., 1.4 mmol) and aminoalcohol **135** (1.0 equiv., 0.2 mmol, 49.1 mg) in CH_2Cl_2 (0.8 mL, 0.25 mol/L) at 0 °C (water/ice bath) and the reaction was stirred for 5 min. Subsequently, the cooling

bath was removed and the reaction mixture was stirred for 1 h at room temperature. After addition of a sat. aq. NH_4Cl solution, the phases were separated and the aqueous layer was extracted with CH_2Cl_2 (3 x 10 mL). The combined extracts were dried over sodium sulfate, concentrated under reduced pressure, and directly purified by flash column chromatography on silica gel (hexanes/EtOAc = 9:1). The title compound was obtained as a colorless oil in 93 % yield (64.8 mg).

^{1}H NMR (500 MHz, CD_2Cl_2): δ 8.06–8.00 (m, 2H), 7.61–7.54 (m, 1H), 7.46 (t, J = 7.8 Hz, 2H), 4.45 (d, J = 9.1 Hz, 1H), 4.40–4.32 (m, 2H), 3.74 (s, 1H), 1.98 (dt, J = 14.4, 6.4 Hz, 1H), 1.83–1.71 (m, 1H), 1.40 (s, 18H), 0.92–0.85 (m, 3H).
^{13}C NMR (126 MHz, CD_2Cl_2): δ 166.9, 156.0, 133.4, 131.1, 130.0, 128.9, 79.2, 62.9, 48.9, 36.0, 34.8, 32.2, 28.7, 26.1, 23.2, 14.4.
ESI-HRMS: calculated for $C_{20}H_{31}NO_4Na$ $[M+Na]^+$: 372.214 620, found: 372.214 527.
HPLC (AD-3, *n*-heptane/*i*-PrOH 95:5, 1.0 mL/min, λ = 230 nm, 298 K): t_r(major) = 11.7 min, t_r(minor) = 16.3 min, 95:5 er.

(*R*)-4-pentylazetidin-2-one (138):

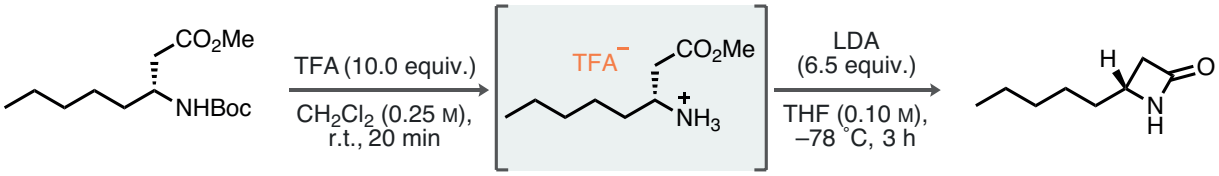

131 **137** **138**

TFA (10.0 equiv., 3.66 mmol, 0.3 mL) was added dropwise to a solution of **131** (1.0 equiv., 0.37 mmol, 105.0 mg) in CH_2Cl_2 (1.5 mL, 0.25 mol/L) and the reaction was stirred for 20 min at room temperature. Subsequenty, the solvent and excess TFA were removed under high vacuum and the crude product was directly used in the next step. For NMR data of unpurified **137**, please see below.

^{1}H NMR (500 MHz, CD_2Cl_2): δ 7.73 (s, 4H), 6.00 (s, 5H), 3.76 (s, 3H), 3.58 (s, 1H), 2.82 (dd, J = 18.0, 3.3 Hz, 1H), 2.71 (dd, J = 18.0, 9.1 Hz, 1H), 1.83–1.72 (m, 1H), 1.65 (dq, J = 14.2, 7.8 Hz, 1H), 1.50–1.23 (m, 6H), 0.94–0.85 (m, 3H).
^{13}C NMR (126 MHz, CD_2Cl_2): δ 173.3, 161.3 (q, J = 38.8 Hz), 53.2, 50.3, 35.3, 32.8, 31.6, 25.4, 22.8, 14.1.
^{19}F NMR (471 MHz, CD_2Cl_2): δ −76.36.

Following a literature procedure,[377] *n*-BuLi (2.5 mol/L in hexanes, 6.5 equiv., 2.38 mmol, 0.95 mL) was added dropwise to a solution of diisopropylamine (6.5 equiv., 2.38 mmol,

0.33 mL) in THF (1.2 mL, 2.0 mol/L) at 0 °C (water/ice bath), and the reaction was stirred for 10 min. Subsequently, this freshly prepared solution of LDA was added dropwise to a solution of **137** in THF (3.7 mL, 0.1 mol/L) at −78 °C and the resulting yellow reaction mixture was stirred for 3 h. After addition of sat. aq. NH_4Cl solution, the phases were separated and the organic layer extracted with ethyl acetate (2 x 15 mL). The combined extracted were dried over Na_2SO_4, concentrated under reduced pressure, and directly purified by flash column chromatography on silica gel (hexanes/EtOAc = 1:2). The title compound was isolated as a colorless oil in 89 % yield (45.9 mg).

^{1}H NMR (500 MHz, CD_2Cl_2): δ 5.98 (s, 1H), 3.62–3.53 (m, 1H), 2.99 (ddd, J = 14.6, 5.0, 2.3 Hz, 1H), 2.51 (ddd, J = 14.6, 2.3, 1.4 Hz, 1H), 1.68–1.51 (m, 2H), 1.38–1.23 (m, 6H), 0.94–0.84 (m, 3H).
^{13}C NMR (126 MHz, CD_2Cl_2): δ 168.3, 48.6, 44.0, 36.0, 32.1, 26.5, 23.1, 14.3.
ESI-HRMS: calculated for $C_8H_{15}NONa$ $[M + Na]^+$: 164.104 583, found: 164.104 570.
HPLC (AD-3, *n*-heptane/*i*-PrOH 98:2, 1.0 mL/min, λ = 210 nm, 298 K): t_r(major) = 9.8 min, t_r(minor) = 11.5 min, 95:5 er.

Methyl ((*R*)-3-((*tert*-butoxycarbonyl)amino)octanoyl)-L-phenylalaninate (140):

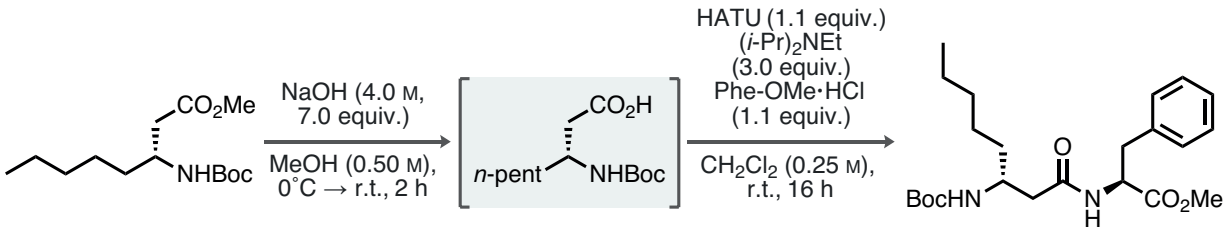

131 **139** **140**

NaOH (4.0 mol/L in H_2O, 7.0 equiv., 3.3 mL) was added to a solution of **131** in methanol (3.8 mL, 0.5 mol/L) at 0 °C. The reaction was allowed to warm to room temperature and was stirred for additional 2 h. Subsequently, the volatiles were removed under reduced pressure and the aqueous mixture carefully acidified to pH = 3 by addition of HCl (1.0 mol/L). Extraction of the aqueous phase with CH_2Cl_2 (3 x 20 mL) yielded the carboxylic acid **139** that was used without further purification in the next step. For analytical data of unpurified **139**, please see below.

^{1}H NMR (500 MHz, CD_2Cl_2): δ 4.89–4.84 (m, 1H), 3.89–3.84 (m, 1H), 2.63–2.43 (m, 2H), 1.65–1.21 (m, 18H), 0.89 (t, J = 6.6 Hz, 3H).
ESI-HRMS: calculated for $C_{13}H_{25}NO_4Na$ $[M + Na]^+$: 282.167 578, found: 282.167 640.

Following a literature procedure,[378] the carboxylic acid **139** (1.0 equiv., 0.77 mmol, 200.0 mg)

was reacted with HATU (1.1 equiv., 0.85 mmol, 323.0 mg) and $(i\text{-Pr})_2$NEt (3.0 equiv., 2.31 mmol, 0.4 mL) in CH_2Cl_2 (3.1 mL, 0.25 mol/L) at room temperature for 10 min, until L-phenylalanine methyl ester hydrochloride (1.1 equiv., 0.85 mmol, 183.0 mg) was added. The reaction mixture was subsequently stirred for 16 h at room temperature. The reaction was terminated by dilution with EtOAc, and the mixture was washed with HCl (1.0 mol/L) and brine. The organic layer was dried over Na_2SO_4, concentrated under reduced pressure, and directly purified by flash column chromatography on silica gel (hexanes/EtOAc 1:2). The title compound was obtained as a white powder in 83 % yield (270.0 mg).

^{1}H NMR (500 MHz, CD_2Cl_2): δ 7.33–7.27 (m, 2H), 7.27–7.22 (m, 1H), 7.17–7.11 (m, 2H), 6.20 (s, 1H), 5.12 (s, 1H), 4.84–4.75 (m, 1H), 3.82–3.71 (m, 1H), 3.70 (s, 3H), 3.13 (dd, J = 13.9, 5.6 Hz, 1H), 3.04 (dd, J = 13.9, 6.7 Hz, 1H), 2.37 (dd, J = 14.9, 5.2 Hz, 1H), 2.30 (dd, J = 14.9, 5.9 Hz, 1H), 1.48–1.36 (m, 18H), 0.89 (t, J = 6.8 Hz, 3H).
^{13}C NMR (126 MHz, CD_2Cl_2): δ 172.5, 171.1, 156.0, 136.9, 129.8, 129.1, 127.6, 79.4, 53.8, 52.7, 48.7, 41.6, 38.4, 35.2, 32.1, 28.7, 26.5, 23.2, 14.4.
ESI-HRMS: calculated for $C_{23}H_{36}N_2O_5Na$ $[M + Na]^+$: 443.251 641, found: 443.251 630.

Methyl ((*R*)-3-((*tert*-butoxycarbonyl)amino)octanoyl)-L-phenylalaninate (140):

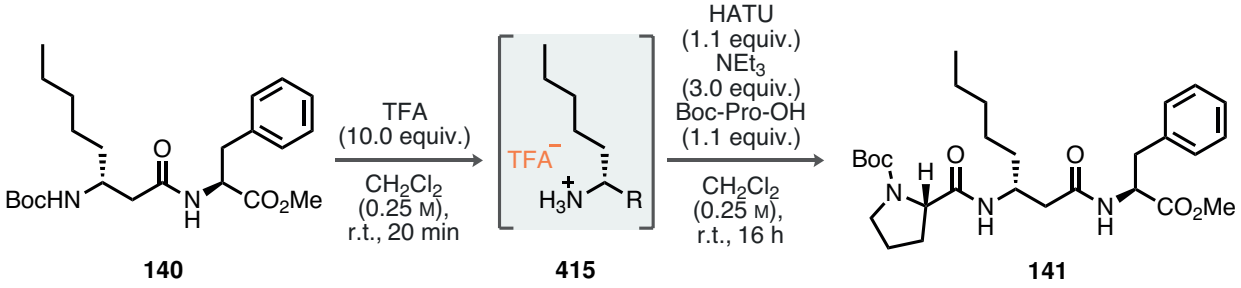

140 **415** **141**

TFA (10.0 equiv., 1.19 mmol, 91 µL) was added dropwise to a solution of **140** (1.0 equiv., 0.12 mmol, 50.0 mg) in CH_2Cl_2 (0.5 mL, 0.25 mol/L) and the reaction was stirred for 20 min at room temperature. Subsequenty, the solvent and excess TFA were removed under high vacuum and the crude product was directly used in the next step. For NMR data of unpurified **415**, please see below.

^{1}H NMR (500 MHz, CD_2Cl_2): δ 7.35–7.23 (m, 3H), 7.14–7.08 (m, 2H), 6.62 (d, J = 7.9 Hz, 1H), 4.89–4.81 (m, 1H), 3.77 (s, 3H), 3.56 (s, 1H), 3.20 (dd, J = 14.0, 5.4 Hz, 1H), 3.06 (dd, J = 14.0, 7.0 Hz, 1H), 2.70 (dd, J = 16.5, 3.3 Hz, 1H), 2.54 (dd, J = 16.5, 8.6 Hz, 1H), 1.74–1.53 (m, 2H), 1.39–1.23 (m, 6H), 0.89 (t, J = 6.7 Hz, 3H).

N-Boc-L-proline (1.1 equiv., 0.13 mmol, 28.2 mg) was reacted with HATU (1.1 equiv.,

0.13 mmol, 49.7 mg) and NEt_3 (3.0 equiv., 0.36 mmol, 50 µL) in CH_2Cl_2 (0.5 mL, 0.25 mol/L) at room temperature for 10 min, until the freshly deprotected dipeptide **415** (1.0 equiv., 0.12 mmole, 25.8 mg) was added and the resulting reaction mixture stirred for 16 h. The reaction was terminated by dilution with EtOAc, and the mixture was washed with HCl (1.0 mol/L) and brine. The organic layer was dried over Na_2SO_4, concentrated under reduced pressure, and directly purified by flash column chromatography on silica gel (first: hexanes/EtOAc 1:1, second: CH_2Cl_2/MeOH 19:1). The title compound was obtained as a white powder in 70 % yield (43.0 mg).

Due to the presence of rotamers, the complete characterization was conducted for the TFA salt after Boc deprotection, using the conditions shown above.

^{1}H NMR (500 MHz, CD_2Cl_2): δ 7.55 (d, J = 9.4 Hz, 1H), 7.35–7.22 (m, 3H), 7.18–7.10 (m, 2H), 6.94 (d, J = 7.9 Hz, 1H), 4.81–4.72 (m, 1H), 4.50–4.43 (m, 1H), 4.28–4.17 (m, 1H), 3.72 (s, 3H), 3.45 (s, 2H), 3.17 (dd, J = 14.1, 5.3 Hz, 1H), 3.00 (dd, J = 14.1, 8.3 Hz, 1H), 2.54 (dd, J = 14.7, 4.7 Hz, 1H), 2.49–2.37 (m, 1H), 2.33 (dd, J = 14.7, 6.4 Hz, 1H), 2.17–1.99 (m, 3H), 1.55–1.43 (m, 2H), 1.34–1.20 (m, 6H), 0.91–0.83 (m, 3H).

^{13}C NMR (126 MHz, CD_2Cl_2): δ 173.4, 172.4, 168.7, 161.5 (q, J = 38.8 Hz), 161.2, 160.9, 160.6, 136.6, 129.6, 129.2, 127.7, 119.8, 117.2, 115.0 (q, J = 288.8 Hz), 112.7, 60.7, 54.6, 53.2, 48.1, 47.6, 40.7, 37.7, 34.5, 31.9, 30.4, 26.4, 25.4, 23.0, 14.3.

ESI-HRMS: calculated for $C_{23}H_{36}N_3O_4$ $[M+H]^+$: 418.270 031, found: 418.270 120.

3.7 Ion Pair Studies

3.7.1 Bis(siloxy)iminium IDPi Ion Pair

In an NMR tube (5 mm diameter), a solution of IDPi **91** (1.0 equiv., 7.6 µmol, 12.8 mg) in CD_2Cl_2 (0.50 mL) was reacted with *tert*-butyldimethyl(2-methylallyl)silane (10.0 equiv., 0.08 mmol, 13.0 mg) at room temperature for 15 min. Subsequently, the NMR tube was inserted into the NMR spectrometer precooled to −80 °C and the first spectrum indicated complete activation (Chapter 2, Scheme 2.11 ii). Subsequent iterative addition of silyl nitronate **85** was followed by ^{31}P measurements, as indicated in the remaining spectra in Scheme 2.11. The 2D NMR data as well as the 1D-selective ROESY data are discussed in Chapter 2, Section 3.5.1.

3.7.2 Triethylammonium IDPi Ion Pair

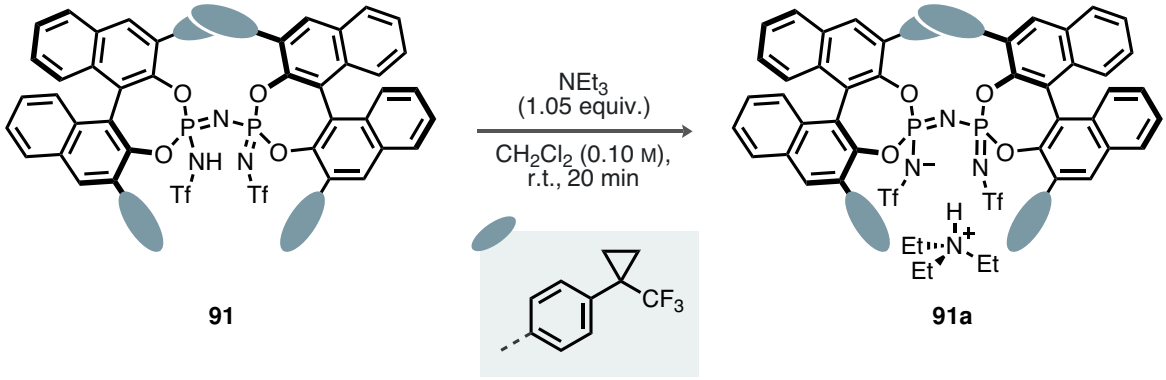

NEt_3 (1.05 equiv., 13.1 µmol, 1.8 µL) was added to a solution of IDPi **91** (1.00 equiv., 12.5 µmol, 20.9 mg) in CH_2Cl_2 (125 µL, 0.10 mol/L) at room temperature. The reaction was stirred for 20 min at room temperature, and subsequently filtered over a glass frit. The off-white amorphous solid was washed with *n*-pentane and dried under high vacuum, providing the title compound in 99 % yield (22.2 mg).

^{1}H NMR (500 MHz, CD_2Cl_2): δ 8.15–8.08 (m, 4H), 8.02 (d, J = 8.3 Hz, 2H), 7.72 (ddd, J = 8.1, 6.7, 1.2 Hz, 2H), 7.57–7.48 (m, 4H), 7.48–7.40 (m, 10H), 7.38 (s, 2H), 7.35–7.28 (m, 4H), 6.85 (d, J = 8.0 Hz, 4H), 6.71–6.61 (m, 4H), 2.70–2.58 (m, 6H), 1.38–1.32 (m, 4H), 1.11 (d, J = 9.7 Hz, 2H), 1.07–0.93 (m, 6H), 0.88 (t, J = 7.2 Hz, 1H), 0.83 (t, J = 7.3 Hz, 9H), 0.73 (d, J = 5.8 Hz, 2H), 0.39 (s, 2H).
^{19}F NMR (471 MHz, CD_2Cl_2): δ −69.78, −70.16, −79.30.
^{31}P NMR (203 MHz, CD_2Cl_2): δ −10.28.

The ^{1}H,^{1}H-NOESY spectrum as well as key interactions are depicted in Chapter 2, Section 3.6.1, Scheme 2.14.

3.8 Synthesis of Quinuclidinium Salts

Quinuclidinium trifluoromethanesulfonate (154):

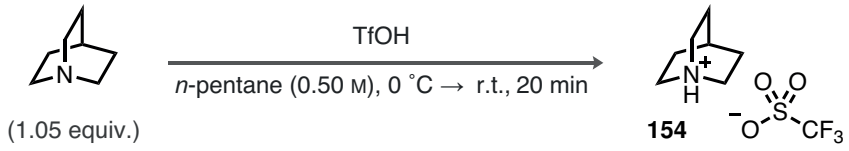

Triflic acid (1.00 equiv., 5.00 mmol, 442 µL) was added dropwise to a solution of quinuclidine (1.05 equiv., 5.25 mmol, 583.7 mg) in *n*-pentane (10.0 mL, 0.50 mol/L) at 0 °C. Upon

complete addition, the reaction was allowed to warm to room temperature and stirred for 20 min. The white precipitate was separated by filtration, washed with *n*-pentane, and dried under high vacuum to provide the title compound in 83 % yield (1.08 g).

^{1}H NMR (500 MHz, CD_2Cl_2): δ 8.61–8.28 (m, 1H), 3.32 (td, J = 2.2, 7.9 Hz, 6H), 2.17 (hept, J = 3.3 Hz, 1H), 1.93 (td, J = 3.3, 8.4 Hz, 6H).

^{13}C NMR (126 MHz, CD_2Cl_2): δ 120.7 (q, J = 319.0 Hz), 47.6, 23.2, 19.4.

^{19}F NMR (471 MHz, CD_2Cl_2): δ −78.99.

ESI-HRMS: calculated for $C_7H_{14}N$ $[M+H]^+$: 112.112 08, found: 112.111 99.

ESI-HRMS: calculated for CF_3O_3S $[M]^-$: 148.952 57, found: 148.952 52.

Quinuclidinium trifluoroacetate (**155**):

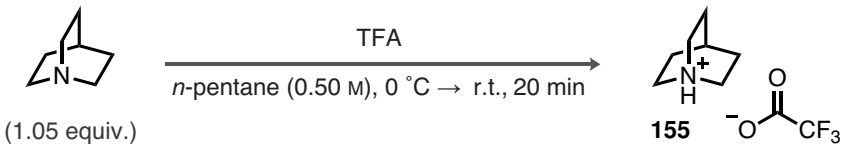

TFA (1.00 equiv., 5.00 mmol, 383 µL) was added dropwise to a solution of quinuclidine (1.05 equiv., 5.25 mmol, 583.7 mg) in *n*-pentane (10.0 mL, 0.50 mol/L) at 0 °C. Upon complete addition, the reaction was allowed to warm to room temperature and stirred for 20 min. The white precipitate was separated by filtration, washed with *n*-pentane, and dried under high vacuum to provide the title compound in 85 % yield (959 mg).

^{1}H NMR (500 MHz, CD_2Cl_2): δ 12.35 (s, 1H), 3.39–3.13 (m, 6H), 2.14 (hept, J = 3.3 Hz, 1H), 1.98–1.78 (m, 6H).

^{13}C NMR (126 MHz, CD_2Cl_2): δ 162.0 (q, J = 34.6 Hz), 117.2 (q, J = 293.2 Hz), 46.6, 23.4, 19.9.

^{19}F NMR (471 MHz, CD_2Cl_2): δ −75.82.

ESI-HRMS: calculated for $C_7H_{14}N$ $[M+H]^+$: 112.112 08, found: 112.112 01.

ESI-HRMS: calculated for CF_3CO_2 $[M]^-$: 112.985 59, found: 112.985 62.

The protodesilylation of silyl ketene acetal **69** by quinuclidinium triflate **154** and trifluoroacetate **155** was investigated by NMR spectroscopy. To a solution of the respective salt **154** or **155** (1.0 equiv., 0.05 mmol) in CD_2Cl_2 (0.50 mL, 0.10 mol/L) was added silyl ketene acetal **69** (20.0 equiv., 1.00 mmol, 218 µL) at room temperature, followed by immediate NMR measurement. The corresponding reaction mixtures were analyzed by ^{1}H,^{29}Si-HMBC, and the related discussion can be found in Chapter 2, Section 3.6.2, Scheme 2.16.

3.9 Catalytic Polarity Inversion of Silyl Nitronates from Nitroalkanes (GP4)

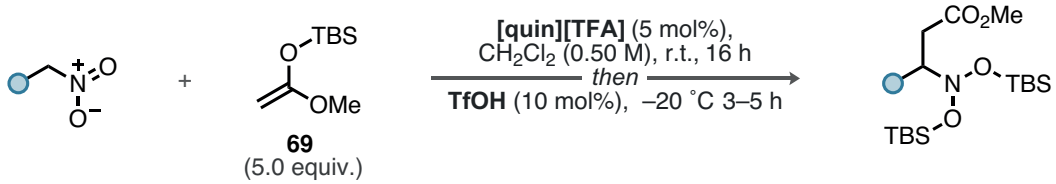

Silyl ketene acetal **69** (5.0 equiv., 2.5 mmol, 546 µL) was added to a solution of quinuclidinium trifluoroacetate (**155**, 5.0 mol%, 5.63 mg) in CH_2Cl_2 (1.0 mL, 0.50 mol/L) at room temperature, and the resulting reaction mixture was stirred for 16 h. Upon complete conversion towards the silyl nitronate (as monitored by crude ^{1}H NMR spectroscopy), the reaction was cooled to −20 °C by transfer to a suitable pre-cooled cryostat. Triflic acid (10 mol%, 4.4 µL) was added and the reaction was stirred for additional 3–5 h at −20 °C. Subsequently, the reaction was terminated by addition of NEt_3 and MeOH (1:1 *v*/*v*, 200 µL/mmol of nitroalkane), stirred for 10 min at −20 °C and then allowed to warm to room temperature. The crude mixture was directly purified *via* flash column chromatography on silica gel (19:1 hexanes/MTBE, silica gel flushed with hexanes/EtOAc/NEt_3 18:1:1 prior to application of the crude mixture) to give the desired nitroso acetal.

Methyl 3-(bis((*tert*-butyldimethylsilyl)oxy)amino)-3-phenylpropanoate (127):

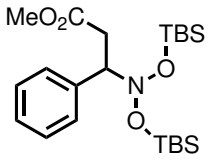

Obtained according to GP4; the title compound was isolated in 88 % yield (194.0 mg) after flash column chromatography.

^{1}H NMR (500 MHz, $CDCl_3$): δ 7.38–7.27 (m, 5H), 4.57 (dd, J = 9.3, 4.6 Hz, 1H), 3.61 (s, 3H), 3.52 (dd, J = 16.1, 4.6 Hz, 1H), 3.08 (dd, J = 16.1, 9.3 Hz, 1H), 0.94 (s, 9H), 0.76 (s, 9H), 0.28 (s, 3H), 0.22 (s, 3H), 0.08 (s, 3H), −0.39 (s, 3H).
^{13}C NMR (126 MHz, $CDCl_3$): δ 173.1, 137.3, 129.8, 128.0, 73.4, 51.8, 30.5, 26.2, 26.1, 18.1, 18.0, −3.6, −3.7, −4.0, −5.2.
ESI-HRMS: calculated for $C_{22}H_{41}NO_4Si_2Na$ $[M + Na]^+$: 462.246 635, found: 462.246 570.

Methyl 3-(bis((*tert*-butyldimethylsilyl)oxy)amino)-4-phenylbutanoate (**86**):

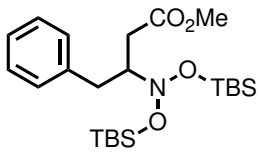

Obtained according to GP4; the title compound was isolated in 97 % yield (221.0 mg) after flash column chromatography.

^{1}H NMR (500 MHz, $CDCl_3$): δ 7.27 (dd, J = 8.1, 7.0 Hz, 2H), 7.21–7.14 (m, 3H), 3.66 (dddd, J = 9.1, 7.1, 5.9, 4.7 Hz, 1H), 3.52 (s, 3H), 3.34 (dd, J = 13.8, 4.7 Hz, 1H), 2.87 (dd, J = 16.0, 7.1 Hz, 1H), 2.63 (dd, J = 13.8, 9.1 Hz, 1H), 2.34 (dd, J = 16.0, 5.9 Hz, 1H), 0.96 (s, 9H), 0.92 (s, 9H), 0.21 (s, 3H), 0.20 (s, 3H), 0.17 (s, 3H), 0.09 (s, 3H).
^{13}C NMR (126 MHz, $CDCl_3$): δ 172.9, 139.4, 129.6, 128.5, 126.2, 72.2, 51.4, 35.1, 33.9, 26.2, 26.2, 18.1, 18.1, −3.5, −3.6, −4.2, −4.7.
ESI-HRMS: calculated for $C_{23}H_{43}NO_4Si_2Na$ $[M + Na]^+$: 476.262 520, found: 476.262 285.

Methyl 3-(bis((*tert*-butyldimethylsilyl)oxy)amino)-5-phenylpentanoate (**93**):

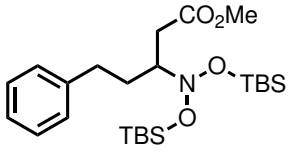

Obtained according to GP4 with 10 mol% quinuclidinium trifluoroacetate and 15 mol% TfOH; the title compound was isolated in 95 % yield (221.8 mg) after flash column chromatography.

^{1}H NMR (500 MHz, $CDCl_3$): δ 7.31–7.27 (m, 2H), 7.21–7.15 (m, 3H), 3.66 (s, 3H), 3.44–3.35 (m, 1H), 3.19 (dd, J = 16.0, 4.7 Hz, 1H), 2.80 (ddd, J = 13.9, 10.5, 5.9 Hz, 1H), 2.65 (ddd, J = 13.9, 10.5, 5.9 Hz, 1H), 2.38 (dd, J = 16.0, 7.6 Hz, 1H), 2.02 (dddd, J = 13.8, 10.4, 7.8, 6.0 Hz, 1H), 1.73 (ddt, J = 13.8, 11.0, 5.7 Hz, 1H), 0.89 (s, 18H), 0.20 (s, 3H), 0.17 (s, 6H), 0.08 (s, 3H).
^{13}C NMR (126 MHz, $CDCl_3$): δ 173.8, 142.1, 128.5, 128.5, 126.0, 70.2, 51.6, 33.1, 33.0, 32.8, 26.1, 18.1, 17.9, −3.5, −3.6, −4.2, −4.5.
ESI-HRMS: calculated for $C_{24}H_{45}NO_4Si_2Na$ $[M + Na]^+$: 490.277 935, found: 490.278 120.

In an alternative procedure on 0.10 mmol scale using 3.0 mol% of quinuclidinium trifluoroacetate for 48 h in toluene/*n*-pentane (1:1 *v*/*v*, 200 µL), followed by addition of IDPi **414** (5.0 mol%, 10.2 mg) at −40 °C and subsequent reaction for 22 h, the title compound **93** was obtained in 92 % yield (43.0 mg) after flash column chromatography.

HPLC (OJ-3R, MeCN/H_2O = 60:40, 1.0 mL/min, λ = 215 nm, 298 K): t_r(minor) = 15.9 min, t_r(major) = 17.4 min, 98.5:1.5 er.

Methyl 3-(bis((*tert*-butyldimethylsilyl)oxy)amino)-6-phenylhexanoate (**161**):

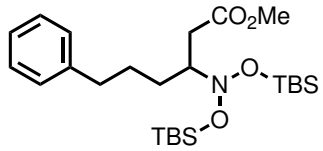

Obtained according to GP4 with 10 mol% quinuclidinium trifluoroacetate and 15 mol% TfOH; the title compound was isolated in 86 % yield (208.0 mg) after flash column chromatography.

^{1}H NMR (500 MHz, $CDCl_3$): δ 7.39–7.33 (m, 2H), 7.31–7.23 (m, 3H), 3.75 (s, 3H), 3.45 (dtd, J = 9.6, 4.8, 3.4 Hz, 1H), 3.31 (dd, J = 16.0, 4.1 Hz, 1H), 2.78–2.61 (m, 2H), 2.39 (dd, J = 16.0, 7.9 Hz, 1H), 1.92–1.68 (m, 3H), 1.58–1.46 (m, 1H), 0.98 (s, 9H), 0.95 (s, 9H), 0.28 (s, 3H), 0.23 (s, 3H), 0.22 (s, 3H), 0.21 (s, 3H).
^{13}C NMR (126 MHz, $CDCl_3$): δ 174.0, 142.5, 128.6, 128.4, 125.9, 70.5, 51.6, 36.3, 32.7, 31.5, 28.8, 26.1, 26.1, 18.1, 17.9, −3.5, −3.6, −4.0, −4.6.
ESI-HRMS: calculated for $C_{25}H_{47}NO_4Si_2Na$ $[M + Na]^+$: 504.293 585, found: 504.293 830.

Methyl 3-(bis((*tert*-butyldimethylsilyl)oxy)amino)-7-phenylheptanoate (**98**):

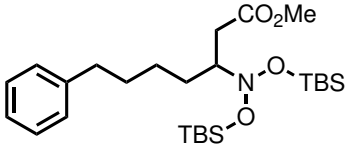

Obtained according to GP4 with 10 mol% quinuclidinium trifluoroacetate and 15 mol% TfOH; the title compound was isolated in 96 % yield (237.0 mg) after flash column chromatography.

^{1}H NMR (500 MHz, $CDCl_3$): δ 7.38–7.34 (m, 2H), 7.29–7.23 (m, 3H), 3.74 (s, 3H), 3.41 (tt, J = 8.0, 4.8 Hz, 1H), 3.34–3.24 (m, 1H), 2.70 (t, J = 7.7 Hz, 2H), 2.39 (dd, J = 16.0, 7.8 Hz, 1H), 1.82–1.39 (m, 6H), 0.98 (s, 9H), 0.97 (s, 9H), 0.27 (s, 3H), 0.23 (s, 3H), 0.22 (s, 3H), 0.20 (s, 3H).
^{13}C NMR (126 MHz, $CDCl_3$): δ 174.0, 142.7, 128.5, 128.4, 125.8, 70.6, 51.6, 36.1, 32.8, 31.8, 31.3, 26.5, 26.1, 18.1, 17.9, −3.5, −3.6, −4.1, −4.7.
ESI-HRMS: calculated for $C_{26}H_{49}NO_4Si_2Na$ $[M + Na]^+$: 518.309 235, found: 518.309 700.

Methyl 3-(bis((*tert*-butyldimethylsilyl)oxy)amino)octanoate (**116**):

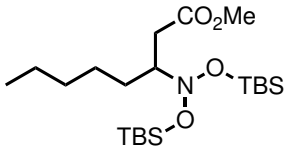

Obtained according to GP4 with 10 mol% quinuclidinium trifluoroacetate and 15 mol% TfOH; the title compound was isolated in 83 % yield (180.2 mg) after flash column chromatography.

^{1}H NMR (500 MHz, $CDCl_3$): δ 3.66 (s, 3H), 3.32 (tdd, J = 7.7, 5.4, 4.4 Hz, 1H), 3.18 (dd, J = 15.9, 4.4 Hz, 1H), 2.31 (dd, J = 15.9, 7.7 Hz, 1H), 1.68–1.58 (m, 1H), 1.49–1.20 (m, 7H), 0.89 (s, 18H), 0.19 (s, 3H), 0.15 (s, 6H), 0.14 (s, 3H).
^{13}C NMR (126 MHz, $CDCl_3$): δ 174.1, 70.7, 51.6, 32.9, 32.1, 31.5, 26.4, 26.1, 22.7, 18.1, 17.9, 14.2, −3.5, −3.6, −4.1, −4.6.
ESI-HRMS: calculated for $C_{21}H_{47}NO_4Si_2Na$ $[M + Na]^+$: 456.293 58, found: 456.293 51.

Methyl 3-(bis((*tert*-butyldimethylsilyl)oxy)amino)-4-(4-methoxyphenyl)buta noate (**103**):

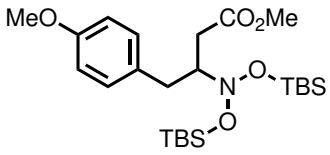

Obtained according to GP4; the title compound was isolated in 72 % yield (175.0 mg) after flash column chromatography.

^{1}H NMR (500 MHz, $CDCl_3$): δ 7.09 (d, J = 8.6 Hz, 2H), 6.81 (d, J = 8.6 Hz, 2H), 3.78 (s, 3H), 3.66–3.58 (m, 1H), 3.52 (s, 3H), 3.26 (dd, J = 13.9, 4.7 Hz, 1H), 2.86 (dd, J = 16.0, 7.0 Hz, 1H), 2.56 (dd, J = 13.9, 9.2 Hz, 1H), 2.33 (dd, J = 16.0, 5.8 Hz, 1H), 0.96 (s, 9H), 0.91 (s, 9H), 0.21 (s, 3H), 0.19 (s, 3H), 0.17 (s, 3H), 0.09 (s, 3H).
^{13}C NMR (126 MHz, $CDCl_3$): δ 173.0, 158.2, 131.4, 130.4, 113.9, 72.4, 55.4, 51.4, 34.3, 33.8, 26.2, 26.2, 18.1, 18.1, −3.5, −3.6, −4.2, −4.7.
ESI-HRMS: calculated for $C_{24}H_{45}NO_5Si_2Na$ $[M + Na]^+$: 506.272 850, found: 506.273 070.

Methyl 3-(bis((*tert*-butyldimethylsilyl)oxy)amino)-4-(4-chlorophenyl)butanoate (159):

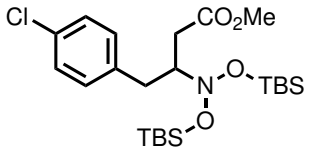

Obtained according to GP4; the title compound was isolated in 99 % yield (242.0 mg) after flash column chromatography.

^{1}H NMR (500 MHz, $CDCl_3$): δ 7.24 (d, J = 8.4 Hz, 2H), 7.11 (d, J = 8.4 Hz, 2H), 3.63–3.57 (m, 1H), 3.54 (s, 3H), 3.27 (dd, J = 14.0, 5.0 Hz, 1H), 2.88 (dd, J = 16.1, 6.8 Hz, 1H), 2.66–2.56 (m, 1H), 2.31 (dd, J = 16.1, 6.1 Hz, 1H), 0.90 (s, 18H), 0.16 (s, 3H), 0.13 (s, 6H), 0.07 (s, 3H).

Methyl 3-(bis((*tert*-butyldimethylsilyl)oxy)amino)-4-(3-chlorophenyl)butanoate (160):

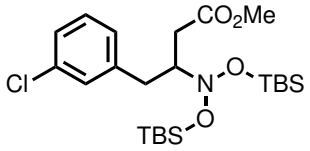

Obtained according to GP4; the title compound was isolated in 67 % yield (164.0 mg) after flash column chromatography.

^{1}H NMR (500 MHz, $CDCl_3$): δ 7.23–7.14 (m, 3H), 7.07 (dt, J = 7.3, 1.6 Hz, 1H), 3.62 (dtd, J = 8.5, 6.6, 5.3 Hz, 1H), 3.57 (s, 3H), 3.28 (dd, J = 13.9, 5.3 Hz, 1H), 2.90 (dd, J = 16.1, 6.6 Hz, 1H), 2.62 (dd, J = 13.9, 8.5 Hz, 1H), 2.34 (dd, J = 16.1, 6.1 Hz, 1H), 0.95 (s, 9H), 0.91 (s, 9H), 0.19 (s, 6H), 0.16 (s, 3H), 0.07 (s, 3H).

4 Synthetic Procedures for Chapter 3

4.1 Bistriflimide Alkylation Kinetics

In an NMR tube (5 mm diameter), the corresponding ester (30.0 equiv., 0.3 mmol) was added to a solution of bistriflimide (1.0 equiv., 10.0 µmol, 2.81 mg) in toluene-d_8 (0.50 mL) at room temperature. Triisopropyl(2-methylallyl)silane (10.0 equiv., 0.1 mmol, 26.1 µL) was added to the reaction mixture, followed by immediate measurements of ^{1}H and ^{19}F NMR spectra at room temperature. The corresponding concentration profiles, along with a discussion of the observed results, can be found in Chapter 3, Section 3.2.1, Fig. 3.1.

4.2 IDPi Methylation

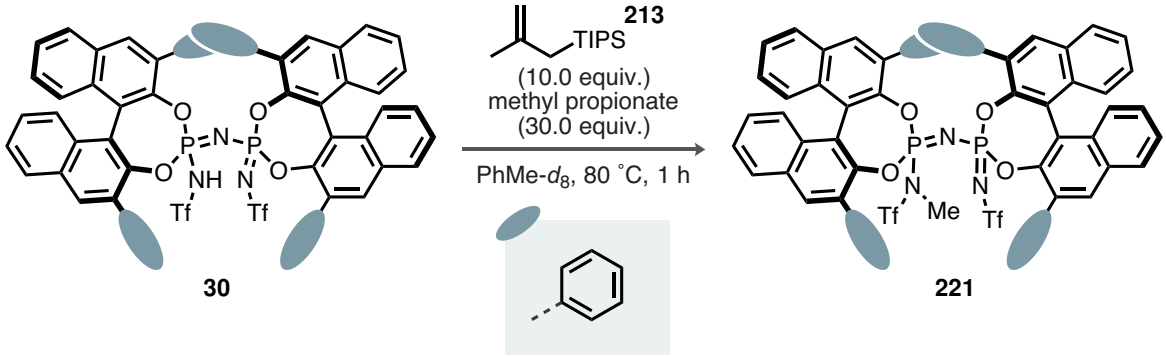

In an NMR tube (5 mm diameter), methyl propionate (30.0 equiv., 0.3 mmol) was added to a solution of IDPi **30** (1.0 equiv., 10.0 µmol, 12.4 mg) in toluene-d_8 (0.50 mL) at room temperature. Triisopropyl(2-methylallyl)silane (10.0 equiv., 0.1 mmol, 26.1 µL) was added to the reaction mixture, followed by transfer of the NMR tube to an oil bath pre-heated to 80 °C. Aliquots were taken every 20 min, inidicating full conversion towards the *N*-methylated IDPi **221** after 1 h at 80 °C. The reaction was allowed to cool to room temperature, concentrated under reduced pressure, and directly purified by preparative TLC (silica gel, hexanes/EtOAc 3:1). The title compound was obtained as a white solid in 98 % yield (11.7 mg).

^{1}H NMR (500 MHz, CD_2Cl_2): δ 8.24–8.03 (m, 6H), 7.88–7.81 (m, 1H), 7.75 (t, J = 7.5 Hz, 1H), 7.68–7.53 (m, 6H), 7.46–7.33 (m, 13H), 7.26 (dd, J = 5.1, 1.9 Hz, 3H), 7.21–7.11 (m, 2H), 7.01 (t, J = 7.8 Hz, 2H), 6.94 (t, J = 7.8 Hz, 2H), 6.68–6.62 (m, 2H), 6.44 (d, J = 7.6 Hz, 2H), 2.05 (d, J = 10.2 Hz, 3H).
^{19}F NMR (471 MHz, CD_2Cl_2): δ −74.65, −80.13.
^{31}P NMR (203 MHz, CD_2Cl_2): δ −14.11 (d, J = 132.4 Hz), −17.03 (d, J = 132.4 Hz).
ESI-HRMS: calculated for $C_{67}H_{43}N_3O_8P_2F_6S_2Na$ $[M+Na]^+$: 1280.176 330, found: 1280.176 770.

4.3 Synthesis of Imines (GP5)

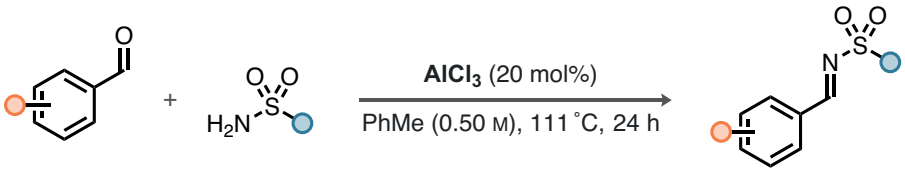

The corresponding sulfonamide (1.0 equiv.) and aromatic aldehyde (1.5 equiv.) were added to a suspension of anhydrous $AlCl_3$ (20 mol%) in toluene (0.50 mol/L) at room temperature. After a reflux condenser with additional Dean–Stark apparatus were attached, the reaction mixture was transferred to an oil bath (set to 140 °C) and refluxed for 24 h. Subsequently, the reaction was allowed to cool to room temperature, concentrated under reduced pressure, and the resulting slurry suspended in EtOAc. The suspension was filtered over a glass frit, and the organic layer washed with sat. aq. $NaHCO_3$ solution. The organic layer was dried over Na_2SO_4, concentrated under reduced pressure, and the resulting yellow solid recrystallized from hexanes/EtOAc (9:1, oil bath set to 85 °C). The title compounds were obtained after filtration, washing with hexanes, and drying under high vacuum.

***N*-benzylidenemethanesulfonamide (224):**

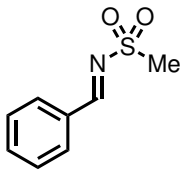

Obtained according to GP5; the title compound was isolated as white needles in 49 % yield (1.89 g).

^{1}H NMR (500 MHz, $CDCl_3$): δ 9.04 (s, 1H), 8.07–7.91 (m, 2H), 7.76–7.63 (m, 1H), 7.54 (t, $J = 7.8$ Hz, 2H), 3.14 (s, 3H).
^{13}C NMR (126 MHz, $CDCl_3$): δ 171.8, 135.3, 132.3, 131.5, 129.4, 40.4.

***N*-benzylideneethanesulfonamide (416):**

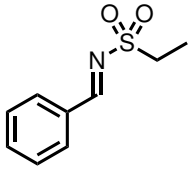

Obtained according to GP5; the title compound was isolated as white needles in 81 % yield (3.21 g).

^{1}H NMR (500 MHz, $CDCl_3$): δ 9.03 (s, 1H), 8.03–7.89 (m, 2H), 7.74–7.62 (m, 1H), 7.52 (t, $J = 7.8$ Hz, 2H), 3.24 (q, $J = 7.4$ Hz, 2H), 1.47–1.33 (m, 3H).
^{13}C NMR (126 MHz, $CDCl_3$): δ 172.4, 135.2, 132.4, 131.4, 129.4, 47.1, 7.9.

***N*-(4-methylbenzylidene)methanesulfonamide** (**417**):

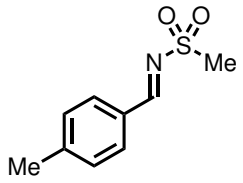

Obtained according to GP5; the title compound was isolated as white needles in 40 % yield (1.65 g).

^{1}H NMR (500 MHz, $CDCl_3$): δ 8.98 (s, 1H), 7.84 (d, $J = 8.0$ Hz, 2H), 7.32 (d, $J = 8.0$ Hz, 2H), 3.12 (s, 3H), 2.45 (s, 3H).
^{13}C NMR (126 MHz, $CDCl_3$): δ 171.5, 146.8, 131.5, 130.2, 129.7, 40.4, 22.1.

***N*-benzylidene-4-methylbenzenesulfonamide** (**201**):

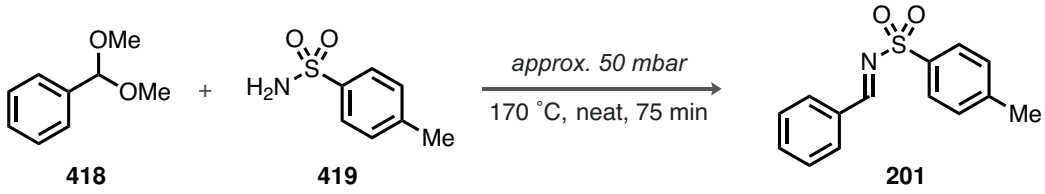

418 **419** **201**

Following a literature procedure,[379] 4-methylbenzenesulfonamide **419** (1.0 equiv., 20.0 mmol, 3.42 g) was dried under high vacuum for 1 h while initially gently heating with a heat gun (250 °C) for 15 min. Subsequently, benzaldehyde dimethylacetal (1.0 equiv., 20.0 mmol, 3.0 mL) was added, followed by attachment of a cooling trap (dry ice). The reaction was transferred to a pre-heated oil bath (set to 170 °C) and stirred for 75 min while maintaining a pressure of approximately 50 mbar. After 75 min, the pressure was reduced to high vacuum (<0.001 mbar) for 15 min, followed by cooling of the reaction mixture to room temperature. After solidification over night, the title compound **201** was obtained as an off-white solid in 91 % yield (4.13 g).

^{1}H NMR (500 MHz, $CDCl_3$): δ 9.03 (s, 1H), 7.94–7.87 (m, 4H), 7.66–7.57 (m, 1H), 7.48 (t, $J = 7.8$ Hz, 2H), 7.34 (d, $J = 8.1$ Hz, 2H), 2.44 (s, 3H).
^{13}C NMR (126 MHz, $CDCl_3$): δ 170.3, 144.7, 135.1, 131.4, 129.9, 129.3, 128.2, 21.8.

4.4 Bistriflimide-Catalyzed Silicon-Catalytic Mukaiyama–Mannich Reaction (GP6)

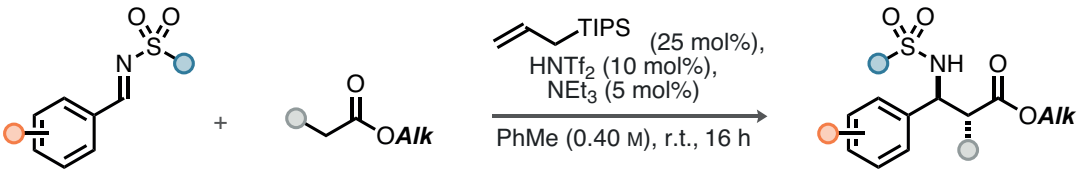

Allyltriisopropylsilane (25 mol%, 0.10 mmol, 24 µL) was dissolved in toluene (1.9 mL) in a flame-dried Schlenk flask at room temperature. A solution of bistriflimide (0.40 mol/L in toluene, 10 mol%, 0.04 mmol, 100 µL) was added, followed by the respective ester (3.0 equiv., 1.20 mmol) and imine (1.0 equiv., 0.40 mmol). The reaction was stirred for 5 min at room temperature. Subsequently, NEt_3 (5 mol%, 0.02 mmol, 2.8 µL) was added and the reaction stirred at room temperature for the indicated time. Upon complete conversion of the imine, the reaction was terminated by addition of a mixture of triethylamine/methanol 1:1 (20 µL), concentrated under reduced pressure, and directly purified by flash column chromatography on silica gel (hexanes/ethyl acetate 4:1).

***anti*-Methyl 2-methyl-3-(methylsulfonamido)-3-phenylpropanoate (229):**

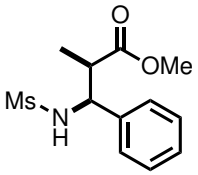

Obtained according to GP6; the title compound was isolated as a white solid in 87 % yield (94.4 mg) as a mixture of diastereomers (87:13 dr, crude dr: 87:13). The following NMR data are given for the *anti*-diastereomer.

^{1}H NMR (500 MHz, $CDCl_3$): δ 7.40–7.33 (m, 2H), 7.33–7.27 (m, 3H), 5.94 (d, $J = 9.1$ Hz, 1H), 4.58 (dd, $J = 9.1, 6.8$ Hz, 1H), 3.65 (s, 3H), 2.88 (p, $J = 7.0$ Hz, 1H), 2.61 (s, 3H), 1.23 (d, $J = 7.1$ Hz, 3H).
^{13}C NMR (126 MHz, $CDCl_3$): δ 175.2, 139.7, 129.1, 128.4, 126.8, 60.4, 52.2, 46.1, 42.0, 15.8.
ESI-HRMS: calculated for $C_{12}H_{16}NO_4S$ $[M - H]^-$: 270.080 85, found: 270.080 89.

***anti*-Ethyl 2-methyl-3-(methylsulfonamido)-3-phenylpropanoate (230):**

Obtained according to GP6; the title compound was isolated as a white solid in 98 % yield (111.8 mg) as a mixture of diastereomers (87:13 dr, crude dr: 87:13). The following NMR

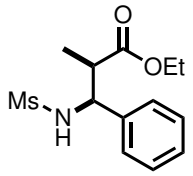

data are given for the *anti*-diastereomer.

^{1}H NMR (500 MHz, $CDCl_3$): δ 7.34 (m, 2H), 7.33–7.27 (m, 3H), 5.91 (d, $J = 9.0$ Hz, 1H), 4.58 (dd, $J = 9.0$, 6.6 Hz, 1H), 4.14–4.06 (m, 2H), 2.84 (p, $J = 7.0$ Hz, 1H), 2.61 (s, 3H), 1.25 (d, $J = 7.1$ Hz, 3H), 1.18 (t, $J = 7.1$ Hz, 3H).
^{13}C NMR (126 MHz, $CDCl_3$): δ 174.8, 139.8, 129.1, 128.3, 126.8, 61.2, 60.3, 46.0, 42.1, 15.9, 14.2.
ESI-HRMS: calculated for $C_{13}H_{19}NO_4SNa$ $[M + Na]^+$: 308.092 70, found: 308.092 80.

***anti*-Isobutyl 2-methyl-3-(methylsulfonamido)-3-phenylpropanoate (226)**:

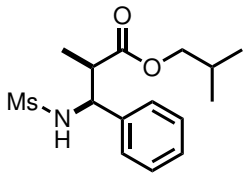

Obtained according to GP6; the title compound was isolated as a white solid in 92 % yield (115.0 mg) as a mixture of diastereomers (89:11 dr, crude dr: 89:11). The following NMR data are given for the *anti*-diastereomer.

^{1}H NMR (500 MHz, $CDCl_3$): δ 7.39–7.33 (m, 2H), 7.32–7.27 (m, 3H), 5.93 (d, $J = 8.9$ Hz, 1H), 4.59 (dd, $J = 8.9$, 6.2 Hz, 1H), 3.81 (d, $J = 6.6$ Hz, 2H), 2.92–2.83 (m, 1H), 2.63 (s, 3H), 1.89–1.77 (m, 1H), 1.29 (d, $J = 7.1$ Hz, 3H), 0.82 (d, $J = 6.7$ Hz, 6H).
^{13}C NMR (126 MHz, $CDCl_3$): δ 174.9, 139.8, 129.1, 128.3, 126.8, 71.2, 60.3, 46.0, 42.1, 27.7, 19.0, 16.1.
ESI-HRMS: calculated for $C_{15}H_{23}NO_4SNa$ $[M + Na]^+$: 336.124 00, found: 336.123 94.

***anti*-Methyl 2-methylsulfonamido(phenyl)methyl)butanoate (233)**:

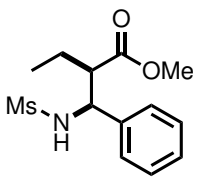

Obtained according to GP6; the title compound was isolated as a white solid in 63 % yield (71.8 mg) as a mixture of diastereomers (86:14 dr, crude dr: 86:14). The following NMR data are given for the *anti*-diastereomer.

^{1}H NMR (500 MHz, $CDCl_3$): δ 7.40–7.33 (m, 2H), 7.32–7.28 (m, 1H), 7.28–7.20 (m, 2H), 5.92 (d, J = 9.2 Hz, 1H), 4.67 (dd, J = 9.2, 6.0 Hz, 1H), 3.62 (s, 3H), 2.66 (dt, J = 9.1, 6.0 Hz, 1H), 2.61 (s, 3H), 1.85–1.70 (m, 1H), 1.68–1.56 (m, 1H), 0.96 (t, J = 7.4 Hz, 3H).
^{13}C NMR (126 MHz, $CDCl_3$): δ 174.9, 140.0, 129.1, 128.3, 126.6, 58.6, 53.7, 52.0, 42.2, 23.9, 11.9.
ESI-HRMS: calculated for $C_{13}H_{19}NO_4SNa$ $[M + Na]^+$: 308.092 39, found: 308.092 70.

***anti*-Isobutyl 2-methylsulfonamido(phenyl)methyl)butanoate (234)**:

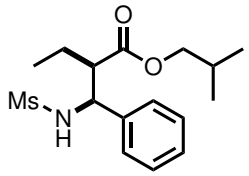

Obtained according to GP6; the title compound was isolated as a white solid in 81 % yield (106.0 mg) as a mixture of diastereomers (96:4 dr, crude dr: 89:11). The following NMR data are given for the *anti*-diastereomer.

^{1}H NMR (500 MHz, $CDCl_3$): δ 7.42–7.32 (m, 2H), 7.32–7.19 (m, 3H), 5.97 (d, J = 9.1 Hz, 1H), 4.69 (dd, J = 9.1, 5.6 Hz, 1H), 3.78 (d, J = 6.6 Hz Hz, 2H), 2.68–2.61 (m, 4H), 1.88–1.74 (m, 2H), 1.74–1.62 (m, 1H), 0.99 (t, J = 7.4 Hz, 3H), 0.78 (d, J = 6.7 Hz, 6H).
^{13}C NMR (126 MHz, $CDCl_3$): δ 174.7, 140.0, 129.1, 128.2, 126.5, 71.1, 58.5, 53.7, 42.3, 27.6, 24.1, 19.0, 11.9.
ESI-HRMS: calculated for $C_{16}H_{25}NO_4SNa$ $[M + Na]^+$: 350.139 65, found: 350.139 42.

***anti*-Isobutyl 2-methyl-3-(methylsulfonamido)-3-(4-tolyl)propanoate (231)**:

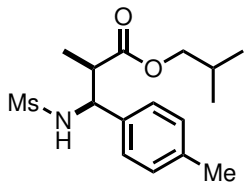

Obtained according to GP6; the title compound was isolated as a white solid in 86 % yield (112.2 mg) as a mixture of diastereomers (95:5 dr, crude dr: 87:13). The following NMR data are given for the *anti*-diastereomer.

^{1}H NMR (500 MHz, $CDCl_3$): δ 7.23–7.08 (m, 4H), 5.93 (d, J = 9.0 Hz, 1H), 4.55 (dd, J = 9.0, 6.6 Hz, 1H), 3.90–3.78 (m, 2H), 2.85 (p, J = 7.0 Hz, 1H), 2.60 (s, 3H), 2.32 (s, 3H), 1.94–1.77 (m, 1H), 1.24 (d, J = 7.1 Hz, 3H), 0.84 (dd, J = 6.8, 1.1 Hz, 6H).

^{13}C NMR (126 MHz, $CDCl_3$): δ 175.0, 138.0, 136.7, 129.7, 126.7, 71.1, 60.1, 46.2, 42.0, 27.7, 21.2, 19.1, 19.0, 15.9..

ESI-HRMS: calculated for $C_{16}H_{25}NO_4SNa$ $[M + Na]^+$: 350.139 65, found: 350.139 54.

***anti*-Isobutyl 3-(ethylsulfonamido)-2-methyl-3-phenylpropanoate (232)**:

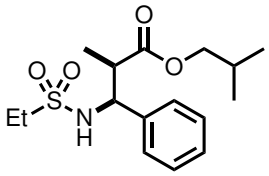

Obtained according to GP6; the title compound was isolated as a white solid in 96 % yield (126.1 mg) as a mixture of diastereomers (94:6 dr, crude dr: 88:12). The following NMR data are given for the *anti*-diastereomer.

^{1}H NMR (500 MHz, $CDCl_3$): δ 7.38–7.31 (m, 2H), 7.31–7.24 (m, 3H), 5.90 (d, J = 9.0 Hz, 1H), 4.57 (dd, J = 9.0, 6.5 Hz, 1H), 3.87–3.76 (m, 2H), 2.91–2.82 (m, 1H), 2.75 (dq, J = 14.6, 7.3 Hz, 1H), 2.63 (dq, J = 14.6, 7.3 Hz, 1H), 1.94–1.77 (m, 1H), 1.26 (d, J = 7.1 Hz, 3H), 1.15 (t, J = 7.3 Hz, 3H), 0.83 (d, J = 6.7 Hz, 6H).

^{13}C NMR (126 MHz, $CDCl_3$): δ 175.0, 140.2, 128.9, 128.2, 126.8, 71.2, 60.2, 48.4, 46.2, 27.7, 19.1, 19.0, 16.0, 8.2.

ESI-HRMS: calculated for $C_{16}H_{25}NO_4SNa$ $[M + Na]^+$: 350.139 65, found: 350.139 48.

***anti*-Methyl 2-methyl-3-((4-methylphenyl)sulfonamido)-3-phenylpropanoate (223)**:

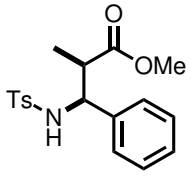

Obtained according to GP6 on 0.5 mmol scale; the title compound was isolated as a white solid in 87 % yield (152.2 mg) as a mixture of diastereomers (86:14 dr, crude dr: 84:16). The following NMR data are given for the *anti*-diastereomer.

^{1}H NMR (500 MHz, CD_2Cl_2): δ 7.52–7.47 (m, 2H), 7.16 (dt, J = 4.6, 1.7 Hz, 3H), 7.14–7.09 (m, 2H), 7.08–7.00 (m, 2H), 5.81 (d, J = 8.9 Hz, 1H), 4.44 (dd, J = 8.9, 6.4 Hz, 1H), 3.54 (s, 3H), 2.81 (m, 1H), 2.33 (s, 3H), 1.07 (d, J = 7.0 Hz, 3H).

***anti*-Ethyl 2-methyl-3-((4-methylphenyl)sulfonamido)-3-phenylpropanoate (227)**:

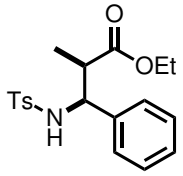

Obtained according to GP6 on 0.05 mmol scale; the title compound was not isolated, the yield was determined by crude ^{1}H NMR analysis with mesitylene as the internal standard (99 %, 73:27 dr). The following incomplete NMR data (signal overlap) are given for the *anti*-diastereomer.

^{1}H NMR (500 MHz, PhMe-d_8): δ 7.49 (d, J = 8.2 Hz, 2H), 6.91–6.84 (m, 5H), 6.65–6.59 (m, 2H), 5.98 (d, J = 9.2 Hz, 1H), 4.62 (t, J = 7.7 Hz, 1H), 3.84 (qd, J = 7.1, 1.7 Hz, 2H), 2.68–2.60 (m, 1H), 2.28 (s, 3H), 2.18 (s, 13H), 0.91 (t, J = 7.1 Hz, 3H).

***anti*-Isobutyl 2-methyl-3-((4-methylphenyl)sulfonamido)-3-phenylpropanoate (225)**:

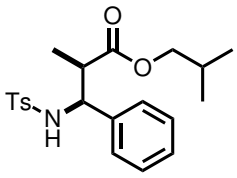

Obtained according to GP6 on 0.1 mmol scale; the title compound was isolated after preparative TLC as a white solid in 78 % yield (30.2 mg) as a mixture of diastereomers (83:17 dr, crude dr: 83:17). The following NMR data are given for the *anti*-diastereomer.

^{1}H NMR (500 MHz, CD_2Cl_2): δ 7.49 (d, J = 8.3 Hz, 2H), 7.17–7.13 (m, 3H), 7.11 (d, J = 8.3 Hz, 2H), 7.03 (dd, J = 6.7, 2.9 Hz, 2H), 5.98 (d, J = 8.8 Hz, 1H), 4.43 (dd, J = 8.8, 6.3 Hz, 1H), 3.74–3.65 (m, 2H), 2.86–2.75 (m, 1H), 2.32 (s, 3H), 1.80–1.70 (m, 1H), 1.06 (d, J = 7.1 Hz, 3H), 0.77 (d, J = 6.7 Hz, 6H).

^{13}C NMR (126 MHz, CD_2Cl_2): δ 174.8, 143.4, 139.5, 137.9, 129.5, 128.6, 127.7, 127.1, 126.8, 71.1, 60.3, 46.2, 27.8, 21.5, 18.9, 15.6.

ESI-HRMS: calculated for $C_{21}H_{27}NO_4SNa$ $[M + Na]^+$: 412.155 300, found: 412.155 510.

***anti*-Phenyl 2-methyl-3-((4-methylphenyl)sulfonamido)-3-phenylpropanoate (228):**

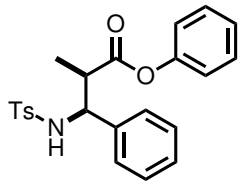

Obtained according to GP6 on 0.1 mmol scale; the title compound was isolated after filtration as a white solid in 68 % yield (28.0 mg) as a mixture of diastereomers (93:7 dr). The following NMR data are given for the *anti*-diastereomer.

^{1}H NMR (500 MHz, CD_2Cl_2): δ 7.51 (d, J = 8.4 Hz, 2H), 7.40 (dd, J = 8.5, 7.4 Hz, 2H), 7.32–7.24 (m, 1H), 7.23–7.16 (m, 2H), 7.12–7.06 (m, 5H), 7.00–6.93 (m, 2H), 5.98 (d, J = 9.6 Hz, 1H), 4.63 (dd, J = 9.6, 7.5 Hz, 1H), 3.12–3.02 (m, 1H), 2.34 (s, 3H), 1.22 (d, J = 7.1 Hz, 3H).
^{13}C NMR (126 MHz, CD_2Cl_2): δ 173.3, 150.3, 143.3, 138.4, 137.4, 129.5, 129.3, 128.5, 127.7, 126.9, 126.7, 126.1, 121.6, 60.4, 46.4, 21.2, 15.0.

4.5 Chiral Tertiary Amine-Catalyzed Silicon-Catalytic Mukaiyama–Mannich Reaction

(1*R*)-(6-methoxyquinolin-4-yl)((2*S*,5*S*)-5-vinylquinuclidin-2-yl)methanol (244):

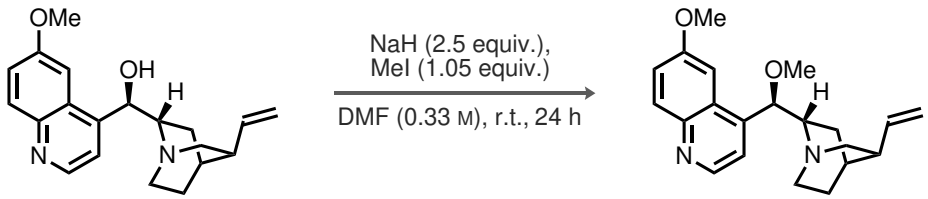

420 **244**

Following a literature procedure,[380] NaH (60 % in mineral oil, 2.50 equiv., 15.4 mmol, 616.4 mg) was added in three equally sized portions to a solution of quinine (1.00 equiv., 6.16 mmol, 2.00 g) in DMF (18.7 mL, 0.33 mol/L) at room temperature. Upon complete addition, the reaction was stirred for 1.5 h at room temperature. Subsequently, methyl iodide (1.05 equiv., 6.47 mmol, 407 µL) was added dropwise to the reaction mixture, followed by stirring for 24 h at room temperature. The reaction was terminated by careful addition of brine, and the aqueous layer was extracted with EtOAc (2 x). The combined organic extracts

were dried over Na_2SO_4, concentrated under reduced pressure, and directly purified by flash column chromatography on silica gel (first: EtOAc/MeOH 9:1, second: CH_2Cl_2/MeOH 19:1). The title compound was obtained in 79 % yield (1.64 g) as a colorless oil.

^{1}H NMR (500 MHz, CD_3OD): δ 8.68 (d, J = 4.6 Hz, 1H), 8.02–7.92 (m, 1H), 7.57 (d, J = 4.6 Hz, 1H), 7.48–7.40 (m, 2H), 5.74 (ddd, J = 17.5, 10.4, 7.5 Hz, 1H), 5.10 (d, J = 3.5 Hz, 1H), 4.96 (dt, J = 17.5, 1.5 Hz, 1H), 4.90 (dt, J = 10.4, 1.5 Hz, 1H), 4.10 (q, J = 7.1 Hz, 1H), 3.98 (s, 3H), 3.49 (dddd, J = 13.2, 10.3, 5.0, 2.5 Hz, 1H), 3.34 (s, 3H), 3.09 (dt, J = 10.8, 8.7 Hz, 2H), 2.79–2.69 (m, 1H), 2.64 (ddd, J = 13.7, 4.9, 2.6 Hz, 1H), 2.41–2.29 (m, 1H), 1.91–1.74 (m, 2H), 1.59 (ddp, J = 12.0, 7.9, 2.5 Hz, 1H), 1.56–1.45 (m, 1H).

The corresponding Mukaiyama–Mannich reactions with **244** were conducted according to the following procedure. Methyl propionate (3.0 equiv., 0.3 mmol, 28.9 µL) and allyltriisopropylsilane (1.0 equiv., 0.1 mmol, 24.1 µL) were added to a solution of bistriflimide (0.56 mol/L in DCE, 20 mol%, 35.7 µL) in CH_2Cl_2 or toluene (0.25 mL, 0.40 mol/L) at room temperature. The reaction was stirred for 1 h, until **244** (20 mol%, 6.77 mg) and imine **201** (1.0 equiv., 0.1 mmol, 25.93 mg) were added, followed by stirring for additional 16 h at room temperature. The reaction was terminated by addition of a mixture of triethylamine/methanol 1:1 (20 µL), and the yield determined by crude ^{1}H NMR analysis with mesitylene as the internal standard. An aliquot of the crude mixture was purified by preparative TLC (hexanes/EtOAc 7:3), and the enantiomeric ratio determined by subsequent HPLC measurement (OJ-3R, MeCN/H_2O 60:40, 1.0 mL/min, λ = 220 nm).

The discussion of the results can be found in Chapter 3, Section 3.4, Scheme 3.13.

4.6 Chiral Silane-Catalyzed Mukaiyama–Mannich Reaction

(*S*)-[1,1'-binaphthalene]-2,2'-diyl bis(trifluoromethanesulfonate) (**251**):

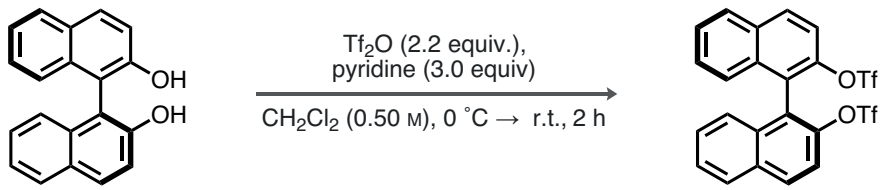

249 **251**

Tf_2O (2.2 equiv., 38.4 mmol, 6.5 mL) was added dropwise to a solution of pyridine (3.0 equiv., 52.4 mmol, 4.2 mL) and (*S*)-BINOL (1.0 equiv., 17.5 mmol, 5.00 g) in CH_2Cl_2 (35.0 mL, 0.50 mol/L) at 0 °C (ice/water bath). The reaction was allowed to warm to room temperature,

stirred for 2 h, and terminated by careful addition of water. The phases were separated, and the aqueous layer was extracted with CH_2Cl_2 (2 x). The combined organic extracts were dried over Na_2SO_4, concentrated under reduced pressure, and directly subjected to purification by flash column chromatography on silica gel (hexanes/CH_2Cl_2 7:3). The title compound was obtained in 99 % yield (9.56 g) as a white solid.[381]

^{1}H NMR (500 MHz, $CDCl_3$): δ 8.16 (d, J = 9.1 Hz, 2H), 8.03 (d, J = 8.3 Hz, 2H), 7.67 (d, J = 9.1 Hz, 2H), 7.60 (t, J = 7.5 Hz, 2H), 7.44 (t, J = 7.7 Hz, 2H), 7.32 (d, J = 8.5 Hz, 2H).
^{13}C NMR (126 MHz, $CDCl_3$): δ 145.6, 133.3, 132.5, 132.1, 128.5, 128.1, 127.5, 126.9, 123.6, 119.5, 118.3 (q, J = 319.1 Hz).
^{19}F NMR (471 MHz, $CDCl_3$): δ −74.58.

(*S*)-3,3'-diphenyl-[1,1'-binaphthalene]-2,2'-diyl bis(trifluoromethanesulfonate) (252):

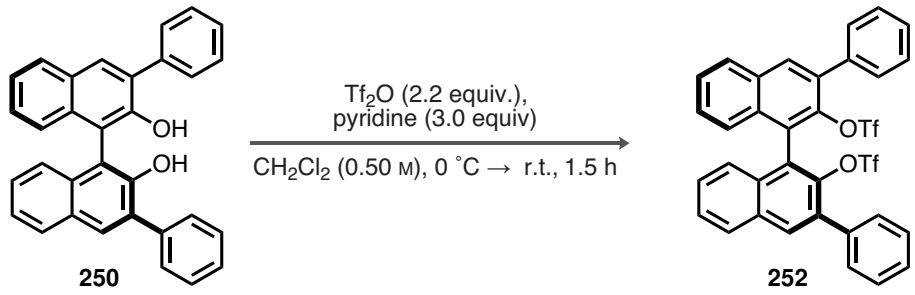

Tf_2O (2.2 equiv., 10.0 mmol, 1.7 mL) was added dropwise to a solution of pyridine (3.0 equiv., 13.7 mmol, 1.1 mL) and (*S*)-BINOL **250** (1.0 equiv., 4.6 mmol, 2.00 g) in CH_2Cl_2 (9.1 mL, 0.50 mol/L) at 0 °C. The reaction was allowed to warm to room temperature, stirred for 1.5 h, and terminated by careful addition of water. The phases were separated, and the aqueous layer was extracted with CH_2Cl_2 (2 x). The combined organic extracts were dried over Na_2SO_4, concentrated under reduced pressure, and directly subjected to purification by flash column chromatography on silica gel (hexanes/CH_2Cl_2 7:3). The title compound was obtained in 99 % yield (3.16 g) as a white solid.[381]

^{1}H NMR (500 MHz, $CDCl_3$): δ 8.12 (s, 2H), 7.99 (d, J = 8.2 Hz, 2H), 7.66–7.63 (m, 4H), 7.59 (ddd, J = 8.1, 6.6, 1.4 Hz, 2H), 7.53 (dd, J = 8.2, 6.6 Hz, 4H), 7.50–7.44 (m, 2H), 7.43–7.33 (m, 4H).
^{13}C NMR (126 MHz, $CDCl_3$): δ 144.2, 136.4, 134.6, 133.4, 133.0, 132.6, 130.0, 128.7, 128.6, 128.4, 127.8, 127.7, 127.7, 125.3.
^{19}F NMR (471 MHz, $CDCl_3$): δ −74.89.

(*S*)-2,2'-dimethyl-1,1'-binaphthalene (253):

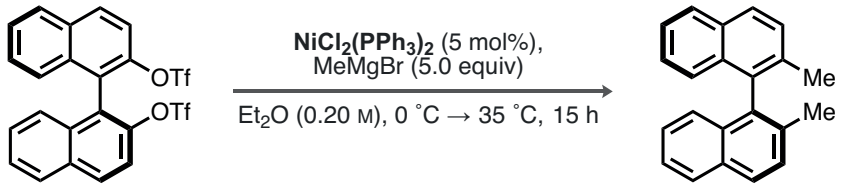

251 **253**

MeMgBr (3.0 mol/L in Et_2O, 5.0 equiv., 45.4 mmol, 15.1 mL) was added dropwise to a solution of **251** (1.0 equiv., 9.1 mmol, 5.00 g) and $NiCl_2(PPh_3)_2$ (5 mol%, 297.1 mg) in Et_2O (30 mL, final concentration 0.20 mol/L) at 0 °C (water/ice bath). The reaction mixture was subsequently transferred to an oil bath (set to 45 °C), and refluxed for 15 h. The reaction was terminated by careful addition of HCl (1.0 mol/L) at 0 °C, allowed to warm to room temperature, and diluted with CH_2Cl_2. The phases were separated, the aqueous layer extracted with CH_2Cl_2 (2 x), the combined organic extracts dried over Na_2SO_4, and concentrated under reduced pressure. The crude product was purified by flash column chromatography on silica gel (hexanes/CH_2Cl_2 39:1), providing the title compound in 68 % yield (1.75 g) as a white solid.[381]

^{1}H NMR (500 MHz, $CDCl_3$): δ 7.89 (t, J = 7.7 Hz, 4H), 7.51 (d, J = 8.4 Hz, 2H), 7.39 (ddd, J = 8.1, 6.7, 1.2 Hz, 2H), 7.21 (ddd, J = 8.3, 6.7, 1.3 Hz, 2H), 7.05 (dd, J = 8.5, 1.1 Hz, 2H), 2.04 (s, 6H).
^{13}C NMR (126 MHz, $CDCl_3$): δ 135.3, 134.4, 132.9, 132.4, 128.9, 128.1, 127.6, 126.2, 125.8, 125.0, 20.2.

(*S*)-2,2'-dimethyl-1,1'-binaphthalene (254):

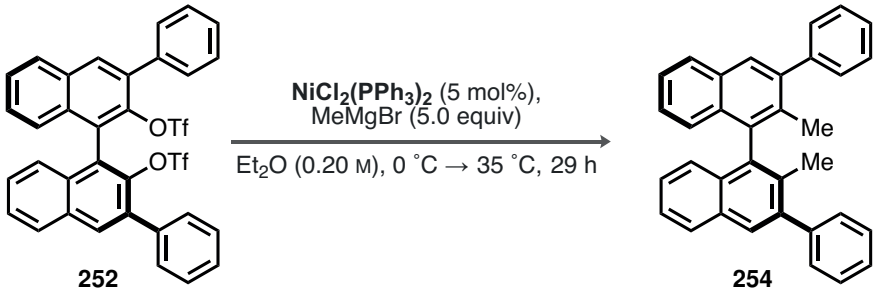

252 **254**

MeMgBr (3.0 mol/L in Et_2O, 5.0 equiv., 19.6 mmol, 6.5 mL) was added dropwise to a solution of **252** (1.0 equiv., 3.9 mmol, 2.75 g) and $NiCl_2(PPh_3)_2$ (5 mol%, 128.0 mg) in Et_2O (13.5 mL, final concentration 0.20 mol/L) at 0 °C (ice/water bath). The reaction mixture was subsequently transferred to an oil bath (set to 45 °C), and refluxed for 15 h.

The reaction was terminated by careful addition of HCl (1.0 mol/L) at 0 °C, allowed to warm to room temperature, and diluted with CH_2Cl_2. The phases were separated, the aqueous layer extracted with CH_2Cl_2 (2 x), the combined organic extracts dried over Na_2SO_4, and concentrated under reduced pressure. The crude product was purified by flash column chromatography on silica gel (hexanes/CH_2Cl_2 9:1), and subsequently recrystallized from hexanes/CH_2Cl_2, providing the title compound in 84 % yield (1.43 g) as a white solid.[381]

^{1}H NMR (500 MHz, $CDCl_3$): δ 7.90 (d, $J = 8.1$ Hz, 2H), 7.85 (s, 2H), 7.54–7.35 (m, 12H), 7.28–7.21 (m, 2H), 7.13 (d, $J = 8.5$ Hz, 2H), 1.96 (s, 6H).
^{13}C NMR (126 MHz, $CDCl_3$): δ 142.5, 141.5, 136.7, 132.8, 132.2, 129.7, 128.4, 128.2, 128.1, 127.1, 126.3, 125.9, 125.5, 18.4.

(*S*)-4-methyl-4-phenyl-4,5-dihydro-3*H*-dinaphtho[2,1-*c*:1',2'-*e*]silepine (255):

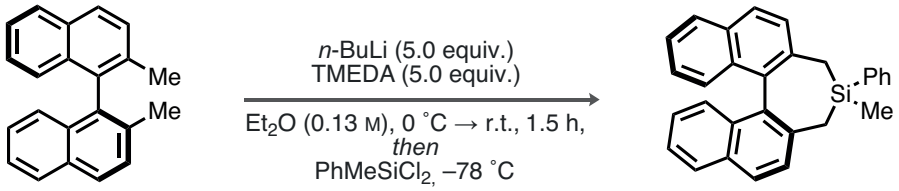

253 **255**

n-BuLi (2.5 mol/L in hexanes, 2.4 equiv., 0.85 mmol, 340 µL) was concentrated under high vacuum for 10 min at room temperature, followed by dissolution in Et_2O (0.51 mL). (*S*)-2,2'-dimethyl-1,1'-binaphthalene (1.0 equiv., 0.35 mmol, 100 mg) was added at 0 °C (ice/water bath), followed by stirring for 5 min, and subsequent addition of TMEDA (3.2 equiv., 1.15 mmol, 172 µL). The dark red solution was stirred for 15 h at room temperature. THF (0.50 mL) was added, followed by $PhSiMeCl_2$ (3.0 equiv., 1.06 mmol, 173 µL) at −78 °C (dry ice/acetone bath). The reaction was stirred for 7 h at −78 °C, and terminated by careful addition of water upon warm-up to room temperature. The crude mixture was diluted with CH_2Cl_2, the phases separated, and the aqueous layer extracted with CH_2Cl_2 (2 x). The combined organic extracts were dried over Na_2SO_4, concentrated under reduced pressure, and directly subjected to flash column chromatography on silica gel (hexanes/CH_2Cl_2 19:1 → 9:1). The title compound was obtained in 45 % yield (63.4 mg) as a white solid.

^{1}H NMR (500 MHz, $CDCl_3$): δ 7.95–7.92 (m, 2H), 7.92–7.88 (m, 1H), 7.82 (d, $J = 8.4$ Hz, 1H), 7.52 (d, $J = 8.4$ Hz, 1H), 7.43–7.36 (m, 4H), 7.36–7.28 (m, 4H), 7.19 (ddt, $J = 8.2$, 6.6, 1.4 Hz, 2H), 7.11 (ddd, $J = 13.2$, 8.6, 1.1 Hz, 2H), 2.29 (d, $J = 13.1$ Hz, 1H), 2.25 (d, $J = 13.4$ Hz, 1H), 2.18 (d, $J = 13.1$ Hz, 1H), 2.05 (d, $J = 13.4$ Hz, 1H), 0.32 (s, 3H).
^{13}C NMR (126 MHz, $CDCl_3$): δ 137.2, 136.8, 136.7, 134.3, 133.1, 133.1, 132.8, 132.7, 132.4, 132.3, 129.9, 128.6, 128.5, 128.5, 128.4, 128.3, 128.2, 128.0, 126.6, 126.2, 126.1, 124.7, 124.7,

23.3, 22.9, –4.8.
^{29}Si NMR (99 MHz, $CDCl_3$): δ 12.77.

(*S*)-2'-methoxy-[1,1'-binaphthalen]-2-yl trifluoromethanesulfonate (421):

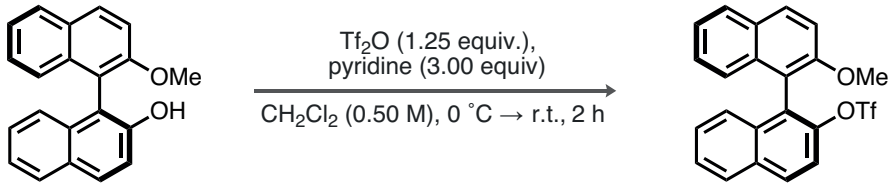

422 **421**

Tf_2O (1.25 equiv., 7.6 mmol, 1.3 mL) was added dropwise to a solution of pyridine (3.00 equiv., 18.3 mmol, 1.5 mL) and (*S*)-2'-methoxy-[1,1'-binaphthalen]-2-ol **422** (1.00 equiv., 6.1 mmol, 1.83 g) in CH_2Cl_2 (12.2 mL, 0.50 mol/L) at 0 °C (ice/water bath). The reaction was allowed to warm to room temperature, stirred for 2 h, and terminated by careful addition of water. The phases were separated, and the aqueous layer was extracted with CH_2Cl_2 (2 x). The combined organic extracts were dried over Na_2SO_4, concentrated under reduced pressure, and directly subjected to purification by flash column chromatography on silica gel (hexanes/CH_2Cl_2 1:1). The title compound was obtained in 79 % yield (2.08 g) as a white solid.[381]

^{1}H NMR (500 MHz, $CDCl_3$): δ 8.05 (t, J = 8.8 Hz, 2H), 7.98 (d, J = 8.2 Hz, 1H), 7.92–7.87 (m, 1H), 7.59–7.51 (m, 2H), 7.46 (d, J = 9.1 Hz, 1H), 7.40–7.29 (m, 3H), 7.29–7.21 (m, 1H), 7.02 (dd, J = 8.6, 1.0 Hz, 1H), 3.83 (s, 3H).
^{13}C NMR (126 MHz, $CDCl_3$): δ 155.3, 145.8, 133.8, 133.7, 132.7, 131.2, 129.0, 128.4, 128.2, 127.5, 127.4, 127.1, 127.0, 127.0, 124.9, 123.8, 119.7, 115.3, 113.1, 56.3.
^{19}F NMR (471 MHz, $CDCl_3$): δ –74.91.

(*R*)-2-methoxy-2'-methyl-1,1'-binaphthalene (423):

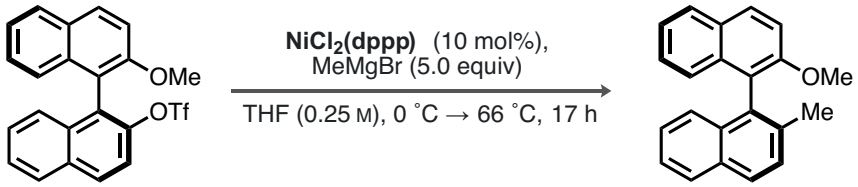

421 **423**

MeMgBr (3.0 mol/L in Et_2O, 5.0 equiv., 23.1 mmol, 7.7 mL) was added dropwise to a solution of **421** (1.0 equiv., 4.6 mmol, 2.00 g) and $NiCl_2$(dppp) (10 mol%, 250.7 mg) in THF (10.8 mL, final concentration 0.25 mol/L) at 0 °C (ice/water bath). The reaction

mixture was subsequently transferred to an oil bath (set to 70 °C), and refluxed for 17 h. The reaction was terminated by careful addition of HCl (1.0 mol/L) at 0 °C, allowed to warm to room temperature, and diluted with CH_2Cl_2. The phases were separated, the aqueous layer extracted with CH_2Cl_2 (2 x), the combined organic extracts dried over Na_2SO_4, and concentrated under reduced pressure. The crude product was purified by flash column chromatography on silica gel (hexanes → hexanes/CH_2Cl_2 9:1 → 4:1), and subsequently recrystallized from hexanes/CH_2Cl_2, providing the title compound in 99 % yield (1.36 g) as a white solid.[249]

^{1}H NMR (500 MHz, $CDCl_3$): δ 7.99 (d, J = 8.9 Hz, 1H), 7.88 (dd, J = 8.3, 4.8 Hz, 3H), 7.51 (d, J = 8.3 Hz, 1H), 7.46 (d, J = 9.0 Hz, 1H), 7.38 (ddd, J = 8.1, 6.6, 1.3 Hz, 1H), 7.32 (ddd, J = 8.1, 6.7, 1.2 Hz, 1H), 7.20 (ddt, J = 8.1, 6.6, 1.2 Hz, 2H), 7.13 (dd, J = 8.5, 1.1 Hz, 1H), 7.00 (dd, J = 8.6, 1.1 Hz, 1H), 3.76 (s, 3H), 2.10 (s, 3H).
^{13}C NMR (126 MHz, $CDCl_3$): δ 154.5, 135.0, 133.7, 133.2, 132.4, 132.1, 129.4, 129.2, 128.7, 127.9, 127.9, 127.5, 126.5, 125.8, 125.1, 124.7, 123.6, 122.1, 113.9, 56.6, 20.3.

(*R*)-2-methoxy-2'-methyl-1,1'-binaphthalene (424):

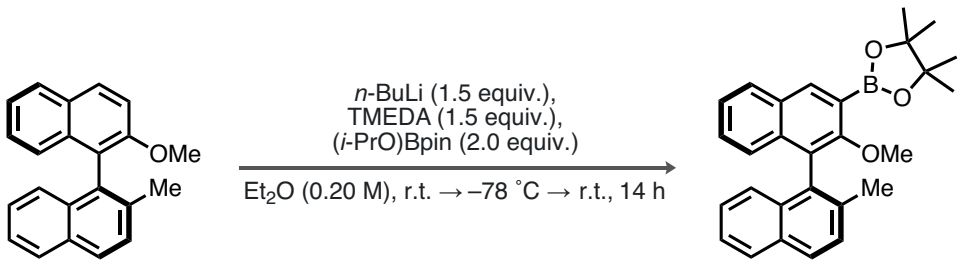

423 **424**

n-BuLi (2.5 mol/L in hexanes, 1.5 equiv., 5.0 mmol, 2.0 mL) was added to a solution of TMEDA (1.5 equiv., 5.0 mmol, 754 µL) in Et_2O (16.8 mL, 0.20 mol/L) at room temperature and the reaction was stirred for 30 min, until (*R*)-2-methoxy-2'-methyl-1,1'-binaphthalene **423** (1.0 equiv., 3.4 mmol, 1.00 g) was added. The reaction was stirred for 8 h at room temperature, followed by cooling to −78 °C (dry ice/acetone bath). 2-Isopropoxy-4,4,5,5-tetramethyl-1,3,2-dioxaborolane (2.0 equiv., 6.7 mmol, 1.4 mL) was added, and the reaction was subsequently allowed to warm to room temperature. The reaction was terminated after 14 h at room temperature by careful addition of sat. aq. NH_4Cl solution, the phases were separated, and the aqueous layer was extracted with CH_2Cl_2 (2 x). The combined extracts were dried over Na_2SO_4, concentrated under reduced pressure, and directly subjected to flash column chromatography on silica gel (hexanes/MTBE 9:1). The title compound was obtained in 74 % yield (1.05 g) as a white solid.

^{1}H NMR (500 MHz, $CDCl_3$): δ 8.44 (s, 1H), 7.96–7.91 (m, 1H), 7.87 (d, J = 8.3 Hz, 2H), 7.50 (d, J = 8.4 Hz, 1H), 7.37 (tdd, J = 8.1, 3.8, 1.3 Hz, 2H), 7.28–7.12 (m, 3H), 7.07–7.00 (m, 1H), 3.39 (s, 3H), 2.13 (s, 3H), 1.42 (s, 9H), 1.42 (s, 9H).

(*R*)-2-methoxy-2'-methyl-3-phenyl-1,1'-binaphthalene (425):

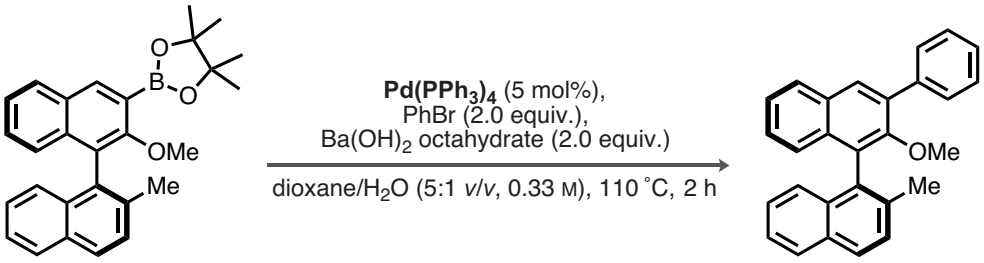

424 **425**

(*R*)-2-methoxy-2'-methyl-1,1'-binaphthalene **424** (1.0 equiv., 2.0 mmol, 850.0 mg), bromobenzene (2.0 equiv., 4.0 mmol, 422 µL), and $BaOH_2$ octahydrate (2.0 equiv., 4.0 mmol, 1.26 g) were suspended in 1,4-dioxane/H_2O (5:1, 6.0 mL, 0.33 mol/L) at room temperature. The suspension was degassed by a constant flow of Ar for 10 min, followed by the addition of $Pd(PPh_3)_4$ (5 mol%, 115.7 mg). The reaction was transferred to an oil bath (set to 130 °C) and refluxed for 2 h. After cooling to room temperature, the reaction was terminated by addition of HCl (3.0 mol/L), the phases were separated, and the aqueous layer was extracted with CH_2Cl_2 (3 x). The combined organic extracts were dried over Na_2SO_4, concentrated under reduced pressure, and directly subjected to flash column chromatography on silica gel (hexanes/CH_2Cl_2 49:1 → 9:1 → 4:1). The title compound was obtained in 87 % yield (651.0 mg) as a white solid.

^{1}H NMR (500 MHz, $CDCl_3$): δ 7.97 (s, 1H), 7.91 (dd, J = 13.2, 8.2 Hz, 3H), 7.80–7.72 (m, 2H), 7.53 (d, J = 8.4 Hz, 1H), 7.47 (t, J = 7.6 Hz, 2H), 7.44–7.35 (m, 3H), 7.31–7.20 (m, 3H), 7.06 (d, J = 8.5 Hz, 1H), 3.03 (s, 3H), 2.22 (s, 3H).
^{13}C NMR (126 MHz, $CDCl_3$): δ 139.0, 135.3, 135.1, 133.5, 133.2, 132.6, 132.2, 131.1, 130.4, 129.5, 128.8, 128.4, 128.2, 128.1, 127.8, 127.4, 126.5, 126.2, 126.1, 125.6, 125.2, 124.9, 60.4, 20.8.

(*R*)-2'-methyl-3-phenyl-[1,1'-binaphthalen]-2-ol (263):

BBr_3 (1.0 mol/L in CH_2Cl_2, 1.25 equiv., 1.5 mmol, 1.5 mL) was added dropwise to a solution of (*R*)-2-methoxy-2'-methyl-3-phenyl-1,1'-binaphthalene **425** (1.00 equiv., 1.2 mmol, 450.0 mg) in CH_2Cl_2 (12.0 mL, 0.10 mol/L) at 0 °C (ice/water bath). The reaction mixture was stirred for 90 min at 0 °C, followed by the careful addition of HCl (1.0 mol/L) at the

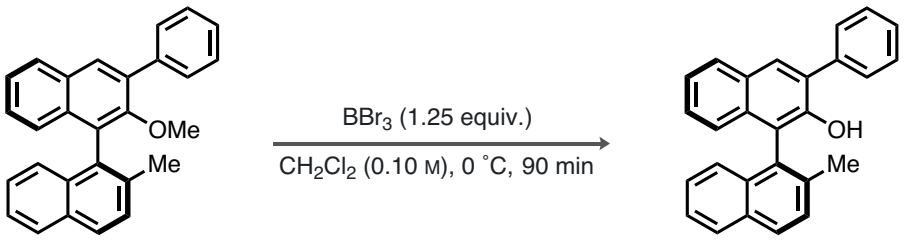

425 **263**

same temperature. Upon warming to room temperature, the phases were separated and the aqueous layer was extracted with CH_2Cl_2 (2 x). The combined organic extracts were dried over Na_2SO_4, concentrated under reduced pressure, and directly subjected to flash column chromatography on silica gel (hexanes/MTBE 39:1). The title compound was obtained in 90 % yield (435.0 mg) as a white solid.

^{1}H NMR (500 MHz, $CDCl_3$): δ 7.98–7.86 (m, 4H), 7.79–7.71 (m, 2H), 7.57 (d, $J = 8.4$ Hz, 1H), 7.52–7.43 (m, 3H), 7.42–7.37 (m, 1H), 7.35 (ddd, $J = 8.1$, 6.7, 1.2 Hz, 1H), 7.33–7.29 (m, 2H), 7.23 (ddd, $J = 8.2$, 6.7, 1.3 Hz, 1H), 6.97 (d, $J = 8.4$ Hz, 1H), 5.00 (s, 1H), 2.20 (s, 3H).

(*S*)-2'-methoxy-3,3'-diphenyl-[1,1'-binaphthalen]-2-ol (**426**):

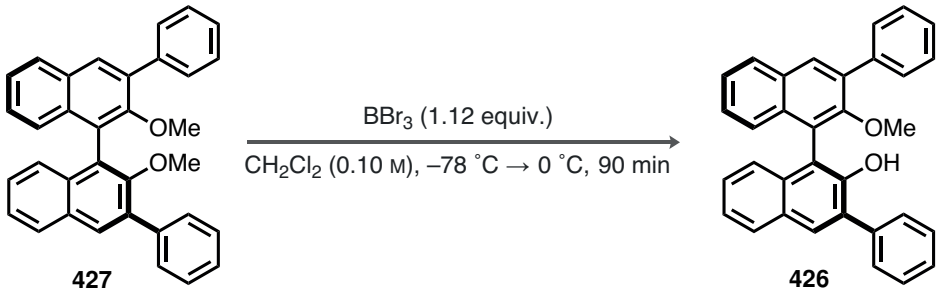

427 **426**

BBr_3 (1.0 mol/L in CH_2Cl_2, 1.12 equiv., 1.8 mmol, 1.8 mL) was added dropwise to a solution of (*S*)-2,2'-dimethoxy-3,3'-diphenyl-1,1'-binaphthalene **427** (1.00 equiv., 1.6 mmol, 758.0 mg) in CH_2Cl_2 (18.0 mL, 0.10 mol/L) at −78 °C (dry ice/acetone bath). The reaction mixture was stirred for 90 min at −78 °C, warmed up to 0 °C (ice/water bath), and was stirred for additional 10 min. The reaction was terminated by the careful addition of HCl (1.0 mol/L) at 0 °C. Upon warming to room temperature, the phases were separated and the aqueous layer was extracted with CH_2Cl_2 (2 x). The combined organic extracts were dried over Na_2SO_4, concentrated under reduced pressure, and directly subjected to flash column chromatography on silica gel (hexanes/EtOAc 19:1). The title compound was obtained in 85 % yield (626.0 mg) as a white solid.

^{1}H NMR (500 MHz, $CDCl_3$): δ 8.04 (s, 1H), 7.98–7.93 (m, 2H), 7.92–7.88 (m, 1H), 7.75 (dt, J = 8.1, 1.2 Hz, 4H), 7.53–7.38 (m, 7H), 7.36 (ddd, J = 8.1, 6.8, 1.3 Hz, 1H), 7.33–7.25 (m, 3H), 7.19 (dd, J = 8.4, 1.2 Hz, 1H), 5.32 (s, 1H), 3.18 (s, 3H).
^{13}C NMR (126 MHz, $CDCl_3$): δ 155.3, 148.9, 138.5, 138.0, 135.6, 133.7, 133.4, 131.7, 131.4, 130.6, 130.3, 129.8, 129.5, 129.2, 128.6, 128.5, 128.4, 128.3, 127.8, 127.6, 127.1, 126.8, 125.8, 125.6, 125.0, 123.9, 123.1, 116.4, 60.9.

(*S*)-2'-methoxy-3,3'-diphenyl-[1,1'-binaphthalen]-2-ol (**428**):

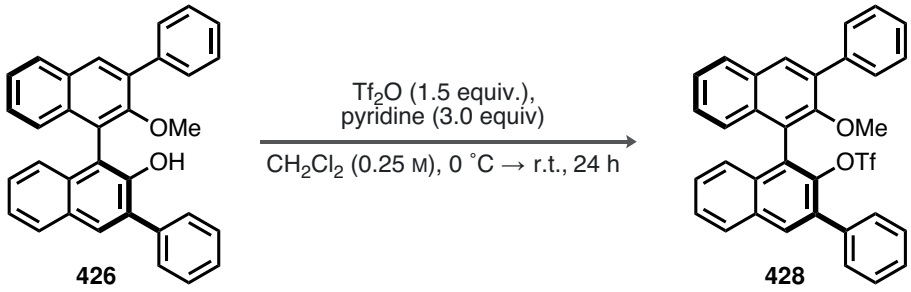

Tf_2O (1.5 equiv., 1.8 mmol, 296 µL) was added dropwise to a solution of pyridine (3.0 equiv., 3.5 mmol, 285 µL) and (*S*)-2'-methoxy-3,3'-diphenyl-[1,1'-binaphthalen]-2-ol **426** (1.0 equiv., 1.2 mmol, 531.0 mg) in CH_2Cl_2 (4.7 mL, 0.25 mol/L) at 0 °C (ice/water bath). The reaction was allowed to warm to room temperature, stirred for 24 h, and terminated by careful addition of water. The phases were separated, and the aqueous layer was extracted with CH_2Cl_2 (2 x). The combined organic extracts were dried over Na_2SO_4, concentrated under reduced pressure, and directly subjected to purification by flash column chromatography on silica gel (hexanes/MTBE 19:1). The title compound was obtained in 99 % yield (681.0 g) as a white solid.[381]

^{1}H NMR (500 MHz, $CDCl_3$): δ 8.03 (d, J = 6.1 Hz, 2H), 7.99 (d, J = 8.2 Hz, 1H), 7.92 (d, J = 8.1 Hz, 1H), 7.78–7.73 (m, 2H), 7.68–7.63 (m, 2H), 7.57 (ddd, J = 8.2, 6.3, 1.7 Hz, 1H), 7.53–7.35 (m, 9H), 7.31 (ddd, J = 8.2, 6.8, 1.3 Hz, 1H), 7.22 (d, J = 8.5 Hz, 1H), 3.17 (s, 3H).
^{13}C NMR (126 MHz, $CDCl_3$): δ 154.9, 143.9, 138.8, 136.8, 135.0, 134.7, 133.4, 133.1, 132.6, 132.3, 131.7, 130.8, 130.1, 129.3, 128.6, 128.6, 128.5, 128.4, 128.4, 128.2, 127.6, 127.4, 127.4, 127.2, 126.7, 126.2, 125.3, 122.4, 60.8.
^{19}F NMR (471 MHz, $CDCl_3$): δ −74.91.

(*R*)-2-methoxy-2'-methyl-3,3'-diphenyl-1,1'-binaphthalene (**429**):

MeMgBr (3.0 mol/L in Et_2O, 5.0 equiv., 2.6 mmol, 855 µL) was added dropwise to a solution of **428** (1.0 equiv., 0.5 mmol, 300.0 mg) and $NiCl_2$(dppp) (10 mol%, 27.8 mg) in THF

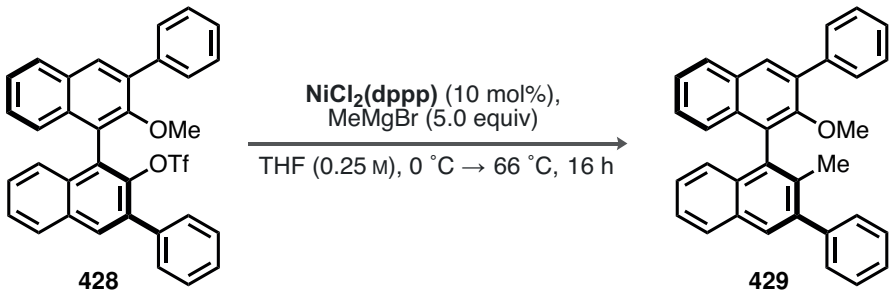

428 **429**

(1.2 mL, final concentration 0.25 mol/L) at 0 °C (ice/water bath). The reaction mixture was subsequently transferred to an oil bath (set to 70 °C), and refluxed for 16 h. The reaction was terminated by careful addition of HCl (1.0 mol/L) at 0 °C, allowed to warm to room temperature, and diluted with CH_2Cl_2. The phases were separated, the aqueous layer extracted with CH_2Cl_2 (2 x), the combined organic extracts dried over Na_2SO_4, and concentrated under reduced pressure. The crude product was purified by flash column chromatography on silica gel (hexanes/MTBE 33:1), providing the title compound in 95 % yield (219.0 mg) as a white solid.[249]

^{1}H NMR (500 MHz, $CDCl_3$): δ 7.97 (s, 1H), 7.95–7.91 (m, 1H), 7.91–7.87 (m, 1H), 7.86 (s, 1H), 7.77–7.73 (m, 2H), 7.54–7.35 (m, 10H), 7.29–7.23 (m, 3H), 7.15 (dd, J = 8.5, 1.1 Hz, 1H), 3.08 (s, 3H), 2.08 (s, 3H).
^{13}C NMR (126 MHz, $CDCl_3$): δ 153.7, 142.5, 141.3, 139.0, 135.4, 133.5, 133.2, 132.8, 132.0, 131.1, 130.4, 129.7, 129.5, 128.7, 128.5, 128.2, 128.1, 127.4, 127.0, 126.6, 126.2, 126.1, 125.7, 125.4, 125.3, 60.4, 19.0.

(*R*)-2'-methyl-3,3'-diphenyl-[1,1'-binaphthalen]-2-ol (**264**):

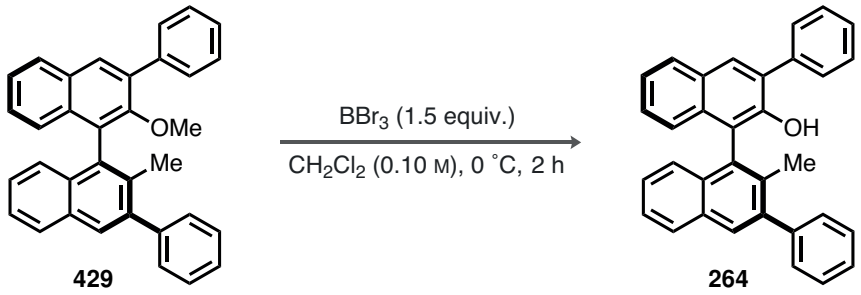

429 **264**

BBr_3 (1.0 mol/L in CH_2Cl_2, 1.5 equiv., 0.73 mmol, 729 µL) was added dropwise to a solution of **429** (1.00 equiv., 0.49 mmol, 219.0 mg) in CH_2Cl_2 (5.0 mL) at 0 °C (ice/water bath). The reaction mixture was stirred for 2 h at 0 °C, then terminated by the careful addition of HCl (1.0 mol/L) at 0 °C. Upon warming to room temperature, the phases were separated and the aqueous layer was extracted with CH_2Cl_2 (2 x). The combined organic extracts were dried over Na_2SO_4, concentrated under reduced pressure, and directly subjected to flash column

chromatography on silica gel (hexanes/MTBE 50:1). The title compound was obtained in 87 % yield (185.0 mg) as a white solid.

^{1}H NMR (500 MHz, $CDCl_3$): δ 7.99 (s, 1H), 7.97–7.91 (m, 3H), 7.81 – 7.74 (m, 2H), 7.56–7.46 (m, 6H), 7.46–7.36 (m, 3H), 7.35–7.26 (m, 2H), 7.09 (dd, J = 8.5, 1.1 Hz, 1H), 5.12 (s, 1H), 2.09 (s, 3H).
^{13}C NMR (126 MHz, $CDCl_3$): δ 148.4, 142.1, 141.7, 138.0, 135.6, 133.0, 132.6, 132.5, 130.1, 129.9, 129.8, 129.6, 129.4, 128.5, 128.4, 128.3, 128.3, 127.7, 127.3, 126.9, 126.9, 126.1, 125.7, 124.6, 124.0, 119.2, 18.5.

(*S*)-3'-methoxy-[2,2':4',1":3",2"']-quaternaphthalen]-2"-yl trifluoromethanesulfonate (430):

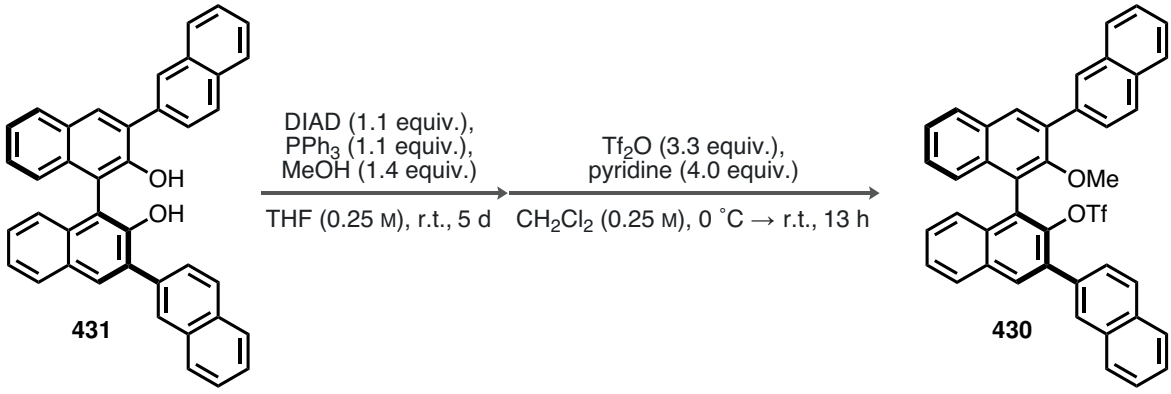

MeOH (1.4 equiv., 1.37 mmol, 55.4 µL) and diisopropyl diazene-1,2-dicarboxylate (DIAD, 1.1 equiv., 1.07 mmol, 225 µL) were added to a solution of (*S*)-BINOL **431** (1.0 equiv., 0.98 mmol, 526.0 mg) and PPh_3 (1.1 equiv., 1.07 mmol, 281.7 mg) in tetrahydrofuran (3.9 mL, 0.25 mol/L) at room temperature, followed by stirring for 5 d. The crude mixture was concentrated under reduced pressure and directly used in the subsequent step without further purification.[382]
The crude product was dissolved in CH_2Cl_2 (3.9 mL, 0.25 mol/L) at room temperature, followed by the addition of Tf_2O (3.3 equiv., 3.22 mmol, 542 µL) and pyridine (4.0 equiv., 3.91 mmol, 316 µL) at 0 °C (ice/water bath). The reaction was allowed to warm to room temperature and stirred for 13 h, followed by the careful addition of water. The phases were separated, and the aqueous layer was extracted with CH_2Cl_2 (2 x). The combined organic extracts were dried over Na_2SO_4, concentrated under reduced pressure, and filtered over a pad of Celite (hexanes/MTBE 4:1). The obtained mixture was directly used in the next sequence of steps without further purification.

(*R*)-3'-methyl-[2,2':4',1":3",2"']-quaternaphthalen]-2"-ol (**265**):

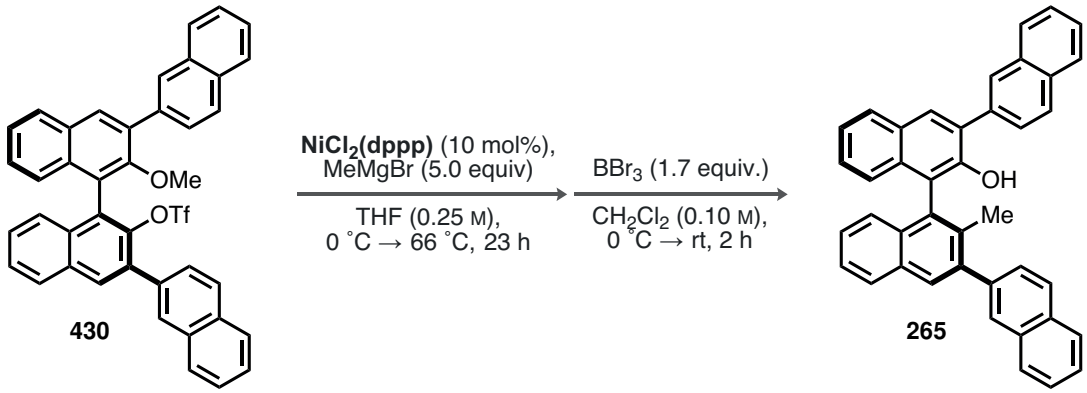

MeMgBr (3.0 mol/L in Et_2O, 5.0 equiv., 4.9 mmol, 1.6 mL) was added dropwise to a solution of the crude product from the previous step and $NiCl_2$(dppp) (10 mol%, 52.9 mg) in THF (2.3 mL, final concentration 0.25 mol/L) at 0 °C (ice/water bath). The reaction mixture was subsequently transferred to an oil bath (set to 70 °C), and refluxed for 23 h. The reaction was terminated by careful addition of HCl (1.0 mol/L) at 0 °C, allowed to warm to room temperature, and diluted with CH_2Cl_2. The phases were separated, the aqueous layer extracted with CH_2Cl_2 (2 x), the combined organic extracts dried over Na_2SO_4, and concentrated under reduced pressure. The crude product was filtered over a pad of Celite, and directly used in the next step without further purification.[249]

The crude product of the Kumada coupling was dissolved in CH_2Cl_2 (12.0 mL) at room temperature. BBr_3 (1.0 mol/L in CH_2Cl_2, 1.7 equiv., 1.7 mmol, 1.7 mL) was added dropwise at 0 °C (ice/water bath). The reaction mixture was allowed to warm to room temperature and stirred for 2 h, then terminated by the careful addition of HCl (1.0 mol/L) at 0 °C. Upon warming to room temperature, the phases were separated and the aqueous layer was extracted with CH_2Cl_2 (2 x). The combined organic extracts were dried over Na_2SO_4, concentrated under reduced pressure, and directly subjected to flash column chromatography on silica gel (hexanes/MTBE 50:1). The title compound was obtained in 32 % yield (167.0 mg, over four steps) as a white solid.

^{1}H NMR (500 MHz, $CDCl_3$): δ 8.25–8.18 (m, 1H), 8.09 (s, 1H), 8.02 (s, 1H), 7.98–7.87 (m, 10H), 7.62 (dd, J = 8.4, 1.7 Hz, 1H), 7.57–7.47 (m, 5H), 7.42–7.28 (m, 4H), 7.13 (dd, J = 8.4, 1.1 Hz, 1H), 5.21 (s, 1H), 2.14 (s, 3H).

^{13}C NMR (126 MHz, $CDCl_3$): δ 148.6, 141.7, 139.6, 135.8, 135.6, 133.7, 133.5, 133.1, 132.9, 132.7, 132.6, 132.6, 130.5, 130.4, 130.2, 129.4, 128.6, 128.5, 128.3, 128.3, 128.2, 128.1, 128.0, 127.9, 127.9, 127.8, 127.8, 127.0, 127.0, 126.5, 126.4, 126.3, 126.2, 126.2, 125.8, 124.7, 124.1, 119.2, 18.7.

4.6.1 Synthesis of Allyl(diisopropyl)aryloxysilanes (GP7)

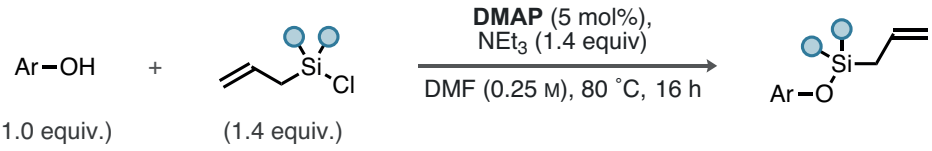

Following a literature procedure,[383] the respective allyl(dialkyl)chlorosilane (1.4 equiv.) was added to a solution of NEt_3 (1.4 equiv.), DMAP (5 mol%), and the hydroxyarene (1.0 equiv.) at room temperature. The reaction was transferred to an oil bath (set to 80 °C), and stirred for 16 h at 80 °C. Upon full conversion of the hydroxyarene, the reaction was allowed to cool to room temperature, and diluted with water and CH_2Cl_2. The phases were separated, and the aqueous layer was extracted with CH_2Cl_2 (2 x). The combined organic extracts were dried over Na_2SO_4, concentrated under reduced pressure, and directly purified by flash column chromatography on silica gel (hexanes/MTBE 39:1).

Allyldiisopropyl(mesityloxy)silane (**261**):

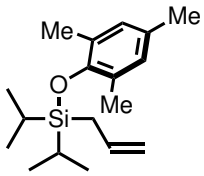

Obtained according to GP7 with allyl(diisopropylchlorosilane) and mesitol on 0.75 mmol scale; the title compound was isolated in 84 % yield (182.0 mg) as a clear oil.

^{1}H NMR (500 MHz, CD_2Cl_2): δ 6.83–6.70 (m, 2H), 5.87 (ddt, J = 16.9, 10.1, 8.1 Hz, 1H), 4.94 (dq, J = 16.9, 1.7 Hz, 1H), 4.85 (dq, J = 10.1, 2.3 Hz, 1H), 2.19 (s, 9H), 1.89 (dt, J = 8.1, 1.4 Hz, 2H), 1.25–1.16 (m, 2H), 1.06 (dd, J = 7.4, 1.6 Hz, 12H).

(*R*)-Allyldiisopropyl((2'-methyl-3-phenyl-[1,1'-binaphthalen]-2-yl)oxy)silane (**266**):

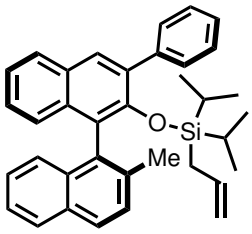

Obtained according to GP7 with allyl(diisopropyl)chlorosilane and (*R*)-2'-methyl-3-phenyl-[1,1'-binaphthalen]-2-ol (**263**) on 0.83 mmol scale after 20 h; the title compound was isolated in 56 % yield (241.0 mg) as a clear oil.

^{1}H NMR (500 MHz, CD_2Cl_2): δ 7.96–7.88 (m, 4H), 7.73–7.65 (m, 2H), 7.57 (d, J = 8.4 Hz, 1H), 7.49 (t, J = 7.5 Hz, 2H), 7.46–7.34 (m, 4H), 7.30 (ddd, J = 8.3, 6.6, 1.3 Hz, 1H), 7.21 (ddd, J = 8.2, 6.8, 1.3 Hz, 1H), 7.01 (d, J = 8.5 Hz, 1H), 5.21 (dq, J = 16.6, 10.0 Hz, 1H), 4.54 (dd, J = 10.0, 2.3 Hz, 1H), 4.50 (dd, J = 16.6, 2.2 Hz, 1H), 2.31 (s, 3H), 0.67 (qd, J = 14.0, 8.1 Hz, 2H), 0.56 (d, J = 7.5 Hz, 2H), 0.53 (d, J = 7.6 Hz, 6H), 0.50 (d, J = 7.5 Hz, 3H), 0.15 (p, J = 7.5 Hz, 1H), 0.06 (p, J = 7.5 Hz, 1H).
^{13}C NMR (126 MHz, CD_2Cl_2): δ 150.0, 140.4, 136.3, 136.1, 135.1, 133.9, 133.7, 133.4, 132.9, 131.0, 130.6, 130.1, 129.4, 128.6, 128.4, 128.4, 128.2, 127.7, 127.1, 126.6, 126.2, 126.0, 125.4, 125.2, 124.6, 113.4, 21.0, 20.0, 17.4, 17.4, 13.8, 13.7.
ESI-HRMS: calculated for $C_{36}H_{38}OSiNa$ $[M + Na]^+$: 537.258 41, found: 537.258 21.

(*R*)-Allyldiisopropyl((2'-methyl-3,3'-diphenyl-[1,1'-binaphthalen]-2-yl)oxy)silane (267):

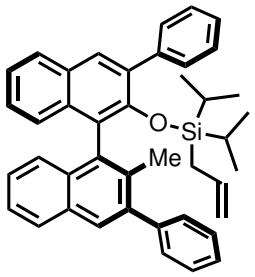

Obtained according to GP7 with allyl(diisopropyl)chlorosilane and (*R*)-2'-methyl-3,3'-diphenyl-[1,1'-binaphthalen]-2-ol (**264**) on 0.29 mmol scale after 14 h; the title compound was isolated in 76 % yield (127.9 mg) as a clear oil.

^{1}H NMR (500 MHz, CD_2Cl_2): δ 7.96–7.89 (m, 3H), 7.87 (s, 1H), 7.67 (dd, J = 8.2, 1.4 Hz, 2H), 7.53–7.22 (m, 13H), 7.11 (d, J = 8.5 Hz, 1H), 5.24 (ddt, J = 16.6, 10.3, 8.1 Hz, 1H), 4.61–4.49 (m, 2H), 2.14 (s, 3H), 0.83–0.75 (m, 1H), 0.73–0.63 (m, 1H), 0.57 (dd, J = 7.5, 2.8 Hz, 6H), 0.53 (dd, J = 7.5, 2.2 Hz, 6H), 0.23 (p, J = 7.5 Hz, 1H), 0.11 (p, J = 7.5 Hz, 1H).
ESI-HRMS: calculated for $C_{42}H_{42}OSiNa$ $[M + Na]^+$: 613.289 71, found: 613.290 25.

(*R*)-Allyldiisopropyl((3'-methyl-[1,2':4',1":3",1"'-quaternaphthalen]-2"-yl)oxy)silane (268):

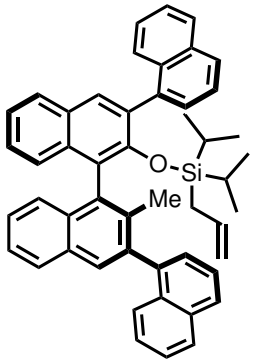

Obtained according to GP7 with allyl(diisopropyl)chlorosilane and (*R*)-3'-methyl-[2,2':4',1":3",2"'-quaternaphthalen]-2"-ol (**265**) on 0.12 mmol scale after 14 h; the title compound was isolated in 45 % yield (37.2 mg) as a clear oil.

^{1}H NMR (500 MHz, $CDCl_3$): δ 8.09 (d, J = 1.7 Hz, 1H), 7.99–7.86 (m, 9H), 7.76 (dd, J = 8.4, 1.7 Hz, 1H), 7.62 (dd, J = 8.3, 1.8 Hz, 1H), 7.53 (ddt, J = 11.7, 6.0, 2.6 Hz, 6H), 7.47–7.27 (m, 5H), 7.17 (d, J = 8.5 Hz, 1H), 5.24–5.10 (m, 1H), 4.58–4.49 (m, 1H), 4.45 (dd, J = 16.8, 2.2 Hz, 1H), 2.19 (s, 3H), 0.68–0.59 (m, 2H), 0.52 (d, J = 7.5 Hz, 3H), 0.50 (d, J = 7.5 Hz, 3H), 0.46 (t, J = 7.3 Hz, 6H), 0.17 (dq, J = 15.0, 8.0 Hz, 1H), 0.03 (dq, J = 15.0, 7.5 Hz, 1H).
ESI-HRMS: calculated for $C_{50}H_{46}OSiNa$ $[M+Na]^+$: 713.321 013, found: 713.321 140.

4.6.2 Alternative Synthesis of Allyl(diisopropyl)aryloxysilanes (GP8)

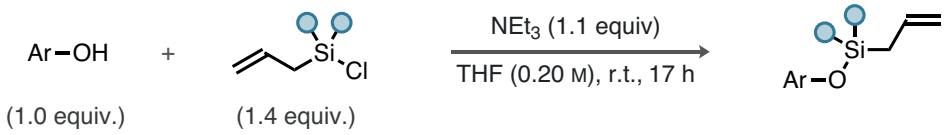

A solution of the hydroxyarene (1.0 equiv.) and NEt_3 (1.1 equiv.) in THF (0.38 mol/L) was added dropwise to a solution of the allyl(dialkyl)chlorosilane (1.4 equiv.) in THF (0.62 mol/L) at room temperature. Upon complete addition, the reaction was stirred for 17 h at room temperature. Subsequently, the reaction was filtered over a glass frit, concentrated under reduced pressure, and directly purified by flash column chromatography on silica gel (hexanes).

Allyldimethyl(phenoxy)silane (**257**):

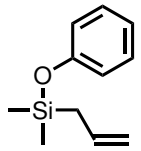

Obtained according to GP8 with allyl(dimethyl)chlorosilane and phenol on 10.6 mmol scale for 19 h; the title compound was isolated in 97 % yield (1.99 g) as a clear oil.

^{1}H NMR (500 MHz, $CDCl_3$): δ 7.34–7.23 (m, 2H), 7.06–6.94 (m, 1H), 6.88 (dt, J = 8.5, 1.3 Hz, 2H), 5.95–5.70 (m, 1H), 5.01–4.89 (m, 2H), 1.79 (dd, J = 8.0, 1.3 Hz, 2H), 0.29 (d, J = 1.5 Hz, 6H).
^{13}C NMR (126 MHz, $CDCl_3$): δ 155.2, 133.4, 129.6, 121.7, 120.3, 114.6, 24.6, −1.7.
^{29}Si NMR (99 MHz, $CDCl_3$): δ 18.03.

Allyldiisopropyl(phenoxy)silane (**259**):

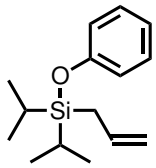

Obtained according to GP8 with allyl(diisopropyl)chlorosilane and phenol on 0.75 mmol scale; the title compound was isolated in 19 % yield (36.2 mg) as a clear oil.

^{1}H NMR (500 MHz, CD_2Cl_2): δ 7.33–7.20 (m, 2H), 7.02–6.95 (m, 1H), 6.93–6.85 (m, 2H), 5.88 (ddt, J = 16.9, 10.1, 8.0 Hz, 1H), 4.99 (dd, J = 16.9, 1.9 Hz, 1H), 4.91 (ddt, J = 10.1, 2.2, 1.1 Hz, 1H), 1.87 (dt, J = 8.0, 1.3 Hz, 2H), 1.23 (ddt, J = 13.7, 8.5, 6.6 Hz, 2H), 1.14–1.10 (m, 12H).

2,2-Diisopropyl-4-methyl-3,4-dihydro-2H-benzo[*e*][1,2]oxasiline (**260**):

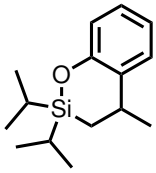

In an NMR tube (5 mm diameter), $HNTf_2$ (0.41 mol/L in toluene, 1.0 equiv., 10.0 µmol, 24.4 µL) was added to a solution of allyldiisopropyl(phenoxy)silane (10.0 equiv., 0.10 mmol, 24.8 mg) in toluene-d_8 (0.50 mL) at room temperature. Upon the first measurement of an ^{1}H

NMR spectrum, the reaction inidicated full conversion. Subsequently, the crude mixture was concentrated under reduced pressure and directly purified by flash column chromatography on silica gel (hexanes). The title compound was obtained in 94 % yield (23.4 mg) as a colorless oil.

^{1}H NMR (500 MHz, $CDCl_3$): δ 7.13 (ddt, J = 9.7, 7.4, 1.6 Hz, 2H), 6.89 (ddd, J = 7.4, 3.7, 2.3 Hz, 2H), 3.01 (tt, J = 11.1, 6.7 Hz, 1H), 1.42 (d, J = 6.7 Hz, 3H), 1.18 – 1.02 (m, 9H), 0.97 (dd, J = 11.4, 7.1 Hz, 6H), 0.74 (dd, J = 14.7, 11.3 Hz, 1H).
^{13}C NMR (126 MHz, $CDCl_3$): δ 155.4, 134.7, 127.6, 126.2, 120.8, 119.5, 30.4, 22.9, 17.4, 17.3, 17.2, 17.1, 15.8, 13.4, 13.0.
^{29}Si NMR (99 MHz, $CDCl_3$): δ 21.35.

The corresponding Mukaiyama–Mannich reactions with the newly synthesized allyl(dialkyl)aryloxysilanes were conducted according to the following procedure. Bistriflimide (0.41 mol/L in toluene, 10 mol%, 24.4 µL) was added to a solution of the corresponding allyl(dialkyl)aryloxysilanes (50 mol%) in toluene (0.5 mL, 0.2 mol/L) at room temperature. After 5 min, isobutyl propionate (3.0 equiv., 0.3 mmol, 28.9 µL) and the corresponding imine **201** or **224** (1.0 equiv.) were added, followed by NEt_3 (5 mol%, 0.7 µL). The reaction was stirred for 16 h at room temperature, then terminated by addition of a mixture of NEt_3/MeOH 1:1 (20 µL), and the yield determined by crude ^{1}H NMR analysis with mesitylene as the internal standard. An aliquot of the crude mixture was purified by preparative TLC (hexanes/EtOAc 7:3), and the enantiomeric ratio determined by subsequent HPLC measurement (OJ-3R, MeCN/H_2O 60:40, 1.0 mL/min, λ = 220 nm).

4.7 Synthesis of Silylsulfonamides

4.7.1 Synthesis of Tetrasubstituted Silyl Ketene Acetals (GP9)

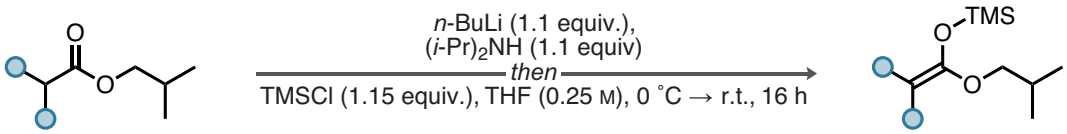

Diisopropylamine (1.00 equiv.) was dissolved in THF (0.25 mol/L) at room temperature. Subsequently, *n*-BuLi (25 mol/L in hexanes, 1.10 equiv.) was added dropwise at 0 °C (ice/water bath) and the reaction was stirred for 30 min at 0 °C. The respective ester (1.00 equiv.) was added dropwise to the reaction mixture followed by stirring for 1 h at 0 °C. TMSCl (1.15 equiv.) was added dropwise and, after removal of the cooling bath, the reaction was stirred at room temperature for 16 h. The crude reaction mixture was concentrated under

reduced pressure, the residue suspended in hexanes, and the organic layer washed with sat. aq. $NaHCO_3$ solution, sat. aq. $CuSO_4$ (3 x), water, and brine. The organic layer was dried over Na_2SO_4 and concentrated under reduced pressure to provide the pure silyl ketene acetals that were used without further purification.

Isobutyl cyclohexanecarboxylate (**432**):

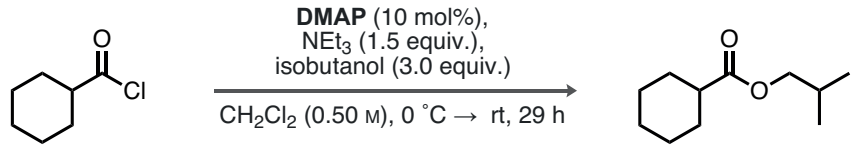

433 **432**

Isobutanol (3.0 equiv., 120.0 mmol, 11.1 mL), NEt_3 (1.5 equiv., 60.0 mmol, 8.4 mL), and DMAP (10 mol%, 488.7 mg) were added to a solution of cyclohexanecarbonyl chloride (**433**, 1.0 equiv., 40.0 mmol, 5.4 mL) in CH_2Cl_2 (80.0 mL, 0.50 mol/L) at 0 °C (ice/water bath). After stirring for 5 min, the cooling bath was removed, and the resulting reaction mixture stirred for 29 h at room temperature. Subsequently, the reaction was diluted with water, the phases separated, and the aqueous layer extracted with CH_2Cl_2 (2 x). The combined organic extracts were dried over Na_2SO_4, concentrated under reduced pressure, and directly subjected to flash column chromatography on silica gel (hexanes/Et_2O 25:1) to provide the title compound in 95 % yield (7.01 g) as a clear oil.

^{1}H NMR (500 MHz, $CDCl_3$): δ 3.84 (d, J = 6.6 Hz, 2H), 2.30 (tt, J = 11.3, 3.6 Hz, 1H), 1.95–1.87 (m, 3H), 1.80–1.71 (m, 2H), 1.69–1.61 (m, 1H), 1.49–1.39 (m, 2H), 1.35–1.19 (m, 3H), 0.92 (d, J = 6.7 Hz, 6H).
^{13}C NMR (126 MHz, $CDCl_3$): δ 176.3, 70.3, 43.5, 29.2, 27.9, 25.9, 25.6, 19.2.

Isobutyl adamantanecarboxylate (**434**):

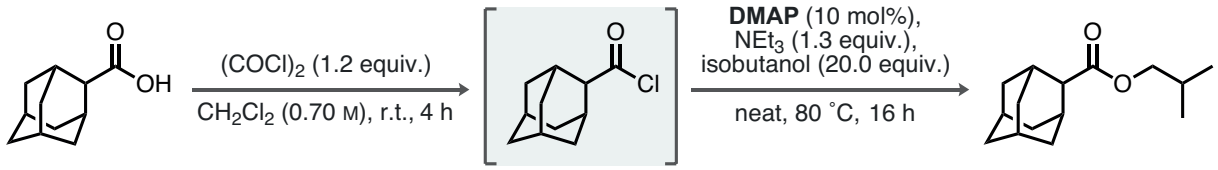

435 **436** **434**

Adamantane-2-carboxylic acid (**435**, 1.0 equiv., 13.9 mmol, 2.50 g) was dissolved in CH_2Cl_2 (20.0 mL, 0.70 mol/L) at room temperature and reacted with a few drops of DMF. The reaction was stirred for 5 min at room temperature, followed by careful addition of oxalyl chloride (1.2 equiv., 16.6 mmol, 1.4 mL). After stirring at room temperature for 4 h, the

reaction was concentrated under reduced pressure and the residue dissolved in isobutanol (20.0 equiv., 403.1 mmol, 25.7 mL). Subsequently, NEt_3 (1.3 equiv., 18.0 mmol, 2.5 mL) as well as DMAP (10 mol%, 169.4 mg) were added and, after attaching a reflux condenser, the reaction was stirred for 16 h at 80 °C. Upon cooling to room temperature, the mixture was diluted with water and CH_2Cl_2, the phases were separated, and the aqueous layer was extracted with CH_2Cl_2 (2 x). The combined organic extracts were dried over Na_2SO_4, concentrated under reduced pressure, and directly subjected to flash column chromatography on silica gel (hexanes/EtOAc 19:1) to provide the title compound in 88 % yield (2.90 g) as clear oil.

^{1}H NMR (500 MHz, $CDCl_3$): δ 3.88 (d, J = 6.5 Hz, 2H), 2.65–2.56 (m, 1H), 2.40–2.31 (m, 2H), 2.00–1.79 (m, 7H), 1.79–1.71 (m, 4H), 1.67–1.58 (m, 2H), 0.94 (d, J = 6.7 Hz, 6H).
^{13}C NMR (126 MHz, $CDCl_3$): δ 174.8, 70.3, 49.8, 38.3, 37.6, 33.7, 29.7, 28.0, 27.7, 27.6, 19.3.
ESI-HRMS: calculated for $C_{15}H_{25}O_2$ $[M+H]^+$: 237.184 905, found: 237.184 740.

(Cyclohexylidene(isobutoxy)methoxy)trimethylsilane (**437**):

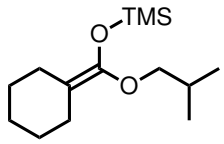

Obtained according to GP9 on 25.0 mmol scale; the title compound was isolated in 74 % yield (4.72 g) as a clear oil.

^{1}H NMR (500 MHz, $CDCl_3$): δ 3.44 (d, J = 6.5 Hz, 2H), 2.13–2.08 (m, 2H), 2.04–1.98 (m, 2H), 1.91–1.82 (m, 1H), 1.52–1.39 (m, 6H), 0.93 (d, J = 6.7 Hz Hz, 9H), 0.18 (s, 12H).

(Adamantan-2-ylidene(isobutoxy)methoxy)trimethylsilane (**438**):

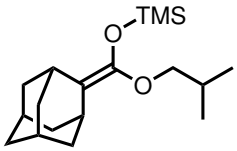

Obtained according to GP9 on 8.5 mmol scale; the title compound was isolated in 98 % yield (2.58 g) as a clear oil.

^{1}H NMR (500 MHz, $CDCl_3$): δ 3.47 (d, J = 6.5 Hz, 2H), 2.81 (t, J = 3.4 Hz, 1H), 2.61 (t, J = 3.3 Hz, 1H), 1.98–1.65 (m, 13H), 0.93 (d, J = 6.7 Hz, 6H), 0.20 (s, 9H).

^{13}C NMR (126 MHz, $CDCl_3$): δ 143.6, 107.7, 76.5, 39.1, 38.8, 37.5, 30.3, 30.0, 28.6, 28.5, 19.6, 0.2.

ESI-HRMS: calculated for $C_{18}H_{32}O_2Si$ $[M+H]^+$: 308.216 609, found: 308.216 150.

4.7.2 Mukaiyama–Mannich Reactions with *N*-Tosylmethylene Imine Equivalents (GP10)

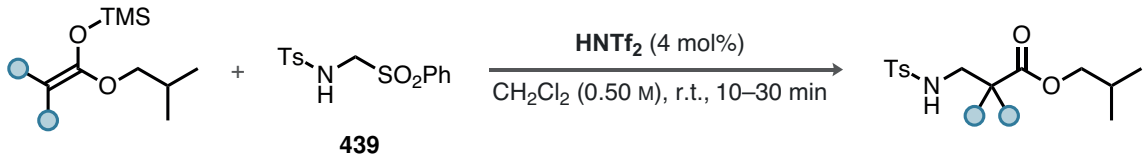

To a suspension of 4-methyl-*N*-((phenylsulfonyl)methyl)benzenesulfonamide **439** (1.0 equiv.) and the corresponding tetrasubstituted silyl ketene acetal (2.1 equiv.) in CH_2Cl_2 (0.50 mol/L) was added bistriflimide (0.40 mol/L in toluene, 4 mol%). The reaction was stirred for 10–30 min at room temperature until it became homogeneous, and directly transferred to a separatory funnel containing sat. aq. $NaHCO_3$ solution. The phases were separated, the aqueous layer was extracted with CH_2Cl_2 (2 x), the combined organic extracts were dried over Na_2SO_4, and concentrated under reduced pressure. The title compounds were obtained after flash column chromatography on silica gel (hexanes/MTBE 3:2 or hexanes/EtOAc 9:1).

4-Methyl-*N*-((phenylsulfonyl)methyl)benzenesulfonamide (**439**):

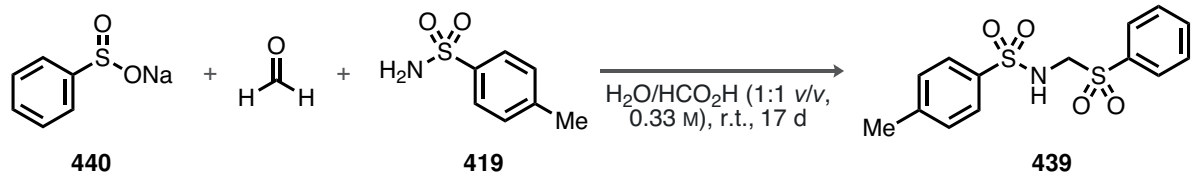

Following literature procedures,[384,385] 4-methylbenzenesulfonamide (1.0 equiv., 30.0 mmol, 5.14 g) and sodium phenylsulfanolate (**440**, 1.1 equiv., 5.42 g) were dissolved in a mixture of water and formic acid (1:1, 90.0 mL, 0.33 mol/L) at room temperature. Formaldehyde (37 % in water, 1.0 equiv., 30.0 mmol, 2.2 mL) was added and the reaction was stirred at room temperature for 17 h. The precipitate was separated by filtration, washed with hexanes and cold MTBE, and dried under high vacuum to provide the title compound in 98 % yield (9.56 g) as a white solid.

^{1}H NMR (500 MHz, DMSO-d_6): δ 8.93 (t, J = 7.0 Hz, 1H), 7.82 (dd, J = 8.4, 1.3 Hz, 2H), 7.79–7.71 (m, 1H), 7.67–7.56 (m, 4H), 7.33 (d, J = 8.0 Hz, 2H), 4.50 (d, J = 7.0 Hz, 2H), 2.36 (s, 3H).

^{13}C NMR (126 MHz, DMSO-d_6): δ 143.0, 138.1, 136.7, 134.1, 129.5, 129.2, 128.7, 126.3, 63.2, 20.9.

Isobutyl 2,2-dimethyl-3-((4-methylphenyl)sulfonamido)propanoate (**441**):

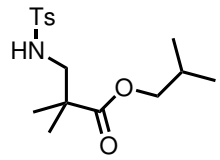

Obtained according to GP10 on 4.2 mmol scale; the title compound was isolated in 61 % yield (828.0 mg) as a white solid.

^{1}H NMR (500 MHz, $CDCl_3$): δ 7.76–7.70 (m, 2H), 7.34–7.27 (m, 2H), 5.07 (t, J = 7.0 Hz, 1H), 3.83 (d, J = 6.6 Hz, 2H), 2.93 (d, J = 7.0 Hz, 2H), 2.42 (s, 3H), 1.97–1.83 (m, 1H), 1.21 (s, 6H), 0.91 (d, J = 6.8 Hz, 6H).
^{13}C NMR (126 MHz, $CDCl_3$): δ 176.9, 143.3, 137.1, 129.7, 127.0, 71.0, 51.0, 43.0, 27.7, 23.4, 21.5, 19.0.

Isobutyl 1-(((4-methylphenyl)sulfonamido)methyl)cyclohexane-1-carboxylate (**442**):

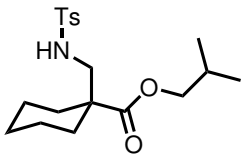

Obtained according to GP10 on 7.0 mmol scale; the title compound was isolated in 90 % yield (2.30 g) as a white solid.

^{1}H NMR (500 MHz, CD_2Cl_2): δ 7.70 (d, J = 8.3 Hz, 2H), 7.40–7.22 (m, 2H), 4.81 (t, J = 6.7 Hz, 1H), 3.79 (d, J = 6.5 Hz, 2H), 2.99 (d, J = 6.7 Hz, 2H), 2.42 (s, 4H), 1.89 (ddd, J = 17.4, 12.1, 7.6 Hz, 3H), 1.52–1.21 (m, 7H), 0.90 (d, J = 6.8 Hz, 6H).
^{13}C NMR (126 MHz, CD_2Cl_2): δ 176.0, 144.0, 137.4, 130.1, 127.3, 71.3, 49.4, 47.4, 31.6, 28.1, 25.9, 22.4, 21.6, 19.3.
ESI-HRMS: calculated for $C_{19}H_{28}NO_4Si$ $[M-H]^-$: 366.174 45, found: 366.174 82.

Isobutyl 2-(((4-methylphenyl)sulfonamido)methyl)adamantane-2-carboxylate (**443**):

Obtained according to GP10 on 2.6 mmol scale; the title compound was isolated in 73 % yield (787.0 mg) as a white solid.

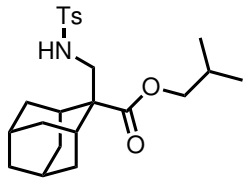

^{1}H NMR (500 MHz, $CDCl_3$): δ 7.71 (d, $J = 8.0$ Hz, 2H), 7.29 (d, $J = 8.0$ Hz, 2H), 4.42 (t, $J = 5.8$ Hz, 1H), 3.75 (d, $J = 6.6$ Hz, 2H), 3.20 (d, $J = 5.8$ Hz, 2H), 2.42 (s, 3H), 2.13 (t, $J = 3.1$ Hz, 2H), 1.86–1.52 (m, 13H), 0.87 (d, $J = 6.8$ Hz, 6H).
^{13}C NMR (126 MHz, $CDCl_3$): δ 175.6, 143.5, 136.8, 129.8, 127.3, 71.1, 52.1, 47.1, 38.1, 35.3, 32.1, 30.6, 27.8, 27.4, 26.8, 21.7, 19.3.
ESI-HRMS: calculated for $C_{23}H_{33}NO_4SNa$ $[M + Na]^+$: 442.202 25, found: 442.202 57.

Ethyl 3-((4-methylphenyl)sulfonamido)propanoate (**444**):

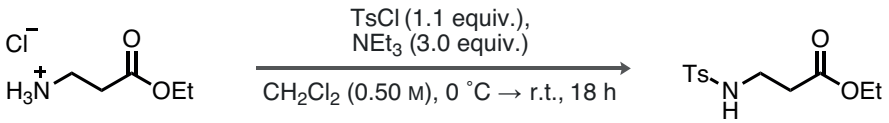

TsCl (1.1 equiv., 33.0 mmol, 6.29 g) was added to a solution of ethyl β-alanine hydrochloride (**445**, 1.0 equiv., 30.0 mmol, 4.61 g) in CH_2Cl_2 (60.0 mL, 0.50 mol/L) at room temperature. The reaction was cooled to 0 °C (ice/water bath), followed by the dropwise addition of NEt_3 (3.0 equiv., 90.0 mmol, 12.5 mL). The cooling bath was removed, allowing the reaction to warm to room temperature, and the reaction was stirred for 18 h at room temperature. The reaction was terminated by the addition of water and HCl (1.0 mol/L), the phases were separated, and the aqueous layer was extracted with CH_2Cl_2 (2 x). The combined organic extracts were dried over Na_2SO_4, concentrated under reduced pressure, and directly subjected to flash column chromatography on silica gel (hexanes/EtOAc 1:1). The title compound was obtained in 87 % yield (7.10 g) as a white solid.

^{1}H NMR (500 MHz, $CDCl_3$): δ 7.74 (d, $J = 8.3$ Hz, 2H), 7.30 (d, $J = 8.3$ Hz, 2H), 5.19 (t, $J = 6.6$ Hz, 1H), 4.11 (q, $J = 7.1$ Hz, 2H), 3.18 (q, $J = 6.3$ Hz, 2H), 2.51 (t, $J = 6.0$ Hz, 2H), 2.42 (s, 4H), 1.23 (t, $J = 7.1$ Hz, 4H).
^{13}C NMR (126 MHz, CD_2Cl_2): δ 172.2, 143.6, 137.1, 129.9, 127.2, 61.1, 38.9, 34.1, 21.6, 14.2.

4-Methyl-*N*-neopentylbenzenesulfonamide (446):

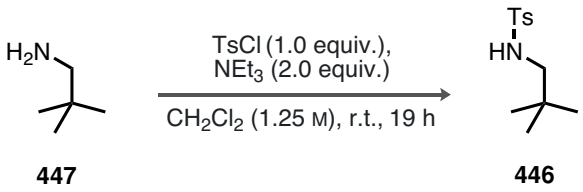

TsCl (1.0 equiv., 15.0 mmol, 2.86 g) was added in portions to a solution of neopentylamine (**447**, 1.0 equiv., 15.0 mmol, 1.8 mL) and NEt_3 (2.0 equiv., 30.0 mmol, 4.2 mL) in CH_2Cl_2 (12.0 mL, 1.25 mol/L) at room temperature. Upon complete addition, the reaction was stirred for 19 h at room temperature. The reaction was terminated by the addition of water, the phases were separated, and the aqueous layer was extracted with CH_2Cl_2 (3 x). The combined organic extracts were dried over Na_2SO_4, concentrated under reduced pressure, and used without further purification. The title compound was obtained in 98 % yield (3.55 g) as a white solid.

^{1}H NMR (500 MHz, CD_2Cl_2): δ 7.71 (d, J = 8.4 Hz, 2H), 7.33 (d, J = 8.4 Hz, 2H), 4.43 (s, 1H), 2.64 (d, J = 7.0 Hz, 2H), 2.42 (s, 3H), 0.87 (s, 9H).
^{13}C NMR (126 MHz, CD_2Cl_2): δ 143.9, 137.6, 130.1, 127.4, 55.1, 31.6, 27.1, 21.6.
ESI-HRMS: calculated for $C_{12}H_{20}NO_2S$ $[M+H]^+$: 242.120 926, found: 242.120 840.

4.7.3 Synthesis of Sodium Sulfonimidates (GP11)

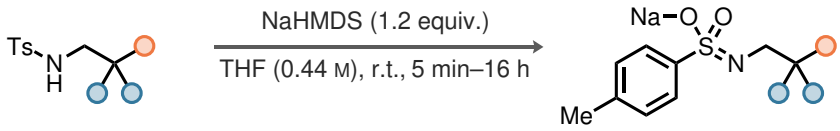

NaHMDS (1.0 mol/L in THF, 1.2 equiv.) was added dropwise to a solution of the corresponding sulfonamide (1.0 equiv.) in THF (0.87 mol/L) at room temperature. The reaction was stirred at room temperature for the indicated time, then terminated by filtration. The obtained solids were washed with THF and hexanes, and provided the title compounds after drying under high vacuum.

Sodium *N*-(3-isobutoxy-2,2-dimethyl-3-oxopropyl)-4-methylbenzenesulfonimidate (448):

Obtained according to GP11 after 5 min on 1.5 mmol scale; the title compound was isolated in 96 % yield (513.0 mg) as a white solid.

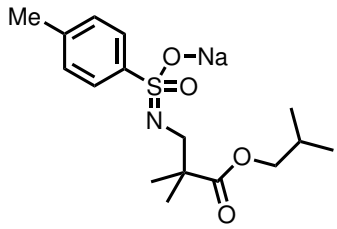

^{1}H NMR (500 MHz, DMSO-d_6): δ 7.43 (d, $J = 8.0$ Hz, 2H), 7.08 (d, $J = 8.0$ Hz, 2H), 3.66 (d, $J = 6.6$ Hz, 2H), 2.66 (s, 2H), 2.28 (s, 3H), 1.76 (hept, $J = 6.7$ Hz, 1H), 0.99 (s, 6H), 0.83 (d, $J = 6.7$ Hz, 6H).
^{13}C NMR (126 MHz, DMSO-d_6): δ 177.3, 145.5, 137.1, 127.9, 126.3, 69.1, 55.6, 44.1, 27.3, 23.3, 20.7, 18.9.
ESI-HRMS: calculated for $C_{16}H_{24}NO_4S$ $[M - Na]^-$: 326.143 15, found: 326.143 36.

Sodium *N*-((1-(isobutoxycarbonyl)cyclohexyl)methyl)-4-methylbenzenesulfonimidate (449):

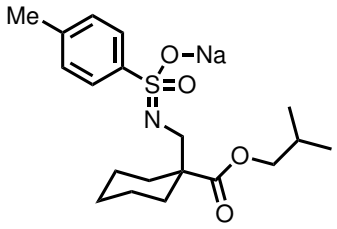

Obtained according to GP11 after 45 min on 3.9 mmol scale; the title compound was isolated in 94 % yield (1.16 g) as a white solid.

^{1}H NMR (500 MHz, DMSO-d_6): δ 7.41 (d, $J = 8.1$ Hz, 2H), 7.08 (d, $J = 7.8$ Hz, 2H), 3.68 (d, $J = 6.5$ Hz, 2H), 2.63 (s, 2H), 2.27 (s, 3H), 1.83 (d, $J = 12.8$ Hz, 2H), 1.80–1.70 (m, 1H), 1.50–1.41 (m, 3H), 1.36–1.06 (m, 5H), 0.84 (d, $J = 6.7$ Hz, 6H).
^{13}C NMR (126 MHz, DMSO-d_6): δ 176.8, 146.0, 137.5, 128.4, 126.7, 69.6, 56.2, 49.6, 32.1, 27.8, 26.1, 23.5, 21.2, 19.5.

Sodium *N*-((2-(isobutoxycarbonyl)adamantan-2-yl)methyl)-4-methylbenzenesulfonimidate (450):

Obtained according to GP11 after 16 h on 1.9 mmol scale; the title compound was isolated in 83 % yield (691.0 mg) as a white solid.

^{1}H NMR (500 MHz, DMSO-d_6): δ 7.44 (d, $J = 7.8$ Hz, 2H), 7.09 (d, $J = 7.8$ Hz, 2H), 3.70 (d, $J = 6.5$ Hz, 2H), 2.88 (s, 2H), 2.28 (s, 3H), 2.08 (s, 2H), 1.88–1.70 (m, 6H), 1.69–1.64 (m,

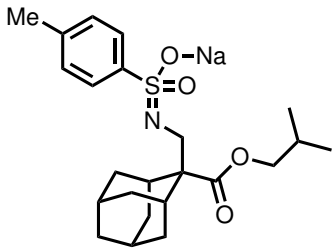

1H), 1.57 (d, $J = 12.0$ Hz, 4H), 1.39 (d, $J = 12.6$ Hz, 2H), 0.83 (d, $J = 6.5$ Hz, 6H).
^{13}C NMR (126 MHz, DMSO-d_6): δ 176.7, 144.9, 137.4, 127.9, 126.3, 69.2, 53.6, 51.0, 38.1, 35.2, 31.9, 30.4, 27.3, 27.2, 26.5, 20.7, 19.0.
ESI-HRMS: calculated for $C_{23}H_{32}O_4NSNa_2$ $[M + Na]^+$: 464.184 195, found: 464.184 020.

Sodium 4-methyl-*N*-neopentylbenzenesulfonimidate (451):

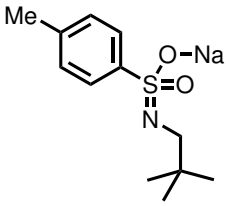

Obtained according to GP11 after 1.5 h on 13.8 mmol scale; the title compound was isolated in 90 % yield (3.28 g) as a white solid.

^{1}H NMR (500 MHz, DMSO-d_6): δ 7.43 (d, $J = 8.1$ Hz, 2H), 7.07 (d, $J = 8.1$ Hz, 2H), 2.29 (s, 2H), 2.27 (s, 3H), 0.73 (s, 9H).
^{13}C NMR (126 MHz, DMSO-d_6): δ 145.7, 136.9, 127.9, 126.4, 58.6, 32.2, 28.1, 20.7.
ESI-HRMS: calculated for $C_{12}H_{18}O_2NS$ $[M - Na]^-$: 240.106 376, found: 240.106 590.

4.7.4 Synthesis of Silylsulfonamides (GP12)

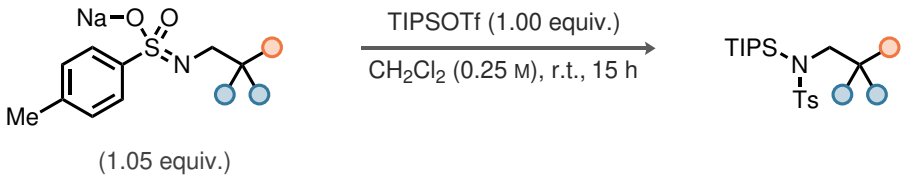

TIPSOTf (1.05 equiv.) was added dropwise to a suspension of the corresponding sodium sulfonimidate (1.05 equiv.) in CH_2Cl_2 (0.25 mol/L) at room temperature. The reaction was stirred at room temperature for the indicated time, followed by concentration under high vacuum. *n*-Pentane was added to the resulting slurry, and the solid was removed by

filtration using a syringe filter (pore size: 0.45 µm) under an atmosphere of Ar into a flame-dried Schlenk. The title compound was obtained after removal of the solvent under high vacuum.

_N_,4-dimethyl-_N_-(triisopropylsilyl)benzenesulfonamide (269):

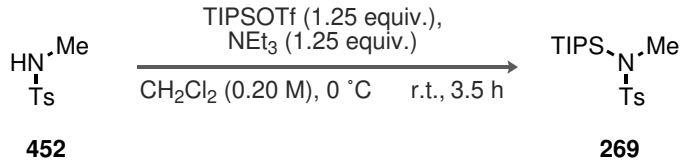

452 **269**

NEt_3 (1.25 equiv., 2.5 mmol, 349 µL) was added dropwise to a solution of TIPSOTf (1.25 equiv., 2.5 mmol, 672 µL) and _N_,4-dimethylbenzenesulfonamide (**452**, 1.0 equiv., 2.0 mmol, 370.5 mg) in CH_2Cl_2 (10.0 mL, 0.20 mol/L) at 0 °C (ice/water bath). The reaction was stirred for 30 min at 0 °C, until the cooling bath was removed, followed by stirring for addition 3 h at room temperature. The crude reaction mixture was concentrated under reduced pressure, and directly subjected to flash column chromatography on silica gel (hexanes/EtOAc 9:1). The title compound was obtained in 92 % yield (630.0 mg) as a colorless solid.

^{1}H NMR (500 MHz, CD_2Cl_2): δ 7.76–7.72 (m, 2H), 7.32 (d, $J = 8.1$ Hz, 2H), 2.70 (s, 3H), 2.42 (s, 3H), 1.53–1.45 (m, 3H), 1.15 (d, $J = 7.5$ Hz, 18H).
^{13}C NMR (126 MHz, CD_2Cl_2): δ 143.5, 137.6, 129.8, 128.1, 34.0, 21.6, 18.6, 13.6.
^{29}Si NMR (99 MHz, CD_2Cl_2): δ 19.98.

Ethyl 3-((4-methyl-_N_-(triisopropylsilyl)phenyl)sulfonamido)propanoate (270):

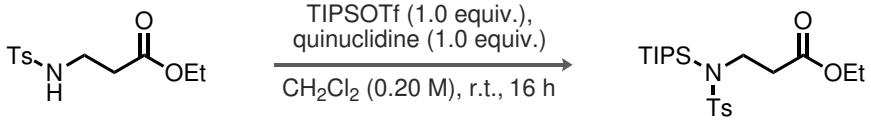

444 (1.2 equiv.) **270**

Quinuclidine (1.0 equiv., 3.1 mmol, 341.5 mg) was added dropwise to a solution of TIPSOTf (1.0 equiv., 3.1 mmol, 826 µL) and ethyl 3-((4-methylphenyl)sulfonamido)propanoate (**444**, 1.2 equiv., 3.7 mmol, 1.00 g) in CH_2Cl_2 (15.5 mL, 0.20 mol/L) at room temperature, followed by stirring for 16 h at room temperature. The crude reaction mixture was concentrated under reduced pressure, and directly subjected to flash column chromatography on silica gel (hexanes/EtOAc 9:1). The title compound was obtained in 90 % yield (1.18 g) as a colorless oil.

^{1}H NMR (500 MHz, CD_2Cl_2): δ 7.81–7.74 (m, 2H), 7.33 (d, J = 8.0 Hz, 2H), 4.06 (q, J = 7.1 Hz, 2H), 3.39–3.28 (m, 2H), 2.67–2.51 (m, 2H), 2.43 (s, 3H), 1.49 (hept, J = 7.5 Hz, 3H), 1.21 (t, J = 7.1 Hz, 3H), 1.17 (d, J = 7.5 Hz, 18H).
^{13}C NMR (126 MHz, CD_2Cl_2): δ 171.5, 144.0, 137.8, 129.9, 128.3, 60.9, 42.1, 36.2, 21.6, 19.0, 14.3, 13.9.
^{29}Si NMR (99 MHz, CD_2Cl_2): δ 20.46.

Isobutyl 2,2-dimethyl-3-((4-methyl-*N*-(triisopropylsilyl)phenyl)sulfonamido)propanoate (277):

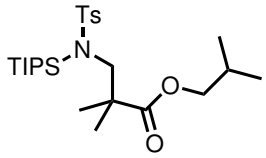

Obtained according to GP12 on 0.77 mmol scale; the title compound was isolated in 75 % yield (280.0 mg) as a colorless oil (N/O-TIPS = 94.3/5.7 at 298 K in toluene-d_8). Below are the NMR data for both N- and O-silatropisomers, if assignment was unambiguously possible.

^{1}H NMR (600 MHz, PhMe-d_8, N-TIPS): δ 8.18–8.11 (m, 2H), 6.91–6.86 (m, 2H), 3.98 (d, J = 6.7 Hz, 2H), 3.59 (s, 2H), 1.95 (s, 3H), 1.94–1.90 (m, 1H), 1.47–1.41 (m, 3H), 1.40 (s, 6H), 1.08 (d, J = 7.5 Hz, 18H), 0.87 (d, J = 6.7 Hz, 6H).
^{1}H NMR (600 MHz, PhMe-d_8, O-TIPS): δ 7.93–7.87 (m, 2H), 6.82 (d, J = 7.9 Hz, 2H), 3.85–3.75 (m, 2H), 3.51 (d, J = 11.4 Hz, 1H), 3.41 (d, J = 11.4 Hz, 1H), 1.95 (s, 3H), 1.94–1.89 (m, 1H), 1.47–1.41 (m, 3H), 1.40 (s, 6H), 1.08 (d, J = 7.5 Hz, 18H), 0.87 (d, J = 6.7 Hz, 6H).
^{13}C NMR (151 MHz, PhMe-d_8): δ 177.6, 142.5, 138.8, 71.0, 53.1, 44.1, 28.1, 25.4, 21.0, 19.3, 19.3, 14.5.
^{29}Si NMR (119 MHz, PhMe-d_8, N-TIPS): δ 17.67.
^{29}Si NMR (119 MHz, PhMe-d_8, O-TIPS): δ 26.18.

Isobutyl 1-(((4-methyl-*N*-(triisopropylsilyl)phenyl)sulfonamido)methyl)cyclohexane-1-carb-oxylate (278):

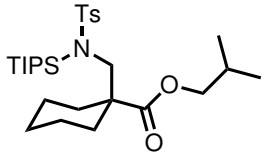

Obtained according to GP12 on 0.70 mmol scale; the title compound was isolated in 83 % yield (307.0 mg) as a colorless oil (N/O-TIPS = 71.3/28.7 at 298 K in toluene-d_8). Below

are the NMR data for both *N*- and *O*-silatropisomers, if assignment was unambiguously possible.

^{1}H NMR (600 MHz, PhMe-d_8, *N*-TIPS): δ 8.05–8.00 (m, 2H), 6.87–6.84 (m, 2H), 4.01 (d, J = 6.6 Hz, 2H), 3.59 (s, 2H), 2.47–2.41 (m, 2H), 1.94 (d, J = 0.8 Hz, 3H), 1.92–1.86 (m, 1H), 1.72–1.61 (m, 6H), 1.54 (dt, J = 14.9, 7.6 Hz, 3H), 1.42 (td, J = 12.8, 4.3 Hz, 2H), 1.14 (d, J = 7.5 Hz, 18H), 0.87 (d, J = 6.7 Hz, 6H).
^{13}C NMR (151 MHz, PhMe-d_8): δ 176.9, 142.6, 138.9, 71.1, 55.8, 48.5, 32.6, 28.0, 26.2, 23.6, 21.0, 19.4, 14.6.
^{29}Si NMR (119 MHz, PhMe-d_8, *N*-TIPS): δ 17.99.
^{29}Si NMR (119 MHz, PhMe-d_8, *O*-TIPS): δ 25.99.

Isobutyl 2-(((4-methyl-N-(triisopropylsilyl)phenyl)sulfonamido)methyl)adamantane-2-carb-oxylate (**279**):

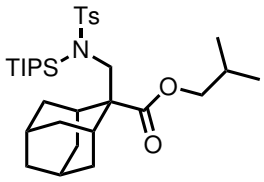

Obtained according to GP12 on 1.25 mmol scale; the title compound was isolated in 70 % yield (536.0 mg) as a colorless oil (*N*/*O*-TIPS = 6.0/94.0 at 298 K in toluene-d_8). Below are the NMR data for both *N*- and *O*-silatropisomers, if assignment was unambiguously possible.

^{1}H NMR (600 MHz, PhMe-d_8, *O*-TIPS): δ 7.98 (d, J = 8.2 Hz, 2H), 6.86–6.79 (m, 2H), 3.89 (dd, J = 6.6, 2.8 Hz, 2H), 3.87 (d, J = 11.9 Hz, 1H), 3.68 (d, J = 11.9 Hz, 1H), 2.53 (d, J = 3.8 Hz, 1H), 2.40 (d, J = 3.8 Hz, 1H), 2.23–2.15 (m, 2H), 2.08–2.04 (m, 1H), 1.91 (s, 4H), 1.88–1.82 (m, 1H), 1.82–1.79 (m, 1H), 1.75–1.48 (m, 7H), 1.35–1.27 (m, 3H), 1.15–1.09 (m, 18H), 0.87 (dd, J = 6.7, 5.0 Hz, 6H).
^{13}C NMR (151 MHz, PhMe-d_8, *O*-TIPS): δ 175.0, 142.1, 140.4, 70.1, 54.3, 49.9, 39.0, 36.0, 35.8, 33.0, 32.9, 31.9, 31.4, 28.4, 28.2, 27.8, 21.0, 19.5, 17.9, 17.8, 12.9.
^{29}Si NMR (119 MHz, PhMe-d_8, *N*-TIPS): δ 20.09.
^{29}Si NMR (119 MHz, PhMe-d_8, *O*-TIPS): δ 25.78.

4-Methyl-*N*-neopentyl-*N*-(triisopropylsilyl)benzenesulfonamide (**281**):

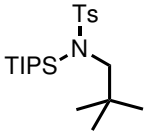

Obtained according to GP12 on 1.6 mmol scale; the title compound was isolated in 80 % yield (467.0 mg) as a colorless oil (N/O-TIPS = 76.3/23.7 at 298 K in toluene-d_8). Below are the NMR data for both N- and O-silatropisomers, if assignment was unambiguously possible.

^{1}H NMR (600 MHz, PhMe-d_8, N-TIPS): δ 7.88–7.82 (m, 2H), 6.82–6.76 (m, 2H), 3.10 (s, 2H), 1.94 (s, 3H), 1.92 (s, 3H), 1.60 (hept, J = 7.5 Hz, 3H), 1.23 (d, J = 7.5 Hz, 18H), 0.99 (s, 9H).
^{1}H NMR (600 MHz, PhMe-d_8, O-TIPS): δ 7.92–7.87 (m, 2H), 6.82–6.76 (m, 2H), 3.08 (d, J = 11.4 Hz, 1H), 3.04 (d, J = 11.4 Hz, 1H), 1.92 (s, 3H), 1.31 (hept, J = 7.5 Hz, 3H), 1.14 (d, J = 7.5 Hz, 6H), 1.10 (d, J = 7.5 Hz, 6H), 1.05 (s, 9H).
^{13}C NMR (151 MHz, PhMe-d_8, N-TIPS): δ 142.5, 139.1, 129.1, 128.9, 57.5, 33.1, 30.1, 21.0, 19.6, 15.1, 13.0.
^{13}C NMR (151 MHz, PhMe-d_8, O-TIPS): δ 141.9, 140.2, 129.3, 127.3, 57.0f, 32.9, 27.9, 21.0, 17.9, 17.8, 13.0.
^{29}Si NMR (119 MHz, PhMe-d_8, N-TIPS): δ 17.80.
^{29}Si NMR (119 MHz, PhMe-d_8, O-TIPS): δ 25.31.
ESI-HRMS: calculated for $C_{21}H_{40}NO_2SiS$ $[M+H]^+$: 398.254 355, found: 398.254 110.

4.8 IDPi-Catalyzed Silicon-Catalytic Mukaiyama-Mannich Reaction (GP13)

The corresponding IDPi catalyst (4 mol%), N-silylsulfonamide (25–75 mol%), and ester (3.0–12.0 equiv.) were dissolved in the solvent of choice and stirred for 15 min at room temperature. After transfer of the reaction flask to a cryostat maintaining the desired temperature, the imine (1.0 equiv., 0.025 mmol) was either added as a stock solution in the respective solvent or ester, or as a solid, to the reaction mixture, after which it was stirred for the indicated time. The reaction was terminated by addition of a mixture of NEt_3/MeOH 1:1 (20 µL), allowed to warm to room temperature, and directly analyzed by crude ^{1}H NMR using mesitylene as internal standard. An aliquot of the reaction mixture was purified by preparative TLC (hexanes/MTBE 7:3), and the enantiomeric ratio determined by HPLC measurement (OJ-3R).

5 Synthetic Procedures for Chapter 4

5.1 Direct *C*-Glycosylation of Arenes (GP14)

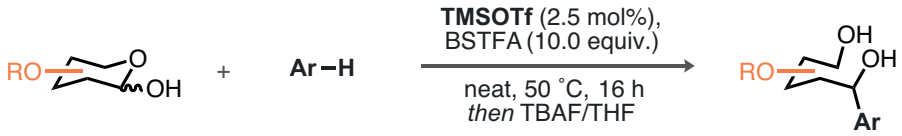

TMSOTf (25 mol%) was slowly added to a suspension of the carbohydrate (1.0 equiv., 0.20 mmol) and arene (1.5 equiv., 0.30 mmol) in BSTFA (10.0 equiv., 2.0 mmol) at room temperature. The mixture was stirred for 5 min at room temperature, after which point the solution became homogeneous, and was then heated to 50 °C. Upon full conversion, as determined by TLC analysis, the reaction was cooled to 0 °C (ice/water bath). TBAF (1.0 mol/L in THF, 11.0 equiv., 22.0 mmol) was then slowly added and the solution was stirred at 0 °C for 2 h, before concentrating under reduced pressure. The crude product was directly subjected to flash column chromatography on silica (EtOAc/MeOH 9:1) to provide the title compound.

(1*S*,2*S*,3*R*,4*R*)-1-(4-aminopyrrolo[2,1-*f*][1,2,4]triazin-7-yl)pentane-1,2,3,4,5-pentaol (344):

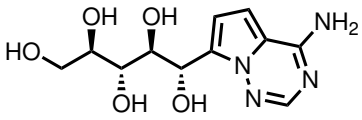

Obtained according to GP13 with aminopyrrolotriazine (**341**) and D-ribose (**342**); the title compound was isolated in 86 % yield (48.7 mg) as a white solid.

^{1}H NMR (600 MHz, DMSO-d_6): δ 7.80 (s, 1H), 7.59 (s, 2H), 6.82 (d, $J = 4.3$ Hz, 1H), 6.64 (d, $J = 4.3$ Hz, 1H), 5.32 (t, $J = 5.7$ Hz, 1H), 5.29 (d, $J = 5.7$ Hz, 1H), 4.87 (d, $J = 5.2$ Hz, 1H), 4.63 (d, $J = 4.8$ Hz, 1H), 4.60 (d, $J = 5.4$ Hz, 1H), 4.35 (t, $J = 5.7$ Hz, 1H), 3.94 (dt, $J = 6.6$, 5.4 Hz, 1H), 3.72–3.65 (m, 1H), 3.60–3.53 (m, 1H), 3.44–3.38 (m, 1H), 3.38 (dd, $J = 6.9$, 5.0 Hz, 1H).
^{13}C NMR (151 MHz, DMSO-d_6): δ 155.6, 147.4, 131.8, 113.6, 109.8, 100.7, 74.9, 72.9, 72.5, 65.4, 62.7.
ESI-HRMS: calculated for $C_{11}H_{17}N_4O_5$ $[M+H]^+$: 285.119 345, found: 285.119 410.

(1*S*,2*S*,3*S*,4*R*)-1-(4-aminopyrrolo[2,1-*f*][1,2,4]triazin-7-yl)pentane-1,2,3,4,5-pentaol (**349**):

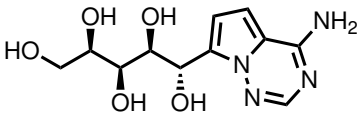

Obtained according to GP13 with arene **341** (1.0 equiv.) and D-xylose (1.5 equiv.); the title compound was isolated in 53 % yield (30.1 mg) as an off-white solid.

^{1}H NMR (600 MHz, DMSO-d_6): δ 7.79 (s, 1H), 7.56 (s, 2H), 6.82 (d, J = 4.4 Hz, 1H), 6.59 (d, J = 4.4 Hz, 1H), 5.19–5.14 (m, 2H), 4.53 (d, J = 4.8 Hz, 1H), 4.44 (dd, J = 6.0, 5.2 Hz, 1H), 4.31 (d, J = 6.3 Hz, 1H), 4.23 (d, J = 6.7 Hz, 1H), 3.89 (tt, J = 6.2, 2.1 Hz, 1H), 3.76 (ddd, J = 6.7, 4.4, 2.2 Hz, 1H), 3.55 (dq, J = 6.0, 4.7 Hz, 1H), 3.45 (ddd, J = 11.1, 6.0, 5.2 Hz, 1H), 3.38–3.32 (m, 1H).
^{13}C NMR (151 MHz, DMSO-d_6): δ 155.6, 147.3, 132.9, 113.7, 108.9, 100.6, 73.7, 73.5, 69.0, 64.5, 62.5.
ESI-HRMS: calculated for $C_{11}H_{17}N_4O_5$ $[M+H]^+$: 285.119 345, found: 285.119 100.

(1*S*,2*S*,3*R*,4*R*)-1-(5-bromo-1-methyl-1*H*-indol-3-yl)pentane-1,2,3,4,5-pentaol (**350**):

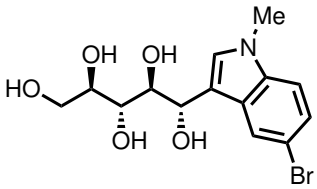

Obtained according to GP13 with 5-bromo-1-methyl-1*H*-indole (1.0 equiv.) and D-ribose (**342**, 1.5 equiv.); the title compound was isolated in 69 % yield (49.8 mg) as a white foam. The product was isolated along with approximately 30 % NEt_3. Otherwise, cyclization towards the furanose occurred upon further concentration.

^{1}H NMR (600 MHz, DMSO-d_6): δ 7.88 (d, J = 2.0 Hz, 1H), 7.35 (d, J = 8.7 Hz, 1H), 7.26 (s, 1H), 7.20 (dd, J = 8.7, 2.0 Hz, 1H), 5.11 (dd, J = 4.5, 1.6 Hz, 1H), 4.97–4.92 (m, 1H), 4.81 (dd, J = 4.9, 2.0 Hz, 1H), 4.66 (dd, J = 5.5, 1.3 Hz, 1H), 4.62 (dd, J = 4.8, 1.4 Hz, 1H), 4.36 (td, J = 5.6, 1.5 Hz, 1H), 3.81–3.75 (m, 1H), 3.74 (s, 3H), 3.69–3.64 (m, 1H), 3.59–3.53 (m, 1H), 3.43 (ddd, J = 11.0, 8.5, 6.5 Hz, 1H), 3.35–3.31 (m, 1H).
^{13}C NMR (151 MHz, DMSO-d_6): δ 135.2, 129.6, 129.2, 123.0, 122.8, 115.1, 111.4, 111.0, 75.4, 72.9, 72.6, 68.1, 62.3, 32.5.
ESI-HRMS: calculated for $C_{14}H_{18}NO_5BrNa$ $[M+Na]^+$: 382.026 068, found: 382.026 000.

(1*S*,2*S*,3*R*,4*R*)-1-(2,4,6-trimethoxyphenyl)pentane-1,2,3,4,5-pentaol (**351**):

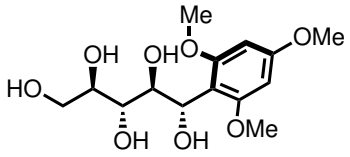

Obtained according to GP13 with 1,3,5-trimethoxybenzene (1.0 equiv.) and D-ribose (**342**, 1.5 equiv.); the title compound was isolated in 71 % yield (45.1 mg) as a white solid. The product was isolated along with approximately 30 % NEt_3. Otherwise, cyclization towards the furanose occurred upon further concentration.

^{1}H NMR (600 MHz, DMSO-d_6): δ 6.19 (s, 2H), 5.05 (dd, J = 8.9, 7.2 Hz, 1H), 4.62–4.58 (m, 2H), 4.56 (d, J = 5.0 Hz, 1H), 4.38 (t, J = 5.8 Hz, 1H), 4.24 (d, J = 6.1 Hz, 1H), 4.07 (ddd, J = 8.9, 6.1, 4.9 Hz, 1H), 3.76 (s, 3H), 3.72 (s, 6H), 3.69 (ddt, J = 6.2, 4.9, 3.0 Hz, 1H), 3.63–3.56 (m, 2H), 3.39 (dt, J = 11.0, 6.0 Hz, 1H).
^{13}C NMR (151 MHz, DMSO-d_6): δ 159.9, 159.3, 111.4, 91.3, 74.7, 72.8, 72.7, 66.8, 63.0, 55.8, 55.1.
ESI-HRMS: calculated for $C_{14}H_{22}O_8Na$ $[M + Na]^+$: 341.120 689, found: 341.120 290.

7-((4*S*,5*S*,6*R*,7*R*)-2,2,10,10-tetramethyl-5,6,7-tris((trimethylsilyl)oxy)-3,9-dioxa-2,10-disilaundecan-4-yl)pyrrolo[2,1-*f*][1,2,4]triazin-4-amine (**343**):

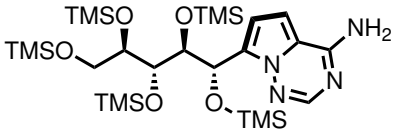

Obtained according to GP13 with aminopyrrolotriazine **341** and D-ribose (**342**) without the subsequent desilylation step; the title compound was isolated after preparative TLC (EtOAc) for structural analysis. Crude ^{1}H NMR analysis with benzene as internal standard indicated quantitative formation of **343**.

^{1}H NMR (600 MHz, PhMe-d_8): δ 7.96 (s, 1H), 7.01 (d, J = 4.5 Hz, 1H), 6.21 (d, J = 4.5 Hz, 1H), 5.96 (d, J = 5.6 Hz, 1H), 5.11 (s, 2H), 4.47 (t, J = 5.4 Hz, 1H), 4.36 (ddd, J = 6.7, 4.9, 2.8 Hz, 1H), 3.96 (dd, J = 10.3, 2.8 Hz, 1H), 3.87 (t, J = 5.4, 4.9 Hz, 1H), 3.74 (dd, J = 10.3, 6.7 Hz, 1H), 0.31 (s, 8H), 0.21 (s, 8H), 0.19 (s, 8H), 0.16 (s, 9H), 0.10 (s, 8H).
^{13}C NMR (151 MHz, PhMe-d_8): δ 55.7, 147.1, 132.9, 113.7, 111.8, 100.1, 78.2, 77.4, 74.7, 66.4, 64.5, 0.9, 0.6, 0.6, 0.2, −0.3.

5.2 Ribose Persilylation

TMSOTf (25 mol%, 10.0 µL) was added to a suspension of D-ribose (**342**, 1.0 equiv., 0.20 mmol, 30.0 mg) in BSTFA (10.0 equiv., 2.0 mmol, 540 µL). The mixture was stirred at room temperature for 15 min, followed by transfer into an NMR tube under an atmosphere of Ar. After introducing a coaxial insert (filled with DMSO-d_6), the sample was immediately subjected to NMR measurements.

The discussion of these results can be found in Chapter 4, Section 3.1.2, and the NMR data are depicted in Scheme 4.8.

5.3 Kinetic Profile of the *C*-Glycosylation Reaction

TMSOTf (25 mol%, 10.0 µL) was added to a suspension of D-ribose (**342**, 1.0 equiv., 0.20 mmol, 30.0 mg) in BSTFA (10.0 equiv., 2.0 mmol, 540 µL). Aminopyrrolotriazine **341** (1.2 equiv., 0.22 mmol, 30.0 mg) was added to the reaction and stirred for another 10 min. The mixture was stirred at room temperature for 15 min, followed by transfer into an NMR tube under an atmosphere of Ar. After introducing a coaxial insert (filled with DMSO-d_6), the sample was immediately subjected to NMR measurements (NMR spectrometer pre-heated to 50 °C).

The discussion of these results can be found in Chapter 4, Section 3.1.3, and the concentration data are depicted in Fig. 4.2.

5.4 Polyol Cyclization Toward *C*-Furanosides

(2*R*,3*R*,4*S*,5*R*)-2-(4-aminopyrrolo[2,1-*f*][1,2,4]triazin-7-yl)-5-(hydroxymethyl)tetrahydrofuran-3,4-diol (**340a**):

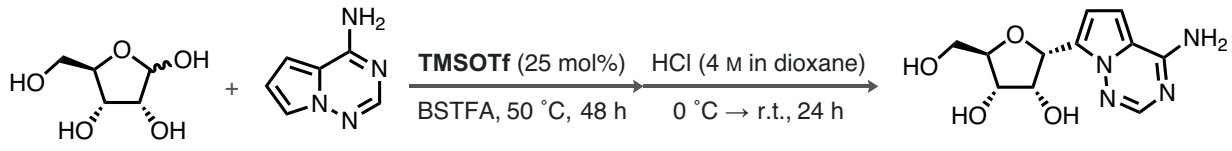

342 **341** (1.2 equiv.) **340a**

TMSOTf (25 mol%, 90.0 µL) was slowly added to a suspension of D-ribose (**342**, 1.0 equiv., 2.0 mmol, 302.0 mg) and aminopyrrolotriazine **341** (1.2 equiv., 2.4 mmol, 326.0 mg) in BSTFA (10.0 equiv., 20.0 mmol, 5.0 mL) at room temperature. The mixture was stirred for 5 min at room temperature, after which point the solution became homogeneous, and was then heated to 50 °C. After 48 h, the reaction was cooled to 0 °C (ice/water bath).

HCl (4.0 mol/L in 1,4-dioxane, 40.0 equiv., 80.0 mmol, 20.0 mL) was then slowly added and the solution was stirred at 0 °C for 10 min, before warming to room temperature. After 24 h, the mixture was diluted with Et_2O, filtered over a glass frit, and the solid was washed with Et_2O, before drying under vacuum. The crude mixture was then dissolved in MeOH (20.0 mL, 0.10 mol/L) and $NaHCO_3$ (11.0 g) was added. The mixture was then stirred for 30 min before filtering, washing with MeOH, and concentrating under reduced pressure. The crude product was directly subjected to flash column chromatography on silica (EtOAc → EtOAc/MeOH 9:1) to provide the title compound in 71 % yield (377.0 mg, 90:10 dr) as an off-white solid.

^{1}H NMR (600 MHz, DMSO-d_6): δ 7.79 (s, 1H), 7.60 (s, 2H), 6.83 (d, $J = 4.4$ Hz, 1H), 6.66 (d, $J = 4.5$ Hz, 1H), 5.45 (d, $J = 3.1$ Hz, 1H), 4.88 (d, $J = 7.0$ Hz, 1H), 4.70 (dd, $J = 6.2$, 5.3 Hz, 1H), 4.68 (d, $J = 4.6$ Hz, 1H), 4.18–4.10 (m, 2H), 3.84 (ddd, $J = 7.5$, 4.9, 2.6 Hz, 1H), 3.64 (ddd, $J = 11.8$, 5.2, 2.6 Hz, 1H), 3.47 (ddd, $J = 11.5$, 6.3, 5.0 Hz, 1H).
^{13}C NMR (151 MHz, DMSO-d_6): δ 155.5, 147.5, 127.9, 113.9, 110.8, 100.7, 81.9, 74.8, 72.5, 71.6, 61.7.
ESI-HRMS: calculated for $C_{11}H_{15}N_4O_4$ $[M+H]^+$: 267.108 780, found: 267.108 860.

(2*S*,3*R*,4*S*,5*R*)-2-(4-aminopyrrolo[2,1-*f*][1,2,4]triazin-7-yl)-5-(hydroxymethyl)tetrahydrofuran-3,4-diol (**340a**):

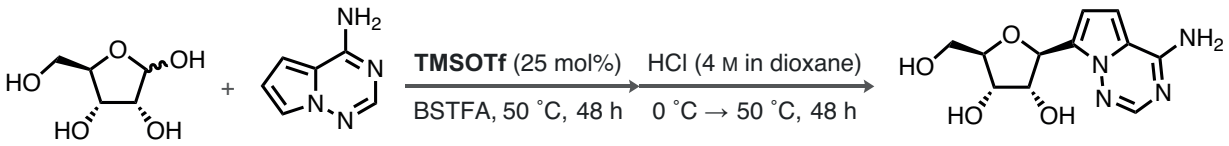

342 **341** (1.5 equiv.) **340b**

TMSOTf (25 mol%, 45.0 µL) was slowly added to a suspension of D-ribose (**342**, 1.0 equiv., 1.0 mmol, 150.0 mg) and aminopyrrolotriazine **341** (1.5 equiv., 1.5 mmol, 202.0 mg) in BSTFA (10.0 equiv., 10.0 mmol, 2.5 mL) at room temperature. The mixture was stirred for 5 min at room temperature, after which point the solution became homogeneous, and was then heated to 50 °C. After 48 h, the reaction was cooled to 0 °C (ice/water bath). HCl (4.0 mol/L in 1,4-dioxane, 40.0 equiv., 40.0 mmol, 10.0 mL) was then slowly added and the solution was stirred at 0 °C for 10 min, before warming to 50 °C. After 48 h, the mixture was diluted with Et_2O, filtered over a glass frit, and the solid was washed with Et_2O, before drying under vacuum. The crude mixture was then dissolved in MeOH (10.0 mL, 0.10 mol/L) and $NaHCO_3$ (5.5 g) was added. The mixture was then stirred for 30 min before filtering, washing with MeOH, and concentrating under reduced pressure. The crude product was

directly subjected to flash column chromatography on silica (EtOAc → EtOAc/MeOH 9:1) to provide the title compound in 48 % yield (127.5 mg, 86:14 dr) as an off-white solid.

^{1}H NMR (600 MHz, DMSO-d_6): δ 7.82 (s, 1H), 6.84 (d, J = 4.4 Hz, 1H), 6.68 (d, J = 4.4 Hz, 1H), 5.11 (d, J = 6.4 Hz, 1H), 4.96 (d, J = 6.3 Hz, 1H), 4.88 (d, J = 5.3 Hz, 1H), 4.77 (dd, J = 6.2, 5.3 Hz, 1H), 4.23 (td, J = 6.3, 5.2 Hz, 1H), 3.94 (q, J = 5.1 Hz, 1H), 3.79 (q, J = 4.5 Hz, 1H), 3.58–3.51 (m, 1H), 3.45 (ddd, J = 11.5, 6.3, 4.8 Hz, 1H).
^{13}C NMR (151 MHz, DMSO-d_6): δ 155.6, 147.7, 128.9, 114.9, 109.7, 100.7, 84.5, 75.4, 73.7, 71.3, 62.1.
ESI-HRMS: calculated for $C_{11}H_{13}N_4O_4$ $[M-H]^-$: 265.094 230, found: 265.094 460.

5.5 Peracetylation of the Furanoside Diastereomers (GP14)

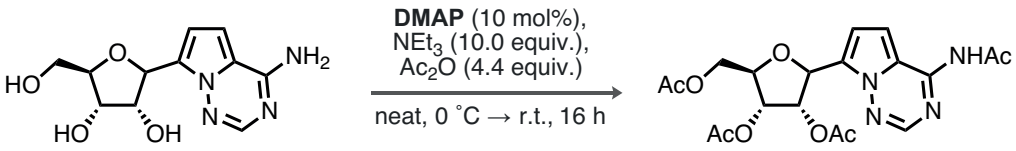

Ac_2O (4.4 equiv.) was added to a suspension of the nucleoside **340a** or **340b** (1.0 equiv.) and DMAP (10 mol%) in NEt_3 (10.0 equiv.) at 0 °C (ice/water bath). The reaction was allowed to warm to room temperature and stirred for 16 h. The mixture was then diluted with EtOAc and water, the phases were separated, and the organic layer was washed with water (2 x). The organic layer was dried over Na_2SO_4, concentrated under reduced pressure, and directly subjected to flash column chromatography on silica gel (CH_2Cl_2/EtOAc 1:1) to provide the title compound.

(2*R*,3*S*,4*R*,5*R*)-2-(4-acetamidopyrrolo[2,1-*f*][1,2,4]triazin-7-yl)-5-(acetoxymethyl)-tetrahydrofuran-3,4-diyl diacetate (**368a**):

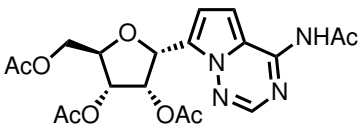

Obtained according to GP14 on 0.50 mmol scale; the title compound was isolated in 86 % yield (187.0 mg, 90:10 dr) as an off-white solid.

^{1}H NMR (600 MHz, CD_2Cl_2): δ 8.43 (s, 1H), 8.10 (s, 1H), 7.13 (d, J = 4.7 Hz, 1H), 6.97 (d, J = 4.7 Hz, 1H), 5.97 (d, J = 3.8 Hz, 1H), 5.83–5.75 (m, 1H), 5.45 (dd, J = 7.8, 4.7 Hz,

1H), 4.46 (dddd, J = 7.7, 4.5, 3.1, 0.5 Hz, 1H), 4.42 (dd, J = 12.0, 3.2 Hz, 1H), 4.19 (dd, J = 12.0, 4.6 Hz, 1H), 2.52 (s, 3H), 2.10 (s, 3H), 2.04 (s, 3H), 1.84 (s, 3H).
^{13}C NMR (151 MHz, CD_2Cl_2): δ 171.0, 170.2, 170.2, 169.6, 150.8, 146.3, 128.0, 115.7, 113.3, 104.7, 77.8, 74.4, 72.8, 71.9, 63.9, 26.0, 21.0, 20.7, 20.6.
ESI-HRMS: calculated for $C_{19}H_{22}N_4O_8Na$ $[M + Na]^+$: 457.132 984, found: 457.133 320.

(2*S*,3*S*,4*R*,5*R*)-2-(4-acetamidopyrrolo[2,1-*f*][1,2,4]triazin-7-yl)-5-(acetoxymethyl)-tetrahydrofuran-3,4-diyl diacetate (368a):

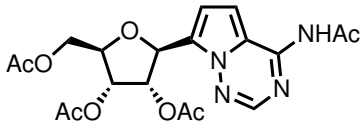

Obtained according to GP14 on 0.20 mmol scale; the title compound was isolated in 38 % yield (85.8 mg, 86:14 dr) as an off-white solid.

^{1}H NMR (600 MHz, CD_2Cl_2): δ 8.58 (s, 1H), 8.15 (s, 1H), 7.12 (d, J = 4.7 Hz, 1H), 6.90 (d, J = 4.7 Hz, 1H), 5.66 (t, J = 5.9 Hz, 1H), 5.58 (d, J = 6.1 Hz, 1H), 5.41 (t, J = 5.5 Hz, 1H), 4.38 (dd, J = 11.9, 3.3 Hz, 1H), 4.34 (td, J = 4.9, 3.4 Hz, 1H), 4.22 (dd, J = 11.9, 4.7 Hz, 1H), 2.54 (s, 3H), 2.10 (s, 3H), 2.08 (s, 3H), 2.04 (s, 3H).
^{13}C NMR (151 MHz, CD_2Cl_2): δ 171.2, 170.8, 170.2, 170.0, 151.1, 146.5, 128.8, 116.6, 112.5, 104.4, 79.9, 75.1, 73.4, 71.9, 63.8, 26.0, 21.0, 20.8, 20.8.
ESI-HRMS: calculated for $C_{19}H_{22}N_4O_8$ $[M]^+$: 434.143 76, found: 434.143 60.

5.6 Telescoped Process

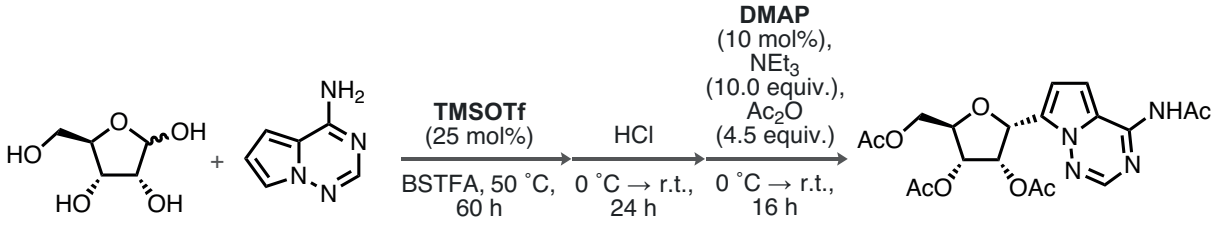

342 **341** (1.2 equiv.) **368a**

TMSOTf (25 mol%, 0.7 mL) was slowly added to a suspension of D-ribose (**342**, 1.0 equiv., 15.0 mmol, 2.25 g) and aminopyrrolotriazine **341** (1.2 equiv., 18.0 mmol, 2.41 g) in BSTFA (10.0 equiv., 150.0 mmol, 40.0 mL) at room temperature. The mixture was stirred for 5 min at room temperature, after which point the solution became homogeneous, and was then heated to 50 °C. After 60 h, the reaction was cooled to 0 °C (ice/water bath). HCl (4.0 mol/L in

1,4-dioxane, 40.0 equiv., 600.0 mmol, 150.0 mL) was then slowly added and the solution was stirred at 0 °C for 10 min, before warming to room temperature. After 24 h, the mixture was diluted with Et_2O, filtered over a glass frit, and the solid was washed with Et_2O, before drying under vacuum. The crude solid and DMAP (10 mol%, 183.0 mg) were suspended in NEt_3 (10.0 equiv., 150.0 mmol, 22.0 mL) at 0 °C (ice/water bath). Ac_2O (4.4 equiv., 67.7 mmol, 6.4 mL) was added dropwise and the reaction was warmed to room temperature and stirred for 16 h. As TLC analysis indicated incomplete conversion, the reaction was cooled to 0 °C, followed by the addition of Ac_2O (1.0 equiv., 15.0 mmol, 1.4 mL). After warming up and stirring at room temperature for 6 h, the mixture was diluted with EtOAc and water, the organic layer was washed with water (2 x), dried over Na_2SO_4, and concentrated under reduced pressure. The title compound was obtained in 60 % yield (3.91 g, 90:10 dr) after flash chromatography on silica gel (CH_2Cl_2/EtOAc 4:3 → 1:1).

5.7 Mn-Catalyzed C−H Oxidation

(3*R*,4*R*,5*R*)-2-(4-acetamidopyrrolo[2,1-*f*][1,2,4]triazin-7-yl)-5-(acetoxymethyl)-2-hydroxytetrahydrofuran-3,4-diyl diacetate (**370**):

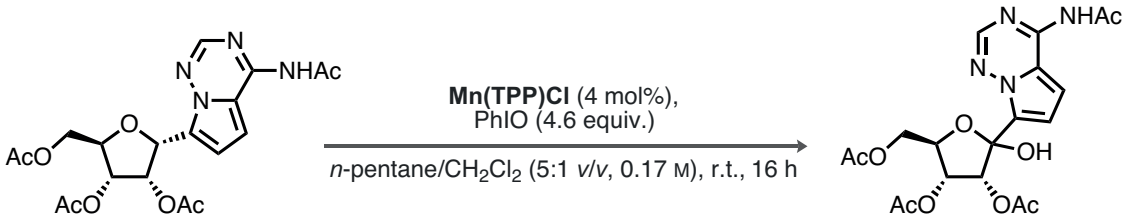

368a **370**

Mn(TPP)Cl (4 mol%) and the acetylated ribonucleoside (**368a**, 1.0 equiv.) were dissolved in a mixture of freshly degassed *n*-pentane and CH_2Cl_2 (5:1 v/v, 0.17 mol/L). Iodosylbenzene (4.6 equiv. in total, 0.58 equiv. per batch) was added in portions over a period of 10.5 h (90 min intervals) and, upon complete addition, the reaction was stirred for additional 6 h. The crude reaction was diluted with EtOAc and filtered over a glass frit. The solvent was removed under reduced pressure, and the crude mixture subjected to flash column chromatography on silica gel (CH_2Cl_2/EtOAc 1:1 → EtOAc) to provide the title compound.

ESI-HRMS: calculated for $C_{19}H_{21}N_4O_9$ $[M-H]^-$: 449.131 405, found: 449.131 880.

The product **370** exhibited dynamic stereoisomerism at the anomeric center, which is related to the lactol–ketone equilibrium. The discussion regarding this observation can be found in Chapter 4, Section 3.4.2, Scheme 4.15. The NMR data of all isomers can be found below.

Table 5.1: Overview of multiple oxidation reactions reproduced in our lab following the procedure given above.

scale / mmol	scale / mg	yield **370** / mmol	yield **370**
1.25	543.0	0.56	45 %
0.50	220.0	0.19	37 %

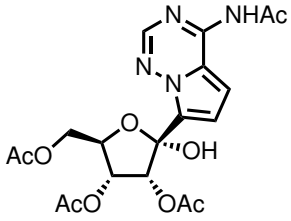

^{1}H NMR (600 MHz, CD_2Cl_2): δ 8.28 (s, 1H), 8.15 (s, 1H), 7.08 (d, J = 4.8 Hz, 1H), 6.93 (d, J = 4.7 Hz, 1H), 5.72 (d, J = 6.9 Hz, 1H), 5.37 (dd, J = 6.9, 3.8 Hz, 1H), 4.56 (q, J = 3.7 Hz, 1H), 4.44 (dd, J = 12.0, 3.5 Hz, 1H), 4.27 (dd, J = 12.0, 4.7 Hz, 1H), 2.53 (s, 3H), 2.14 (s, 3H), 2.07 (s, 3H), 2.06 (s, 3H).
^{13}C NMR (151 MHz, CD_2Cl_2): δ 170.8, 170.7, 170.5, 169.7, 151.3, 146.2, 129.3, 116.5, 112.1, 104.5, 100.5, 80.4, 73.0, 70.7, 63.7, 26.0, 21.0, 20.9, 20.7.

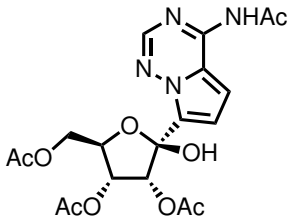

^{1}H NMR (600 MHz, CD_2Cl_2): δ 8.28 (s, 1H), 8.14 (s, 1H), 7.10 (d, J = 4.7 Hz, 1H), 6.97 (d, J = 4.7 Hz, 1H), 5.69 (d, J = 4.5 Hz, 1H), 5.63 (dd, J = 7.7, 4.5 Hz, 1H), 4.53–4.47 (m, 2H), 4.27–4.21 (m, 1H), 2.53 (s, 3H), 2.10 (s, 3H), 2.03 (s, 3H), 1.76 (s, 3H).
^{13}C NMR (151 MHz, CD_2Cl_2): δ 171.0, 170.7, 170.1, 169.3, 151.2, 146.2, 128.3, 116.0, 113.5, 104.6, 103.6, 78.8, 75.9, 72.3, 65.1, 26.0, 21.0, 20.7, 20.5.

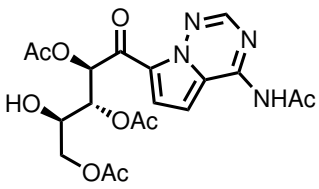

^{1}H NMR (600 MHz, CD_2Cl_2): δ 8.45 (s, 1H), 8.35 (s, 1H), 7.69 (d, J = 5.0 Hz, 1H), 7.13 (d, J = 5.0 Hz, 1H), 6.39 (d, J = 3.3 Hz, 1H), 5.46 (dd, J = 7.8, 3.3 Hz, 1H), 4.31 (t,

J = 7.0 Hz, 1H), 4.19 (dd, J = 11.8, 2.8 Hz, 1H), 4.10 (dd, J = 11.8, 6.2 Hz, 1H), 2.57 (s, 3H), 2.21 (s, 3H), 2.03 (s, 3H), 2.00 (s, 3H).
^{13}C NMR (151 MHz, CD_2Cl_2): δ 183.0, 171.3, 171.0, 170.4, 170.1, 151.7, 147.7, 128.4, 119.7, 119.6, 105.4, 76.6, 72.0, 68.5, 65.5, 26.1, 21.0, 20.9, 20.8.

5.8 Diastereoselective Deoxycyanation

The discussion regarding the deoxycyanation can be found in Chapter 4, Section 3.5. Initial experiments after substitution of TfOH with $HNTf_2$ (Table 4.2, entry 3) indicated formation of gem-dicyanodhydro-1,3-oxazine **380**. The structural assignment of **380** was made based on crude 2D NMR analysis without isolation, and the spectroscopic evidence for this assignment is provided below.

(6*R*,7*R*)-4a-(4-acetamidopyrrolo[2,1-*f*][1,2,4]triazin-7-yl)-6-(acetoxymethyl)-4,4-dicyano-2-methyl-4a,6,7,7a-tetrahydro-4*H*-furo[2,3-*e*][1,3]oxazin-7-yl acetate (**380**):

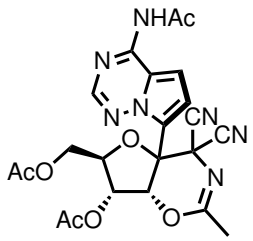

^{1}H NMR (600 MHz, CD_2Cl_2): δ 8.21 (s, 1H), 7.30 (d, J = 4.8 Hz, 1H), 7.16 (d, J = 4.9 Hz, 1H), 6.84 (d, J = 3.8 Hz, 1H), 5.06 (dd, J = 8.5, 3.8 Hz, 1H), 4.44–4.39 (m, 1H, C5H), 4.35 (dd, J = 12.5, 3.0 Hz, 1H), 4.04 (dd, J = 12.5, 4.7 Hz, 1H), 2.23 (s, 3H).
^{13}C NMR (151 MHz, CD_2Cl_2): δ 146.3, 116.6, 104.9, 74.1, 73.0, 62.8, 62.5.
^{15}N NMR (61 MHz, CD_2Cl_2): δ 180.0.
ESI-HRMS: calculated for $C_{22}H_{20}N_7O_7$ $[M-H]^-$: 494.142 971, found: 449.143 490.

(2*S*,3*R*,4*R*,5*R*)-2-(4-acetamidopyrrolo[2,1-*f*][1,2,4]triazin-7-yl)-5-(acetoxymethyl)-2-((trimethylsilyl)oxy)tetrahydrofuran-3,4-diyl diacetate (**377**):

We additionally observed the presence of β-silylated lactol **377** in reactions that did not proceed to full conversion. Similar to the assignment of **380**, we identified several key signals by virtue of 2D NMR analysis.

^{1}H NMR (600 MHz, CD_2Cl_2): δ 7.24 (d, J = 4.8 Hz, 1H), 7.05–7.04 (m, 1H), 6.01 (d, J = 4.4 Hz, 1H), 5.65 (dd, J = 8.4, 4.4 Hz, 1H), 4.44–4.40 (m, 1H), 4.40–4.37 (m, 1H), 4.28–4.25 (m, 1H).

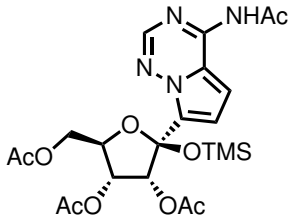

^{13}C NMR (151 MHz, CD_2Cl_2): δ 113.3, 105.2, 104.0, 78.0, 76.8, 72.3, 65.3.
ESI-HRMS: calculated for $C_{22}H_{29}N_4O_9Si$ $[M-H]^-$: 521.170 934, found: 521.171 070.

(2*R*,3*R*,4*R*,5*R*)-2-(4-acetamidopyrrolo[2,1-*f*][1,2,4]triazin-7-yl)-5-(acetoxymethyl)-2-cyanotetrahydrofuran-3,4-diyl diacetate (**378**):

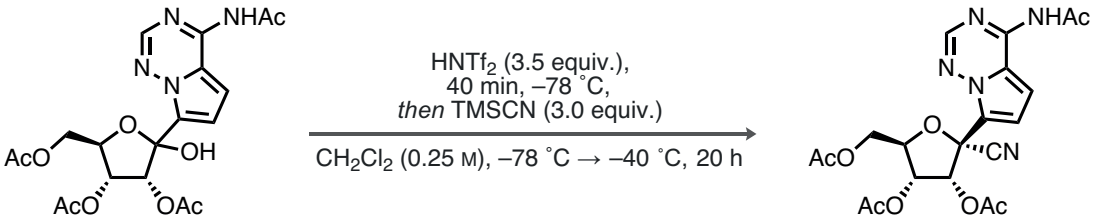

Bistriflimide (0.88 mol/L solution in CH_2Cl_2, 3.5 equiv., 0.35 mmol, 400 µL) was added to lactol **370** (1.0 equiv., 0.10 mmol, 45.0 mg) in at −78 °C (dry ice/acetone bath). The reaction was stirred for 40 min at −78 °C, followed by the addition of TMSCN (3.0 equiv., 0.30 mmol, 38.0 µL). The reaction was allowed to warm to −40 °C (using a suitable cryostat), and was stirred for 20 h at this temperature. The reaction was terminated by the addition of NEt_3 (4.0 equiv., 0.40 mmol, 56.0 µL), and the volatiles were removed under high vacuum using an additional cooling trap filled with liquid N_2. ^{1}H NMR analysis of the crude mixture indicated full conversion towards **378** (87:13 dr). The crude mixture was then treated with additional NEt_3 (1.0 mL) and directly subjected to flash column chromatography (CH_2Cl_2/EtOAc 1:1) to provide the title compound in 84 % yield (38.5 mg, 89:11 dr) as an off-white solid.

^{1}H NMR (600 MHz, CD_2Cl_2): δ 8.33 (s, 1H), 8.24 (s, 1H), 7.14 (d, J = 4.8 Hz, 1H), 7.10 (d, J = 4.9 Hz, 1H), 6.17 (d, J = 5.9 Hz, 1H), 5.43 (dd, J = 5.9, 5.2 Hz, 1H), 4.63 (td, J = 5.0, 3.4 Hz, 1H), 4.46 (dd, J = 12.3, 3.5 Hz, 1H), 4.29 (dd, J = 12.3, 4.9 Hz, 1H), 2.54 (s, 3H), 2.15 (s, 3H), 2.14 (s, 3H), 2.05 (s, 3H).
^{13}C NMR (151 MHz, CD_2Cl_2): δ 170.9, 170.8, 170.3, 169.5, 151.5, 146.8, 123.7, 118.4, 115.4, 114.1, 104.7, 81.5, 77.8, 72.5, 71.0, 63.0, 21.1, 20.9, 20.9.
ESI-HRMS: calculated for $C_{20}H_{20}N_5O_8$ $[M-H]^-$: 458.131 738, found: 458.131 900.

5.9 Deacetylation of the Cyanated Furanoside

(2*R*,3*R*,4*S*,5*R*)-2-(4-aminopyrrolo[2,1-*f*][1,2,4]triazin-7-yl)-3,4-dihydroxy-5-(hydroxymethyl)tetrahydrofuran-2-carbonitrile (305):

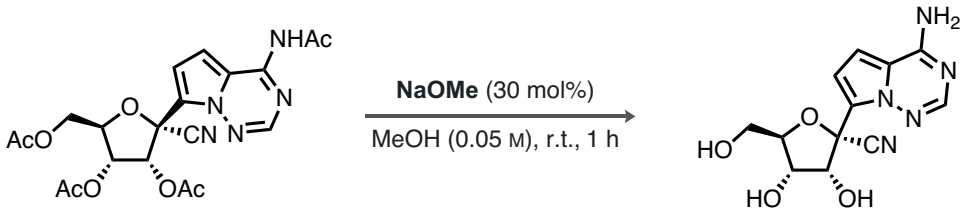

378 **305**

Following a literature procedure,[386] NaOMe (25 % solution in MeOH, 30 mol%, 8.0 µL) was added to a solution of **378** (1.0 equiv., 0.12 mmol, 54.0 mg) in MeOH (2.4 mL, 0.05 mol/L) and the reaction was stirred for 1 h at room temperature. The visible precipitate was separated by decanting the solvent, followed by addition of hexanes, and additional decanting. Subsequently, the white solid was dried under high vacuum to provide the title compound in 81 % yield (27.6 mg, >95:5 dr, 92 % based on the correct diastereomer).

^{1}H NMR (600 MHz, DMSO-d_6): δ 7.91 (s, 1H), 7.89 (s, 2H), 6.90 (d, J = 4.5 Hz, 1H), 6.88 (d, J = 4.5 Hz, 1H), 6.09 (s, 1H), 5.19 (d, J = 4.5 Hz, 1H), 4.91 (t, J = 5.7 Hz, 1H), 4.64 (d, J = 5.1 Hz, 1H), 4.09–4.03 (m, 1H), 3.96 (d, J = 5.9 Hz, 1H), 3.64 (ddd, J = 12.2, 5.1, 3.4 Hz, 1H), 3.51 (ddd, J = 12.1, 6.1, 4.5 Hz, 1H).
^{13}C NMR (151 MHz, CD_2Cl_2): δ 155.6, 147.9, 123.9, 117.3, 116.5, 110.8, 100.8, 85.4, 78.5, 74.2, 70.1, 60.9.
ESI-HRMS: calculated for $C_{12}H_{14}N_5O_4$ $[M+H]^+$: 292.104 028, found: 292.103 860.

Spectral data matches those provide in the literature.[282]

6 Synthesis of Catalysts

(*S*)-3,3'-bis(4-(1-(trifluoromethyl)cyclopropyl)phenyl)-[1,1'-binaphthalene]-2,2'-diol: (**453**):

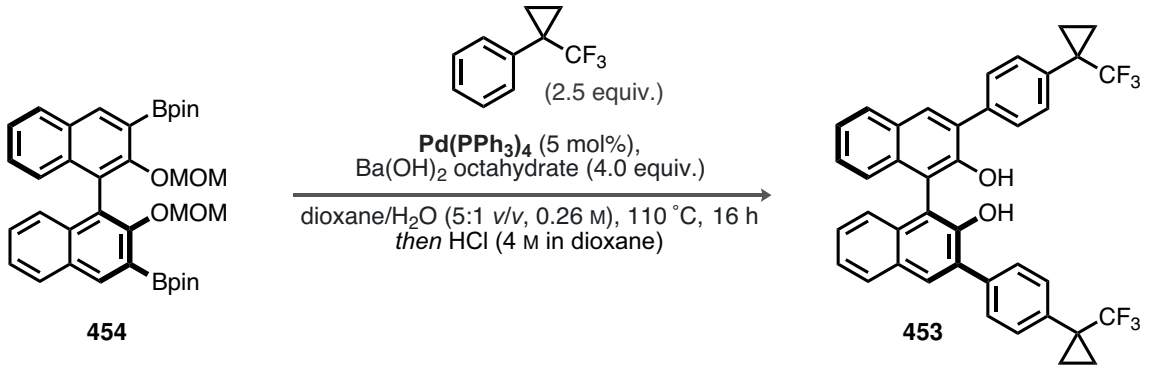

(*S*)-MOM-BINOL-Bpin ester **454** (1.0 equiv., 6.6 mmol, 4.15 g), 1-bromo-4-(1-(trifluoromethyl)cyclopropyl)benzene (2.5 equiv., 16.7 mmol, 4.39 g), and $BaOH_2$ octahydrate (4.0 equiv., 25.5 mmol, 8.36 g) were suspended in 1,4-dioxane/H_2O (5:1 *v*/*v*, 17.0 mL, 0.26 mol/L) at room temperature. The suspension was degassed by the freeze-pump-thaw method at −78 °C, followed by the addition of $Pd(PPh_3)_4$ (5 mol%, 381.0 mg). The reaction was transferred to an oil bath (set to 130 °C) and refluxed for 16 h. After cooling to room temperature, the reaction was terminated by addition of HCl (1.0 mol/L), the phases were separated, and the aqueous layer was extracted with CH_2Cl_2 (3 x). The combined organic extracts were dried over Na_2SO_4 and concentrated under reduced pressure. Then, HCl (4.0 mol/L in 1,4-dioxane, 20.0 mL) was added to the mixture, followed by stirring for 2 h at room temperature. The solvent was removed under reduced pressure, and the crude mixture directly subjected to flash column chromatography on silica (hexanes/EtOAc 19:1 → 7:3). The title compound was obtained in 92 % yield (4.51 g) as a white solid.

^{1}H NMR (500 MHz, $CDCl_3$): δ 8.05 (d, J = 1.8 Hz, 2H), 7.93 (d, J = 8.1 Hz, 2H), 7.81–7.67 (m, 4H), 7.59 (dd, J = 8.3, 2.0 Hz, 4H), 7.40 (ddd, J = 8.2, 6.7, 1.3 Hz, 2H), 7.33 (td, J = 7.6, 6.9, 1.4 Hz, 2H), 7.29–7.13 (m, 2H), 5.34 (s, 2H), 1.40 (s, 4H), 1.10 (s, 4H).
^{13}C NMR (126 MHz, $CDCl_3$): δ 150.3, 137.7, 135.7, 133.1, 131.8, 131.4, 130.2, 129.7, 129.6, 129.2, 128.7, 128.4, 127.7, 127.6, 125.5, 125.4, 124.6, 124.3, 112.3, 28.5, 28.3, 28.0, 27.7, 21.6, 10.0, 9.9.
^{19}F NMR (471 MHz, $CDCl_3$): δ −69.89.
ESI-HRMS: calculated for $C_{40}H_{27}F_6O_2$ $[M-H]^-$: 653.192 076, found: 653.192 620.

IDPi 91:

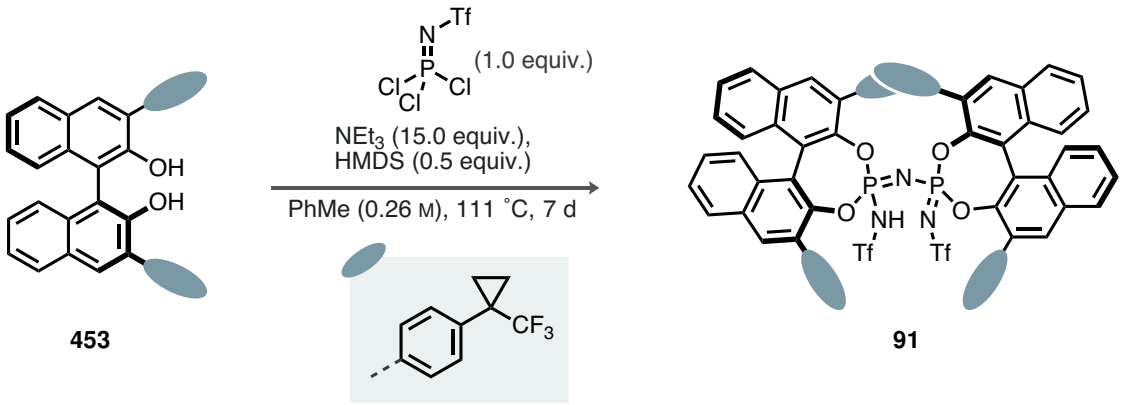

453 **91**

Phosphorimidoyl trichloride (1.0 equiv., 2.3 mmol, 652 mg) and NEt_3 (15.0 equiv., 34.4 mmol, 4.8 mL) was added to a solution of (*S*)-BINOL **453** in toluene (9.0 mL, 0.26 mol/L) and the reaction was stirred for 30 min at room temperature. Then, HMDS (0.5 equiv., 1.1 mmol, 239 µL) was added, and the reaction was stirred at room temperature for 10 min, followed by transfer to a pre-heated oil bath (set to 140 °C). The reaction was refluxed for 7 d. After cooling to room temperature, the mixture was diluted with CH_2Cl_2 and HCl (3.0 mol/L). The phases were separated, the aqueous layer extracted with CH_2Cl_2 (2 x), the combined extracts dried over Na_2SO_4, and concentrated under reduced pressure. Purification by flash column chromatography on silica gel (*n*-pentane/Et_2O 2:3) followed by acidification in CH_2Cl_2 with HCl (6.0 mol/L) afforded the title compound in 89 % yield (1.72 g) as ann off-white solid.

^{1}H NMR (500 MHz, $CDCl_3$): δ 8.17 (s, 2H), 8.03 (d, J = 8.3 Hz, 2H), 8.00 (d, J = 8.2 Hz, 2H), 7.80 (ddd, J = 8.1, 5.7, 2.2 Hz, 2H), 7.68–7.59 (m, 4H), 7.56 (ddd, J = 8.1, 6.5, 1.4 Hz, 2H), 7.41–7.27 (m, 8H), 7.16–7.09 (m, 6H), 7.06 (d, J = 8.0 Hz, 4H), 6.59 (d, J = 8.4 Hz, 4H), 1.32–1.21 (m, 4H), 1.19 (ddd, J = 10.0, 6.6, 5.0 Hz, 2H), 1.09 (ddd, J = 10.0, 6.4, 4.9 Hz, 2H), 1.03–0.89 (m, 6H), 0.61 (dt, J = 11.0, 5.9 Hz, 2H).
^{13}C NMR (126 MHz, $CDCl_3$): δ 148.0, 147.9, 147.8, 145.9, 145.2, 144.9, 143.0, 142.5, 142.0, 141.7, 135.6, 135.5, 135.3, 135.1, 134.7, 134.6, 134.4, 134.3, 130.7, 130.4, 130.0, 129.8, 128.3, 128.2, 125.64, 125.62, 125.3, 125.1, 125.0, 124.7, 122.0, 121.9, 121.84, 121.82, 120.7, 120.6, 28.81, 28.80, 27.5, 27.0, 26.8, 16.1, 15.3, 15.2, 15.18, 14.7, 14.5.
^{19}F NMR (471 MHz, $CDCl_3$): δ −69.94, −70.00, −78.47.
^{31}P NMR (203 MHz, $CDCl_3$): δ −15.79.
ESI-HRMS: calculated for $C_{82}H_{52}F_{18}N_3O_8P_2S_2$ $[M-H]^-$: 1674.238 928, found: 1674.240 510.

6.1 Catalysts from Other Group Members

The following catalysts were provided by the technicians of the List group: **25**, **30**, **87**, **88**, **89**, **90**. IDPi catalysts **94**, **94a**, **94b**, **94c**, **94d**, **94e** were provided by Dr. Hui Zhou. IDPi catalyst **99a** was provided by Dr. Santanu Ghosh. IDPi catalyst **122** was provided by Dr. Oleg Grossmann and Dr. Chendan Zhu. IDPi catalysts **151a**, **122**, **122a**, **122b**, **152a**, **153**, **153a** were provided by Dr. Chendan Zhu. IDPi catalyst **87a** was provided by Dr. Vikas Singh. IDPi catalyst **150b** was provided by Sebastian Brunen, as well as IDPis **282a**, **282b**, and **292a**. IDPi catalyst **282** was provided by Mathias Turberg. IDPi catalysts **284**, **284a**, **284b**, **285**, **286**, **287**, **288**, **289**, **290**, **291** were provided by Dr. Manuel Scharf.

7 X-Ray Data

Methyl-3-((*tert*-butoxycarbonyl)amino)-2-methyl-4-phenylbutanoate (133a):

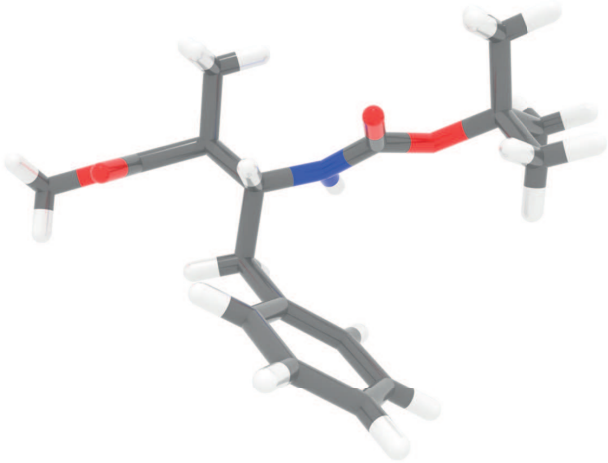

Fig. 5.1: X-ray crystal structure of **133a**.

Identification code	13001
Empirical formula	$C_{17}H_{25}NO_4$
Color	colorless
Formula weight	307.38 g/mol
Temperature	100(2) K
Wavelength	1.54178 Å
Crystal system	MONOCLINIC
Space group	*Cc*, (no. 9)
Unit cell dimensions	
a	20.5518(16) Å
b	5.2194(4) Å
c	17.6501(14) Å
α	90°
β	116.247(4)°
γ	90°
Volume	1698.1(2) $Å^3$
Z	4
Density (calculated)	1.202 $Mg \cdot m^{-3}$
Absorption coefficient	0.691 mm^{-1}
F(000)	664 e
Crystal size	0.142 x 0.142 x 0.060 mm^3
θ range for data collection	4.798 to 63.206°
Index ranges	$-23 \leq h \leq 23$, $-5 \leq k \leq 4$, $-20 \leq l \leq 20$

Reflections collected	16924
Independent reflections	2562 [R_{int} = 0.0412]
Reflections with I>2σ(I)	2364
Completeness to θ = 63.206°	98.2 %
Absorption correction	Gaussian
Max. and min. transmission	0.97 and 0.94
Refinement method	Full-matrix least-squares on F^2
Data / restraints / parameters	2562 / 2 / 208
Goodness-of-fit on F^2	1.107
Final R indices [I>2σ(I)]	R_1 = 0.0287 wR_2 = 0.0655
R indices (all data)	R_1 = 0.0388 wR_2 = 0.0716
Absolute structure parameter	0.11(6)
Largest diff. peak and hole	0.2 and -0.2 e · $Å^{-3}$

Table 5.2: Bond lengths [Å] and angles [°].

Bond	**Length [Å]**	**Bond**	**Length [Å]**
O(1)–C(1)	1.206(3)	O(2)–C(1)	1.340(3)
O(2)–C(5)	1.450(3)	O(3)–C(7)	1.224(3)
O(4)–C(7)	1.346(3)	O(4)–C(8)	1.477(3)
N(1)–H(1)	0.86(4)	N(1)–C(3)	1.453(3)
N(1)–C(7)	1.347(3)	C(1)–C(2)	1.500(4)
C(2)–C(3)	1.539(4)	C(2)–C(6)	1.536(4)
C(3)–C(4)	1.543(4)	C(4)–C(12)	1.508(4)
C(8)–C(9)	1.516(4)	C(8)–C(10)	1.519(4)
C(8)–C(11)	1.520(4)	C(12)–C(13)	1.386(4)
C(12)–C(17)	1.388(4)	C(13)–C(14)	1.388(4)
C(14)–C(15)	1.383(4)	C(15)–C(16)	1.385(4)
C(16)–C(17)	1.383(4)		
C(1)–O(2)–C(5)	115.9(2)	C(7)–O(4)–C(8)	120.79(19)
C(3)–N(1)–H(1)	118(2)	C(7)–N(1)–H(1)	116(2)
C(7)–N(1)–C(3)	124.8(2)	O(1)–C(1)–O(2)	122.8(2)
O(1)–C(1)–C(2)	125.5(2)	O(2)–C(1)–C(2)	111.7(2)
C(1)–C(2)–C(3)	111.03(19)	C(1)–C(2)–C(6)	107.9(2)
C(6)–C(2)–C(3)	110.5(2)	N(1)–C(3)–C(2)	109.23(19)
N(1)–C(3)–C(4)	109.0(2)	C(2)–C(3)–C(4)	113.2(2)
C(12)–C(4)–C(3)	111.8(2)	O(3)–C(7)–O(4)	125.5(2)
O(3)–C(7)–N(1)	124.8(2)	O(4)–C(7)–N(1)	109.6(2)
O(4)–C(8)–C(9)	110.4(2)	O(4)–C(8)–C(10)	102.1(2)
O(4)–C(8)–C(11)	110.0(2)	C(9)–C(8)–C(10)	110.4(2)

Table 5.2: Bond lengths [Å] and angles [°] (continued).

Bond	**Length [Å]**	**Bond**	**Length [Å]**
C(9)–C(8)–C(11)	113.1(2)	C(10)–C(8)–C(11)	110.2(2)
C(13)–C(12)–C(4)	121.8(2)	C(13)–C(12)–C(17)	118.1(2)
C(17)–C(12)–C(4)	120.0(2)	C(12)–C(13)–C(14)	120.8(3)
C(15)–C(14)–C(13)	120.4(3)	C(14)–C(15)–C(16)	119.3(3)
C(17)–C(16)–C(15)	120.0(3)	C(16)–C(17)–C(12)	121.4(2)

Methyl 2-methyl-3-((4-methylphenyl)sulfonamido)-3-phenylpropanoate (223):

Fig. 5.2: X-ray crystal structure of **223**, omitting the disorder found for the ester fragment.

Identification code	14902
Empirical formula	$C_{18}H_{21}NO_4S$
Color	colorless
Formula weight	347.42 g·mol^{-1}
Temperature	100(2) K
Wavelength	0.71073 Å
Crystal system	MONOCLINIC
Space group	$P2_1/n$, (no. 14)
Unit cell dimensions	
a = 10.3300(8) Å	$\alpha = 90°$
b = 13.8707(11) Å	$\beta = 100.469(3)°$
c = 12.4306(10) Å	$\gamma = 90°$
Volume	1751.5(2) Å^3
Z	4
Density (calculated)	1.318 Mg·m^{-3}
Absorption coefficient	0.206 mm^{-1}
F(000)	736 e
Crystal size	0.32 x 0.069 x 0.061 mm^3
θ range for data collection	2.221 to 33.241°
Index ranges	$-15 \leq h \leq 15$, $-21 \leq k \leq 21$, $-19 \leq l \leq 19$
Reflections collected	225856
Independent reflections	6722 [$R_{int} = 0.0825$]
Reflections with I>2σ(I)	6001
Completeness to $\theta = 25.242°$	99.9 %
Absorption correction	Semi-empirical from equivalents

Max. and min. transmission	0.95 and 0.93
Refinement method	Full-matrix least-squares on F^2
Data / restraints / parameters	6722 / 0 / 238
Goodness-of-fit on F^2	1.061
Final R indices [I>2σ(I)]	$R_1 = 0.0437$ $wR_2 = 0.1205$
R indices (all data)	$R_1 = 0.0483$ $wR_2 = 0.1236$
Largest diff. peak and hole	1.0 and -0.4 e·Å^{-3}

Table 5.3: Bond lengths [Å] and angles [°].

Bond	**Length [Å]**	**Bond**	**Length [Å]**
S(1)–O(3)	1.4453(8)	S(1)–O(4)	1.4294(8)
S(1)–N(1)	1.6249(10)	S(1)–C(12)	1.7590(11)
O(1)–C(3)	1.2398(16)	O(1)–C(4B)	1.372(4)
O(2)–C(3)	1.2965(17)	O(2)–C(4A)	1.426(2)
N(1)–H(1)	0.85(2)	N(1)–C(1)	1.4774(14)
C(1)–H(1A)	0.974(17)	C(1)–C(2)	1.5418(15)
C(1)–C(6)	1.5150(15)	C(2)–C(3)	1.5172(17)
C(2)–C(5)	1.510(2)	C(6)–C(7)	1.4017(17)
C(6)–C(11)	1.3830(17)	C(7)–C(8)	1.3912(18)
C(8)–C(9)	1.388(2)	C(9)–C(10)	1.373(3)
C(10)–C(11)	1.3977(19)	C(12)–C(13)	1.3857(15)
C(12)–C(17)	1.3897(16)	C(13)–C(14)	1.3904(18)
C(14)–C(15)	1.397(2)	C(15)–C(16)	1.387(2)
C(15)–C(18)	1.5091(19)	C(16)–C(17)	1.3871(18)
O(3)–S(1)–N(1)	104.62(5)	O(3)–S(1)–C(12)	108.60(5)
O(4)–S(1)–O(3)	118.98(5)	O(4)–S(1)–N(1)	108.45(5)
O(4)–S(1)–C(12)	107.91(5)	N(1)–S(1)–C(12)	107.80(5)
C(3)–O(1)–C(4B)	121.4(3)	C(3)–O(2)–C(4A)	117.80(13)
S(1)–N(1)–H(1)	108.5(13)	C(1)–N(1)–S(1)	121.64(7)
C(1)–N(1)–H(1)	117.4(13)	N(1)–C(1)–H(1A)	107.3(10)
N(1)–C(1)–C(2)	106.60(9)	N(1)–C(1)–C(6)	113.79(9)
C(2)–C(1)–H(1A)	106.3(10)	C(6)–C(1)–H(1A)	109.9(10)
C(6)–C(1)–C(2)	112.54(9)	C(3)–C(2)–C(1)	108.01(9)
C(5)–C(2)–C(1)	113.66(11)	C(5)–C(2)–C(3)	109.93(10)
O(1)–C(3)–O(2)	124.55(12)	O(1)–C(3)–C(2)	120.19(12)
O(2)–C(3)–C(2)	115.21(11)	C(7)–C(6)–C(1)	121.24(10)
C(11)–C(6)–C(1)	119.88(11)	C(11)–C(6)–C(7)	118.88(11)
C(8)–C(7)–C(6)	120.49(13)	C(9)–C(8)–C(7)	119.84(14)

Table 5.3: Bond lengths [Å] and angles [°] (continued).

Bond	**Length [Å]**	**Bond**	**Length [Å]**
C(10)–C(9)–C(8)	119.95(12)	C(9)–C(10)–C(11)	120.50(14)
C(6)–C(11)–C(10)	120.33(14)	C(13)–C(12)–S(1)	119.49(9)
C(13)–C(12)–C(17)	120.59(11)	C(17)–C(12)–S(1)	119.66(8)
C(14)–C(15)–C(18)	120.63(14)	C(13)–C(12)–C(17)	120.73(12)
C(16)–C(15)–C(18)	120.72(14)	C(15)–C(16)–C(17)	121.35(12)
C(16)–C(17)–C(12)	119.18(12)		

***N*,4-dimethyl-*N*-(triisopropylsilyl)benzenesulfonamide (269):**

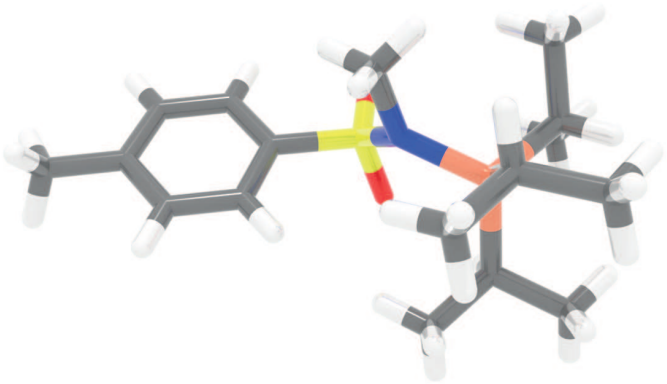

Fig. 5.3: X-ray crystal structure of **269**

Identification code	15391
Empirical formula	$C_{17}H_{31}N\ O_2\ S\ Si$
Color	clear colorless
Formula weight	341.58 g·mol^{-1}
Temperature	150(2) K
Wavelength	0.71073 Å
Crystal system	TRICLINIC
Space group	*P1*, (no. 2)
Unit cell dimensions	
a = 8.1927(3) Å	α = 90.688(2)°
b = 8.4286(3) Å	β = 91.941(2)°
c = 15.4791(6) Å	γ = 117.389(2)°
Volume	948.06(6) Å^3
Z	2
Density (calculated)	1.197 Mg·m^{-3}
Absorption coefficient	0.241 mm^{-1}
F(000)	372 e
Crystal size	0.376 x 0.106 x 0.087 mm^3
θ range for data collection	2.634 to 33.212°
Index ranges	-12 $\leq$ h $\leq$ 12, -12 $\leq$ k $\leq$ 12, -23 $\leq$ l $\leq$ 23
Reflections collected	132128
Independent reflections	7246 [R_{int} = 0.0777]
Reflections with I>2σ(I)	6309
Completeness to θ = 25.242°	99.8 %
Absorption correction	Numerical

Max. and min. transmission	0.98 and 0.95
Refinement method	Full-matrix least-squares on F^2
Data / restraints / parameters	7246 / 0 / 207
Goodness-of-fit on F^2	1.047
Final R indices [I>2σ(I)]	$R_1 = 0.0449$ $wR_2 = 0.1174$
R indices (all data)	$R_1 = 0.0521$ $wR_2 = 0.1236$
Largest diff. peak and hole	0.7 and -0.7 e·Å^{-3}

Table 5.4: Bond lengths [Å] and angles [°].

Bond	**Length [Å]**	**Bond**	**Length [Å]**
S(1)–O(1)	1.4400(11)	S(1)–O(2)	1.4345(11)
S(1)–N(1)	1.6213(12)	S(1)–C(2)	1.7724(11)
Si(1)–N(1)	1.8017(10)	Si(1)–C(9)	1.8848(11)
Si(1)–C(12)	1.8876(13)	Si(1)–C(15)	1.8826(12)
N(1)–C(1)	1.4878(17)	C(2)–C(3)	1.3839(16)
C(2)–C(7)	1.3883(16)	C(3)–C(4)	1.3983(18)
C(4)–C(5)	1.3841(19)	C(5)–C(6)	1.3943(18)
C(5)–C(8)	1.5072(17)	C(6)–C(7)	1.3869(16)
C(9)–C(10)	1.5311(18)	C(9)–C(11)	1.5344(19)
C(10)–C(11)	1.3977(19)	C(12)–C(14)	1.545(2)
C(12)–C(13)	1.525(2)	C(15)–C(17)	1.5380(17)
C(15)–C(16)	1.5279(18)		
O(1)–S(1)–N(1)	110.79(8)	O(1)–S(1)–C(2)	106.09(6)
O(2)–S(1)–O(1)	118.35(8)	O(2)–S(1)–N(1)	107.35(5)
O(2)–S(1)–C(2)	109.32(6)	N(1)–S(1)–C(2)	104.02(5)
N(1)–Si(1)–C(9)	109.41(5)	N(1)–Si(1)–C(12)	102.76(6)
N(1)–Si(1)–C(15)	111.97(5)	C(9)–Si(1)–C(12)	108.38(6)
C(15)–Si(1)–C(9)	109.16(5)	C(15)–Si(1)–C(12)	114.91(6)
S(1)–N(1)–Si(1)	123.72(6)	C(1)–N(1)–S(1)	112.52(10)
C(1)–N(1)–Si(1)	119.30(9)	C(3)–C(2)–S(1)	119.06(9)
C(3)–C(2)–C(7)	120.46(11)	C(7)–C(2)–S(1)	120.46(8)
C(2)–C(3)–C(4)	119.19(12)	C(5)–C(4)–C(3)	121.20(12)
C(4)–C(5)–C(6)	118.57(11)	C(4)–C(5)–C(8)	121.11(12)
C(6)–C(5)–C(8)	120.31(12)	C(7)–C(6)–C(5)	120.96(12)
C(6)–C(7)–C(2)	119.62(11)	C(10)–C(9)–Si(1)	113.99(9)
C(10)–C(9)–C(11)	109.81(11)	C(11)–C(9)–Si(1)	112.57(8)
C(13)–C(12)–Si(1)	113.95(11)	C(13)–C(12)–C(14)	109.95(16)
C(14)–C(12)–Si(1)	113.53(10)	C(16)–C(15)–Si(1)	116.09(8)

Table 5.4: Bond lengths [Å] and angles [°] (continued).

Bond	**Length [Å]**	**Bond**	**Length [Å]**
C(16)–C(15)–C(17)	110.44(11)	C(17)–C(15)–Si(1)	110.73(8)

(1*S*,2*S*,3*R*,4*R*)-1-(4-aminopyrrolo[2,1-*f*][1,2,4]triazin-7-yl)pentane-1,2,3,4,5-pentaol (344):

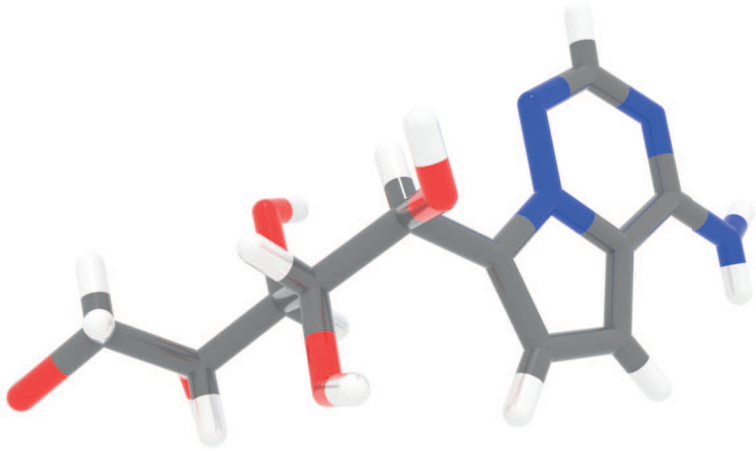

Fig. 5.4: X-ray crystal structure of **344**

Identification code	13994
Empirical formula	$C_{11}H_{16}N_4O_5$
Color	colorless
Formula weight	284.28 g·mol^{-1}
Temperature	100(2) K
Wavelength	1.54178 Å
Crystal system	MONOCLINIC
Space group	$P2_1$, (no. 4)
Unit cell dimensions	
a = 9.0404(5) Å	$\alpha = 90°$
b = 5.2892(3) Å	$\beta = 101.113(2)°$
c = 12.6527(7) Å	$\gamma = 90°$
Volume	593.66(6) Å^3
Z	2
Density (calculated)	1.590 Mg·m^{-3}
Absorption coefficient	1.082 mm^{-1}
F(000)	300 e
Crystal size	0.247 x 0.185 x 0.071 mm^3
θ range for data collection	3.560 to 72.004°
Index ranges	-11 ≤ h ≤ 10, -6 ≤ k ≤ 6, -15 ≤ l ≤ 15
Reflections collected	21970
Independent reflections	2218 [R_{int} = 0.0357]

Reflections with I>2σ(I)	2209
Completeness to $\theta = 67.500°$	100.0 %
Absorption correction	Gaussian
Max. and min. transmission	0.94 and 0.83
Refinement method	Full-matrix least-squares on F^2
Data / restraints / parameters	2218 / 1 / 225
Goodness-of-fit on F^2	1.082
Final R indices [I>2σ(I)]	$R_1 = 0.0238$ $wR_2 = 0.0621$
R indices (all data)	$R_1 = 0.0240$ $wR_2 = 0.0623$
Absolute structure parameter	0.07(5)
Largest diff. peak and hole	0.2 and -0.2 e·Å^{-3}

Table 5.5: Bond lengths [Å] and angles [°].

Bond	**Length [Å]**	**Bond**	**Length [Å]**
O(1)–H(1)	0.79(3)	O(1)–C(1)	1.435(2)
O(2)–H(2)	0.83(4)	O(2)–C(2)	1.429(2)
O(3)–H(3)	0.88(3)	O(3)–C(3)	1.427(2)
O(4)–H(4)	0.85(3)	O(4)–C(4)	1.430(2)
O(5)–H(5)	0.86(3)	O(5)–C(5)	1.438(2)
N(1)–H(1A)	0.86(3)	N(1)–H(1B)	0.89(3)
N(1)–C(10)	1.333(3)	N(2)–C(10)	1.334(2)
N(2)–C(11)	1.365(2)	N(3)–N(4)	1.376(2)
N(3)–C(11)	1.308(2)	N(4)–C(6)	1.369(2)
N(4)–C(9)	1.389(2)	C(1)–C(2)	1.519(2)
C(2)–H(2A)	0.99(2)	C(2)–C(3)	1.540(2)
C(3)–H(3A)	0.98(2)	C(3)–C(4)	1.532(2)
C(4)–H(4A)	0.99(2)	C(4)–C(5)	1.535(3)
C(5)–H(5A)	0.94(3)	C(5)–C(6)	1.499(2)
C(6)–C(7)	1.386(3)	C(7)–C(8)	1.401(2)
C(8)–C(9)	1.384(3)	C(9)–C(10)	1.425(2)
C(1)–O(1)–H(1)	106(2)	C(2)–O(2)–H(2)	112.9(19)
C(3)–O(3)–H(3)	109(2)	C(4)–O(4)–H(4)	108.6(19)
C(5)–O(5)–H(5)	109.8(18)	H(1A)–N(1)–H(1B)	119(2)
C(10)–N(1)–H(1A)	121.2(16)	C(10)–N(1)–H(1B)	116.9(17)
C(10)–N(2)–C(11)	117.01(15)	C(11)–N(3)–N(4)	112.35(15)
N(3)–N(4)–C(9)	124.65(15)	C(6)–N(4)–N(3)	125.61(14)
C(6)–N(4)–C(9)	109.74(15)	O(1)–C(1)–C(2)	110.81(16)
O(2)–C(2)–C(1)	107.09(14)	O(2)–C(2)–H(2A)	107.3(12)

Table 5.5: Bond lengths [Å] and angles [°] (continued).

Bond	**Length [Å]**	**Bond**	**Length [Å]**
O(2)–C(2)–C(3)	109.36(14)	C(1)–C(2)–H(2A)	110.3(11)
C(1)–C(2)–C(3)	112.90(16)	C(3)–C(2)–H(2A)	109.7(11)
O(3)–C(3)–C(2)	109.97(13)	O(3)–C(3)–H(3A)	110.0(3)
O(3)–C(3)–C(4)	108.30(15)	C(2)–C(3)–H(3A)	106.4(14)
C(4)–C(3)–C(2)	113.06(14)	C(4)–C(3)–H(3A)	109.1(13)
O(4)–C(4)–C(3)	107.68(15)	O(4)–C(4)–H(4A)	110.0(13)
O(4)–C(4)–C(5)	112.30(14)	C(3)–C(4)–H(4A)	108.4(13)
C(3)–C(4)–C(5)	112.78(14)	C(5)–C(4)–H(4A)	105.6(14)
O(5)–C(5)–C(4)	107.96(14)	O(5)–C(5)–H(5A)	113.9(17)
O(5)–C(5)–C(6)	108.27(14)	C(4)–C(5)–H(5A)	105.9(15)
C(6)–C(5)–C(4)	114.50(16)	C(6)–C(5)–H(5A)	106.5(15)
N(4)–C(6)–C(5)	120.26(17)	N(4)–C(6)–C(7)	106.7(15)
C(7)–C(6)–C(5)	132.66(16)	C(6)–C(7)–C(8)	108.99(16)
C(9)–C(8)–C(7)	106.94(16)	N(4)–C(9)–C(10)	116.48(17)
C(8)–C(9)–N(4)	107.56(15)	C(8)–C(9)–C(10)	135.90(17)
N(1)–C(10)–N(2)	119.53(17)	N(1)–C(10)–C(9)	120.57(18)
N(2)–C(10)–C(9)	119.89(17)	N(3)–C(11)–N(2)	129.59(18)

BIBLIOGRAPHY

[1] J. J. Berzelius, *Edinburgh New Philos. J.* **1836**, *21*, 223–236.

[2] B. M. Trost, *Angew. Chem. Int. Ed.* **1995**, *34*, 259–281.

[3] G. Rothenberg, *Catalysis – Concepts and Green Applications*, Wiley, **2008**.

[4] L. Pasteur, *Ann. Chim. Phys.* **1848**, *24*, 442 459.

[5] J. H. v. Hoff, *Archives Néerlandaises des Sciences Exactes et Naturelles* **1874**, *9*, 445–454.

[6] J. A. L. Bel, *Bulletin de la Société Chimique de Paris* **1874**, *22*, 337–347.

[7] W. S. Knowles, *Angew. Chem. Int. Ed.* **2002**, *41*, 1998–2007.

[8] R. Noyori, *Angew. Chem. Int. Ed.* **2002**, *41*, 2008–2022.

[9] K. B. Sharpless, *Angew. Chem. Int. Ed.* **2002**, *41*, 2024–2032.

[10] P. A. Wender, V. A. Verma, T. J. Paxton, T. H. Pillow, *Acc. Chem. Res.* **2008**, *41*, 40–49.

[11] B. List, R. A. Lerner, C. F. Barbas, *J. Am. Chem. Soc.* **2000**, *122*, 2395–2396.

[12] K. A. Ahrendt, C. J. Borths, D. W. C. MacMillan, *J. Am. Chem. Soc.* **2000**, *122*, 4243 4244.

[13] M. Mahlau, B. List, *Angew. Chem. Int. Ed.* **2013**, *52*, 518–533.

[14] J.-i. Matsuo, M. Murakami, *Angew. Chem. Int. Ed.* **2013**, *52*, 9109–9118.

[15] T. Mukaiyama, *Organic Reactions* **1982**, (Ed.: W. Dauben).

[16] L. Schreyer, R. Properzi, B. List, *Angew. Chem. Int. Ed.* **2019**, *58*, 12761–12777.

[17] B. Mitschke, M. Turberg, B. List, *Chem* **2020**, *6*, 2515–2532.

[18] H. O. House, D. S. Crumrine, A. Y. Teranishi, H. D. Olmstead, *J. Am. Chem. Soc.* **1973**, *95*, 3310–3324.

[19] T. Mukaiyama, K. Narasaka, K. Banno, *Chem. Lett.* **1973**, *2*, 1011–1014.

[20] G. Stork, P. F. Hudrlik, *J. Am. Chem. Soc.* **1968**, *90*, 4462–4464.

[21] S. Murai, Y. Kuroki, T. Aya, N. Sonoda, S. Tsutsumi, *J. Chem. Soc. Chem. Commun.* **1972**, *0*, 741–741.

[22] S. Murai, Y. Kuroki, K. Hasegawa, S. Tsutsumi, *J. Chem. Soc. Chem. Commun.* **1972**, *0*, 946–947.

[23] T. Mukaiyama, K. Banno, K. Narasaka, *J. Am. Chem. Soc.* **1974**, *96*, 7503–7509.

[24] K. Saigo, M. Osaki, T. Mukaiyama, *Chem. Lett.* **1975**, *4*, 989–990.

[25] A. Hosomi, H. Sakurai, *Tetrahedron Lett.* **1976**, *17*, 1295–1298.

[26] S. Danishefsky, J. F. Kerwin, S. Kobayashi, *J. Am. Chem. Soc.* **1982**, *104*, 358–360.

[27] T. Mukaiyama, N. Iwasawa, *Chem. Lett.* **1982**, *11*, 1903–1906.

[28] T. Mukaiyama, R. W. Stevens, N. Iwasawa, *Chem. Lett.* **1982**, *11*, 353–356.

[29] N. Iwasawa, T. Mukaiyama, *Chem. Lett.* **1982**, *11*, 1441–1444.

[30] S. Kobayashi, T. Mukaiyama, *Chem. Lett.* **1989**, *18*, 297–300.

[31] T. Mukaiyama, S. Kobayashi, H. Uchiro, I. Shiina, *Chem. Lett.* **1990**, *19*, 129–132.

[32] T. Tsunoda, M. Suzuki, R. Noyori, *Tetrahedron Lett.* **1980**, *21*, 71–74.

[33] E. M. Carreira, R. A. Singer, *Tetrahedron Lett.* **1994**, *35*, 4323–4326.

[34] S. E. Denmark, S. B. D. Winter, X. Su, K.-T. Wong, *J. Am. Chem. Soc.* **1996**, *118*, 7404–7405.

[35] E. M. Carreira, R. A. Singer, W. Lee, *J. Am. Chem. Soc.* **1994**, *116*, 8837 8838.

[36] E. R. Parmee, O. Tempkin, S. Masamune, A. Abiko, *J. Am. Chem. Soc.* **1991**, *113*, 9365–9366.

[37] D. A. Evans, J. A. Murry, M. C. Kozlowski, *J. Am. Chem. Soc.* **1996**, *118*, 5814–5815.

[38] S. E. Denmark, K.-T. Wong, R. A. Stavenger, *J. Am. Chem. Soc.* **1997**, *119*, 2333–2334.

[39] T. Mukaiyama, A. Ishida, *Chem. Lett.* **1975**, *4*, 319–322.

[40] K. Narasaka, K. Soai, T. Mukaiyama, *Chem. Lett.* **1974**, *3*, 1223–1224.

[41] I. Ojima, S.-i. Inaba, K. Yoshida, *Tetrahedron Letters* **1977**, *18*, 3643–3646.

[42] H. Yamamoto, K. Ishihara, *Acid Catalysis in Modern Organic Synthesis*, Wiley VCH, Weinheim, **2008**.

[43] M. Dusselier, M. E. Davis, *Chem. Rev.* **2018**, *118*, 5265–5329.

[44] R. Breslow, *Acc. Chem. Res.* **1995**, *28*, 146–153.

[45] S. Grimme, *The Chemical Bond*, (Eds.: G. Frenking, S. Shaik), Wiley VCH, Weinheim, **2014**.

[46] J. P. Wagner, P. R. Schreiner, *Angew. Chem. Int. Ed.* **2017**, *54*, 12274–12296.

[47] H. Eyring, *J. Chem. Phys.* **1935**, *3*, 107–115.

[48] M. G. Evans, M. Polanyi, *Trans. Faraday Soc.* **1935**, *31*, 875–894.

[49] S. Mukherjee, J. W. Yang, S. Hoffmann, B. List, *Chem. Rev.* **2007**, *107*, 5471–5569.

[50] S. Mayer, B. List, *Angew. Chem. Int. Ed.* **2006**, *45*, 4193–4195.

[51] T. Akiyama, J. Itoh, K. Yokota, K. Fuchibe, *Angew. Chem. Int. Ed.* **2004**, *43*, 1566 1568.

[52] D. Uraguchi, M. Terada, *J. Am. Chem. Soc.* **2004**, *126*, 5356–5357.

[53] S. Hoffmann, A. M. Seayad, B. List, *Angew. Chem. Int. Ed.* **2005**, *44*, 7424–7427.

[54] J. Seayad, A. M. Seayad, B. List, *J. Am. Chem. Soc.* **2006**, *128*, 1086–1087.

[55] J. W. Yang, M. T. H. Fonseca, N. Vignola, B. List, *Angew. Chem. Int. Ed.* **2004**, *44*, 108–110.

[56] S. G. Ouellet, J. B. Tuttle, D. W. C. MacMillan, *J. Am. Chem. Soc.* **2005**, *127*, 32 33.

[57] G. L. Hamilton, E. J. Kang, M. Mba, F. D. Toste, *Science* **2007**, *317*, 496–499.

[58] M. S. Taylor, E. N. Jacobsen, *Angew. Chem. Int. Ed.* **2006**, *45*, 1520 1543.

[59] A. G. Doyle, E. N. Jacobsen, *Chem. Rev.* **2007**, *107*, 5713–5743.

[60] R. R. Knowles, E. N. Jacobsen, *Proc. Natl. Acad. Sci.* **2010**, *107*, 20678–20685.

[61] L. P. Hammett, A. J. Deyrup, *J. Am. Chem. Soc.* **1932**, *54*, 4239–4247.

[62] N. F. Hall, J. B. Conant, *J. Am. Chem. Soc.* **1927**, *49*, 3047–3061.

[63] A. Kütt, T. Rodima, J. Saame, E. Raamat, V. Mäemets, I. Kaljurand, I. A. Koppel, R. Y. Garlyauskayte, Y. L. Yagupolskii, L. M. Yagupolskii, E. Bernhardt, H. Willner, I. Leito, *J. Org. Chem.* **2011**, *76*, 391–395.

[64] A. Kütt, S. Selberg, I. Kaljurand, S. Tshepelevitsh, A. Heering, A. Darnell, K. Kaupmees, M. Piirsalu, I. Leito, *Tetrahedron Lett.* **2018**, *59*, 3738–3748.

[65] A. Kütt, S. Tshepelevitsh, J. Saame, M. Lõkov, I. Kaljurand, S. Selberg, I. Leito, *Eur. J. Org. Chem.* **2021**, 1407–1419.

[66] K. Kaupmees, N. Tolstoluzhsky, S. Raja, M. Rueping, I. Leito, *Angew. Chem. Int. Ed.* **2013**, *52*, 11569–11572.

[67] M. Klussmann, L. Ratjen, S. Hoffmann, V. Wakchaure, R. Goddard, B. List, *Synlett* **2010**, 2189–2192.

[68] G. A. Olah, G. K. S. Prakash, Á. Molnár, J. Sommer, *Superacid Chemistry*, John Wiley & Sons, Inc., Hoboken, New Jersey, **2009**.

[69] G. A. Olah, G. Klopman, R. H. Schlosberg, *J. Am. Chem. Soc.* **1969**, *91*, 3261–3268.

[70] J. M. Brunel, *Chem. Rev.* **2005**, *105*, 857–898.

[71] D. Parmar, E. Sugiono, S. Raja, M. Rueping, *Chem. Rev.* **2014**, *114*, 9047–9153.

[72] S. Bahmanyar, K. N. Houk, H. J. Martin, B. List, *J. Am. Chem. Soc.* **2003**, *125*, 2475–2479.

[73] S. Bahmanyar, K. N. Houk, *J. Am. Chem. Soc.* **2001**, *123*, 12911–12912.

[74] I. Felker, G. Pupo, P. Kraft, B. List, *Angew. Chem. Int. Ed.* **2015**, *54*, 1960–1964.

[75] G. A. Shevchenko, B. Oppelaar, B. List, *Angew. Chem. Int. Ed.* **2018**, *57*, 10756–10759.

[76] P. Burk, I. A. Koppel, I. Koppel, L. M. Yagupolskii, R. W. Taft, *J. Comput. Chem.* **1996**, *17*, 30–41.

[77] D. Nakashima, H. Yamamoto, *J. Am. Chem. Soc.* **2006**, *128*, 9626–9627.

[78] S. C. Pan, B. List, *Chem. Asian J.* **2008**, *3*, 430–437.

[79] D. Kampen, A. Ladépêche, G. Claßen, B. List, *Adv. Synth. Catal.* **2008**, *350*, 962–966.

[80] M. Hatano, T. Maki, K. Moriyama, M. Arinobe, K. Ishihara, *J. Am. Chem. Soc.* **2008**, *130*, 16858–16860.

[81] A. Berkessel, P. Christ, N. Leconte, J.-M. Neudörfl, M. Schäfer, *Eur. J. Org. Chem.* **2010**, 5165–5170.

[82] P. García-García, F. Lay, P. García-García, C. Rabalakos, B. List, *Angew. Chem. Int. Ed.* **2009**, *48*, 4363–4366.

[83] M. Treskow, J. Neudörfl, R. Giernoth, *Eur. J. Org. Chem.* **2009**, 3693–3697.

[84] B. Mathieu, L. Ghosez, *Tetrahedron Lett.* **1997**, *38*, 5497–5500.

[85] Z. Zhang, H. Y. Bae, J. Guin, C. Rabalakos, M. v. Gemmeren, M. Leutzsch, M. Klussmann, B. List, *Nat. Commun.* **2016**, *7*, 12478.

[86] K. P. Kepp, *Inorg. Chem.* **2016**, *55*, 9461–9470.

[87] G. Hilt, A. Nödling, *Eur. J. Org. Chem.* **2011**, 7071–7075.

[88] L. Rummel, H. F. König, H. Hausmann, P. R. Schreiner, *J. Org. Chem.* **2022**, *87*, 13168–13177.

[89] H. F. T. Klare, L. Albers, L. Süsse, S. Keess, T. Müller, M. Oestreich, *Chem. Rev.* **2021**, *121*, 5889–5985.

[90] U. Mayer, V. Gutmann, W. Gerger, *Monatsh. Chem.* **1975**, *106*, 1235–1257.

[91] V. Gutmann, *Coord. Chem. Rev.* **1976**, *18*, 225–255.

[92] M. A. Beckett, G. C. Strickland, J. R. Holland, K. S. Varma, *Polymer* **1996**, *37*, 4629–4631.

[93] R. K. Schmidt, K. Müther, C. Mück-Lichtenfeld, S. Grimme, M. Oestreich, *J. Am. Chem. Soc.* **2012**, *134*, 4421–4428.

[94] T. James, M. v. Gemmeren, B. List, *Chem. Rev.* **2015**, *115*, 9388–9409.

[95] T. Gatzenmeier, M. v. Gemmeren, Y. Xie, D. Höfler, M. Leutzsch, B. List, *Science* **2016**, *351*, 949–952.

[96] V. K. Singh, C. Zhu, C. K. De, M. Leutzsch, L. Baldinelli, R. Mitra, G. Bistoni, B. List, *Science* **2023**, *382*, 325–329.

[97] H. Zhou, Y. Zhou, H. Y. Bae, M. Leutzsch, Y. Li, C. K. De, G.-J. Cheng, B. List, *Nature* **2022**, *605*, 84–89.

[98] V. N. Wakchaure, W. DeSnoo, C. J. Laconsay, M. Leutzsch, N. Tsuji, D. J. Tantillo, B. List, *Nature* **2024**, *625*, 287–292.

[99] M. Hatano, T. Mizuno, A. Izumiseki, R. Usami, T. Asai, M. Akakura, K. Ishihara, *Angew. Chem. Int. Ed.* **2011**, *50*, 12189–12192.

[100] M. Hatano, K. Ishihara, *Chem. Commun.* **2012**, *48*, 4273.

[101] M. Hatano, T. Sakamoto, T. Mizuno, Y. Goto, K. Ishihara, *J. Am. Chem. Soc.* **2018**, *140*, 16253–16263.

[102] K. Maruoka, T. Itoh, H. Yamamoto, *J. Am. Chem. Soc.* **1985**, *107*, 4573–4576.

[103] K. Maruoka, T. Itoh, M. Sakurai, K. Nonoshita, H. Yamamoto, *J. Am. Chem. Soc.* **1988**, *110*, 3588–3597.

[104] K. Maruoka, S. Saito, H. Yamamoto, *J. Am. Chem. Soc.* **1992**, *114*, 1089–1090.

[105] K. Maruoka, H. Imoto, H. Yamamoto, *J. Am. Chem. Soc.* **1994**, *116*, 12115–12116.

[106] I. Čorić, B. List, *Nature* **2012**, *483*, 315–319.

[107] Z. Sun, G. A. Winschel, A. Borovika, P. Nagorny, *J. Am. Chem. Soc.* **2012**, *134*, 8074–8077.

[108] R. M. Beesley, C. K. Ingold, J. F. Thorpe, *J. Chem. Soc. Trans.* **1915**, *107*, 1080–1106.

[109] L. Schreyer, P. S. J. Kaib, V. N. Wakchaure, C. Obradors, R. Properzi, S. Lee, B. List, *Science* **2018**, *362*, 216–219.

[110] M. B. Boxer, H. Yamamoto, *J. Am. Chem. Soc.* **2007**, *129*, 2762–2763.

[111] P. Woulfe, *Philos. Trans. Roy. Soc. London* **1771**, *61*, 114–130.

[112] E. Mitscherlich, *Ann. Phar.* **1834**, *12*, 305–311.

[113] A. Laurent, *Ann. Chem. Phys.* **1832**, *49*, 214–221.

[114] J. S. Muspratt, A. W. Hofmann, *Mem. Proc. Chem. Soc.* **1843**, *2*, 367–383.

[115] N. Zinin, *J. Prakt. Chem.* **1842**, *27*, 140–153.

[116] R. Willstätter, H. Kubli, *Ber. Dtsch. Chem. Ges.* **1908**, *41*, 1936–1940.

[117] A. Béchamp, *Ann. Chem. Phys.* **1854**, *42*, 186–196.

[118] K. Hübner, *Chem. unserer Zeit* **2006**, *40*, 274–275.

[119] G. Booth, *Ullmann's Encyclopedia of Industrial Chemistry*, **2013**.

[120] V. Meyer, *Justus Liebigs Ann. Chem.* **1874**, *171*, 1–56.

[121] L. C. R. Henry, *Acad. Sci. Ser. C.* **1895**, 1265.

[122] L. C. R. Henry, *Bull. Soc. Chim. Fr.* **1895**, *13*, 999.

[123] L. C. R. Henry, *Bull. Acad. Roy. Belg.* **1896**, *32*, 33.

[124] H. Sasai, T. Suzuki, S. Arai, T. Arai, M. Shibasaki, *J. Am. Chem. Soc.* **1992**, *114*, 4418–4420.

[125] M. Shibasaki, H. Sasai, T. Arai, *Angew. Chem. Int. Ed.* **1997**, *36*, 1236–1256.

[126] H. Sasai, T. Suzuki, N. Itoh, S. Arai, M. Shibasaki, *Tetrahedron Lett.* **1993**, *34*, 2657–2660.

[127] H. Sasai, N. Itoh, T. Suzuki, M. Shibasaki, *Tetrahedron Lett.* **1993**, *34*, 855–858.

[128] M. Shibasaki, M. Kanai, S. Matsunaga, N. Kumagai, *Acc. Chem. Res.* **2009**, *42*, 1117–1127.

[129] T. Marcelli, R. N. v. d. Haas, J. H. v. Maarseveen, H. Hiemstra, *Synlett* **2005**, 2817–2819.

[130] P. R. Schreiner, A. Wittkopp, *Org. Lett.* **2002**, *4*, 217–220.

[131] T. Marcelli, R. N. S. v. d. Haas, J. H. v. Maarseveen, H. Hiemstra, *Angew. Chem. Int. Ed.* **2006**, *45*, 929–931.

[132] H. Fu, J. Cao, T. Qiao, Y. Qi, S. J. Charnock, S. Garfinkle, T. K. Hyster, *Nature* **2022**, *610*, 302–307.

[133] M. V. Kashutina, S. L. Ioffe, V. A. Tartakovskii, *Dokl. Akad. Nauk SSSR* **1974**, *218*, 607–610.

[134] K. Torssell, O. Zeuthen, R. Servin, C. R. Enzell, J.-E. Berg, A.-M. Pilotti, *Acta Chem. Scand.* **1978**, *32b*, 118–124.

[135] E. W. Colvin, D. Seebach, *J. Chem. Soc. Chem. Commun.* **1978**, 689–691.

[136] E. W. Colvin, A. K. Beck, D. Seebach, *Helv. Chim. Acta* **1981**, *64*, 2264–2271.

[137] D. Seebach, A. K. Beck, T. Mukhopadhyay, E. Thomas, *Helv. Chim. Acta* **1982**, *65*, 1101–1133.

[138] F. Lehr, J. Gonnermann, D. Seebach, *Helv. Chim. Acta* **1979**, *62*, 2258–2275.

[139] E. W. Colvin, A. K. Beck, B. Bastani, D. Seebach, Y. Kai, J. D. Dunitz, *Helv. Chim. Acta* **1980**, *63*, 697–710.

[140] T. Ooi, K. Doda, K. Maruoka, *J. Am. Chem. Soc.* **2003**, *125*, 2054–2055.

[141] J. U. Nef, *Justus Liebigs Ann. Chem.* **1894**, *280*, 263–291.

[142] D. Seebach, *Angew. Chem. Int. Ed.* **1979**, *18*, 239–258.

[143] S. E. Denmark, A. Thorarensen, *Chem. Rev.* **1996**, *96*, 137–166.

[144] V. O. Smirnov, S. L. Ioffe, A. A. Tishkov, Y. A. Khomutova, I. D. Nesterov, M. Y. Antipin, W. A. Smit, V. A. Tartakovsky, *J. Org. Chem.* **2004**, *69*, 8485–8488.

[145] A. A. Mikhaylov, A. D. Dilman, Y. A. Khomutova, D. E. Arkhipov, A. A. Korlyukov, S. L. Ioffe, *Eur. J. Org. Chem.* **2013**, 5670–5677.

[146] A. A. Mikhaylov, Y. A. Khomutova, D. E. Arkhipov, A. A. Korlyukov, S. L. Ioffe, *Mendeleev Commun.* **2014**, *24*, 374–376.

[147] A. Tabolin, A. Sukhorukov, S. Ioffe, A. Dilman, *Synthesis* **2017**, *49*, 3255–3268.

[148] Y. A. Khomutova, V. O. Smirnov, H. Mayr, S. L. Ioffe, *J. Org. Chem.* **2007**, *72*, 9134–9140.

[149] V. O. Smirnov, Y. A. Khomutova, V. A. Tartakovsky, S. L. Ioffe, *Eur. J. Org. Chem.* **2012**, 3377–3384.

[150] D. W. Stephan, *Acc. Chem. Res.* **2015**, *48*, 306–316.

[151] D. J. Scott, M. J. Fuchter, A. E. Ashley, *Chem. Soc. Rev.* **2017**, *46*, 5689–5700.

[152] H. Feger, G. Simchen, *Liebigs Ann. Chem.* **1986**, *1986*, 1456–1465.

[153] H. Feger, G. Simchen, *Liebigs Ann. Chem.* **1986**, *1986*, 428–437.

[154] K. R. Knudsen, T. Risgaard, N. Nishiwaki, K. V. Gothelf, K. A. Jørgensen, *J. Am. Chem. Soc.* **2001**, *123*, 5843–5844.

[155] T. Risgaard, K. V. Gothelf, K. A. Jørgensen, *Org. Biomol. Chem.* **2002**, *1*, 153–156.

[156] J. E. Wilson, A. D. Casarez, D. W. C. MacMillan, *J. Am. Chem. Soc.* **2009**, *131*, 11332–11334.

[157] A. E. Reed, R. B. Weinstock, F. Weinhold, *J. Chem. Phys.* **1985**, *83*, 735–746.

[158] C. Mannich, W. Krösche, *Arch. Pharm.* **1912**, *250*, 647–667.

[159] C. Mannich, E. Ganz, *Ber. Dtsch. Chem. Ges.* **1922**, *55*, 3486–3504.

[160] C. Zhu, F. Mandrelli, H. Zhou, R. Maji, B. List, *J. Am. Chem. Soc.* **2021**, *143*, 3312–3317.

[161] R. P. Cheng, S. H. Gellman, W. F. DeGrado, *Chem. Rev.* **2001**, *101*, 3219–3232.

[162] B. List, P. Pojarliev, W. T. Biller, H. J. Martin, *J. Am. Chem. Soc.* **2002**, *124*, 827–833.

[163] H. Y. Bae, M. J. Kim, J. H. Sim, C. E. Song, *Angew. Chem. Int. Ed.* **2016**, *55*, 10825–10829.

[164] A. K. Beck, D. Seebach, *Encyclopedia of Reagents for Organic Synthesis* **1995**, DOI `10.1002/047084289x.rt313m`.

[165] H. Y. Bae, D. Höfler, P. S. J. Kaib, P. Kasaplar, C. K. De, A. Döhring, S. Lee, K. Kaupmees, I. Leito, B. List, *Nat. Chem.* **2018**, *10*, 888 894.

[166] T. Gatzenmeier, P. S. J. Kaib, J. B. Lingnau, R. Goddard, B. List, *Angew. Chem. Int. Ed.* **2018**, *57*, 2464–2468.

[167] T. Gatzenmeier, M. Turberg, D. Yepes, Y. Xie, F. Neese, G. Bistoni, B. List, *J. Am. Chem. Soc.* **2018**, *140*, 12671–12676.

[168] X. Gao, H. B. Kagan, *Chirality* **1998**, *10*, 120–124.

[169] H. Kim, G. Gerosa, J. Aronow, P. Kasaplar, J. Ouyang, J. B. Lingnau, P. Guerry, C. Farès, B. List, *Nat. Commun.* **2019**, *10*, 770.

[170] C. C. Wagen, S. E. McMinn, E. E. Kwan, E. N. Jacobsen, *Nature* **2022**, *610*, 680–686.

[171] S. E. Denmark, G. L. Beutner, T. Wynn, M. D. Eastgate, *J. Am. Chem. Soc.* **2005**, *127*, 3774–3789.

[172] J. W. Yang, M. Stadler, B. List, *Angew. Chem. Int. Ed.* **2007**, *46*, 609–611.

[173] Q. Wang, M. Leutzsch, M. v. Gemmeren, B. List, *J. Am. Chem. Soc.* **2013**, *135*, 15334–15337.

[174] H. Mayr, B. Kempf, A. R. Ofial, *Acc. Chem. Res.* **2003**, *36*, 66–77.

[175] P. C. Maria, J. F. Gal, *J. Phys. Chem.* **1985**, *89*, 1296–1304.

[176] S. E. Denmark, M. E. Schnute, C. B. W. Senanayake, *J. Org. Chem.* **1993**, *58*, 1859–1874.

[177] S. E. Denmark, A. Thorarensen, *J. Org. Chem.* **1994**, *59*, 5672–5680.

[178] H. Zhou, J. T. Han, N. Nöthling, M. M. Lindner, J. Jenniches, C. Kühn, N. Tsuji, L. Zhang, B. List, *J. Am. Chem. Soc.* **2022**, *144*, 10156–10161.

[179] P. S. Pregosin, *Pure Appl. Chem.* **2009**, *81*, 615–633.

[180] H. Zhou, H. Y. Bae, M. Leutzsch, J. L. Kennemur, D. Bécart, B. List, *J. Am. Chem. Soc.* **2020**, *142*, 13695–13700.

[181] K. Kurahashi, Y. Yamaoka, Y. Takemoto, K. Takasu, *React. Chem. Eng.* **2018**, *3*, 626–630.

[182] Evans pKa Table *(accessed in June 2024)*, `http://ccc.chem.pitt.edu/wipf/MechOMs/evans_pKa_table`.

[183] S. Lee, P. S. J. Kaib, B. List, *J. Am. Chem. Soc.* **2017**, *139*, 2156–2159.

[184] S. Lee, H. Y. Bae, B. List, *Angew. Chem. Int. Ed.* **2018**, *57*, 12162–12166.

[185] J. Ouyang, H. Bae, S. Jordi, Q. M. Dao, S. Dossenbach, S. Dehn, J. B. Lingnau, C. K. De, P. Kraft, B. List, *Angew. Chem. Int. Ed.* **2021**, *60*, 5666–5672.

[186] S. Das, B. Mitschke, C. K. De, I. Harden, G. Bistoni, B. List, *Nat. Catal.* **2021**, *4*, 1043–1049.

[187] W. Riemenschneider, H. M. Bolt, *Ullmann's Encyclopedia of Industrial Chemistry: Esters, Organic*, Wiley-VCH, **2012**.

[188] J. Kubitschke, H. Lange, H. Strutz, *Ullmann's Encyclopedia of Industrial Chemistry: Carboxylic Acids, Aliphatic*, Wiley-VCH, **2014**.

[189] S. E. Denmark, T. Wynn, G. L. Beutner, *J. Am. Chem. Soc.* **2002**, *124*, 13405–13407.

[190] A. G. Wenzel, E. N. Jacobsen, *J. Am. Chem. Soc.* **2002**, *124*, 12964–12965.

[191] S. E. Reisman, A. G. Doyle, E. N. Jacobsen, *J. Am. Chem. Soc.* **2008**, *130*, 7198–7199.

[192] J. A. Birrell, J.-N. Desrosiers, E. N. Jacobsen, *J. Am. Chem. Soc.* **2011**, *133*, 13872–13875.

[193] M. Sickert, C. Schneider, *Angew. Chem. Int. Ed.* **2008**, *47*, 3631–3634.

[194] Y. M. A. Yamada, N. Yoshikawa, H. Sasai, M. Shibasaki, *Angew. Chem. Int. Ed.* **1997**, *36*, 1871–1873.

[195] H. E. Zimmerman, M. D. Traxler, *J. Am. Chem. Soc.* **1957**, *79*, 1920–1923.

[196] J.-E. Dubois, M. Dubois, *Tetrahedron Lett.* **1967**, *8*, 4215–4219.

[197] J. Dubois, P. Fellmann, *Tetrahedron Lett.* **1975**, *16*, 1225–1228.

[198] W. A. Kleschick, C. T. Buse, C. H. Heathcock, *J. Am. Chem. Soc.* **1977**, *99*, 247–248.

[199] C. T. Buse, C. H. Heathcock, *J. Am. Chem. Soc.* **1977**, *99*, 8109–8110.

[200] T. Mukaiyama, K. Inomata, M. Muraki, *J. Am. Chem. Soc.* **1973**, *95*, 967–968.

[201] M. Hirama, S. Masamune, *Tetrahedron Lett.* **1979**, *20*, 2225–2228.

[202] D. A. Evans, E. Vogel, J. V. Nelson, *J. Am. Chem. Soc.* **1979**, *101*, 6120–6123.

[203] T. Mukaiyama, T. Inoue, *Chem. Lett.* **1976**, *5*, 559–562.

[204] S. Masamune, T. Sato, B. Kim, T. A. Wollmann, *J. Am. Chem. Soc.* **1986**, *108*, 8279–8281.

[205] E. Corey, C. P. Decicco, R. C. Newbold, *Tetrahedron Lett.* **1991**, *32*, 5287–5290.

[206] D. A. Evans, J. Bartroli, T. L. Shih, *J. Am. Chem. Soc.* **1981**, *103*, 2127–2129.

[207] D. A. Evans, J. M. Takacs, L. R. McGee, M. D. Ennis, D. J. Mathre, J. Bartroli, *Pure Appl. Chem.* **1981**, *53*, 1109–1127.

[208] A. Abiko, J.-F. Liu, S. Masamune, *J. Am. Chem. Soc.* **1997**, *119*, 2586–2587.

[209] Y. Suzuki, R. Yazaki, N. Kumagai, M. Shibasaki, *Angew. Chem. Int. Ed.* **2009**, *48*, 5026–5029.

[210] Y. Yamashita, S. Fushimi, T. Banik, T. Kimura, S. Kobayashi, *Org. Lett.* **2024**, *26*, 1579–1583.

[211] Y. Morita, T. Yamamoto, H. Nagai, Y. Shimizu, M. Kanai, *J. Am. Chem. Soc.* **2015**, *137*, 7075–7078.

[212] T. Fujita, M. Yamane, W. M. C. Sameera, H. Mitsunuma, M. Kanai, *Angew. Chem. Int. Ed.* **2021**, *60*, 24598–24604.

[213] M. W. Rathke, A. Lindert, *J. Am. Chem. Soc.* **1971**, *93*, 2318–2320.

[214] R. E. Ireland, R. H. Mueller, *J. Am. Chem. Soc.* **1972**, *94*, 5897–5898.

[215] R. E. Ireland, A. K. Willard, *Tetrahedron Lett.* **1975**, *16*, 3975 3978.

[216] R. E. Ireland, R. H. Mueller, A. K. Willard, *J. Am. Chem. Soc.* **1976**, *98*, 2868–2877.

[217] W. E. Doering, W. Roth, *Tetrahedron* **1962**, *18*, 67–74.

[218] R. E. Ireland, P. Wipf, J. D. Armstrong, *J. Org. Chem.* **1991**, *56*, 650–657.

[219] Z. A. Fataftah, I. E. Kopka, M. W. Rathke, *J. Am. Chem. Soc.* **1980**, *102*, 3959–3960.

[220] T. Oesterle, G. Simchen, *Liebigs Ann. Chem.* **1987**, *1987*, 687–692.

[221] K. Krägeloh, G. Simchen, K. Schweiker, *Liebigs Ann. Chem.* **2010**, *1985*, 2352–2362.

[222] U. Frick, G. Simchen, *Liebigs Ann. Chem.* **2010**, *1987*, 839–845.

[223] H. Emde, G. Simchen, *Liebigs Ann. Chem.* **1983**, *1983*, 816–834.

[224] C. S. Wilcox, R. E. Babston, *J. Org. Chem.* **1984**, *49*, 1451–1453.

[225] S. Kobayashi, H. Kiyohara, M. Yamaguchi, *J. Am. Chem. Soc.* **2011**, *133*, 708–711.

[226] S. E. Wheeler, K. N. Houk, P. v. R. Schleyer, W. D. Allen, *J. Am. Chem. Soc.* **2009**, *131*, 2547–2560.

[227] W. J. Hehre, R. Ditchfield, L. Radom, J. A. Pople, *J. Am. Chem. Soc.* **1970**, *92*, 4796–4801.

[228] J. A. Pople, L. Radom, W. J. Hehre, *J. Am. Chem. Soc.* **1971**, *93*, 289–300.

[229] A. Krapcho, E. Jahngen, A. Lovey, F. W. Short, *Tetrahedron Lett.* **1974**, *15*, 1091–1094.

[230] M. F. Jung, M. A. Lyster, *J. Am. Chem. Soc.* **1977**, *99*, 968–969.

[231] T.-L. Ho, G. A. Olah, *Angew. Chem. Int. Ed.* **1976**, *15*, 774–775.

[232] M. G. Voronkov, V. G. Komarov, A. I. Albanov, É. I. Kositsina, É. I. Dubinskaya, *Bull. Acad. Sci. USSR Div. Chem. Sci.* **1978**, *27*, 1482–1482.

[233] P. S. J. Kaib, L. Schreyer, S. Lee, R. Properzi, B. List, *Angew. Chem. Int. Ed.* **2016**, *55*, 13200–13203.

[234] H. Mayr, T. Bug, M. F. Gotta, N. Hering, B. Irrgang, B. Janker, B. Kempf, R. Loos, A. R. Ofial, G. Remennikov, H. Schimmel, *J. Am. Chem. Soc.* **2001**, *123*, 9500–9512.

[235] G. Helmchen, R. Schmierer, *Tetrahedron Lett.* **1983**, *24*, 1235–1238.

[236] G. Helmchen, U. Leikauf, I. Taufer-Knöpfel, *Angew. Chem.* **1985**, *97*, 874–876.

[237] G. Bredig, P. S. Fiske, *Biochem. Z.* **1912**, *687*, 7–23.

[238] H. Pracejus, *Justus Liebigs Ann. Chem.* **1960**, *634*, 9 22.

[239] S.-s. Jew, H.-g. Park, *Chem. Commun.* **2009**, *0*, 7090–7103.

[240] H. C. Kolb, M. S. VanNieuwenhze, K. B. Sharpless, *Chem. Rev.* **1994**, *94*, 2483 2547.

[241] M. Johannsen, K. A. Jørgensen, G. Helmchen, *J. Am. Chem. Soc.* **1998**, *120*, 7637 7638.

[242] Y. Sakaguchi, Y. Iwade, T. Sekikawa, T. Minami, Y. Hatanaka, *Chem. Commun.* **2013**, *49*, 11173–11175.

[243] B. Mathieu, L. d. Fays, L. Ghosez, *Tetrahedron Lett.* **2000**, *41*, 9561–9564.

[244] K. Kubota, C. L. Hamblett, X. Wang, J. L. Leighton, *Tetrahedron* **2006**, *62*, 11397–11401.

[245] V. H. G. Rohde, M. F. Müller, M. Oestreich, *Organometallics* **2015**, *34*, 3358–3373.

[246] P. Shaykhutdinova, M. Oestreich, *Organometallics* **2016**, *35*, 2768–2771.

[247] P. Shaykhutdinova, S. Kemper, M. Oestreich, *Eur. J. Org. Chem.* **2018**, 2896–2901.

[248] P. Shaykhutdinova, M. Oestreich, *Org. Lett.* **2018**, *20*, 7029–7033.

[249] P. Shaykhutdinova, M. Oestreich, *Synthesis* **2019**, *51*, 2221–2229.

[250] R. Noyori, N. Sano, S. Murata, Y. Okamoto, H. Yuki, T. Ito, *Tetrahedron Lett.* **1982**, *23*, 2969–2972.

[251] G. A. Olah, G. Rasul, G. K. S. Prakash, *J. Am. Chem. Soc.* **1999**, *121*, 9615–9617.

[252] S. Shirakawa, R. Berger, J. L. Leighton, *J. Am. Chem. Soc.* **2005**, *127*, 2858–2859.

[253] L. M. Engelhardt, W.-P. Leung, C. L. Raston, G. Salem, P. Twiss, A. H. White, *J. Chem. Soc. Dalton Trans.* **1988**, *0*, 2403–2409.

[254] J. M. Chong, G. K. MacDonald, S. B. Park, S. H. Wilkinson, *J. Org. Chem.* **1993**, *58*, 1266–1268.

[255] P. Stanetty, M. D. Mihovilovic, *J. Org. Chem.* **1997**, *62*, 1514–1515.

[256] H. J. Reich, *Chem. Rev.* **2013**, *113*, 7130–7178.

[257] E. E. V. Tamelen, J. I. Brauman, L. E. Ellis, *J. Am. Chem. Soc.* **1971**, *93*, 6141–6144.

[258] Z. Y. Wei, D. Wang, J. S. Li, T. H. Chan, *J. Org. Chem.* **1989**, *54*, 5768–5774.

[259] J. F. Klebe, H. Finkbeiner, D. M. White, *J. Am. Chem. Soc.* **1966**, *88*, 3390–3395.

[260] D. L. Stalling, C. W. Gehrke, R. W. Zumwalt, *Biochem. Biophys. Res. Commun.* **1968**, *31*, 616–622.

[261] F. G. Bordwell, D. Algrim, *J. Org. Chem.* **1976**, *41*, 2507–2508.

[262] F. G. Bordwell, J. A. Harrelson, T. Y. Lynch, *J. Org. Chem.* **1990**, *55*, 3337–3341.

[263] D. A. Adsmond, D. J. Grant, *J. Pharm. Sci.* **2001**, *90*, 2058–2077.

[264] M. J. Scharf, B. List, *J. Am. Chem. Soc.* **2022**, *144*, 15451–15456.

[265] O. J. Benedictow, *The Complete History of the Black Death*, Boydell & Brewer, **2021**.

[266] D. I. Andersson, D. Hughes, *FEMS Microbiol. Rev.* **2011**, *35*, 901–911.

[267] W. Msemburi, A. Karlinsky, V. Knutson, S. Aleshin-Guendel, S. Chatterji, J. Wakefield, *Nature* **2023**, *613*, 130–137.

[268] K. Karikó, M. Buckstein, H. Ni, D. Weissman, *Immunity* **2005**, *23*, 165–175.

[269] D. R. Owen, C. M. N. Allerton, A. S. Anderson, L. Aschenbrenner, M. Avery, S. Berritt, B. Boras, R. D. Cardin, A. Carlo, K. J. Coffman, A. Dantonio, L. Di, H. Eng, R. Ferre, K. S. Gajiwala, S. A. Gibson, S. E. Greasley, B. L. Hurst, E. P. Kadar, A. S. Kalgutkar, J. C. Lee, J. Lee, W. Liu, S. W. Mason, S. Noell, J. J. Novak, R. S. Obach, K. Ogilvie, N. C. Patel, M. Pettersson, D. K. Rai, M. R. Reese, M. F. Sammons, J. G. Sathish, R. S. P. Singh, C. M. Steppan, A. E. Stewart, J. B. Tuttle, L. Updyke, P. R. Verhoest, L. Wei, Q. Yang, Y. Zhu, *Science* **2021**, *374*, 1586–1593.

[270] E. D. Clercq, G. Li, *Clin. Microbiol. Rev.* **2016**, *29*, 695–747.

[271] P. Naumov, N. Yasuda, W. M. Rabeh, J. Bernstein, *Chem. Commun.* **2013**, *49*, 1948–1950.

[272] S. Cuffini, R. A. Howie, E. R. T. Tiekink, J. L. Wardell, S. M. S. V. Wardell, *Acta Crystallogr. E.* **2009**, *65*, o3170–o3171.

[273] N. Camerman, J. Trotter, *Acta Crystallogr.* **1965**, *18*, 203–211.

[274] D. Wei, T. Hu, Y. Zhang, W. Zheng, H. Xue, J. Shen, Y. Xie, H. A. Aisa, *Bioorg. Med.Chem.* **2021**, *46*, 116364.

[275] K. McClellan, C. M. Perry, *Drugs* **2001**, *61*, 263–283.

[276] Y. Fukuta, T. Mita, N. Fukuda, M. Kanai, M. Shibasaki, *J. Am. Chem. Soc.* **2006**, *128*, 6312–6313.

[277] B. M. Trost, T. Zhang, *Chem. Eur. J.* **2011**, *17*, 3630–3643.

[278] Yeung, S. Hong, E. J. Corey, *J. Am. Chem. Soc.* **2006**, *128*, 6310–6311.

[279] V. A. Braz, M. D. Barkley, R. A. Jockusch, P. L. Wintrode, *Biochemistry* **2010**, *49*, 10565–10573.

[280] N. G. Sharaf, R. Ishima, A. M. Gronenborn, *Biochemistry* **2016**, *55*, 3864–3873.

[281] J. K. Aronson, *Meyler's Side Effects of Drugs*, 15th ed., Elsevier B.V., **2016**.

[282] T. K. Warren, R. Jordan, M. K. Lo, A. S. Ray, R. L. Mackman, V. Soloveva, D. Siegel, M. Perron, R. Bannister, H. C. Hui, N. Larson, R. Strickley, J. Wells, K. S. Stuthman, S. A. V. Tongeren, N. L. Garza, G. Donnelly, A. C. Shurtleff, C. J. Retterer, D. Gharaibeh, R. Zamani, T. Kenny, B. P. Eaton, E. Grimes, L. S. Welch, L. Gomba, C. L. Wilhelmsen, D. K. Nichols, J. E. Nuss, E. R. Nagle, J. R. Kugelman, G. Palacios, E. Doerffler, S. Neville, E. Carra, M. O. Clarke, L. Zhang, W. Lew, B. Ross, Q. Wang, K. Chun, L. Wolfe, D. Babusis, Y. Park, K. M. Stray, I. Trancheva, J. Y. Feng, O. Barauskas, Y. Xu, P. Wong, M. R. Braun, M. Flint, L. K. McMullan, S.-S. Chen, R. Fearns, S. Swaminathan, D. L. Mayers, C. F. Spiropoulou, W. A. Lee, S. T. Nichol, T. Cihlar, S. Bavari, *Nature* **2016**, *531*, 381–385.

[283] D. Siegel, H. C. Hui, E. Doerffler, M. O. Clarke, K. Chun, L. Zhang, S. Neville, E. Carra, W. Lew, B. Ross, Q. Wang, L. Wolfe, R. Jordan, V. Soloveva, J. Knox, J. Perry, M. Perron, K. M. Stray, O. Barauskas, J. Y. Feng, Y. Xu, G. Lee, A. L. Rheingold, A. S. Ray, R. Bannister, R. Strickley, S. Swaminathan, W. A. Lee, S. Bavari, T. Cihlar, M. K. Lo, T. K. Warren, R. L. Mackman, *J. Med. Chem.* **2017**, *60*, 1648–1661.

[284] H. Pan et al., *The Lancet* **2022**, *399*, 1941–1953.

[285] Antivirale Therapie in der Frühphase einer SARS-CoV-2-Infektion *(accessed in May 2024)*, `https://www.rki.de/DE/Content/InfAZ/N/Neuartiges_Coronavirus/COVRIIN_Dok/Antivirale_Therapie_Fruehphase.pdf`.

[286] Veterinary advancements in managing Feline Infectious Peritonitis (FIP) in cats *(accessed in May 2024)*, `https://www.vetvoice.com.au/articles/veterinary-advancements-in-managing-feline-infectious-peritonitis-fip-in-cats-in/`.

[287] B. Murphy, M. Perron, E. Murakami, K. Bauer, Y. Park, C. Eckstrand, M. Liepnieks, N. Pedersen, *Vet. Microbiol.* **2018**, *219*, 226–233.

[288] Y. Mehellou, J. Balzarini, C. McGuigan, *ChemMedChem* **2009**, *4*, 1779–1791.

[289] A. S. Alanazi, E. James, Y. Mehellou, *ACS Med. Chem. Lett.* **2019**, *10*, 2–5.

[290] E. D. Clercq, A. Holý, I. Rosenberg, T. Sakuma, J. Balzarini, P. C. Maudgal, *Nature* **1986**, *323*, 464–467.

[291] E. D. Clercq, A. Holý, I. Rosenberg, *Antimicrob. Agents Chemother.* **1989**, *33*, 185–191.

[292] E. D. Clercq, A. Holý, *Nat. Rev. Drug Discovery* **2005**, *4*, 928–940.

[293] S. E. Denmark, S. K. Ghosh, *Angew. Chem. Int. Ed.* **2001**, *40*, 4759–4762.

[294] R. G. Konsler, J. Karl, E. N. Jacobsen, *J. Am. Chem. Soc.* **1998**, *120*, 10780–10781.

[295] D. A. DiRocco, Y. Ji, E. C. Sherer, A. Klapars, M. Reibarkh, J. Dropinski, R. Mathew, P. Maligres, A. M. Hyde, J. Limanto, A. Brunskill, R. T. Ruck, L.-C. Campeau, I. W. Davies, *Science* **2017**, *356*, 426–430.

[296] M. Wang, L. Zhang, X. Huo, Z. Zhang, Q. Yuan, P. Li, J. Chen, Y. Zou, Z. Wu, W. Zhang, *Angew. Chem.* **2020**, *132*, 21000–21005.

[297] D. A. Theodore, R. L. Mackman, J. P. Parrish, A. S. Ray, WO2012012776A1, **2012**.

[298] B. K. Chun, M. O. N. H. Clarke, E. Doerffler, H. C. Hui, R. Jordan, R. L. Mackman, J. P. Parrish, A. S. Ray, D. Siegel, US9724360B2, **2016**.

[299] S. D. Axt, P. R. Badalov, K. Brak, S. Campagna, A. Chtchemelinine, E. Doerffler, M. M. Frick, D. Gao, L. V. Heumann, B. Hoang, W. Lew, R. R. Milburn, S. T. Neville, B. Ross, E. Rueden, R. W. Scott, D. Siegel, A. C. Stevens, C. Tadeus, T. Vieira, A. W. Waltman, X. Wang, M. C. Whitcomb, L. Wolfe, C.-Y. Yu, WO2016069825A1, **2016**.

[300] D. F. Vargas, E. L. Larghi, T. S. Kaufman, *ACS Omega* **2021**, *6*, 19356–19363.

[301] C. D. Savi, D. L. Hughes, L. Kvaerno, *Org. Process Res. Dev.* **2020**, *24*, 940–976.

[302] C. J.-M. Frédéric, A. Tikad, J. Fu, W. Pan, R. B. Zheng, A. Koizumi, X. Xue, T. L. Lowary, S. P. Vincent, *Chem. Eur. J.* **2016**, *22*, 15913–15920.

[303] J. Bouton, S. V. Calenbergh, J. Hullaert, *Org. Lett.* **2020**, *22*, 9287–9291.

[304] S. A. Patil, B. A. Otter, R. S. Klein, *J. Heterocycl. Chem.* **1994**, *31*, 781–786.

[305] B. V. Juan, J. A. A. Diez, A. M. A. Buil, P. R. Eastwood, C. E. Trias, M. E. L. Toribio, R. S. Roberts, L. V. Gispert, J. G. Rodriguez, M. M. Cepeda, WO2013010880A1, **2013**.

[306] R. R. Knapp, V. Tona, T. Okada, R. Sarpong, N. K. Garg, *Org. Lett.* **2020**, *22*, 8430–8435.

[307] A. Krasovskiy, P. Knochel, *Angew. Chem. Int. Ed.* **2004**, *43*, 3333–3336.

[308] T. Vieira, A. C. Stevens, A. Chtchemelinine, D. Gao, P. Badalov, L. Heumann, *Org. Process Res. Dev.* **2020**, *24*, 2113–2121.

[309] G. Yang, J. Schmieg, M. Tsuji, R. W. Franck, *Angew. Chem. Int. Ed.* **2004**, *43*, 3818–3822.

[310] Y. Yang, B. Yu, *Chem. Rev.* **2017**, *117*, 12281–12356.

[311] G. Butora, D. B. Olsen, S. S. Carroll, D. R. McMasters, C. Schmitt, J. F. Leone, M. Stahlhut, C. Burlein, M. MacCoss, *Bioorg. Med. Chem.* **2007**, *15*, 5219–5229.

[312] K. V. Booth, F. P. d. Cruz, D. J. Hotchkiss, S. F. Jenkinson, N. A. Jones, A. C. Weymouth-Wilson, R. Clarkson, T. Heinz, G. W. Fleet, *Tetrahedron: Asymmetry* **2008**, *19*, 2417–2424.

[313] K. S. Gudmundsson, J. C. Drach, L. B. Townsend, *J. Org. Chem.* **1998**, *63*, 984–989.

[314] G. E. Hilbert, T. B. Johnson, *J. Am. Chem. Soc.* **1930**, *52*, 4489–4494.

[315] E. Wittenburg, *Chem. Ber.* **1966**, *99*, 2380–2390.

[316] U. Niedballa, H. Vorbrüggen, *Angew. Chem. Int. Ed.* **1970**, *9*, 461–462.

[317] H. Vorbrüggen, K. Krolikiewicz, *Angew. Chem. Int. Ed.* **1975**, *14*, 421–422.

[318] S. D. Taylor, F. Mirzaei, A. Sharifi, S. L. Bearne, *J. Org. Chem.* **2006**, *71*, 9420–9430.

[319] S. Hanessian, B. Lou, *Chem. Rev.* **2000**, *100*, 4443–4464.

[320] J. A. Bennek, G. R. Gray, *J. Org. Chem.* **1987**, *52*, 892–897.

[321] K. Toshima, G. Matsuo, T. Ishizuka, M. Nakata, M. Kinoshita, *J. Chem. Soc. Chem. Commun.* **1992**, 1641–1642.

[322] K. Toshima, T. Ishizuka, G. Matsuo, M. Nakata, *Tetrahedron Lett.* **1994**, *35*, 5673–5676.

[323] K. Toshima, G. Matsuo, T. Ishizuka, Y. Ushiki, M. Nakata, S. Matsumura, *J. Org. Chem.* **1998**, *63*, 2307–2313.

[324] S. C. Collet, J.-F. Rémi, C. Cariou, S. Laïb, A. Y. Guingant, N. Q. Vu, G. Dujardin, *Tetrahedron Lett.* **2004**, *45*, 4911–4915.

[325] V. C. Yan, F. L. Muller, *ACS Med. Chem. Lett.* **2020**, *11*, 1361–1366.

[326] First-in-Human Study of Orally Administered GS-441524 for COVID-19 *(accessed in May 2024)*, `https://www.clinicaltrials.gov/study/NCT04859244`.

[327] D. Šišak, L. B. McCusker, G. Zandomeneghi, B. H. Meier, D. Bläser, R. Boese, W. B. Schweizer, R. Gilmour, J. D. Dunitz, *Angew. Chem. Int. Ed.* **2010**, *49*, 4503–4505.

[328] J.-S. Chen, Y.-F. Ke, H.-Y. Lin, W. Lin, W.-C. Yen, H.-R. Wu, S.-Y. Luo, *Synthesis* **2021**, *53*, 2000–2006.

[329] J. Zhang, S. Park, S. Chang, *Angew. Chem.* **2017**, *129*, 13945–13949.

[330] R. X. .-. Ren, N. C. Chaudhuri, P. L. Paris, Rumney, E. T. Kool, *J. Am. Chem. Soc.* **1996**, *118*, 7671–7678.

[331] J. A. Buss, A. Vasilopoulos, D. L. Golden, S. S. Stahl, *Org. Lett.* **2020**, *22*, 5749–5752.

[332] D. P. Hruszkewycz, K. C. Miles, O. R. Thiel, S. S. Stahl, *Chem. Sci.* **2016**, *8*, 1282–1287.

[333] A. Gunay, K. H. Theopold, *Chem. Rev.* **2010**, *110*, 1060–1081.

[334] M. Costas, *Coord. Chem. Rev.* **2011**, *255*, 2912–2932.

[335] J. T. Groves, T. E. Nemo, R. S. Myers, *J. Am. Chem. Soc.* **1979**, *101*, 1032–1033.

[336] T. Higuchi, H. Ohtake, M. Hirobe, *Tetrahedron Lett.* **1989**, *30*, 6545–6548.

[337] T. Shingaki, K. Miura, T. Higuchi, M. Hirobe, T. Nagano, *Chem. Commun.* **1997**, *0*, 861–862.

[338] K. Wang, J. M. Mayer, *J. Am. Chem. Soc.* **1997**, *119*, 1470–1471.

[339] F. Burg, M. Gicquel, S. Breitenlechner, A. Pöthig, T. Bach, *Angew. Chem. Int. Ed.* **2018**, *57*, 2953–2957.

[340] G. R. Fulmer, A. J. M. Miller, N. H. Sherden, H. E. Gottlieb, A. Nudelman, B. M. Stoltz, J. E. Bercaw, K. I. Goldberg, *Organometallics* **2010**, *29*, 2176–2179.

[341] R. K. Harris, E. D. Becker, S. M. C. d. Menezes, P. Granger, R. E. Hoffman, K. W. Zilm, *Pure Appl. Chem.* **2008**, *80*, 59–84.

[342] C. Bannwarth, S. Ehlert, S. Grimme, *J. Chem. Theory Comput.* **2019**, *15*, 1652–1671.

[343] P. Pracht, F. Bohle, S. Grimme, *Phys. Chem. Chem. Phys.* **2020**, *22*, 7169–7192.

[344] F. Neese, *WIREs Comput. Mol. Sci.* **2022**, *12*, DOI 10.1002/wcms.1606.

[345] F. Weigend, R. Ahlrichs, *Phys. Chem. Chem. Phys.* **2005**, *7*, 3297–3305.

[346] S. Grimme, A. Hansen, S. Ehlert, J.-M. Mewes, *J. Chem. Phys.* **2021**, *154*, 064103.

[347] T. Gasevic, J. B. Stückrath, S. Grimme, M. Bursch, *J. Phys. Chem. A* **2022**, *126*, 3826–3838.

[348] K. Eichkorn, O. Treutler, H. Öhm, M. Häser, R. Ahlrichs, *Chem. Phys. Lett.* **1995**, *240*, 283–290.

[349] F. Neese, *J. Comput. Chem.* **2003**, *24*, 1740–1747.

[350] F. Weigend, *Phys. Chem. Chem. Phys.* **2006**, *8*, 1057–1065.

[351] Y. Zhao, D. G. Truhlar, *Theoretical Chemistry Accounts: Theory* **2007**, *120*, 215 241.

[352] F. Neese, A. Hansen, F. Wennmohs, S. Grimme, *Acc. Chem. Res.* **2009**, *42*, 641–648.

[353] F. Neese, A. Hansen, D. G. Liakos, *J. Chem. Phys.* **2009**, *131*, 064103.

[354] D. G. Liakos, A. Hansen, F. Neese, *J. Chem. Theory Comput.* **2011**, *7*, 76–87.

[355] A. Hansen, D. G. Liakos, F. Neese, *J. Chem. Phys.* **2011**, *135*, 214102.

[356] C. Riplinger, F. Neese, *J. Chem. Phys.* **2013**, *138*, 034106.

[357] C. Riplinger, B. Sandhoefer, A. Hansen, F. Neese, *J. Chem. Phys.* **2013**, *139*, 134101.

[358] C. Riplinger, P. Pinski, U. Becker, E. F. Valeev, F. Neese, *J. Chem. Phys.* **2016**, *144*, 024109.

[359] T. H. Dunning, *J. Chem. Phys.* **1989**, *90*, 1007–1023.

[360] otherm.py, `https://github.com/duartegroup/otherm`.

[361] E. D. Glendening, C. R. Landis, F. Weinhold, *J. Comput. Chem.* **2019**, *40*, 2234–2241.

[362] E. R. Johnson, S. Keinan, P. Mori-Sánchez, J. Contreras-García, A. J. Cohen, W. Yang, *J. Am. Chem. Soc.* **2010**, *132*, 6498–6506.

[363] J. Contreras-García, E. R. Johnson, S. Keinan, R. Chaudret, J.-P. Piquemal, D. N. Beratan, W. Yang, *J. Chem. Theory Comput.* **2011**, *7*, 625–632.

[364] T. D. Goddard, C. C. Huang, E. C. Meng, E. F. Pettersen, G. S. Couch, J. H. Morris, T. E. Ferrin, *Protein Sci.* **2018**, *27*, 14–25.

[365] C. Yang, W. Liu, Z. He, Z. He, *Org. Lett.* **2016**, *18*, 4936–4939.

[366] W. Dehaen, A. Hassner, *J. Org. Chem.* **1991**, *56*, 896–900.

[367] A. Goti, A. Brandi, G. Danza, A. Guarna, D. Donati, F. D. Sarlo, *J. Chem. Soc. Perkin Trans. 1* **1989**, *0*, 1253–1258.

[368] M. Takeshita, S. Yoshida, Y. Kohno, *Heterocycles* **1994**, *37*, 553.

[369] A. Leyva, A. Corma, *J. Org. Chem.* **2009**, *74*, 2067–2074.

[370] C. W. Cavanagh, M. H. Aukland, Q. Laurent, A. Hennessy, D. J. Procter, *Org. Biomol. Chem.* **2016**, *14*, 5286–5292.

[371] M. Marčeková, P. Gerža, M. Šoral, J. Moncol, D. Berkeš, A. Kolarovič, P. Jakubec, *Org. Lett.* **2019**, *21*, 4580–4584.

[372] H. A. Patel, M. Rawat, A. L. Patel, A. V. Bedekar, *Appl. Organomet. Chem.* **2019**, *33*, e4767.

[373] P. Vojáčková, D. Chalupa, J. Prieboj, M. Nečas, J. Švenda, *Org. Lett.* **2018**, *20*, 7085–7089.

[374] S. E. Denmark, G. L. Beutner, *J. Am. Chem. Soc.* **2003**, *125*, 7800–7801.

[375] S. Kondaparla, A. Soni, A. Manhas, K. Srivastava, S. K. Puri, S. B. Katti, *RSC Adv.* **2016**, *6*, 105676–105689.

[376] M. Terada, Y. Toda, *J. Am. Chem. Soc.* **2009**, *131*, 6354–6355.

[377] Y.-C. Lin, A. Ribaucourt, Y. Moazami, J. G. Pierce, *J. Am. Chem. Soc.* **2020**, *142*, 9850–9857.

[378] R. J. H. Scanes, O. Grossmann, A. Grossmann, D. R. Spring, *Org. Lett.* **2015**, *17*, 2462–2465.

[379] R. Albrecht, G. Kresze, B. Mlakar, *Chem. Ber.* **1964**, *97*, 483–489.

[380] D. J. Foley, S. Zinken, D. Corkery, L. Laraia, A. Pahl, Y.-W. Wu, H. Waldmann, *Angew. Chem. Int. Ed.* **2020**, *59*, 12470–12476.

[381] H. Nie, Y. Zhu, X. Hu, Z. Wei, L. Yao, G. Zhou, P. Wang, R. Jiang, S. Zhang, *Org. Lett.* **2019**, *21*, 8641–8645.

[382] D. Sälinger, R. Brückner, *Chem. Eur. J.* **2009**, *15*, 6688–6703.

[383] J. Robertson, M. J. Hall, P. M. Stafford, S. P. Green, *Org. Biomol. Chem.* **2003**, *1*, 3758–3767.

[384] F. Chemla, V. Hebbe, J.-F. Normant, *Synthesis* **2000**, *2000*, 75–77.

[385] H. Zhou, H. H. C. Lakmal, J. M. Baine, H. U. Valle, X. Xu, X. Cui, *Chem. Sci.* **2017**, *8*, 6520–6524.

[386] O.-M. Soueidan, B. J. Trayner, T. N. Grant, J. R. Henderson, F. Wuest, F. G. West, C. I. Cheeseman, *Org. Biomol. Chem.* **2015**, *13*, 6511–6521.

APPENDIX

Enantiomeric Ratios of the Multi-Substrate Screening

Table A.1: Enantiomeric ratios of nitroso acetals **96**, **86**, **97**, and **98** with various IDPi catalysts, as obtained by the multi-substrate screening.

entry	IDPi	er **96**	er **86**	er **97**	er **98**
1	**30**	29:71	28:72	20:80	82:18
1	**99b**	55.5:44.5	33.5:66.5	65:35	91.5:8.5
1	**99a**	92:8	90:10	98.5:1.5	88:12
1	**90**	63:37	91:9	96:4	93:7
1	**91**	84.5:15.5	93:7	93.5:6.5	94:6
1	**94**	80:20	92.5:7.5	66:34	99.5:0.5

Concentration Data for the Resting State Determination of the Silyl Nitronate Polarity Inversion

The reaction between **393** (1.0 equiv.) and silyl ketene acetal **69** (2.0 equiv.) catalyzed by IDPi **99a** (2.5 mol%) at −80 °C in toluene-d_8 was monitored by ^{1}H and ^{31}P NMR spectroscopy. We believe that due to viscosity problems, the reaction came to a halt at approximately 6 h, and regained activity upon warm-up to room temperature. However, the NMR data indicated the silylated IDPi to be the resting state over the whole course of the reaction.

Table A.2: Concentration data of the reaction between **393** and **69**.

t/h	**393** / (mmol/L)	**96** / (mmol/L)
0.00	219.39	32.64
0.09	219.38	33.07
0.15	211.75	34.89
0.23	205.79	35.07
0.32	195.13	38.96
0.40	191.57	42.51
0.48	186.85	44.33
0.57	182.02	45.32
0.65	172.87	51.09

t/h	**393** / (mmol/L)	**96** / (mmol/L), continued.
0.73	170.44	52.88
0.82	173.50	58.42
0.90	168.91	57.66
0.98	166.60	61.48
1.08	161.77	63.44
1.15	160.43	65.91
1.23	158.69	68.74
1.32	154.11	71.84
1.40	154.83	74.57
1.48	152.20	78.54
1.57	148.95	79.45
1.65	147.84	85.70
1.73	146.69	85.64
1.82	147.42	89.52
1.90	145.59	92.53
1.98	142.86	94.35
2.08	139.32	97.98
2.15	139.05	100.63
2.23	138.88	102.85
2.32	135.48	107.78
2.40	135.80	108.02
2.48	133.66	112.80
2.57	132.25	113.21
2.65	128.23	113.93
2.73	126.60	116.31
2.82	128.08	122.16
2.90	126.85	125.49
2.98	125.30	124.17
3.08	121.78	126.93
3.15	121.31	126.96
3.23	118.31	129.14
3.32	118.48	130.82
3.40	117.02	132.10
3.48	114.03	133.89
3.57	115.48	136.74

t/h	**393** / (mmol/L)	**96** / (mmol/L), continued.
3.65	113.86	136.96
3.74	112.11	137.70
3.82	109.99	139.96
3.90	108.81	139.22
3.99	106.44	141.75
4.08	106.50	143.84
4.15	101.40	139.58
4.24	101.60	143.98
4.32	101.93	144.98
4.40	100.50	145.39
4.49	99.90	146.82
4.57	98.78	149.40
4.65	95.26	148.30
4.74	94.26	147.70
4.82	95.92	150.43
4.90	94.17	151.16
4.99	92.28	153.20
5.08	91.66	152.75
5.15	90.23	155.51
5.24	89.03	153.02
5.32	85.85	153.03
5.40	86.16	154.97
5.49	80.58	147.34
5.57	85.61	158.80
5.65	94.08	160.08
5.74	93.93	152.09
5.82	94.41	163.74
5.90	80.77	159.19
5.99	73.10	165.12
6.08	64.17	174.16
6.15	56.39	182.53
6.24	45.59	191.44
6.32	36.88	201.69
6.40	29.68	208.46
6.49	24.18	217.24

t/h	**393** / (mmol/L)	**96** / (mmol/L), continued.
6.57	19.49	219.86
6.65	16.16	226.74
6.74	13.40	226.32
6.82	11.31	229.55
6.90	9.37	230.43
6.99	8.81	233.24
7.08	6.92	240.02
7.15	6.05	235.66
7.24	5.42	233.86
7.32	5.45	236.59
7.40	4.34	237.74

Effect of Substituting $HNTf_2$ with IDPis in the Silicon-Catalytic Mukaiyama–Mannich Reaction of Alkyl Esters with NEt_3

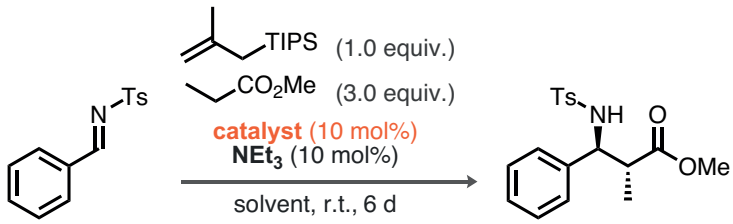

201 **223**

IDPi	*solvent*	*result*
99b	CH_2Cl_2	21%, 62:38 dr, 47.5:52.5 er (*anti*)
99b	PhMe	traces, dr n.d., 51.5:48.5 er (*anti*)
150	CH_2Cl_2	24%, 58:42 dr, 49.5:50.5 er (*anti*)
150	PhMe	11%, 45:55 dr, 44.5:55.5 er (*anti*)

Scheme A.1: Reactions on 0.10 mmol scale, yield determined by crude ^{1}H NMR analysis with mesitylene as internal standard.

Screening Data of the IDPi-Catalyzed Mukaiyama–Mannich Reaction of the *N*-Tosyl Benzaldimine

All of these reactions were conducted according to GP13.

Table A.3: Screening of the reactivity and enantioselectivity in the reaction between imine **201** and isobutyl propionate (**217**, 3.0 equiv.) with 100 mol% TIPS-**D**; all reactions were conducted on 0.025 mmol scale; yield and diastereoselectivities were determined by crude ^{1}H NMR analysis with mesitylene as internal standard.

entry	solvent	IDPi	yield	dr	er (*anti*)	er (*syn*)
1	CH_2Cl_2	**150** (10 mol%)	92 %	73:27	50:50	50:50
2	$CHCl_3$	**150** (10 mol%)	quant.	83:17	50:50	51:49
3	CyH	**150** (10 mol%)	quant.	82:18	53.5:46.5	nd
4	*n*-pentane	**150** (10 mol%)	quant.	82:18	51.5:48.5	47:53
5	$CHCl_3$/PhMe 1:1 *v*/*v*	**150** (10 mol%)	quant.	83:17	51:49	53:47
6	$CHCl_3$	**30** (10 mol%)	–	–	–	–
6	$CHCl_3$	**455** (10 mol%)	–	–	–	–

Cartesian Coordinates of DFT-Optimized Structures

Table A.4: Cartesian coordinates of **75** (Scheme 2.5).

atom	*x*	*y*	*z*
C	-5.052132	1.217585	-0.082060
C	-3.797972	2.093843	-0.033334
C	-2.553066	1.278645	-0.122628
H	-3.815348	2.698147	0.891579
H	-3.846786	2.839226	-0.847743
N	-1.352451	1.876867	-0.093340
H	-2.556062	0.199361	-0.213693
O	-0.274812	1.188026	-0.170487
O	-1.297328	3.155040	0.013436
C	-6.346476	2.026493	-0.003342
H	-5.019119	0.492644	0.744081
H	-5.042782	0.625199	-1.008437
H	-6.385779	2.607863	0.925910
H	-7.237177	1.386470	-0.037992
H	-6.410910	2.738440	-0.835129

Table A.5: Cartesian coordinates of **76** (Scheme 2.5).

atom	x	y	z
C	-4.399875	1.561606	0.765828
C	-3.965347	1.721154	-0.703258
C	-2.589185	1.219611	-0.964546
H	-4.020820	2.783935	-0.974546
H	-4.661672	1.177313	-1.352704
N	-1.568304	1.950208	-0.612134
H	-2.356210	0.259643	-1.404581
O	-0.308682	1.378554	-0.886558
O	-1.574300	3.076074	-0.077974
C	-5.800152	2.118797	1.006360
H	-3.672838	2.079767	1.401511
H	-4.363606	0.499235	1.037655
H	-5.841679	3.187617	0.769433
H	-6.101622	1.995620	2.051151
H	-6.542632	1.609345	0.381352
Si	1.073345	2.301135	-0.434816
C	2.399845	1.110412	-1.004804
H	2.325512	0.150078	-0.483993
H	3.394077	1.525736	-0.803889
H	2.327130	0.919418	-2.080595
C	1.163629	2.547669	1.414885
H	0.969007	1.606576	1.941013
H	0.435717	3.288135	1.755615
H	2.166410	2.886805	1.701312
C	1.180356	3.903334	-1.389050
H	0.991478	3.733394	-2.454794
H	2.186085	4.330494	-1.294666
H	0.455632	4.635855	-1.025310

Table A.6: Cartesian coordinates of **77** (Scheme 2.5).

atom	x	y	z
C	-4.284659	1.153803	1.012854
C	-3.519725	1.433688	-0.306115

Table A.6: Cartesian coordinates of **77** (Scheme 2.5), continued.

atom	x	y	z
C	-2.074103	1.622666	-0.063269
H	-3.941989	2.317182	-0.794290
H	-3.636893	0.575036	-0.976701
N	-1.548379	2.773786	0.191314
H	-1.365403	0.799776	-0.047951
O	-0.237421	2.923146	0.479712
O	-2.276316	3.891510	0.194730
C	-5.760570	0.883526	0.739458
H	-4.173370	2.022358	1.672681
H	-3.829498	0.298684	1.526402
H	-6.235699	1.737779	0.246618
H	-6.292788	0.695250	1.675707
H	-5.890566	0.005866	0.098524
Si	0.912276	3.093566	-0.866094
C	0.916347	1.464426	-1.767904
H	1.142018	0.622965	-1.103999
H	1.700630	1.487952	-2.534629
H	-0.023433	1.262481	-2.293693
C	2.464475	3.428248	0.086173
H	2.690445	2.613770	0.782049
H	2.400544	4.361139	0.655050
H	3.311302	3.519370	-0.603765
C	0.316840	4.483973	-1.944330
H	-0.709138	4.326011	-2.294941
H	0.953898	4.551777	-2.834395
H	0.361313	5.449274	-1.431732
Si	-2.209542	4.999864	1.591662
C	-3.891902	5.765052	1.440968
H	-4.034196	6.220894	0.455360
H	-4.011114	6.557262	2.189090
H	-4.690097	5.032940	1.600181
C	-0.832352	6.211925	1.305780
H	-0.950251	6.736355	0.351974
H	0.152015	5.735096	1.330333

Table A.6: Cartesian coordinates of **77** (Scheme 2.5), continued.

atom	x	y	z
H	-0.849527	6.970500	2.097760
C	-1.959646	3.946682	3.103061
H	-2.738761	3.187284	3.224695
H	-2.000147	4.591194	3.989666
H	-0.982756	3.452952	3.107327

Table A.7: Cartesian coordinates of **144** (Fig. 2.2).

atom	x	y	z
C	3.65067	-2.93883	0.99704
C	4.77049	-3.79224	0.97175
C	5.66257	-3.81456	2.05583
C	5.42731	-3.00729	3.18201
C	4.29717	-2.17359	3.21907
C	3.41218	-2.14025	2.13294
H	2.52932	-1.48271	2.15959
H	4.09882	-1.53841	4.09535
H	6.12540	-3.03180	4.03272
H	6.54850	-4.46685	2.01943
H	4.96388	-4.41023	0.08233
C	2.65589	-2.93171	-0.16263
C	1.55328	-3.76419	0.37192
N	1.27959	-4.98246	0.01196
O	1.80853	-5.58268	-1.06830
Si	0.61507	-5.93319	-2.38775
C	-0.64832	-4.56970	-2.26296
H	-0.17000	-3.57223	-2.31509
H	-1.22293	-4.65129	-1.31894
H	-1.37540	-4.64017	-3.09633
C	-0.12642	-7.62037	-2.02336
H	-0.67250	-7.99714	-2.91286
H	0.65061	-8.36579	-1.76150
H	-0.84595	-7.54084	-1.18533
C	1.71379	-5.92249	-3.94373

Table A.7: Cartesian coordinates of **144** (Fig. 2.2), continued.

atom	x	y	z
C	0.75554	-5.85478	-5.15356
H	1.33754	-5.93217	-6.09810
H	0.01193	-6.68038	-5.16133
H	0.20474	-4.89233	-5.18578
C	2.54952	-7.21560	-3.99925
H	3.22309	-7.30743	-3.12172
H	1.91732	-8.12623	-4.04282
H	3.19136	-7.21415	-4.90746
C	2.64090	-4.69490	-3.95460
H	2.08564	-3.74053	-3.86014
H	3.21000	-4.66747	-4.91026
H	3.38563	-4.73489	-3.13693
O	0.38771	-5.73561	0.70139
Si	1.02765	-6.87843	1.93951
C	2.79507	-7.25299	1.42288
H	3.24644	-7.96475	2.14395
H	2.83279	-7.70641	0.41356
H	3.42403	-6.33946	1.41708
C	-0.14151	-8.32702	1.73411
H	0.00178	-8.81095	0.74859
H	0.03755	-9.08569	2.52201
H	-1.19386	-7.99016	1.80579
C	0.92295	-6.08864	3.67444
C	1.33119	-7.19318	4.67536
H	2.36909	-7.55202	4.51201
H	1.28700	-6.78757	5.70980
H	0.65300	-8.07057	4.64049
C	-0.52076	-5.63346	3.95377
H	-0.83555	-4.83679	3.25349
H	-1.24558	-6.47029	3.88674
H	-0.59005	-5.20916	4.97970
C	1.88378	-4.89392	3.81553
H	2.93469	-5.14894	3.56821
H	1.87236	-4.52500	4.86463

Table A.7: Cartesian coordinates of **144** (Fig. 2.2), continued.

atom	x	y	z
H	1.57840	-4.03866	3.18632
H	3.08896	-3.33316	-1.09334
H	2.27682	-1.90942	-0.35806
H	0.95319	-3.40425	1.23069
P	-1.13634	0.97678	-1.11462
N	-0.75296	1.60864	0.28934
P	0.25978	1.19580	1.43599
N	0.52030	-0.35336	1.84800
S	-0.58121	-1.24018	2.61267
O	-0.33891	-2.68473	2.32059
O	-1.97739	-0.74609	2.56005
C	-0.08516	-1.14267	4.44098
F	1.22755	-1.39681	4.58258
F	-0.35392	0.06296	4.95236
F	-0.78181	-2.07238	5.11466
O	1.69838	1.88731	1.03291
C	2.71550	2.04212	1.96748
C	2.50655	2.90685	3.05318
C	3.47985	2.91938	4.11275
C	3.26791	3.61033	5.34179
C	4.22699	3.58951	6.34415
C	5.44772	2.88612	6.16119
C	5.67895	2.19639	4.98164
C	4.70479	2.18129	3.93845
C	4.92782	1.47781	2.72615
C	3.96366	1.37157	1.72168
C	4.27341	0.66484	0.45075
C	5.31117	-0.29309	0.39480
C	5.64585	-0.95782	-0.78899
C	4.94753	-0.70779	-1.98972
C	3.94493	0.28206	-1.95082
C	3.61055	0.94700	-0.76865
H	2.81502	1.69860	-0.81099
H	3.36319	0.53469	-2.84621

Table A.7: Cartesian coordinates of **144** (Fig. 2.2), continued.

atom	x	y	z
C	5.23760	-1.43628	-3.27499
H	5.85154	-0.57449	1.30896
H	5.91313	1.01460	2.57655
H	6.61683	1.63902	4.83220
H	6.20376	2.88397	6.96072
H	4.03830	4.11891	7.29016
H	2.32327	4.15166	5.49123
C	1.34292	3.84186	3.05841
C	0.04718	3.35362	2.89836
C	-1.11748	4.17585	2.78622
C	-0.92216	5.55083	2.88280
C	0.37074	6.12438	3.03573
C	0.54446	7.54076	3.05681
C	1.80789	8.10706	3.11928
C	2.95332	7.27038	3.16622
C	2.81825	5.88924	3.16725
C	1.53337	5.27139	3.11184
H	3.71642	5.26003	3.18652
H	3.95803	7.71808	3.18422
H	1.92584	9.20091	3.11927
H	-0.35195	8.17796	3.00275
H	-1.79355	6.22049	2.82030
C	-2.44439	3.58449	2.48853
C	-3.26756	4.17692	1.50451
C	-4.48230	3.59022	1.13405
C	-4.90153	2.38622	1.73129
C	-4.10268	1.81347	2.73670
C	-2.89224	2.40036	3.11358
H	-2.27552	1.91153	3.87756
H	-4.41835	0.87322	3.21112
C	-6.18481	1.71976	1.31951
C	-7.40022	2.24633	2.04671
F	-7.58893	3.56986	1.81083
H	-2.92469	5.08134	0.98097

Table A.7: Cartesian coordinates of **144** (Fig. 2.2), continued.

atom	x	y	z
O	-0.10998	1.97382	2.82953
N	-0.36188	-0.34931	-1.60485
S	0.50591	-0.60656	-2.92469
O	1.28427	-1.85858	-2.73393
O	1.20155	0.57654	-3.49140
C	-0.75024	-1.06328	-4.27125
F	-1.62649	-1.97871	-3.82007
F	-1.42343	0.02100	-4.67103
F	-0.08551	-1.58563	-5.31525
O	-1.04371	2.07459	-2.33324
C	-1.87233	3.18786	-2.25915
C	-3.22248	3.00939	-2.55980
C	-4.11678	4.12332	-2.37656
C	-5.53200	4.01537	-2.51757
C	-6.35976	5.10300	-2.27690
C	-5.81252	6.35665	-1.89658
C	-4.44131	6.49468	-1.74870
C	-3.56305	5.39130	-1.96607
C	-2.16294	5.51463	-1.74936
C	-1.29260	4.43238	-1.86411
C	0.15503	4.57112	-1.56841
C	1.15214	3.93298	-2.34201
C	2.50953	4.14975	-2.07114
C	2.91870	4.98669	-1.01567
C	1.92560	5.60593	-0.23111
C	0.57047	5.39923	-0.50199
H	-0.18280	5.86811	0.14749
H	2.22174	6.25617	0.60211
C	4.37463	5.25760	-0.74373
C	4.81180	6.65267	-1.13931
H	0.87216	3.26181	-3.16463
H	-1.75884	6.50001	-1.47187
H	-4.00594	7.45830	-1.44148
H	-6.47860	7.21240	-1.71076

Table A.7: Cartesian coordinates of **144** (Fig. 2.2), continued.

atom	x	y	z
H	-7.44981	4.98917	-2.37354
H	-5.97027	3.04979	-2.80219
C	-3.71436	1.66778	-2.98368
C	-3.51181	0.55533	-2.15886
C	-4.14071	-0.71207	-2.39008
C	-4.88587	-0.84911	-3.55807
C	-5.01179	0.20097	-4.50733
C	-5.71321	0.01472	-5.73539
C	-5.81940	1.04313	-6.65844
C	-5.21786	2.30124	-6.38959
C	-4.53683	2.51805	-5.20034
C	-4.42231	1.48579	-4.22339
H	-4.06523	3.49111	-5.00532
H	-5.28568	3.10916	-7.13361
H	-6.36024	0.88494	-7.60360
H	-6.16361	-0.96938	-5.93842
H	-5.37372	-1.81335	-3.76722
C	-4.10903	-1.79017	-1.36878
C	-5.31872	-2.41092	-0.98176
C	-5.34584	-3.34371	0.06329
C	-4.16574	-3.66945	0.75694
C	-2.95227	-3.10163	0.33125
C	-2.92014	-2.18030	-0.71767
H	-1.95743	-1.75166	-1.02086
H	-2.02395	-3.34953	0.86341
C	-4.17383	-4.59332	1.94386
C	-3.83467	-6.02221	1.59733
H	-6.25882	-2.10987	-1.46816
O	-2.76239	0.71583	-0.99685
C	-3.70248	-4.05831	3.28315
F	-2.61254	-6.11940	0.99152
F	-4.73451	-6.56328	0.74318
F	-3.78357	-6.83243	2.69158
C	6.02151	-2.72376	-3.16069

Table A.7: Cartesian coordinates of **144** (Fig. 2.2), continued.

atom	x	y	z
C	5.49707	-0.61562	-4.53983
C	4.22569	-1.39355	-4.41435
H	6.44911	-1.70345	-0.75267
F	6.13631	-3.36656	-4.34941
F	5.42692	-3.60472	-2.29759
F	7.28701	-2.53438	-2.70411
C	-5.16252	-4.35805	3.06766
H	-6.30129	-3.79393	0.37321
H	-3.35354	-3.01418	3.28882
H	-3.13671	-4.73940	3.93350
H	6.26994	-0.97856	-5.23472
H	5.46785	0.47578	-4.40143
H	3.27528	-0.87825	-4.22022
H	4.12747	-2.30856	-5.01439
H	-5.58701	-5.23816	3.57350
H	-5.85921	-3.51699	2.93343
C	-6.38305	1.27937	-0.11590
C	-6.16824	0.24853	0.96265
H	-5.09922	4.05282	0.34981
F	-7.28608	2.09401	3.38873
F	-8.54280	1.61008	1.66907
H	-5.55575	1.48892	-0.80743
H	-7.39035	1.37808	-0.54721
H	-7.02742	-0.36829	1.26492
H	-5.19017	-0.25332	1.00991
C	5.04424	4.67215	0.48590
C	5.40919	4.16052	-0.88260
H	3.26801	3.66046	-2.70037
F	6.14239	6.85106	-0.93469
F	4.16297	7.60994	-0.42335
F	4.56655	6.90029	-2.44681
H	4.41458	4.03598	1.12324
H	5.77261	5.29937	1.02154
H	6.39193	4.43678	-1.29119

Table A.7: Cartesian coordinates of **144** (Fig. 2.2), continued.

atom	x	y	z
H	5.04518	3.16380	-1.17269

Table A.8: Cartesian coordinates of **208** (Scheme 3.8).

atom	x	y	z
C	1.284618	-0.699496	-0.005876
C	-0.000010	0.100213	-0.000145
H	1.240737	-1.510394	-0.741301
H	1.416352	-1.169975	0.976556
H	2.135737	-0.047340	-0.206908
C	-1.284432	-0.699822	0.005854
H	-1.240174	-1.510782	0.741188
H	-1.416283	-1.170230	-0.976595
H	-2.135667	-0.047898	0.207146
O	-0.000164	1.313301	0.000043

Table A.9: Cartesian coordinates of **210** (Scheme 3.8).

atom	x	y	z
C	-1.767166	0.627343	0.000657
C	-0.462369	-0.118127	-0.042427
O	0.587350	0.736994	0.015314
O	-0.341396	-1.319246	-0.096662
C	1.884054	0.105321	0.028008
H	2.030269	-0.485593	-0.880465
H	1.982176	-0.550162	0.898017
H	2.605769	0.921156	0.077154
H	-2.553240	0.003477	-0.425320
H	-1.698794	1.582394	-0.524153
H	-2.015261	0.835912	1.047099

Table A.10: Cartesian coordinates of **209** (Scheme 3.8).

atom	x	y	z
C	-2.560249	-0.002058	1.446507
C	-2.408622	-0.003649	0.117310
C	-3.543397	-0.008372	-0.857394
H	-3.477171	-0.891148	-1.503756
H	-3.481922	0.872486	-1.506830
H	-4.507699	-0.010078	-0.346177
O	-1.210887	-0.001263	-0.526617
H	-3.553683	-0.004211	1.876777
H	-1.715144	0.001576	2.126247
Si	0.366512	0.000782	0.074321
C	0.651198	-1.555550	1.131429
C	1.388016	0.001992	-1.519237
C	0.647998	1.557848	1.131210
C	-0.212981	-2.750353	0.699958
H	-0.060768	-3.597474	1.381447
H	0.044501	-3.092075	-0.307992
H	-1.277993	-2.499598	0.706592
C	2.136097	-1.950576	1.196998
H	0.341962	-1.278679	2.151744
H	2.516477	-2.241113	0.211177
H	2.277223	-2.808969	1.866028
H	2.770638	-1.138855	1.568616
C	1.128362	1.258680	-2.366650
H	1.700310	1.215052	-3.302586
H	1.415339	2.179409	-1.850140
H	0.067564	1.338742	-2.630432
C	1.131289	-1.255040	-2.367032
H	2.448003	0.003158	-1.218872
H	1.420932	-2.175196	-1.850993
H	1.702741	-1.209528	-3.303179
H	0.070599	-1.337821	-2.630425
C	2.131763	1.957488	1.194515
H	2.509458	2.250033	0.208262
H	2.769533	1.147470	1.564323

Table A.10: Cartesian coordinates of **209** (Scheme 3.8), continued.

atom	x	y	z
H	2.271349	2.815780	1.863998
C	-0.220557	2.750026	0.701238
H	0.341264	1.279842	2.151983
H	-0.069674	3.597653	1.382390
H	-1.284793	2.496045	0.709718
H	0.034117	3.092410	-0.307202

Table A.11: Cartesian coordinates of **211** (Scheme 3.8).

atom	x	y	z
C	3.152608	0.989399	-0.913503
C	2.060352	0.277630	-0.608305
O	1.943322	-1.082001	-0.637939
O	0.909457	0.840766	-0.223517
C	3.093170	-1.824525	-1.037701
H	3.930281	-1.645629	-0.351281
H	3.392274	-1.558165	-2.059218
H	2.801416	-2.875250	-0.999441
H	4.077249	0.526120	-1.221695
H	3.100358	2.066821	-0.845879
Si	-0.542687	0.053785	0.170677
C	-0.267662	-1.099308	1.656273
C	0.870256	-0.642896	2.582102
H	1.812752	-0.516272	2.040529
H	1.035836	-1.382746	3.376182
H	0.640234	0.311130	3.068401
C	-1.556911	-1.340162	2.458637
H	0.036109	-2.059879	1.212869
H	-1.912530	-0.417680	2.931504
H	-1.382035	-2.069166	3.260222
H	-2.371913	-1.727068	1.837472
C	-1.156385	-0.947449	-1.323692
C	-2.677170	-1.172054	-1.294783
H	-3.225215	-0.228380	-1.396526

Table A.11: Cartesian coordinates of **211** (Scheme 3.8), continued.

atom	x	y	z
H	-3.012157	-1.648865	-0.367254
H	-2.987592	-1.819157	-2.125129
C	-0.717561	-0.365101	-2.675592
H	-0.671304	-1.929907	-1.218214
H	0.368554	-0.245209	-2.736989
H	-1.167055	0.616146	-2.860747
H	-1.029186	-1.026502	-3.494581
C	-1.656803	1.527832	0.580224
C	-1.124891	2.335647	1.775747
H	-1.089546	1.745075	2.695934
H	-1.767383	3.204803	1.966834
H	-0.113440	2.707778	1.577169
C	-1.849423	2.456243	-0.630241
H	-2.640768	1.115494	0.855691
H	-2.342258	1.953274	-1.467457
H	-0.886242	2.837135	-0.988178
H	-2.467285	3.321029	-0.355894

Table A.12: Cartesian coordinates of allyltriisopropylsilane (Scheme 3.8).

atom	x	y	z
C	-3.587261	-0.146368	0.936617
C	-2.387452	-0.707199	1.085759
C	-1.129451	0.009978	1.444594
Si	0.201902	-0.021880	0.075291
H	-0.669403	-0.460545	2.326983
H	-1.345701	1.050053	1.719389
H	-4.454411	-0.733799	0.651226
H	-3.738677	0.919293	1.094846
H	-2.295973	-1.782469	0.919168
C	1.798487	0.769274	0.779326
C	-0.391625	0.925908	-1.465639
C	0.536561	-1.841469	-0.377688
C	1.668055	-1.983014	-1.406487

Table A.12: Cartesian coordinates of allyltriisopropylsilane (Scheme 3.8), continued.

atom	x	y	z
H	1.498092	-1.373218	-2.301308
H	1.775592	-3.025962	-1.731807
H	2.629253	-1.679219	-0.974401
C	0.823598	-2.712436	0.853737
H	-0.390573	-2.212665	-0.841878
H	1.719216	-2.369174	1.386279
H	1.002435	-3.755583	0.561943
H	-0.006953	-2.708725	1.567662
C	-1.388052	0.133042	-2.325158
H	-1.697066	0.722305	-3.198854
H	-2.291244	-0.115124	-1.757237
H	-0.958673	-0.803571	-2.696518
C	-0.980620	2.294569	-1.090105
H	0.508072	1.103172	-2.075396
H	-0.289038	2.896779	-0.490027
H	-1.904760	2.174088	-0.512971
H	-1.229842	2.874029	-1.988495
C	1.547501	1.782254	1.906815
H	0.964347	2.640031	1.551099
H	2.497669	2.174732	2.292209
H	1.005520	1.341958	2.749481
C	2.678196	1.405832	-0.308703
H	2.366122	-0.070000	1.213326
H	2.891887	0.718547	-1.133800
H	3.639250	1.730579	0.110787
H	2.195027	2.292278	-0.736486

Table A.13: Cartesian coordinates of propene (Scheme 3.8).

atom	x	y	z
C	-1.254819	-0.227228	-0.000024
C	-0.107695	0.444962	0.000081
C	1.251833	-0.178040	0.000049
H	1.191924	-1.270305	-0.000121

Table A.13: Cartesian coordinates of propene (Scheme 3.8), continued.

atom	x	y	z
H	1.827154	0.136501	0.879534
H	1.827239	0.136771	-0.879283
H	-2.212423	0.284262	0.000010
H	-1.273514	-1.314874	-0.000147
H	-0.136316	1.535492	0.000201

Table A.14: Cartesian coordinates of the silyl ketene acetal formed from **267** (Fig. 3.3).

atom	x	y	z
C	0.437792	0.320469	3.278441
C	0.075596	-1.033503	3.435454
C	1.287663	0.685770	2.264397
C	0.585014	-1.997809	2.599325
C	1.486548	-1.659360	1.559395
C	1.820138	-0.282756	1.380202
C	2.044945	-2.640464	0.685614
C	2.632087	0.082334	0.287319
C	3.101790	-0.847721	-0.612543
C	2.829598	-2.230061	-0.383157
H	2.841111	1.135601	0.113641
H	0.031252	1.071175	3.949633
H	1.556299	1.729015	2.116625
H	-0.619914	-1.315498	4.220908
H	0.290934	-3.036281	2.718811
C	1.786335	-4.080178	0.934001
C	1.014261	-4.828347	-0.000878
C	2.307440	-4.678713	2.074246
C	0.819498	-6.224285	0.223912
C	1.343414	-6.803149	1.397109
C	2.046255	-6.059914	2.320809
H	1.155135	-7.856579	1.593398
C	0.081043	-6.982921	-0.716823
C	-0.448330	-6.391416	-1.836577
C	-0.279283	-5.006726	-2.048337

Table A.14: Cartesian coordinates of the silyl ketene acetal formed from **267** (Fig. 3.3), continued.

atom	x	y	z
C	0.427397	-4.244148	-1.150448
H	-0.719271	-4.539642	-2.924974
H	0.542008	-3.176860	-1.312737
H	-0.064906	-8.044626	-0.532126
H	-1.011519	-6.982706	-2.552852
C	3.817789	-0.379661	-1.819692
C	3.326688	-0.683441	-3.094173
C	4.936876	0.450895	-1.709202
C	3.937656	-0.163706	-4.228736
C	5.054821	0.659941	-4.109122
C	5.553048	0.963951	-2.846165
H	6.427405	1.600548	-2.744527
H	5.329070	0.683794	-0.722493
H	2.451854	-1.319211	-3.188158
H	3.539240	-0.401913	-5.211046
H	5.534636	1.061321	-4.996933
C	2.510890	-6.727180	3.560703
C	2.176979	-6.223064	4.823018
C	3.260273	-7.905220	3.490356
C	2.586083	-6.876522	5.979371
C	3.674845	-8.557228	4.646536
C	3.340311	-8.044321	5.896110
H	4.266316	-9.465613	4.570789
H	3.663482	-8.551520	6.800565
H	1.577005	-5.319812	4.894646
H	2.310811	-6.475089	6.950604
H	3.540028	-8.285464	2.512699
C	3.204787	-3.901611	3.001983
H	3.788767	-3.165133	2.443077
H	3.888478	-4.567068	3.530642
H	2.635418	-3.344543	3.756177
O	3.285307	-3.129200	-1.294040
Si	4.472022	-4.267280	-1.518498
O	4.462600	-5.219032	-0.134111

Table A.14: Cartesian coordinates of the silyl ketene acetal formed from **267** (Fig. 3.3), continued.

atom	x	y	z
C	3.911722	-5.190105	-3.062266
C	3.223187	-4.269998	-4.082645
H	2.889410	-4.854949	-4.949456
H	3.902501	-3.491710	-4.451219
H	2.348051	-3.778463	-3.649659
C	5.039728	-5.984119	-3.741331
H	3.162851	-5.907342	-2.693386
H	4.630596	-6.615004	-4.540499
H	5.573000	-6.635551	-3.043625
H	5.771807	-5.313488	-4.203841
C	6.162587	-3.435426	-1.563481
C	6.434218	-2.651347	-2.855243
H	5.626422	-1.959969	-3.104074
H	6.572385	-3.329265	-3.704766
H	7.355197	-2.062785	-2.758656
C	7.313844	-4.412910	-1.274997
H	6.117859	-2.711002	-0.731284
H	7.174469	-4.957810	-0.337223
H	8.266041	-3.870593	-1.215278
H	7.414095	-5.152725	-2.078032
C	4.914095	-6.471651	0.080833
O	4.473789	-7.305969	-0.905930
C	5.665458	-6.807336	1.137813
C	6.168443	-5.836679	2.158613
H	7.264075	-5.860536	2.227909
H	5.780428	-6.076499	3.157815
H	5.865733	-4.815123	1.917633
H	5.924552	-7.850973	1.273773
C	5.049600	-8.613703	-1.021229
C	4.320516	-9.676468	-0.202542
H	6.117556	-8.568867	-0.764772
H	4.960004	-8.862832	-2.087572
C	5.012568	-11.024611	-0.408999
H	4.981307	-11.319583	-1.465316

Table A.14: Cartesian coordinates of the silyl ketene acetal formed from **267** (Fig. 3.3), continued.

atom	x	y	z
H	4.512637	-11.808835	0.168019
H	6.062686	-10.993442	-0.097443
C	2.843650	-9.734494	-0.585703
H	4.396084	-9.408550	0.859642
H	2.378232	-8.749887	-0.490229
H	2.301470	-10.439921	0.053566
H	2.728087	-10.063781	-1.626310

Table A.15: Cartesian coordinates of **277a** (Fig. 3.8).

atom	x	y	z
C	2.932078	-0.832952	0.141359
C	3.810120	-1.782735	0.650279
C	1.822055	-1.263311	-0.580877
C	3.612136	-3.148031	0.429195
C	1.606820	-2.615992	-0.827960
C	2.503100	-3.547366	-0.322203
C	4.593225	-4.161110	0.949597
H	5.062929	-3.820146	1.876503
H	5.393584	-4.332386	0.219239
H	4.110126	-5.123790	1.139114
S	0.661413	-0.063818	-1.251044
H	0.753924	-2.928237	-1.420815
H	2.340126	-4.604334	-0.518230
H	3.113467	0.225870	0.296387
H	4.673783	-1.450846	1.221255
O	-0.119425	-0.756015	-2.287899
O	1.439843	1.142273	-1.572735
N	-0.440262	0.326239	-0.045992
C	0.116348	1.086876	1.093765
C	0.361198	2.615471	0.914531
H	1.051641	0.628506	1.445229
H	-0.594208	0.979119	1.913179
C	-0.671032	3.274309	0.005511

Table A.15: Cartesian coordinates of **277a** (Fig. 3.8), continued.

atom	x	y	z
H	-0.589582	2.908666	-1.018976
H	-0.538309	4.359088	-0.002398
H	-1.680214	3.059891	0.372132
C	0.287467	3.231766	2.329590
H	-0.734874	3.148596	2.716000
H	0.557403	4.292602	2.304373
H	0.970955	2.719424	3.014171
C	1.799472	2.862597	0.461108
O	1.898171	3.822956	-0.468913
O	2.762219	2.316387	0.961923
C	3.234336	4.063215	-0.955836
H	3.625263	3.152733	-1.418364
H	3.892985	4.370523	-0.138727
H	3.135103	4.858602	-1.694907
Si	-2.088165	-0.434928	-0.039473
C	-1.919970	-2.312581	0.187481
C	-3.137642	-0.093676	-1.592499
C	-2.983599	0.414912	1.438440
C	-3.028462	-1.055077	-2.785682
H	-3.012755	-2.106904	-2.483214
H	-2.124140	-0.865720	-3.364675
H	-3.893031	-0.915098	-3.447531
C	-3.020284	1.359396	-2.071923
H	-4.155028	-0.224569	-1.189860
H	-3.751550	1.565018	-2.864212
H	-2.022845	1.546223	-2.484434
H	-3.189280	2.083998	-1.267351
C	-0.992417	-2.768707	1.324373
H	-0.716919	-3.823612	1.197264
H	-1.486276	-2.679289	2.296426
H	-0.061771	-2.193575	1.366536
C	-3.291768	-2.998959	0.307335
H	-1.472273	-2.638155	-0.764253
H	-3.181758	-4.090828	0.286078

Table A.15: Cartesian coordinates of **277a** (Fig. 3.8), continued.

atom	x	y	z
H	-3.974266	-2.720787	-0.502622
H	-3.780784	-2.743861	1.254543
C	-2.698481	-0.222733	2.811038
H	-3.093546	0.410974	3.615275
H	-1.635219	-0.388768	3.009766
H	-3.194950	-1.195166	2.893691
C	-4.508447	0.511235	1.253679
H	-2.611307	1.449472	1.465766
H	-4.967279	-0.477394	1.135385
H	-4.787959	1.117798	0.387940
H	-4.961175	0.974071	2.140103

Table A.16: Cartesian coordinates of **278a** (Fig. 3.8).

atom	x	y	z
C	-0.169151	-3.032488	-0.204701
C	0.055013	-4.538125	-0.394639
C	0.779780	-2.128449	-1.003538
H	-0.118966	-2.768121	0.855134
H	-1.188928	-2.798460	-0.537986
C	0.843325	-2.606388	-2.478624
C	1.186228	-4.089838	-2.599197
H	1.558593	-1.982414	-3.027573
H	-0.149583	-2.443455	-2.924791
C	0.138362	-4.932059	-1.870023
H	-0.766422	-5.077374	0.093859
H	0.976451	-4.842566	0.111105
H	-0.838369	-4.776596	-2.353190
H	0.369980	-6.000191	-1.962836
H	2.181805	-4.283443	-2.174124
H	1.237232	-4.368553	-3.658820
C	0.274777	-0.648987	-1.062502
C	2.226224	-2.127740	-0.503197
N	-0.443572	-0.091273	0.103201

Table A.16: Cartesian coordinates of **278a** (Fig. 3.8), continued.

atom	x	y	z
H	-0.419137	-0.593051	-1.900624
H	1.124806	-0.007884	-1.334168
S	0.532804	0.419982	1.369093
C	1.466314	1.852425	0.812228
C	1.008862	3.123201	1.148010
C	1.736393	4.233586	0.742405
C	2.912052	4.094234	-0.000792
C	3.357424	2.805750	-0.307654
C	2.651672	1.680409	0.101500
H	4.282956	2.675522	-0.862910
H	3.028470	0.685106	-0.112583
H	0.105512	3.233356	1.738285
H	1.388244	5.226837	1.014995
C	3.674361	5.303078	-0.466658
H	3.328711	5.617236	-1.459227
H	4.744907	5.093471	-0.543805
H	3.534810	6.148819	0.212546
O	1.517569	-0.635616	1.648909
O	-0.391761	0.888078	2.413188
O	2.473150	-3.026982	0.458327
C	3.802666	-2.976744	1.014679
H	3.830680	-3.764153	1.768413
H	3.970714	-1.998423	1.473016
H	4.552289	-3.153175	0.238239
O	3.087045	-1.412847	-0.978493
Si	-2.204352	0.351158	0.079362
C	-2.385824	2.240196	0.006323
C	-1.536650	2.952942	-1.057809
H	-1.977018	2.845868	-2.053209
H	-0.510522	2.573927	-1.101367
H	-1.476692	4.028119	-0.844502
C	-3.859988	2.664322	-0.113533
H	-2.028550	2.566447	0.995313
H	-4.271326	2.390748	-1.091807

Table A.16: Cartesian coordinates of **278a** (Fig. 3.8), continued.

atom	x	y	z
H	-3.958688	3.753073	-0.015523
H	-4.494228	2.205694	0.652380
C	-3.215349	-0.308908	1.553465
C	-2.855643	-1.756869	1.913982
H	-2.897996	-2.430800	1.050772
H	-3.544268	-2.147283	2.674312
H	-1.842004	-1.806940	2.326342
C	-3.300563	0.545283	2.827802
H	-4.230631	-0.318334	1.125270
H	-2.393291	0.453085	3.425407
H	-4.148221	0.207860	3.438453
H	-3.449826	1.608847	2.616799
C	-2.887332	-0.513825	-1.501175
C	-4.371713	-0.904661	-1.385597
H	-5.010748	-0.033025	-1.202528
H	-4.553083	-1.628192	-0.586004
H	-4.708744	-1.361220	-2.325285
C	-2.690327	0.278078	-2.807110
H	-2.330073	-1.456367	-1.601290
H	-3.354242	1.148290	-2.837814
H	-2.942346	-0.349188	-3.671783
H	-1.670038	0.646890	-2.951944

Table A.17: Cartesian coordinates of **278a** (Fig. 3.8).

atom	x	y	z
C	-0.169151	-3.032488	-0.204701
C	0.055013	-4.538125	-0.394639
C	0.779780	-2.128449	-1.003538
H	-0.118966	-2.768121	0.855134
H	-1.188928	-2.798460	-0.537986
C	0.843325	-2.606388	-2.478624
C	1.186228	-4.089838	-2.599197
H	1.558593	-1.982414	-3.027573

Table A.17: Cartesian coordinates of **278a** (Fig. 3.8), continued.

atom	x	y	z
H	-0.149583	-2.443455	-2.924791
C	0.138362	-4.932059	-1.870023
H	-0.766422	-5.077374	0.093859
H	0.976451	-4.842566	0.111105
H	-0.838369	-4.776596	-2.353190
H	0.369980	-6.000191	-1.962836
H	2.181805	-4.283443	-2.174124
H	1.237232	-4.368553	-3.658820
C	0.274777	-0.648987	-1.062502
C	2.226224	-2.127740	-0.503197
N	-0.443572	-0.091273	0.103201
H	-0.419137	-0.593051	-1.900624
H	1.124806	-0.007884	-1.334168
S	0.532804	0.419982	1.369093
C	1.466314	1.852425	0.812228
C	1.008862	3.123201	1.148010
C	1.736393	4.233586	0.742405
C	2.912052	4.094234	-0.000792
C	3.357424	2.805750	-0.307654
C	2.651672	1.680409	0.101500
H	4.282956	2.675522	-0.862910
H	3.028470	0.685106	-0.112583
H	0.105512	3.233356	1.738285
H	1.388244	5.226837	1.014995
C	3.674361	5.303078	-0.466658
H	3.328711	5.617236	-1.459227
H	4.744907	5.093471	-0.543805
H	3.534810	6.148819	0.212546
O	1.517569	-0.635616	1.648909
O	-0.391761	0.888078	2.413188
O	2.473150	-3.026982	0.458327
C	3.802666	-2.976744	1.014679
H	3.830680	-3.764153	1.768413
H	3.970714	-1.998423	1.473016

Table A.17: Cartesian coordinates of **278a** (Fig. 3.8), continued.

atom	x	y	z
H	4.552289	-3.153175	0.238239
O	3.087045	-1.412847	-0.978493
Si	-2.204352	0.351158	0.079362
C	-2.385824	2.240196	0.006323
C	-1.536650	2.952942	-1.057809
H	-1.977018	2.845868	-2.053209
H	-0.510522	2.573927	-1.101367
H	-1.476692	4.028119	-0.844502
C	-3.859988	2.664322	-0.113533
H	-2.028550	2.566447	0.995313
H	-4.271326	2.390748	-1.091807
H	-3.958688	3.753073	-0.015523
H	-4.494228	2.205694	0.652380
C	-3.215349	-0.308908	1.553465
C	-2.855643	-1.756869	1.913982
H	-2.897996	-2.430800	1.050772
H	-3.544268	-2.147283	2.674312
H	-1.842004	-1.806940	2.326342
C	-3.300563	0.545283	2.827802
H	-4.230631	-0.318334	1.125270
H	-2.393291	0.453085	3.425407
H	-4.148221	0.207860	3.438453
H	-3.449826	1.608847	2.616799
C	-2.887332	-0.513825	-1.501175
C	-4.371713	-0.904661	-1.385597
H	-5.010748	-0.033025	-1.202528
H	-4.553083	-1.628192	-0.586004
H	-4.708744	-1.361220	-2.325285
C	-2.690327	0.278078	-2.807110
H	-2.330073	-1.456367	-1.601290
H	-3.354242	1.148290	-2.837814
H	-2.942346	-0.349188	-3.671783
H	-1.670038	0.646890	-2.951944

Table A.18: Cartesian coordinates of **278a** (Fig. 3.8).

atom	x	y	z
C	-0.169151	-3.032488	-0.204701
C	0.055013	-4.538125	-0.394639
C	0.779780	-2.128449	-1.003538
H	-0.118966	-2.768121	0.855134
H	-1.188928	-2.798460	-0.537986
C	0.843325	-2.606388	-2.478624
C	1.186228	-4.089838	-2.599197
H	1.558593	-1.982414	-3.027573
H	-0.149583	-2.443455	-2.924791
C	0.138362	-4.932059	-1.870023
H	-0.766422	-5.077374	0.093859
H	0.976451	-4.842566	0.111105
H	-0.838369	-4.776596	-2.353190
H	0.369980	-6.000191	-1.962836
H	2.181805	-4.283443	-2.174124
H	1.237232	-4.368553	-3.658820
C	0.274777	-0.648987	-1.062502
C	2.226224	-2.127740	-0.503197
N	-0.443572	-0.091273	0.103201
H	-0.419137	-0.593051	-1.900624
H	1.124806	-0.007884	-1.334168
S	0.532804	0.419982	1.369093
C	1.466314	1.852425	0.812228
C	1.008862	3.123201	1.148010
C	1.736393	4.233586	0.742405
C	2.912052	4.094234	-0.000792
C	3.357424	2.805750	-0.307654
C	2.651672	1.680409	0.101500
H	4.282956	2.675522	-0.862910
H	3.028470	0.685106	-0.112583
H	0.105512	3.233356	1.738285
H	1.388244	5.226837	1.014995
C	3.674361	5.303078	-0.466658
H	3.328711	5.617236	-1.459227

Table A.18: Cartesian coordinates of **278a** (Fig. 3.8), continued.

atom	x	y	z
H	4.744907	5.093471	-0.543805
H	3.534810	6.148819	0.212546
O	1.517569	-0.635616	1.648909
O	-0.391761	0.888078	2.413188
O	2.473150	-3.026982	0.458327
C	3.802666	-2.976744	1.014679
H	3.830680	-3.764153	1.768413
H	3.970714	-1.998423	1.473016
H	4.552289	-3.153175	0.238239
O	3.087045	-1.412847	-0.978493
Si	-2.204352	0.351158	0.079362
C	-2.385824	2.240196	0.006323
C	-1.536650	2.952942	-1.057809
H	-1.977018	2.845868	-2.053209
H	-0.510522	2.573927	-1.101367
H	-1.476692	4.028119	-0.844502
C	-3.859988	2.664322	-0.113533
H	-2.028550	2.566447	0.995313
H	-4.271326	2.390748	-1.091807
H	-3.958688	3.753073	-0.015523
H	-4.494228	2.205694	0.652380
C	-3.215349	-0.308908	1.553465
C	-2.855643	-1.756869	1.913982
H	-2.897996	-2.430800	1.050772
H	-3.544268	-2.147283	2.674312
H	-1.842004	-1.806940	2.326342
C	-3.300563	0.545283	2.827802
H	-4.230631	-0.318334	1.125270
H	-2.393291	0.453085	3.425407
H	-4.148221	0.207860	3.438453
H	-3.449826	1.608847	2.616799
C	-2.887332	-0.513825	-1.501175
C	-4.371713	-0.904661	-1.385597
H	-5.010748	-0.033025	-1.202528

Table A.18: Cartesian coordinates of **278a** (Fig. 3.8), continued.

atom	x	y	z
H	-4.553083	-1.628192	-0.586004
H	-4.708744	-1.361220	-2.325285
C	-2.690327	0.278078	-2.807110
H	-2.330073	-1.456367	-1.601290
H	-3.354242	1.148290	-2.837814
H	-2.942346	-0.349188	-3.671783
H	-1.670038	0.646890	-2.951944

Table A.19: Cartesian coordinates of TIPS-**G** (Scheme 3.26).

atom	x	y	z
N	0.2504949772	0.1796289577	0.5523795040
S	-0.9357704004	-0.9783349767	0.7939673369
C	-0.1680928802	1.5975805337	0.6627741178
C	-0.2602640247	2.2897960792	2.0640277329
H	-1.1315934124	1.7268913025	0.1463340927
H	0.5518974033	2.1602710816	0.0668585714
C	0.1871754084	3.7462046288	1.8505480282
H	0.0818035321	4.3204387608	2.7772856972
H	-0.4213303737	4.2389062697	1.0816405697
H	1.2370969194	3.7995504693	1.5368605473
C	0.6370664694	1.6259707627	3.1084988502
H	0.3428329881	0.5872465105	3.2773635960
H	0.5560928301	2.1670719871	4.0582096800
H	1.6903337709	1.6408728619	2.8099746951
C	-1.7052541744	2.3108903626	2.5846357058
H	-1.7618245507	2.8982972058	3.5083518769
H	-2.0630984185	1.3025242711	2.8031701860
H	-2.3771167826	2.7785826194	1.8537170015
Si	1.8633457133	-0.3414578263	-0.0988987200
C	2.9344773642	1.2572787113	0.0175050966
C	4.4242001496	0.9737297746	0.2814966307
H	4.8703329978	0.3646713975	-0.5136651504
H	4.5906281075	0.4594261167	1.2318802772

Table A.19: Cartesian coordinates of TIPS-**G** (Scheme 3.26), continued.

atom	x	y	z
H	4.9817015825	1.9187594940	0.3161654471
C	2.8296048921	2.2105422001	-1.1872234050
H	2.5618369730	1.7988393314	0.8978404966
H	1.8015665188	2.4426201328	-1.4814396800
H	3.3277868079	1.7855085743	-2.0649346898
H	3.3312526003	3.1604091736	-0.9616196595
C	2.7393705413	-1.6724777769	0.9462355612
C	2.5894400255	-1.4241975562	2.4541901792
H	3.2248240757	-2.1151419110	3.0230798264
H	1.5535376492	-1.5906212868	2.7706028767
H	2.8629672282	-0.4042208161	2.7451370641
C	2.4760215817	-3.1525685580	0.6293671659
H	3.7940548453	-1.4879924406	0.6861680351
H	2.4650724976	-3.3634543608	-0.4446924291
H	1.5178531507	-3.4791388294	1.0352120541
H	3.2658037069	-3.7681371958	1.0794491706
C	1.6796210824	-0.9612298640	-1.8855008819
C	0.8727139046	-0.0447143243	-2.8183314656
H	1.4691161154	0.8099444601	-3.1506864467
H	-0.0315745594	0.3465508644	-2.3397069042
H	0.5590794317	-0.5881461411	-3.7195304418
C	3.0424600738	-1.3022120944	-2.5108344460
H	1.1213020336	-1.9026645240	-1.7728031781
H	3.6280886354	-1.9885620981	-1.8899074016
H	3.6453230827	-0.4003922492	-2.6672683940
H	2.9110503673	-1.7765607393	-3.4920336267
C	-2.2639394892	-0.6202903549	-0.3675686356
C	-2.2019177570	-1.1629765909	-1.6482108536
C	-3.2324642339	-0.9090467621	-2.5414475587
C	-4.3299038504	-0.1217491698	-2.1755080495
C	-4.3741100691	0.3985229864	-0.8807251986
C	-3.3527435306	0.1478216404	0.0293328639
H	-3.4071502094	0.5268771381	1.0438178629
H	-5.2257307355	0.9996712835	-0.5725070360

Table A.19: Cartesian coordinates of TIPS-**G** (Scheme 3.26), continued.

atom	x	y	z
H	-1.3644165566	-1.7929275487	-1.9286567310
H	-3.1901811609	-1.3372022657	-3.5401021591
C	-5.4511717735	0.1193418188	-3.1470171475
H	-5.0676473883	0.3351122328	-4.1490845785
H	-6.0819684581	0.9545047690	-2.8316648429
H	-6.0895473638	-0.7687980418	-3.2269745237
O	-1.5147146561	-0.8467094143	2.1387196426
O	-0.3211494207	-2.2489621451	0.3734664480

Table A.20: Cartesian coordinates of TIPS-**X** (Scheme 3.26).

atom	x	y	z
N	0.5763259192	-0.0980902748	0.1779837682
C	1.6101962160	-0.5267563945	-0.8298321071
C	2.7157972653	0.5091789037	-1.2811773012
C	4.0482957835	0.3718426632	-0.5247736285
H	4.5337244690	-0.5889535711	-0.7259169416
H	3.9258158346	0.4914988060	0.5523644830
H	4.7322567789	1.1547983306	-0.8709453481
C	3.0037931695	0.2124730537	-2.7679769382
H	3.8044499623	0.8671858360	-3.1285171542
H	2.1214581375	0.3906766074	-3.3933877651
H	3.3309149027	-0.8208111122	-2.9283899696
C	2.2289842226	1.9561449140	-1.1799398416
H	2.0342043423	2.2494111843	-0.1471446812
H	1.3170236494	2.1113202621	-1.7621724375
H	2.9954976779	2.6240670683	-1.5888623092
C	2.2253907033	-1.8877208788	-0.4972702882
H	1.0006710563	-0.6767576653	-1.7241442137
H	2.9129519862	-1.8340038684	0.3488764557
H	2.7991547790	-2.2575868936	-1.3516986609
H	1.4521618887	-2.6260207465	-0.2745451431
S	0.9810229618	0.1742921547	1.7784875758
C	1.3230120604	-1.4165585205	2.6003429215

Table A.20: Cartesian coordinates of TIPS-**X** (Scheme 3.26), continued.

atom	x	y	z
H	0.6058004842	-2.1682307038	2.2664187364
H	1.1975305467	-1.2153798019	3.6676630165
H	2.3473343284	-1.7239339824	2.3915178156
O	2.2122339711	0.9638507354	1.9113462451
O	-0.2721988721	0.6698559424	2.3841789141
Si	-1.2391357184	-0.1521930348	-0.1160511413
C	-2.1005172606	1.5477368000	0.0772929425
C	-1.1166127605	2.7179332720	-0.0689627958
H	-1.6666300471	3.6674639753	-0.0818976448
H	-0.5346203052	2.6596933835	-0.9911201738
H	-0.4149450606	2.7468548511	0.7702212025
C	-2.9938329870	1.7702418113	1.3068070909
H	-2.7637485079	1.5786097665	-0.8032529974
H	-2.4550258416	1.5824581163	2.2385631150
H	-3.8874419469	1.1425102037	1.2849841829
H	-3.3348766225	2.8134950381	1.3240821680
C	-1.4545377430	-0.6113679360	-1.9663281686
C	-1.0609111725	0.5070422558	-2.9449769652
H	-1.7191779509	1.3751647211	-2.8283725159
H	-1.1598680898	0.1617634768	-3.9821982481
H	-0.0352786265	0.8592253738	-2.8115060335
C	-2.9155065217	-1.0067719080	-2.2536766908
H	-0.8367492183	-1.4976842755	-2.1787147344
H	-3.6119513913	-0.2030317272	-1.9852343202
H	-3.2242730312	-1.9069297975	-1.7180001734
H	-3.0470412495	-1.1998237092	-3.3261207818
C	-1.9398440455	-1.5904043985	0.9467639360
C	-3.4595216620	-1.5979494009	1.1934705538
H	-3.7542368854	-0.8161941864	1.8948909232
H	-3.7573364059	-2.5585859234	1.6335608540
H	-4.0464708047	-1.4667853548	0.2792007163
C	-1.4919720423	-2.9582190770	0.4047728675
H	-1.4792016747	-1.4569995131	1.9339508860
H	-1.7556623393	-3.7546123686	1.1128042277

Table A.20: Cartesian coordinates of TIPS-**X** (Scheme 3.26), continued.

atom	x	y	z
H	-0.4120629747	-3.0130459038	0.2382705937
H	-1.9773587737	-3.2019152458	-0.5461048368

Table A.21: Cartesian coordinates of methyl propionate (Scheme 3.26).

atom	x	y	z
C	-1.2342569344	0.7342802206	0.1793314840
C	0.0287644816	-0.0371147243	-0.1187645399
O	1.1234950831	0.6753701189	0.2398781403
O	0.0824497145	-1.1405972820	-0.6094851391
C	2.3842241254	0.0189105468	-0.0057343452
H	2.4413932523	-0.9199101413	0.5523973882
H	3.1481345575	0.7178096495	0.3360749741
H	2.5040973167	-0.1932310482	-1.0719447137
C	-2.4923652136	-0.0320174772	-0.2030072250
H	-1.2241664155	0.9880838772	1.2470044368
H	-2.4995707122	-0.2624943642	-1.2714930940
H	-3.3833622123	0.5571921763	0.0321498258
H	-2.5500490131	-0.9810350084	0.3362729513
H	-1.1697997816	1.6941492441	-0.3488921177

Table A.22: Cartesian coordinates of the (Z)-TIPS silyl ketene acetal of methyl propionate (Scheme 3.26).

atom	x	y	z
C	-1.2342569344	0.7342802206	0.1793314840
C	0.0287644816	-0.0371147243	-0.1187645399
O	1.1234950831	0.6753701189	0.2398781403
O	0.0824497145	-1.1405972820	-0.6094851391
C	2.3842241254	0.0189105468	-0.0057343452
H	2.4413932523	-0.9199101413	0.5523973882
H	3.1481345575	0.7178096495	0.3360749741
H	2.5040973167	-0.1932310482	-1.0719447137
C	-2.4923652136	-0.0320174772	-0.2030072250

Table A.22: Cartesian coordinates of the (*Z*)-TIPS silyl ketene acetal of methyl propionate (Scheme 3.26), continued.

atom	x	y	z
H	-1.2241664155	0.9880838772	1.2470044368
H	-2.4995707122	-0.2624943642	-1.2714930940
H	-3.3833622123	0.5571921763	0.0321498258
H	-2.5500490131	-0.9810350084	0.3362729513
H	-1.1697997816	1.6941492441	-0.3488921177
C	2.9521416563	-0.6644498821	-0.7858532873
C	1.8193677425	-0.1008170716	-0.3455785303
O	1.6996221413	1.1193036711	0.2668728981
O	0.6173826683	-0.6864821426	-0.4532518049
C	2.8880018523	1.8837993588	0.4429752978
H	3.6074629341	1.3494665169	1.0767468128
H	2.5811628541	2.8088091272	0.9346851659
H	3.3525296903	2.1142492679	-0.5246437396
Si	-0.8816741295	-0.0624723384	0.0314766849
C	-2.0415715321	-1.4786792258	-0.4488784509
C	-2.0734824998	-1.6932547391	-1.9708391696
H	-1.0801568342	-1.9616497442	-2.3492172324
H	-2.4078288082	-0.8000963680	-2.5088160125
H	-2.7584802283	-2.5107239373	-2.2302936202
C	-1.7017659652	-2.7967919262	0.2631658773
H	-3.0500454768	-1.1659781937	-0.1320204254
H	-0.6739405767	-3.1072323537	0.0426817305
H	-2.3706154822	-3.6003572029	-0.0716064654
H	-1.8006678661	-2.7191883927	1.3500818002
C	-1.3245439380	1.4870754915	-0.9840903566
C	-1.2247718059	2.8105249877	-0.2133411896
H	-1.5287192559	3.6504907006	-0.8513834723
H	-0.1941164744	2.9955971205	0.1086916879
H	-1.8620272467	2.8251225749	0.6772584696
C	-0.4981239492	1.5676157703	-2.2794573866
H	-2.3806970560	1.3459461895	-1.2683697357
H	0.5544987481	1.7666839176	-2.0503624317
H	-0.8602504850	2.3832962407	-2.9182480816

Table A.22: Cartesian coordinates of the (*Z*)-TIPS silyl ketene acetal of methyl propionate (Scheme 3.26), continued.

atom	x	y	z
H	-0.5352158440	0.6416010595	-2.8612646401
C	-0.8834932004	0.2831247864	1.8955264316
C	-2.3150511777	0.2747802339	2.4560373797
H	-2.9852251605	0.9426378162	1.9007409417
H	-2.3250421118	0.5979636456	3.5047228804
H	-2.7506190289	-0.7306101349	2.4203266287
C	0.0335339092	-0.6497360297	2.6988503698
H	-0.4860286653	1.3024441022	2.0040890026
H	-0.3000586721	-1.6914452721	2.6490716305
H	0.0428948704	-0.3596046277	3.7576550039
H	1.0644004188	-0.6163010952	2.3322779269
C	2.9916566818	-2.0079285912	-1.4469779978
H	3.8860136134	-0.1303177384	-0.6605455336
H	3.4007548679	-1.9432049368	-2.4633112345
H	1.9910481336	-2.4406835754	-1.5150115936
H	3.6254946417	-2.7106928918	-0.8912559742

Table A.23: Cartesian coordinates of GFN2-xTB conformer 2/13 of **368a** (Scheme 4.16).

atom	x	y	z
O	1.725635	1.742078	-1.620899
C	2.646523	1.855785	-0.543974
C	2.280576	0.769674	0.469370
C	1.608552	-0.277185	-0.440855
C	0.876343	0.624727	-1.456011
C	-0.482780	1.003218	-0.955619
H	0.770921	0.120128	-2.423663
N	-1.518738	0.142490	-1.063874
C	-0.938736	2.140330	-0.314425
C	-2.291870	1.964714	-0.021316
C	-2.654500	0.709041	-0.489284
H	-0.344829	3.003113	-0.090856
H	-2.924210	2.677108	0.472941

Table A.23: Cartesian coordinates of GFN2-xTB conformer 2/13 of **368a** (Scheme 4.16), continued.

atom	x	y	z
N	-1.471359	-1.058283	-1.631253
C	-2.573255	-1.746150	-1.624874
C	-3.844541	-0.059293	-0.501855
C	-3.794071	-1.310655	-1.073164
H	-2.503561	-2.717075	-2.091216
H	-4.663265	-1.941446	-1.108402
N	-4.975958	0.511945	0.062575
C	-6.234443	-0.026049	0.176011
H	-4.841430	1.449859	0.413006
C	-7.204354	0.932935	0.830056
H	-8.179136	0.459907	0.901447
H	-7.290355	1.841515	0.237506
H	-6.859750	1.195428	1.828185
O	-6.533035	-1.132506	-0.198601
O	0.741383	-1.138549	0.258127
H	2.382688	-0.865977	-0.945626
O	1.346021	1.310344	1.393002
H	3.134437	0.364049	1.019592
C	4.089172	1.711754	-1.060030
H	2.534287	2.850951	-0.096853
O	4.418652	0.359939	-1.340119
H	4.791024	2.101288	-0.314918
H	4.178964	2.261723	-1.998732
C	1.233703	-2.346164	0.595298
C	0.253782	-3.093352	1.445651
H	-0.761599	-2.873272	1.130129
H	0.388391	-2.748227	2.470248
H	0.457199	-4.158456	1.398560
O	2.317220	-2.738195	0.256102
C	1.085866	0.612794	2.508374
C	-0.017933	1.280075	3.283152
H	-0.933577	1.222899	2.698253
H	0.223417	2.328463	3.434302

Table A.23: Cartesian coordinates of GFN2-xTB conformer 2/13 of **368a** (Scheme 4.16), continued.

atom	x	y	z
H	-0.152182	0.781094	4.237614
O	1.657638	-0.392311	2.831147
C	5.190476	-0.295059	-0.444420
C	5.343863	-1.733402	-0.827309
H	5.332732	-1.841021	-1.907377
H	4.497697	-2.285022	-0.413538
H	6.259414	-2.133322	-0.402951
O	5.658640	0.233602	0.527980

Table A.24: Cartesian coordinates of GFN2-xTB conformer 3/13 of **368a** (Scheme 4.16).

atom	x	y	z
O	1.778194	0.778535	-2.037404
C	2.619266	0.979224	-0.913060
C	2.339716	-0.160350	0.086056
C	1.421248	-1.106624	-0.703362
C	0.758248	-0.140912	-1.718770
C	-0.464189	0.490792	-1.129041
H	0.477298	-0.664089	-2.639120
N	-1.648289	-0.160024	-1.171926
C	-0.663019	1.686426	-0.462441
C	-2.005932	1.764845	-0.092428
C	-2.623431	0.603501	-0.534575
H	0.084808	2.429541	-0.274373
H	-2.463072	2.578676	0.436494
N	-1.858518	-1.345012	-1.735884
C	-3.069619	-1.812039	-1.671620
C	-3.934615	0.071103	-0.477119
C	-4.153902	-1.160196	-1.053267
H	-3.207890	-2.773944	-2.141933
H	-5.127033	-1.615660	-1.039497
N	-4.903372	0.835566	0.155621
C	-6.227126	0.532589	0.360285

Table A.24: Cartesian coordinates of GFN2-xTB conformer 3/13 of **368a** (Scheme 4.16), continued.

atom	x	y	z
H	-4.575117	1.727966	0.497017
C	-6.959518	1.645418	1.076502
H	-6.505220	1.831365	2.047568
H	-7.996848	1.356671	1.216640
H	-6.919040	2.560137	0.488620
O	-6.746030	-0.499054	0.013241
O	0.491941	-1.756969	0.133609
H	2.019278	-1.856401	-1.235522
O	1.656178	0.354273	1.219423
H	3.257177	-0.653431	0.425641
C	4.077503	1.005965	-1.397621
H	2.383357	1.935954	-0.429816
O	5.015881	0.824061	-0.348929
H	4.262657	1.957189	-1.905998
H	4.247712	0.179810	-2.090097
C	0.279898	-3.071469	-0.070468
C	-0.793883	-3.573879	0.852270
H	-0.801236	-2.995793	1.770940
H	-0.638208	-4.628855	1.056618
H	-1.753302	-3.452260	0.352325
O	0.873844	-3.727641	-0.878854
C	2.291747	0.352569	2.396104
C	1.453876	1.024465	3.446089
H	1.760250	2.067882	3.502194
H	1.629694	0.560740	4.412293
H	0.404845	0.976965	3.172368
O	3.389181	-0.108246	2.571290
C	5.053563	1.740159	0.635393
C	6.066239	1.361673	1.673029
H	5.573329	0.690390	2.375973
H	6.402147	2.246630	2.204307
H	6.898948	0.837735	1.215301
O	4.344090	2.710884	0.665071

Table A.25: Cartesian coordinates of GFN2-xTB conformer 4/13 of **368a** (Scheme 4.16).

atom	x	y	z
O	1.364989	1.307377	-1.102965
C	2.405574	1.385985	-0.151837
C	2.540520	-0.043867	0.391221
C	1.070265	-0.464562	0.465104
C	0.502775	0.210789	-0.810440
C	-0.912337	0.640101	-0.635371
H	0.544899	-0.504635	-1.643469
N	-1.930557	-0.155970	-1.033128
C	-1.457555	1.754947	-0.022916
C	-2.847073	1.634036	-0.053843
C	-3.140280	0.430327	-0.681849
H	-0.895117	2.569569	0.388841
H	-3.548071	2.345701	0.338198
N	-1.798534	-1.322303	-1.652384
C	-2.896836	-1.953364	-1.937862
C	-4.325035	-0.276953	-1.005054
C	-4.193196	-1.489516	-1.641309
H	-2.759216	-2.898760	-2.439547
H	-5.054958	-2.074096	-1.906831
N	-5.531741	0.308698	-0.651332
C	-6.803058	-0.155680	-0.881343
H	-5.443255	1.191495	-0.168419
C	-7.856520	0.780678	-0.330571
H	-8.840374	0.368075	-0.532681
H	-7.774564	1.757612	-0.802685
H	-7.730886	0.897290	0.743881
O	-7.055078	-1.185014	-1.456350
O	0.511770	0.089718	1.647087
H	0.905479	-1.545543	0.458838
O	3.219047	-0.080719	1.624352
H	3.054856	-0.685566	-0.335897
C	3.673484	1.959319	-0.799254
H	2.108518	2.043242	0.680483
O	4.492598	0.961828	-1.389384

Table A.25: Cartesian coordinates of GFN2-xTB conformer 4/13 of **368a** (Scheme 4.16), continued.

atom	x	y	z
H	4.260708	2.491952	-0.044268
H	3.371917	2.633995	-1.602155
C	-0.624990	-0.451984	2.108647
C	-1.115233	0.304806	3.312760
H	-0.277336	0.740405	3.847446
H	-1.685019	-0.359199	3.955695
H	-1.767786	1.104832	2.968075
O	-1.165086	-1.406718	1.618955
C	4.208891	-0.982764	1.762865
C	4.939541	-0.771649	3.051971
H	4.270112	-0.370118	3.805604
H	5.725549	-0.043580	2.853981
H	5.392789	-1.701661	3.380801
O	4.465406	-1.817668	0.936583
C	5.545923	0.526379	-0.676204
C	6.260683	-0.579469	-1.391185
H	5.946710	-1.517698	-0.933155
H	7.333086	-0.475626	-1.254023
H	5.998159	-0.583705	-2.443798
O	5.848137	0.971003	0.400961

Table A.26: Cartesian coordinates of GFN2-xTB conformer 5/13 of **368a** (Scheme 4.16).

atom	x	y	z
O	1.344353	1.305423	-1.073569
C	2.396988	1.389242	-0.136551
C	2.546903	-0.040072	0.403661
C	1.080244	-0.469821	0.496036
C	0.494239	0.201009	-0.773010
C	-0.922265	0.621169	-0.588980
H	0.534520	-0.513727	-1.606758
N	-1.938607	-0.166930	-1.006712
C	-1.470483	1.726788	0.037516

Table A.26: Cartesian coordinates of GFN2-xTB conformer 5/13 of **368a** (Scheme 4.16), continued.

atom	x	y	z
C	-2.859840	1.608964	-0.006203
C	-3.150117	0.416651	-0.656859
H	-0.910050	2.533850	0.466584
H	-3.562686	2.314948	0.392694
N	-1.804046	-1.323513	-1.643532
C	-2.901343	-1.946492	-1.950044
C	-4.333830	-0.278933	-1.008103
C	-4.199301	-1.482018	-1.661647
H	-2.761395	-2.884438	-2.464927
H	-5.060199	-2.057551	-1.948840
N	-5.542481	0.309791	-0.666301
C	-6.812618	-0.135735	-0.936588
H	-5.456223	1.184536	-0.168536
C	-7.869242	0.806042	-0.401371
H	-7.775008	0.901847	0.678334
H	-8.852127	0.411388	-0.640646
H	-7.759084	1.789845	-0.853044
O	-7.061338	-1.154083	-1.532239
O	0.531614	0.079577	1.684745
H	0.923010	-1.551975	0.491318
O	3.244199	-0.074666	1.626222
H	3.054066	-0.678296	-0.331593
C	3.653144	1.968812	-0.800875
H	2.108189	2.045195	0.699738
O	4.460898	0.975910	-1.413787
H	4.253538	2.494687	-0.051525
H	3.337646	2.650499	-1.592396
C	-0.597981	-0.469240	2.155723
C	-1.077699	0.277971	3.370003
H	-1.741424	1.074405	3.038606
H	-0.235974	0.717355	3.895608
H	-1.633489	-0.393766	4.017238
O	-1.139493	-1.423184	1.666090

Table A.26: Cartesian coordinates of GFN2-xTB conformer 5/13 of **368a** (Scheme 4.16), continued.

atom	x	y	z
C	4.238809	-0.974140	1.748755
C	4.991198	-0.759608	3.024665
H	5.456226	-1.687039	3.344214
H	4.333158	-0.362958	3.790833
H	5.768862	-0.026420	2.813066
O	4.482726	-1.809585	0.919273
C	5.526679	0.534255	-0.723232
C	6.224251	-0.569961	-1.457459
H	7.299793	-0.463802	-1.349729
H	5.933185	-0.574530	-2.502554
H	5.925211	-1.508849	-0.990883
O	5.850722	0.972678	0.350113

Table A.27: Cartesian coordinates of GFN2-xTB conformer 6/13 of **368a** (Scheme 4.16).

atom	x	y	z
O	1.7986347022	0.7835685426	-2.0363099946
C	2.6330027852	0.9830709600	-0.9068725710
C	2.3424185970	-0.1532707042	0.0928550776
C	1.4300159816	-1.0996269767	-0.7018044691
C	0.7761475834	-0.1354667250	-1.7247380844
C	-0.4500960012	0.4978340656	-1.1440641403
H	0.5027363045	-0.6611303501	-2.6459875282
N	-1.6274847377	-0.1664328605	-1.1641866237
C	-0.6575088418	1.7067713037	-0.5051127451
C	-1.9992091822	1.7798312125	-0.1287985145
C	-2.6067504012	0.6015701398	-0.5388260831
H	0.0838295868	2.4618737882	-0.3402861742
H	-2.4617316783	2.6011082345	0.3837382368
N	-1.8279164764	-1.3664961059	-1.6993075387
C	-3.0318553543	-1.8467514030	-1.6136838734
C	-3.9114052706	0.0554049489	-0.4600767865
C	-4.1193409430	-1.1925011510	-1.0031781221

Table A.27: Cartesian coordinates of GFN2-xTB conformer 6/13 of **368a** (Scheme 4.16), continued.

atom	x	y	z
H	-3.1613621896	-2.8212758654	-2.0588893932
H	-5.0867646707	-1.6589483120	-0.9705872732
N	-4.8854231889	0.8248743466	0.1592219359
C	-6.2039341445	0.5117478533	0.3806183221
H	-4.5662642320	1.7307712508	0.4725563524
C	-6.9461880841	1.6357744856	1.0689009029
H	-6.4859499830	1.8591285563	2.0292019530
H	-7.9778406021	1.3365157944	1.2278303285
H	-6.9247596633	2.5318592052	0.4519943581
O	-6.7122221565	-0.5357170904	0.0667050970
O	0.4958534099	-1.7460687958	0.1333056079
H	2.0293836817	-1.8510221796	-1.2300892510
O	1.6506622935	0.3660592463	1.2189172586
H	3.2558893597	-0.6471091319	0.4418836240
C	4.0948526675	1.0018561983	-1.3814829452
H	2.3978478711	1.9416651648	-0.4269096309
O	5.0241069459	0.8112263334	-0.3261627700
H	4.2900386568	1.9529842511	-1.8861779166
H	4.2644369378	0.1761200874	-2.0745807028
C	0.1906713940	-3.0266403610	-0.1519831864
C	-0.8350406914	-3.5484374542	0.8148001831
H	-1.5654836013	-4.1448339223	0.2758578596
H	-1.3174418577	-2.7262239598	1.3328344380
H	-0.3374121833	-4.1910637530	1.5387416540
O	0.7002260843	-3.6536520666	-1.0373028095
C	2.2730522016	0.3560175029	2.4025701836
C	1.4303696137	1.0335898496	3.4448058719
H	0.3824134351	0.9817041622	3.1680113029
H	1.7336556612	2.0782768923	3.4938501298
H	1.6039660103	0.5772073959	4.4148226487
O	3.3646925528	-0.1144152946	2.5885607017
C	5.0630756528	1.7282151148	0.6574675606
C	6.0607120699	1.3389107998	1.7056631530

Table A.27: Cartesian coordinates of GFN2-xTB conformer 6/13 of **368a** (Scheme 4.16), continued.

atom	x	y	z
H	6.4061626699	2.2209043114	2.2357151535
H	6.8888378663	0.7993811145	1.2578200750
H	5.5509426134	0.6790733922	2.4075481087
O	4.3646635518	2.7070689695	0.6788536355

Table A.28: Cartesian coordinates of GFN2-xTB conformer 7/13 of **368a** (Scheme 4.16).

atom	x	y	z
O	1.2909344733	1.5602701008	-0.6841946441
C	2.6093429498	1.1778096306	-0.3571679727
C	2.5328036987	-0.2037021111	0.3361204986
C	1.0259181553	-0.4901715504	0.4252165652
C	0.4691021224	0.4092797878	-0.7078904603
C	-0.9586800919	0.7640826697	-0.5068616897
H	0.5727057077	-0.1368126875	-1.6597779663
N	-1.9424700896	-0.0057730958	-1.0233776465
C	-1.5469115285	1.7601310098	0.2521839981
C	-2.9303937604	1.5944629265	0.1881677017
C	-3.1751994413	0.4814023334	-0.6060595526
H	-1.0114937480	2.5249385187	0.7781432501
H	-3.6602626121	2.2169249924	0.6690358138
N	-1.7627981329	-1.0681966080	-1.7992323377
C	-2.8361912856	-1.6906418723	-2.1839457614
C	-4.3304574200	-0.2157171211	-1.0385207509
C	-4.1500307717	-1.3199017289	-1.8396567570
H	-2.6607720187	-2.5502616788	-2.8123597894
H	-4.9879789618	-1.8913834095	-2.1947904635
N	-5.5599579746	0.2681588086	-0.6173170038
C	-6.8117743392	-0.2016773262	-0.9288000948
H	-5.5065771533	1.0696085576	-0.0047491166
C	-7.9023670271	0.6008142260	-0.2533758805
H	-8.8695330398	0.1967980911	-0.5370139428
H	-7.8464368479	1.6437507699	-0.5583993801

Table A.28: Cartesian coordinates of GFN2-xTB conformer 7/13 of **368a** (Scheme 4.16), continued.

atom	x	y	z
H	-7.7941106729	0.5440377389	0.8278135615
O	-7.0219963680	-1.1400045006	-1.6562495877
O	0.5515808597	-0.0627981776	1.6900174260
H	0.7623750606	-1.5413956566	0.2746201621
O	3.1330288998	-0.1469165737	1.6152326818
H	3.0341147753	-0.9769056481	-0.2597988434
C	3.4672928180	1.1544519435	-1.6398183454
H	3.0107983829	1.9136907547	0.3473819445
O	4.6259486113	0.3369395320	-1.5724982864
H	3.7557814161	2.1813053500	-1.8860368759
H	2.8768993794	0.7372447339	-2.4584467424
C	-0.5995446936	-0.5881204182	2.1282276278
C	-1.0021007024	0.0429221230	3.4330791661
H	-0.1371491636	0.4843093410	3.9168933623
H	-1.4693507252	-0.7013003008	4.0714539538
H	-1.7303200409	0.8236665553	3.2220767167
O	-1.2139015308	-1.4468971041	1.5528181557
C	4.2133169564	-0.9024561892	1.8482585808
C	4.7967145398	-0.5845717777	3.1930708131
H	5.4467668265	0.2808381561	3.0716105249
H	5.3844403182	-1.4237686578	3.5522628340
H	4.0080664808	-0.3296410643	3.8936047874
O	4.6557329379	-1.7040331774	1.0673811270
C	5.5647912854	0.6268031101	-0.6574388449
C	6.7296618419	-0.3103922341	-0.7792242716
H	6.4676874039	-1.2338251873	-0.2642357076
H	7.6052936469	0.1260804621	-0.3090234560
H	6.9194531753	-0.5388022197	-1.8232095676
O	5.4567001773	1.5133865881	0.1486343894

Table A.29: Cartesian coordinates of GFN2-xTB conformer 8/13 of **368a** (Scheme 4.16).

atom	x	y	z
O	1.6794769559	0.9012307585	-2.0449163341
C	2.5504197993	0.9421364512	-0.9250962153
C	2.2655695292	-0.3058752596	-0.0677250204
C	1.2876609741	-1.1206649300	-0.9367316829
C	0.6459796664	-0.0308574283	-1.8234824699
C	-0.5591903299	0.5501898931	-1.1510355125
H	0.3433867682	-0.4332810863	-2.7959578501
N	-1.7637477096	-0.0482099471	-1.2877985598
C	-0.7201167624	1.6414187391	-0.3164417299
C	-2.0611567810	1.7094517685	0.0627797054
C	-2.7144946000	0.6456657441	-0.5435181726
H	0.0512736440	2.3239583459	-0.0226687632
H	-2.4931662011	2.4520613857	0.7054565273
N	-2.0109171825	-1.1303967289	-2.0178965629
C	-3.2355696952	-1.5642055785	-2.0150949610
C	-4.0427897945	0.1536081875	-0.5598169042
C	-4.2998043971	-0.9747972444	-1.3051006950
H	-3.4060768775	-2.4435326123	-2.6174547536
H	-5.2868091563	-1.3969420286	-1.3530933065
N	-4.9879238577	0.8510501479	0.1783600104
C	-6.3222934512	0.5689245915	0.3357868880
H	-4.6307022868	1.6726895465	0.6452046324
C	-7.0191608723	1.5901068055	1.2075551315
H	-6.9396624323	2.5800028624	0.7629269592
H	-6.5666692709	1.6118373534	2.1968684608
H	-8.0676399647	1.3232793779	1.3001081912
O	-6.8758347135	-0.3814502816	-0.1588511664
O	0.3018917178	-1.7977648729	-0.1887893672
H	1.8561539222	-1.8397960820	-1.5385022761
O	1.6145886411	0.0578892499	1.1420780795
H	3.1771582788	-0.8617981960	0.1762099754
C	3.9926067705	0.9956814307	-1.4510796515
H	2.3544407212	1.8399329481	-0.3248486454
O	4.9657723433	0.7486010728	-0.4509031558

Table A.29: Cartesian coordinates of GFN2-xTB conformer 8/13 of **368a** (Scheme 4.16), continued.

atom	x	y	z
H	4.1595802672	1.9786439446	-1.9032102621
H	4.1371334775	0.2162914323	-2.2013485963
C	0.7076480159	-2.8695277448	0.5118430046
C	-0.4423689527	-3.4637599830	1.2761074221
H	-1.3606179354	-3.3515266131	0.7075668481
H	-0.5474601904	-2.9280799237	2.2177581201
H	-0.2406475508	-4.5094287450	1.4873376379
O	1.8385161813	-3.2714666619	0.5131686139
C	2.3366857353	0.0716380582	2.2700416179
C	1.4965115556	0.5417979330	3.4247137217
H	1.7817420178	1.5665835333	3.6561514129
H	1.6988773309	-0.0724982046	4.2978208897
H	0.4443459976	0.5102596328	3.1605708391
O	3.4955110285	-0.2372592262	2.3342279113
C	5.0684293432	1.6278172562	0.5618235711
C	6.1394811294	1.2091189902	1.5220049103
H	5.6942469091	0.4908561784	2.2088985587
H	6.4913528102	2.0693201910	2.0827519874
H	6.9530477497	0.7254146932	0.9912533730
O	4.3742814240	2.6051926369	0.6617570843

Table A.30: Cartesian coordinates of GFN2-xTB conformer 9/13 of **368a** (Scheme 4.16).

atom	x	y	z
O	1.3522959484	0.3960337831	-1.9844996518
C	2.2607104825	0.7696798994	-0.9668378891
C	2.4049690891	-0.4435421218	-0.0218490568
C	1.3436909526	-1.4455814599	-0.5405241583
C	0.4699237332	-0.5946035760	-1.4869764224
C	-0.7303475597	-0.0304902878	-0.7952152238
H	0.1166604136	-1.1637299774	-2.3521140508
N	-1.9718840741	-0.2435654925	-1.2926532551
C	-0.8614256822	0.7474863970	0.3435208820

Table A.30: Cartesian coordinates of GFN2-xTB conformer 9/13 of **368a** (Scheme 4.16), continued.

atom	x	y	z
C	-2.2152680876	1.0153825543	0.5403383981
C	-2.9111055646	0.3931387008	-0.4875023955
H	-0.0572293710	1.0735361046	0.9716151775
H	-2.6295689137	1.5969389166	1.3411825886
N	-2.2617694550	-0.9598603016	-2.3733470179
C	-3.5182607199	-1.0538801556	-2.6902311352
C	-4.2746289971	0.2798041485	-0.8558916045
C	-4.5767831508	-0.4583549291	-1.9776179581
H	-3.7197229352	-1.6416315181	-3.5726701195
H	-5.5924227137	-0.5811405135	-2.3062863417
N	-5.2040676289	0.9256003004	-0.0543251528
C	-6.5704046177	0.9529395415	-0.1877230520
H	-4.8047029861	1.4396244444	0.7182861651
C	-7.2285691398	1.7842612145	0.8912790921
H	-8.3045897647	1.7689237394	0.7464289158
H	-6.8753941700	2.8121915203	0.8402081103
H	-6.9936087985	1.3802361685	1.8738767382
O	-7.1767031699	0.3818104940	-1.0595848336
O	0.5527368164	-1.9989665845	0.4903277092
H	1.8487655695	-2.2505523621	-1.0869316648
O	2.1012437634	-0.0679984855	1.3119486107
H	3.4129406887	-0.8716961964	-0.0422429262
C	3.5648753988	1.1861296311	-1.6606351445
H	1.8632702147	1.6124282240	-0.3851884247
O	4.7128747029	1.1868276865	-0.8283943167
H	3.4234261561	2.1809859967	-2.0955584234
H	3.7856294620	0.4702661997	-2.4549053305
C	1.1697159568	-2.8470091261	1.3304897646
C	0.2168416430	-3.3280595664	2.3899100422
H	-0.5712443226	-2.5974329751	2.5414008155
H	0.7600024886	-3.5154653933	3.3115915374
H	-0.2276981971	-4.2636757878	2.0556039259
O	2.3180748020	-3.1764137745	1.2172324195

Table A.30: Cartesian coordinates of GFN2-xTB conformer 9/13 of **368a** (Scheme 4.16), continued.

atom	x	y	z
C	3.0951736243	-0.0395459818	2.2118084441
C	2.5855812690	0.4560046894	3.5354536532
H	3.1995506393	0.0584617131	4.3378217921
H	1.5440840536	0.1803172744	3.6682425699
H	2.6663393703	1.5422167054	3.5346401286
O	4.2317812303	-0.3418401579	1.9732875196
C	4.7297971169	1.9784290451	0.2547088518
C	6.0528163256	1.8880790331	0.9553634951
H	6.0422379633	0.9848603827	1.5634856311
H	6.1905260864	2.7526401726	1.5971947793
H	6.8557360624	1.8071109479	0.2296042219
O	3.7962896137	2.6543704346	0.6025217756

Table A.31: Cartesian coordinates of GFN2-xTB conformer 10/13 of **368a** (Scheme 4.16).

atom	x	y	z
O	1.3173703027	0.3244638732	-1.9755982619
C	2.2161883239	0.7361380422	-0.9646715323
C	2.4094879845	-0.4694641015	-0.0180855787
C	1.3572117136	-1.4962834013	-0.5081357534
C	0.4563804338	-0.6739823233	-1.4542034162
C	-0.7430813619	-0.1137680067	-0.7584874312
H	0.1027249213	-1.2581212004	-2.3089612156
N	-1.9803677371	-0.2764956551	-1.2850310073
C	-0.8749048573	0.6290014305	0.4035273631
C	-2.2247508540	0.9255848070	0.5857779445
C	-2.9172898905	0.3578756791	-0.4754178662
H	-0.0734793696	0.9122215142	1.0555504458
H	-2.6387303916	1.4903477492	1.3987142149
N	-2.2685928673	-0.9476087131	-2.3945972611
C	-3.5206659107	-0.9953298777	-2.7380536662
C	-4.2758239281	0.2965871555	-0.8734923049
C	-4.5759848854	-0.3937514056	-2.0257780195

Table A.31: Cartesian coordinates of GFN2-xTB conformer 10/13 of **368a** (Scheme 4.16), continued.

atom	x	y	z
H	-3.7209551614	-1.5473980581	-3.6434906439
H	-5.5877717161	-0.4750590260	-2.3783250930
N	-5.2027988298	0.9416629664	-0.0684570392
C	-6.5636063372	1.0216952590	-0.2333123432
H	-4.8055339495	1.4139438379	0.7314033449
C	-7.2203239203	1.8347122637	0.8604551946
H	-8.2918290328	1.8650590100	0.6872249988
H	-6.8289159621	2.8499881759	0.8598113995
H	-7.0272188546	1.3840736551	1.8318283033
O	-7.1668936881	0.5053057672	-1.1406800415
O	0.5922200639	-2.0495390643	0.5420332227
H	1.8679778466	-2.2997210813	-1.0515299302
O	2.1292740648	-0.0952399703	1.3210845992
H	3.4255678451	-0.8760938797	-0.0612353306
C	3.4975023453	1.2010039640	-1.6692863533
H	1.7891072900	1.5633257748	-0.3813430940
O	4.6536087442	1.2474102741	-0.8496625049
H	3.3138481830	2.1891116994	-2.1039507899
H	3.7375608730	0.4930850627	-2.4651145504
C	1.2383865743	-2.8723854428	1.3853440470
C	0.3122114722	-3.3519952483	2.4688732612
H	-0.1612605913	-4.2738030476	2.1360080737
H	-0.4577484130	-2.6101441589	2.6554868548
H	0.8815740224	-3.5613902697	3.3696568090
O	2.3902600928	-3.1838721643	1.2579043571
C	3.1437511586	-0.0356914607	2.1961883927
C	2.6535068582	0.4550373528	3.5289371720
H	1.6293056231	0.1368314360	3.6970994687
H	2.6865567144	1.5436446052	3.5119955022
H	3.3076563086	0.0944590391	4.3168178266
O	4.2816490806	-0.3099451821	1.9316475936
C	4.6516993446	2.0372361918	0.2344178634
C	5.9886632374	2.0063977380	0.9138108084

Table A.31: Cartesian coordinates of GFN2-xTB conformer 10/13 of **368a** (Scheme 4.16), continued.

atom	x	y	z
H	6.0956927462	2.8739873207	1.5574130574
H	6.7825794006	1.9668712056	0.1748012305
H	6.0311724641	1.1010788394	1.5172570939
O	3.6945845835	2.6704426067	0.5984283792

Table A.32: Cartesian coordinates of GFN2-xTB conformer 11/13 of **368a** (Scheme 4.16).

atom	x	y	z
O	1.4781808223	0.1813186289	-1.8717394648
C	2.3488485708	0.7733192131	-0.9330046305
C	2.6107437738	-0.2850531615	0.1622777960
C	1.6066891396	-1.4126035372	-0.1581088699
C	0.6641181751	-0.7787031549	-1.2149326314
C	-0.5689456155	-0.2001654742	-0.6020499385
H	0.3508437185	-1.4975583743	-1.9777942099
N	-1.7838704185	-0.4208791999	-1.1598903430
C	-0.7592780741	0.5745899133	0.5308147584
C	-2.1238083307	0.8301772404	0.6637560540
C	-2.7645177752	0.2044894973	-0.3979998780
H	0.0159665484	0.9049687280	1.1930306045
H	-2.5810150648	1.4056378930	1.4456413923
N	-2.0127941842	-1.1277011597	-2.2585649225
C	-3.2508022269	-1.2396721918	-2.6318755079
C	-4.1082940114	0.0797077697	-0.8313085088
C	-4.3491267450	-0.6606786517	-1.9653243483
H	-3.4032743419	-1.8233442238	-3.5264332085
H	-5.3469834923	-0.7933586440	-2.3414311145
N	-5.0807986455	0.7196924433	-0.0759373318
C	-6.4366685380	0.7542323023	-0.2878287676
H	-4.7241928295	1.2323067873	0.7181630238
C	-7.1527159507	1.5825740837	0.7565850425
H	-8.2189878258	1.5692868314	0.5518173961
H	-6.7961418948	2.6102557785	0.7284548431

Table A.32: Cartesian coordinates of GFN2-xTB conformer 11/13 of **368a** (Scheme 4.16), continued.

atom	x	y	z
H	-6.9733746224	1.1750244331	1.7493793181
O	-6.9947528083	0.1915253419	-1.1965592403
O	0.9588468222	-1.8207252302	1.0306427058
H	2.1207954772	-2.2717935166	-0.6040545509
O	2.3456905725	0.2839916499	1.4327055545
H	3.6432954162	-0.6510122298	0.1502346859
C	3.6081518388	1.2183346094	-1.6919819985
H	1.8723064109	1.6388316713	-0.4513212694
O	4.7862544654	1.2795264440	-0.9028530163
H	3.4208101731	2.1946686252	-2.1493716826
H	3.8222741297	0.4848560399	-2.4716189727
C	0.0344360913	-2.7877551389	0.9169629519
C	-0.6191754414	-3.0450932353	2.2465315703
H	-1.3077498985	-2.2284018102	2.4543724129
H	0.1314986237	-3.0689103929	3.0309228682
H	-1.1682148927	-3.9806793228	2.2105203607
O	-0.2207972895	-3.3493762167	-0.1122531660
C	3.3298548989	0.3196975381	2.3374702578
C	2.8912397290	1.0751581751	3.5581457072
H	1.8601674368	0.8341305933	3.7976660903
H	2.9557851672	2.1377596974	3.3284355768
H	3.5473729097	0.8468055289	4.3921801713
O	4.4185558180	-0.1643362784	2.1708379474
C	4.8188227560	2.1199431083	0.1429585831
C	6.1558118566	2.0678149588	0.8218677312
H	6.1507775569	1.2152862142	1.5002334006
H	6.3161906923	2.9769396169	1.3930493409
H	6.9429629825	1.9223097890	0.0890128227
O	3.8854317275	2.7996236042	0.4819158371

Table A.33: Cartesian coordinates of GFN2-xTB conformer 12/13 of **368a** (Scheme 4.16).

atom	x	y	z
O	1.6690905819	0.8858435904	-2.0453969902
C	2.5445273928	0.9403376254	-0.9298524171
C	2.2736779912	-0.3050016745	-0.0638860360
C	1.2880112598	-1.1275664995	-0.9174235096
C	0.6392357622	-0.0470322197	-1.8103512261
C	-0.5652671063	0.5356233840	-1.1383040055
H	0.3327498985	-0.4583752487	-2.7778443740
N	-1.7727504690	-0.0542867283	-1.2870951374
C	-0.7242237645	1.6197814994	-0.2940830406
C	-2.0669294869	1.6925140180	0.0782368878
C	-2.7233800164	0.6386446834	-0.5419171527
H	0.0495584658	2.2943212542	0.0114803181
H	-2.4979590964	2.4316060765	0.7256116466
N	-2.0224688968	-1.1282580537	-2.0284481722
C	-3.2497399222	-1.5543033448	-2.0363736441
C	-4.0547920808	0.1555534638	-0.5706785003
C	-4.3144940787	-0.9644061600	-1.3275257015
H	-3.4225270785	-2.4267884561	-2.6478608140
H	-5.3038914484	-1.3796784277	-1.3851167111
N	-4.9996136242	0.8532818309	0.1677759719
C	-6.3368584828	0.5792367037	0.3147391114
H	-4.6398040301	1.6692323249	0.6425522433
C	-7.0321910949	1.5994348157	1.1889177660
H	-8.0830424357	1.3393224135	1.2732485339
H	-6.9430766362	2.5916084452	0.7512419866
H	-6.5857373085	1.6116561212	2.1811347688
O	-6.8935627480	-0.3640622061	-0.1897545783
O	0.3078422556	-1.7950562968	-0.1532056758
H	1.8509386714	-1.8536378212	-1.5159895128
O	1.6373031124	0.0622457576	1.1522448786
H	3.1896202104	-0.8576223832	0.1712346599
C	3.9836458352	1.0032352102	-1.4632018930
H	2.3436647977	1.8395714135	-0.3334035070
O	4.9643402647	0.7620598267	-0.4689265324

Table A.33: Cartesian coordinates of GFN2-xTB conformer 12/13 of **368a** (Scheme 4.16), continued.

atom	x	y	z
H	4.1422050676	1.9872032526	-1.9161853412
H	4.1288170130	0.2248975976	-2.2144477180
C	0.7182003002	-2.8629627510	0.5508398253
C	-0.4352154875	-3.4815736116	1.2899976331
H	-0.0687351452	-4.0217957251	2.1576445922
H	-0.9330502685	-4.1834594621	0.6233515332
H	-1.1471887284	-2.7148427555	1.5790951954
O	1.8512343338	-3.2587783191	0.5545810602
C	2.3693504059	0.0661018495	2.2740917900
C	1.5432493387	0.5402931118	3.4368346190
H	1.7861945521	-0.0431187957	4.3203662877
H	0.4865453511	0.4689744090	3.2001938064
H	1.7998144942	1.5802153209	3.6321238285
O	3.5265784771	-0.2508391001	2.3264855464
C	5.0647607420	1.6386342592	0.5461811928
C	6.1460464143	1.2269832982	1.4979771821
H	5.7171203748	0.4898414602	2.1751961049
H	6.4824442840	2.0857864700	2.0702227660
H	6.9677214177	0.7674218214	0.9582664694
O	4.3613421403	2.6084856721	0.6545455822

Table A.34: Cartesian coordinates of GFN2-xTB conformer 13/13 of **368a** (Scheme 4.16).

atom	x	y	z
O	1.4854858880	0.1869017399	-1.8749421924
C	2.3569708695	0.7744688103	-0.9342423627
C	2.6110733109	-0.2852421058	0.1615258960
C	1.6029403273	-1.4084550731	-0.1611844443
C	0.6661133387	-0.7701930438	-1.2206963377
C	-0.5666775419	-0.1884974259	-0.6101906710
H	0.3521353659	-1.4877741698	-1.9844614419
N	-1.7822695430	-0.4147868041	-1.1643261955
C	-0.7564807213	0.5907816579	0.5196630665

Table A.34: Cartesian coordinates of GFN2-xTB conformer 13/13 of **368a** (Scheme 4.16), continued.

atom	x	y	z
C	-2.1213948025	0.8431864203	0.6546826519
C	-2.7628738024	0.2109439732	-0.4027164862
H	0.0193064124	0.9259618246	1.1788372738
H	-2.5783276169	1.4210148033	1.4349797226
N	-2.0117441163	-1.1268303034	-2.2594973944
C	-3.2503665577	-1.2445789113	-2.6289440681
C	-4.1075001723	0.0788107295	-0.8311465132
C	-4.3488965962	-0.6670772176	-1.9614212955
H	-3.4032550413	-1.8323664969	-3.5207305617
H	-5.3474279076	-0.8056713274	-2.3335889626
N	-5.0803383755	0.7164857522	-0.0742512024
C	-6.4376129075	0.7398720423	-0.2784869059
H	-4.7233104334	1.2336586111	0.7166864209
C	-7.1542040581	1.5646796678	0.7683642672
H	-6.9734738131	1.1538303858	1.7595741472
H	-8.2206351787	1.5499333945	0.5645617638
H	-6.7994117562	2.5930234352	0.7437097148
O	-6.9963668999	0.1711210534	-1.1830069237
O	0.9498555889	-1.8126561787	1.0260622272
H	2.1142797097	-2.2702661530	-0.6052393284
O	2.3456609603	0.2850438692	1.4313255329
H	3.6419723637	-0.6558740226	0.1519697702
C	3.6206311584	1.2129760507	-1.6898023056
H	1.8838006358	1.6425183997	-0.4538432559
O	4.7959225900	1.2699880113	-0.8961829433
H	3.4391762462	2.1895062798	-2.1491387455
H	3.8344065065	0.4774921694	-2.4676434972
C	0.0188873577	-2.7731408347	0.9103495295
C	-0.6398292045	-3.0251191665	2.2384439335
H	-1.2094626316	-3.9480194556	2.1961174661
H	-1.3090830079	-2.1943928608	2.4533768346
H	0.1108626487	-3.0719736808	3.0218609143
O	-0.2375805530	-3.3336504494	-0.1191507984

Table A.34: Cartesian coordinates of GFN2-xTB conformer 13/13 of **368a** (Scheme 4.16), continued.

atom	x	y	z
C	3.3273814300	0.3144473218	2.3389652395
C	2.8895279237	1.0712399570	3.5590973677
H	3.5430565712	0.8397041289	4.3943039266
H	1.8569992103	0.8343382160	3.7964688839
H	2.9588465488	2.1336992335	3.3301541708
O	4.4138653657	-0.1754519888	2.1750021788
C	4.8282649488	2.1123974127	0.1480999033
C	6.1618194993	2.0542551020	0.8332697970
H	6.1533466161	1.1963936828	1.5048278318
H	6.3199174299	2.9589745958	1.4120058730
H	6.9524559230	1.9140570803	0.1030930457
O	3.8969905133	2.7976541040	0.4814963718

Table A.35: Cartesian coordinates of GFN2-xTB conformer 1/8 of **368b** (Scheme 4.16).

atom	x	y	z
O	-1.6085170513	-1.5148091529	-2.0305591034
C	-1.8321260742	-0.1284332890	-1.8967044710
C	-1.9810169444	0.1574459412	-0.3871983015
C	-1.9430781626	-1.2454215610	0.2576529227
C	-1.1474422321	-2.0348190342	-0.7802472931
C	0.3446225954	-1.9203612526	-0.6643031429
H	-1.4388022307	-3.0902131665	-0.7827918526
N	1.0473322763	-1.0909698635	0.1481267006
C	1.2576658372	-2.5823308217	-1.4737723120
C	2.5388797711	-2.1469756368	-1.1504449868
C	2.4037738042	-1.2101973939	-0.1341226920
H	0.9960727341	-3.2991536080	-2.2267018065
H	3.4506253965	-2.4798300563	-1.6067852023
N	0.5523162663	-0.2912578619	1.0885843641
C	1.3978106579	0.4328421222	1.7584978107
C	3.3063408226	-0.4031995955	0.6013205938
C	2.7892543914	0.4280247113	1.5673570483

Table A.35: Cartesian coordinates of GFN2-xTB conformer 1/8 of **368b** (Scheme 4.16), continued.

atom	x	y	z
H	0.9444239972	1.0731680389	2.4995902568
H	3.4243806117	1.0673508925	2.1522740384
N	4.6511140292	-0.5102252585	0.2849775432
C	5.7175335511	0.1158371612	0.8797883524
H	4.8490512152	-1.1101505610	-0.5032287000
C	7.0263847779	-0.2307277235	0.2031004204
H	7.0042920028	0.0862839615	-0.8374886350
H	7.1972343702	-1.3046465761	0.2403886683
H	7.8379583100	0.2782233895	0.7144279059
O	5.6303503520	0.8480200618	1.8339978205
O	-3.2472452714	-1.8062682858	0.3290937590
H	-1.4940420922	-1.2161876211	1.2528373349
O	-3.1929785746	0.8268235187	-0.0994188469
H	-1.1463893420	0.7471695965	0.0067260800
C	-0.6711200734	0.6541805808	-2.5453639676
H	-2.7732656131	0.1099352787	-2.4051477556
O	-0.6193260557	1.9942344293	-2.0839654043
H	-0.8033979232	0.6768882775	-3.6296526556
H	0.2742710036	0.1543623783	-2.3079556003
C	-4.0203025366	-1.4398687972	1.3594718980
C	-5.3986417783	-2.0271899091	1.2134995300
H	-5.9713626018	-1.3946975873	0.5380569399
H	-5.8918472697	-2.0542213552	2.1803536202
H	-5.3359323608	-3.0215538009	0.7826250262
O	-3.6563179241	-0.7440884158	2.2692298228
C	-3.1340850276	1.9439347831	0.6451517750
C	-4.5152800026	2.3900225174	1.0248869195
H	-4.5047892999	3.4389146245	1.3040157872
H	-4.8213783354	1.7932345879	1.8834248384
H	-5.2096091442	2.2097472150	0.2099785457
O	-2.1124344009	2.4916478683	0.9589308345
C	0.4373918303	2.3505748122	-1.3285411674
C	0.2694254904	3.7406608509	-0.8010462304
H	-0.1722783147	4.3811495187	-1.5581603681

Table A.35: Cartesian coordinates of GFN2-xTB conformer 1/8 of **368b** (Scheme 4.16), continued.

atom	x	y	z
H	1.2258576635	4.1297205215	-0.4669004384
H	-0.4154874712	3.6853147992	0.0454577806
O	1.3724765379	1.6242386251	-1.1116154895

Table A.36: Cartesian coordinates of GFN2-xTB conformer 2/8 of **368b** (Scheme 4.16).

atom	x	y	z
O	-1.6058520801	-1.5072574805	-2.0337362230
C	-1.8340707028	-0.1218710543	-1.8996098767
C	-1.9872640200	0.1633189569	-0.3902593126
C	-1.9334802889	-1.2382078201	0.2567631844
C	-1.1403155591	-2.0256448606	-0.7847134967
C	0.3519234017	-1.9119496803	-0.6717120278
H	-1.4305022434	-3.0814358238	-0.7857760452
N	1.0567853309	-1.0799738461	0.1362956807
C	1.2634063000	-2.5842674564	-1.4742473801
C	2.5461610224	-2.1541001524	-1.1501014255
C	2.4134477126	-1.2099923402	-0.1402456422
H	0.9999768143	-3.3049783061	-2.2227886782
H	3.4572931089	-2.4951567933	-1.6015892887
N	0.5635496055	-0.2694589609	1.0684070781
C	1.4114659103	0.4534714296	1.7363683813
C	3.3193420076	-0.4083005039	0.5970040045
C	2.8040778488	0.4345927368	1.5537452591
H	0.9598384945	1.1031139085	2.4703624695
H	3.4417084107	1.0706180507	2.1395427099
N	4.6655691267	-0.5347698920	0.2935940906
C	5.7357335800	0.0705286479	0.9031031846
H	4.8629085501	-1.1411752767	-0.4897843317
C	7.0467908577	-0.3019260478	0.2447271649
H	7.1899320089	-1.3801360608	0.2709726185
H	7.8622113204	0.1802819020	0.7754770964
H	7.0502072851	0.0284498929	-0.7919194004
O	5.6493883932	0.8052527460	1.8553718908

Table A.36: Cartesian coordinates of GFN2-xTB conformer 2/8 of **368b** (Scheme 4.16), continued.

atom	x	y	z
O	-3.2322485879	-1.8093586544	0.3421694095
H	-1.4760661599	-1.2029007406	1.2479849785
O	-3.2080060950	0.8176821464	-0.1044658204
H	-1.1601065955	0.7637821090	0.0032397146
C	-0.6742631448	0.6648074935	-2.5447941709
H	-2.7744691166	0.1139170322	-2.4106344144
O	-0.6407934496	2.0096732276	-2.0962180709
H	-0.7964298028	0.6749441647	-3.6305020056
H	0.2737595173	0.1770905132	-2.2933098194
C	-3.9979141316	-1.4460537497	1.3792283231
C	-5.3709392286	-2.0499508712	1.2524095256
H	-5.9584505220	-1.4292920381	0.5787198420
H	-5.8530893092	-2.0756005480	2.2248796896
H	-5.3013220334	-3.0467576722	0.8282449715
O	-3.6314213958	-0.7412714316	2.2809799724
C	-3.1641460939	1.9415998597	0.6306153890
C	-4.5512942087	2.3714078571	1.0078393787
H	-4.8441539807	1.7854584913	1.8783691748
H	-5.2455314275	2.1649423271	0.1991016093
H	-4.5573691568	3.4251618235	1.2682265766
O	-2.1501467789	2.5064329143	0.9386811900
C	0.4054888035	2.3847013710	-1.3351762261
C	0.2173231490	3.7780023638	-0.8230684573
H	-0.2283649128	4.4049666743	-1.5891115663
H	1.1668121136	4.1826902431	-0.4877518351
H	-0.4713640798	3.7223810865	0.0203359856
O	1.3463636298	1.6707079846	-1.1031467751

Table A.37: Cartesian coordinates of GFN2-xTB conformer 3/8 of **368b** (Scheme 4.16).

atom	x	y	z
O	-1.6058520801	-1.5072574805	-2.0337362230
C	-1.8340707028	-0.1218710543	-1.8996098767
C	-1.9872640200	0.1633189569	-0.3902593126

Table A.37: Cartesian coordinates of GFN2-xTB conformer 3/8 of **368b** (Scheme 4.16), continued.

atom	x	y	z
C	-1.9334802889	-1.2382078201	0.2567631844
C	-1.1403155591	-2.0256448606	-0.7847134967
C	0.3519234017	-1.9119496803	-0.6717120278
H	-1.4305022434	-3.0814358238	-0.7857760452
N	1.0567853309	-1.0799738461	0.1362956807
C	1.2634063000	-2.5842674564	-1.4742473801
C	2.5461610224	-2.1541001524	-1.1501014255
C	2.4134477126	-1.2099923402	-0.1402456422
H	0.9999768143	-3.3049783061	-2.2227886782
H	3.4572931089	-2.4951567933	-1.6015892887
N	0.5635496055	-0.2694589609	1.0684070781
C	1.4114659103	0.4534714296	1.7363683813
C	3.3193420076	-0.4083005039	0.5970040045
C	2.8040778488	0.4345927368	1.5537452591
H	0.9598384945	1.1031139085	2.4703624695
H	3.4417084107	1.0706180507	2.1395427099
N	4.6655691267	-0.5347698920	0.2935940906
C	5.7357335800	0.0705286479	0.9031031846
H	4.8629085501	-1.1411752767	-0.4897843317
C	7.0467908577	-0.3019260478	0.2447271649
H	7.1899320089	-1.3801360608	0.2709726185
H	7.8622113204	0.1802819020	0.7754770964
H	7.0502072851	0.0284498929	-0.7919194004
O	5.6493883932	0.8052527460	1.8553718908
O	-3.2322485879	-1.8093586544	0.3421694095
H	-1.4760661599	-1.2029007406	1.2479849785
O	-3.2080060950	0.8176821464	-0.1044658204
H	-1.1601065955	0.7637821090	0.0032397146
C	-0.6742631448	0.6648074935	-2.5447941709
H	-2.7744691166	0.1139170322	-2.4106344144
O	-0.6407934496	2.0096732276	-2.0962180709
H	-0.7964298028	0.6749441647	-3.6305020056
H	0.2737595173	0.1770905132	-2.2933098194
C	-3.9979141316	-1.4460537497	1.3792283231

Table A.37: Cartesian coordinates of GFN2-xTB conformer 3/8 of **368b** (Scheme 4.16), continued.

atom	x	y	z
C	-5.3709392286	-2.0499508712	1.2524095256
H	-5.9584505220	-1.4292920381	0.5787198420
H	-5.8530893092	-2.0756005480	2.2248796896
H	-5.3013220334	-3.0467576722	0.8282449715
O	-3.6314213958	-0.7412714316	2.2809799724
C	-3.1641460939	1.9415998597	0.6306153890
C	-4.5512942087	2.3714078571	1.0078393787
H	-4.8441539807	1.7854584913	1.8783691748
H	-5.2455314275	2.1649423271	0.1991016093
H	-4.5573691568	3.4251618235	1.2682265766
O	-2.1501467789	2.5064329143	0.9386811900
C	0.4054888035	2.3847013710	-1.3351762261
C	0.2173231490	3.7780023638	-0.8230684573
H	-0.2283649128	4.4049666743	-1.5891115663
H	1.1668121136	4.1826902431	-0.4877518351
H	-0.4713640798	3.7223810865	0.0203359856
O	1.3463636298	1.6707079846	-1.1031467751

Table A.38: Cartesian coordinates of GFN2-xTB conformer 4/8 of **368b** (Scheme 4.16).

atom	x	y	z
O	-0.4004280043	0.2359699810	-2.2074391369
C	-1.7168402370	0.7446776698	-2.2881101283
C	-2.1342169815	1.1724284203	-0.8615266504
C	-0.9235067008	0.7827286722	0.0032941589
C	-0.1862152397	-0.2421521794	-0.8968688990
C	1.2663705106	-0.3386964392	-0.5991228956
H	-0.6649293983	-1.2239991484	-0.7455456338
N	1.7372527404	-1.1941321508	0.3342763661
C	2.3353694318	0.3889679601	-1.0907957856
C	3.4907957764	-0.0401496874	-0.4401146214
C	3.1127712488	-1.0267457386	0.4605527924
H	2.2668344452	1.1396448909	-1.8518475925
H	4.4817448723	0.3341566402	-0.6089129836

Table A.38: Cartesian coordinates of GFN2-xTB conformer 4/8 of **368b** (Scheme 4.16), continued.

atom	x	y	z
N	1.0058116130	-2.0491978072	1.0421048588
C	1.6456859117	-2.7785352542	1.9078430091
C	3.7822373595	-1.8265609568	1.4178471883
C	3.0298906533	-2.7186231535	2.1488449560
H	1.0281808747	-3.4682884262	2.4636270989
H	3.4817100089	-3.3506212100	2.8911653258
N	5.1499950410	-1.6468678666	1.5508202254
C	6.0185388817	-2.3057804832	2.3850950283
H	5.5356565803	-0.9262898308	0.9569323229
C	7.4369438405	-1.8003038412	2.2397230844
H	7.4839873562	-0.7408569224	2.4829370966
H	7.7835870612	-1.9422585566	1.2181719686
H	8.0831755129	-2.3514789120	2.9162661818
O	5.6940309656	-3.1863299974	3.1426133793
O	-1.3339434588	0.2320167800	1.2349923257
H	-0.2730893546	1.6483475433	0.1812219506
O	-3.2796142996	0.4313264273	-0.4747166471
H	-2.3654936236	2.2410425761	-0.7920294109
C	-1.7178967279	1.8943705545	-3.3059421235
H	-2.4095996243	-0.0457132124	-2.6114376114
O	-2.7854646936	2.8140090913	-3.1396659095
H	-1.7438547700	1.4745302683	-4.3162627757
H	-0.8073784159	2.4823582960	-3.1767079844
C	-0.4645552436	0.2883347431	2.2576167169
C	-1.0216160636	-0.4271814150	3.4543592531
H	-0.4499868262	-0.1656714173	4.3391795800
H	-0.9423346263	-1.4969602868	3.2737318456
H	-2.0701900538	-0.1759947459	3.5829876895
O	0.6021169161	0.8376178062	2.2012585651
C	-4.4058534133	1.0980903961	-0.1988936202
C	-5.5315659377	0.1419205481	0.0654458298
H	-5.1564127923	-0.7519689327	0.5533236235
H	-5.9591102535	-0.1388729871	-0.8960171307
H	-6.2965240390	0.6249720741	0.6656477123

Table A.38: Cartesian coordinates of GFN2-xTB conformer 4/8 of **368b** (Scheme 4.16), continued.

atom	x	y	z
O	-4.4949248313	2.2983379811	-0.1930537364
C	-4.0455136069	2.3612913433	-3.2603312080
C	-5.0294224133	3.4740082876	-3.0556748295
H	-5.1939309586	3.5728788069	-1.9829850616
H	-5.9706204298	3.2289814494	-3.5378221754
H	-4.6262654015	4.4079979157	-3.4335218378
O	-4.3199244558	1.2117779680	-3.4833248831

Table A.39: Cartesian coordinates of GFN2-xTB conformer 5/8 of **368b** (Scheme 4.16).

atom	x	y	z
O	-1.6117055066	-1.4925995437	-2.0361304662
C	-1.8335016551	-0.1079031232	-1.8872167486
C	-1.9914042657	0.1613738715	-0.3745466664
C	-1.9435085630	-1.2467390441	0.2565817649
C	-1.1509030648	-2.0260064233	-0.7916942121
C	0.3415688863	-1.9171359139	-0.6750177398
H	-1.4442263576	-3.0807925676	-0.8047307069
N	1.0468555210	-1.0911938053	0.1389359578
C	1.2528759018	-2.5829784002	-1.4831761075
C	2.5356588275	-2.1540933237	-1.1572665804
C	2.4033243442	-1.2173554754	-0.1405205038
H	0.9893706108	-3.2983545512	-2.2368109864
H	3.4465898016	-2.4912836887	-1.6120516354
N	0.5540637923	-0.2891734451	1.0785283270
C	1.4019684863	0.4291193065	1.7514791013
C	3.3087922801	-0.4170314481	0.5988052977
C	2.7939740848	0.4159244097	1.5644870089
H	0.9505468105	1.0711831676	2.4922369043
H	3.4312946668	1.0503613293	2.1523116175
N	4.6539923826	-0.5325009928	0.2869134339
C	5.7221624007	0.0878503570	0.8846378611
H	4.8511236896	-1.1352576201	-0.4993286677
C	7.0314942001	-0.2687687456	0.2141019722

Table A.39: Cartesian coordinates of GFN2-xTB conformer 5/8 of **368b** (Scheme 4.16), continued.

atom	x	y	z
H	7.1970173647	-1.3432531582	0.2582621869
H	7.8437560679	0.2391380265	0.7253608400
H	7.0144419281	0.0422950416	-0.8283131430
O	5.6360869837	0.8221170077	1.8373102032
O	-3.2451935712	-1.8110936032	0.3359410618
H	-1.4869322800	-1.2240553254	1.2486347863
O	-3.2122498715	0.8186396135	-0.0918563690
H	-1.1652118408	0.7566074942	0.0288365969
C	-0.6681968110	0.6796601940	-2.5210667833
H	-2.7713347477	0.1377854333	-2.3984978661
O	-0.6259720328	2.0190890624	-2.0566691709
H	-0.7889529587	0.7032408131	-3.6068267307
H	0.2765357003	0.1830739149	-2.2748066172
C	-3.9855399968	-1.4897353228	1.4067239175
C	-5.3502266780	-2.1179216040	1.3054884383
H	-5.2563810108	-3.1903062876	1.4620565156
H	-5.7578366616	-1.9530048219	0.3124099025
H	-6.0037050379	-1.6987463787	2.0642759315
O	-3.5952494930	-0.8177504964	2.3221047486
C	-3.1658204080	1.9745628809	0.5871075389
C	-4.5524533391	2.4979077386	0.8342218336
H	-4.7900372554	3.2332710916	0.0674155768
H	-4.5835313160	2.9870617524	1.8033875268
H	-5.2723924397	1.6874745106	0.7909763116
O	-2.1497917496	2.5233142250	0.9182611390
C	0.4304618695	2.3818935426	-1.3035144832
C	0.2574075698	3.7730017611	-0.7802892395
H	-0.4415433682	3.7211290447	0.0546949237
H	-0.1700961548	4.4135073263	-1.5455980576
H	1.2096143084	4.1601625379	-0.4322679089
O	1.3690397680	1.6602699990	-1.0867143228

Table A.40: Cartesian coordinates of GFN2-xTB conformer 6/8 of **368b** (Scheme 4.16).

atom	x	y	z
O	-0.6079017768	-0.0672968299	-1.9711931478
C	-1.3896313577	1.0956485249	-1.7788415298
C	-2.2371056318	0.8846685183	-0.5140074198
C	-1.4507610113	-0.1956403393	0.2306746606
C	-0.8077273674	-1.0002441870	-0.9185691360
C	0.4719605149	-1.6514008821	-0.5282292851
H	-1.5188845629	-1.7753924970	-1.2465951442
N	1.5077167654	-0.9656694948	0.0073773532
C	0.8375527363	-2.9851322728	-0.5955599149
C	2.1267790291	-3.1154063995	-0.0849736240
C	2.5445988073	-1.8463591332	0.2933522974
H	0.2226106093	-3.7766516830	-0.9767601987
H	2.6809700347	-4.0301814846	-0.0030013478
N	1.5429205908	0.3423119720	0.2392729726
C	2.6332424298	0.8126302858	0.7690674547
C	3.7210679574	-1.3110573973	0.8725306705
C	3.7607580952	0.0444564850	1.1095350688
H	2.6277699372	1.8776136768	0.9468193623
H	4.6253784620	0.5085410484	1.5474433231
N	4.7472582076	-2.1969850566	1.1603270917
C	5.9806155636	-1.9253766608	1.6992831411
H	4.5391308689	-3.1617848340	0.9449349533
C	6.8119729107	-3.1776235036	1.8706460579
H	7.7735609645	-2.9113057453	2.2990525260
H	6.9700677592	-3.6582824729	0.9073736772
H	6.3056739777	-3.8762963486	2.5334830402
O	6.3608129466	-0.8209939025	1.9988390015
O	-2.2853602870	-0.9840854348	1.0559360562
H	-0.6628867995	0.2703546382	0.8343237435
O	-3.5339272956	0.4119035955	-0.8521992811
H	-2.3443484756	1.8063278670	0.0674705601
C	-0.4621544570	2.3163622977	-1.6374408774
H	-2.0424244647	1.2307692083	-2.6503744758
O	-1.1564916311	3.4564395066	-1.1530397793

Table A.40: Cartesian coordinates of GFN2-xTB conformer 6/8 of **368b** (Scheme 4.16), continued.

atom	x	y	z
H	-0.0146243079	2.5328698681	-2.6119490276
H	0.3170943872	2.0931532842	-0.9057501648
C	-1.7031623778	-1.6039407744	2.0955630880
C	-2.7091574780	-2.4274394462	2.8503343950
H	-3.7088473897	-2.0355895338	2.6936964353
H	-2.4554996968	-2.4357748660	3.9063042961
H	-2.6661789626	-3.4494552264	2.4781790685
O	-0.5364950243	-1.5079732020	2.3646961179
C	-4.5567188108	1.2666582623	-0.7192789124
C	-5.8388899460	0.6357197204	-1.1822146486
H	-5.9944115730	0.9078883902	-2.2248764951
H	-6.6697740236	1.0215054529	-0.5988691235
H	-5.7751320478	-0.4446683500	-1.1045524527
O	-4.4468182643	2.3883698722	-0.2987775589
C	-2.0914432055	3.9986215739	-1.9555162042
C	-2.8193520228	5.1041439587	-1.2516863066
H	-2.1600244498	5.6074225991	-0.5520686973
H	-3.6377005702	4.6452040007	-0.6969942349
H	-3.2299888375	5.8004543411	-1.9759509573
O	-2.3098147771	3.6118232163	-3.0724510841

Table A.41: Cartesian coordinates of GFN2-xTB conformer 7/8 of **368b** (Scheme 4.16).

atom	x	y	z
O	-1.3812294155	-0.7317213758	-2.2920349320
C	-2.5994557965	-0.0233916257	-2.4374996511
C	-3.0438974965	0.4203404553	-1.0385031211
C	-1.7261770338	0.3845509826	-0.2511837697
C	-0.9772956359	-0.7795460597	-0.9385768174
C	0.5021714589	-0.6645797676	-0.8106789042
H	-1.3151905373	-1.7189745795	-0.4685526083
N	1.1342715224	-1.0553717657	0.3186624408
C	1.4497792461	-0.1430631155	-1.6735277809
C	2.6942543088	-0.2172619790	-1.0482876468

Table A.41: Cartesian coordinates of GFN2-xTB conformer 7/8 of **368b** (Scheme 4.16), continued.

atom	x	y	z
C	2.4947736759	-0.7832983853	0.2031404578
H	1.2516152946	0.2309058582	-2.6574451347
H	3.6256023087	0.1074542001	-1.4696914785
N	0.5558229900	-1.6066809547	1.3817211918
C	1.3384429120	-1.9038547660	2.3766264495
C	3.3216597682	-1.1104672156	1.3047863044
C	2.7268094233	-1.6815762926	2.4074006099
H	0.8432488229	-2.3541813944	3.2237628238
H	3.3024080713	-1.9498999888	3.2741195447
N	4.6737234998	-0.8282232121	1.1892522835
C	5.6744995611	-1.0692206040	2.0974271854
H	4.9350586491	-0.3869515473	0.3187450224
C	7.0217752258	-0.6009072037	1.5934991789
H	6.9996949340	0.4705410492	1.4054118147
H	7.2768477835	-1.1148242345	0.6689965243
H	7.7774863354	-0.8167523134	2.3427915949
O	5.5043518946	-1.5940714899	3.1699109032
O	-1.9453653513	0.1569224518	1.1216677603
H	-1.1782015171	1.3241753175	-0.3875294502
O	-3.9613803010	-0.5231860883	-0.5093848810
H	-3.5012145103	1.4143343020	-1.0276013342
C	-2.3957251156	1.1780125475	-3.3741535649
H	-3.3478082241	-0.6943786739	-2.8785803368
O	-1.6577210147	2.1934052938	-2.7099656059
H	-3.3604973091	1.6043808611	-3.6586989487
H	-1.8423263932	0.8531691177	-4.2610879210
C	-1.0819130288	0.7218580555	1.9820498340
C	-1.4627525128	0.3865876036	3.3938027033
H	-2.4703784859	0.7491714168	3.5835365008
H	-0.7614504770	0.8452859263	4.0833682034
H	-1.4573156952	-0.6933534540	3.5135491203
O	-0.1540235305	1.4059036668	1.6429648196
C	-4.7453919475	-0.1036045844	0.5006747727
C	-5.5499965632	-1.2483832293	1.0485145460

Table A.41: Cartesian coordinates of GFN2-xTB conformer 7/8 of **368b** (Scheme 4.16), continued.

atom	x	y	z
H	-6.4169617299	-0.8684498164	1.5801650927
H	-4.9221327394	-1.8047634977	1.7417977536
H	-5.8487241749	-1.9141637108	0.2446963717
O	-4.7883287251	1.0313326538	0.8877625821
C	-0.3944550443	2.4273479478	-3.1137934816
C	0.2803318822	3.3937178151	-2.1825418966
H	1.0809672961	3.9099573796	-2.7033534058
H	0.7082811236	2.8287373483	-1.3545440206
H	-0.4413729869	4.0995249472	-1.7832520995
O	0.1053121184	1.9209474399	-4.0798816452

Table A.42: Cartesian coordinates of GFN2-xTB conformer 8/8 of **368b** (Scheme 4.16).

atom	x	y	z
O	-0.6181065124	-0.0661786211	-1.9721003973
C	-1.3917010036	1.1013352522	-1.7748473935
C	-2.2472145668	0.8848497406	-0.5165629387
C	-1.4564202036	-0.1893699078	0.2319559433
C	-0.8140708898	-0.9964370212	-0.9158437800
C	0.4663222824	-1.6470041505	-0.5266965767
H	-1.5252132692	-1.7728895429	-1.2407631794
N	1.5021384448	-0.9633544697	0.0114642333
C	0.8319832417	-2.9805131142	-0.5991180848
C	2.1212586041	-3.1127837453	-0.0893168324
C	2.5390280234	-1.8451878390	0.2938973119
H	0.2169258071	-3.7705029122	-0.9832961589
H	2.6754912081	-4.0278522532	-0.0109490772
N	1.5376165531	0.3435990602	0.2490035501
C	2.6279592624	0.8116152103	0.7808674844
C	3.7157322761	-1.3124131710	0.8748766171
C	3.7555230847	0.0420463531	1.1178123859
H	2.6225715742	1.8758637555	0.9629839799
H	4.6203257560	0.5042671117	1.5573327868
N	4.7420901513	-2.1996066464	1.1580679844

Table A.42: Cartesian coordinates of GFN2-xTB conformer 8/8 of **368b** (Scheme 4.16), continued.

atom	x	y	z
C	5.9762484921	-1.9303202693	1.6963937449
H	4.5337722770	-3.1634532006	0.9386303963
C	6.8077459600	-3.1833499239	1.8612575829
H	7.7719327502	-2.9182934935	2.2845856883
H	6.9598786815	-3.6633212215	0.8966922318
H	6.3046218190	-3.8821652746	2.5264031886
O	6.3568161518	-0.8272635609	2.0002934891
O	-2.2865594545	-0.9768369915	1.0629213751
H	-0.6684776075	0.2816582922	0.8316094701
O	-3.5372246689	0.3990312868	-0.8625928949
H	-2.3656643154	1.8065505510	0.0625032250
C	-0.4580481960	2.3153951538	-1.6161201997
H	-2.0373061273	1.2488968873	-2.6496287904
O	-1.1551367332	3.4552175910	-1.1356383832
H	0.0019253992	2.5342372441	-2.5842850574
H	0.3112456067	2.0850869440	-0.8762090764
C	-1.6981199735	-1.5957850939	2.0995000196
C	-2.6986168063	-2.4198505118	2.8611003553
H	-2.4688416474	-2.3831714683	3.9220913997
H	-2.6175809287	-3.4533033604	2.5291391477
H	-3.7047654971	-2.0620129421	2.6691806732
O	-0.5302020377	-1.4983075183	2.3626055149
C	-4.5682398884	1.2460351647	-0.7438774058
C	-5.8528346565	0.5755698008	-1.1414794243
H	-5.6739551366	-0.1171240933	-1.9577771446
H	-6.5849688701	1.3260607105	-1.4235153192
H	-6.2306834792	0.0158529558	-0.2878771753
O	-4.4665391187	2.3804578931	-0.3572261612
C	-2.0591930622	4.0174607598	-1.9602412205
C	-2.8054578745	5.1138509352	-1.2613739471
H	-3.6390888668	4.6479578691	-0.7360275647
H	-3.1949708000	5.8210262544	-1.9867372140
H	-2.1654666600	5.6062605788	-0.5364588788
O	-2.2395415956	3.6523803642	-3.0909060458

EIDESSTATTLICHE ERKLÄRUNG

Ich versichere, dass ich die von mir vorgelegte Dissertation selbstständig angefertigt, die benutzten Quellen und Hilfsmittel vollständig angegeben und die Stellen der Arbeit – einschließlich Tabellen, Karten und Abbildungen –, die anderen Werken im Wortlaut oder dem Sinn nach entnommen sind, in jedem Einzelfall als Entlehnung kenntlich gemacht habe; dass diese Dissertation noch keiner anderen Fakultät oder Universität zur Prüfung vorgelegen hat; dass sie – abgesehen von unten angegebenen Teilpublikationen – noch nicht veröffentlicht worden ist, sowie, dass ich eine solche Veröffentlichung vor Abschluss des Promotionsverfahrens nicht vornehmen werde. Die Bestimmungen der Promotionsordnung sind mit bekannt. Die von mir vorgelegte Dissertation ist von Prof. Dr. Dr. h.c. Dr. h.c. Benjamin List betreut worden.

Benjamin Mitschke — Mülheim an der Ruhr, 1. Juli 2024

Bisher sind folgende Teilpublikationen und Patente veröffentlicht worden:

1. "Asymmetric Friedel–Crafts Reactions of Unactivated Arenes"
   S. Brunen, B. Mitschke, M. Leutzsch, B. List
   J. Am. Chem. Soc. **2023**, *145*, 15708–15713.

2. "Direct Regioselective Dehydrogenation of alpha-Substituted Cyclic Ketones"
   S. A. Schwengers‡, G. G. Gerosa‡, T. Amatov, N. Yasukawa, S. Brunen, M. Leutzsch, B. Mitschke, G. Shevchenko, B. List
   Angew. Chem. Int. Ed. **2023**, *62*, e202307081. ‡: equal contribution.

3. "Toward a Formyl-to-Phenyl Conversion: An Unexpected Photochemical Fulvene Rearrangement"
   M. Lindner, M. W. Alachraf, B. Mitschke, P. Schulze, M. Leutzsch, B. List
   Angew. Chem. Int. Ed. **2023**, *62*, e202303119.

4. "Design of an Organocatalytic (4 + 3) Cycloaddition of 2-Indolylalcohols with Dienolsilanes"
   J. Ouyang, R. Maji, M. Leutzsch, B. Mitschke, B. List
   J. Am. Chem. Soc. **2022**, *144*, 8460–8466.

5. "Direct and Catalytic *C*-Glycosylation of Arenes: Expeditious Synthesis of the Remdesivir Nucleoside"
   C. Obradors[‡], B. Mitschke[‡], M. H. Aukland[‡], M. Leutzsch, O. Grossmann, S. Brunen, S. A. Schwengers, B. List
   Angew. Chem. Int. Ed. **2022**, *61*, e202114619. [‡]: equal contribution.

6. "Harnessing the ambiphilicity of silyl nitronates in a catalytic asymmetric approach to aliphatic β^3-amino acids"
   S. Das[‡], B. Mitschke[‡], C. K. De[‡], I. Harden, G. Bistoni, B. List
   Nat. Catal. **2021**, *4*, 1043–1049. [‡]: equal contribution.

7. "Confinement as a unifying element in selective catalysis"
   B. Mitschke, M. Turberg, B. List
   Chem **2021**, *6*, 2515–2532.

8. "Process for a stereoselective polyene cyclization"
   M. Schelwies, R. Pelzer, B. List, N. Luo, M. Turberg, S. Das, B. Mitschke, C. K. De, S. Brunen, V. N. Wakchaure, D. Danielsson, P. Kaib, A. Blond
   Submitted on November 2, 2023.

9. "Process for the preparation of cyclohomogeranates"
   M. Schelwies, B. Brunner, R. Pelzer, B. List, M. Turberg, B. Mitschke, S. Das, C. K. De
   WO2023247609A1.

10. "Process for the catalytic glycosylation of arenes"
    B. List, C. Obradors, B. Mitschke, M. H. Aukland
    WO 2023/011994.